# DEVELOPMENT AND CHARACTERIZATION OF MECHANICALLY ACTUATED MICROTWEEZERS FOR USE IN A SINGLE-CELL NEURAL INJURY MODEL

A Dissertation
Presented to
The Academic Faculty

by

Brock Wester

In Partial Fulfillment
of the Requirements for the Degree
Doctor of Philosophy in the
School of Biomedical Engineering


Georgia Institute of Technology
May 2011

# DEVELOPMENT AND CHARACTERIZATION OF MECHANICALLY ACTUATED MICROTWEEZERS FOR USE IN A SINGLE-CELL NEURAL INJURY MODEL

Approved by:


Dr. Michelle LaPlaca, Advisor
School of Biomedical Engineering
*Georgia Institute of Technology*

Dr. Mark Allen, Advisor
School of Electrical and Computer Engineering
*Georgia Institute of Technology*

Dr. Ken Gall
School of Material Science Engineering
*Georgia Institute of Technology*

Mr. Franklin Bost
School of Biomedical Engineering
*Georgia Institute of Technology*

Dr. Qi Wang
School of Biomedical Engineering
*Georgia Institute of Technology*



Date Approved: August 01, 2010

## ACKNOWLEDGEMENTS

I wish to thank and acknowledge the following people:

My advisors, Dr. Michelle LaPlaca and Dr. Mark Allen, my thesis committee members, Dr. Ken Gall, Mr. Franklin Bost, and Dr. Qi Wang, and my former advisor Dr. Robert Lee for agreeing to mentor me; I appreciate all of the direction and guidance that has been provided both in the past few years and in recent time, their willingness to entertain/attend my ad-hoc meetings, and for the help and assistance, the thoughtful contributions, and the post-graduate relationship that is forthcoming.

Dr. Yoon-Su Choi, for getting me prepared and comfortable in the microfabrication cleanroom; Yoonsu is a true expert in MEMS and helped to get me running and independent very quickly. I wish to also thank him for originally inventing the mechanically actuated microtweezer, a wonderfully simple and elegant engineering design that has enabled this thesis work.

Dr. Swami Rajaraman, for guidance, advice, and direction with the microfabrication processing and MEMS design; his expertise and considerate help on this project has saved me an immeasurable amount of design time and taught me a great deal, and I am indebted to him. It has been fantastic to work with Swami over the last few years of my thesis; he has been a great mentor, colleague, and friend (and a hell of a lot of fun to travel with). Swami assisted with a variety of aspects of this project, from microfabrication, to laser micromachining, to even proof-reading. He is an all-star.

Mr. J.T. Shoemaker for surgical training and assistance, and limitless knowledge of cell culture; incredible reliability leads to low variability, and he provided both. J.T. is a neuronal harvest, histology, microscopy, and culture wizard. I will miss the random

movie quoting and consistent catching up with both the important and non-important news, he is one of my favorite people in Atlanta.

Dr. Scott Kasprzak and Ms. Angela Lin for support with mechanical testing, and for access to their mechanical testing facilities.

Ms. Michelle Kuykendal and Mr. Gareth Guvanasen for letting me use the calcium imaging station (sorry for the having to break down my staging systems), the initial instruction on the rig and software, the excellent fluorescence processing software, and the occasional generously donated conical tube of ACSF.

Dr. Jevin Scrivens and Dr. Shane Migliore for helping me to learn computer-assisted-design and for the mechanical engineering assistance; four years ago this was a whole new world for me, and as the microtweezer system design progressed it was both increasingly more important as well as fun. Jevin completed a great deal of the CAD design for the preliminary manual mechanical controller and actuator from a machined prototype developed by Scott Bair, who I also thank for his design contributions.

My undergraduate assistants, Mr. Ashish Patil, Mr. Nick Vafai, Mr. Stuart Boyer, and Ms. Savannah Cookson for assistance with mechanical/electrical evaluation and characterization and cell culturing, for helping to keep the lab in working order, and for the occasional sanity check (thanks for the proof-reading!).

To all the gifted and talented researchers that I worked with on projects over the past few years who have helped me develop into the engineer and researcher I am today: neuronal modeling with Dr. Randy Weinstein; molecular motor modeling with Dr. Cassie Mitchell and Dr. Victoria Stahl; histology and cellular analysis with Dr. Kacy Cullen; spinal cord injury and behavioral studies with Dr. Crystal Simon; photo-patterning of a

novel thiol-acrylate material with Dr. Scott Kasprzak; MEMS packaging of microneedle array devices with Dr. Seong-Hyok Kim, Dr. Seung-Joon Paik, Mr. Po-Chun (Kirk) Wang, and Mr. Richard Shafer; redesign and revitalization of the 3D neuronal translational injury device with Mr. J.T. Shoemaker; and the microfabrication of resilient micro-molds to create stamps for cell adhesion patterning with Mr. Dave Dumbauld.

My fellow entrepreneurs at Teneo Microsystems and NanoGrip Technologies: Dr. Jim Ross, Dr. Swami Rajaraman, Mr. Tom O'Brien, Dr. Mark Allen, Dr. Yoonsu Choi, and Dr. Jevin Scrivens. Thank you for the incredible opportunities, exciting experiences and the invaluable business training.

Dr. Maxine McClain for advice with microfabrication and MEMS packaging; Mr. Kaelin Brewster, Mr. J.T. Shoemaker, Mr. Edgar Brown, Mr. Brian Williams, Mr. Jon Hall, and Mr. John Holthaus for helping to keep everything running in the lab; Mr. Gary Spinner and the MiRC cleanroom staff for the "unfair advantage" provided to each of the users; Mr. Essy Behravesh, for the primer in lab view, and the excellent coding examples to getting me going; Mr. Garrett Schemmel, a great friend who originally taught me to use Adobe Illustrator and how to draw vector-based graphics, a very useful skill for creating figures to clarify ideas that I may struggle to explain with the English language; and Mrs. Sally Gerrish, Mrs. Shannon Sullivan, Mrs. Beth Bullock Spencer, Mrs. Purnima Sharma, Mrs. Sandra Wilson, Mrs. Penelope Pollard, and Mrs. Amber Burris for all of the precious logistical, book-keeping, and administrative support.

The members of LaPlaca Lab: Dr. Gustavo Prado, Dr. Kacy Cullen, Dr. Ciara Tate, Dr. Hilary Irons, Dr. Chris Lessing, Dr. Sarah Stabenfeldt, Dr. Crystal Simon, Dr. Maxine McClain, Dr. Varad Vernekar, Mr. J.T. Shoemaker, I will miss the "scientifically

pertinent" cubical discussions, Halloween and themed house parties, outings to Virginia Highlands, and the Friday nights at Atlanta Brewing Company.

The members of the Lee Lab: Dr. Randy Weinstein, Mr. Matt Sown, Mr. Nick Shapiro, Mr. Jamie Lazin, Mr. Chris Church, Dr. Cassie Mitchell, Ms. Sarah Jones, I will miss the Thursday lunch runs to Rusan's all-you-can-eat sushi bar and the mad scramble for the eel pieces. For you guys, I will also try to make sure to hang an American flag over my desk when I get to my next job, which will hopefully draw less criticism then what we got here (at a public institution).

The members of the Allen Lab that I worked with (it's a giant lab): Dr. Yoon-Su Choi, Dr. Swami Rajaraman, Dr. Maxine McClain, Dr. Seong-Hyok Kim, Dr. Seung-Joon Paik, Dr. Florian Herrault, Mr. Richard Shafer, Mr. Po-Chun 'Kirk' Wang, and Mr. Preston Galle, you have been fantastic instructors and liaisons to microfabrication and the GT MiRC and have helped make my transition back into 'real' engineering so much more enjoyable. Thank you for the help in microfabrication, packaging, linear actuator, and manufacturing technologies.

My long-term roommates (and important house affiliates) throughout graduate school in my 'fraternity-house style home': Mr. Christian Lease and Dr. Randy Ankeny, thank you so much for the help working on the house during the most stressful time of my life. Mr. Min Cho, Mr. Christian Lease, Dr. Blaine Zern, Dr. Torrence Welch, and Mr. Vince Fiore, you have all profoundly impacted my life in grad school, and made the tougher times a great deal more tolerable. Blaine and Torrence, I miss you guys more than you know and appreciate the empathy and motivation to help me keep going, and I look forward to seeing you all more once I get some cash in my pocket. Min, you have

been my ‘rock’ in the house, and I will have to find some way to pay you back for everything (including the fantastic cooking).

Dr. Jim Ross, who even as a graduate student prior to defending his thesis, acted as a close mentor and colleague. Jim brought me onto this project 4 years ago, and the two of us saw the microtweezer go from an extremely clever idea all the way to a commercial product. Jim is a true entrepreneur, and with Swami and myself, started a couple companies around this microtweezer technology. However, without Jim’s business and project management savvy, tireless work ethic, and thoughtful negotiation skills, we would never have navigated the complex and challenge-filled path of commercialization and small-company development. Thank you again Jim.

My close friends in Atlanta, DC, and other now spread throughout the country, you have been incredibly supportive, and I greatly appreciate how you have enriched my life and helped to provide me the fortitude to go on.

Dr. Kelly Scheinberg for helping me to get through one of the most arduous years of my life; despite your terribly busy schedule, you have been there to give care, support, and an open ear, and have made everything so much easier.

My family, for always being incredibly supportive of all of my endeavors, even the crazy ones that result in me being a student of the same university for just over 11 years. You’ve always been there without question, and given me everything I could ever need. I love you all, thank you so much.

The flexible electrode work described in Chapter 7 was supported by the NSF (DGE-0333411) and the NIH (NINDS/NIMH/NIBIB NS046851 and NIBIB EB000786).

# TABLE OF CONTENTS

# LIST OF TABLES

# LIST OF FIGURES

# LIST OF SYMBOLS

Units

| | |
|---|---|
| m | Meter |
| cm | Centimeter ($10^{-2}$ m) |
| dm | Decimeter ($10^{-1}$ m) |
| mm | Millimeter ($10^{-3}$ m) |
| µm | Micrometer ($10^{-6}$ m) |
| in | Inches |
| L | Liter |
| mL | Milliliter ($10^{-3}$ L) |
| g | Grams |
| mg | Milligrams ($10^{-3}$ g) |
| ug | Micrograms ($10^{-6}$ g) |
| sec | Seconds |
| Hz | Hertz (1/sec) |
| N | Newton |
| µN | Micronewton ($10^{-6}$ N) |
| Pa | Pascal (N/m) |
| KPa | Kilopascal ($10^{6}$ Pa) |
| MPa | Megapascal ($10^{6}$ Pa) |
| GPa | Gigapascal ($10^{9}$ Pa) |
| bar | Bar ($10^{2}$ KPa) |
| mbar | Millibar ($10^{-3}$ bar) |
| lb | Pounds |

| | |
|---|---|
| mol | Moles |
| M | Molar (mol/L) |
| μM | Micromolar ($10^{-6}$ M) |
| pH | Potential for Hydronium ($H_3O^+$), Measure of Acidity/Basicity |
| A | Amps |
| mA | Milliamps |

Materials

| | |
|---|---|
| Ni | Nickel |
| Cu | Copper |
| Cr | Chrome |
| Ti | Titanium |
| Al | Aluminum |
| Au | Gold |
| Ca | Calcium |
| Na | Sodium |
| K | Potassium |
| Cl | Chlorine |
| Mg | Magnesium |
| Rd | Rodium |

Nomenclature

| | |
|---|---|
| 2D | Two-Dimensional |
| 3D | Three-Dimensional |

Tweezer Geometric Modeling

Tweezer Beam

Constants

| | |
|---|---|
| $C_U$ | Tweezer Beam Upper Arm Length |
| $C_F$ | Tweezer Beam Forearm Length |
| $T_{TIP}$ | Tweezer Beam Width (Y dimension) |
| $T_{BODY}$ | Tweezer Body Width |

Variables

| | |
|---|---|
| $\Theta$ | Tweezer Beam Elbow Angle |
| $\Phi$ | Tweezer Beam Shoulder Angle |
| $B_{UX}$ | Tweezer Beam Upper Arm Length (Horizontal Vector) |
| $A_{UY}$ | Tweezer Beam Upper Arm Length (Vertical Vector) |
| $B_{FX}$ | Tweezer Beam Forearm Length (Horizontal Vector) |
| $A_{FY}$ | Tweezer Beam Forearm Length (Vertical Vector) |
| $\Theta_U$ | Tweezer Beam Elbow Angle (Upper Arm Segment) |
| $\Theta_F$ | Tweezer Beam Elbow Angle (Forearm Segment) |
| W | Tweezer Beam Elbow Separation (from opposite side elbow) |
| $L_M$ | Tweezer Beam Moment (From shoulder to contact point on channel) |
| $L_{MX}$ | Tweezer Beam Moment (Horizontal Vector) |
| $L_{MY}$ | Tweezer Beam Moment (Vertical Vector) |
| A | Tweezer Box Actuation Distance (Vertical Direction) |
| $A_{TRANS}$ | Tweezer Box Actuation Transition from Drive to Overdrive |
| $T_{TIP}$ | Tweezer Tip Separation (from opposite side tip) |

Tweezer Box

Constants

| | |
|---|---|
| N | Tweezer Box Channel Notch Separation (from opposite side notch) |
| Ω | Tweezer Box Channel Overdrive Angle |

Tweezer Tip Force Modeling

| | |
|---|---|
| Q | Force, Applied |
| U | Strain Energy |
| δ | Beam Displacement/Deflection |
| M | Tweezer Beam Moment |
| E | Elastic/Young's Modulus |
| I | Moment of Inertia |
| $L_M$ | Moment Arm Length |

# LIST OF ABBREVIATIONS

Microfabrication Technologies, Materials, and Dimensions

| | |
|---|---|
| AFM | Atomic Force Microscopy |
| ALD | Atomic Layer Deposition |
| CAD | Computer Assisted Design |
| CCD | Charge-Coupled Device |
| DC | Direct Current |
| ICP | Inductively Coupled Plasma |
| ID | Inner Diameter |
| IR | Infrared |
| LIGA | Lithographie-Galvanoformung-Abformung |
| LED | Light-Emitting Diode |
| MEMS | Micro-electro-mechanical-systems |
| OD | Outer Diameter |
| PECVD | Plasma Enhanced Chemical Vapor Deposition |
| PEEK | Polyether-Ether-Ketone |
| PDMS | Poly-Dimethyl-Siloxane |
| PR | Photoresist |
| SEM | Scanning Electron Microscope |
| SAM | Self-Assembled-Monolayer |
| SU-8 | Photo Sensitive Photoresist Epoxy |
| UV | Ultra-violet (light) |

Physiology and Chemistry

| | |
|---|---|
| ACSF | Artificial Cerebral Spinal Fluid |
| AMPA | α-Amino-3-Hydroxy-5-Methyl-4-Isoxazolepropionic Acid |
| APV | 2-Amino-5-Phosphonova-Leric Acid |
| BMI | Bicuculline Methiodide |
| CCI | Controlled Cortical Impact |
| CNQX | 6-Cyano-7-Nitroquinoxaline-2,3-Dione |
| CNS | Central Nervous System |
| DAI | Diffuse Axonal Injury |
| DI | De-Ionized Water |
| DNA | Deoxyribonucleic Acid |
| DNAse | Deoxyribonucleic Acid Digestive Enzyme |
| D-PBS | Dulbecco's Phosphate Buffered Saline |
| ECM | Extra-Cellular Matrix |
| EEG | Electro-Encephalogram |
| EDTA | Ethylenediaminetetraacetic acid |
| EGTA | Ethylene glycol tetraacetic acid |
| FITC | Fluorescein-isothiocyanate |
| GABA | γ-Aminobutric Acid |
| GFAP | Glial Fibrillary Acidic Protein |
| HBSS | Hank's Buffered Salt Solution |
| HBSS-CMF | Hank's Buffered Salt Solution (Calcium and Magnesium Free) |
| IPA | Iso-Propanol Alcohol |
| NBM | Neural Basal Medium |
| NMDA | N-Methyl D-Aspartate |
| NT | Neurotransmitter |

| | |
|---|---|
| PBS | Phosphate Buffered Saline |
| PDL | Poly-D-Lysine Amino Acid |
| SAM | Self Assembled Monolayer |
| SCI | Spinal Cord Injury |
| TBI | Traumatic Brain Injury |
| TCE | Tri-Chloro-Ethylene |
| TTX | Tetrodotoxin |

# SUMMARY

Very few clinical treatments are available to reduce the damage and subsequent dysfunction following traumatic brain injury (TBI). This is partially due to the fact that cellular mechanisms of dysfunction and death are yet to be fully elucidated. To better understand the various mechanical, electrical, and chemical events during neural injury, and to establish cell tolerances to mechanical insult, it is critical to establish injury models that precisely control cell strain, the physical event that initiates the trauma cascade.

To this end, this thesis project focuses on the creation of a novel single-cell injury model of TBI. The implementation of the model requires the development of a novel injury device that allows direct micro-interfacing with neural environments.

This device consists of a high–resolution micro-electro-mechanical-system (MEMS) microtweezer microactuator that is compatible with aqueous environments and can be proximally positioned within neural tissue and neural cultures. This microtweezer is constructed using traditional photolithography and micromachining processes, and is packaged into a custom machined stainless steel luer needle. The packaged device is controllable by a custom developed software-automated controller that incorporates a high precision linear actuator and utilizes a modular luer-based docking interface.

Following mechanical characterization and biocompatibility assessment, the microtweezer system was used to induce mechanical insults with prescribed strain and strain rate onto the somata of primary cortical neurons in 2D culture. Real-time injury-induced intracellular calcium change and post-injury neuronal plasma membrane

permeability were evaluated. Membrane permeability is a significant contributor to secondary injury cascades during TBI. By evaluating cellular response to mechanical input using models like these, strain and strain rate input tolerance criteria can be used to determined thresholds for membrane integrity, cellular injury, and death. These findings provide a new platform for traumatic single-cell injury and can be integrated with results from bulk injury models, where the entire culture or tissue is injured, to gain a better understanding of the collective cell response to injury.

# CHAPTER 1

# INTRODUCTION

## 1.1 - Introduction

### 1.1.1 – Motivation

#### 1.1.1.1 - Traumatic Brain Injury

Traumatic brain injury (TBI) affects 1.4 million people a year in the United States and despite the fact that 96% of people survive a TBI, the health and socioeconomic consequences can be grave, partially due to the fact that very few clinical treatments are available to reduce the damage and subsequent dysfunction following TBI [1] (Figure 1.1). To better understand the various mechanical, electrical, and chemical events during neural injury so that therapies and treatments can be improved, engineers and scientists have developed a number of in vivo and in vitro models. These models endeavor to recreate the environmental conditions during injury so that specific cellular events and mechanisms that result in cell death, cell and network dysfunction, or high level functional deficits, can be elucidated.

Various 2D and 3D cell culture, tissue slice, and live animal models have been developed so that injury scenarios can be recreated and examined. Most current in vivo and in vitro TBI models induce system-wide injury mechanisms. While they emulate conditions seen during injury, these systemic mechanical, chemical and electrical injury paradigms can have limited experimental throughput. Additionally, due to conformational and physiological inconsistencies from one system injury to the next, they can ultimately lead to variability in the localized injury environments. To improve

assessment and understanding of the localized neuronal injury environment, new models are required that allow for controllable and high-throughput examination of cellular response [2].

1.1.1.2 - Membrane Permeability

Central to this proposed research is the hypothesis that membrane permeability may contribute to secondary injury following initial mechanical insult [3-12]. Mechanical input to the neuron at the soma or cellular processes that originates from shear forces or stress loading onto bulk tissue can compromise the integrity of the fluid cellular plasma membrane (Figure 1.2). Localized and wide spread electrical and chemical events can ensue following compromise of cellular membranes and alterations in ionic gradients. These events can then result in a variety of cellular, molecular, mechanical, and chemical outcomes, including increases in neuronal discharge, which, if generally excitatory, can result in further depolarizing pressures [3, 12-48]. Under this scenario, the neuronal response could greatly exacerbate and even propagate an excitotoxic wave of activity across neighboring regions. Recordings in the somatosensory cortex following mechanical insult present preliminary evidence of this effect [49]. Determining the cellular response criteria to injury is important to understanding the secondary injury cascades that are initiated during the acute period following initial insult, as well as its analysis and correlation with mechanical input.

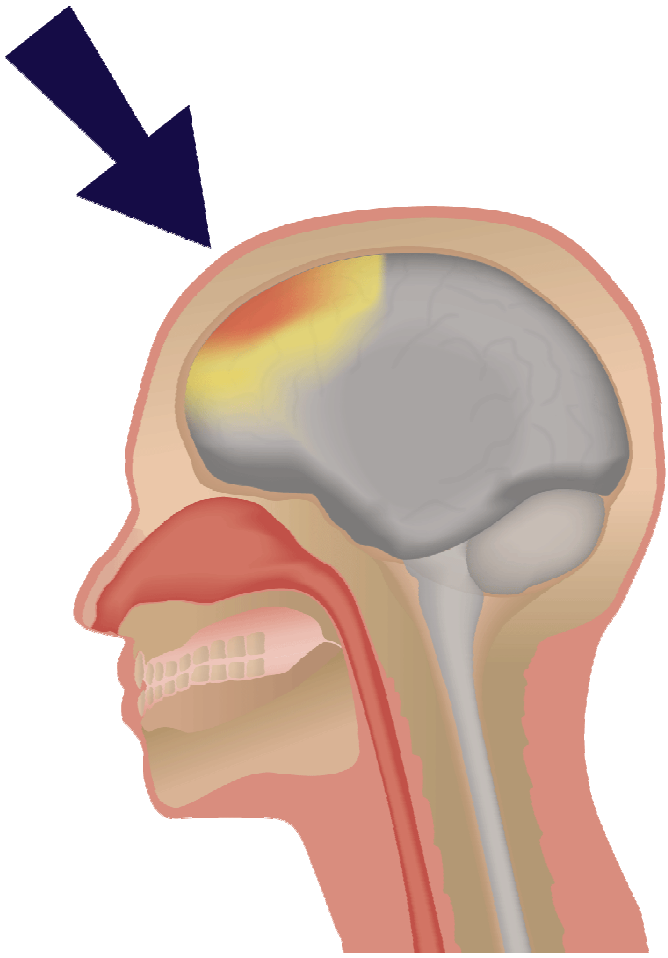

**Figure 1.1**: Cartoon demonstrating the mechanical insult that initiates traumatic brain injury.

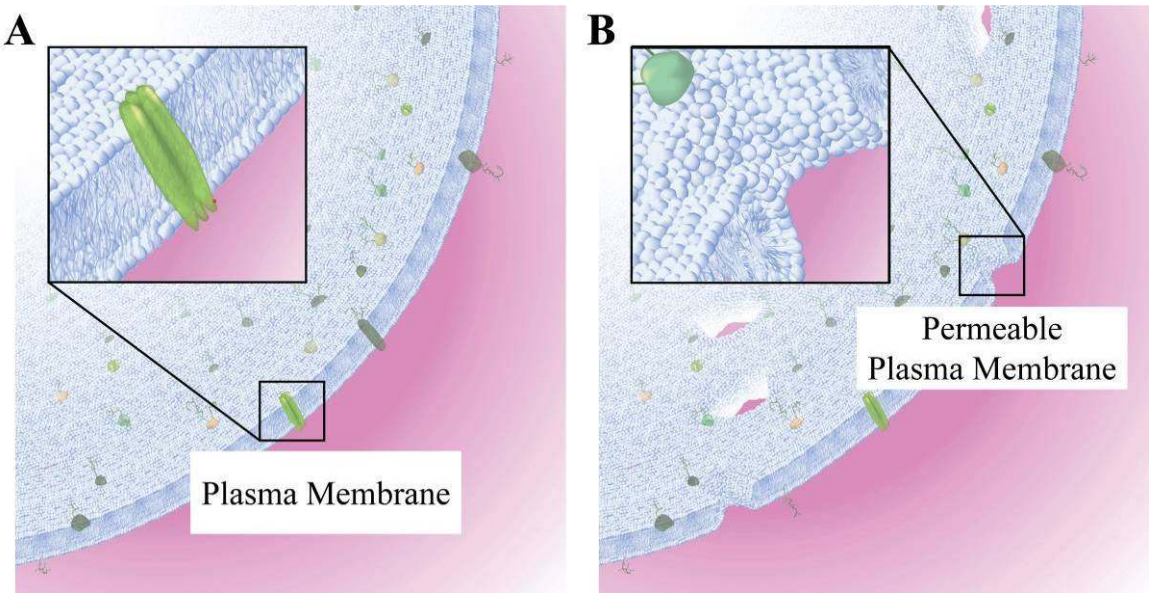


**Figure 1.2**: Cartoon highlighting the opening of holes in the cellular plasma membrane (A) following mechanical insult (B). This permeability of the cell membrane disrupts the cell's ability to maintain ionic gradients.

### 1.1.2 - Research Focus and Methodology

This dissertation focuses on the creation of a novel and clinically relevant single-cell injury model of traumatic brain injury (TBI). The implementation of the model will initially require the development of a novel injury device that will allow specialized micro-interfacing functionality with neural micro environments. This will include the induction of prescribed strain and strain rates onto neural tissue, such as groups of cells, individual cells, and cell processes.

A large portion of this thesis work will focus on the device design, construction, and characterization. This will be accomplished using iterative cycles, with each assessment and characterization leading to substantive design changes (Figure 1.3). The device will consist of a high–resolution micro-electro-mechanical-system (MEMS) microtweezer microactuator tool that can be both introduced into biological and aqueous environments and be proximally positioned to specific targets in neural tissue and neural culture systems to allow delivery of mechanical injury. To ensure device performance and limit disturbance of the local environment, a mechanically-actuated microactuator solution will be considered over more traditionally developed MEMS microactuators that use thermally and electrically sensitive materials. The scope of this development will include the production of microtool fabrication processes, implementation of mechanical tool packaging and proof-of-concept controller technology that enables device verification and characterization, as well as experimental demonstration and use of the tool to address a critical need to better examine acute cellular responses during TBI (Figure 1.4). Aim 1 will focus on the development of viable and repeatable fabrication processes for the MEMS microtweezer, mechanical packaging for the micro device, and

then a high resolution software and manually drivable microtool controller to power and control the device. Traditional photolithography and micromachining processes will be used for fabrication, and this controller and packaging will incorporate high precision linear actuators and utilize the luer-based microtool docking interface. Aim 2 will mechanically characterize the tool, focusing on the substrate structural integrity, performance precision, and determination of long term performance and wear, all to ensure consistent device behavior, which is paramount to limiting variability during experimental use.

Following verification of the device's performance, a high-throughput cell culture and injury system that is compatible with the injury device was developed. This injury system was incorporated into a calcium imaging setup that used a high speed camera mounted to an upright microscope with a light-blocking enclosure. The microtweezer device was micropositioned into the culture using a 3-axis robotic-arm-like stage. In Aim 3, this system was used to induce prescribed strains onto neurons to create traumatic brain injury conditions at the cellular level (Figure 1.5). Simultaneous mechanical induction and visual inspection of calcium sensitive dyes was performed to allow determination of strain thresholds for cell death.

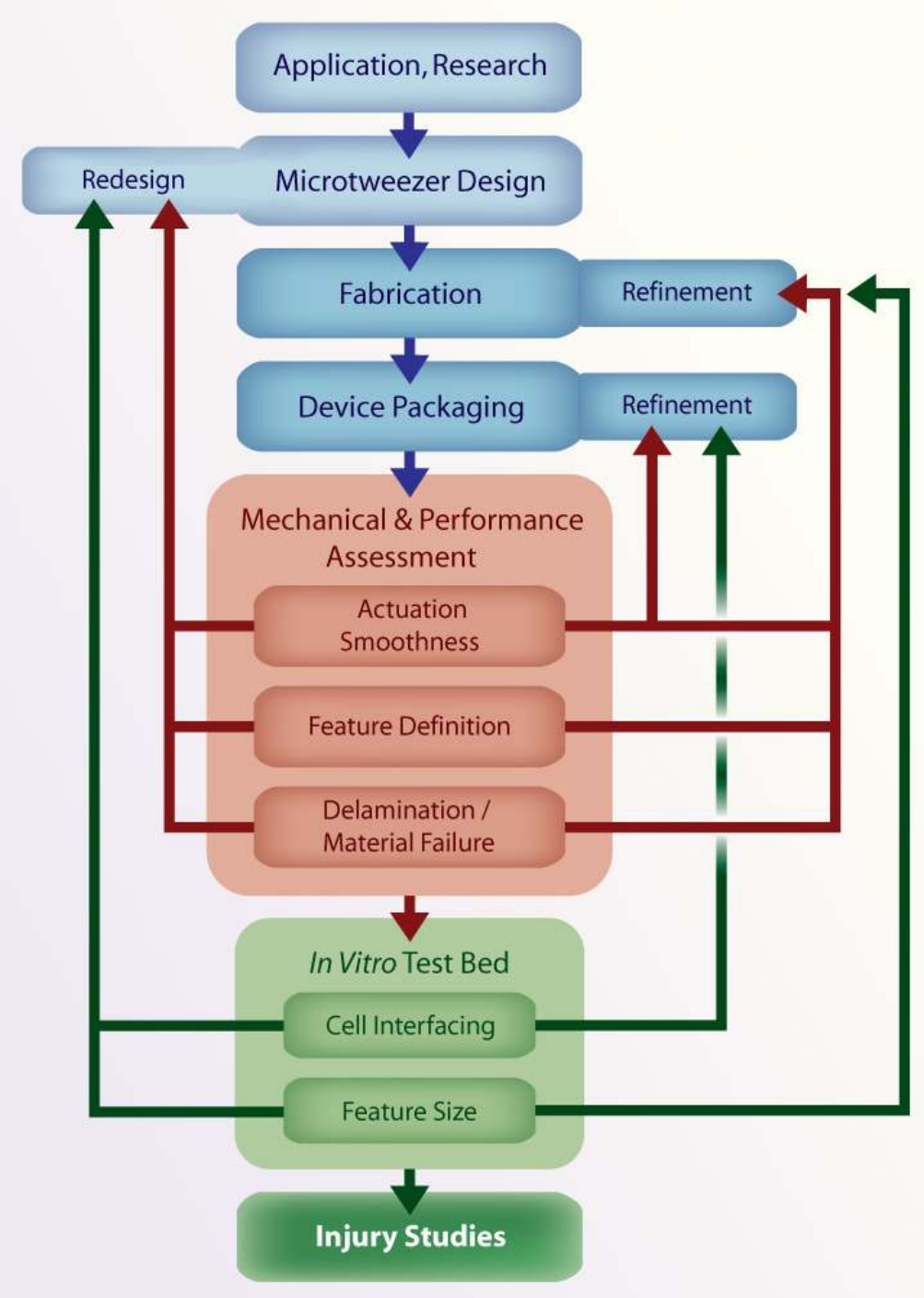


**Figure 1.3**: Flow chart highlighting the iterative design process of design, construction, and then characterization and evaluation, which influences redesign. Successful designs will be used in the in vitro test bed and evaluated for effectiveness, which might result in additional redesign prior to use in the injury studies.

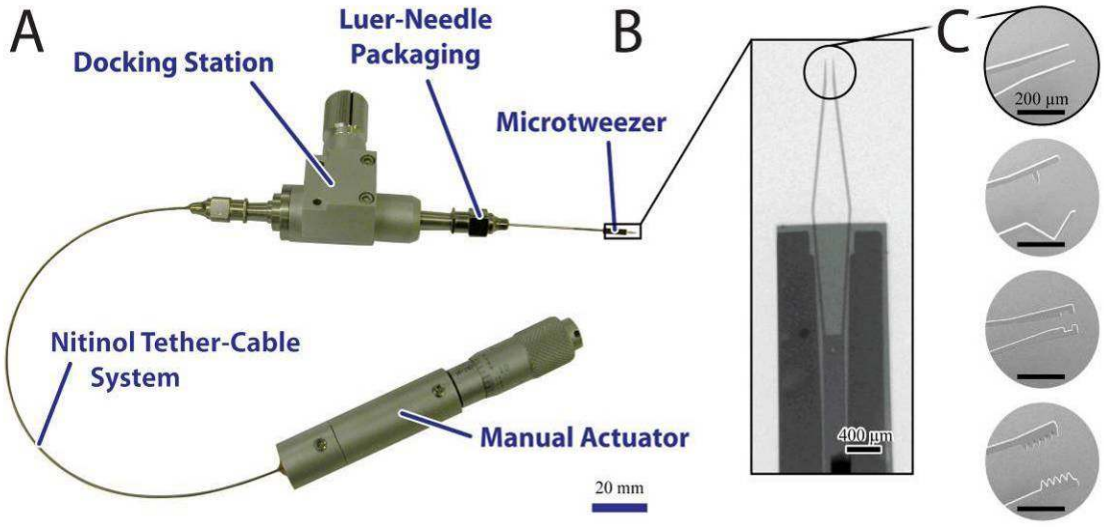


**Figure 1.4**: (A) Photo of the manual microtweezer system. The microtweezer is mechanically packaged with a stainless steel luer needle. The manual mechanical controller consists of a docking station, a manual linear actuator with a micrometer knob, and a nitinol tether-cable system to physically and functionally connect them. (B) X-Ray of assembled microtweezer. (C) SEM images of various tweezer tips.

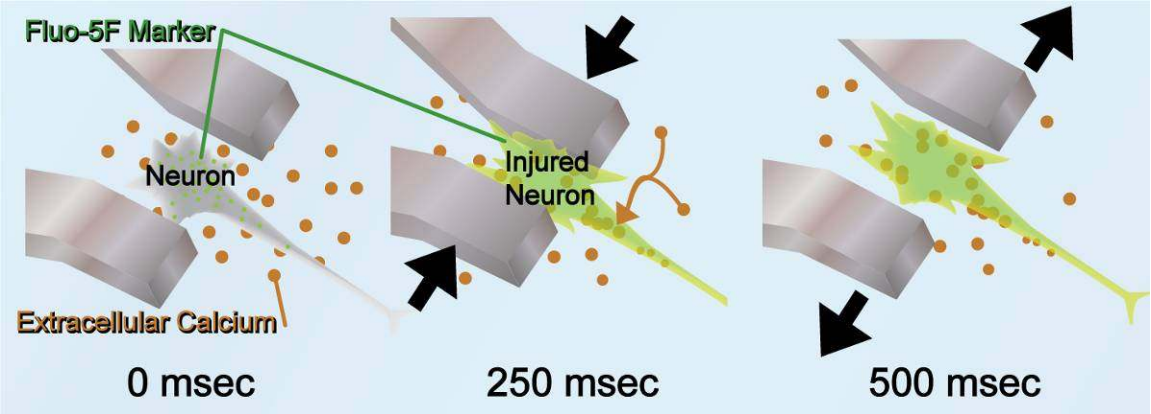


**Figure 1.5**: Cartoon of the use of the microtweezer to induce single-cell injury. The timeline shown is for a sample injury time course (strain rate of 2/s).

The end goal of this research is to develop an injury system that can be used to induce mechanical deformations on the cellular level that relate to those experienced by cells during system-wide mechanical injuries, such as cortical impact. Because the device implementing the injury was viewable under a microscope, viable visual inspection before, during, and immediately following the mechanical insult was possible. In addition to allowing the examination of the injury conditions themselves, real-time cellular response could be recorded.

The individual elements of this system followed iterative cycles of development and characterization to optimize performance for use in the in vitro environment. Several generations of MEMS microtweezers and tool packaging schemes were developed. A manual controller was designed and constructed to allow preliminary mechanical analysis and to facilitate microtweezer packaging assembly. An automated controller was built for endured mechanical testing and for the delivery of repeatable cellular injuries. Multiple microtweezer designs were used in an in vitro environment to induce strain injuries onto neurons. From this preliminary testing, a final design was created and used in the subsequent injury studies.

Future development beyond the scope of this proposal will optimize both the packaging strategy of the microtool and the controller components to allow for sustainable manufacturing. The final device will be a high-resolution, automated micro-instrumentation system that is highly customizable, establishing a micro-instrumentation platform for high throughput examination of cellular response to mechanical input. While this system will initially be validated with a cellular interfacing experiment, the technology developed will provide a platform that allows for new progress in

microsensing, micropositioning, and microinterfacing in semiconductor, MEMS, and life science applications. A system of this capability would enable discovery in cellular and tissue biomechanics, neural physiology and pathophysiology, and general biomedical experimentation. It is believed that this system, once completed, will also have several design and cost advantages over other commercially available piezoelectric, thermal, or optical based actuating microtools. For example, this system can be introduced into aqueous environments and can be used with electrically and thermally sensitive biological materials and constructs without any interference to the experimental condition. In addition, by combining the current microtool and microtweezer technology with integrated microelectrode sensors, real time manipulation and electrical recording and stimulation would be possible. Furthermore, these tools would allow precise micromanipulation of tissue samples, fluorescent markers, and microstructures such as biological and artificial scaffolds, as well as mechanical and electrical characterization of an individual chondrocyte or neuron (for example). Both specific applications, such as inducing prescribed strains and strain rates onto cells to determine mechanical/cell response properties, and general applications like micropositioning identifiable markers for tissue microscopy, will be possible with the same tool system. For these and a variety of other applications, these highly customizable microtools can provide acuity, control, repeatability, and scalability.

## 1.2 - Background

### 1.2.1 - Micro-Electro-Mechanical-Systems

To allow for experimentation and interfacing with biological microenvironments, there have been a number of platform-based (microelectrode array dishes, lab-on-a-chip

devices, platform sensors) and non-platform-based (stand alone insertable-shank electrodes, microgrippers, microtweezers) MEMS devices created [50-52]. Microtweezers were originally developed for use in a variety of semiconductor and MEMS research applications (MEMSPI, Sandia). They expanded on the functionality of micro-scale probe tips by increasing the degrees of movement freedom (Figure 1.6). However, as these tools provide acuity of control and miniaturization, they could also play a major role in biomedical experimentation. Microtweezers and similar microtools offer an attractive option to meet the increasing need to manipulate micro-sized objects such as semiconductor and MEMS components, optical fibers, cells, tissue slices, fluorescent markers, and other biological structures and material constructs.

For devices that actively and mechanically interface with microenvironments, research groups, such as MEMSPI, have historically elected to utilize electrical, thermal, or piezoelectric based actuation mechanisms due to established techniques and microfabrication strategies for these types of mechanisms [53-64]. However the use of these mechanisms have several limitations: (1) material limitations and cost due to required use of silicon and silicon-doping to achieve electrically based actuation; (2) mechanical and electrical characterization can be required for every device due to inherent variations in lithographic processing (i.e. the tuning of a piezo or electro-thermal driving signal for an actuator) [65]; (3) modular construction and functioning of the microdevice and the package can be expensive and unreliable; (4) interference from the microenvironment can alter or inhibit device performance (i.e., aqueous environment, heated systems, etc.); and, (5) most importantly, these electrical and thermal devices can dissipate heat into the local environment, as well as generate unintended yet damaging

electrostatic fields and currents that limit the device's applications, especially when introduced into a biological environment. Due to these concerns in the development of a microtweezer compatible for acute neuronal interfacing, electrical actuation mechanisms were dismissed for the chosen device and a mechanical actuation mechanism was developed instead that mimics macrotweezers or hand-held forceps.

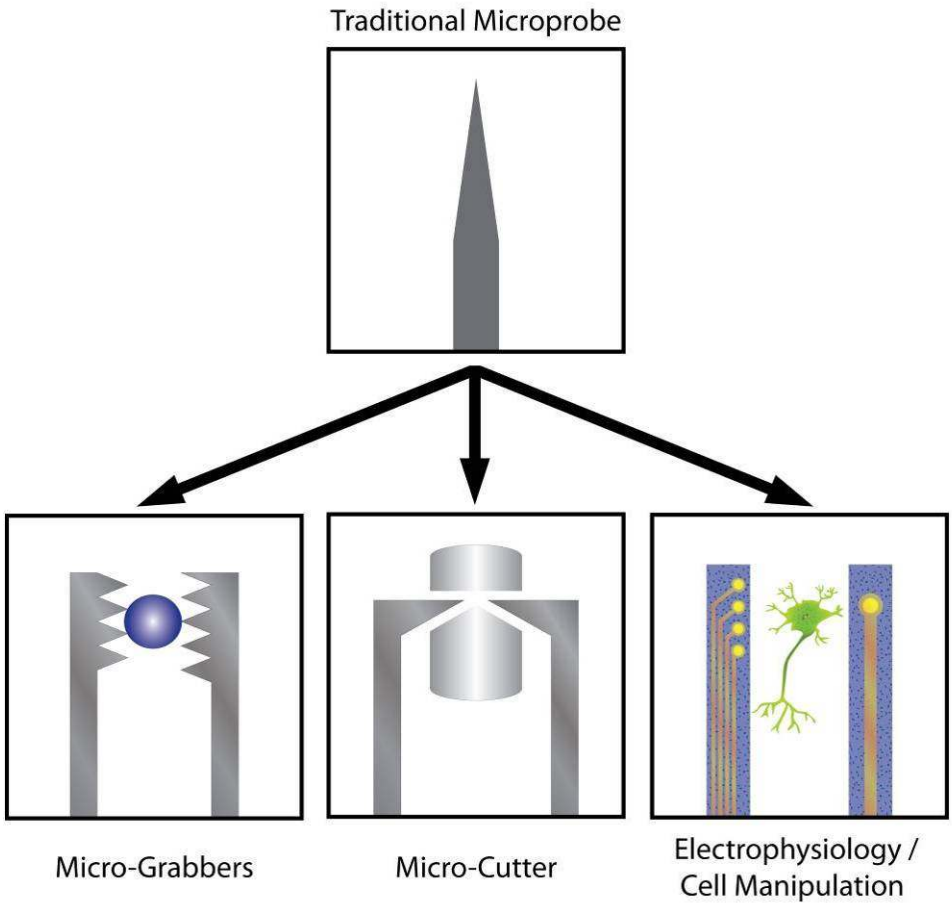


**Figure 1.6**: Micromanipulation systems provide extremely precise control of static probe tips and microneedles; that same precision can be applied to a new class of manipulation tools tips that expand functionality.

### 1.2.2 - Traumatic Brain Injury, Societal Need and Current Models

#### 1.2.2.1 - Societal Need for TBI Research

There is a clinical need for comprehensive studies to examine traumatic brain injury (TBI) and spinal cord injury (SCI). Traumatic brain injury (TBI) affects 1.4 million people a year in the United States, yet less than 4% of these persons die at the time of the event [1]. Despite the fact that most people survive a TBI, the health and socioeconomic consequences can be grave, as very few clinical treatments are available to reduce damage and reverse dysfunction in cognition and sensory and motor function [40, 66-71]. Identifying the critical events that occur acutely following a traumatic insult and their relationship to final outcome may lead to the development of improved clinical therapies [2, 72-74]. There have been a number of studies that examine electrical, chemical, and structural responses following injury [17, 23, 24, 26, 27, 34, 40, 42, 43, 48, 74-84]. The mechanical impact of TBI has been correlated to disruption of intra- and extracellular ionic homeostasis of neurons, neurotransmitter release, and concomitant massive depolarization [3-5, 9-12, 15, 85-95]. Neuronal damage has also been found to be initiated by the excitotoxic release of amino acids [96]. Additionally, glucose levels and oxidative metabolism are depressed from ionic balance reestablishment and ischemia [97].

However, due mainly to experimental and technological limitations, localized biomechanical, chemical, and electrophysiological alterations of brain tissue during and immediately after TBI, remain largely uncharacterized, especially the role of neuronal plasma membrane permeability during mechanical disturbances.

1.2.2.2 - Current TBI Models

Numerous models have been used to assess animal motor, sensory and cognitive function and deficits following injury, changes in electrophysiology and network behavior, and a wide variety of cellular responses [10, 11, 20, 43, 86, 90, 91, 93, 94, 98-103]. Many of the *in vivo* animal models employ compressive loading onto tissue with fluid percussion [23, 77, 104], weight-drop and controlled cortical impact [10, 16, 49, 67, 82, 83, 100], and blast or explosion-induced shock-wave [105, 106] models. Amongst the *in vitro* injury models, a variety of tensile [3, 87, 107-110], and shearing mechanisms are used to induce mechanical loading onto the tissue and cell culture samples. What is common in all of these models is the induction of a system-wide injury mechanism, where a single mechanical input is applied to entire sections of brain, tissue, or cell cultures. The *in vivo* and *in vitro* mechanical injury devices [11, 20, 43, 86, 90, 91, 93, 94, 99-103] that are used in these studies are designed to induce these blanket injuries.

While these blanket mechanical inputs effectively emulate the mechanical loading onto brain tissue during TBI, many factors can affect the variability in localized (cellular) injury environments: (1) conformational, morphological, and physiological inconsistencies in the tissue and cell culture microenvironments; (2) the variability in delivery of mechanical input; and, (3) the adhesion or alignment of the sample to the mechanical input. In the realm of in vitro injury models, for example, mechanical input and the adhesion and alignment of the sample to the mechanical input can be disrupted by inconsistent physical attachment of the cells to a stretchable membrane for tensile loading, or poor/uneven contact-transfer of translational or rotational movement for bulk-load shearing [86].

1.2.2.3 - Single Cell Injury TBI Models

While these models are excellent for examining systemic cellular response, overall viability, and environmental changes, the described variability can limit the examination of mechanical input and response output relationships at the cellular and sub-cellular level, especially in the acute time stages following mechanical input.

A variety of single-cell mechanical input experiments have been conducted. Some preliminary single-cell mechanical input models consisted of poking either ciliated epithelial cells or astrocytes with glass pipettes [111-114]. While these models examined real-time changes in intracellular calcium concentrations, the control of mechanical input was poorly understood (no deflection sizes, strain levels, or forces are provided), and cellular response output could not be easily correlated to input due to: (1) the variable orientation of glass pipette interface angle with cells; (2) the limited surface area of interface between the pipette tip and tissue to induce physiologic shearing and bulk loading effects; and, (3) limited consideration between the size of the cells (ciliated epithelium and astrocyte cell body sizes vary considerably) and their relation to mechanical input. Single-cell injuries that consisted of cell process (axon, dendrite) transection with a laser beam were possible, but control of injury was limited, and unintended cell damage could occur [115-117]. Lastly, software simulations were developed to predict single cell injury mechanics from systemic injury models [118], but ultimately new methods are required that allow for controllable and high-throughput examination of actual cellular response [2].

Some newer technologies that do control induction of prescribed mechanical forces onto cells have been preliminarily developed, which allows for some single-cell

interfacing [57, 63, 88, 93, 119]. However, these devices require either extensive characterization prior to use, can disturb the environment due to their actuation mechanisms (described previously), or lack the ability to measure or visually verify the extent of injury.

To determine the mechanical input criteria needed for the proposed single-cell injury studies, previously presented *in vivo* and *in vitro* models, their levels and types of mechanical input, and the composition of their tissue/culture samples injured were considered. Maximal strain loading of 0.50 and strain rates less than 10 $s^{-1}$ were shown in relatable models to induce membrane permeability [88, 89, 99, 107, 120] (discussed in Section 5.4.1.1). By comparing the cellular response to these levels of mechanical insult, an input-output relationship can possibly be elucidated, which is important to understanding the thresholds for injury.

### 1.2.3 - General Market and Clinical Need

In addition to specific research and clinical needs outlined, this developed microtool will also have much broader application in biomedical engineering research and development. In fact, the biomedical market has consistently shown a demand for innovative tools that support both research and clinical procedures. While device development is focused for the research market, the technology is also well suited to serve some clinical needs.

On the research side, cells and biological constructs are currently positioned with relatively crude blunt and dropper type instruments or with expensive and relatively inflexible optical positioning equipment. This microtool can be used in a variety of cellular research applications to precisely pick and place cells and tissue slices,

manipulate fluorescent markers for use in microscopy, and interface with tissues allowing mechanical and material characterization. In addition to TBI, there are a number of research areas where findings from systemic models could be enhanced with examination of cellular responses, such as muscle tissue damage [121-123], and orthopedic related traumas [124, 125]. For example, it would allow researchers to isolate material and tissue samples for elastic and mechanical characterization, induce prescribed strains into samples via actuation or to examine the cellular response to injury in a precise and highly controlled manner. Access to microtools tailored to biomedical applications will allow a variety of experimental preparations previously not possible. This microtool technology could be disseminated to multiple laboratories to allow for interdisciplinary and collaborative research projects.

There are emerging clinical applications for which this tool would be appropriate, such as minimally invasive manipulation and dissection procedures. These procedures would include including some orthoscopic surgical operations, as well as in vitro fertilization related cellular interfacing. Such surgical and interfacing procedures require acuity, control, repeatability, and miniaturization, which this platform technology could provide.

## 1.3 - Research Aims

### 1.3.1 - Aim 1 - Develop MEMS Microtweezer System

#### 1.3.1.1 - Objective

Develop a MEMS based mechanically actuated microtweezer and associated packaging, controller, and stage system for direction and control.

1.3.1.2 - Approach

Traditional photolithography and micromachining processing will be used to manufacture the MEMS device, and luer-based mechanical packaging will be employed to allow connection of the microdevice to a linear-actuator based mechanical controller. This system will be composed of the following: 1) a microtweezer that opens and closes based on the linear position of a sleeve; 2) a packaging system that mechanically connects the tweezer and sleeve to a spring loaded button, and allows handling and docking of the tool; 3) a housed software and manually controllable linear actuator that drives the button allowing automated and repeatable microtool movement and functionality; 4) a docking interface on the controller housing that allows for modular plug-n-play changing of different microtools; and finally, 5) a mountable interface on the controller housing that can allow the system to be augmented to 3rd party positioning stages and micromanipulators.

1.3.1.3 - Outcome

A high-resolution, automated micro-instrumentation system that is highly customizable was designed and manufactured. The work presented shows the development of a versatile microtool system. Several generations of manually controlled prototype systems were developed to facilitate preliminary mechanical analysis, and an automated system was developed to allow for endured mechanical testing and for consistency in biological experiments.

This mechanically actuated microtweezer platform improves upon commercially available and published microtweezer designs that were potentially expensive to manufacture, difficult to customize, involved complex actuation mechanisms, and had

limited material sets. These developed microtweezers were shown to have robust, repeatable actuation under a variety of fast and slow operational schemes, even while driven with a hand-turned micrometer knob.

The microtweezer system was composed of four main components: 1) a packaged microtool; 2) a docking station; 3) a mechanical linear actuator; and, 4) a stage (Figure. 1.4). The microtool is a microfabricated MEMS microtweezer structure that was packed onto a luer needle. Inside the housing of the luer needle was a spring loaded button that was functionally and physically connected to the microfabricated MEMS structure. This luer needle based packaging allowed for mounting onto the docking station, which had a luer fitting. The docking station provided rotational functionality of the microtool about the luer needle axis, as well as mounting of the system onto a stage using a mounting bracket. The linear actuator powered a rod through the mechanical controller to drive the spring loaded button of the microtool package, which actuated the microtweezer. The various stages utilized in this work allowed for positional movement of the microtool in multiple axes, and in multiple experimental and research environments. In general, because of the modularity of the system, the use of a robotic arm, micromanipulator, or micropositioner stage was possible.

### 1.3.2 - Aim 2 - Mechanical Modeling and Characterization

#### 1.3.2.1 - Objective

Mechanically assess the tool performance, forces and displacements induced by the tweezers and consistency of movement, and lifetime of each tweezer.

#### 1.3.2.2 - Approach

Mechanical characterization will rely on visual inspection and real-time force measurement of the microtweezer tips during use. A NanoUTM system will be used to acquire force data. This information will be used to determine the force output under different actuation schemes, and the wear cycle of each tweezer design. Based on mechanical modeling and geometric design of each tweezer design, force measurement can be used to assess displacement.

1.3.2.3 - Outcome

Mechanical modeling and characterization drove the refinement of the microtweezer geometries and packaging and controller design to ensure repeatable and consistent performance. Preliminarily, geometric and force loading models were created to predict the mechanical performance of tweezer models designed for cell interfacing. The model results and the eventual comparison between these theoretical predictions and the mechanical characterization facilitated substantive design modifications.

Mechanical characterization of the various microtweezer designs was performed prior to use in the cellular studies outlined in Aim 3. This ensured that the microtweezer actuation was capable of delivering established and consistent strain injuries onto the somata (cell bodies) of neurons. Force data was collected from a variety of actuation regimens to examine this consistency in actuation and controllability of tweezer tip velocity and acceleration.

### 1.3.3 - Aim 3 - Biocompatibility and Single Cell Injury Model

1.3.3.1 - Objective

The microtool system will be employed in a single-cell injury model of traumatic brain injury (TBI) to assess cellular injury response in the acute time stages following mechanical insult.

1.3.3.2 - Approach

Following biocompatibility studies, the microtool will induce prescribed strain injuries onto single cortical neurons. In order to assess cellular injury, which in this model is indicated by neuronal membrane permeability following insult, fluorescence changes in intracellular calcium sensitive dyes will be examined following mechanical insult.

1.3.3.3 - Outcome

Biocompatibility studies showed that exposure to the MEMS device for extended periods of time (24 hours, nearly 25 times that of a typical experiment) did not result in any increase in cellular death.

Enhancements in the staging and imaging system were performed to increase the positioning and resolution capabilities for the microtweezer. Preliminary biological studies that examined acute cellular response following mechanical insult were conducted. Measureable differences in occurrence of cell death were observed across experimental groups with varying mechanical insult/injury severity. Changes in fluorescent intensity were also recorded and analyzed and compared against experimental groups.

## 1.4 - Dissertation Organization

This dissertation is composed of six main chapters. This section is the end of Chapter 1, which provided background and motivation for the thesis work. Chapters 2-5 cover the development of the microtweezer system, the mechanical modeling and characterization, and the biological methods and studies. Additional background, and discussion of the design process, results, and analyses is provided in each of the chapters. Chapter 6 provides conclusions, final thoughts, and future directions for the microtweezer system, its performance, and the results of the biological studies.

The design, development, and construction of the various components of the microtweezer system were conducted in parallel. Modularity was incorporated into the system to prevent unnecessary re-design following a change in one of the components. However, substantive design changes in one component would motivate changes in another, and numerous design iterations were developed. For example, a change in the microtweezer package might affect a dimensional constraint or feature of the mechanical controller, and vice versa. Mechanical modeling and characterization also impacted the design process. This development, testing, and refinement took place prior to the majority of the biological studies.

To simplify the description of this iterative and parallel process, the detailing of the development of each component, and then mechanical testing is provided separately. Chapter 2 details the design, fabrication, and assembly of the MEMS microtweezer component of the injury system. Chapter 3 details the design and construction of the microtweezer package, and the design and development of the manual and automated controller systems. Chapter 4 describes the mechanical models used to design the tweezer geometries, and provides the results of mechanical characterization. Chapter 5

explains the cell culture model used, and provides results for the biocompatibility and injury studies.

Following the conclusions and future directions chapter (Chapter 6), a supplemental chapter is included that describes another substantive research project that was worked on during this thesis. While this project did not overlap with the thesis work provided, it included considerable micro-device development, which contributed to the decision making process during the microtweezer system development. The supplemental chapter describes the author's original thesis project, which covered the design, construction, and characterization of a flexible electrode for eventual use in recording sensory information in brain tissue during traumatic brain injury.

Following this supplemental chapter are appendices that provide details for: (1) the fabrication processes; (2) the dimensions and materials for the construction of the packaging, controller, and actuator; (3) sections of software code from the custom-developed mechanical modeling software; and, (4) detailed biological protocols used in the injury testing.

# CHAPTER 2

# MICRO-ELECTRO-MECHANICAL-SYSTEM (MEMS) MICROTWEEZER DEVELOPEMENT

## 2.1 - Introduction

This chapter covers the development of the MEMS microtweezer, which is comprised of a *microtweezer with body, beams, and tips*, and a sleeve or *box*. A brief description of these microtweezer components and their general design is provided first, followed by a discussion of the device materials and biocompatibility, and finally, the device construction. A thorough description of the construction is provided, which covers the microfabrication processing, electroplating, and device assembly. Because of the multiple components involved, modularity was integrated into the design to allow parallel processing and development. Despite this parallel development, the iterative development process for the *microtweezer* is provided first, followed by the iterative development process for the *box*.

## 2.2 - Design

The MEMS microtweezer is composed of two main components: (1) a tool body that contains the tool beams and tips; and, (2) a sleeve, or box that houses the tool body in an inner constrictive channel that physically engages the tool beams to close the tips. Thus, these microtweezers use externally applied linear mechanical motion to achieve high-resolution tip control as the tool tips are opened and closed due to their position within the moving box (Figure 2.1). As the box moves forward, it also provides

additional self alignment of the tips, which is achieved by exerting equal forces from each side of the channel, and by the channel constricting vertical movement of the tweezer beams. The box channel contains multiple segments of varying inner geometries, a regular drive section, and an over-drive section, which provides additional actuation range to allow tool tips with larger separations between them to close completely. The 2D patterned inner-channel geometries are relatively unconstrained, allowing a range of closing schemes to be employed for instrument customization, such as fast closing of bulk microtweezer tip separation, and then slow closing of the remaining tip separation prior to tip contact. Geometric tuning of the beams and channel can also cause, for example, a box movement of 3 μm to translate into 1 μm of tip closure, providing a mechanical advantage, or 3:1 actuation resolution ratio. This enhancement in resolution naturally lends itself to achieving high resolution in the submicron-scale. This tuning can also be used to ensure a more linear relationship between box movement input, and tip closure output.

The tip size of the microtweezer was selected based on the size of primary cortical neurons and expected spacing of neurons in a culture. The injury model demands a tool tip with structural integrity to sufficiently deform the neuron without significant beam deflection from the deformation. The tool tip, however, also needs to be narrow enough allow maneuvering of the tool around a neuron while minimally disturbing neighboring cells or cell processes (neuronal axons and dendrites). The selection of the beam geometries, which dictate the opening and closing resolution of the microtweezer, is described in detail in Chapter 4. The geometries of the inner channel of the box, which also contribute to the tweezer actuation resolution, are discussed in Chapter 4 as well.

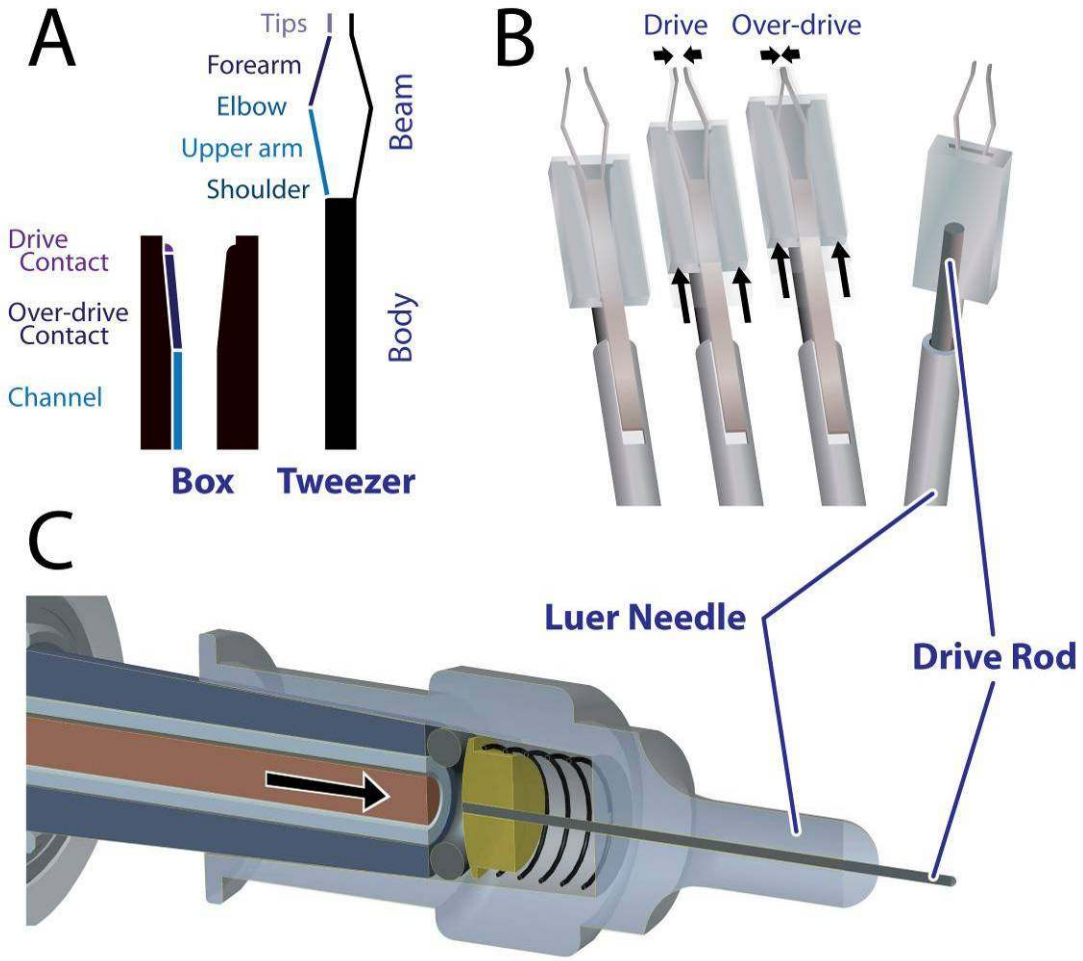


**Figure 2.1**: (A) Schematic of MEMS box and tweezer showing key features, (B) box and tool tips actuation with arrow size demonstrating a 3:1 actuation ratio (linear box movement to tip closing), and (C) mechanical luer-needle packaging of microtweezer with needle and drive rod. The drive shaft (red) meets a rounded interface on the outside of the button resulting in a point contact, which limits torsional loading on the drive rod during axial rotation of the microtweezer.

## 2.3 - Materials and Biocompatibility

The selection of materials is important not only for the mechanical and material properties, such as tensile strength, elastic modulus, and surface attraction, but also for biological compatibility. Microtweezer tips and boxes have been fabricated utilizing a variety of approaches that use single and multiple layers of electroplated nickel, and layers of fusion bonded silicon. Originally fabricated simultaneously, the tweezer and box are now separately constructed using planar photolithography and surface micromachining processes. Nickel was selected as the base material used for the microtweezers, although successful tweezer designs were constructed using SU-8 (which lacks the mechanical properties for this application) [126]. The primary characteristics that made nickel attractive include affordability, mechanical strength (Young's Modulus 200 GPa), durability against fracture, established manufacturing techniques (deposition and electroplating), and limited chemical interactivity [127, 128]. Despite the micro-scale dimensions of the microtweezer beams and tips, the elastic modulus of nickel suggested that forces acting on the tweezer from cell straining will be minimal compared to those from actuation. The current nickel tweezer also provides a suitable base substrate on which to pattern additional features, such as microelectrodes.

### 2.3.1 - Nickel Toxicity

Due to possible galvanic reactions that can take place when nickel is presented into a biological environment with charged ions, the dissociation of nickel from the microtweezer is possible. Provided a sufficient time for the entrance of nickel ions into the cellular media, toxicity from long term exposure could occur.

Nickel has been linked to carcinogenicity, as it can promote mutations and cause damage in genetic material [129]. If high enough ($EC_{50}$=0.29 mM), the concentration of nickel can alter the ability of the cell to proliferate [130]. Given it's propensity to oxidize and create reactive chemical species, the presence of nickel in the cellular medium can also cause damage to other cellular components [131-134]. Additionally, localized millimolar concentrations of nickel can induce ionic currents in the cellular membrane, which can affect neuronal electrophysiology [135]. To address these concerns, a discussion of the time course of exposure and the possible localized concentration is provided below.

### 2.3.2 - Microtweezer and Experimental Biocompatibility

For the experimental protocols conducted in this dissertation, all experiments lasted no longer than an hour, and only the nickel tweezer beams and silicon box and tips are immersed in the cellular medium. Additionally, the used cells are not returned to culture and are disposed. Galvanic reactions and possible dissociation of nickel ions in this time course will minimally affect the biological environment around the cells.

Additionally, the minimal total volume of the tweezers beams is relatively very small compared to the cell medium volume, which for these cell culture well plates, is 1-2 mL per well. Even if both of the upper-arm components of the tweezer beams completely dissolved into the medium, which given the chemical and biomolecular composition of the medium, would not happen in the 1 hour time course of the experiments, this would only raise the total nickel concentration to 0.668 μM (Table 2.1). This calculated value was significantly lower than the values reported to affect cellular proliferation or activate of ionic currents in the cell membrane.

To ensure that the medium concentrations of nickel around the cells were not elevating to a toxic level, a conservative biocompatibility study was conducted. In this study, a portion of the microtweezer body larger than that normally presented into the medium during experiments was immersed into the cell culture medium for 24 hours. This time period was significantly longer than a typical injury study (discussed in Chapter 5). Cell viability was assessed after this 24 hour period, and results showed that no additional death occurred from nickel exposure.

### 2.3.3 - Microtweezer Surface Treatments

While nickel was selected in this design for mechanical, material, and fabrication advantages, the specific experimental application can require surface treatments or coatings so that nickel-related toxicity is decreased. A variety of material coverings can be deposited, sprayed, electroplated, and dip-coated to reduce or eliminate any exposure of nickel to the environment. Some material coverings provide advantages such as a non-polarizing surface (electroplated or deposited gold), reduced surface energy (sprayed or dip-coated Teflon, biomaterial, and protein coatings), and biocompatibility (parylene and protein coatings).

For longer term experiments not carried out in this dissertation, parylene coatings could be an effective surface treatment. Parylene has been successfully deposited on to microtweezer tips as a non-conductive layer, and resulted in minimal or negligible change in mechanical function of the microtweezer [136]. The coatings were also pervasive enough to ensure electrical isolation after several medium immersions.

**Table 2.1**: Modeled nickel concentration of the cellular medium if both of the nickel tweezer beams completely dissolved. The starred length (*) is the length of the tweezer beam counting the upper arm and tip.

# Nickel Toxicity Model

| | | |
|---|---|---|
| Nickel Material Properties: | | |
| Density | 8.908 | g/cm$^3$ |
| Molecular Weight | 58.69 | g/mol |
| Tweezer Beam Properties: | | |
| Length* | 0.22 | cm |
| Width | 0.004 | cm |
| Height | 0.0025 | cm |
| Volume | 2.20 E-06 | cm$^3$ |
| Mass | 1.96 E-05 | g |
| Moles | 3.34 E-07 | Mol |
| Culture Well Properties | | |
| Medium Volume | 1 | mL |
| **Nickel Concentration (both beams dissolved)** | **0.6678** | **uM** |

## 2.4 - Construction

Traditional photolithography and micromachining processes were used to fabricate the MEMS microtweezer. This fabrication protocol for the microtweezer components utilizes a modified LIGA (Lithographie-Galvanoformung-Abformung process, or translated, Lithography-Electroplating-Molding) process [137], where a photoresist (PR) mold was placed on top of a conductive electroplating seed layer, and a metal was electroplated inside of this mold. The deposited materials would take the shape of the mold. A silicon etching and bonding process was developed to replace the photoresist mold process for the final fabrication design used to construct the box component of the microtweezer. Following microfabrication of the two individual components, they were assembled together using forceps under a stereoscope, and eventually incorporated into the luer needle packaging.

As previously stated, the microtweezer and box development was conducted in parallel. For simplicity, however, the iterative development processes for the microtweezer and box are described separately. Additionally, a detailed description of the electroplating process, which was utilized by both components, is provided following the development descriptions for each component. A brief explanation of the process of assembling the microtweezer and box together is provided last.

### 2.4.1 - Microfabrication Process - MEMS Microtweezer Body, Beams, and Tips

The microtweezer body and tips (the same component) were fabricated by electroplating a specified metal into a photolithographically defined photoresist mold on an electroplating seed layer. Nickel was used in this design, but copper, gold or rhodium microtweezers can also be developed using the same process. A variety of substrate,

mold, and seed layer material combinations have been attempted for construction to provide the highest possible resolution of mold feature size, the most flexibility in mold geometries for thick single and multi-layer electroplating steps, convenience and success in microfabrication processing, and chemical resistance to the electroplating bath and lift-off processing steps.

The iterative design process for the microtweezer body and tips is described below. Despite the numerous changes in the construction process during development, three main iterations are provided with detailed descriptions of the successes and failures for each. The preliminary microtweezer fabrication that involved the construction of the microtweezer and box simultaneously is provided first. This is followed by the secondary process where the fabrication of the microtweezer and box is separated and the final process that was used to construct the microtweezer. A brief description of a multi-layer microtweezer fabrication process is provided last.

2.4.1.1 - Preliminary Microtweezer Microfabrication Process

The microtweezer body, tips, and box were originally microfabricated together in the same sample to eliminate the need for post-processing assembly, to limit opportunity for tool damage during assembly, and to ensure body and box alignment. This fabrication protocol followed the modified LIGA process, and consisted of a series of metal electroplating steps in photoresist molds deposited subsequently on top of each other. This original process required five photolithography processing steps (four with alignment), three metal deposition steps, and five electroplating steps (Figure 2.2).

The fabrication process started with the deposition of a blanket metal layer (Ti/Al, 50 nm/0.5 μm) using a DC Metal Sputterer (CVC). In addition to being a conductive

electroplating seed layer, the Ti/Al material was also used as a sacrificial material that can be removed with chemical etchants after the process is completed to lift-off the samples from the substrate. The titanium was deposited first as an adhesion layer between the substrate and the final aluminum metal layer. Both titanium and aluminum can oxidize, allowing them to be removed with a buffered oxide etchant. Despite titanium's predisposition for passivation/oxidizing, which may limit its ability to bond to other materials, the chamber of the DC Sputterer was evacuated to a low pressure with minimal water vapor and oxygen. This environment allowed titanium's chemical adhesion to the substrate surface in the presence of a strong electrical current. Chrome was a possible candidate for an adhesion layer, but it cannot be readily removed with a buffered oxide etch.

This metal deposition was followed by the patterning of the first photoresist electroplating mold. This PR mold was made of AZ-4620 positive resist (Shipley Company, Marlborough, MA), and was spun to a thickness of 20 μm, baked in an oven set at 90$^{o}$ C for 25 minutes, and exposed to 600 mJ of a UV light at a 365 nm wavelength. Following development of the PR mold with the 354 developer for 4 minutes (Shipley Company), the electroplating seed layer was prepared for immersion into the electroplating bath. This required the removal of the superficial aluminum oxide layer exposed by the photoresist mold with a 5 second immersion in a bath of diluted buffered oxide etchant. This etching step was designed to only remove a limited amount of the aluminum surface material so that non-oxidized aluminum is presented for electroplating. After etching and a de-ionized (DI) water rinse, the sample was placed in the electroplating bath to deposit the first layer of nickel in the photoresist mold (bottom of

the box). For electroplating protocols, see Section 2.4.3. A second AZ-4620 mold of 5 μm thickness was photopatterned on top of this bottom layer define the side walls of the box, in which a second nickel layer (sides of box, space between bottom of box and tweezer) was electroplated (Figure 2.2-C). This photoresist layer was baked in an oven set at 90$^{o}$ C for 10 minutes, and received600 mJ of UV exposure. This reduced thickness with comparison to the bottom layer of the box was to prevent too much free vertical movement of the tweezer within the box. Another blanket electroplating seed layer was deposited over the photoresist and nickel from the second electroplating layer to provide complete coverage for a 20 μm thick third mold and electroplating layer (Figure 2.2-D, E, F), which contains the mid-section of the box and the complete body of the microtweezer. Following electroplating of this third layer, a 5 μm fourth mold layer (sides of box, space between tweezer and top of box) was patterned and electroplated (Figure 2.2-G). Again, the reduced thickness was to limit free movement of the tweezer in the vertical direction. A final electroplating seed layer was deposited (Figure 2.2-H), and the final 20 μm PR mold (top of box) was patterned and electroplated. An acetone bath stripped the photoresist molds from all 5 layers (Figure 2.2-I), and a wet acid etch selective for the first electroplating seed layer was used to lift of the completed sample.

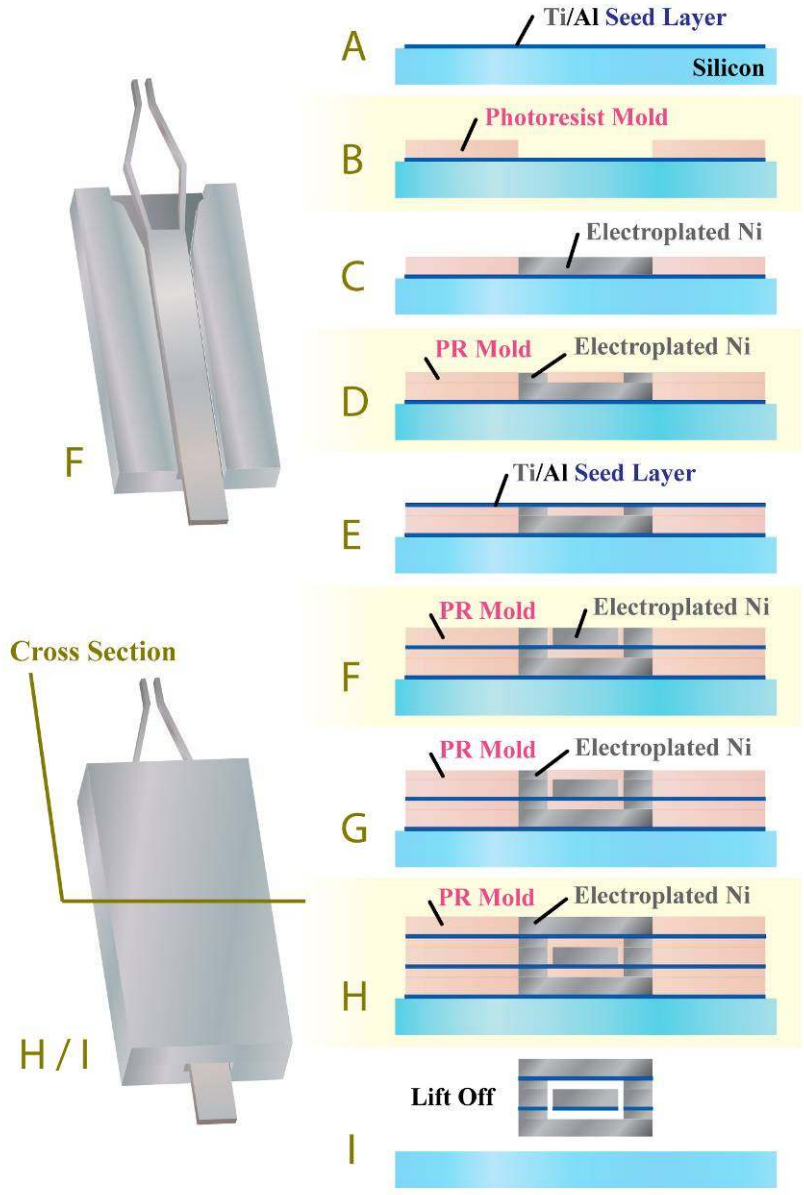


**Figure 2.2**: Fabrication for the microtool box and tweezer in one process flow. (A) Electroplating seed layer was blanket deposited, followed by the patterning of the first photoresist (PR) electroplating mold (B). The first layer of Ni (bottom of the box) was electroplated into the mold (C), and a second Ni layer was electroplated into a thin subsequently patterned mold (D). A second blanket seed layer was deposited to provide complete coverage for the third mold (E), which contained the mid-section of the box and the complete body of the microtweezer (F). After electroplating a third layer, a fourth mold was patterned and electroplated (G). A final seed layer was deposited, and the final mold was patterned and electroplated (H). An acetone bath stripped all PR layers, and a wet acid etch selective for the first electroplating seed layer was used to lift of the completed sample (I).

Many process and recipe refinements were required to the fabrication process flow prior to the completion of a sample. Determination of high fidelity process recipes for each step was not completed considering the degrees of freedom present. Process issues were readily identifiable, however, and the most common source of failure resulted from the choice of the AZ-4620 photoresist. If the entire fabrication took place inside of the UV-light filtered areas of the cleanroom, the chemical integrity of this positive photoresist may have endured the successive baking steps. However, the samples needed to be taken out of the cleanroom to the fume hood of a room without UV-filtered lights where the electroplating station resided. It is likely that exposure to this UV source could have started to break the cross-linking bonds in the positive photoresist material. Following the multiple subsequent photoresist patterning, baking, and electroplating, the photoresist commonly interacted with the electroplating bath, causing it to break down, crack, and delaminate from the substrate.

Additionally, the immersion developer used to develop and remove the un-crosslinked AZ-4620 photoresist interacted with any exposed regions of the aluminum surface of the electroplating seed layer [138]. This interaction with the electroplating seed layer limited the ability to electroplate nickel uniformly across the wafer.

Each of the electroplating seed layers were comprised of a Ti/Al sputtered depositions, which were susceptible to the oxide-etch-based lift-off process. Partial removal of the second and third electroplating seed layers during etching could compromise the lamination of the various electroplated levels. Using a different electroplating seed layer material, or depositing a separate and additional sacrificial layer under the first electroplating seed layer could allow for increased selectivity for the lift-

off process. Originally, soda ash glass was used as the substrate for this process, but the buffered oxide etchant used to remove the Ti/Al electroplating seed layer for lift-off interacted with the silicon oxide present in this glass and diminished the speed of the etching. It also created a glass-slurry that would re-deposit on the sample. For this purpose, silicon wafers were eventually substituted, allowing a cleaner lift-off process to occur. However, the use of pure silicon, which was conductive (soda ash glass, composed mostly of silicon dioxide is insulating), resulted in unpredictable backside electrodeposition of nickel metal during the electroplating process. Without passivation of the silicon surface, this made characterization of the electroplating speed difficult to assess.

The materials for the Ti/Al electroplating seed layer were selected due to their vulnerability to oxide etchants for the lift-off process. While this susceptibility provided a suitable and selective target, the propensity of the exposed aluminum layer to oxidation required that a buffered oxide etch was performed prior to each electroplating step. The etching of this top oxidized layer was timed, but if the sample was left in the etchant bath for too long, the entire aluminum layer could be removed. If this occurred in isolated locations on the wafer, the processing of the sample could continue, but it could significantly reduce yield. If the entire aluminum layer was removed, the top-most layer of photoresist would need to be removed with acetone to allow the deposition of another Ti/Al seed layer. This acetone bath step, however, likely resulted in the removal of all photoresist present in the sample, including any previously patterned electroplating mold layers.

Ultimately the limited yield of units from each sample forced a substantial change in approach to fabricating both the microtweezer body and tips, and the box/sleeve. Bright field photographs of various stages of the microfabrication process can be seen in Figure 2.3.

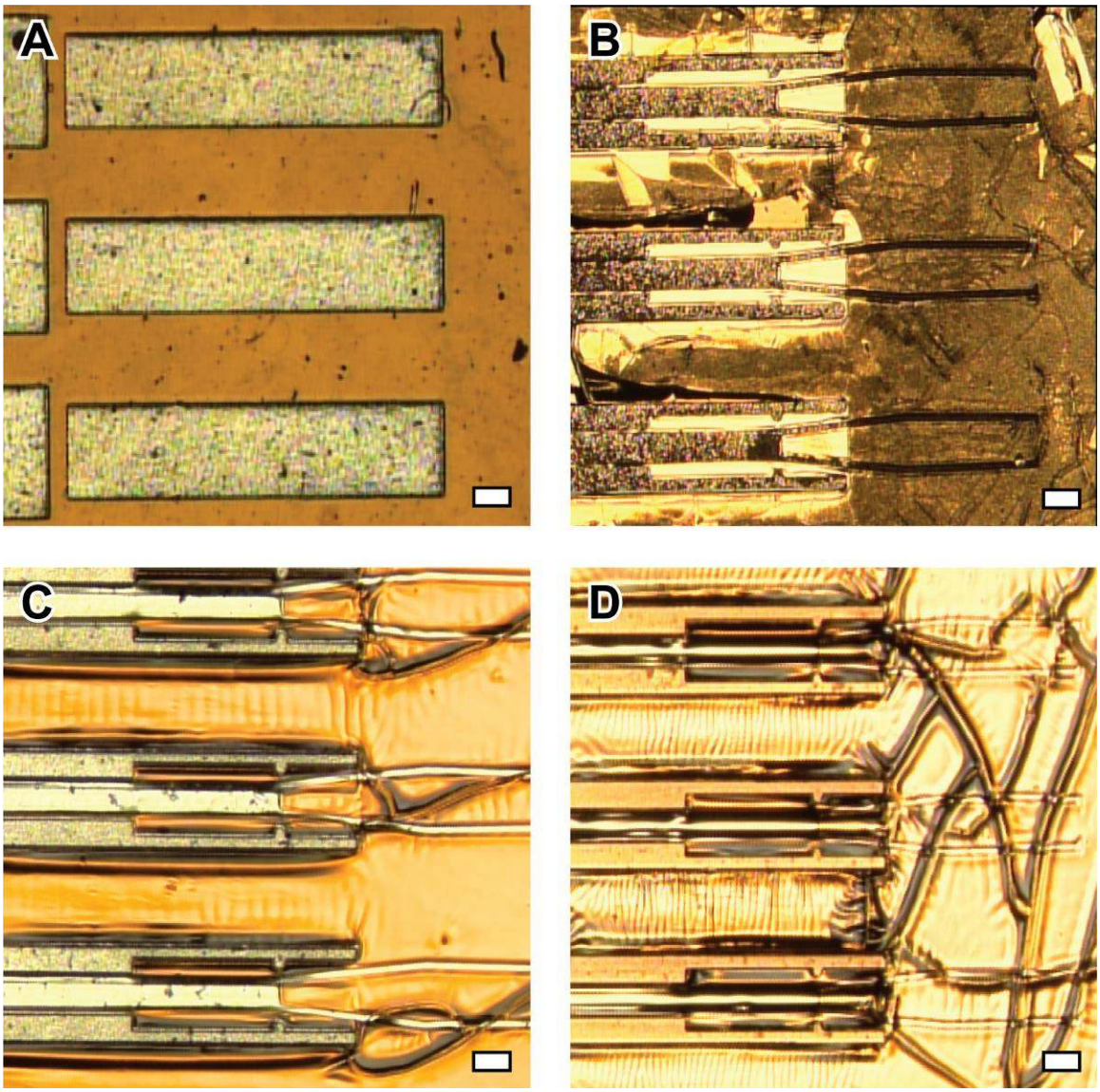


**Figure 2.3**: Bright field photographs of samples from the preliminary microtweezer fabrication process flow. (A) Following the first electroplating stage, (B) after patterning the third electroplating layer, (C) after plating the third layer, and (D) after patterning the fourth electroplating mold layer. All scale bars are 300 μm.

2.4.1.2 - Secondary Microtweezer Microfabrication Process

The next major process flow change resulted in the box and tool body/tips being fabricated separately [139]. While some additional assembly was required, this new process substantially reduced the complexity of the fabrication, replacing a single 13-step process with two shorter more efficacious processes where the parts are produced independently. The total number of alignment steps for fabrication of both the tweezer and box was lowered from four to two. These new processes also reduced the required process integration, allowing for more simplified process refinement, and eventually increased yields for both of the new processes.

In general, fabricating the two components separately allowed for a more versatile selection of materials, tool geometries, and separate post-fabrication processing for tip sharpening, patterning and surface treatments (if required to alleviate mechanical concerns like stiction and wear). This modular design also created a platform that permitted the future integration of various sensors on the tool tips, such as surface microelectrodes, position sensors, and strain gauges.

The photoresist used to define the electroplating molds was switched to the negative resist NR9-8000. This photoresist was selected to pattern the molds to: (1) increase the temporal and chemical stability of the photoresist, as it would resist chemical breakdown from unintended exposure to UV; (2) eliminate chemical reactivity that positive photoresist developers containing hydroxides and borates exhibit with an oxidation-sensitive aluminum electroplating seed layer [138]; (3) reduce chemical reactivity of photoresists while immersed in the electroplating bath; and, (4) allow a large range of thicknesses ranging from 5 μm to 30+ μm to be patterned.

The process started with an initial cleaning of the substrate with *piranha* solution (50:50 ratio of concentrated sulfuric acid and hydrogen peroxide), and a subsequent solvent-based cleaning with tetrachloroethylene (TCE), acetone, isopropanol (IPA), and de-ionized water (DI). The process continued with the spin coating of a thin (3-5 μm) sacrificial negative photoresist (NR7-1500) layer on a silicon wafer (Figure 2.4-A). This sacrificial layer, which was blanket exposed to twice the recommended dosage of UV light at the 365 nm wavelength and baked for 15 minutes in a 90$^{o}$ C oven, remained chemically stable throughout the subsequent microfabrication processes, which included repeated baking steps, photoresist immersion development, and hours in an electroplating bath. This sacrificial layer assisted in lift-off processing as it dissolved in acetone, and electrically isolated the electroplating seed layer from the wafer, preventing metal deposition on the edge and backside of the wafer during electroplating. The Ti/Al electroplating seed layer was then vapor deposited onto the sacrificial photoresist layer (Figure 2.4-A). The subsequent fabrication processes followed the preliminary protocol, and involved the patterning of a photoresist mold in which Ni was electroplated to form the single layer of the tweezer (Figure 2.4-B, C). The NR9-8000 negative resist was spun with a single-coat layer to a thickness of up to 30 μm, baked in an oven set to 90$^{o}$ C for 25 minutes, exposed to 1200 mJ of 365 nm UV light, post-exposure baked in a oven for 90$^{o}$ C for 10 minutes, and then developed in RD6 photoresist developer for 3 minutes. Following electroplating, a gentle acetone bath was used to remove the photoresist mold. For lift-off, the sample was then placed in a fresh acetone bath with sonication to remove the sacrificial photoresist layer and ablate the thin film electroplating seed layer.

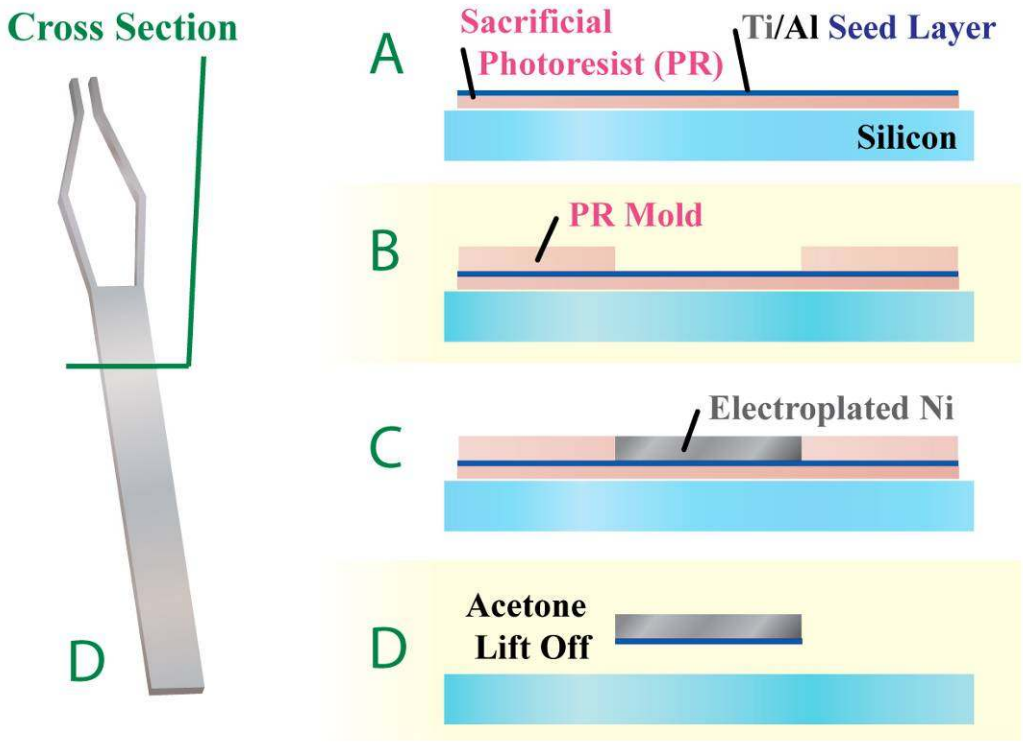


**Figure 2.4**: Fabrication process flow for the single-layer microtweezer body and tips (A-D). Fabrication follows the processes defined in the preliminary fabrication process for both the box and tweezer, however a sacrificial photoresist layer was initially deposited to aid in the final lift-off process.

This separate process for constructing the microtweezer tips and body had a substantially improved yield over the original process, where the microtweezer tips, body, and box were fabricated together. While the sacrificial photoresist layer was effective for providing a specific target for lift-off, for electrically isolating the wafer from the electroplating seed layer, and for resisting chemical breakdown over the fabrication steps used to construct the microtweezer, it was difficult to remove with acetone. This could have resulted from the overall thickness profile available to the wet etchant (the resist was spun to 3-5 μm) and the over-cross-linked structure from the repeated baking steps. Use of this lift-off layer also allowed a variety of electroplating seed layers to be used. In addition to promoting photoresist removal during lift-off, sonicating the acetone solution mechanically broke up the portions of the thin electroplating seed layer that were not attached to the tweezer. While effective in mechanically removing the metal layer, this process resulted in tiny fragments of the metal seed layer remaining attached on the sides of the completed tweezer. This debris could interfere with the mechanical actuation of the tweezer as it would introduce inconsistencies in the surface of the tweezer that contacts the inner channel of the microtweezer box. To alleviate this, the metal seed layer could be etched with the required etchant following the first acetone bath and prior to the second acetone bath with sonication.

The NR9-8000 negative photoresist mold for the electroplating process had improved temporal, thermal, and chemical integrity over the AZ-4620 positive photoresist. The photoresist did not crack as readily following immersion in the electroplating bath, and exposure to unintended UV light did not affect the surface of the

mold. The NR9-8000 photoresist was designed for spinning photoresist thicknesses of 8 μm when spun at speeds of 3000 revolutions per minute, with a ramp of 1000 revolutions per minute per second, and total spin time of 30 seconds. To successfully create photoresist molds over 20 μm in thickness, the spin speed needed to be reduced considerably, which usually affected the uniformity of the photoresist across the wafer, and resulted in exaggerated lips of elevated thickness toward the edge of the wafer. Bubbles present in the photoresist deposited onto the wafer prior to spinning had more significant impacts on the uniformity of the photoresist spin, and special care was required to ensure that prior to spinning, the resist present did not contain any trapped air. Coverage over the entire wafer following a low-speed spin was another issue, which was relieved if additional photoresist was deposited onto the wafer (sometimes roughly 2/3 of the wafer needed to be covered). This resulted in substantial photoresist material waste. Weight-casting the resist was another option, which would prevent this waste in photoresist material, but uniformity would be compromised, and this would impact the evaluation of the electroplated metal thickness, which was paramount to ensuring that the tweezer-thickness and box-channel-height were the proper dimensions. Spins of 800 revs/min resulted in resist thicknesses of 25 μm, which were sufficient to electroplate tweezers of 18-23 μm.

Patterning the NR9-8000 required more refinement than the AZ-4620, as negative resists tend to have undercuts in their profile, which if present in the electroplating mold, would lead to a trapezoidal cross-sectional geometry (Figure 2.5). This trapezoidal shape could alter the function of the microtweezer and box interface, or even prevent possible assembly (Figure 2.6). This undercut profile in negative resist resulted from its UV-

promoted cross-linking mechanism. The UV light source was directed down through the mask from a mercury source above the sample. Therefore, photoresist close to, or touching the mask, received the highest dosage of UV exposure, and deeper photoresist will receive less cumulative UV light, as absorption takes place as the UV light passes through the material. This gradient of UV exposure correlated with a gradient of chemical cross-linking within the photoresist profile. This deeper, less cross-linked photoresist was susceptible to removal by the developer during the development, especially if the sample was submersed into a developer bath. As the development process removes the photoresist of a feature that received no UV exposure and had no cross-linking, deeper areas of the remaining photoresist side wall on the periphery of the patterned feature that are closer to the substrate can eventually be exposed to the developer and dissolved, leading to undercut profiles.

Additionally, this deeper region of photoresist at a mask-feature interface (the boundary between a clear field and dark field region of the mask) received less UV exposure because the lack of refracted light that would have originated from light directed at the mask feature. The UV light source in the mask aligner is collimated, which significantly reduced the volume of light directed at the sample that was not completely vertical. However, at the air-mask and mask-photoresist interfaces, light refraction can occur, which can enhance the angle of any non-vertical light directed at the sample. At the interface between a clear portion of the mask and an opaque feature of the mask, refracted light only originates from the clear field region.

Given the thickness of the photoresist spin, the preliminary baking process used an oven set to 95$^{o}$ C to ensure a more uniform heat transfer to the thickness of the

photoresist for both the initial baking step, and the post-exposure baking step. However, after a few initial spins of the NR9-8000 photoresist, and 1.5x the recommended dosage of UV exposure per thickness, severe undercuts were still present. The post-exposure bake using the convection heat from the oven was not sufficient in completing the cross-linking of the deep regions of photoresist. A baking step using the hotplate (1 min, 120$^{o}$ C) that precedes baking in the oven would transfer heat from the plate to the wafer substrate to the deep regions of the photoresist and promote complete cross-linking of the photoresist at the photoresist-substrate interface. The addition of this baking step mitigated the undercut profile of the photoresist. Given the thermal conduction required through the thick resist profile, baking processes for the complete removal of solvents (pre-expose bake) and for complete cross-linking (post-expose bake) were substantial, and given the heat capacity of the thick resist layer, sufficient cooling time was required to prevent rapid thermal contractions, which would result in cracking of the photoresist. Depending on the photoresist thickness, a cooling time of 2-5x of baking time was required after the post-exposure bake to prevent cracking of the photoresist upon immersion in the developer bath.

Bright field photographs of samples from the secondary microtweezer fabrication process flow are displayed in Figure 2.7.

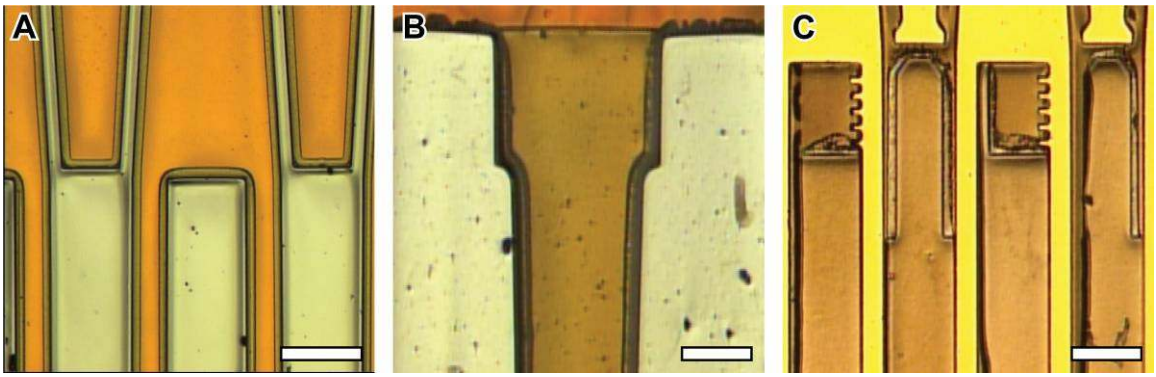


**Figure 2.5**: Bright-field photographs of nickel structures that were electroplated into undercut photoresist: (A) Microtweezer shoulder and beams, (B) second electroplating layer of the nickel box (channel), and (C) a multi-layer microtweezer. This undercut on the resist profile can be reduced by increasing the UV dosage. This overexposure, paired with a combination of hotplate and oven baking, effectively reduced the undercut profile and resulted in an electroplating mold that defined a more rectangular cross-sectional geometry. All scale bars are 300 μm.

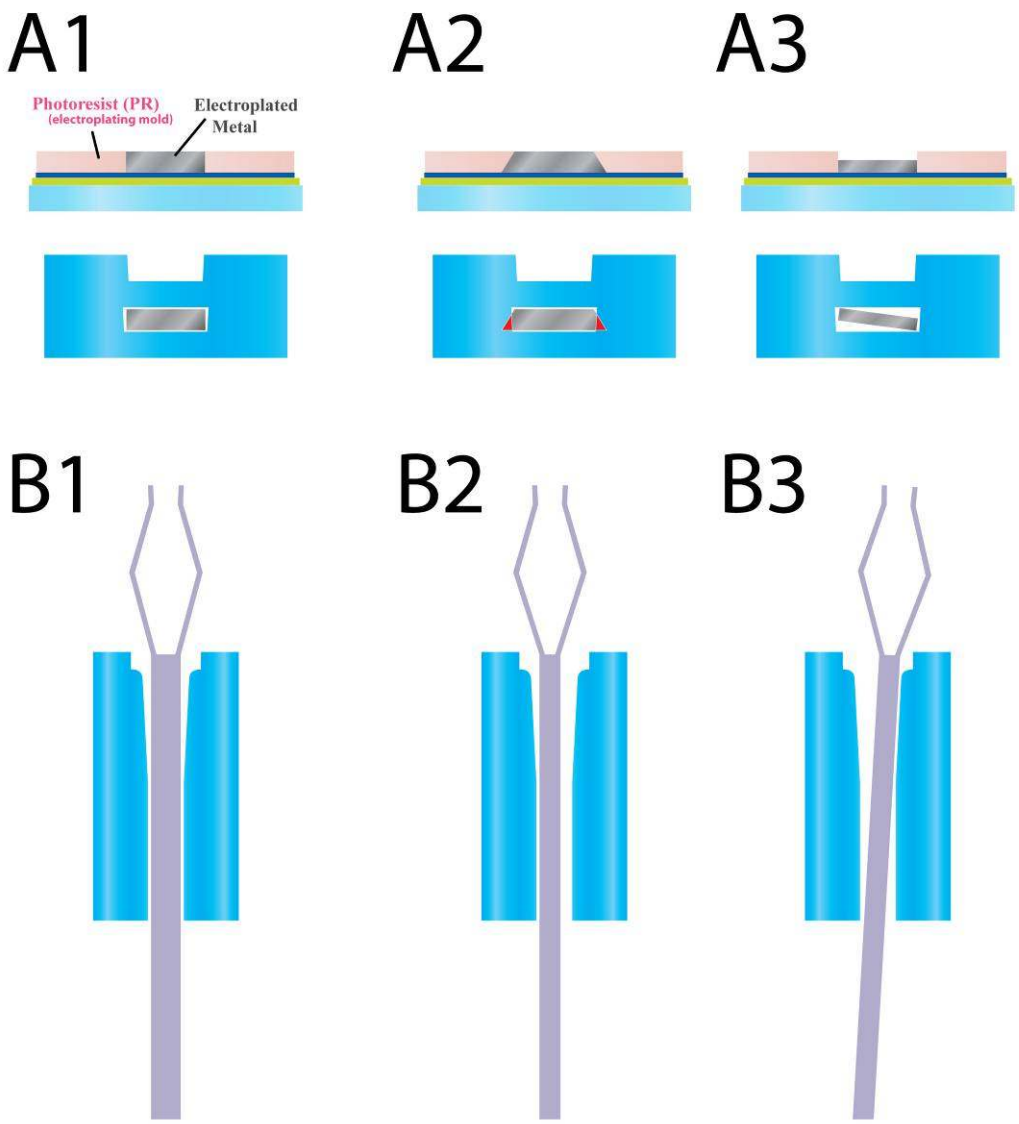


**Figure 2.6**: Cross sectional (A1-3) and top-down (B1-3) views of cartoons highlighting the functional problems that result from poorly formed components. (A1, B1)Ideally fabricated and assembled microtweezers and box. (A2) Tweezer formed from photoresist mold with undercut that cannot be assembled. (A3) Tweezer that has insufficient electroplating, and has too much free space, which allows vertical and torsional movement within channel. (B2, B3) Tweezer that is too thin, and can shift horizontally or rotationally, affecting the symmetry of tweezer beam actuation.

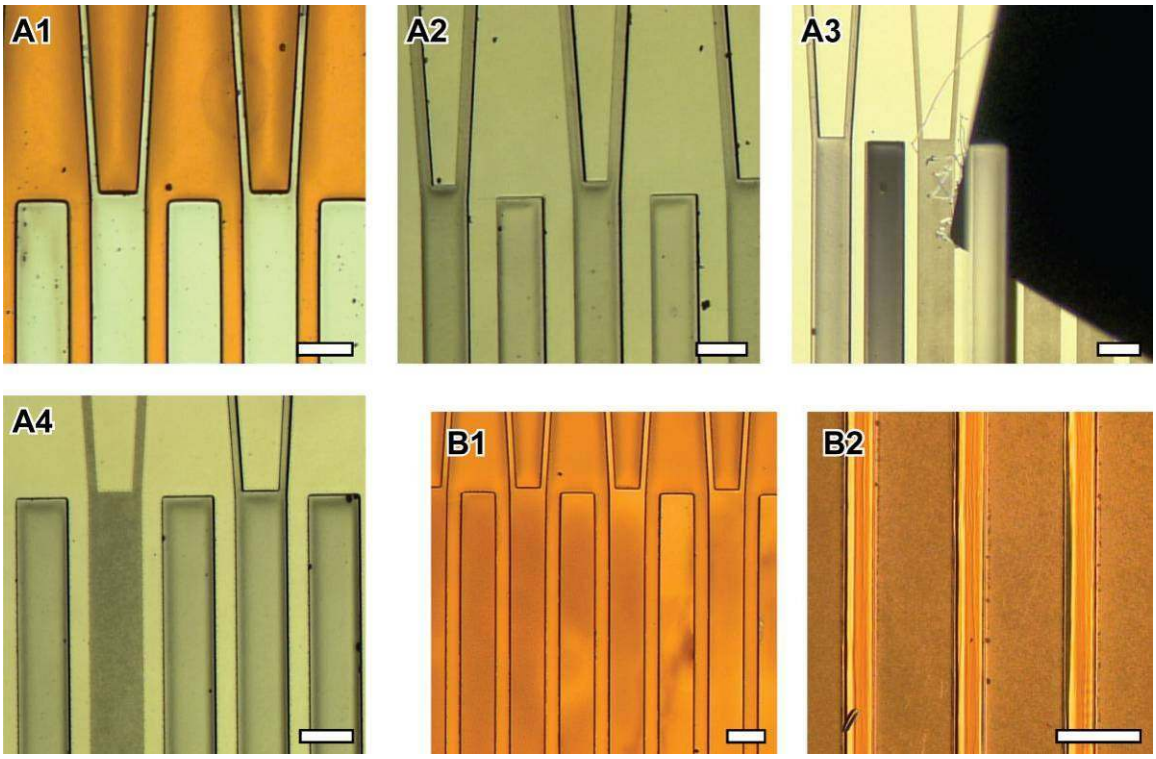


**Figure 2.7**: Bright field photographs of microtweezers constructed using the secondary fabrication process flow with a Ti/Al seed layer (A1-4) and a Ti/Cu seed layer (B1-2): (A1) Following electroplating in the first layer mold, (A2) after photoresist stripping, (A3) mechanical lift-off using a razor-blade edge, (A4) a sample with a single unit lifted off, and (B1) a sample using a copper electroplating seed layer before and after (B2) electroplating nickel into the photoresist mold. All scale bars are 300 μm.

2.4.1.3 - Final Microtweezer Microfabrication Process

In the final manufacturing process, the box and tool body/tips fabrication processes remain separated. The tool body and tips were again fabricated by electroplating a specified metal (for instance Ni, Cu, Au) into a photolithographically defined mold on an electroplating seed layer. For the refinement of this microfabrication process, there were a number of degrees of freedom to consider for every material and process choice. A variety of substrate, mold and seed layer material combinations were attempted for construction to provide: (1) the highest possible resolution of mold feature size; (2) the most flexibility in mold geometries for thick single and multi-layer electroplating steps; (3) convenience and success in microfabrication processing; and, (4) chemical resistance to the electroplating bath and lift-off processing steps.

The material and process selections for many of the degrees of freedom of this problem, such as the materials to use for substrate, sacrificial lift-off layer, electroplating seed layer, and photoresist mold, were hashed out and improved (Table 2.2).

**Table 2.2**: This table displays a list of material choices for each process in the modified LIGA microtweezer fabrication.

| Substrate | Advantage of Use | Drawback to Use |
|---|---|---|
| Glass | · Freely available from cleanroom supply<br>· Electrically non-conductive | · Etched with oxide etchant<br>· Rectangular shapes don't align with equipment<br>· Poor thermal conductivity* |
| ● Silicon | · Wafer shape fits with equipment<br>· Good thermal conductivity<br>· Does not etch with oxide etchants | · Electrically conductive, requiring passavative covering before electroplating |

| Sacrificial Lift-Off Layer | Advantage of Use | Drawback to Use |
|---|---|---|
| Electroplating Seed Layer | · Doesn't require additional deposition step | · Metal layer is usually thin and slow to etch<br>· Requires metal etchant which can etch tweezer material |
| Photoresist | · Allows use of multiple substrate types<br>· Dissolves quickly in solvents<br>· Solvents selected for etching are not selective for metal<br>· Can be used to reduce physical inconsistencies from a scratched substrate | · Photoresist sensitive to excessive heating<br>· Photoresist reacts to plating bath<br>· Adds many additional processing steps<br>· May not create completely flat surface for electroplating seed layer |
| ● Oxide ($SiO_2$) | · Dissolves quickly in oxide etch<br>· Electrically non-conductive<br>· Uniform deposition | · Adds an additional processing step |

| Electroplating Seed Layer | Advantage of Use | Drawback to Use |
|---|---|---|
| Aluminum | · Removed quickly by variety of wet etchants<br>· Dissolves in wet oxide etchant (HF, Buffered Oxide Etchant)<br>· Can be deposited using a variety of metal deposition machines | · Requires adhesion layer of Titanium or Chrome<br>· Reacts to and is etched by certain photoresist developers<br>· Selective etching partially etches Nickel |
| Copper | · Selectively etching is possible ($CuSO_4$ - $NH_4OH$ Solution)<br>· Can be deposited using a variety of metal deposition machines | · Requires adhesion layer of Titanium or Chrome<br>· Selective etching is time consuming<br>· Selective etching partially etches Nickel |
| ● Gold | · Selectively etching is possible (KI - $I_2$) | · Requires adhesion layer of Titanium or Chrome<br>· Limited number of machines supply gold |

| Photoresist Mold | Advantage of Use | Drawback to Use |
|---|---|---|
| AZ-4620 | · High aspect ratio thick photoresist<br>· Dissolves quickly in solvents | · Sensitive to light (begins to breakdown)<br>· Eventualy cracks and delaminates when exposed to electroplating bath<br>· Maximum height of 25-30 microns<br>· Developer chemically reacts to metal seed layer |
| NR-9-8000 | · High aspect ratio thick photoresist<br>· Mildly chemically resistant to electroplating bath | · Maximum height of 25-30 microns<br>· Does not dissolve completely in solvent<br>· Photoresist can undercut from development<br>· Sensitive to multiple thermal baking steps |
| ● NR-21-20000 | · High aspect ratio thick photoresist<br>· Mildly chemically resistant to electroplating bath<br>· Maximum height of roughly 100 microns | · Does not dissolve completely in solvent<br>· Photoresist can undercut from development<br>· Sensitive to multiple thermal baking steps |
| SU-8-2000 Series | · High aspect ratio thick photoresist<br>· Chemically resistant to electroplating bath<br>· Maximum heights of over 100 microns | · Can not be selectively dissolved in wet etchant |

While the different versions of glass (soda-ash, quartz, etc.) are physically durable, inexpensive, and non-conductive, the final substrate chosen for both the tweezer and box fabrication processes was the 4 inch silicon wafer. The photolithography alignment equipment in the Georgia Tech Microfabrication Research Center (MiRC) was mostly designed for these substrate sizes. Additionally, the silicon wafers were good thermal conductors, which allowed the use of hotplates without a significant thermal loss through the substrate medium, ensuring accurate temperatures in the sample during photoresist baking. Most importantly, the silicon substrate was not susceptible to oxide etching, allowed selectivity for removing an oxidizing electroplating seed layer or sacrificial lift-off layer made of silicon dioxide.

The sacrificial lift-off layers used in previous microtweezer fabrication processes were an electroplating seed layer and a thin bed of spun photoresist. While the seed layer was selectively etched, the thickness of the deposited material did not provide much surface area profile available for chemical attack, and this etching process took a substantial amount of time. Most of the chemical etchants used to remove this metal seed layer were also partially selective for the nickel material used in the microtweezer, and while substantial portions of nickel material were not removed, the etching bath needed to be monitored to identify when lift-off had occurred so the bath could be rinsed.

The sacrificial photoresist layer provided a variety of benefits to increase the yield of the process. It was effective in reducing the necessity to prepare the surface of the wafer prior to processing, as the spinning of the photoresist would provide a generally uniform layer for subsequent processing. The sacrificial resist also provided an insulating layer to prevent backside electroplating deposition, and reduced the overall

time of the lift-off process. However, given the exposure of this photoresist layer to several baking steps, and excessive cross-linking, the time of removal with acetone was not improved from metal etching the thin electroplating seed layer. The chemical break-up of this photoresist material also contributed debris in the lift-off bath that was re-deposited onto the microtweezer samples, which created a need for additional cleaning steps.

The final sacrificial lift-off layer that was selected was a 1 μm thick layer of silicon dioxide that was deposited using a standard $SiO_2$ plasma-enhanced-chemical-vapor-deposition (PECVD) process. This oxide layer could be selectively etched with a buffered oxide etchant like the Al/Ti electroplating seed layer, but it was greater in thickness to the seed layer, creating a physical side profile that allowed faster etching. Like the sonication-induced acetone release of the sacrificial photoresist layer, using the oxide sacrificial lift-off layer allowed the use of any type of electroplating seed layer metal, including some that were more chemically inert, such as gold. This oxide layer was also more uniform in deposition then the spun photoresist, and created a better platform for further processing as thermal conduction from hot-plate heating was not compromised. Upon lift-off, the silicon dioxide layer was readily etched with the buffered oxide etchant, and no debris was produced. Lastly, the oxide created an insulating layer between the electroplating seed layer and the silicon substrate, which prevented electro-deposition of metal on the backside of the wafer.

To eliminate the possibility of backside electroplating, a silicon nitride layer was deposited onto the back/bottom of the wafer prior to the deposition of the silicon oxide on

the front/top of the wafer. This nitride layer completed the electrical passivation of the wafer surface, and ensured a consistency in the electroplating process.

As a result of the silicon dioxide sacrificial lift-off layer and its removal being independent of the electroplating seed layer, a variety of seed layer materials were tested, such as aluminum, copper, and gold. Ideally, the electroplating seed layer would: (1) conduct electricity with minimal resistivity to ensure even charge distribution; (2) be selectively removable with an etchant that would not interact with the other materials present in the sample; (3) be easy to deposit onto a variety of substrates; and, (4) not require additional surface treatment processing prior to immersion in the electroplating bath. The preliminary and secondary fabrication processes utilized a Ti/Al layer due to its susceptibility to oxide etching removal, and to simplify deposition, as all metal deposition machines in the cleanroom supported this process. However, the propensity of these materials to oxidize required an oxide-removal step prior to electroplating, which if prolonged, could remove the entire metal layer. While copper oxidized in the presence of air like aluminum, a buffered oxide etch will not readily remove the entire copper layer. Selectively etching copper for removal prior to lift-off, however, required a prolonged immersion in an agitated $CuSO_4$-$NH_2OH$ solution. This solution, if saturated, actually promoted the re-depositing of copper on the sample onto surface locations with limited shear forces within the agitated bath. Gold did not oxidize in the presence of air, and did not require an oxide etch prior to immersion in the electroplating bath. Selective etching with gold was possible using KI-$I_2$, but if deposited thin enough, the gold layer was removed successfully using sonication during stripping of the sacrificial lift-off layer.

Additionally, gold is a chemically inert and biocompatible material, and trace amounts left on the tweezer would minimally affect any biological or environmental applications.

The current density for the electroplating process on the gold surface was controlled to prevent material stressing (discussed below) in the growth the nickel structures within the mold, which promoted the delamination of electroplated structures. However, given enough mechanical input, the physical lift-off of certain high-aspect ratio features in the nickel structure was possible. The structures that most readily delaminated from this lift-off bath agitation were the tips of the tweezers, which had a cross-sectional geometry of 25 μm thick and 40 μm wide. Because of potential plastic deformations in the tweezer tips or beams, which could affect device performance, these particular samples were discarded, lowering the batch yield. However, this reduced adhesion between the nickel and gold surfaces allowed multiple lift-off process combinations to be employed (discussed below).

As a result of the baking and spinning issues with the NR9-8000 photoresist, a similar photoresist, NR21-20000, which was designed for higher spin thicknesses, was used. Like AZ-4620 and NR9-8000, NR21-20000 was a high-aspect ratio thick photoresist. However, this resist had a few key advantages: (1) the maximum height for a single spin thickness was roughly 100 μm, which was greater that of AZ-4620 or NR9-8000; (2) spin recipes for the 25-30 μm range, which were ideal for patterning molds for microtweezers, were achievable using high-speed spin settings; (3) undercuts were less prominent than in NR9-8000; and, (4) the surface following the spin was more uniform than NR9-8000, most likely because the spin speeds for NR21-20000 were much greater than those used for NR9-8000 (3000 rev/min vs. 800 rev/min).

While this new resist shared the same chemical resistivity and temporal integrity of NR9-8000, it also shared it's resistance to acetone or resist-removal stripping. Following patterning and electroplating, each sample required multiple resist remover immersions with agitation to remove all presence of photoresist. Additionally, the level of agitation needed to be controlled and the sample monitored to prevent the delamination of the electroplated nickel features.

In summation, the final fabrication process of the microtweezer took place using a 4" silicon wafer substrate with silicon nitride backside and silicon dioxide topside depositions, an electroplating seed layer of gold, and a patterned mold made of NR21-20000 thick negative photoresist (Figure 2.8).

The process started with an initial piranha cleaning, and a subsequent solvent-based cleaning (TCE, Acetone, IPA, DI). A 1 μm layer of SiN was deposited using a PECVD process onto the backside of the wafer, followed by a second solvent cleaning. This insulated layer ensured no backside or edge deposition during electroplating. This relatively thick layer of nitride also remained in place following any oxide etches, and it was resistant to all subsequent fabrication processes. A 1 μm layer of $SiO_2$ was then deposited using a PECVD process onto the topside of the wafer, followed by another solvent-based cleaning process. This $SiO_2$ layer provided additional electrical isolation (also in the case of pin-holes in the SiN layer), and an etching target for the lift-off process. A 0.5 μm thick gold electroplating seed layer was sputtered on top of the $SiO_2$. The NR21-20000 negative resist was spun with a single-coat layer to a thickness of 25 μm. It was then baked on a plate set to 120$^o$ C for 1 minute and then a hot plate set to 90$^o$ C for 3 minutes, exposed to 3000 mJ of 365 nm UV light, post-exposure baked on a hot

plate set to 90° C for 3 minutes, and then developed in RD6 photoresist developer for 3 minutes. Following development, the sample could be heated to above 90° C (120° C is sufficient) on a hot plate for 1-3 seconds to create re-flow in the resist, which could be used to remove undercuts in the resist profile. Care needed to be taken with this process modification, which could result in the deformation of the patterned features. The sample was then electroplated to just under the mold height (18-23 μm). Following electroplating, an acetone or resist-remover bath with agitation was used to strip the photoresist mold. This step needed to be repeated multiple times to completely remove all photoresist residue along the edges of the electroplated microtweezers. Lift-off was accomplished with multiple methods, including gold etching, oxide etching in an agitated bath, and using the point of a razor blade to delaminate individual samples from the wafer surface. Given the number of samples present on each wafer (hundreds), bulk lift-off resulted in samples floating freely in the etching bath, which made single sample capture difficult. Using a razor blade to remove the samples could result in fragments of gold present on the edges of the tweezers, as well as some gold stripped from the wafer surface and attached to the microtweezer bottom. A combination of etching the gold and physical lift-off worked best to provide both control of individual sample capture and minimal gold debris presence. The etching of the seed layer, which progressed to under the tweezer, is demonstrated in Figure 2.9.

Bright field photographs of tweezers constructed using this fabrication process are displayed in Figure 2.10, and scanning electron microscope (SEM) pictures of the various styles of tweezer tips are displayed in Figure 2.11.

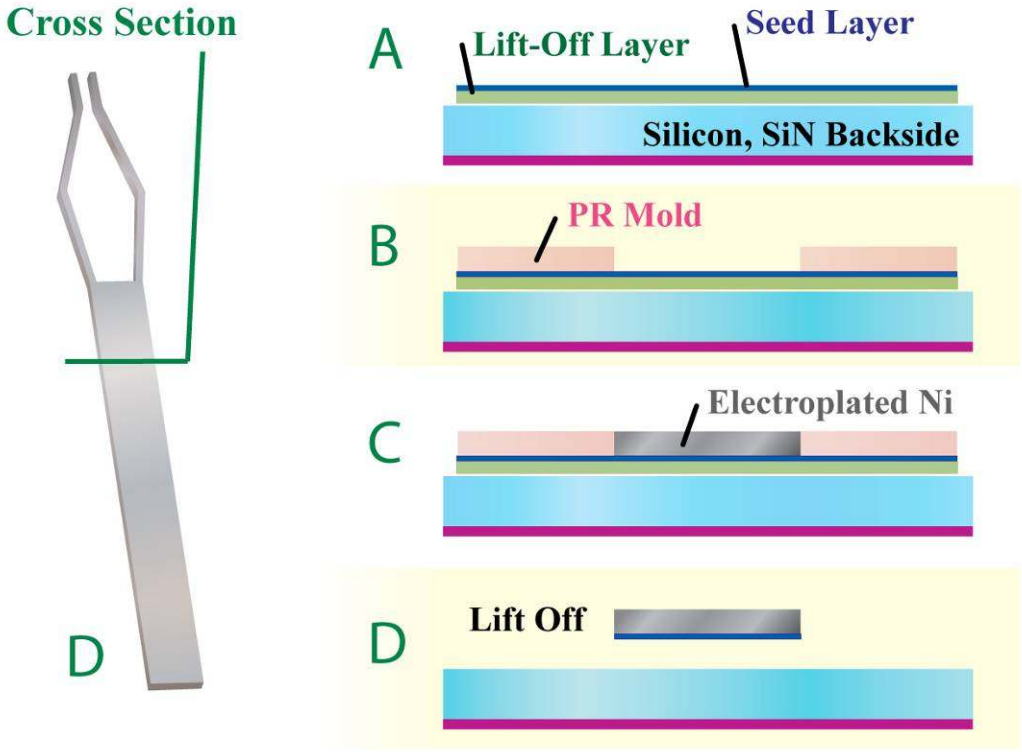


**Figure 2.8**: Final fabrication process flow for the single-layer microtweezer body and tips (A-D). Fabrication followed the processes defined in the preliminary and secondary tweezer fabrication process with the use of a backside silicon nitride layer and a sacrificial silicon oxide layer that was initially deposited to aid in the final lift-off process.

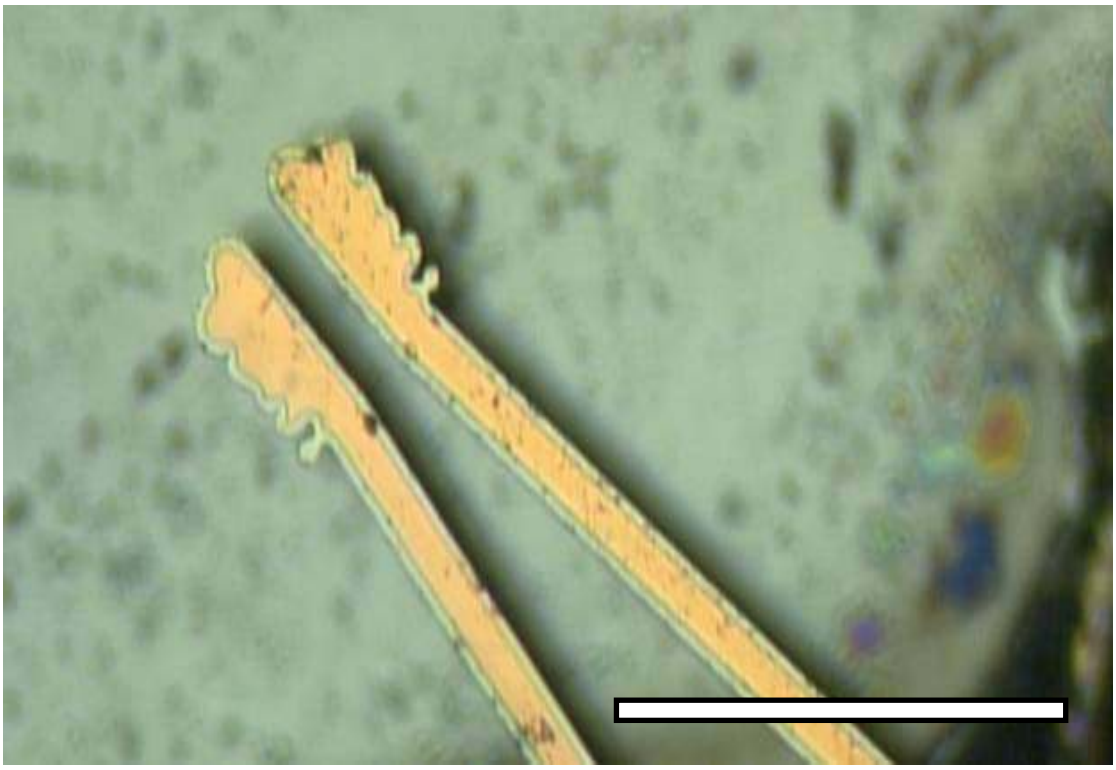

**Figure 2.9**: Bright field photographs of the underside of a microtweezer (with a unique tweezer tip style not used in these experiments) following metal etch of the electroplating seed layer, and then the lift-off process. The etching of the seed layer was carried past the removal of the exposed regions, which resulted in slight underside etching. Scale bar is 300 μm.

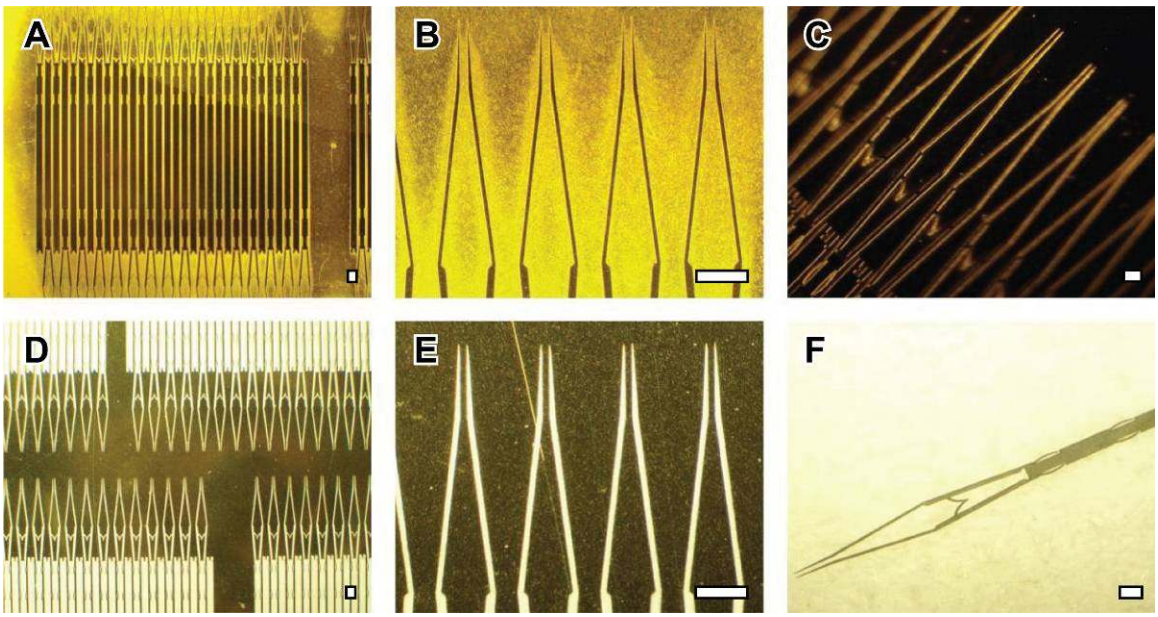


**Figure 2.10**: Bright field photographs of microtweezers constructed using the final fabrication process flow: (A, B, C) Following the patterning of the first electroplating mold, (D, E) after the nickel electroplating step, and (F) after lift-off. All scale bars are 300 µm.

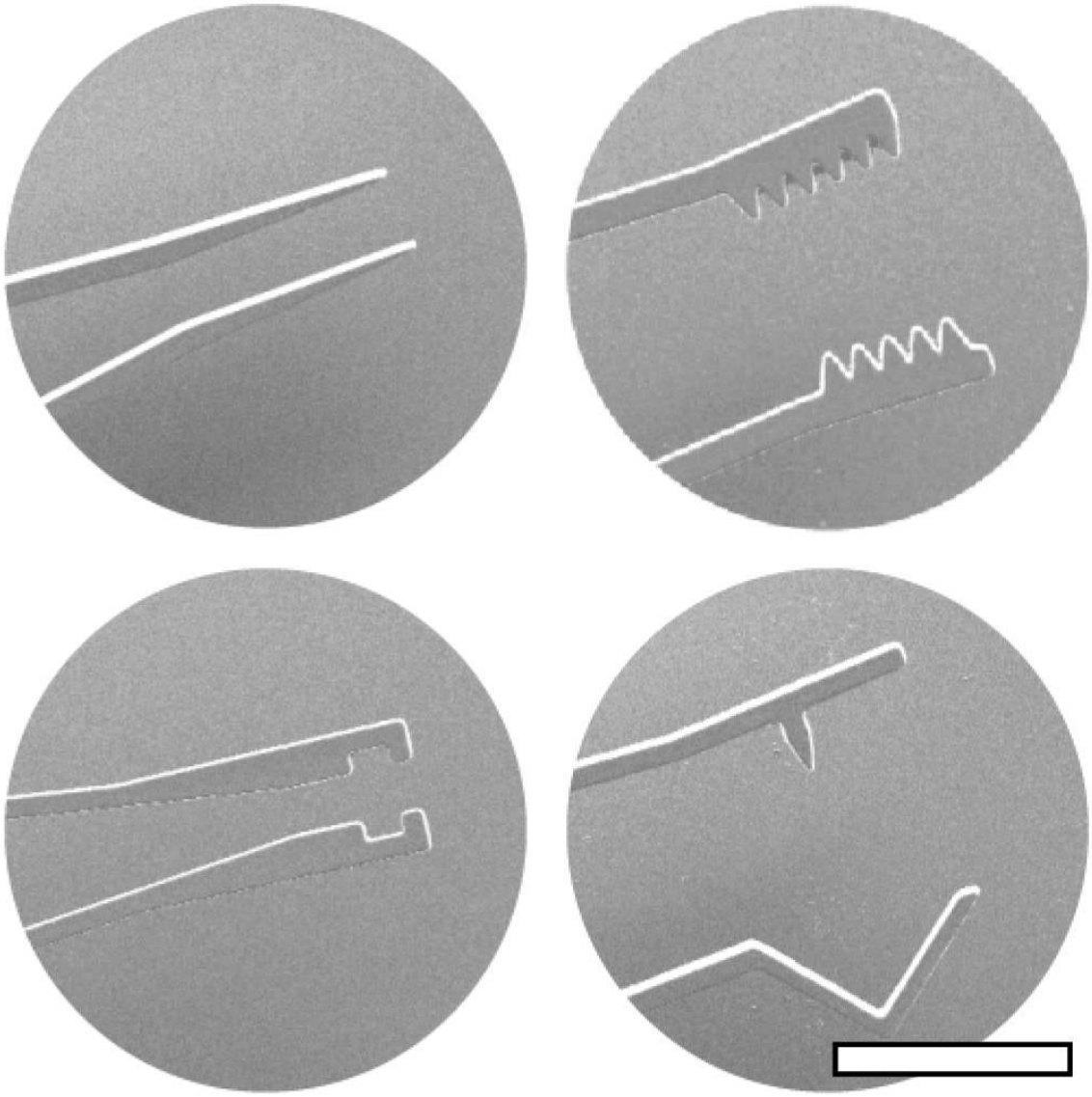

**Figure 2.11**: SEM pictures of various microtweezer tip styles: (Clockwise from upper left corner) Forceps, serrated, square notch, and piercer. Scale bar is 300 μm.

2.4.1.4 - Multi-Layer Microtweezer Microfabrication Process

Following the fabrication process flow outlined in the preliminary tweezer section, multiple layers of nickel could be deposited in sequentially patterned photoresist molds to increase the thickness of the tweezer or to pattern more complex tip shapes. Currently, the tweezer height is dictated by the height of the box, which is fabricated separately. Given the increased processing time in the manufacturing of the box over the tweezer (a multi-layered structure compared to a single-layered structure), creating a basic box that can accompany a variety of different tweezers is ideal. Being able to adjust the thickness of both the tweezer tip, and the overall tweezer body to fit available box units, can be accomplished by depositing multiple layers of nickel. This allows independent control over the thickness of the microtweezer tips, which may need to be tailored based on the application. A secondary photolithography mask was created to pattern an electroplating mold that results in nickel deposition only on the body of the tweezer, allowing control over the tips and beams thicknesses with the first electroplating process.

Bright field photographs of a multi-layer of nickel tweezer can be seen in Figure 2.12.

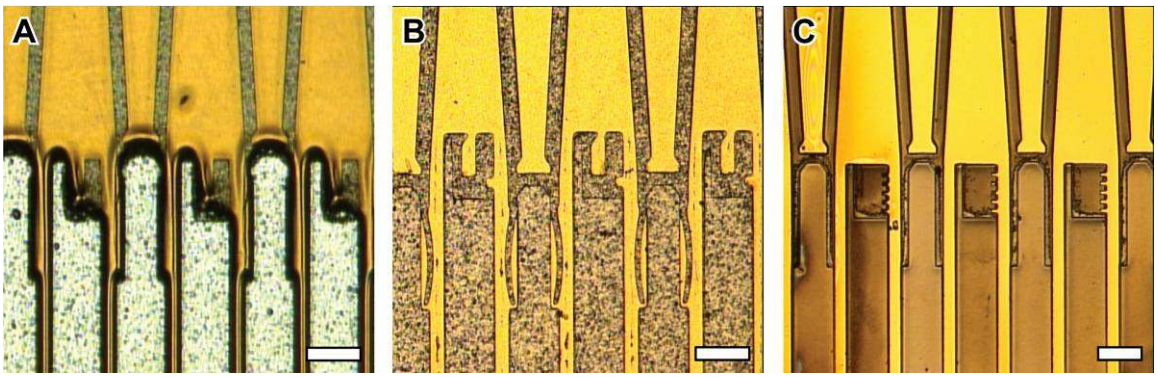


**Figure 2.12**: Bright field photographs of multi-layer microtweezers constructed using the final fabrication process flow: (A) Following electroplating the second layer, mold still present, (B, C) after stripping the photoresist (different samples, different electroplating processes). All scale bars are 300 μm.

### 2.4.2 - Microfabrication Process - MEMS Microtweezer Box

The microtweezer box or sleeve was a covered channel with openings on either side that housed the tweezer and allowed translational movement of the tweezer along one axis. Considering the planar nature of photolithography processing (blanket depositions and wet-etching, planar photoresist patterning, isotropic and anisotropic top-down dry etching, etc.), some exotic microfabrication techniques were required to pattern a covered, debris free and relatively smooth channel so that the tweezer body could slide to allow fluid deflection movement of the tweezer beams.

The iterative design process for the microtweezer box is described below. Despite the numerous changes in the construction process during development, three main iterations are provided with detailed descriptions of the successes and failures for each. The preliminary box fabrication that involved the construction of the microtweezer and box simultaneously is briefly discussed (detailed in Section 2.4.1.1). This is followed by the secondary box process where the fabrication involves a multi-layer molding process similar to the preliminary process. The final box fabrication process used, which involves the bonding of two patterned silicon layers to form the box channel, is provided last.

#### 2.4.2.1 - Preliminary Box Microfabrication Process

The original fabrication process of the microtweezer constructed the box and tweezer body and tips together. This process is described above for the preliminary microfabrication process for the microtweezer body and tips, and is shown in Figure 2.2. Given the total number of steps involved in this process, and the difficulty in assessing

sources of failure for each, refinement during the iterative development was challenging, and limited numbers of viable samples were produced.

2.4.2.2 - Secondary Box Microfabrication Process

To increase yield and establish a means to better troubleshoot process failures, the microtweezer box and body/tips were fabricated separately [139]. The goal was to reduce the complexity of the overall process, and increase yield. The independently-fabricated microtweezer box was constructed using a three-level electroplating process (Figure 2.13), which was similar to the five-level process of the preliminary fabrication process. As before, the channel was created by patterning and then dissolving a central sacrificial photoresist structure that ran the length of the box.

Similar to the secondary tweezer body/tips fabrication process, the photoresist used to define the electroplating molds was switched to the negative resist NR9-8000. This change was especially important in the box fabrication due to the repeated baking and electroplating steps, as the NR9-8000 resist provided better temporal integrity and chemical resistivity than AZ-4620. Also like the body/tips process, a sacrificial photoresist layer was added at the beginning of this process to provide an etching target for the final lift-off step.

Following cleaning steps, the fabrication process started with the spinning, baking, over-exposure, and post-exposure baking of the thin (3-5 μm) sacrificial negative photoresist (NR7-1500) layer (Figure 2.13A). The Ti/Al electroplating seed layer was then vapor deposited onto the sacrificial photoresist layer (Figure 2.13A). The subsequent fabrication processes followed the preliminary box fabrication protocol, and involved the patterning of a series of photoresist molds in which Ni was electroplated to

form the various layers of the box (Figure 2.13B-F). For each layer, the NR9-8000 negative resist was spun with a single-coat layer to a thickness of 25 μm, baked in an oven set to 90$^{o}$ C for 25 minutes, exposed to XXX mJ of 365 nm UV light, post-exposure baked in a oven for 90$^{o}$ C for 10 minutes, and then developed in RD6 photoresist developer for 3 minutes. To prevent rapid thermal expansion, following each baking step, the sample was allowed to cool for over twice the baking step duration. After each mold patterning, the sample was electroplated to just under the height of the mold. Following the electroplating of the second layer, a second electroplating seed layer needed to be deposited to cover the non-conductive photoresist that was defining the box channel. This metal layer was blanket deposited to ensure complete coverage. Following the third electroplating step, a gentle acetone bath was used to remove each of the photoresist molds. For lift-off, the sample was then placed in a fresh acetone bath with sonication to remove the sacrificial photoresist layer, and to ablate the thin film electroplating seed layers (Figure 2.13G).

The scaled geometries and dimensions of the completed 3-layer nickel microtweezer box are depicted in Figure 2.14 and Table 2.3.

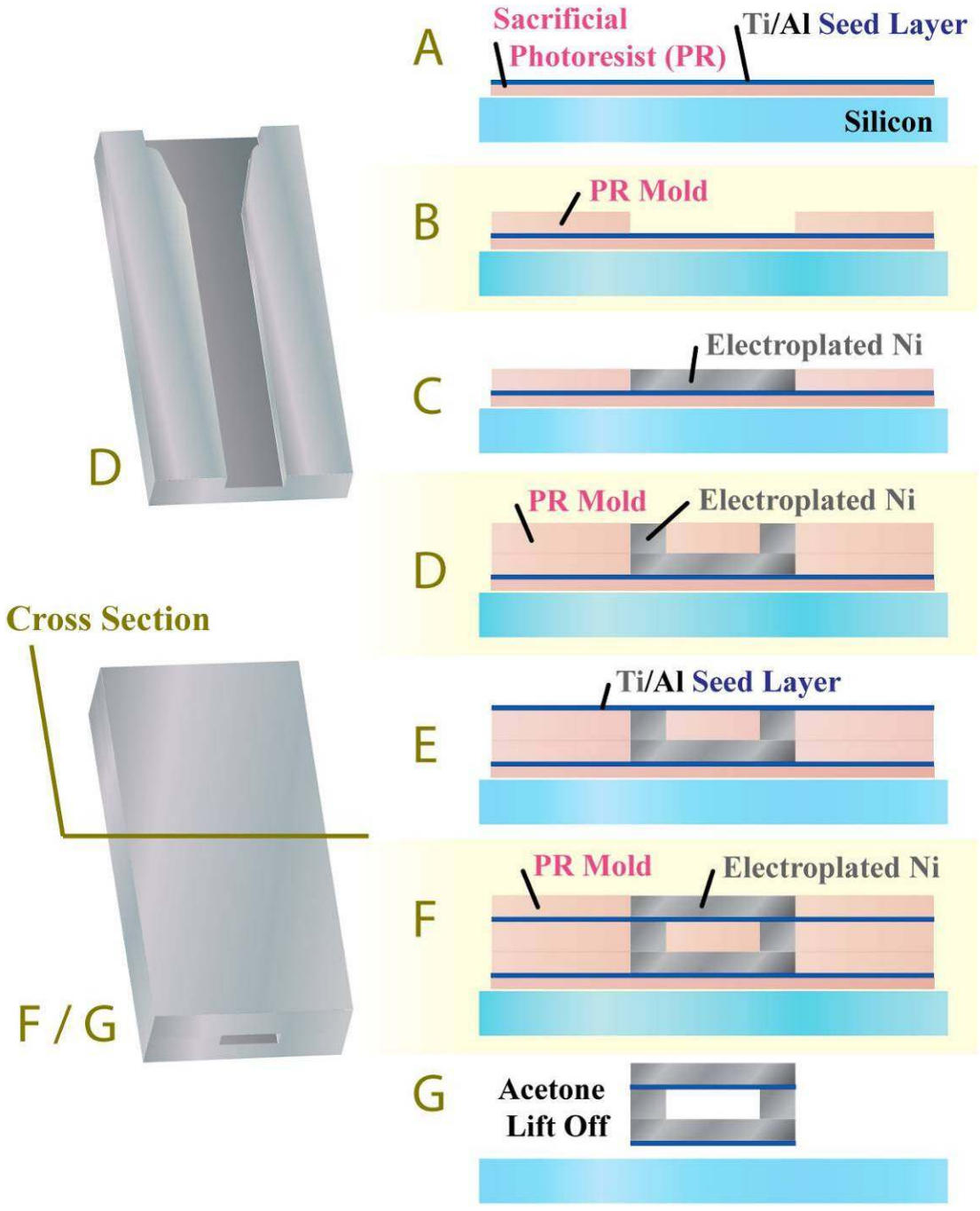


**Figure 2.13**: Secondary fabrication process flow for the three-layer microtweezer box (A-G). Fabrication follows the processes defined in the preliminary fabrication process for both the box and tweezer.

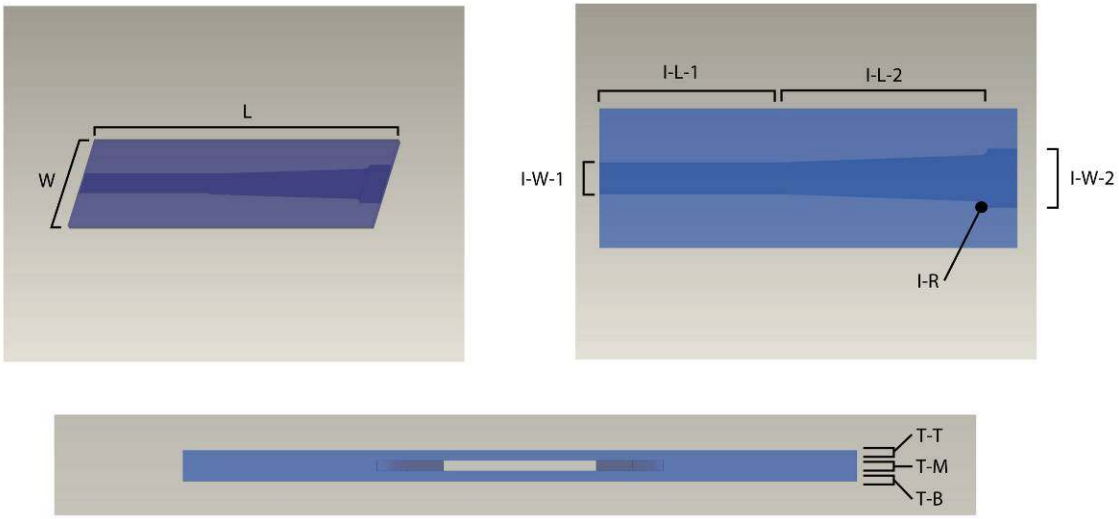


**Figure 2.14**: CAD drawings of the completed nickel box and the relative dimensions of the channel that runs the length of the box.

**Table 2.3**: Table highlighting the dimensions of the complete nickel box depicted in Figure 2.14.

## Nickel Box Dimensions

| | | |
|---|---|---|
| **Box** | | |
| Length | ( L ) | 4.70 mm |
| Width | ( W ) | 1.57 mm |
| Thickness - Top | ( T-T ) | 25 μm |
| Thickness - Channel | ( T-C ) | 25 μm |
| Thickness - Bottom | ( T-B ) | 25 μm |
| **Channel** | | |
| Width - Back | ( I-W-1 ) | 345 μm |
| Width - Front | ( I-W-2 ) | 650 μm |
| Length - Channel | ( I-L-1 ) | 2.02 mm |
| Length - Overdrive | ( I-L-2 ) | 2.225 mm |
| Radius - Drive Contact | ( I-R ) | 70 μm |

Despite the similarities between the preliminary and secondary fabrication processes, the use of the NR9-8000 photoresist greatly increased the sample yield. As long as proper cooling and rinsing procedures were followed, the presence of cracks in the photoresist was greatly reduced following each of the baking and electroplating steps. These cracks were mitigated by using re-flow procedures on the photoresist (heating to above 120$^{o}$ C for a few seconds), but given the photoresist's exposure to the electroplating bath chemicals, this was avoided to prevent possible loss in chemical integrity and the introduction of additional weak points in the resist. However, this could be examined further for use in other modified LIGA processes to increase photoresist integrity for fabrication protocols with additional steps or steps that involve extensive thermal or chemical exposure.

One potential downside of using this negative photoresist was the incomplete resist stripping process. Following each photoresist mold patterning, there were several thermal and chemical exposures during the subsequent photolithography, microfabrication, and electroplating processes, which affected the ability of the photoresist to be removed completely with an immersion in acetone or resist remover. Given the expected contact with the microtweezer beams, the channel features of the box needed to be free of any photoresist debris. However, the material flow of acetone into the channel was constricted due to its cross sectional geometry of 25 μm by 300 μm. Discovery of any photoresist film left in the channel was identified during the assembly process when a microtweezer could not be effectively inserted into the box channel. Mismatch or lack of symmetry in the closing of the two tweezer beams also resulted from photoresist residue within the channel. Visual evidence confirmed this following

deliberate delamination of the second and third electroplated nickel layers (Figure 2.15). In addition to causing problems with the mechanical function of the microtweezer, photoresist residue left on the box, or transferred to the tweezer beam, could cause biocompatibility issues during any experiments where the tweezers are inserted into a cell medium. Multiple photoresist stripping steps were attempted for each sample, some with bath agitation or bath sonication, but depending on the specific thermal and chemical exposures during the microfabrication process, small portions of the resist within the channel seemed impervious to the stripper.

As mentioned previously in the microtweezer body and tips process design, the NR9-8000 photoresist was being spun to a relatively high thickness. To prevent photoresist waste, the presence of edge beads, overall non-uniformity in thickness, and poor thermal curing, a new negative photoresist would be required to continue attempting this process.

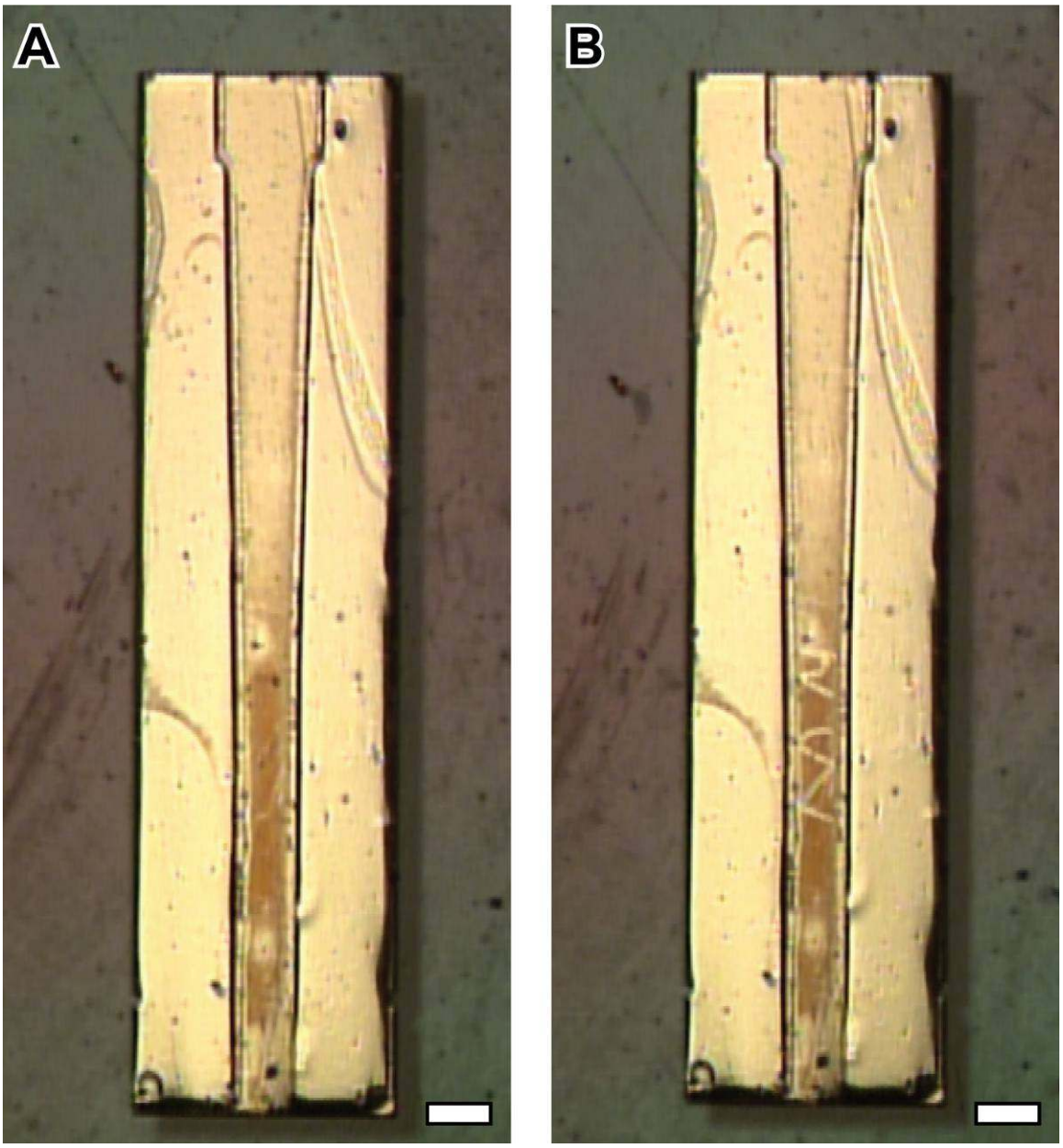


**Figure 2.15**: Bright-field photographs of the inner channel of the nickel box (this box had a delaminated third layer) (A) before, and (B) after the channel floor was scribed with a forceps tip. The channel geometries are visible. Photoresist residue in the narrow portion of the channel, which was difficult to completely remove, can be seen. This residue affected the mechanical function of the combined microtweezer and box. All scale bars are 300 μm.

Following lift-off of the completed box units, insertion of microtweezer units was attempted. A variety of setups were employed to stabilize the box so that the microtweezer could be handled with forceps and inserted. Because this assembly was accomplished using hand-held forceps, training and practice was required. Initially, however, it was noticed during attempted insertion that if alignment of the tweezer and box was not perfect, physical contact and stress from the tweezer body could be placed on either the top or bottom of the box. In some cases, this caused delamination of the sequentially electroplated box layers (Figure 2.16). The delamination occurred at the interface between the second and third electroplating layers; the likely sources of structural weakness being the adhesion between the second electroplated layer and second seed layer. Because sufficient quantities of box samples had structural integrity during and after assembly with the microtweezer, this failure was not examined thoroughly. Additionally, following successful assembly, few box layer delaminations occurred due to the uni-axial restricted movement of the tweezer within the box; little relative stress was placed on the either the top or bottom layer of the box during actuation. It is likely, however, that the source of delamination resulted from oxidation of the nickel surface on the second electroplated layer prior to metal sputtering of the second seed layer. This oxidation could prevent sufficient adhesion between the nickel and titanium.

Completed nickel boxes using the secondary fabrication process are displayed in Figure 2.17.

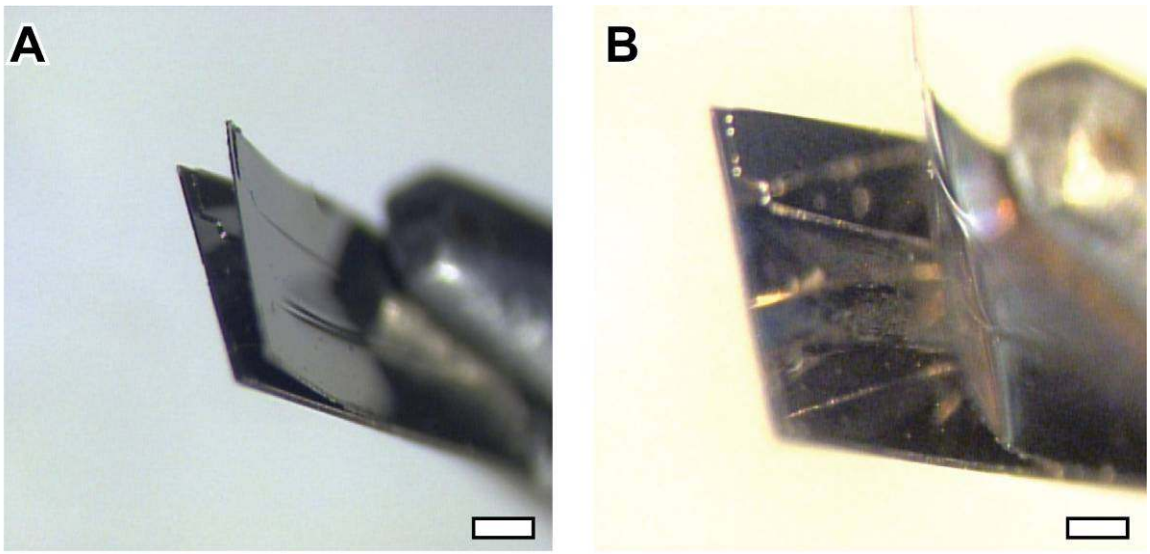


**Figure 2.16**: Bright-field photographs of boxes with delaminating electroplating layers (A, B). The delaminations occurred between the second electroplating layer, and the electroplating seed layer for the third electroplating layer. Boxes in photos are being held by forceps. All scale bars are 300 μm.

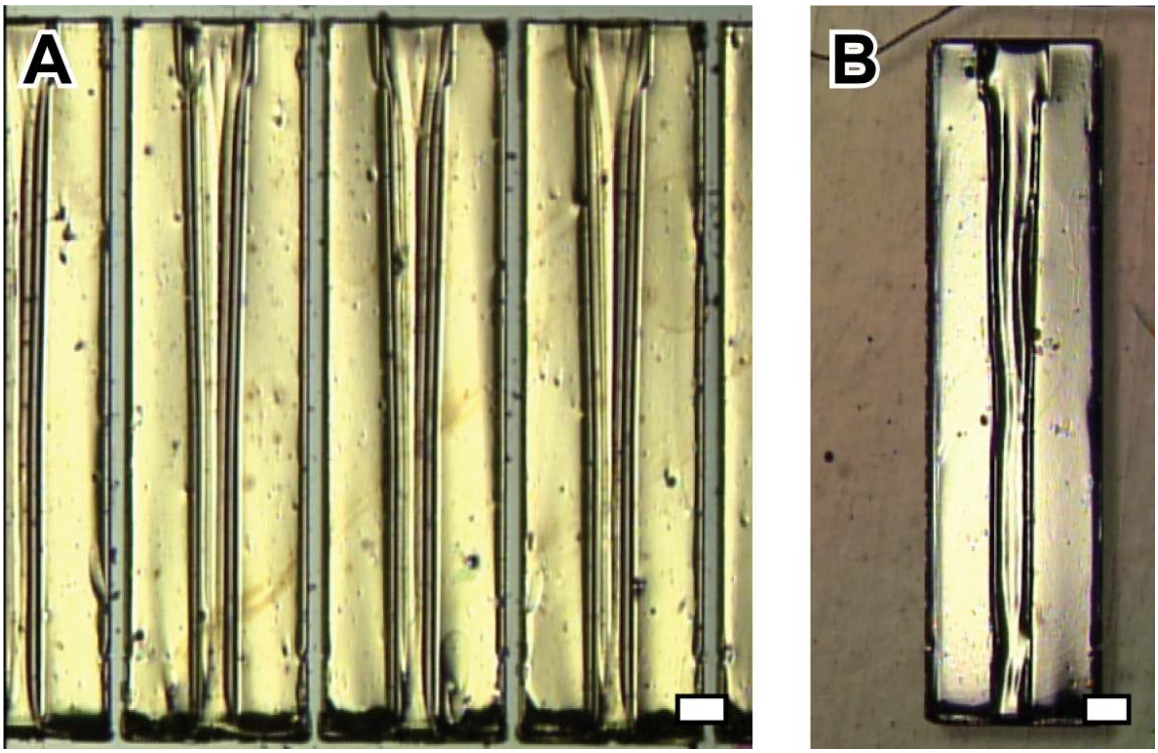


**Figure 2.17**: Bright-field photographs of completed nickel boxes: (A) Following photoresist stripping process, and (B) after the lift-off where sacrificial photoresist and electroplating seed layers were ablated with the second photoresist stripping step that included sonication. All scale bars are 300 μm.

In addition to insertion of the tweezer into the box, the attachment of assembled MEMS devices to the luer needle package was attempted (package design detailed in Chapter 3). It was observed that upon attachment of the tweezer body to the outside of the luer needle, and attachment of the box to the drive cable, there was a slight deflection in the tweezer body between the end of the luer needle and the box. This deflection is proportionally depicted in Figure 2.18. The tweezer cross sectional geometry does allow material flexibility in this dimension, and it was difficult to assess this body deflection's impact on the opening and closing of the tweezer. To reduce this deflection, an alteration in the dimensions of the box bottom thickness, the inner diameter of the luer needle, or the outer diameter of the luer needle was required. The stainless steel luer needle was a commercial product, and there was some variety in inner and outer diameters available, but the no needles were found that have a cannula wall 25 μm thick, which was the thickness of the bottom of the nickel box. Considering the dimensions of the needle cannula wall, the box bottom would have to be increased to 150 μm to completely eliminate the tweezer body deflection. With the secondary box fabrication process outlined here, the thickness of the individual layers of the box was limited by the spin thickness of the NR9-8000 photoresist mold. Additional sequential layers of photoresist could be spun to increase the thickness of the mold. However, the complications and failures that were observed in the preliminary fabrication process related to repeated photoresist baking and thick photoresist baking in general could be encountered again. Alternative photoresists, such as NR21-20000, could be used to create higher molds. However, new electroplating protocols would have to be established to grow the 125 μm tall layer while limiting temporal exposure of the photoresist to the bath, which with the

current 25 µm process, is at least 8 hours. A limited solution to increase thickness could involve the physical attachment of an additional component of known thickness to the box following lift-off, but an alternative sustainable fabrication process was required to create this thicker box layer. Additionally, a portion of the outer layer of the luer needle could be removed using either a laser etching or micromilling process to reduce the thickness of the needle cannula wall.

It was possible that this tweezer body deflection did not affect tweezer actuation, as: (1) the drive cable provided the majority of physical support for the MEMS device given its cross sectional dimension; and, (2) the tweezer beam was stationary during actuation as the box advances forward to contact the beams at the end of the tweezer. However, this deflection of the tweezer beam could induce strain on the top layer of the box, which could eventually result in delamination of the top and middle nickel layers.

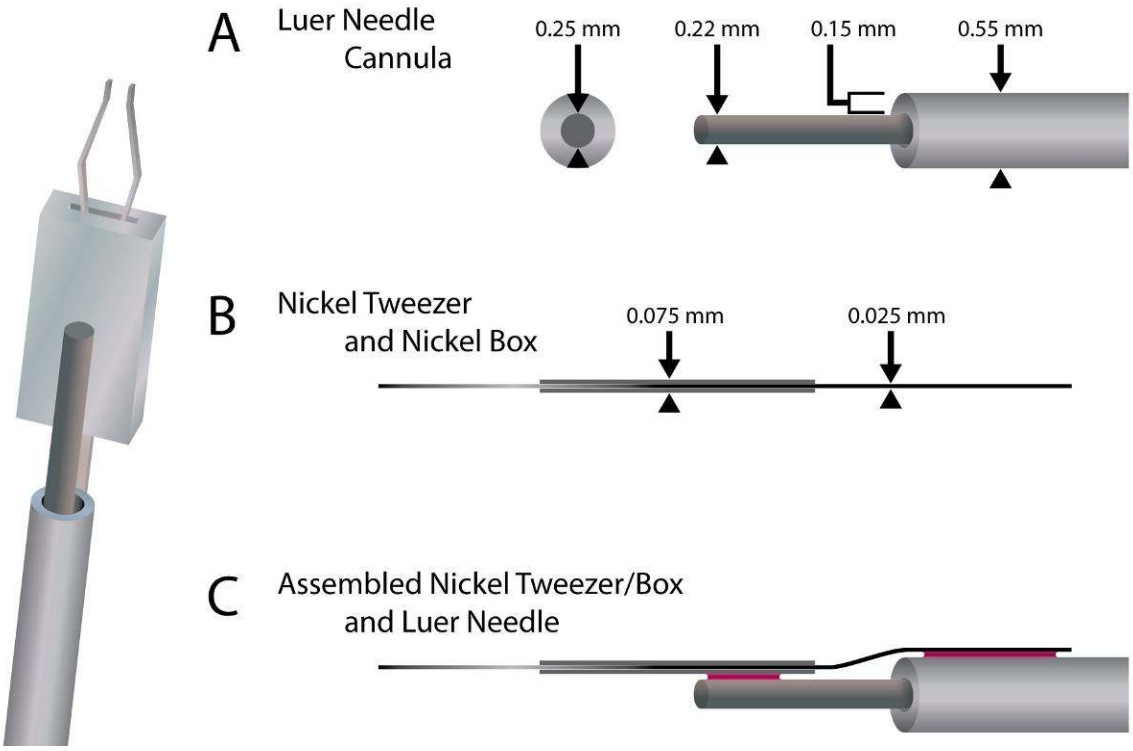


**Figure 2.18**: Cartoon depicting the (A) dimensions of the needle cannula and drive cable, (B) the thickness dimensions of the nickel tweezer and nickel box, and (C) the deflection in the tweezer body with the attachment of the nickel tweezer and nickel box to the luer needle and drive cable. Relative thickness proportions are accurately portrayed. The epoxy used at the various attachment points is colored red.

2.4.2.3 - Final Box Microfabrication Process

There were several sources of failure in the nickel box construction that were experienced in both the preliminary and secondary process flows. The photoresists selected had to endure multiple exposure, heating, and development steps, as well as resist the chemical affects of being immersed in the electroplating bath for hours. Additionally, the spin thicknesses of the photoresist would always dictate the depth of the microtweezer box channel. An increase in the aspect ratio for the photoresist mold would limit the feature size of the tweezer tips.

Instead of using a micromolding approach to constructing the box channel, which involved the addition of material to form the channel, an approach that would utilize a channel created from etching or removing material was considered for this final process. This could result in deeper channels being built, as well as prevent the presence of any photoresist residue in the channel. As previously mentioned, the aspect ratio of the channel was important to ensuring that the microtweezer did not have excess room to move laterally, which could affect the closing symmetry of the tweezer beams. Most wet and plasma enhanced etching of material was isotropic, which would result in non-vertical walls in the channel trench. However, anisotropic vertical etching of a channel was possible using inductively coupled etching (ICP) with silicon as an etching target. Planar etching the channel into the top surface of a material required the deposition or adhesion of a top surface to cover the channel. The attachment of this second component of the box could result in the delamination issues that were present with the multiple layers of electroplated nickel. While a second wafer adhered on top of the first wafer using anodic silicon-silicon fusion provided a sufficiently strong bond, precise alignment

of the two silicon pieces prior to bonding would be required to ensure localization of the covered features. Because this process was subtractive, and the substrate material (silicon wafer) would become the individual units, a selective lift-off process was not possible. Instead, each unit had to be physically separated from the substrate by dicing the wafer into pieces with a thin saw blade, defining the size of each unit. Backside grinding/polishing to thin each of the two silicon wafer substrates (each 500 µm thick) prior to bonding and/or dicing was required to reduce the overall thickness and size of the final unit (450 µm thick, compared to 75 µm thick for the nickel box).

Because the bonding process for the two wafers required alignment, visible features would need to be patterned in the top wafer. As a result of this required step, it was decided that in addition to alignment marks, deep notch features would also be patterned for every other row of boxes in the top wafer. The presence of this notch feature would facilitate alignment of the two overlapping wafers, as features from each wafer could be seen with an infrared (IR) camera. The presence of this notch feature on the top of the completed box also assisted with the physical alignment of the box and luer needle/drive cable during assembly. Given the known needle cannula and drive cable dimensions (Figure 2.18, 19) this notch would allow the thickness of the box between the inner channel and the drive cable to be controlled. This improved alignment prevented flexion in the microtweezer body from its attachment point on the luer needle (Figure 2.19), reduced strain place on the box surfaces by the microtweezer body, and potentially improved actuation performance.

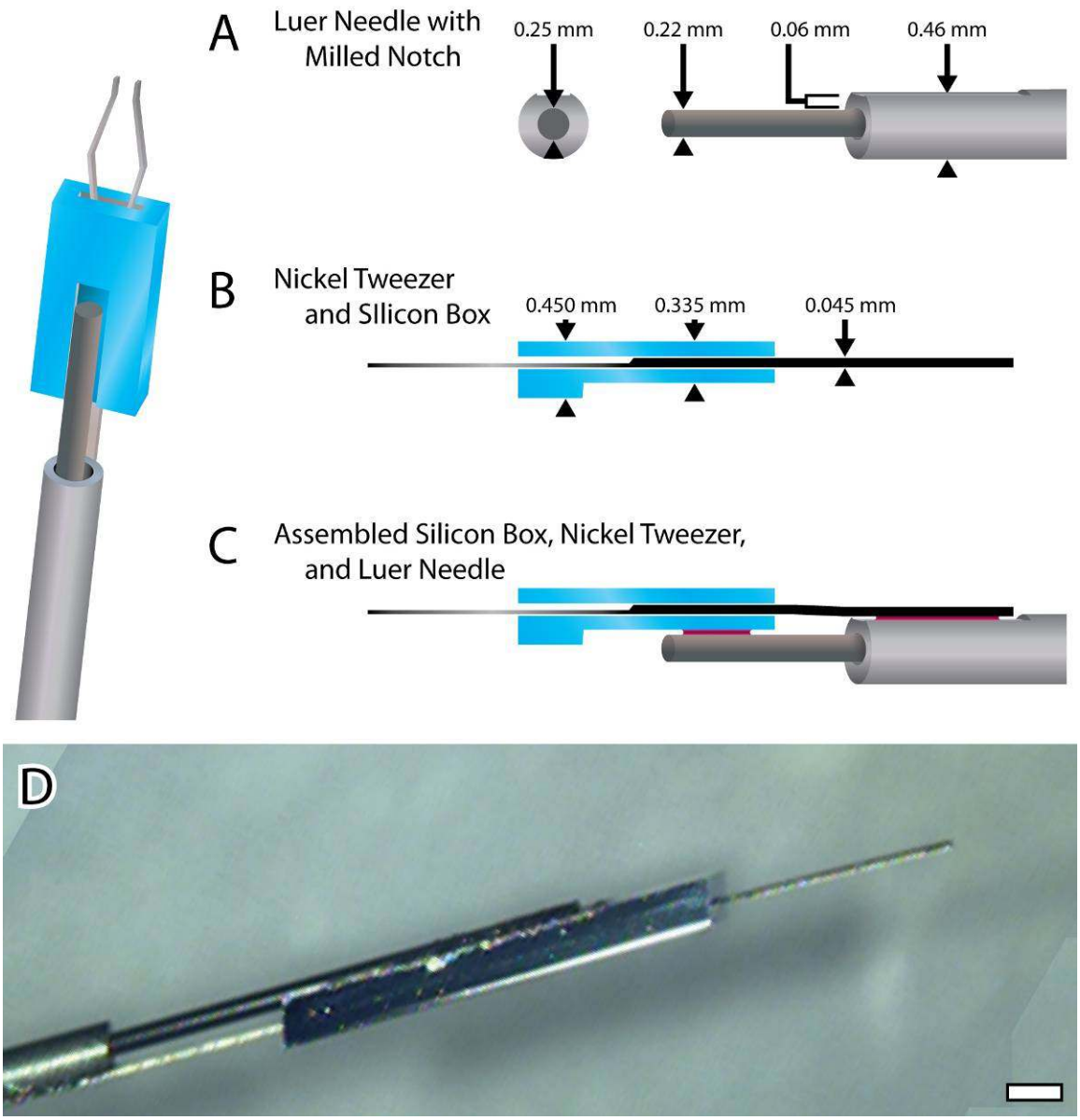


**Figure 2.19**: (A, B, C) Cartoon and (D) bright field photograph depicting the vertical alignment of the box, tweezer body, and luer needle for assembly. The thickness of the different microfabricated parts can affect the angle at which the tweezer lies due to its attachment to the top of the luer needle, and its position in the box channel. This cartoon also depicts the presence of a micromilled notch in the luer needle cannula (described in Chapter 3), and the use of a multi-layered microtweezer body. In addition to improving vertical alignment of the tweezer, the presence of these physical features in the box and needle assisted with alignment and consistency during assembly. Scale bar is 500 µm.

The final fabrication process for the microtweezer boxes started with the etching of the channel in the top surface of a 500 μm thick silicon wafer (Figure 2.20A-D). This required the patterning of a protective photoresist layer to define the planar geometry of the channel. The exposed regions of the silicon were preferentially etched using an ICP etching Bosch process that utilized $SF_6$ gas in a plasma field to remove silicon. The protective photoresist material was minimally etched during this process as well, so a thick layer (15 μm) was patterned to ensure that the resist would endure the etching of the entire channel. After the etching of the channel, the photoresist was stripped using a photoresist remover, and the wafer was then piranha-cleaned. These process steps were repeated for patterning the notch features in the second/top wafer. Bottom wafers with channel depths of 50 μm, 100 μm, and 150 μm were etched (Figure 2. 20). A consistent notch depth of 115 μm was etched into each top wafer, which was roughly half of the final thickness of this wafer following backside grinding/polishing (each wafer was ground to 225 μm). The scaled geometries and dimensions of the completed silicon microtweezer box are depicted in Figure 2. 21 and Table 2.4.

Given the lack of expertise in aligned fusion bonding in the cleanroom facility used, this bonding step was performed by a regional microfabrication foundry that accepts small-batch jobs for research and start-up companies (MEMSCAP, NC, USA). They were contracted to bond multiple sets of wafers; two sets that had 50 μm deep channels, one set with 100 μm deep channels, and one set with 150 μm deep channels (Figure 2.22-25). The bonding of a fifth set failed due to the top wafer cracking, which resulted from the previous backside polish thinning. Prior to the bonding of the each wafer set, each top wafer (with the notch feature) was backside polished to a thickness of

225 µm (Figure 2.20D). Following bonding, the wafers were fusion annealed to increase the adhesion strength of the bond (Figure 2.20E-F, Figure 2.24). The bottom wafer was then backside polished so that the entire device thickness was 450 µm (making the bottom wafer 225 µm thick) (Figure 2.20G). The bonded wafers were then diced into the individual units (Figure 2.20H, Figure 2.25). The maximum yield from a 4-inch wafer-set was roughly 500 units.

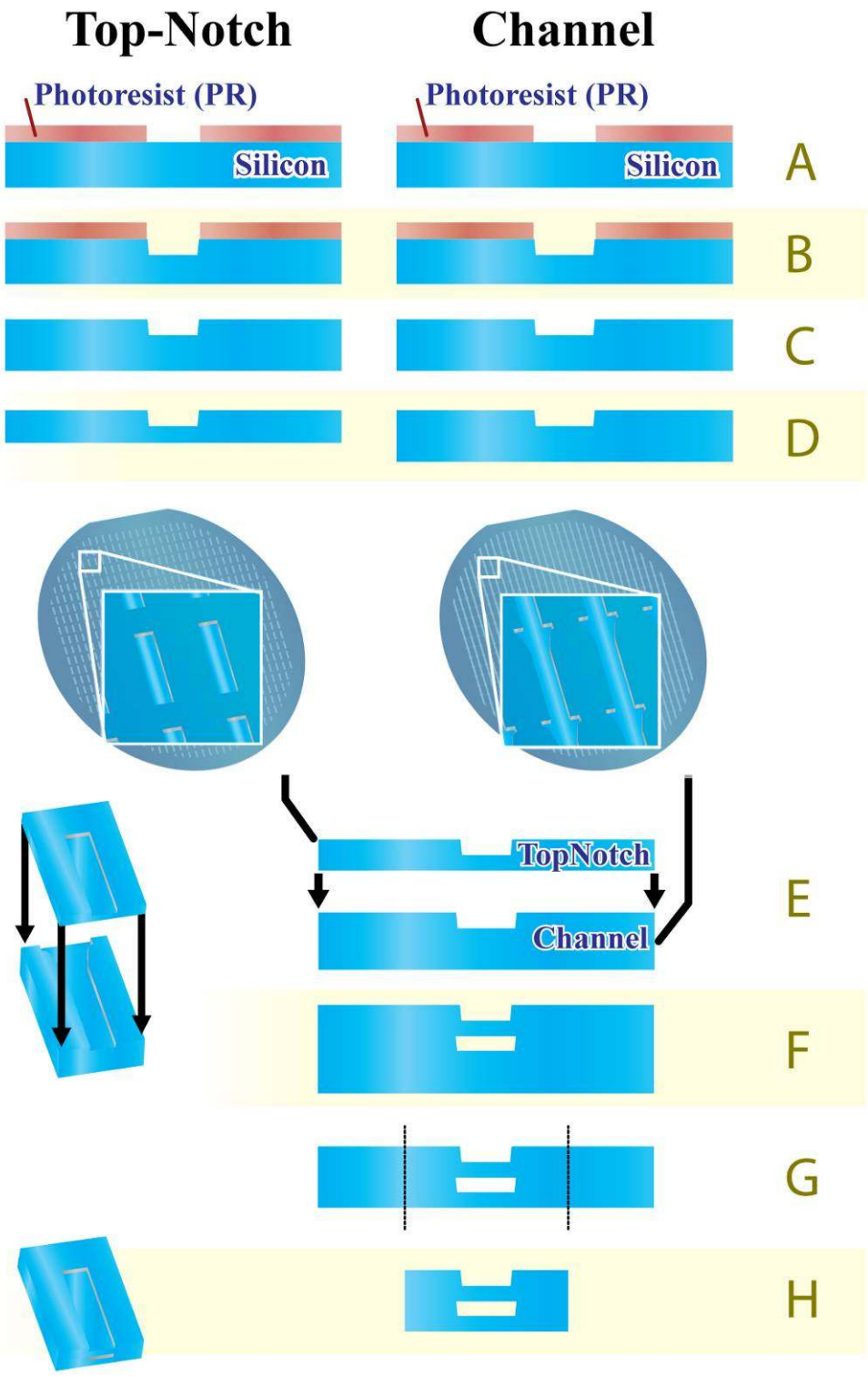


**Figure 2.20**: Fabrication process flow for the silicon microtweezer box.

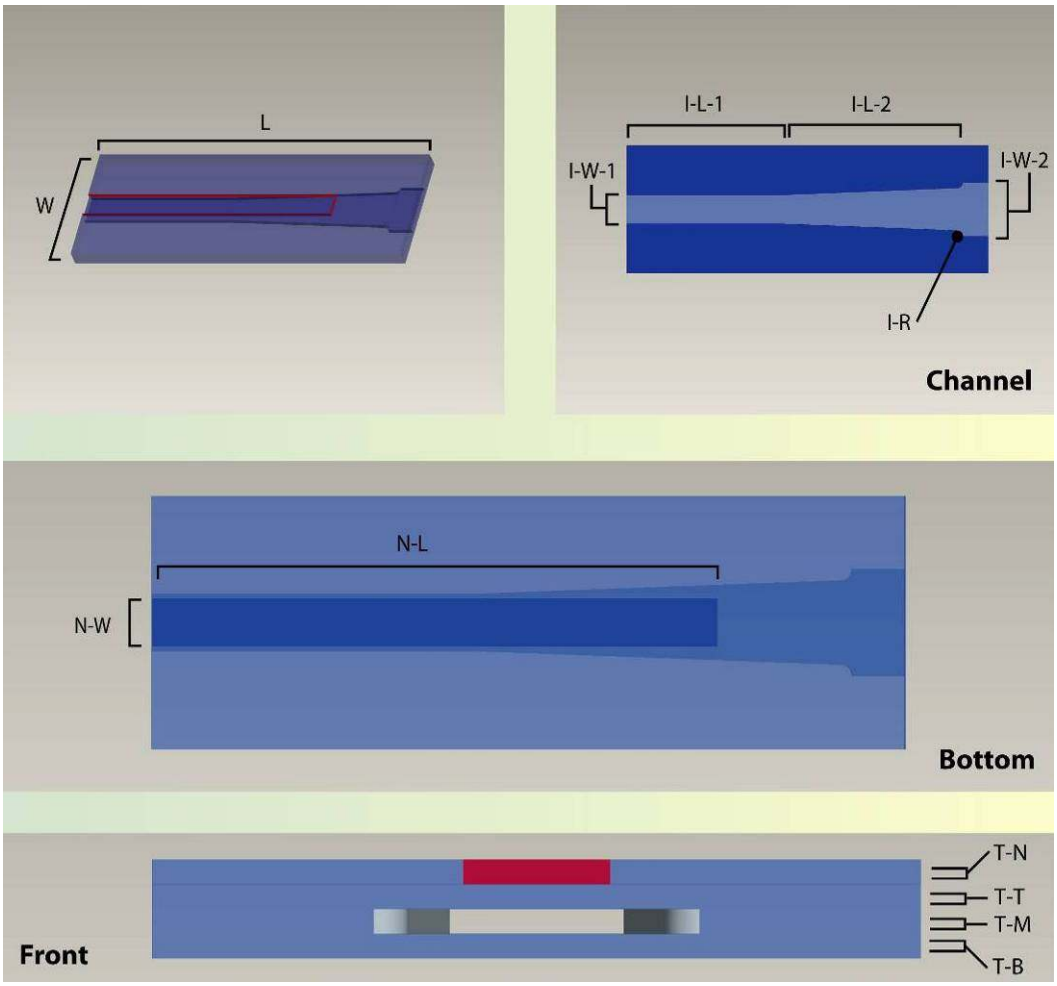


**Figure 2.21**: CAD drawings of the completed silicon box and the relative locations of the alignment notch feature on the top of the box and the channel that runs the length of the box.

**Table 2.4**: Table highlighting the dimensions of the complete silicon box depicted in Figure 2.21. Because these dimensions were determined by dicing, the starred (*) items were confirmed with microscopy.

## Silicon Box Dimensions

| | | |
|---|---|---|
| **Box** | | |
| Length | ( L ) | 4.37 mm* |
| Width | ( W ) | 1.52 mm* |
| Thickness - Notch | ( T-N ) | 115 µm |
| Thickness - Top | ( T-T ) | 110 µm |
| Thickness - Channel | ( T-C ) | *varies* |
| Thickness - Bottom | ( T-B ) | 225 µm – 'T-C' |
| **Channel** | | |
| Width - Back | (I-W-1) | 330 µm |
| Width - Front | (I-W-2) | 650 µm |
| Length - Channel | ( I-L-1 ) | 2.09 mm |
| Length - Overdrive | ( I-L-2 ) | 2.225 mm |
| Radius - Drive Contact | ( I-R ) | 70 µm |
| **Notch** | | |
| Width | ( N-W ) | 300 µm |
| Length (from back) | ( N-L ) | 3.575 mm |

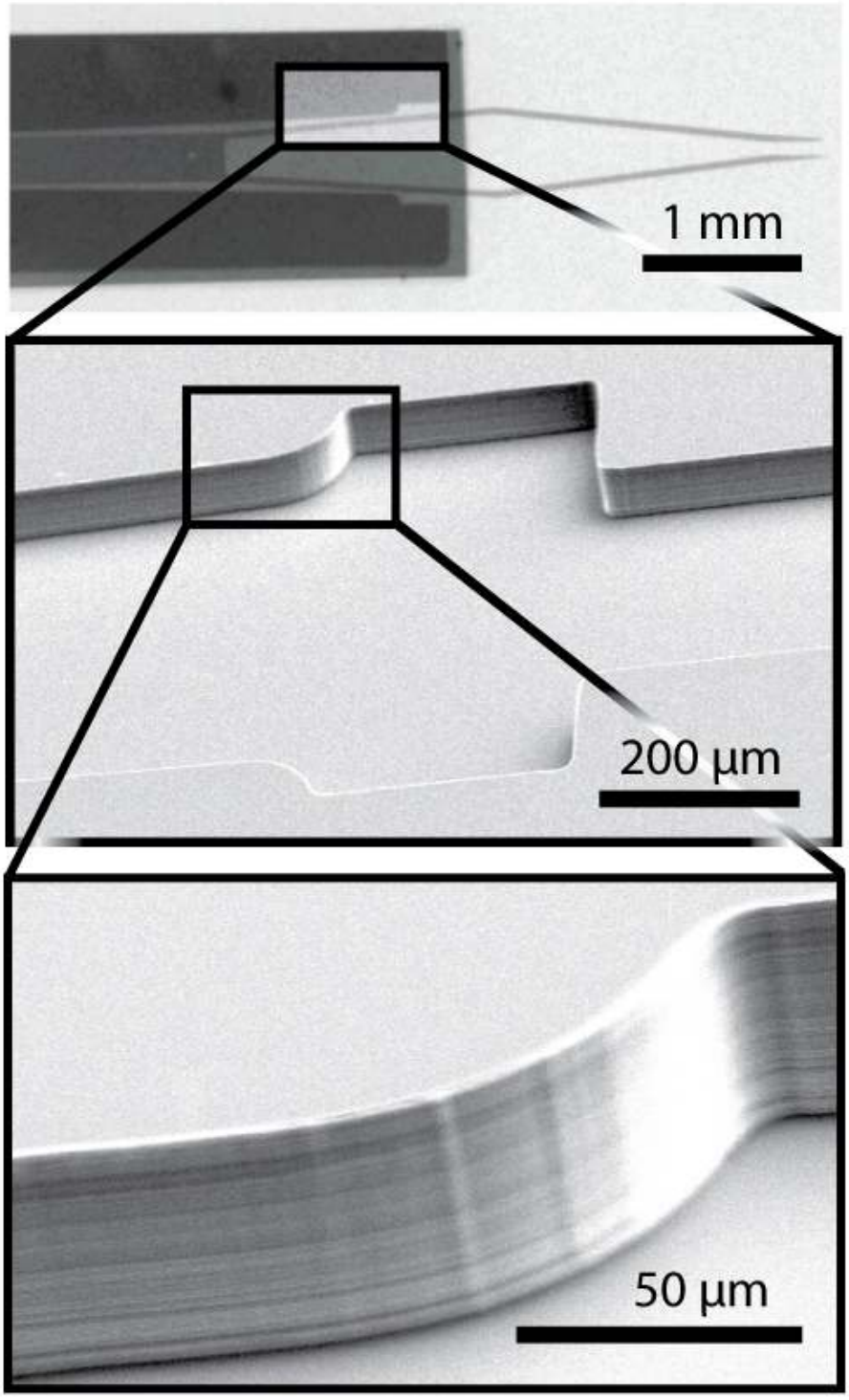


**Figure 2.22**: X-Ray of assembled microtweezer (top, microtweezer device with nickel box, for reference purposes only), and SEM images of an exposed silicon box channel wall (middle and bottom). Visual inspection shows vertical ICP etching lines from the Bosch process can be seen on the wall.

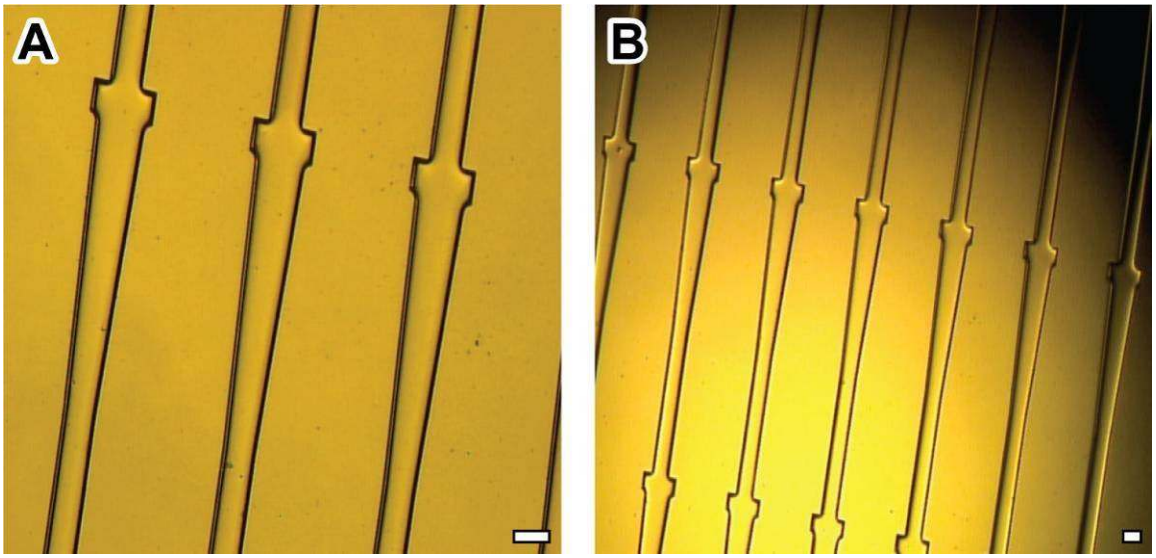


**Figure 2.23**: Bright-field photo of the channel features patterned in rows on the "bottom" silicon wafer.

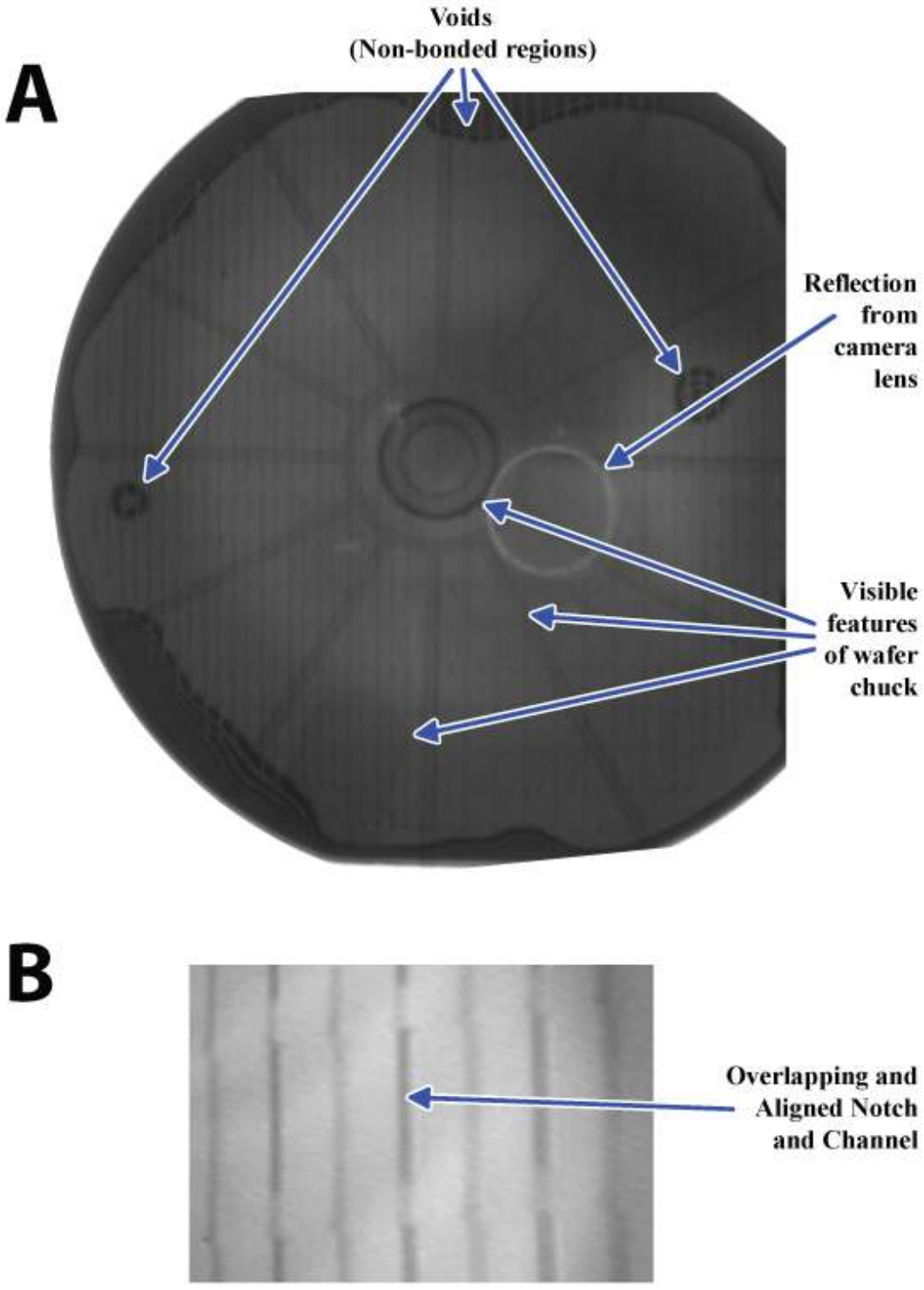


**Figure 2.24**: Infrared images of the top (notch) and bottom (channel) bonded wafers. (A) Roughly 80% of the surface area of overlapping area was bonded, and (B) alignment of the notch and channel was successful.

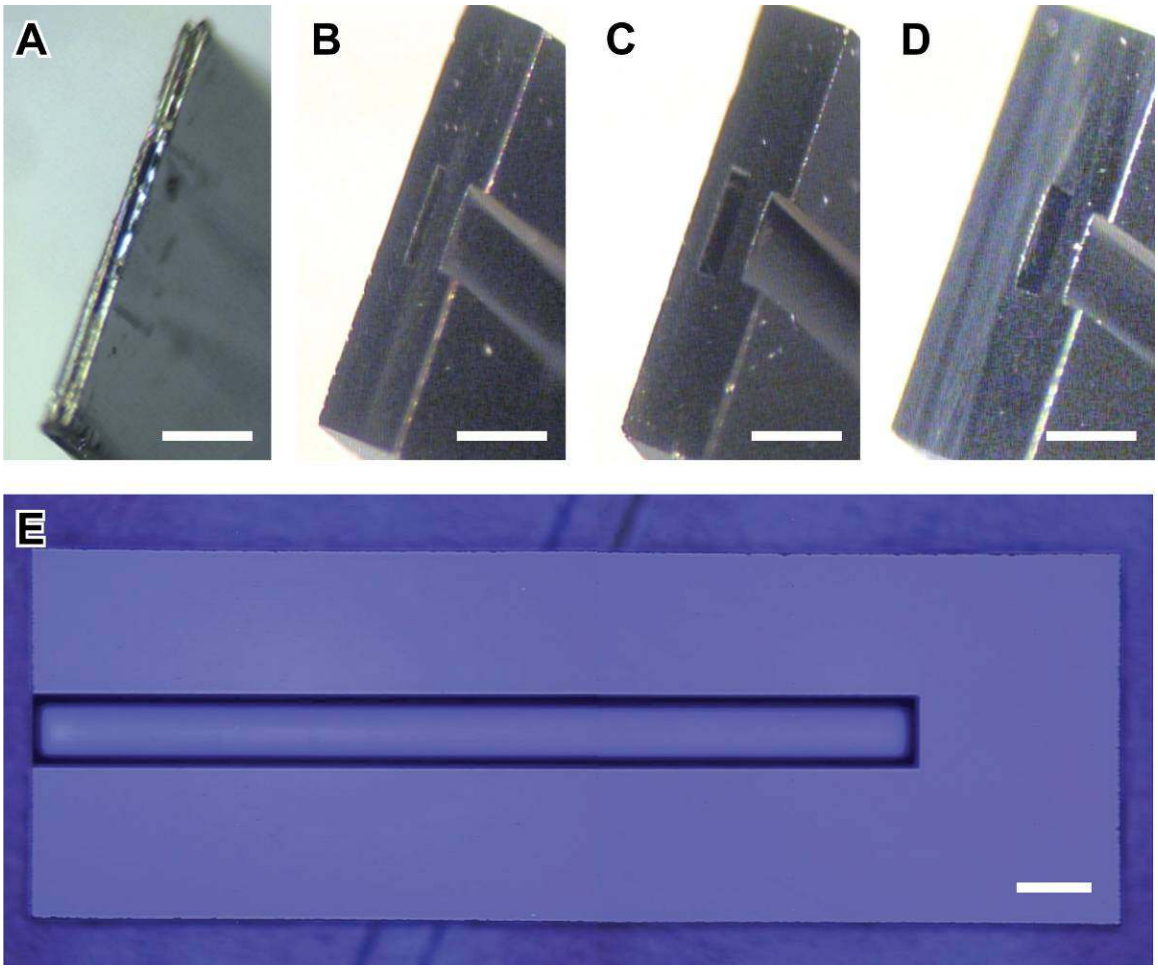


**Figure 2.25**: Bright-field photos of the various channel thicknesses of the (A) nickel box (25µm) and silicon boxes (B: 50 µm, C: 100 µm, D: 150 µm), and a dark-field photo of the silicon box notch (E). To note: the backside polishing of the silicon box with the 150 µm channel was not complete, resulting in a much thicker bottom portion of the box. All scale bars are 300 µm.

While the co-efficient of static friction between nickel and silicon (~0.8) was already relatively low, the incorporation of physical features in the floor of the silicon box channel, such as patterned texture, could reduce the surface area of the contact between the tweezer body and box channel, and reduce the total frictional force resisting relative motion [140]. Creation of these features, however, would require photoresist patterning inside the channel, which could result in photoresist residue present in the channel of final device. Additionally, the texture of the top side of the nickel electroplated surface would already reduce friction against the flat surface of the crystalline silicon channel.

### 2.4.3 - Electroplating Processes

The electroplating step in the fabrication process allowed the patterned growth of the nickel tweezer and box layers. The total thickness of these layers was a function of electroplating current charge density, time, and electroplating material (Ni, Cu, Au, etc.) and bath.

The thickness of an ideally performing tweezer was contingent on a compromise between: (1) a low-friction interface between the tweezer beam and box channel; and, (2) minimal vertical snugness within the channel that would prevent vertical shifting, axial rotation, and length-wise tilting of the tweezer during actuation and positioning. The box channel cross sectional geometry was rectangular in shape, and thus a uniform electroplating surface that resulted in a tweezer with a rectangular shape would provide the best fit.

#### 2.4.3.1 - Current Supply and Charge Density

This electroplating surface uniformity depended on a variety of factors, including the plating current density during electroplating, which was a product of the total current supplied to the electroplating surface and the total surface area. This current density, which determined the amount of charging on the surface to promote metal growth, was used to determine how quickly the deposited metal layer will grow. By using Faraday's Law and calculating for volume deposited, which considers atomic weight and valence, and material density, many simplified formulas have been derived for the plating of various materials. The thickness of nickel deposited per minute of electroplating was approximated using such a formula (2.1), which was verified by multiple runs [141].

$$h = (0.205) \cdot c \cdot J \cdot t \tag{2.1}$$

where,

h = height of electroplated layer

c = coefficient of cathode efficiency (usually above 0.95)

J = electric current density ($A/dm^2$)

t = time (minutes)

Thus, a power source supplying 100 mA of current to the electroplating seed layer on a 4" wafer with 0.50 $dm^2$ of unit surface area resulted in a current density of 0.196 $A/dm^2$ and a plating rate of 2.29 µm/hour (Table 2.5).

**Table 2.5**: Table of dimensions and quantities of specific units on a sample wafer, which were used to determine the total surface area of exposed electroplating seed layer. This value was used to determine the current density on this surface, which is dependent on the current supply. The plating rate (height per time) can then be calculated, and final expected thickness based on the total electroplating time.

Sample Features Dimensions (on 4" wafer)

| | Main Dimensions L | Main Dimensions H | Accessory Dimensions $L_1$ | Accessory Dimensions $H_1$ | Accessory Dimensions $L_2$ | Accessory Dimensions $H_2$ | Surface Area | # | Total Area ($mm^2$) | Total Area ($dm^2$) |
|---|---|---|---|---|---|---|---|---|---|---|
| Tweezer | | | (beams - added) | | | | | | | |
| 300 μm wide body | 0.3 | 14.13 | 0.04 | 3.48 | 0.10 | 0.2 | 4.398 | 432 | 1900.0 | 0.1900 |
| 600 μm wide body | 0.6 | 14.13 | 0.04 | 3.52 | 0.04 | 0.25 | 8.629 | 32 | 276.1 | 0.0276 |
| | | | | | | | **Total Area:** | | 2035.4 | **0.2176** |
| Box - Bottom and Top Layer | | | | | | | | | | |
| 330 μm wide channel | 1.572 | 4.7 | | | | | 7.388 | 309 | 2283.0 | 0.2283 |
| 370 μm wide channel | 1.572 | 4.7 | | | | | 7.388 | 82 | 605.8 | 0.0606 |
| 370 μm wide channel, long channel | 1.572 | 6.7 | | | | | 10.532 | 179 | 1885.3 | 0.1885 |
| 670 μm wide channel | 2.272 | 4.7 | | | | | 10.678 | 29 | 309.7 | 0.0310 |
| | | | | | | | **Total Area:** | | 5083.8 | **0.5084** |
| Boxes - Channel Layer | | | (channels - subtracted) | | | | | | | |
| 330 μm wide channel | 1.572 | 4.7 | 0.37 | 2.02 | 0.65 | 2.69 | 4.886 | 309 | 1509.6 | 0.1510 |
| 370 μm wide channel | 1.572 | 4.7 | 0.33 | 2.02 | 0.65 | 2.69 | 4.970 | 82 | 407.6 | 0.0408 |
| 370 μm wide channel, long channel | 1.572 | 6.7 | 0.37 | 4.01 | 0.65 | 2.69 | 7.286 | 179 | 1304.1 | 0.1304 |
| 670 μm wide channel | 2.272 | 4.7 | 0.67 | 2.02 | 1.23 | 2.69 | 6.007 | 29 | 174.2 | 0.0174 |
| | | | | | | | **Total Area:** | | 3395.5 | **0.3396** |

Electroplating Characteristics

| | Plating Area ($dm^2$) | Current (A) | Current Density ($A/dm^2$) | Time (h) | Expected Thickness (μm) |
|---|---|---|---|---|---|
| Tweezers | 0.2176 | 0.100 | 0.4595 | 3.5 | 18.79 |
| Box (Bottom, Top) | 0.5084 | 0.100 | 0.1967 | 13.0 | 29.88 |
| Box (Channel) | 0.3396 | 0.100 | 0.2945 | 8.5 | 29.25 |

When considering different end-applications for electroplating, such as: (1) electrical functionality; (2) prescribed surface area and topography; or, (3) comprehensive thin-layer, deep-channel, and small-feature coverage; using a more advanced bi-phasic current supply is ideal to provide uniform and complete depositions. During such a process, the current direction will change, dedicating specific amounts of time to charging the surface to promote deposition of metal atoms, and then specific amounts of time charging the surface to promote the removal of metal atoms. Because the deposition and removal of metals ions was dependent on localized availability of charges and metal atoms, these loading and unloading cycles would result in a more uniform surface. For example, areas on the electroplating surface that were adjacent to the mold, or that were generally smaller in feature size, would experience less material flow and availability, and will subsequently electroplate more slowly. Over the course of the electroplating time these areas will experience less material flow and less metal deposition than areas toward the center of the electroplating mold where flow is not constrained. Without a discharging cycle, this will eventually result in a lack of uniformity in total electroplating thickness. As a result, it is likely that minor factors such as distributed feature size and edge-length-to-area ratio could similarly affect the speed of electroplating and overall surface uniformity.

The equipment setup that was being used for our specific electroplating process did not have pre-programmed functionalities to create a repeating bi-phasic current supply. However, for our specific application, which did not include deep channels (even at the end of the tweezer tip, which only had a radius of curvature of 1um), direct current (DC) supply sufficed in providing relatively uniform surface deposition. This was

demonstrated as variations in deposition ranging 2-5um from 25um of total electroplating thickness were seen over the 300um width of a tweezer. This is roughly 10-20% of the total thickness, which would suggest a possible impact on cross sectional geometries, and resultantly, the moment of inertia of a tweezer beam during deflection. However, these variations consistently appeared at the edge of the tweezer, near the photoresist-electroplated material interface, and did not impact the adherence of the electroplated shape to the photoresist mold. Additionally, these variations in the edges of the tweezer would likely result in a reduced contact area between the tweezer beam and channel, which would result in less friction while during actuation.

2.4.3.2 - Electroplating Surface Pretreatment

Depending on the material used for the electroplating seed layer, specific chemical treatments were required to condition the surface to facilitate electrical conductivity, which promoted uniform and undisturbed electroplating. The presence of oxidized regions on the electroplating surface affected the entire electroplating process, as the oxidized regions did not facilitate electroplating and resulted in large irregularities on the electroplating surface. Subsequently the total electroplating surface reduced in area, which altered the plating current density and affected the electroplating surface uniformity and the rate of deposition. When using a metal seed layer that readily oxidized in the presence of air, such as copper and aluminum, removal of this less-conductive oxidation layer with immersion in an oxide etchant bath was required prior to immersion in the electroplating bath.

2.4.3.3 - Electroplating Bath

In addition to current supply function, plating current density, surface area, and pretreatments of the electroplating seed layer, there were a few other considerations that affected the condition of the electroplated material surface, most notably the plating bath condition. The electroplating bath needed to be free from contaminants and debris, and the chemistry needed to be maintained.

Variable size molecules in the electroplating bath created nucleation sites on the sample surface that grew into bubble-like features, creating an uneven topography on the surface. Deposited impurities on the electroplating surface also affected the subsequent deposition of additional metal, creating pits in the final electroplating surface. The bath needed to be constantly filtered to reduce the presence of these contaminants. The pH of the bath needed to be maintained as well, which was important to the electrochemical mechanics of the nickel anode – nickel sulfamate bath – sample interactions. A brightener solution that contained chrome was added to the electroplating bath to provide a smaller grain size and smoother finish on the surface (Figure 2.26).

The electroplating bath container itself needed to be deep enough to allow the vertical immersion of both the sample wafer (cathode) and the nickel anode (Figure 2.27). The sample wafer had a patterned contact pad on the large flat that resided above of the bath fluid line and allowed electrical connection to the electroplating seed layer. The patterned features of the wafer for the individual units were immersed in the bath and were plated. Both electrical connection and physical holding of the wafer was accomplished with the use of a stainless steel alligator clip. The nickel anode was placed inside of a polypropylene bag that acted as a filter to prevent the entrance of large nickel particles from the anode into the bath. This bag also supported the weight of the

2”x4”x0.25” metal bar which was not readily supported by an alligator clip like the wafer. The stirring rod was rotated at a slow rate (lowest setting) to ensure continuous fluid flow within the bath to allow distribution of nickel ions.

The materials present in the electroplating bath provided a buffered, metal ion rich medium in which to promote the deposition of metal onto charged surfaces that were submersed. Even without the presence of a current, precipitation of materials within the bath was possible, so constant agitation was supplied by the stirring rod to reduce this change in the plating bath chemistry and composition. Air-tight containment was used to prevent evaporation, which would also result in precipitation.

During electroplating, while the application of stirring would promote material flow throughout the electroplating bath, which facilitated the deposition of metal ions, the speed of movement of the bath could affect the flow of ions, and thus uniformity of deposition. The stirring flow was circular within the bath. Given the shape of the wafer substrate that contained the electroplating surface and the depth and aspect ratio of the electroplating molds, a trapezoidal flow gradient could start to appear over the features in the electroplating surfaces, resulting in poor plating uniformity. Tailoring the electroplating speed to both maintain bath agitation and promote non-gradient forming material flow was required.

2.4.3.4 - Anode Material, Conditioning

A 2”x4”x0.25” sized anode composed of 99% nickel was used in these electroplating processes. The anode was placed inside of polypropylene bag that acted as a filter to prevent the deposition of large metallic particles that might come off of the nickel anode (Anode Products Company, Inc, IL, USA). These bags were designed for

use in nickel electroplating baths that were maintained under 200$^{o}$ F. They had good resistance to alkalies, mineral acids, organic acids (boric acid in nickel sulfamate solution), oxidizing agents, and organic solvents. This bag was napped on one side, which could provide filtered protection for the directional ion flow present between the anode and sample (cathode).

2.4.3.5 - Wafer Backside Preparation

Following the change in the substrate from non-conductive glass pieces to conductive silicon wafers, the deposition of metal onto the backside of the wafer needed to be considered to allow for better controls and consistency. Because silicon was not as conductive as the seed layer, its distribution and predictability of surface charging was limited. Because a constant current value was supplied using a power source, any charge distributed away from the electroplating seed layer reduced the thickness of the front-side plating. If the plating thickness was not within compliance, additional plating processes would have to be completed to achieve the final thickness. As previously discussed, the addition of subsequent layers of separately electroplated nickel could introduce structural weaknesses in the units, and would ideally need to be avoided. Thus, complete prevention of any backside electroplating was required to ensure consistent feature patterning.

Originally, a sheet of blue silicon wafer tape was applied to the back of the wafer to act as a physical cover. Following immersion in the electroplating bath, however, the adhesion of this tape was compromised along the edges, and air and fluid pockets could form. This could still permit some backside deposition and affect the plating thickness

for the sample. Fresh pieces of tape would be required for each electroplating process, and given the inconsistency in coverage, an improved process was required.

The introduction of an additional photolithography step to electrically isolate the wafer backside was attempted. While the sacrificial photoresist deposition did limit the ability of the backside of the wafer to receive a charge, the blanket metal deposition processes could coat the edge of the wafer and re-establishing the electrical connection. A coating of a non-conductive material to cover the backside was the most successful process. This material would have to be resistant to all of the fabrication processes prior to electroplating. As previously mentioned, using a PECVD process, a layer of silicon nitride was deposited onto the backside prior to any other deposition processes. This layer remained intact throughout the entire process and completely prevented any electroplating of metal on the backside (Figure 2.28).

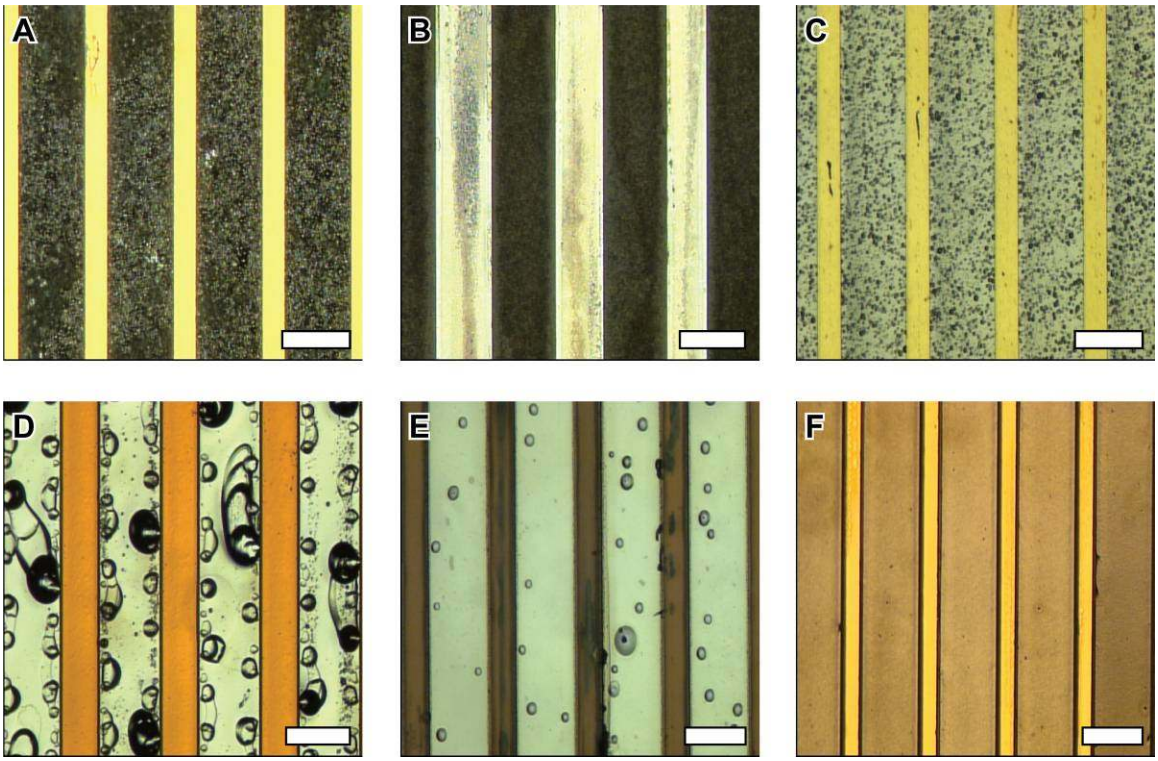


**Figure 2.26**: Bright-field photos of the different surface textures and features given the different conditions of the nickel sulfamate electroplating bath: (A) unfiltered nickel sulfamate without chrome brightener, (B) filtered nickel sulfamate without chrome brightener (dark region is nickel), (C) nickel sulfamate with chrome brightener, (D) nickel sulfamate with chrome brightener, old nickel anode causing particulate depositon, (E) incompletely etched oxide layer on seed layer surface preventing electroplating except at pin-holes, and (F) filtered nickel sulfamate with chrome brightener, anode in a polypropylene anode filtering bag. All scale bars are 300 μm.

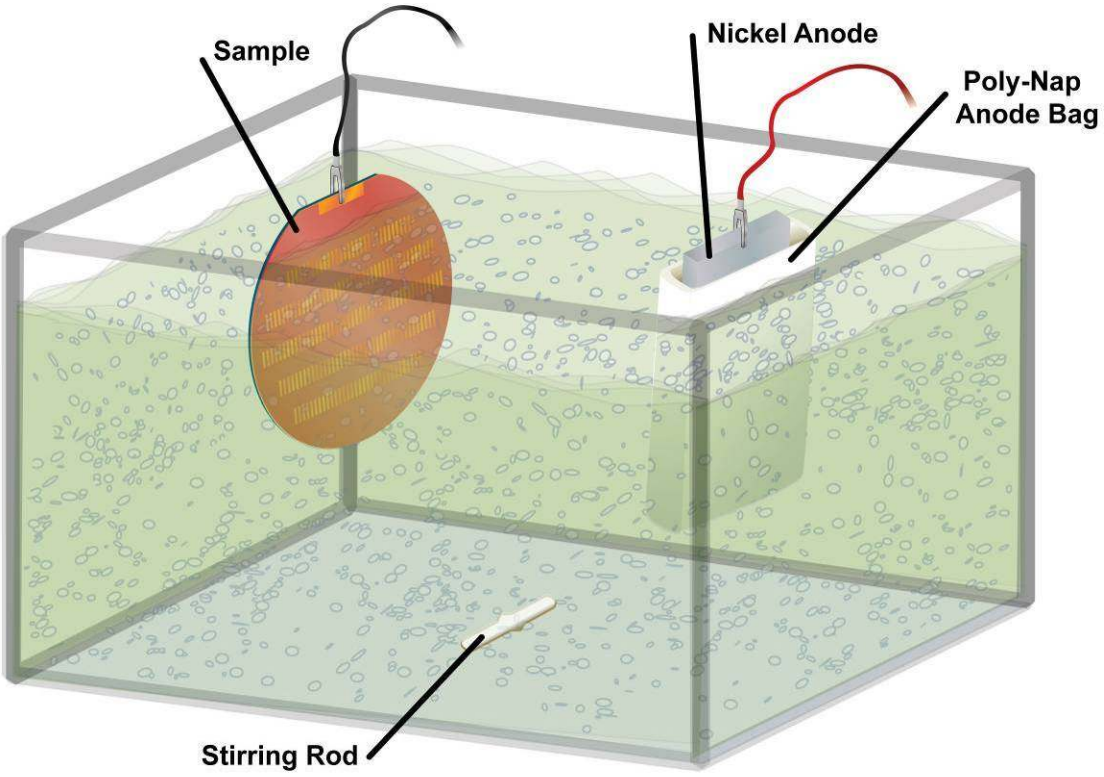


**Figure 2.27**: Cartoon of the electroplating bath setup. The sample wafer had a patterned contact pad on the large flat, which resided above the bath fluid line and allowed electrical connection to the electroplating seed layer. The patterned features of the wafer for the individual units were immersed in the bath and were plated. The nickel anode was placed inside of a polypropylene bag that acted as a filter to prevent the entrance of large nickel particles from the anode into the bath. The stirring rod ensured continuous fluid flow to allow distribution of nickel ions in the bath.

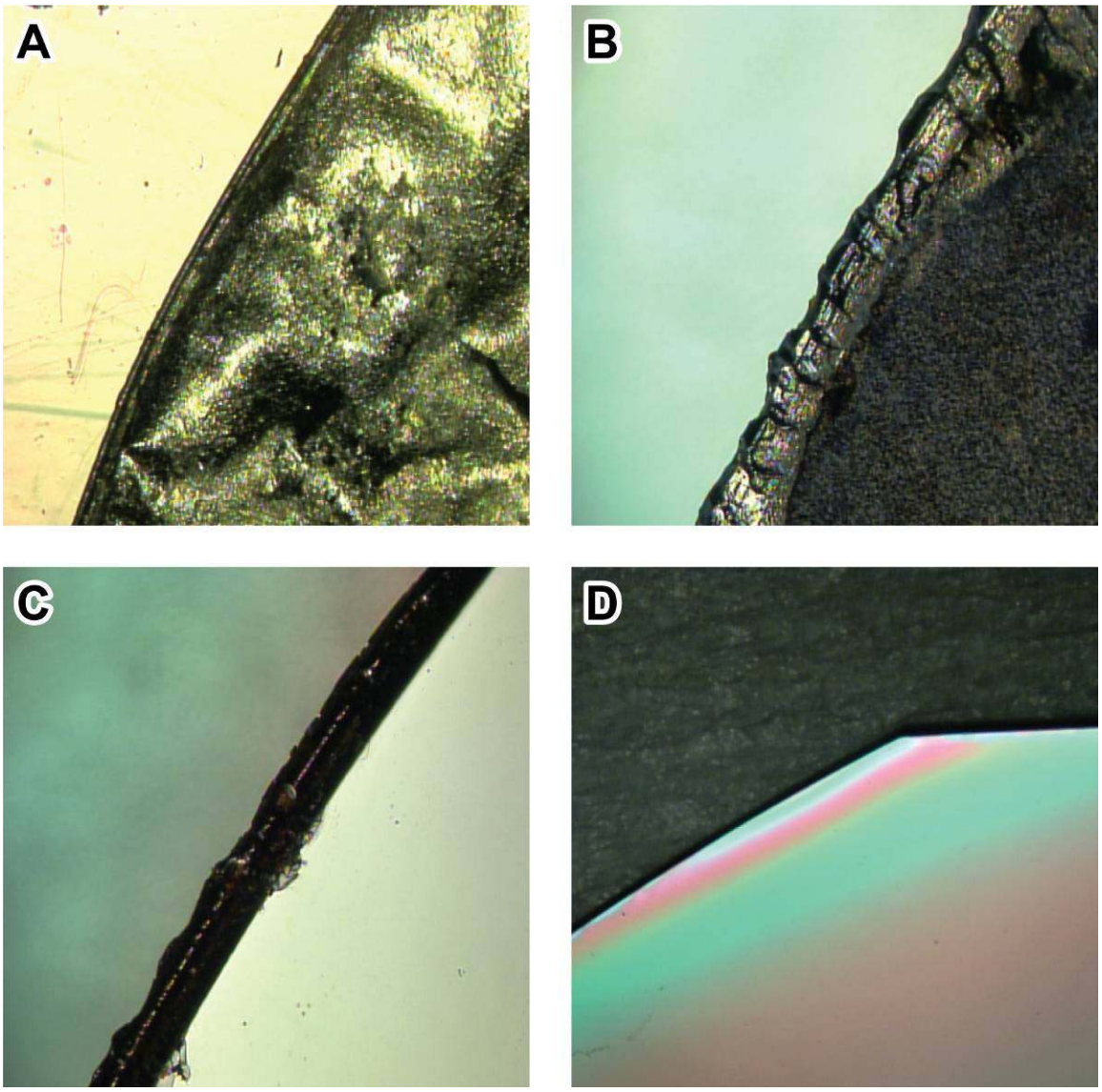


**Figure 2.28**: Bright-field photos of the backside of wafers following different pre-electroplating preparation: (A) bare silicon wafer with no preparation, which resulted in extensive but inconsistent backside deposition, (B, C) silicon wafer with the backside covered in blue wafer tape, which was marginally but inconsistently successful in limiting backside deposition, and (D) silicon wafer with silicon nitride deposited on backside, which resulted in no backside deposition.

### 2.4.4 - Assembly Process - MEMS Microtweezer Box and Body

After the individual microtweezer body/tips and boxes were fabricated, they were then assembled together (Figure 2.29). Assembly required an optical stereoscope, a jig to hold the boxes (and a standing clamp to hold the jig), and hand-held forceps to manipulate and position the tweezer body to be inserted into the box. This assembled MEMS microtweezer device could then be attached to the luer needle mechanical packaging.

An x-ray of the assembled tweezer and box and a bright-field photo of the interface between the tweezer and box are shown in Figure 2.30.

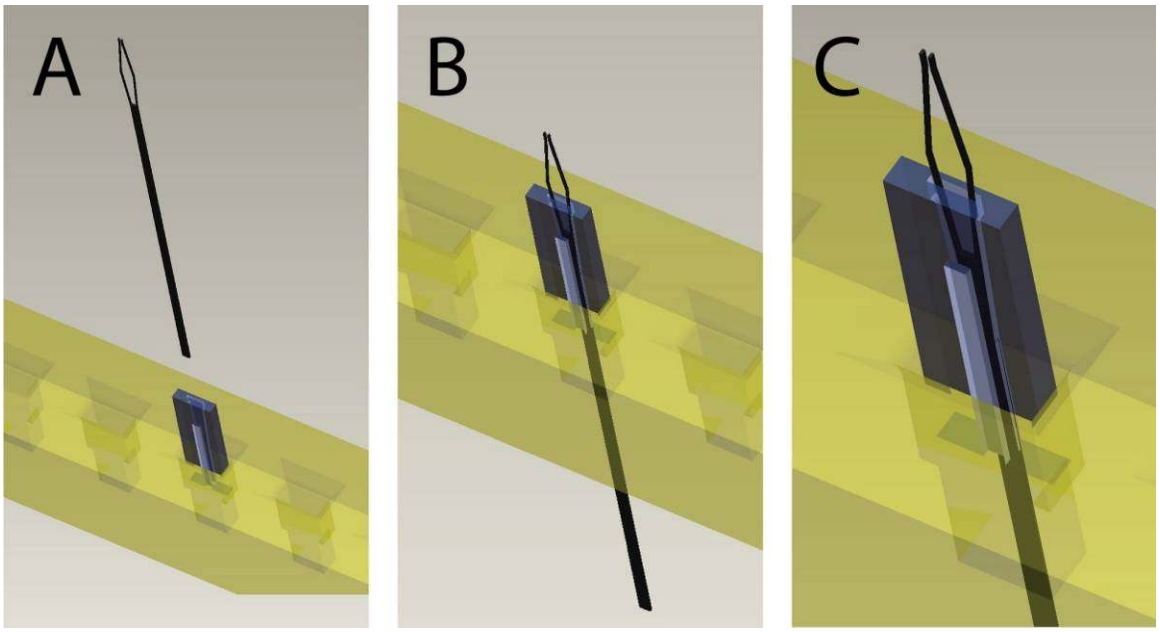


**Figure 2.29**: Assembly process for inserting the microtweezer body and tips into the microtweezer box (A-C). A custom fabricated jig with multiple slots is used to isolate the microtweezer box to facilitate insertion. Forceps are used to hold the microtweezer as it is inserted into the box.

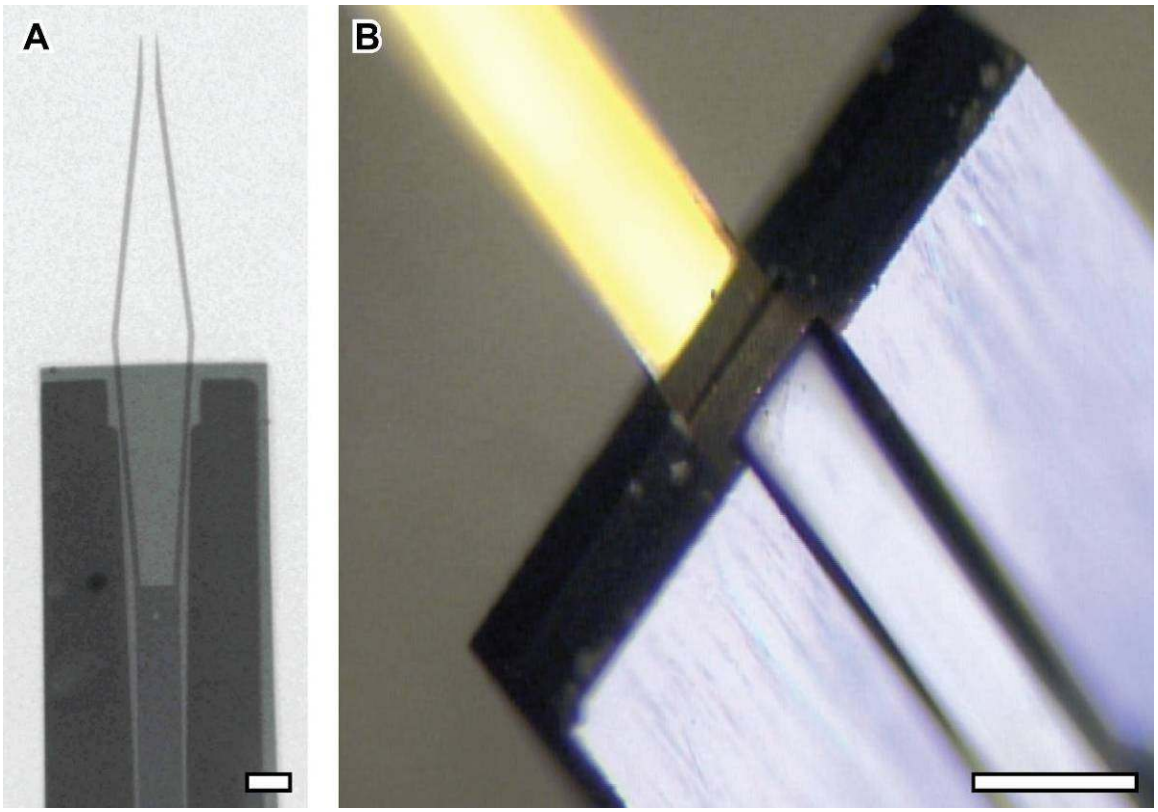


**Figure 2.30**: (A) X-ray of the assembled MEMS microtweezer (nickel box) and (B) bright-field photo showing the rear interface between the inserted tweezer and the box (silicon). The notch, which was used as an attachment point for the drive cable, can be seen. All scale bars are 300 μm.

# CHAPTER 3

# MEMS MICROTWEEZER PACKAGING AND CONTROLLER DEVELOPMENT

## 3.1 - Introduction

This chapter covers the development of the microtweezer tool packaging, mechanical controller that docks the packaged microtweezer, and linear actuator that powers the system actuation. The incorporation of a commercial staging system that positions and orients the complete system is also discussed. Modularity was integrated into each component and into the interfaces between each component so that, like the MEMS microtweezer, these systems could be developed both iteratively and in parallel. In this chapter, the components and their design cycles are presented independently, starting with the microtweezer packaging, then controller and linear actuator, and finally the stage.

## 3.2 - MEMS Mechanical Packaging

Independent of device or use, one of the most critical aspects to MEMS manufacturing is developing an interfacing mechanism, or package, that provides important application-dependent functionalities, such as physical and environmental protection, translation of mechanical movement, and electrical connectivity [142]. Packaging in MEMS, semiconductors, and biomedical devices is particularly important as it typically accounts for over 70% of the cost/development of the final device [143]. Thus, tool packaging for microscale devices needs to be considered at all stages of development to create a reliable and successful device.

These sections outline design considerations for the microtool package and successful implementation of these designs. General design features are examined first, followed by a description of the major design iterations, the materials used, and the construction of the final design.

### 3.2.1 - Features

This section will explain the major elements of the packaging design, which covers the functional connectivity to both the MEMS microtweezer and the mechanical controller. The motivation for design modularity is discussed, and a general description of the final packaging design is provided.

#### 3.2.1.1 - Modularity of Design

The original microtweezer packaging design consisted of the microtweezer components directly connected to a simple micrometer head controller [136]. In this arrangement, one side of a tether-cable sleeve was glued to the assembled MEMS microtweezer device and the opposite end was glued to the end of a manual micrometer head (Figure 3.1). While this setup allowed for preliminary functional assessment of the tweezer performance, it had no modularity in design, and as soon as the MEMS device was damaged during a test, the entire device had to be disassembled.

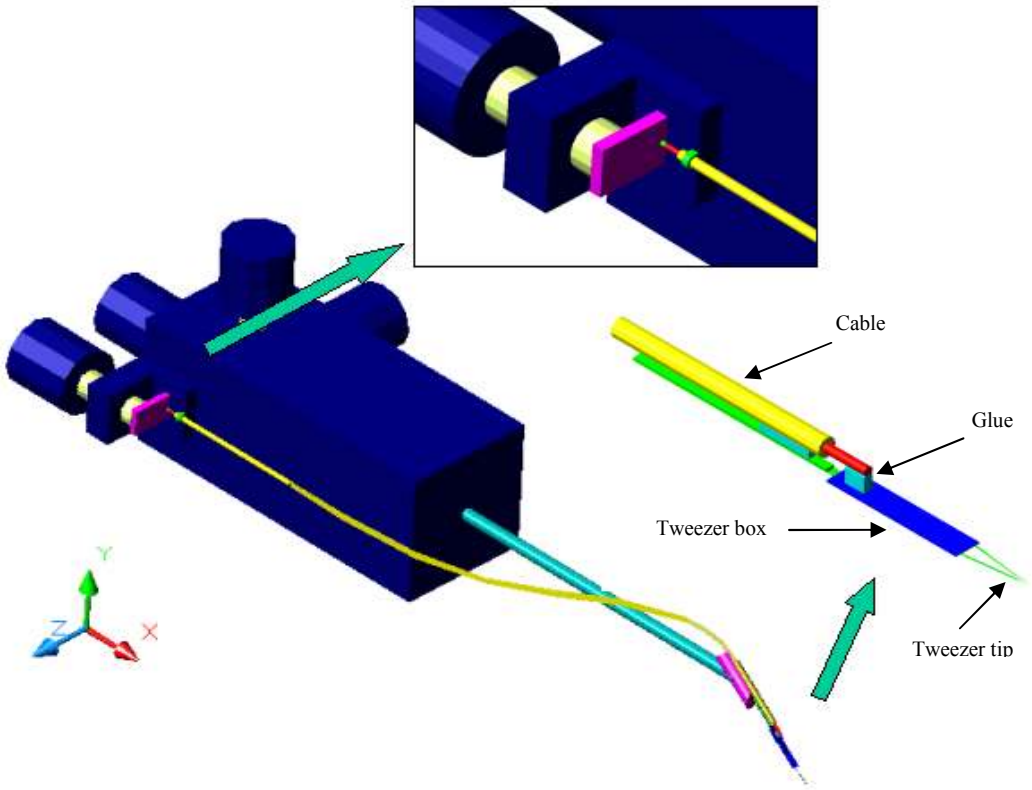


MEMS microtweezer. An axis knob on a microprobe station controls the motion of the microtweezer box through a physically attached tethered cable. Figure courtesy of Dr. Yoonsu Choi (published in Journal of Micromechanics and Microengineering, 2008).

Given that the microtweezers were going to be placed into biological environments for the single-cell injury studies, it was likely that replacement would be necessary after a limited number of experiments. To allow for quick replacement of the microtweezer, a modular system design where each component could be separated was required. This modularity would also allow for easier testing of multiple microtweezer designs, and would facilitate an iterative design process as each component (microtweezer, package, controller, and linear actuator) could be independently developed. Isolation of the microtweezer and packaging from the controller was paramount to achieving this independent design modularity.

3.2.1.2 - Tether-Cable Attachment to MEMS Device

The MEMS microtweezer opened and closed due to the relative position of the microtweezer box and microtweezer body. This relative position needed to be directed by a mechanical controller that could receive user input. Connection of the two components was achieved by a packaging scheme that allowed controller output to be delivered to the MEMS device. Thus, the mechanical packaging consisted of a physical interface between the MEMS microtweezer and a mechanical controller. This interface allowed docking of the microtweezer and included a mechanism to translate mechanical controller motion to the microtweezer box. Because both fixed position and moving elements were required to create this relative motion, a tether-cable system was employed for the packaging design. The tether and the cable were attached to the microtweezer body and box to provide the independent motion and thus opening and closing of the microtweezer tips.

To connect the MEMS component to this luer-based package, the microtweezer box and body were centered on the end of the tether. The microtweezer body was attached to the outside of the tether, which in the final design was a stainless steel luer needle. The microtweezer box was connected to an independently moving drive cable that ran through the needle cannula. Movement of this cable would result in movement of the box.

3.2.1.3 - Tether-Cable Design, Mechanical Controller Interface

A variety of separable tether-cable arrangements that allowed both physical and functional connectivity to a controller were attempted. The final design employed a stainless steel luer needle that housed a protected internal mechanism. This mechanism allowed relative linear motion as the needle acted as a tether, and a wire running through the needle acted as the cable. The cable extended from the needle tip, where it was attached to the microtweezer box, to the luer hub, where it was attached to a spring loaded button. This button was held in place by a friction-locked rubber o-ring, and was presented within the opening of the hub so that it could be pushed or linearly actuated by the output shaft of the mechanical controller (Figure 2.1).

### 3.2.2 - Design Iterations

This section will outline the motivation and reasoning behind the many design decisions made during the iterative design process. Outline and discussion of the design strategy for each component of the package are provided. The tether-cable system and its integration with the MEMS microtweezer box and body are discussed first, and then the internal mechanism and the luer interface to the mechanical controller.

3.2.2.1 - Tether-Cable Attachment to MEMS Device

This section will discuss the major design features of the interface between the tether-cable and the microtweezer body and box. The main objective of this interface was to fix and stabilize the tweezer body, and allow controlled linear motion of the box. The connection between the cable and box will be discussed first, and then the connection between the tether and microtweezer body.

*3.2.2.1.1 - Drive Cable-MEMS Box Interface*

The independently movable drive cable was attached to the MEMS box using epoxy. When advanced forward, the cable would direct the box forward to close the microtweezer tips. In early designs, the cable was attached to the nickel microtweezer box, which had a flat bottom surface. While the bottom of the nickel box provided sufficient surface area for attachment, this process of gluing the round drive cable to the relatively flat surface resulted in axial misalignment, as the width of the box did not have any torsional stability.

Subsequent design iterations incorporated features into the box to correct this torsional instability. First, holed features on to each side of the box provided multiple attachment points that could allow control of rotation during assembly (Figure 3.2-A2-4). Hook-like features that did not require a fastener or epoxy were also incorporated onto each side of the nickel box. Both of these features would provide additional torsional stability, but each required a special attachment component on the end of the drive cable. Instead of developing this additional part, the central notch feature was developed for the silicon box (Figure 2.19-2.21). This notch features allowed a nesting of the drive cable into the box, which reduced twisting during assembly.

*3.2.2.1.2 - Tether-MEMS Microtweezer Interface*

The tether, which remained in the same position regardless of the cable movement, was attached to the microtweezer using epoxy. This consistency in location of the tweezer during actuation was ideal when considering the micromanipulation applications for the final device, all of which require precise positioning of the tweezer itself prior to manipulation. For attachment, only a portion of the tweezer body would overlap with the needle. This would allow the body to extend beyond the tether to provide the box with a wide range of linear motion.

To create the tether, variety of structures such as stripped wire casings, plastic tubing, syringe needles, and blunt-end luer needles were utilized. In initial designs, a stripped wire sheath acted as the tether, and an additional stabilizing rod or post was attached to this sheath using glue to provide additional support (Figure 3.2-A1). Alignment and attachment of the sheath along the outside length of the rod was difficult, and the rod was eventually replaced with a low gauge disposable syringe needle, where the sheath and cable could run through the needle cannula (Figure 3.2-B1-2). The combination of the low gauge needle cannula and sheath would then be replaced by just a needle with a higher gauge.

In addition to being a structurally rigid component with a built-in cannula, the needle also provided a small profile to facilitate the presentation of the microtweezer into small experimental setups. The biological experiments were conducted under a microscope objective, and the luer needle, which was 25 mm in length and 0.55 mm in diameter, allowed for positioning in the limited clearance provided.

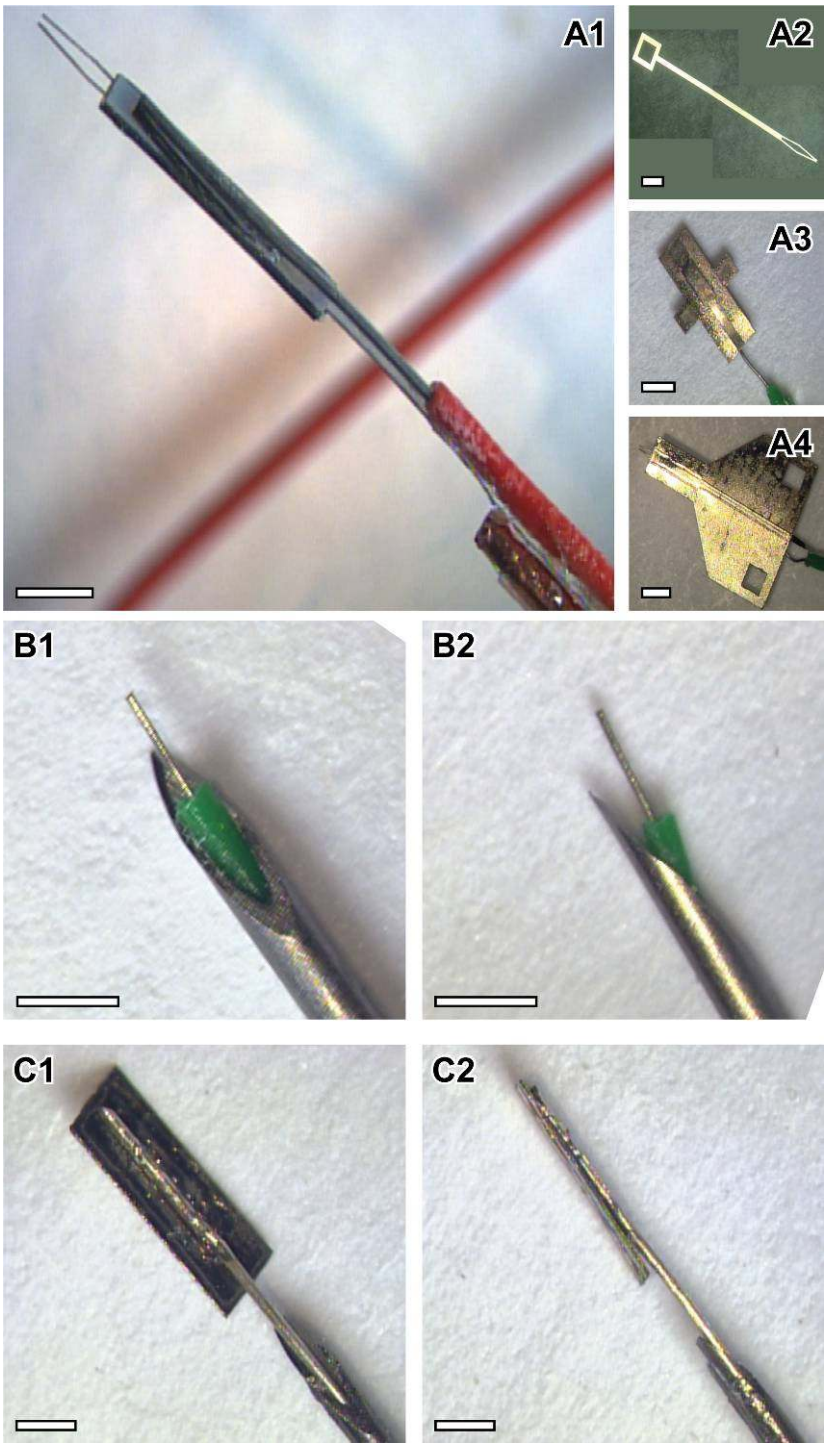


**Figure 3.2**: Preliminary designs for the mechanical tether-cable packaging of the MEMS device. Attachment schemes that utilized stripped wire casings (A), plastic tubing, and syringe needles (B, C) as the tether were attempted. The cable component was usually stainless steel wire, music wire, and small-diameter metal rods. Unique features were augmented to the box to serve as attachment points for the cable (A2-4).

During assembly, rotational and directional alignment of the tweezer with the length of the needle had to be ensured so that the advancement of the cable out of the needle would push the box straight forward so that closing of the tweezer beams was symmetrical. If the tweezer body was rotated slightly, placed laterally from the center of the needle, or directed to one side, then when the box was actuated forward, the box channel would initially only contact one of the tweezer beams. Similar to the attachment of cable and box, the process of gluing the flat surface of the tweezer to the round surface of the needle could also result in axial misalignment.

To provide additional rotational, directional, and torsional stability during attachment of the tweezer to the tether, a notch feature similar to the notch in the bottom of the silicon box described in Chapter 2 was incorporated into the end of the luer needle (discussed below in Section 3.1.4.1). This notch facilitated consistent tweezer attachment to the end of the needle.

3.2.2.2 - Tether-Cable Design, Mechanical Controller Interface

This section will discuss the design of the tether-cable mechanism and its connection and interface with the mechanical controller. The objective of the tether-cable mechanism was to ensure a stable and defined range of motion of the microtweezer box. The objective of the mechanical controller interface was to provide both physical docking and functional connectivity between the packaged microtweezer and controller. This interface needed to have physical isolation from the controller to ensure modularity.

The design considerations for both the tether-cable and interface features will be discussed over the evolution from a preliminary design to the final design.

*3.2.2.2.1 - Preliminary Tether-Cable Mechanism and Controller Interface*

The tether-cable, which is defined by the luer needle cannula and drive cable, needed to be stable and have a defined and consistent range of motion. In a preliminary design, the restriction in range was accomplished by creating physical stops in the drive cable. These stops, which existed on the drive cable that extended into the luer hub and past the needle tip, prevented movement relative to the needle cannula beyond specified points of the cable. This defined range protected the MEMS device, which could be damaged by over-actuation or by withdrawing the drive cable through the cannula (as it was attached to the box). Because of its location, the back stopper inside the luer hub needed to be fashioned prior to insertion of the cable into the needle cannula. To avoid damage to the microtweezer, the stopper at the front of the luer needle needed to be fashioned prior to attachment of the MEMS device. This was accomplished by defining the back stopper, feeding the drive cable through the luer housing to the needle front, and then fashioning the front stopper. Following the creation of both the stoppers, the MEMS device would be attached as described previously in Sections 2.4.2.2, 2.4.2.3, and 3.1.2.1.

A few packaged microtweezers following this preliminary design were created that used physical stoppers, and a concept for the controller that would power this mechanical package was defined (Figure 3.3). This controller was not manufactured, but its design and intended function is discussed below.

This controller design incorporated an internal threaded luer connection on the outer housing to allow the docking of the needle's female luer hub. The controller design also contained a collet that would move forward through a collet chuck on the drive housing, causing it to close and grasp onto the end of the drive cable. Advancement of the collet would be controlled by a rack and pinion type connection. The rack would be

milled onto one side of the collet. The pinion that would engage the rack on the collet would protrude through the drive housing and the outer housing, and would have continuous movement to ensure complete range of motion of the collet. The drive housing would move forward and backward relative to the outer housing to control the relative motion of the drive cable. This relative motion of the drive cable would move the microtweezer box. Physical features in this design could also be incorporated to limit the range of drive housing movement. This would prevent movement of the drive cable beyond the limits defined by the stoppers, limiting unintentional loading on or bending of the drive cable.

While this package and controller scheme provided a modular solution, there were a few key problems associated with its design: 1) Consistency in the stopper location was difficult to ensure, 2) the attachment or milling process of the stopper needed to be well characterized to prevent damage to the MEMS device, 3) the drive cable was free to slide forwards and backwards, 4) the drive cable was free to rotate axially, 5) the collet would have to be disengaged prior to docking and undocking of the luer needle to prevent damage to the drive cable, 6) the drive housing would have to be rotationally fixed to prevent twisting of the clamped drive cable, and 7) to control movement forwards and backwards of the drive cable, the controller would need to physically grab the back stopper of the drive cable.

The freedom of movement of the drive cable was the main source of failure of the packaging design. The cable was free to advance and cause the box to engage the tweezer beams without any preventative loading or force. The rotational freedom could cause the cable to twist, and torsionally load and bend the tweezer body of the MEMS

device, especially if the box was currently engaging the tweezer. The attachment points of the microtweezer to the luer needle and box to the cable were also likely to separate should any torsional loading occur during any movement of the cable.

Prescribed attachment of the collet to the drive cable would be difficult to achieve. Following luer docking of the packaged microtweezer, the controller collet would need to advance forward and clamp onto the end of the drive cable. The drive cable would need to be centrally aligned and un-bent to insure that the collet could effectively grasp the end. Given the freedom of movement of the drive cable, this clamping could take place during any location in the cable's range of motion. If the clamping occurred toward the end of the actuation cycle, then as the collet advanced through the chuck to close completely, this could force the drive cable forward and cause it to buckle between the collet and back of the luer housing. Lastly, this clamping location uncertainty would also prevent the assurance of a home state, and prevent closed loop control. Once clamped, the drive cable would have no freedom of movement, and should the drive housing rotate relative to the outer housing, torsional loading would occur on the MEMS device.

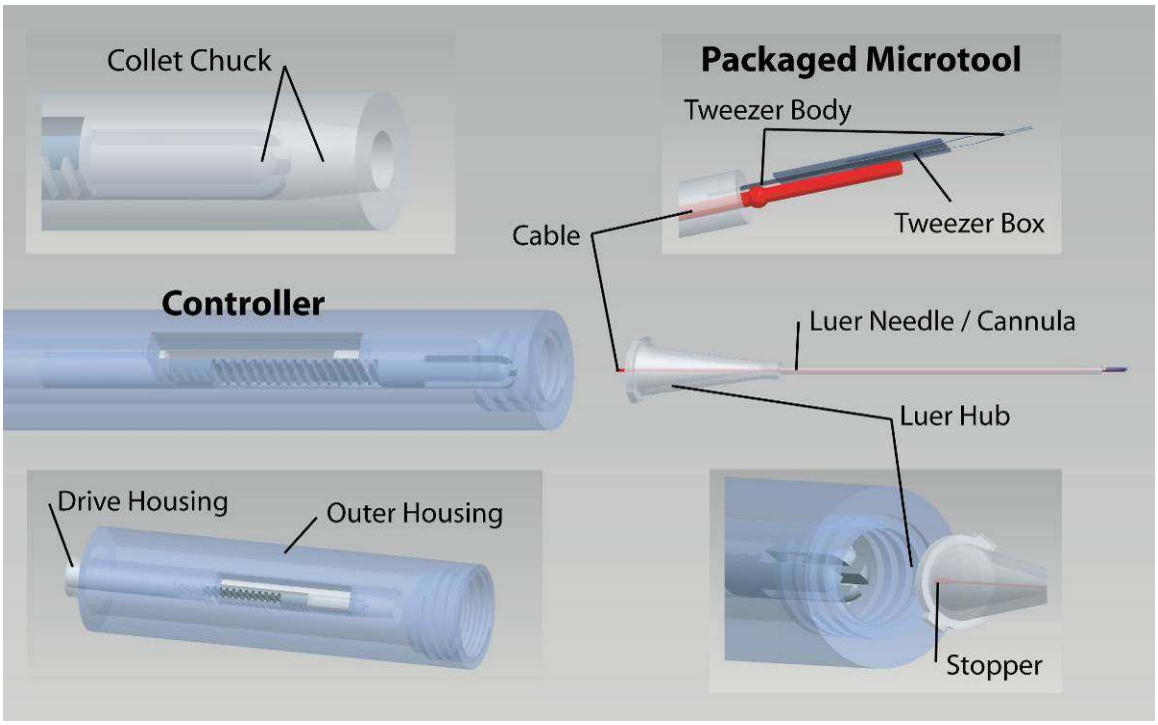


**Figure 3.3**: CAD drawings with labels highlighting the key features of the preliminary luer housing package and controller design. This package design used physical stops on the drive cable to control the actuation range of the MEMS device. The controller outer housing contained a docking interface for the luer needle of the package, and an internal collet to grasp the drive cable. This collet was attached to an internal drive housing that could move linearly independent of the outer housing, causing actuation of the MEMS device.

*3.2.2.2.2 - Final Tether-Cable Mechanism and Controller Interface*

In this section, the multiple design changes that took place from the preliminary design to the final design were condensed into a single iteration for discussion. These changes were made to address the freedom of movement and controller interface concerns. The overall evolution from hard stoppers on a cable to the spring-loaded button mechanism is explained.

In addition to having both a luer fitting that provides a universal docking interface and a needle cannula that can act as a tether, the stainless steel luer needle can also protectively house internal mechanisms in its luer hub. The preliminary packaging design failed to utilize this housing, and ultimately, the controller collet of that design would have had to be positioned to avoid colliding with the housing interior.

In the final design, this hub was utilized to house an internal mechanism that assisted in the positioning and movement of the drive cable and microtweezer box. This mechanism incorporated the physical stop concept of the preliminary design, but also established a home state for the drive cable. This home state was defined by a seated o-ring, and the default home position of the drive cable was insured by an internal spring loaded mechanism (Figure 3.4).

This design prevented uncontrolled movement of the drive cable, limiting unintended actuation and rotational loading on the attached MEMS device. A consistent home position was also defined, which ensured that the engagement of the drive cable by the controller started at the same location. Because the drive cable had tensile loading induced by a compression spring, it returned to the home position without external input, eliminating the need by the controller to pull the cable backwards. This simplified the

interface between the controller and drive cable considerably as only a pushing motion by the controller was required. Additionally, a point-contact interface was defined between the button and the mechanical controller by patterning a ball-face into the button. This limited the surface area of contact and thus static friction, which reduced torsional loading during actuation of the controller.

This package design allowed for positional and rotational isolation from the mechanical controller. Because the spring loaded button was attached to the drive cable, which runs through the needle cannula, its movement was limited to the central axis of the housing. Therefore, the only constraints placed on the controller by this design were the need for a male luer docking interface, and a protruding element or *drive rod* that could physically engage the spring-loaded button.

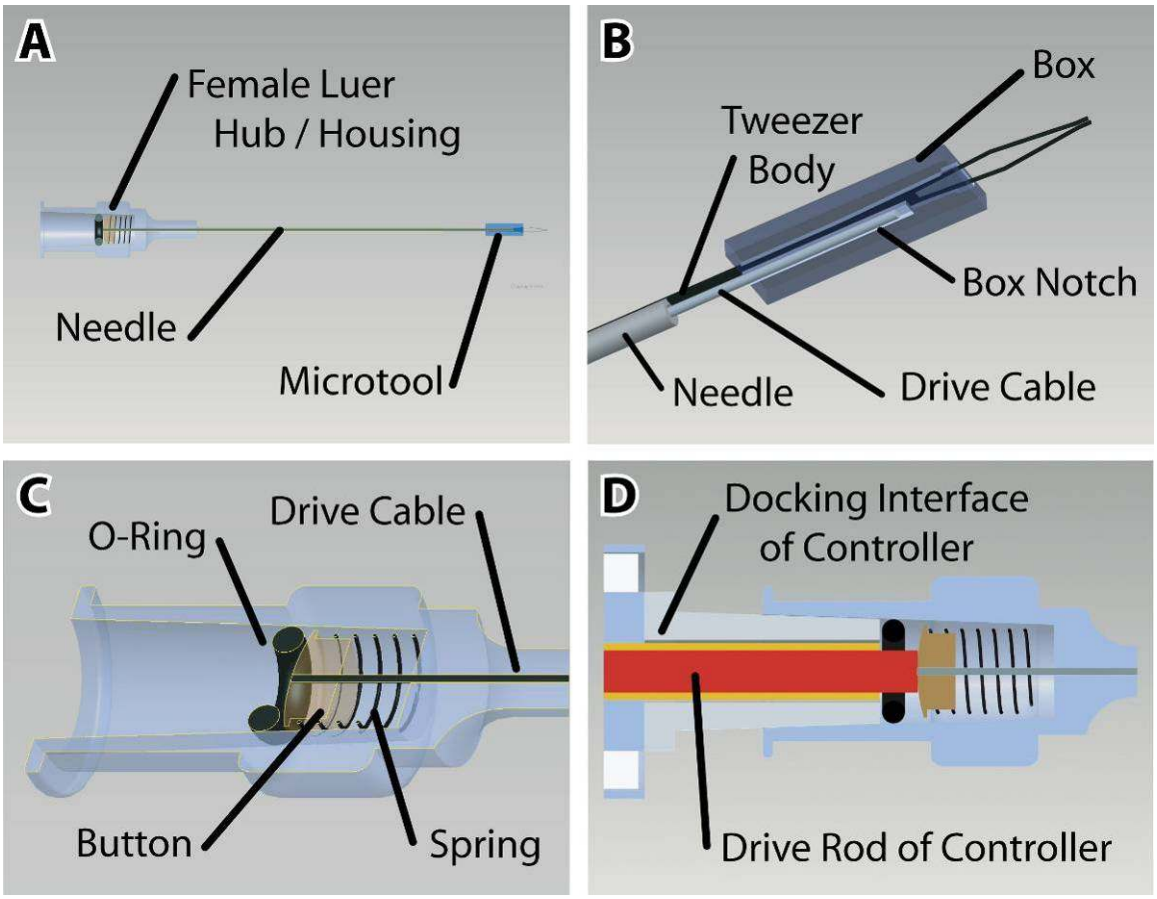


**Figure 3.4**: CAD drawings with labels highlighting the key features of the final luer housing package design. This package design uses a spring-loaded button to create a home position for the drive cable (A, C), which can help to control the actuation range of the MEMS device. The design does not require a physical stop near the MEMS device (B). This new package also allows for more freedom with the controller design, as the only engineering constraints required are the male luer interface and a linearly actuated drive rod to engage the spring loaded button (D).

The dimensional constraints of each component in the spring-loaded button design were defined by the inner geometries of the Popper (Cadence Science, NY, USA) stainless steel luer needle hub. Moving parts of the design needed to travel freely within the interior of the luer housing. The o-ring, which was the only static part, needed to seat firmly and have sufficient friction to prevent being dislodged.

The role of the button component of the package was to create a physical stop at the end of the drive cable. It was circular in shape, and it contained a shallow hole on the back to allow the snug insertion of the drive cable, which was glued in place (Figure 3.5-A-C). The front contained a ball-faced feature to create a point-contact interface with the drive rod of the controller. The button had two outer diameters along its length to create a flange for the seating of the compression spring. The smaller diameter (0.1125") defined the short sleeve that would allow the sliding of the compression spring for a snug and axially concentric placement. The larger outer diameter (0.1385") needed to be small enough to allow unrestricted movement along the central axis of the luer housing but large enough to prevent passage through the inner diameter of the o-ring. The length of the smaller diameter section of the button (0.059") was defined to control the total gross movement of the drive cable within the luer housing, as eventually the front of the button would contact the front of the hub interior. This length, which was longer than the solid height of the compression spring, also prevented the spring coils from stacking.

To constrain the button to the home position, the custom designed stainless steel compression spring needed to have sufficient force to overcome frictional forces that exist along the drive cable-needle cannula interface, as well as any stiction-based forces that might exist in the MEMS device (discussed in Chapter 4). The thickness of the

spring cable (0.005”) and the number of coils per length (pitch set to 0.0633”) determined the overall compression force, which was designated to 0.06 lb/in. Because the spring must seat onto the smaller sleeve diameter of the button and not slide above the larger diameter flange, the inner diameter was constrained to 0.12 inches (Figure 3.5-D). The spring length (0.35”) was set to ensure some compression of the spring in the drive cable home position, and was based on the final position of the seated o-ring and the front (deepest face) of the inner luer housing. To prevent stacking of the coils, the completely compressed or solid height (0.0415”) of the spring was kept below the length of the spring sleeve on the button (0.045”). These springs were originally designed to be just strong enough to keep the button in the home position and to minimize the required force to actuate the whole device. As the microtweezer geometries changed from design to design, additional force was required to prevent stiction from influencing the tweezer tip movement. To compensate, these custom designed springs were nested to double the spring force. From visual inspection, no noticeable mechanical artifacts were observed that resulted from any inner-frictional forces between up to three nested springs.

The o-ring was custom ordered to have an outer diameter dimension of 0.162 inches which would provide a snug friction fit inside the female luer hub of the stainless steel needle where the male luer fitting would rest once entered into the luer hub (Figure 3.5-E). The inner diameter was selected to ensure ample room to allow the drive rod of the controller to pass through the o-ring without making contact. Un-restricted contact of the drive rod was vital to prevent the introduction of mechanical artifacts in the actuation. This inner diameter defined the thickness of the o-ring cross section, which given the

consistent seated location within the luer hub, would have a marginal affect on the total actuation distance of the spring loaded button.

The drive cable was a straight stainless steel rod with an outer diameter of 0.22 mm, which is 30 µm smaller than the needle cannula inner diameter (0.25 mm) (Figure 3.5-C). The stainless steel finish on this rod would ensure a smooth interface with the inner wall of the cannula. The length of the rod (38 mm) was cut from stock, and provided sufficient material to protrude from the needle cannula from the drive cable home position to allow attachment of the MEMS device during assembly.

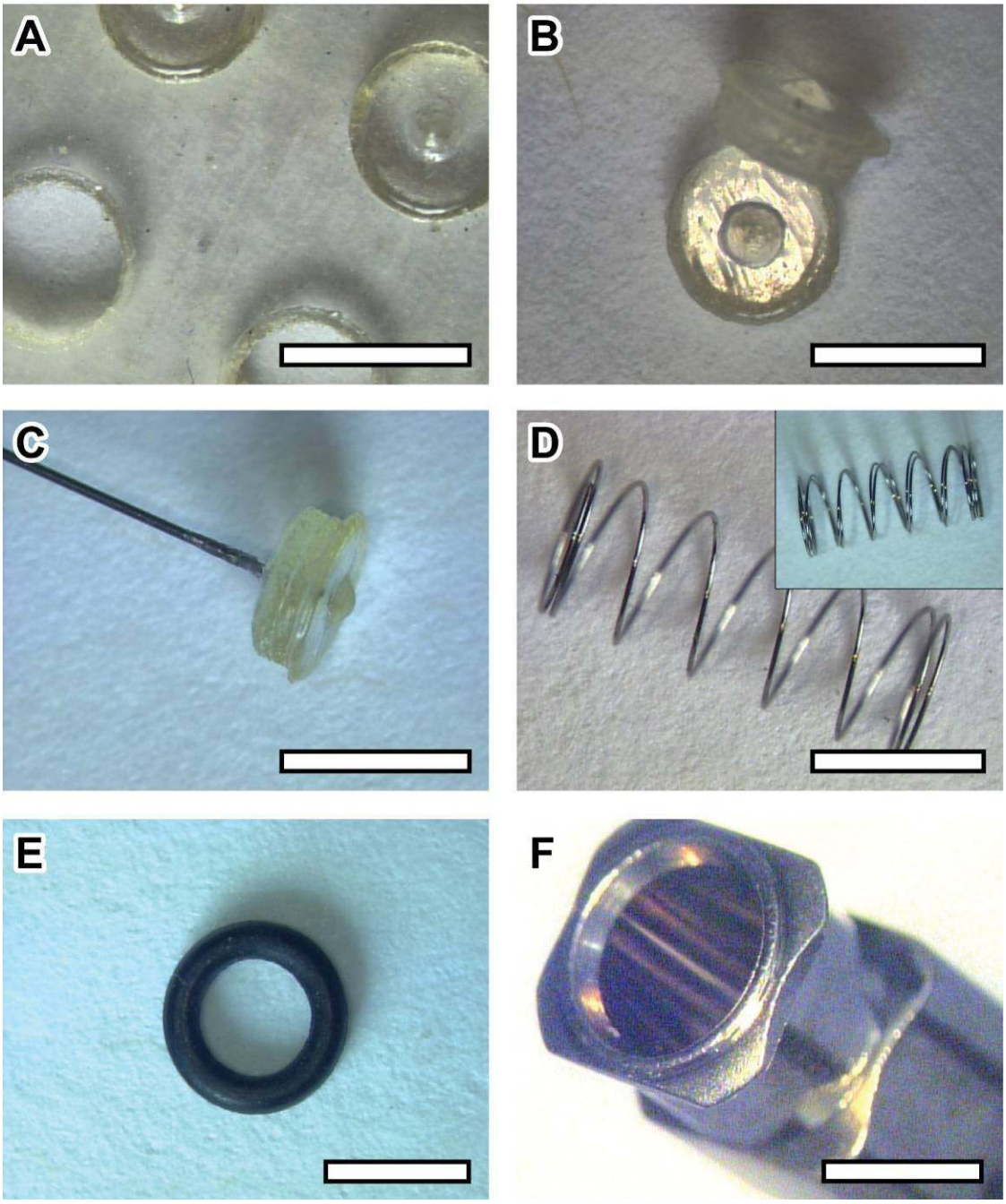


**Figure 3.5**: Bright-field photographs of the various components used in the spring-loaded packaging design: (A) Stereolithographically printed buttons in the supportive sheet prior to separation, (B) completed and cleaned buttons, (C) the assembled button and drive cable, (D) the compression spring, (E) the rubber o-ring, and (F) the luer hub of the stainless steel luer needle. Two to three springs could be successfully nested (D, inset, two springs) to increase the loading on the button without any inter-spring stiction-based interference. All scale bars are 3.5 mm.

### 3.2.3 - Materials

The entire composition of the inner compression spring and luer needle is stainless steel. Stainless steel, which is used in medical equipment and surgical instruments, was also chosen for the drive cable, which should have the tensile strength to limit any material deflection from weight of the adhered MEMS device. The tensile strength and material surface should also mitigate mechanical artifacts from movement of the direct drive cable within the needle cannula.

The resin material that comprises the button is soft enough to allow the insertion of the drive cable into a hole that is smaller than the cable outer diameter, but was stable enough to endure the loading from the drive rod of the controller. The resin button does not contact any moving surfaces except the front of the drive rod, and the point contact on the ball-face of the button would limit any rotational loading that could occur at this interface. Therefore, the frictional forces of this material did not have to be considered. It would also never be introduced into the cellular medium, so biocompatibility was not a concern as well.

The o-ring, which needs to statically seat into the inner female luer channel of the luer hub, is comprised of black rubber (Apple Rubber Co, stock 70BN). This material has the flexibility to allow the driving and compression of the o-ring into the luer channel, as well as a suitable static friction coefficient with stainless steel to seat without displacement from the loading of the spring loaded button. This component would not be introduced into the cell medium.

### 3.2.4 - Construction

The sections that follow detail the machining processes for specific custom components in the package design, the assembly process of the package, and finally the attachment of the MEMS device to the assembled package.

3.2.4.1 - Luer Needle with Grooved Notch

Initially, laser machining and polish machining methods were attempted to create a simple flat surface on the end of the needle. This flatness would provide a surface that was more compatible with the geometries of the tweezer body, facilitating rotational alignment during assembly. The laser micromachining, which used high energy pulses to remove small amounts of material, provided a controlled patterning of the needle surface. As a result of the piecewise removal process, the machined surface was textured. This provided a better surface for the adhesion of epoxy, but adversely affected the positioning of the tweezer during attachment. The process was also slow and low-throughput, and if prolonged, deposited debris into the cannula, which affected the actuation smoothness of the tether-cable arrangement.

The polished milling process was more effective at removing larger amounts of material and at creating a smoother surface for alignment of the tweezer. However, this process was less controlled. While the jigs created to facilitate this machining process aided in alignment of the patterned feature, they were insufficient in providing the control and consistency of the laser machining process. The polished milling process also placed considerable force on the outside of the needle and the shape of the cannula was commonly altered, reducing the inner diameter at the end of the needle. This reduction in diameter was also inconsistent, preventing a compensatory adjustment in the drive cable diameter that would work with the altered cannula shape (Figure 3.6).

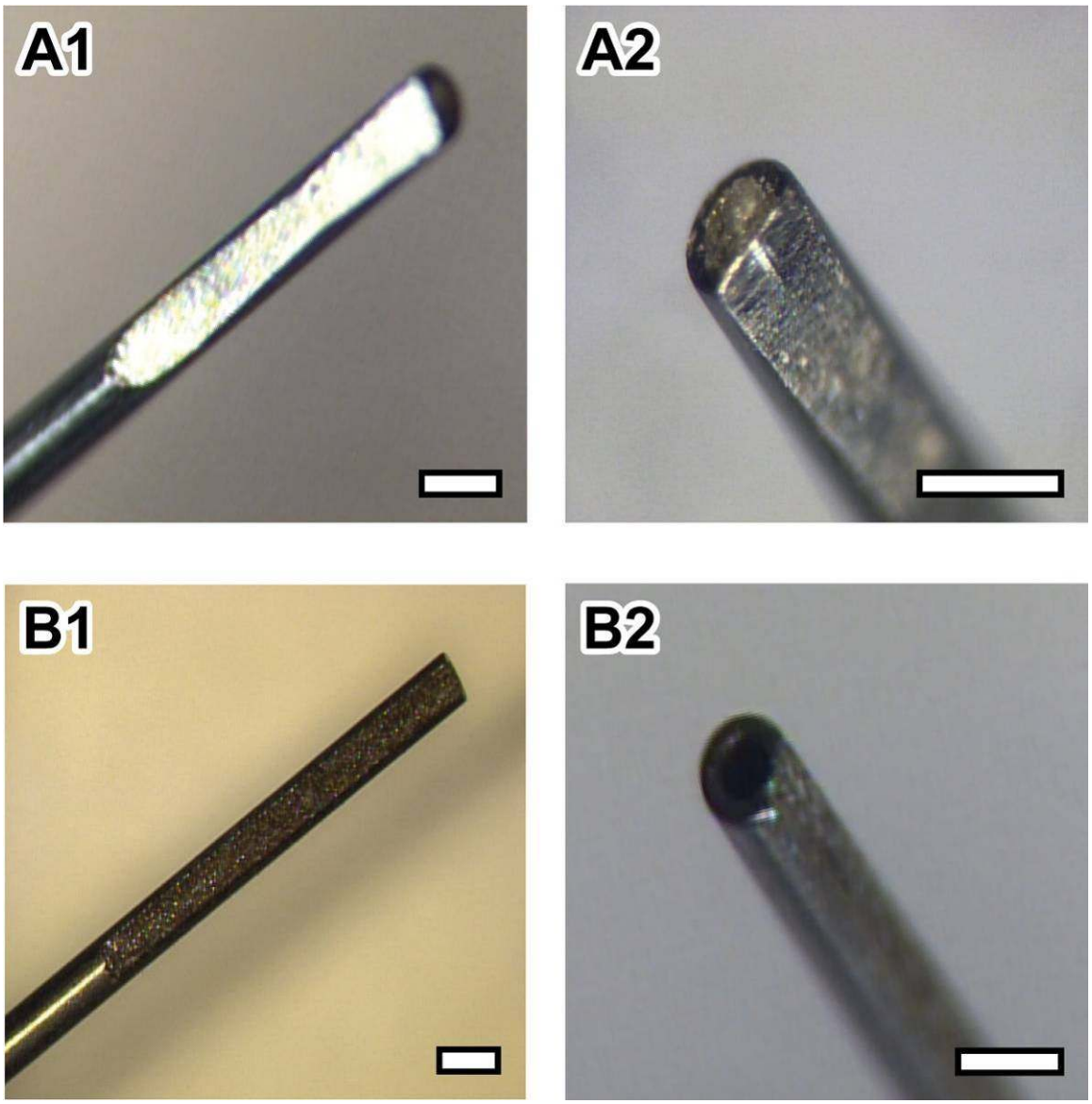


**Figure 3.6**: Bright-field photos of the polish milled (A1-2) and laser etched (B1-2) flats that were machined onto the end of the stainless steel luer needle. The needle inner cannula geometry for both the polish milled and laser etched needles have been altered, which will affect the movement of the drive cable. All scale bars are 500 μm.

This notch machining process was eventually outsourced to a company that specializes in the machining and forming of exotic luer needle shapes and features (UNIMED, Switzerland). They were contracted to pattern a 330 µm wide micro-milled notch that is open from the end of the needle and that would run the length of the needle for 7 mm (Figure 3.7). The 330 µm notch would allow for placement of the 300 µm wide tweezer, prevent translational misalignment from the center of the needle, and limit the ability of the tweezer planar angle to rotate. The 7 mm length of the notch would provide sufficient bonding surface for the beam of the tweezer, and given the 30 µm tolerance of the notch to the cross sectional dimensions of the tweezer beam, would also assist in the rotational and directional alignment towards the end of the needle (Figure 3.8). The flat, which is tangential to the needle cannula, will prevent axial misalignment.

The notch micro-milled by UNIMED had consistent dimensions, and provided a smooth and even surface in which to place the microtweezer body. The side walls of the notch effectively provided rotational and directional alignment, and the flatness of the notch and adherence to tangential geometries with the cannula ensured axial alignment. This milling process did not alter the inner cannula, and drive rods with diameters that were 30 µm less (0.22 mm) than the diameter of the needle cannula (0.25 mm) could travel freely.

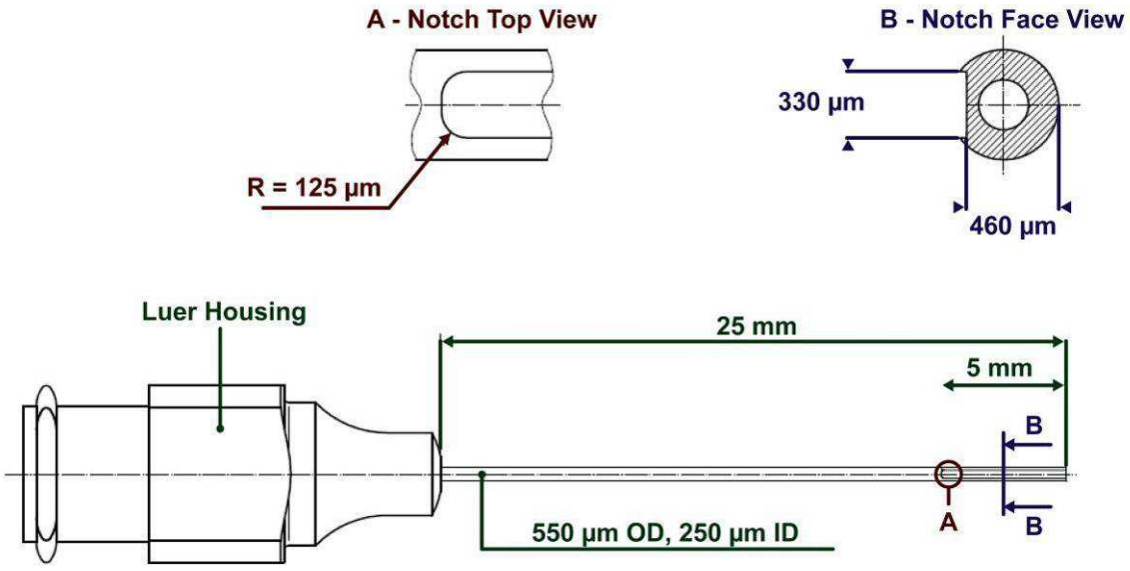


**Figure 3.7**: CAD drawings with labels highlighting the key dimensions of the UNIMED micro-milled notch in the end of the stainless steel luer needle.

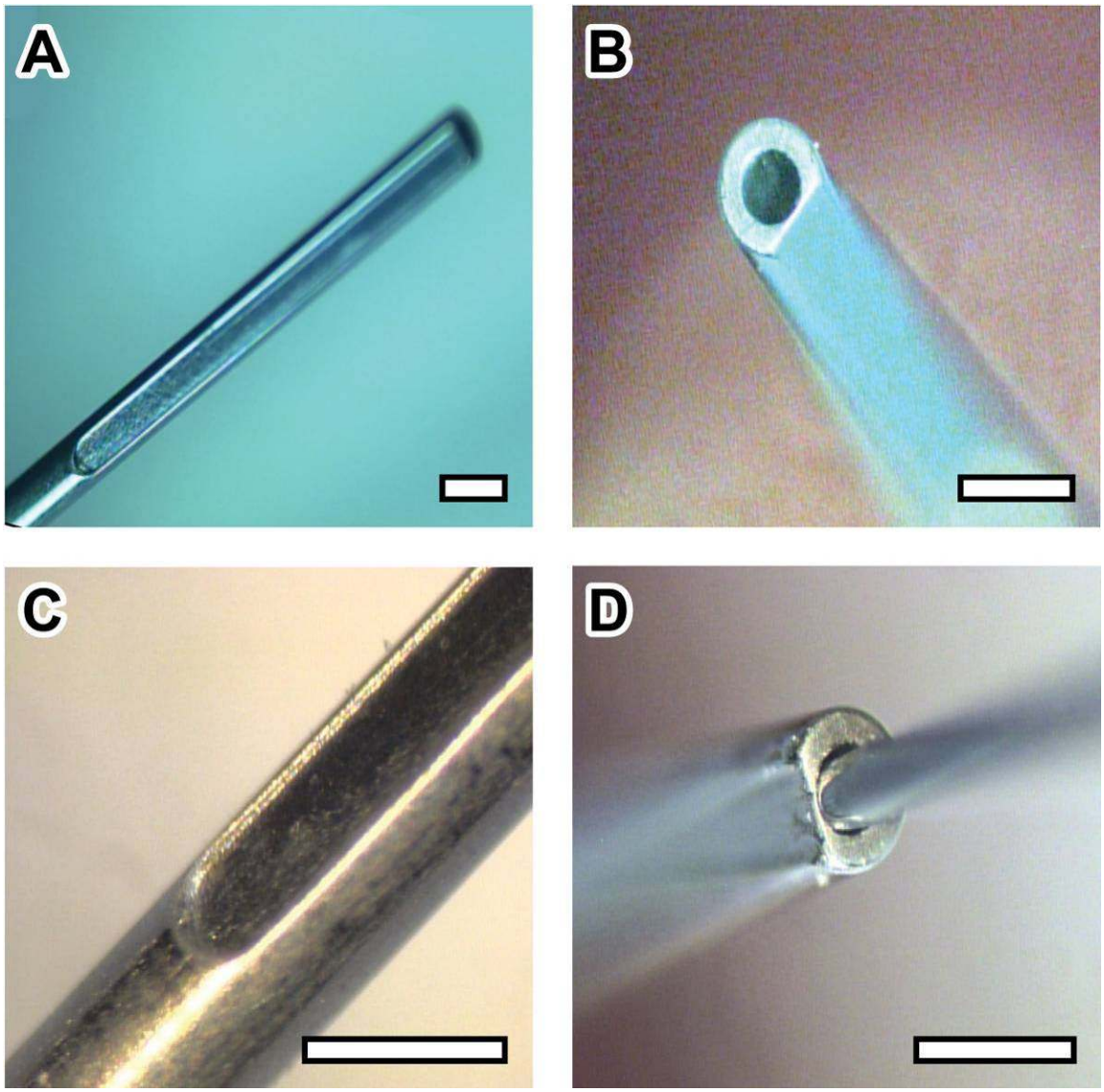


**Figure 3.8**: Bright-field photos of the micro-milled notches that were machined onto the end of the stainless steel luer needle (A-D). The needle inner cannula geometry is unaffected by this milling process (B), and a drive cable inserted into the cannula can freely travel (D). All scale bars are 500 µm.

3.2.4.2 - Stereolithographically Printed Button

The geometries of the button were defined using CAD software (Pro-Engineer), and stereolithographically formed on a three-dimensional printer (OBJET model Eden 250). This printer has planar resolution of less than 100x100 μm and vertical resolution less than 25 μm. The printing process created the part out of polyurethane based resin, which was encased and supported by a removable scaffold material. Following the printing process, the scaffold material was removed and the part was cleaned inside of a chamber with a high pressure water jet. This mechanical cleaning was followed by immersion into a mild NaOH solution for chemical removal of any residual printing scaffold. Because of the overall small size of this button, several pieces were printed at once in an array inside of a sheet to prevent them from getting lost or damaged during the cleaning process. Bright field images of the completed and cleaned button, button parts still inside of the sheet, and the button-drive cable assembly are displayed in Figure 3.5-A-C.

3.2.4.3 - Luer Needle Assembly

Because the MEMS components of the microtool (box and body), and the luer housing and spring-drive components were all manufactured separately, assembly was required. Several jigs were constructed that successfully facilitated the device assembly (Figure 3.9, 3.10). Order of needle packaging assembly was important due to the nesting of the spring loaded button inside the housing of the luer needle and its physical connection with the MEMS components that were on the end of the luer needle. Using a fabricated jig that contains a channel with a prescribed length, one end of the drive cable was inserted into a notch in the button and adhered with epoxy. A compression spring

was inserted over the cable and nested over an outside groove in the button. The opposite end of the cable was then advanced into the luer housing and through the needle cannula until it came out the end of the needle. The o-ring was placed into the needle housing and seated by inserting a male luer fitting into the luer hub. This o-ring created a physical stop for the spring-loaded button, which securely completed assembly.

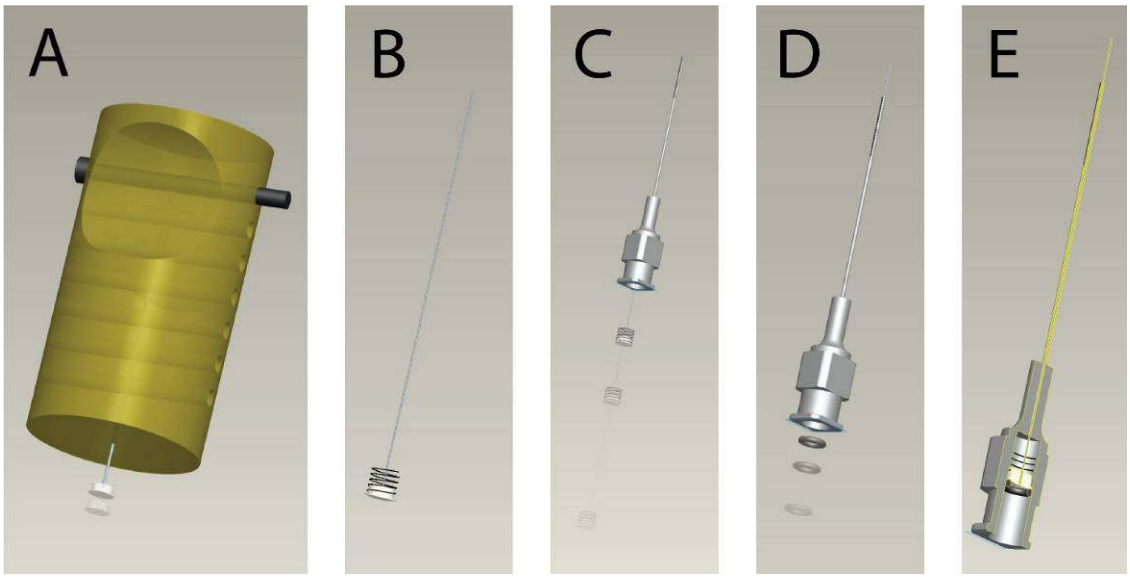


**Figure 3.9**: Cartoons showing the assembly process for the luer needle package. (A) A jig is used to facilitate the directed insertion of the drive cable into the slot of the button, which is adhered with epoxy. (B) A spring is slid over the button sleeve, and the assembled spring loaded button is inserted into the luer housing (C). (D, E) An o-ring is inserted to seat the spring-loaded button and act as a physical stop to ensure spring tension and to provide consistency in the button location.

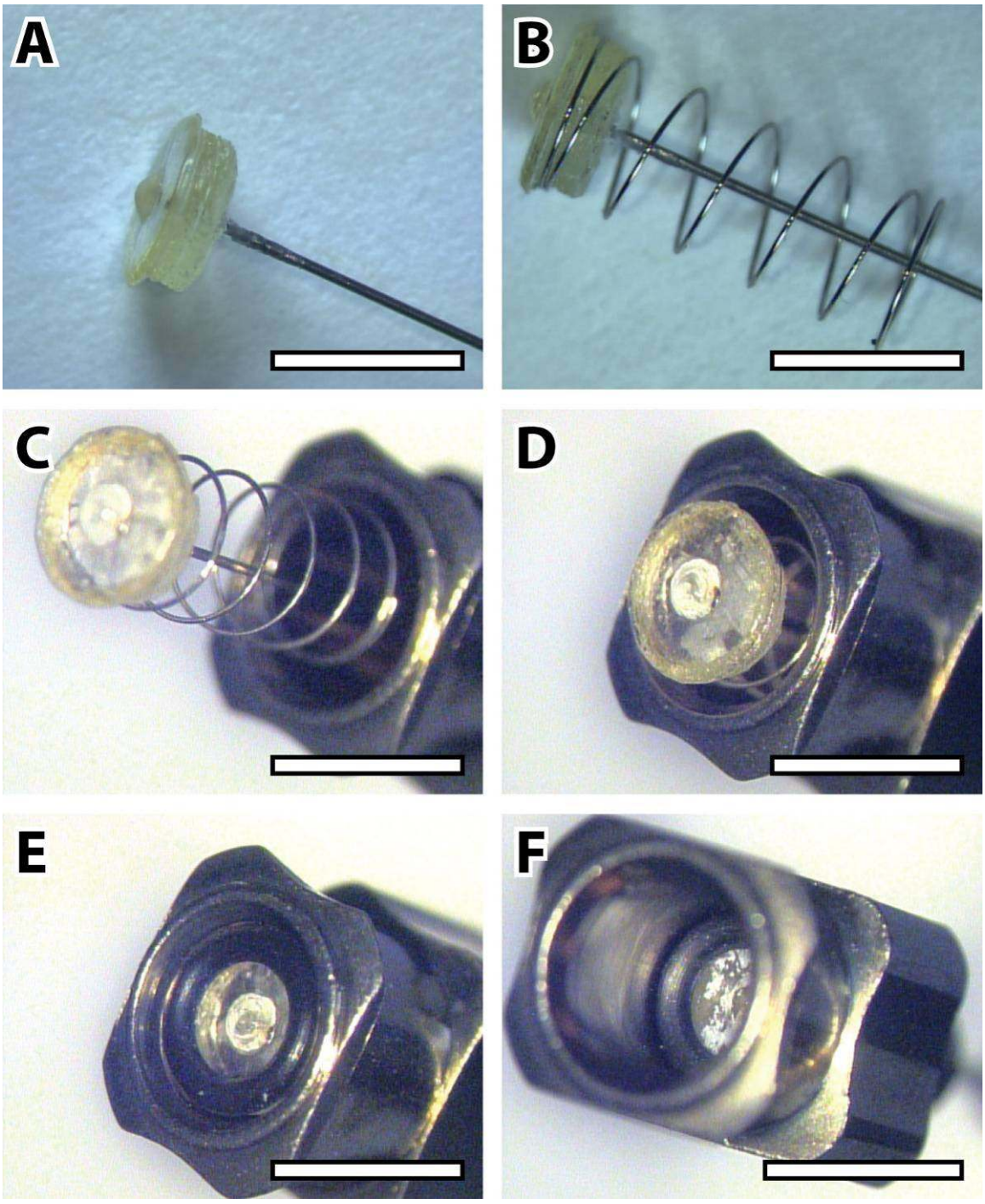


**Figure 3.10**: Bright-field photos of the assembly of process for the luer needle package. (A) The drive cable is inserted into the slot of the button and glued. (B) A spring is seated over the button sleeve, and the assembled button is inserted into the luer housing (C, D). (E, F) An o-ring is inserted to seat the spring-loaded button and act as a physical stop to ensure spring tension and to provide consistency in the button location. All scale bars are 1.0 mm.

3.2.4.4 - Packaged Microtweezer Assembly

Following assembly of the luer needle packaging, the assembled MEMS microtweezer body/tips and box were affixed to the needle shaft and cable to create the tether-cable arrangement and complete the device mechanical packaging.

The weight of the MEMS device rested on the cable, which could cause possible deflection. Therefore, prior to attachment, excess cable longer than 6 mm extending from the front of the needle cannula was cut. The body of the microtweezer was then placed in the notch at the end of the luer needle and glued. Finally, the protruding end of the cable was glued to the notch on the underside of the microtweezer box (Figure 3.11).

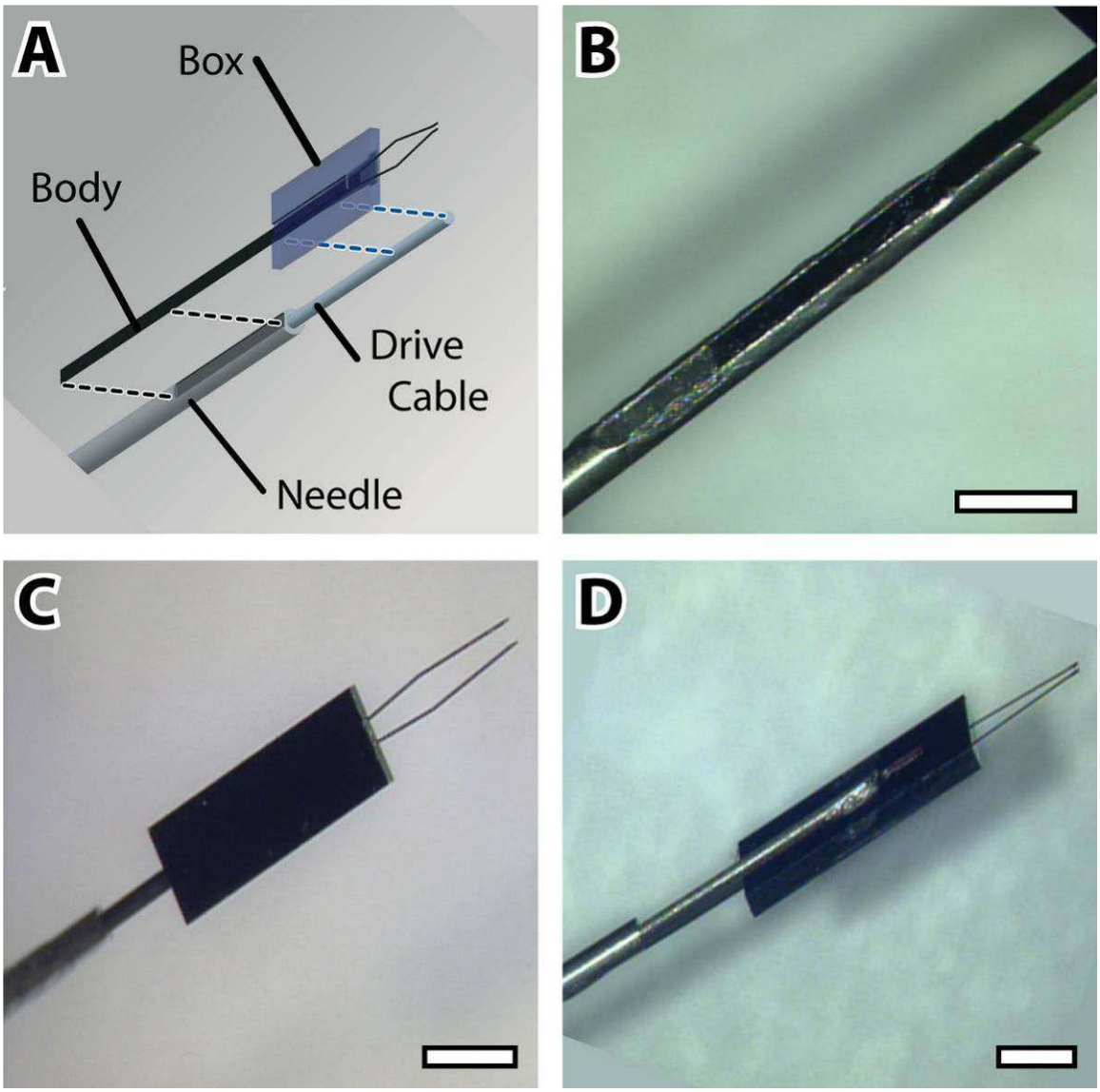


**Figure 3.11**: (A) Cartoon showing the attachment of the MEMS device onto the assembled luer needle package, and (B-D) bright-field photos of the assembled device. The body of the microtweezer is placed in the milled notch at the end of the luer needle and glued (B), and the protruding end of the drive cable is glued to the notch on the underside of the silicon box (D). All scale bars are 1.0 mm.

## 3.3 - Mechanical Controller

The role of the mechanical controller was to dock and position the packaged microtweezer, and to drive the opening and closing of the microtweezer tips based on user input. To direct this actuation, the controller employed a uni-axial, linear-actuation-based, direct-drive mechanism, which was powered by a user-controller linear actuator attached to the rear (discussed in Section 3.3). When a microtweezer was docked onto the mechanical controller, the controller's internal drive rod physically engaged the spring-loaded button of the microtweezer luer-based packaging to actuate the microtweezer. The luer docking interface turned axially, which rotated the microtweezer around the needle axis to facilitate alignment of the tweezer.

### 3.3.1 - Features

The controller was composed of: (1) a male *luer docking interface* where the microtweezer can be mounted; (2) a *drive rod* that travelled through the controller to functionally connect the linear actuator to the drive cable of the microtweezer packaging; (3) a *worm gear assembly* with ball bearings to allow rotation of the microtweezer about its axis; (4) a *mounting bracket* so that the controller can be affixed to a stage or micropositioner; and (5) an interface for either a manual or computer-controlled linear actuator to control the drive rod and thus engage the drive cable of the package and the box of the MEMS device.

Due to modularity in design with the packaged microtweezer, the mechanical controller had few dimensional constraints for the docking interface. When considering the size of the microtweezers themselves, however, and the need to use stereoscopic and microscopic equipment for visualization, the device was introduced into space-

constrained locations. Therefore the mechanical controller, on which the microtweezer physically mounts, needed to have a small profile to allow for positioning under these devices or integration into these devices. In addition to the size constraint and the requirement for a luer interface, the controller also needed to allow the connection of a linear actuator to power the drive rod, and to have a mounting interface to allow for attachment to positioning stages and micromanipulators.

The following sections will discuss the various features of the mechanical controller outlined above.

3.3.1.1 - Luer Docking Interface

The industry standard male luer docking interface provided modular plug and play functionality for the loading and unloading of microtweezers, which had a female luer hub. To physically engage the spring loaded button inside of the female luer, the drive rod of the mechanical controller traveled through a channel in this male luer fitting (Figure 2.1). A low friction and highly constrained interface between the luer channel and drive rod was required to ensure smooth and consistent movement.

During actuation of the drive rod and cable, lateral shifting of either had a direct affect on the microtweezer box position, and thus the microtweezer tips. Given the dimensional accuracy required of the tweezers, this slight movement impacted the tweezer performance. Thus, like the diameter match between the drive cable and luer needle cannula (a difference of 30μm) the inner diameter of the luer channel needed to match the outer diameter of the drive rod.

While a variety of stock metal rod diameters were available, commercially available luer interfaces have limited choices for the inner channel diameter. Because the

diameter of the drive rod was ultimately controlled by both this inner channel diameter, and that of the luer package o-ring, a machinable luer component with a custom channel size was eventually designed. Therefore the design dimensions were constrained to the o-ring inner diameter, as the diameter of the rod that cleared the o-ring dictated the luer channel diameter.

To ensure that this tight interface had low friction during actuation, which if high enough could create stiction, high quality surface machining of the drive rod and luer channel was required. Material selection was also important to reduce the coefficient of static friction and to provide resistivity to corrosion and wear.

To allow for testing of different material interfaces, an inner sleeve was originally glued into the luer channel (Figure 3.12 rotational one below). This reduced the diameter of the drive rod, which could reduce its tensile strength and buckling force (not examined). While the force applied to the rod to drive the spring loaded button was relatively small, the rod still needed to travel the length of the controller without buckling, which would increase actuation friction and affected the actuation resolution.

3.3.1.2 - Drive Rod Control and Actuation

The drive rod of the controller extended axial from the luer channel to physically engage the spring-loaded button of the microtweezer package. Like the drive cable, to limit free movement and provide a home state, this rod was spring loaded. The spring selected was tailored to prevent too much additional loading on the linear actuator system, which pushed both the controller's spring-loaded drive rod, and the package's spring-loaded drive cable. To seat the spring, the drive rod required a flange or collar. This collar mimicked the button attached to the drive cable and acted as a stop to limit the

backward motion of the drive rod, establishing a home position. For various designs, the collar was either incorporated into the construction or machining of the drive rod, or was attached during assembly. While attachment of the collar allowed changes in the home position and more modularity in design, it also created a point of failure on a component that sees regular movement and spring tension.

The range of motion of the drive rod determined the system's overall actuation distance, which also determined the total range of microtweezer tip closure. Given the inherent variability in the home location of the MEMS box due to manual assembly, the range of motion of this drive rod needed to exceed the expected range of motion of the box. However, this range needed to be limited to prevent complete compression of the package's spring loaded button, which if pressed with too much force, would break the friction lock on the luer interface and undock the microtweezer from the mechanical controller.

In addition to establishing a home position, the collar of the drive rod acted as a physical stop to create a maximum actuation limit. As the collar was a separate component from the drive rod, it was positioned to control this limit. Multiple collars could also be attached to the drive rod to establish physical limits in both directions.

The drive rod that traveled throughout this mechanical controller was engaged by both a manual and programmable actuator system. This system was connected to the rear of the controller away from the luer interface and microtweezer. This modularity and versatility in design allowed for a variety of uses, including microtweezer assembly, the preliminary and cyclical mechanical assessment, and the biological interfacing application explored in this dissertation.

3.3.1.3 - Isolated Axial Rotational Functionality

In addition to the X, Y, and Z motion provided by the stage that holds the mechanical controller, the microtweezer required axial rotation control to ensure proper microtweezer orientation during both mechanical evaluation and biological experiments. This control was designed to be continuous to allow a microtweezer docked in any orientation to be rotationally aligned. Given the focal plane width of the expected microscope objective used for experimentation (e.g. a 20x immersion objective can have a working distance less than 5 mm), alignment itself was verified using visual inspection, precluding the necessity for state or closed loop control.

To achieve this rotation, the male luer fitting that docks the microtweezer needed to be able to rotate concentrically with the luer channel and drive rod. This rotation also needed to be externally controllable with either a motor or knob. Similar to the positional restriction created by all of the spring-loaded components, this rotation could not occur freely without user input. A rotating sleeve was originally considered, but this mechanism would provide direct control; if the user rotated 90 degrees then the tool would rotate 90 degrees. Rotation resolution would be limited to user ability. This mechanism would also require some friction-inducing elements to prevent free rotational motion. This incorporated friction would require the user to apply additional force to rotate the controller, which would likely cause a translation in its position, and thus the position of the microtweezer.

A mechanism that conferred mechanical advantage from user input was required to increase rotational resolution. A few gear setups with mechanical down-stepping were considered, but for all iterations of the design, a worm system was chosen to control the

rotation mechanism. Given the torque incorporated by the worm wheel onto the worm gear, and the tight interface of the worm gear teeth and wheel threads, free movement of the luer was restricted (Figure 3.12). A knob was attached to the end of the worm wheel to provide user control. The worm wheel contained a double-thread, where one wheel rotation resulted in a worm gear rotation of two teeth. Because the worm gear had twenty teeth, one full rotation of the luer shaft required 10 rotations of the knob. This provided a substantial mechanical advantage and increase in resolution.

Despite all of the benefits of the worm system, it was by far the largest component in the mechanical controller, and dictated the inner diameter of the controller housing. Because of the teeth and thread angles required in the worm elements to ensure a fluid motion, small worm systems were difficult to find.

The rotation of the worm gear and luer was independent from the internal drive rod's movement, preventing the loading of torsional strain on the drive rod, drive cable, or MEMS device. To avoid torsional loading on any of the linearly moving elements in the controller and package, friction was minimized at the various modular interfaces between the main components of the system: (1) the linear actuator-drive rod interface; (2) the drive rod-luer interface; and (3) the drive rod-drive cable interface. In addition to the finely machined rods and channels, a ball-face interface was incorporated between the drive rod and the head of the linear actuator.

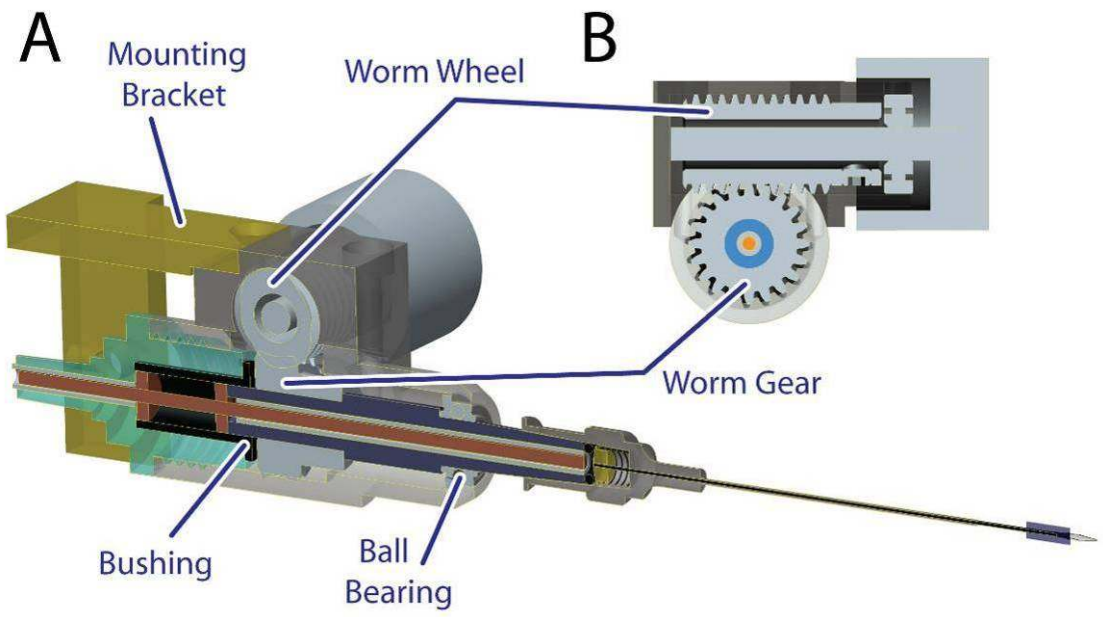


**Figure 3.12**: (A) Cross section of preliminary mechanical controller schematic showing the rotationally isolated worm system that allows axial rotation of the packaged microtweezer. The worm gear and attached luer shaft (blue) can rotate independently with the housing (grey), as well as independently from the inner drive shaft (red), which will limit torsional loading on the spring loaded button of the luer-needle package. (B) Cross section of the worm wheel and manually turn-able knob.

3.3.1.4 - Linear Actuator Interface

One of the last constraining design considerations was the incorporation of an interface for the linear actuator and its translational input. Similar to the engagement of the spring-loaded button in the luer package, only linear pushing onto the rear of the drive rod was required for actuation. A variety of designs for connections to both manual and automated linear actuators were developed. Modular interfaces that connected the components of the system would facilitate parallel development of both the controller and linear actuator, and allow for versatility in the design and for use in a variety of user applications.

3.3.1.5 - Stage Mounting

The housing for the docking station had a number of sockets machined for mounting bracket attachment. These mounting brackets allowed the mechanical controller to be affixed to any standard micropositioning or imaging stage, micromanipulator, or robotic arm. A variety of mounting bracket shapes were designed to conform to these stages, and to the geometries involved in the micromanipulation application.

**3.3.2 - Design Iterations**

This section will explain the motivation and reasoning behind the various decisions made during the iterative design process of the mechanical controller. Outline and discussion of the design strategy for each of the main features of both the manual and automated controllers are provided. The features for the manual controller are discussed

first, and then the design for the automated controller, which incorporates many of the components of the manual controller.

3.3.2.1 - Controller Design for Manual Linear Actuator

The manual controller was originally designed and constructed to allow for preliminary evaluation of the microtweezer performance. Its speed and instant human response was also critical to providing a quick assembly and testing process. Preliminary mechanical assessment of the microtweezer and of the luer packaging system was also provided by the manual controller [144].

The following sections will describe the design features and physical components of the manual controller. The direct-drive and rotational components will be discussed first, followed by the interface with the linear actuator, and finally a discussion of the hierarchy of dimensional constraints encountered during the system design.

*3.3.2.1.1 - Luer Interface, Drive Rod, and Rotational Functionality*

The manual mechanical controller incorporated all of the features required for connection to the microtweezer, linear actuator, and stage (Figure 3.13, 3.14). The male luer hub was incorporated into a shaft that was directly attached to the worm system to provide isolated rotational control of the mounted microtweezer. A ball bearing was seated around the front of the luer shaft to provide a rotationally isolated connection to the controller housing. The rear of the luer shaft resided inside of a bushing that, with the ball bearing, would ensure concentric and smooth rotation. Along with the back of the luer shaft and rear of the controller housing, this bushing formed a cavity. The drive rod ran through the luer shaft and into this cavity where it was connected to the spring and collar elements that defined the drive rod home position. These elements along with a

flat bushing (labeled “rotating plunge assembly”) rotated independently of the luer shaft to prevent any torsional loading. The rod, collar, and spring comprised the spring-loaded drive rod, and the flat bushing acted as a mechanical buffer between the spring and the luer shaft, limiting the ability of the spring to rotationally load the luer shaft and vice-versa. To allow for additional control over the dimensions of the plunge assembly, the drive rod traveled through a stainless steel tube that was glued inside of the channel.

Several of the components in this design were machined, and the multiple copies of these parts could be re-machined to alter the geometries to test new components or to improve performance. The stereolithographic printer was also utilized to rapidly test design changes. The addition of parts, such as the inner tube within the luer shaft, was used to allow for a variety of different drive rod diameters to be tested. The rotating plunge assembly (drive rod, collar, and spring), which was assembled in house, underwent several design iterations to ensure smooth actuation and durable collar attachment.

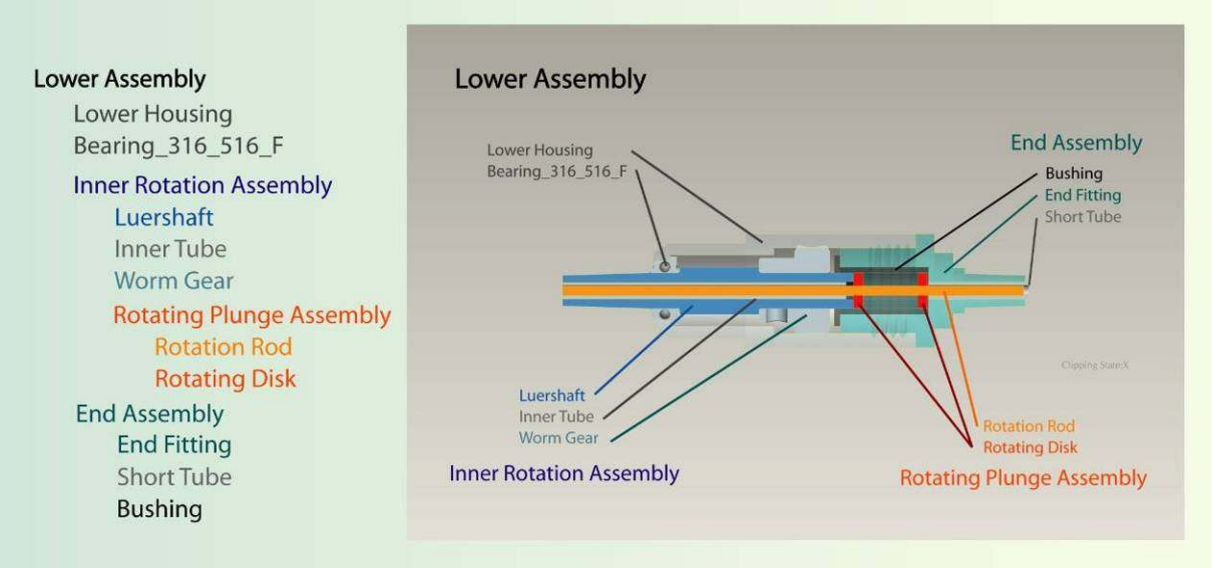


**Figure 3.13**: Lower housing of the mechanical controller with rear linear actuator connection. The direct drive mechanism (orange rod and red stopper) and rotational system (worm gear in gray) are displayed. The "End Assembly" displayed here is for luer connection to a manual linear actuation via a tether-cable system.

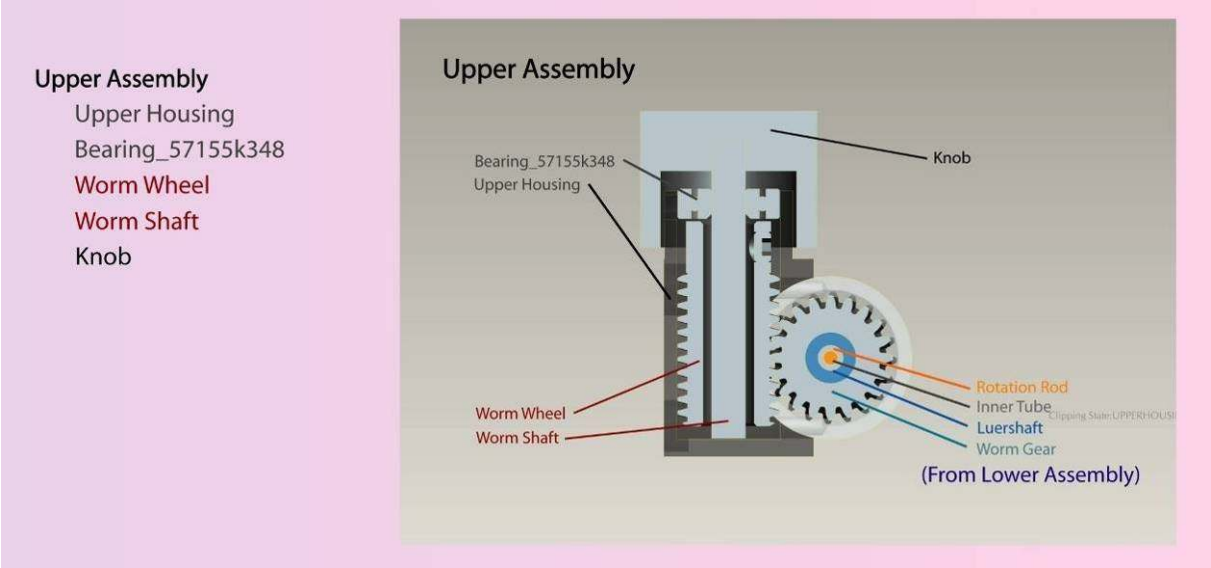


**Figure 3.14**: Upper housing of the mechanical controller. The rotational system (worm gear, worm wheel, and turning knob) are displayed. A transverse cross sectional view of the lower assembly and the direct drive mechanism is also displayed.

*3.3.2.1.2 - Connection to the Manual Linear Actuator*

The rear of this controller was designed to be connected to a manual linear actuator. To follow on the design of the originally packaged microtweezer system that utilized a micrometer head, this connection could be something as simple as a circular clamp or socket and set screw. However, for a manual system that was attached directly to the controller, and thus microtweezer, it would be difficult for a human user to turn a knob without introducing vibration that would travel through the linear actuator, controller, and package, to the microtweezer. In addition to a lack of mechanical buffering, the size of the combined controller and actuator might limit the application space of the system.

When considering the potential size of the linear actuator and the dimensional constraints of the anticipated experimental environment defined in this thesis, an actuator that was physically separate from the controller allowed more flexibility in design. This separation also mitigated the translation of mechanical artifacts and noise from the user's input. To accomplish this separation, an additional tether-cable arrangement was required to connect the controller and linear actuator (discussed below). Therefore, a luer interface similar to the docking port for microtweezers on the front of the mechanical controller was incorporated onto the back of the controller for connection to the tether, and thus linear actuator (Figure 3.15).

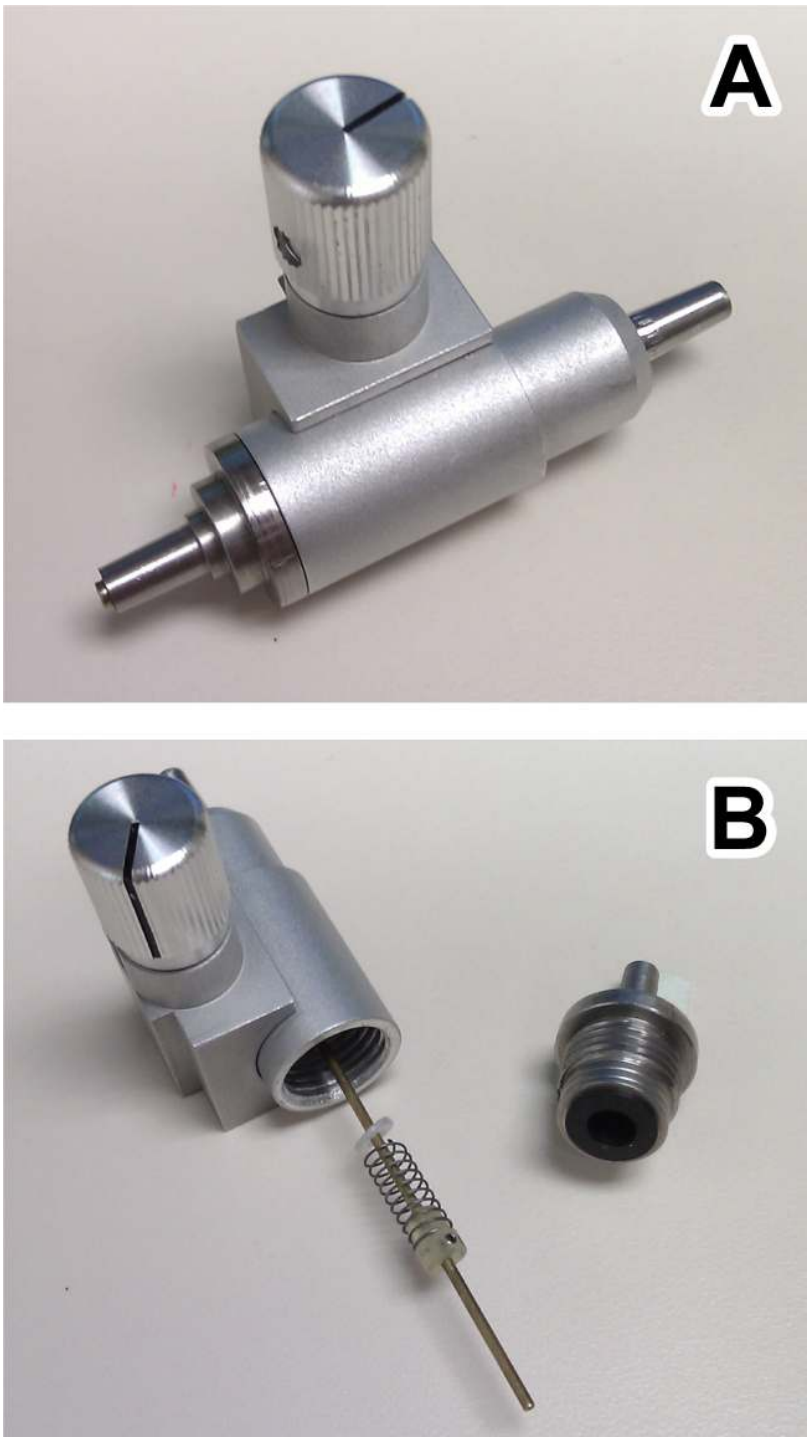


**Figure 3.15**: Bright-field photograph of the (A) docking station and (B) of the docking station separated to show the spring-loaded drive rod and collar, flat bushing (white, far end of spring), and rotation bushing (black, inset with rear luer).

*3.3.2.1.3 - Dimensional Constraints*

The outer diameter of the worm gear teeth (0.42”) and the gear channel’s inner diameter (0.1875”) that was attached to the back of the luer shaft constrained the dimensions for most of the other static and moving parts in the design. The dimensions of the worm gear teeth dictated the minimum diameter of the controller housing (0.5”). Additionally, the gear inner diameter placed a complex hierarchy of constraints on the rotating plunge assembly.

The gear inner diameter dictated the luer shaft diameter, which set the rotational bushing size. This defined the bushing cavity diameter and influenced the rod collar maximal diameter. The outer diameter of the drive rod, which was mostly constrained by the inner diameter of the packaging o-ring that needed to be cleared without contact, also needed to configure to the available collar designs. The collar needed to be securely attached to the drive rod to create a flange along the rod large enough that the spring could seat stably without dislodging. This flange dimension affected both the spring wire thickness, and the inner diameter of the collar, and outer diameter of the drive rod.

To accommodate for all of these interdependencies, a variety of drive rod diameters needed to be tested, which required the addition of the inner tube inside of the luer shaft. These inner tubes had consistent outer diameters that matched the luer shaft channel diameter (0.0965” ID). The thickness of the tubing, however, would vary, allowing different drive rod diameters to be tested.

The collar designs ranged from glued plastic rings, to rubber stoppers, to machined plastic and metal collars with set screws. The attachment of this collar to the

drive rod, and its motion within the rotational bushing was major source of failure in this design. Eventually, a design that used a set screw to secure the collar was successful.

3.3.2.2 - Controller Design for Automated Linear Actuator

While the manual controller was effective for microtweezer assembly and preliminary mechanical evaluation, an automated control system was necessary for precise and directed actuations of the microtweezer. The automation allowed for endured cycle testing and assessment of the actuation speed's impact on microtweezer performance. This ensured consistency in movement also enabled the repeatable actuations necessary during the biological studies.

The following sections will describe the design features and physical components of the automated controller. The direct-drive and rotational components will be discussed first, followed by the interface with the automated linear actuator, and finally, a brief discussion of the dimensional constraints.

*3.3.2.2.1 - Luer Interface, Drive Rod, and Rotational Functionality*

Due to modularity in design, many of the features for the manual controller could be reinstituted for the controller designed for the automated actuator. The use of a worm system was continued, and the same components and mechanism for the luer shaft and ball bearing rotation could be re-used. Because of the complex interdependent constraints placed on the drive rod diameter and collar, and their need for stable attachment, these components were replaced by a single pin blank, which is a finely machined rod with a collar. The pin blank was available in a variety of diameters, which allowed conformity with the luer shaft channel. The pin blank collar diameter also created a sufficient flange to nest the spring. The use of this finely machined part would

preclude the need for an inner tube, which was removed from the design. The increased drive rod diameter, however, did require a slight increase in the inner diameter of the luer packaging o-ring (from 0.092" to 0.098"). The use of a flat bushing between the spring and the luer shaft, which prevented torsional loading of the spring against the luer, was maintained in this design. These design changes eliminated the sources of failure that were present in the manual controller design (Figure 3.16).

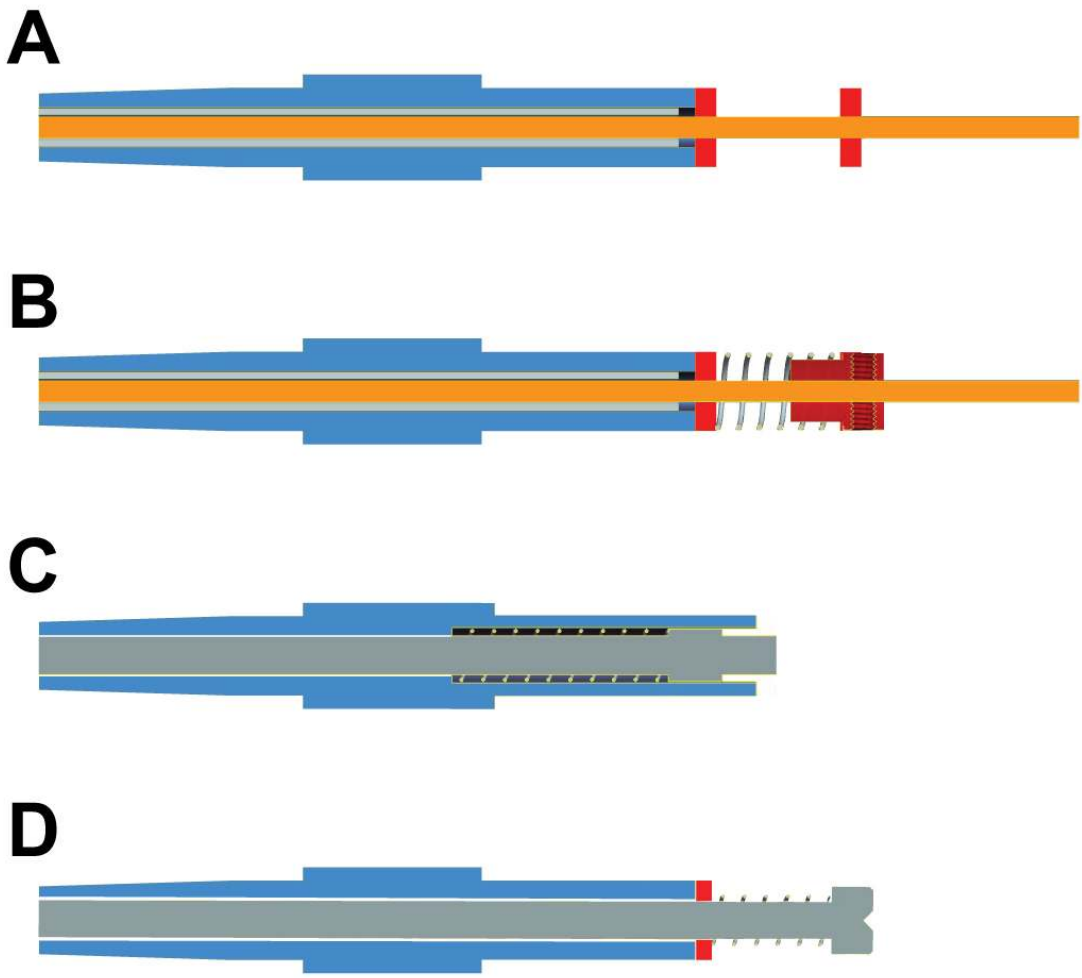


**Figure 3.16**: Evolution of the drive rod, or rotating plunge assembly, with some of the design iterations included. Each design had a spring and a flat bushing between the spring and luer shaft. (A) A preliminary design had a glued stopper (spring not shown), (B) the final manual design had a stopper set with a set screw, (C) a preliminary design for the automatic controller had a nested spring inside of the luer shaft (not described), (D) and the final design for the automatic controller.

*3.3.2.2.2 – Connection to the Automated Linear Actuator*

The rear of this controller was designed to allow the direct connection of an automated linear actuator (Figure 3.17). The introduction of mechanical noise from a high resolution computer controlled linear actuator would be substantially less than that likely to occur from a human user turning a directly attached knob. For attachment, the current controller housing rear threading was maintained, and instead of the end luer fitting attached to the rear of the manual controller, a coupler that was compatible with the front of the linear actuator was attached (described in Section 3.4.2.3).

*3.3.2.2.3 - Dimensional Constraints*

The outer diameter of the linear actuator model selected was 0.5", which matched the diameter of the controller housing. Because the actuator did not increase the profile of the entire device, the ability to position the system under a microscope experimental environment was not affected.

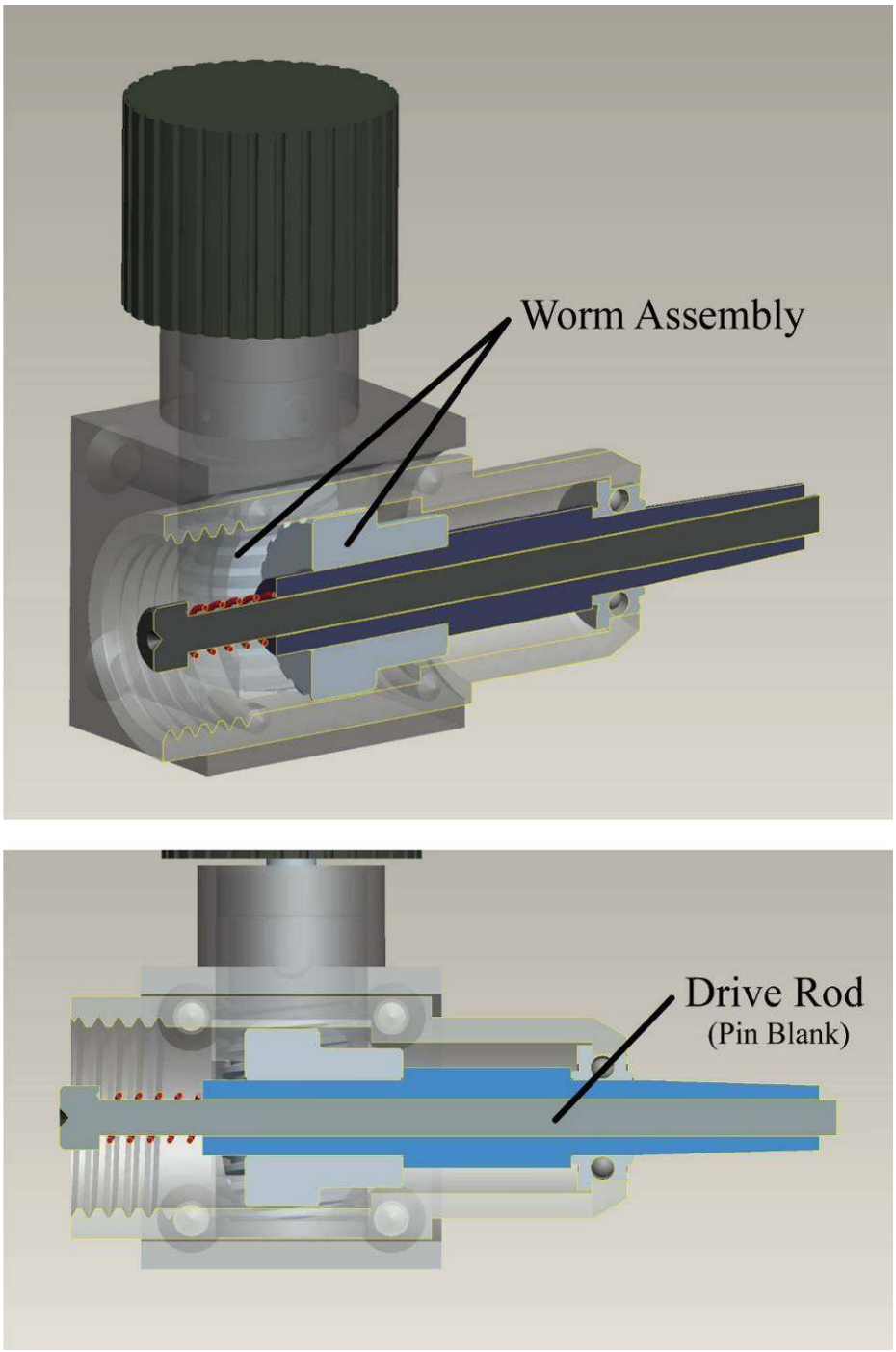


**Figure 3.17**: Lower housing of the docking station with automated actuator connection (threading to right will screw onto Newport TRA12CC Linear Actuator system). The central axis direct drive system consists of a spring loaded pin blank that will rest against the linear actuator motor head.

### 3.3.3 - Materials

The materials for the mechanical controller were selected based on mechanical durability, surface to surface interfacing of moving parts, weight, and ease in machining. For housing and structural components, aluminum was selected unless there was direct metal to metal motion contact, where stainless steel or brass was used. Materials that were resistant to corrosion and wear were required for all of the components that interfaced with any moving parts. The dimensional tolerances were high for most of these parts and interfaces, and any type of oxidation or removal of material would not only affect the performance, but could damage the device. Outside of the mechanical and corrosive considerations there were no chemical or temperature requirements.

For rotating and parts with moving interfaces, ball bearings and plastic bushings were used to reduce friction and wear, and the worm gear interface contained a plastic gear and a stainless steel worm wheel, which allowed a tight connection.

### 3.3.4 - Construction

Most of the interfaces between the commercial parts that were purchased as-is (worm system, bearings and bushings) and the custom machined parts were held intact with friction bonds or by epoxy. The assembly of the housing was accomplished with both threaded interfaces and with the use of a minimal number of fasteners (screws, set screws).

## 3.4 - Linear Actuator

The linear actuator created relative linear motion along one axis, and was used to control the position of the mechanical controller's drive rod, which actuated the microtweezer. To ensure functional connectivity with the controller, the output motion of

the linear actuator was translated to the rear of the mechanical controller where it contacted the drive rod.

Because of modularity of this complete system, and because the actuation required is direct-drive, this mechanism can be fulfilled by a variety of manual and automated actuator types. The versatility in selecting either a manual or automated controller allowed for microtweezer control through either the tactile precision of a human user (assembly, characterization) or automation from a computerized controller (consistent movements, cycle testing).

### 3.4.1 - Features

The linear actuator is composed of: (1) a driving element to create the relative motion that powers the system actuation; (2) a housing component to protect this drive element and create a physical and functional interface that connects to the mechanical controller; and (3) a mechanism for user control.

The following sections will discuss the various features of the linear actuator outlined above.

#### 3.4.1.1 - Driving Element and User Control

The means to convert user input into relative actuation was developed for both the manual and automated actuators. The manual solution utilized a hand turn-able micrometer (Mitutoyo, Japan; Micrometer Model 148-112) to create linear actuation. With a rotational spindle pitch of 0.5 mm, the micrometer head provided ±2 μm of linear actuation precision. With the roughly 3:1 mechanical advantage provided by the box actuation to tip closure down-step, this overall manual solution provided sub-micron precision of the microtweezer tips.

The automatic solution utilized a programmable motorized actuator (Newport, CA, USA; Linear Actuator TRA12CC) that was powered by a software controlled driver board (Newport; SMC100CC). The protruding head of the motorized actuator had a minimum incremental motion of 200 nm, which potentially provided microtweezer tip closing resolution of less than 100 nm.

3.4.1.2 - Mechanical Controller Interface

The controller-actuator interface allowed relative positional control from the driving element of the linear actuator to be physically delivered to engage the drive rod of the controller.

For the manual solution, the linear actuator needed to be physically separated from the controller to ensure mechanical isolation and buffering. This required the use of a special tether-cable element that extended from the driving element of the actuator to a luer fitting that could attach to the rear of the controller. The cable protruding from the end of this element would contact and direct the drive rod of the controller.

For the automated solution, the linear actuator could be attached to the rear of the controller using a custom coupler.

Like the packaging and controller, rotational isolation was incorporated into the interface between the drive rod and the actuator head for both the manual and automated designs.

### 3.4.2 - Design Iterations

This section will outline the motivation and reasoning behind the decisions made during the iterative design process of the manual and automated linear actuator systems. The development of the preliminary manual actuator system is discussed first [144],

followed by subsequent manual actuator designs, and then the development of the automated system.

3.4.2.1 - Preliminary Manual Linear Actuator

A preliminary manually controllable linear actuator system was developed that utilized a hand turn-able micrometer as the driving element (Figure 3.18). To provide mechanical buffering and more flexibility in the dimensional constraints, this manual actuator attached to the mechanical controller via a low-friction and flexible nitinol cable tether-cable system. Nitinol is an elastic shape-memory alloy composed of nickel and titanium, and is commonly used in medical devices [145, 146]. To attach to the luer interface on the rear of the controller, the tether was inserted into the front of a female luer hub. For relative motion, the nitinol cable passed through the nitinol tether and luer hub cannula to be presented to the back of the drive rod (Figure 3.19). On the actuator housing, the movable nitinol cable was attached to the "cable nut" (Figure 3.18, blue piece), which was actuated by the micrometer. The nitinol tether was attached to the "cable sleeve end" component (Figure 3.18, red piece). While linearly static, the "cable sleeve end" was rotationally isolated from the housing components ("actuator cap", "spring container"). This was to ensure that if the controller was attached to a positioning stage with a "theta" or rotational movement control that no torsional loading of the nitinol tether-cable system would occur. Any loading could affect the actuation resolution, un-dock the luer hub from the controller, or damage the nitinol connection.

The nitinol-nitinol interface between the tether and cable had excellent flexibility and minimal frictional loading, and stiction would only occur if excessive bending of the tether-cable length occurred. Despite the material flexibility, nitinol displayed good

tensile strength and provided good translation of position. It is for these properties that this material is commonly used in clinical catheter-type systems [146-150]. The nitinol material, however, was very difficult to adhere to due to its low surface energy from the passivation of the titanium surface [151-153]. Because few materials offered the mechanical benefits of nitinol, a variety of adhesion techniques (gluing, clamping, wrapping, soldering, welding, socket-joints) were attempted to connect the nitinol sleeve to the luer hub and actuator housing, and the nitinol cable to the head of the micrometer. A nitinol manufacturer (Memry, CA, USA) was eventually contracted to construct pre-cut nitinol tubes with welded features on the end of the tube to facilitate attachment.

For the manual linear actuator system, opening and closing of the microtweezer tips was thus achieved through the following steps: (1) turning the micrometer head to push the nitinol cable and create relative linear motion; (2) forward movement of the nitinol cable through the nitinol tether to contact the drive rod; (3) actuation of the spring-loaded drive rod internal to the mechanical controller to contact the spring-loaded button of the microtweezer packaging; (4) actuation of the spring loaded button and advancement of the drive cable; (5) movement of the microtweezer box forward, which causes contact of the microtweezer channel with the tweezer beams; and (6) closing of the microtweezer beams, causing the tweezer tips at the end of the beams to close.

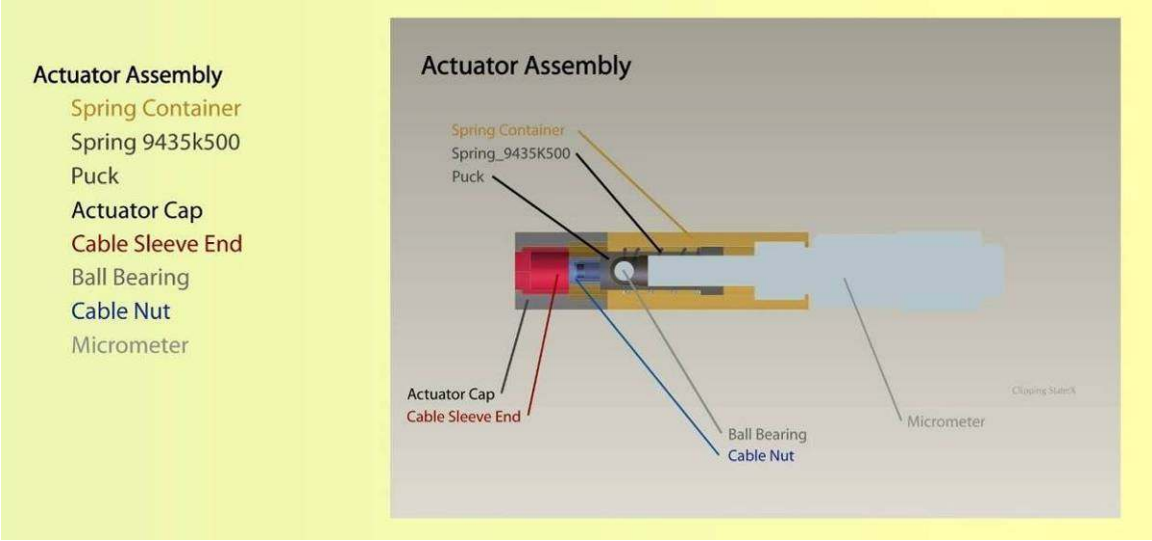


**Figure 3.18**: Manual actuator system that was composed of a manually turn-able micrometer head that connected to a nitinol tether-cable system. A fixed nitinol tube (not shown) is attached to the "Cable Sleeve End" and a moveable nitinol cable (not shown) is attached to the "cable nut", which moves in conjunction with the movement of the micrometer head.

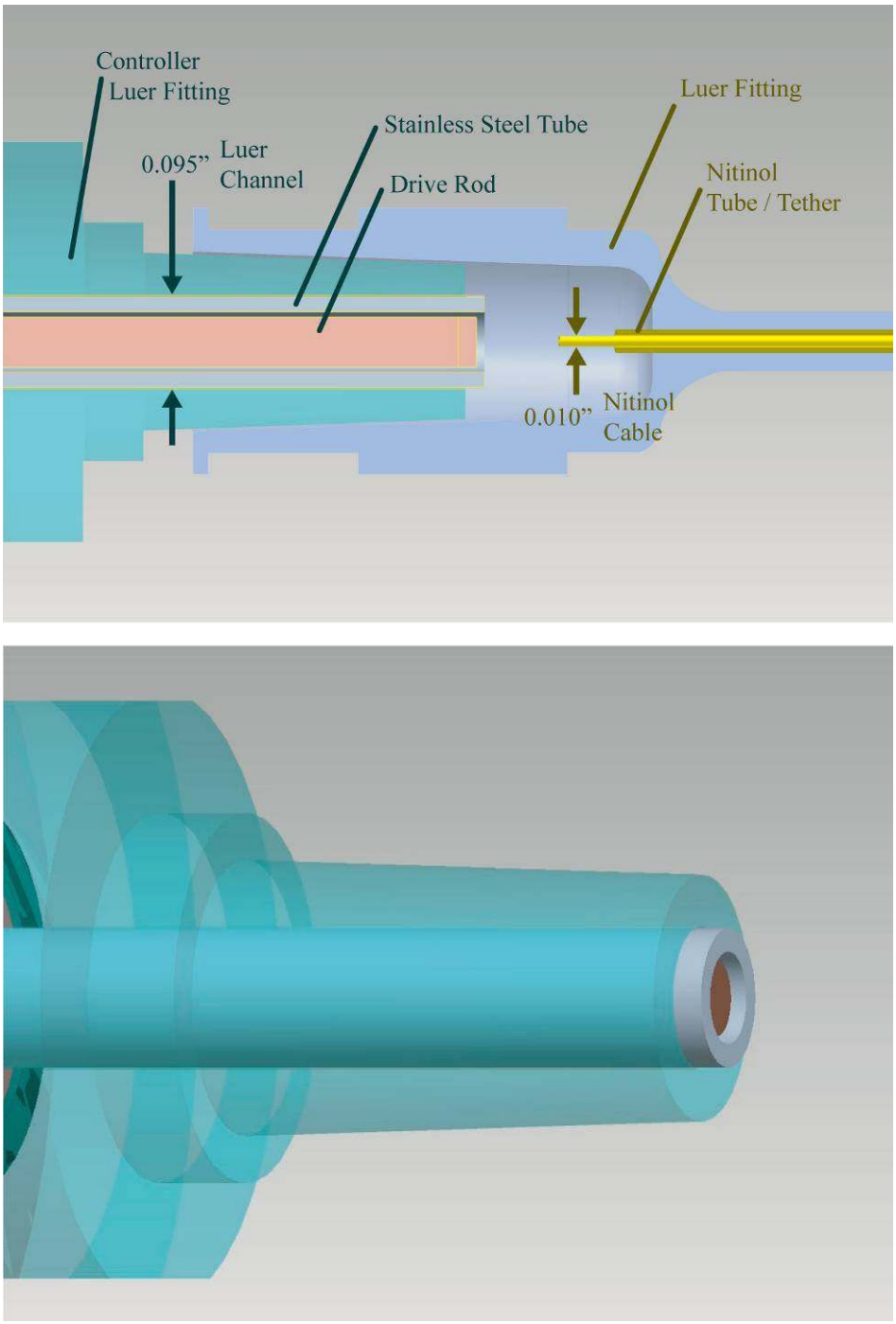


**Figure 3.19**: Cartoon of the luer interface between the mechanical controller and the nitinol tether-cable system highlighting the critical tolerance in the drive rod diameter, inner luer channel diameter, and the nitinol cable diameter. Given the flexibility of the nitinol material, non-axial actuation of the nitinol cable could lead to stiction between the cable and luer channel.

This preliminary manual mechanical controller and actuator system was utilized to facilitate microtweezer assembly, which required testing of the actuation alignment and fluidity. Still photographs of the microtweezer at different positions of tip closure from manual actuation are displayed in Figure 3.20 and Figure 3.21. While this manual system was extremely versatile and provided quick user response to movement, it had limited repeatability required for advanced mechanical testing and for the consistent biological experimentation.

3.4.2.2 - Secondary Manual Linear Actuators

Prior to outsourcing the nitinol welding to Memry, Inc., several design iterations for the manual actuator were created and prototyped to improve the connection between the nitinol tether and the actuator housing. While the "cable sleeve end" was isolated rotationally from the housing, which provided torsional strain relief, the mechanism of this isolation needed to be improved to ensure fluid motion. In the preliminary design, rotation of this component was allowed because the part was simply floating, which could actually affect the relative position of the nitinol tether compared to the cable. In these design changes, a ball bearing is incorporate to prevent linear movement of this part, and to enhance rotational isolation. Several changes to this interface, and the interface between the nitinol tether and housing, and the nitinol cable and micrometer head were designed (Figure 3.22, Figure 3.23)

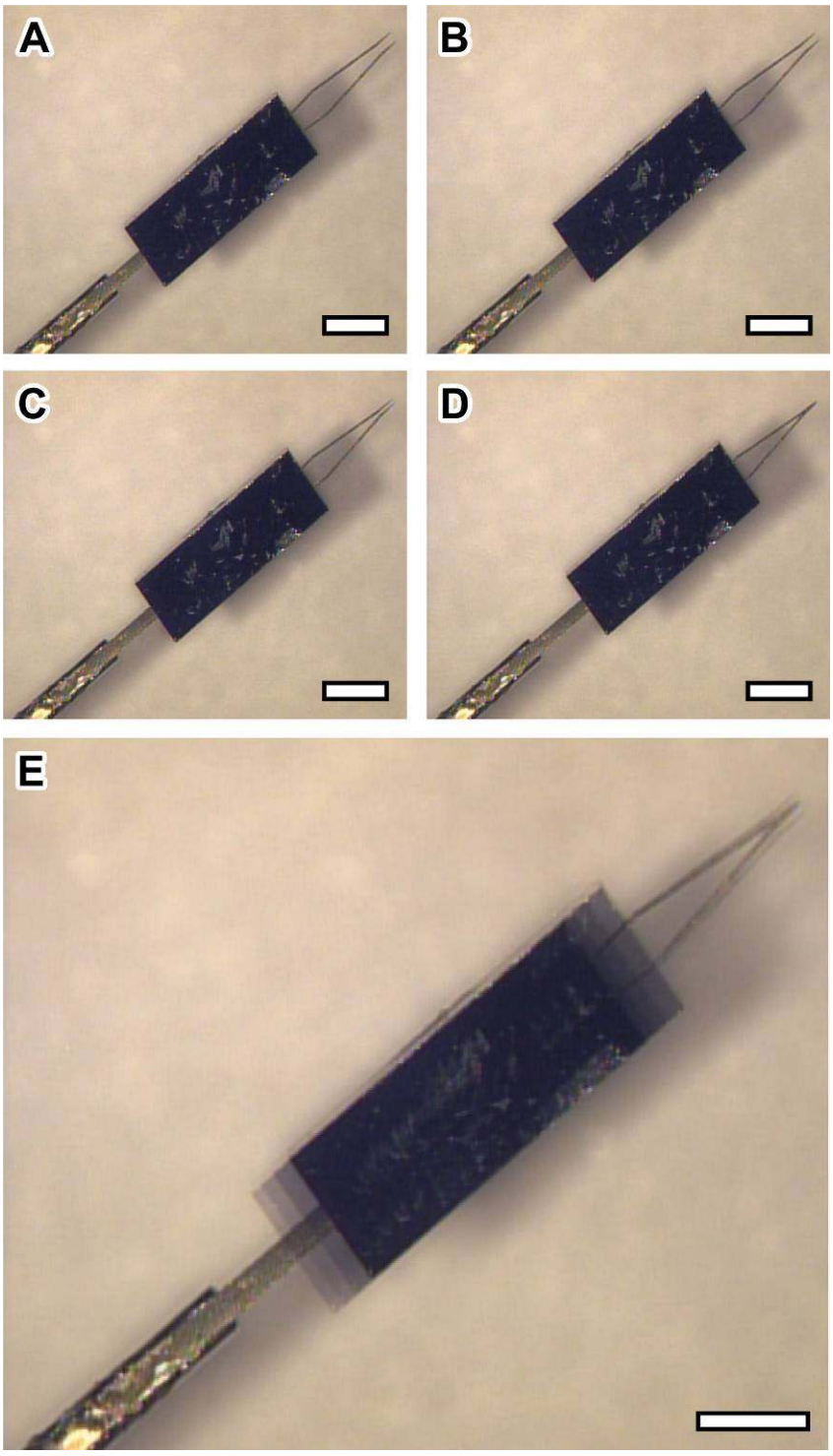


**Figure 3.20**: Bright-field photos of still shots taken over the course of a complete open-to-close actuation of a forceps-tipped tweezer. (A) Tweezer is completely open (320 µm), (B, C) tweezer is partially closed, and (D) tweezer is completely closed. (E) An overlay of the box and tweezer positions is displayed. All scale bars are 1.0 mm.

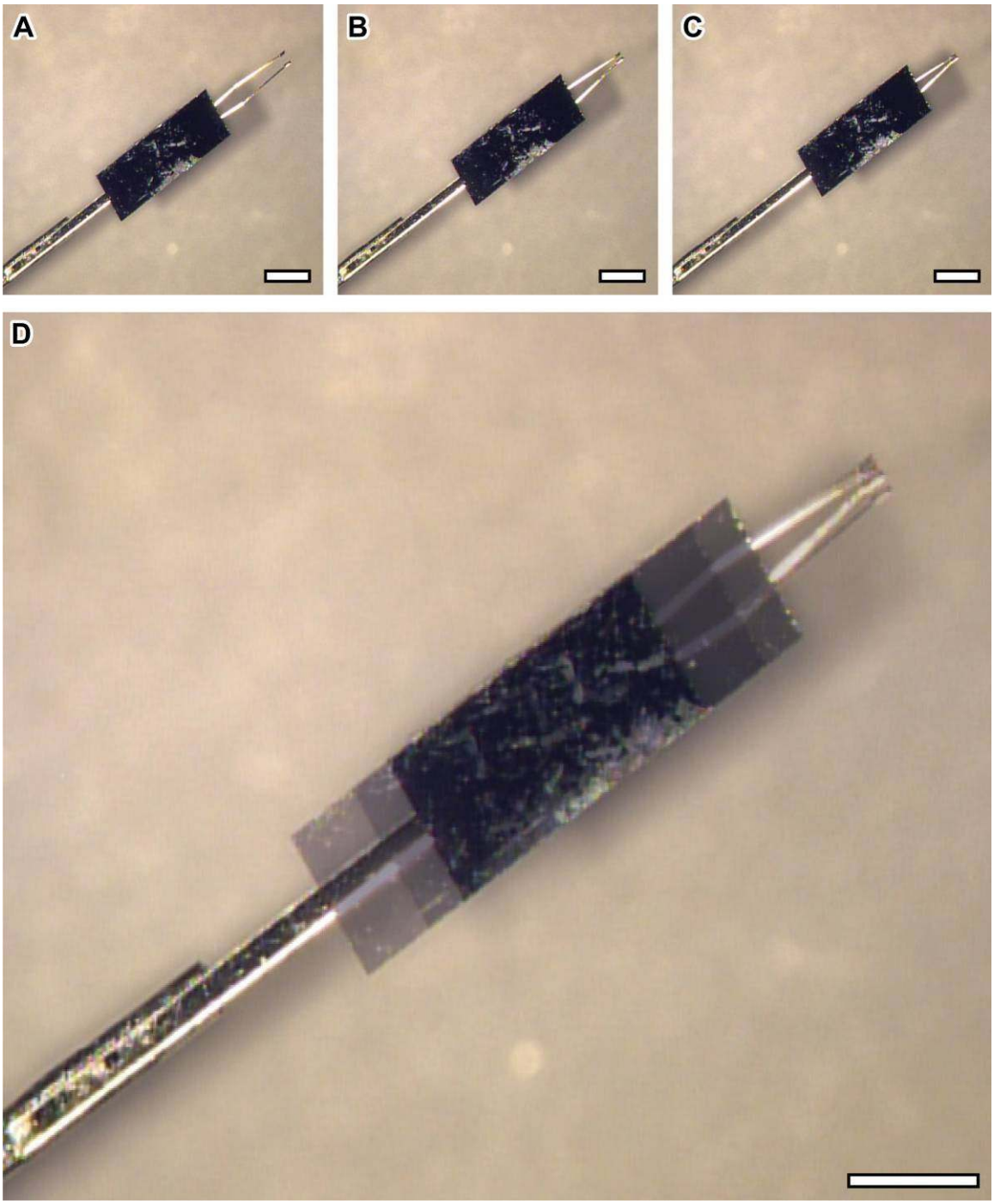


**Figure 3.21**: Bright-field photos of still shots taken over the course of a complete open-to-close actuation of a serrated-tipped tweezer. (A) Tweezer is completely open (320 µm), (B) tweezer is partially closed, and (C) tweezer is completely closed. (D) An overlay of the box and tweezer positions is displayed. All scale bars are 1.0 mm.

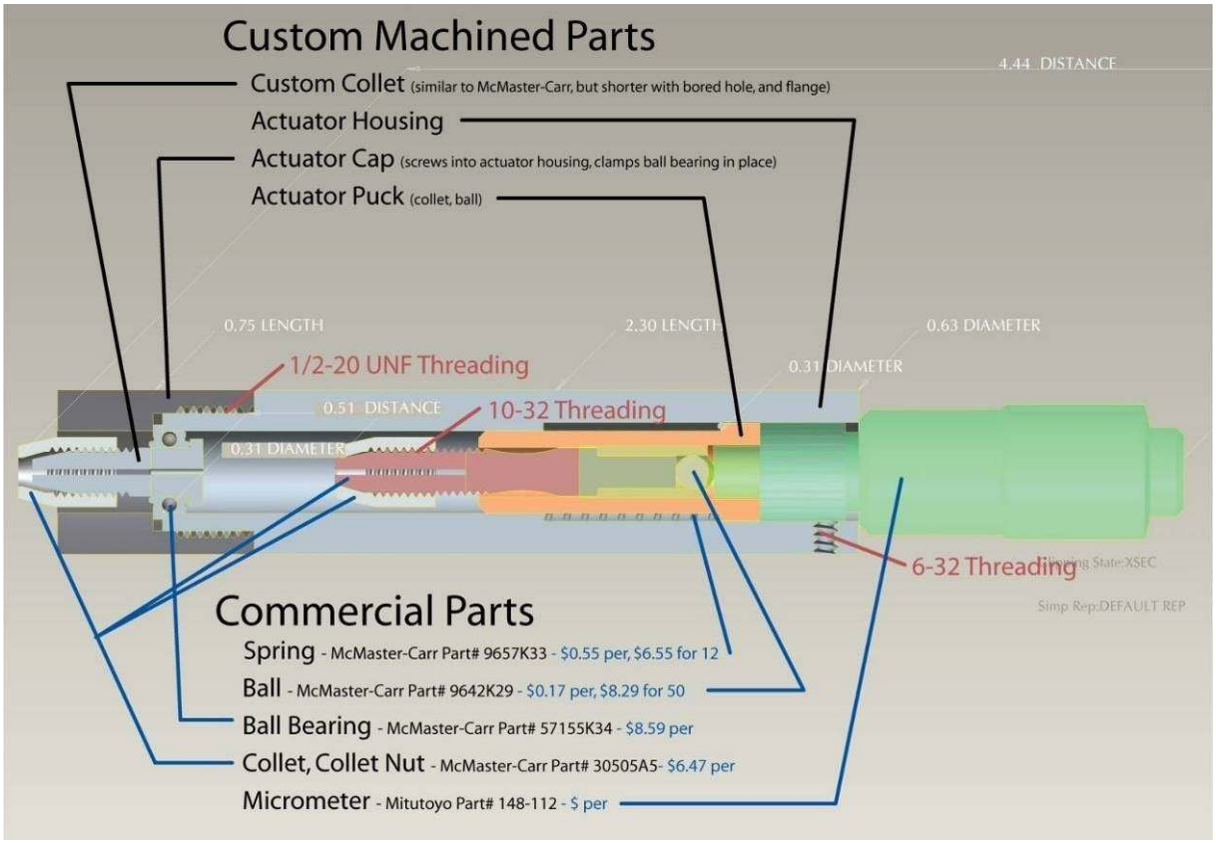


**Figure 3.22**: First alternative manual linear actuator system. A tether cable system for relative motion delivery is utilized in this design. A fixed nitinol tube (not shown) is isolated by the gray collet, and the moveable nitinol cable (not shown) is grasped by the red collet, which moves in conjunction with the movement of the micrometer head.

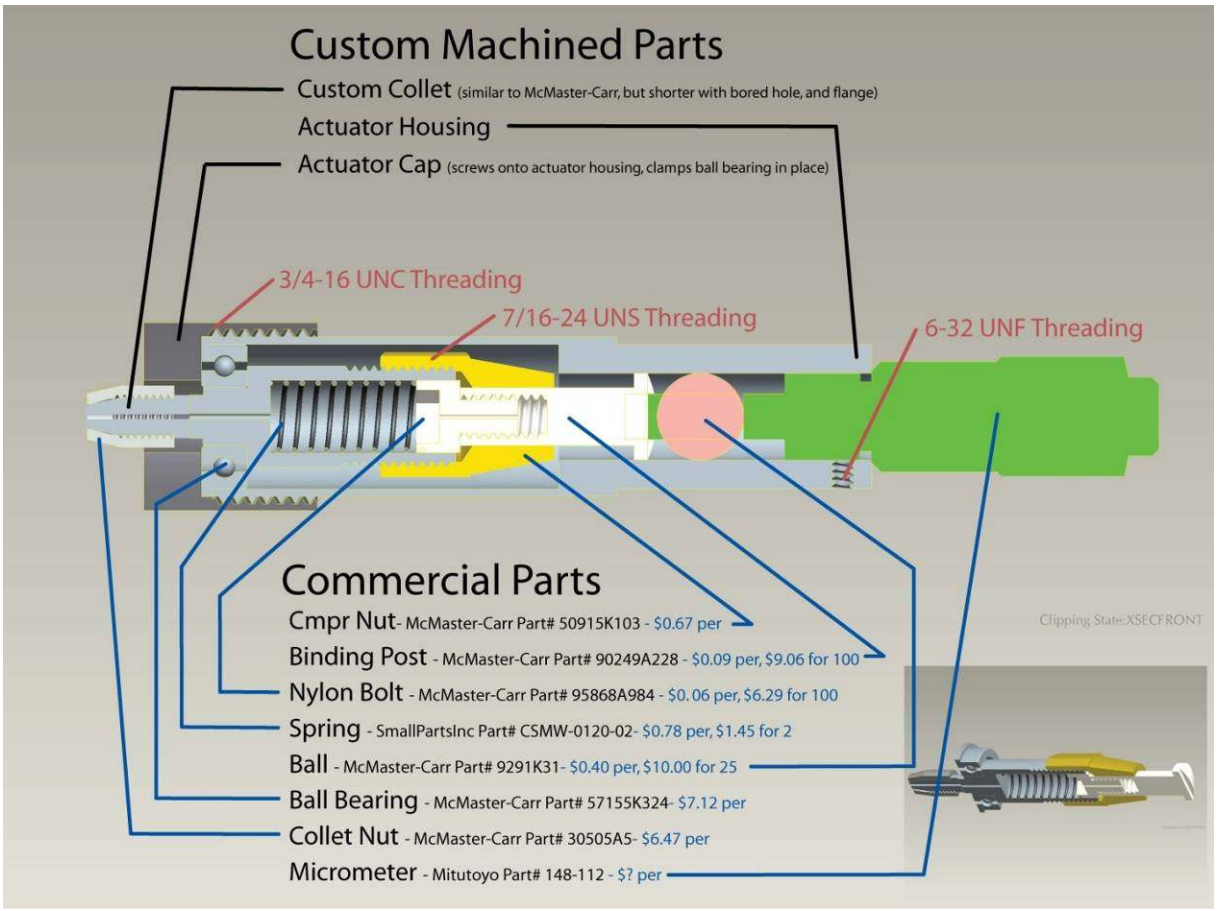


**Figure 3.23**: Second alternative manual linear actuator system. A tether cable system for relative motion delivery is utilized in this design. A fixed nitinol tube (not shown) is isolated by the gray collet, and the moveable nitinol cable (not shown) is glued into the nylon bolt, which moves in conjunction with the movement of the micrometer head.

3.4.2.3 - Automated Linear Actuator

This manual micrometer based system was replaced with a motorized commercial linear actuator that was controllable with software (Figure 3.24). This linear actuator was powered through the Newport SMC100CC single-axis DC motor controller, which sent and received commands to/from a computer through a serial RS-232 connection. A custom built stand-alone software program to communicate with the SMC100CC controller was coded and compiled using LabView 2009 (Figure 3.25, 3.26). This software program allowed a variety of functions, including absolute and relative movements, and repeatable and cyclic movements that ensured repeatability with both cell experimentation and with mechanical testing. This custom designed software also provided the ability to configure the controller to adjust the motor head speed and acceleration.

Instead of an intermediary flexible tether-cable system, the mechanical controller was directly attached to the linear actuator using a custom-designed coupler (Figure 3.27). The internal channel of the coupler was constrained by the need to have contact and engagement of the controller's spring loaded drive rod at the home or default position of the linear actuator. While this engagement needed to be minimal to prevent default actuation of the package's drive cable, it was important to prevent unintended and uncontrolled movement of the drive rod. After fabrication of the linear actuator coupler and assembly, minor adjustments to the length of the drive rod were possible by surface grinding and polishing the tip.

For the automated linear actuator, opening and closing of the microtweezer tips was thus achieved through the following steps (Figure 3.28): (1) the software sends a

command to the control board to move the linear actuator motor head; (2) forward movement of the head advances the spring-loaded drive rod internal to the mechanical controller; (3) actuation of the drive rod contacts the spring-loaded button of the microtweezer packaging; (4) actuation of the spring loaded button and advancement of the drive cable; (5) movement of the microtweezer box forward, which causes contact of the microtweezer channel with the tweezer beams; and (6) closing of the microtweezer beams, causing the tweezer tips at the end of the beams to close.

The computer controlled system, which had higher overall resolution compared the manual system, was used to perform the long term tweezer cycle testing, and to deliver repeatable and controlled cell interfacing tip closures during the biological experiments.

**Figure 3.24**: Automated actuator system (images from www.Newport.com). This system utilizes a Newport TRA12CC DC servo linear actuator motor and a SCM100CC controller board. A RS-232 serial cable can connect the controller board with a computer for sending and receiving commands and configuration information.

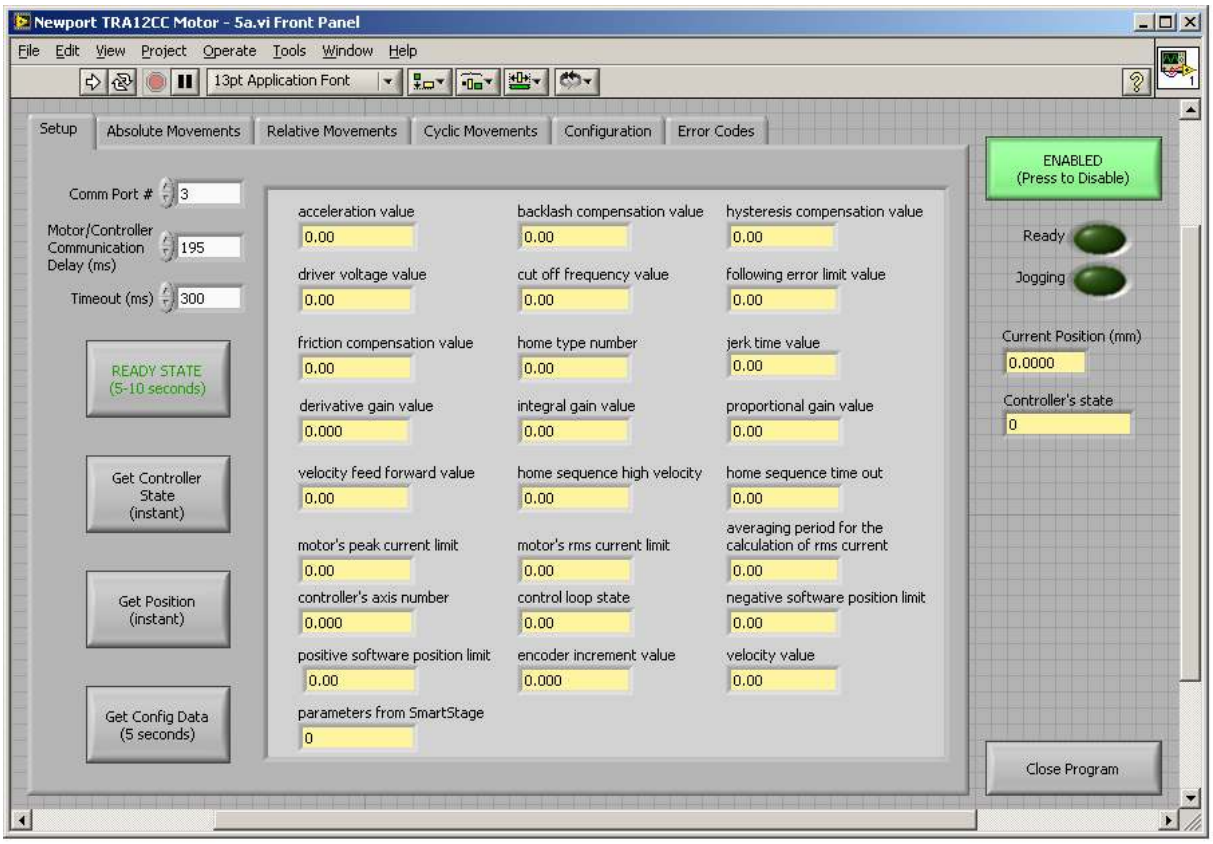


**Figure 3.25**: Graphical user interface (first screen) for custom built software program that enables commands to be sent to the Newport linear actuator controller board. This software was developed using the Labview 2009 programming environment. This screen provides setup and configuration functionality.

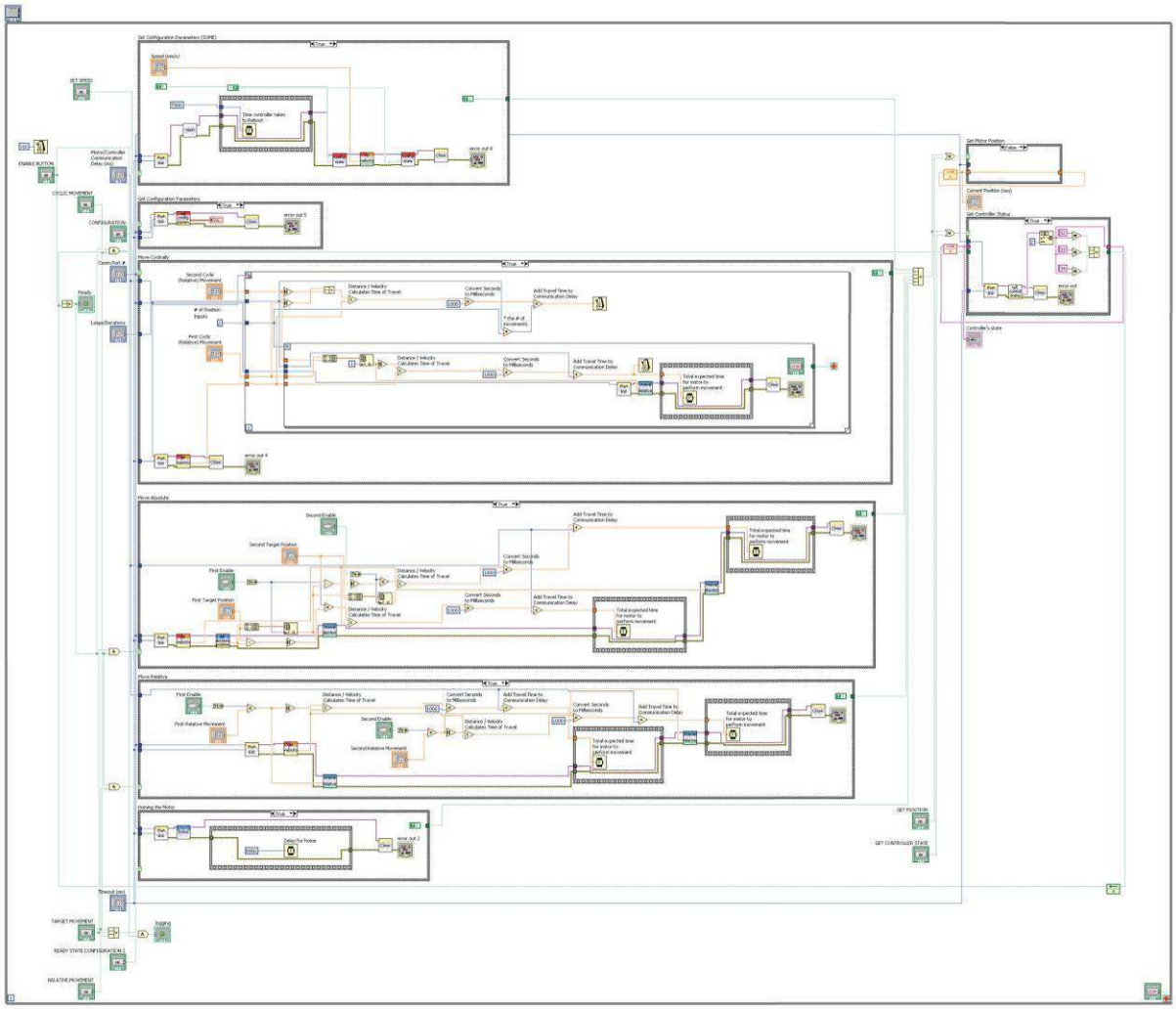

**Figure 3.26**: Screen shot of the programming code for custom built software program that enables commands to be sent to the Newport linear actuator controller board. This software was developed using the Labview 2009 programming environment. This screen shows the run-time code that interprets input from the user and pre-processes it before sending commands to the motor controller. Code for each sub-program block (pre-processing for and communications with the controller) and for each blocked case-statement function for false conditions are not shown.

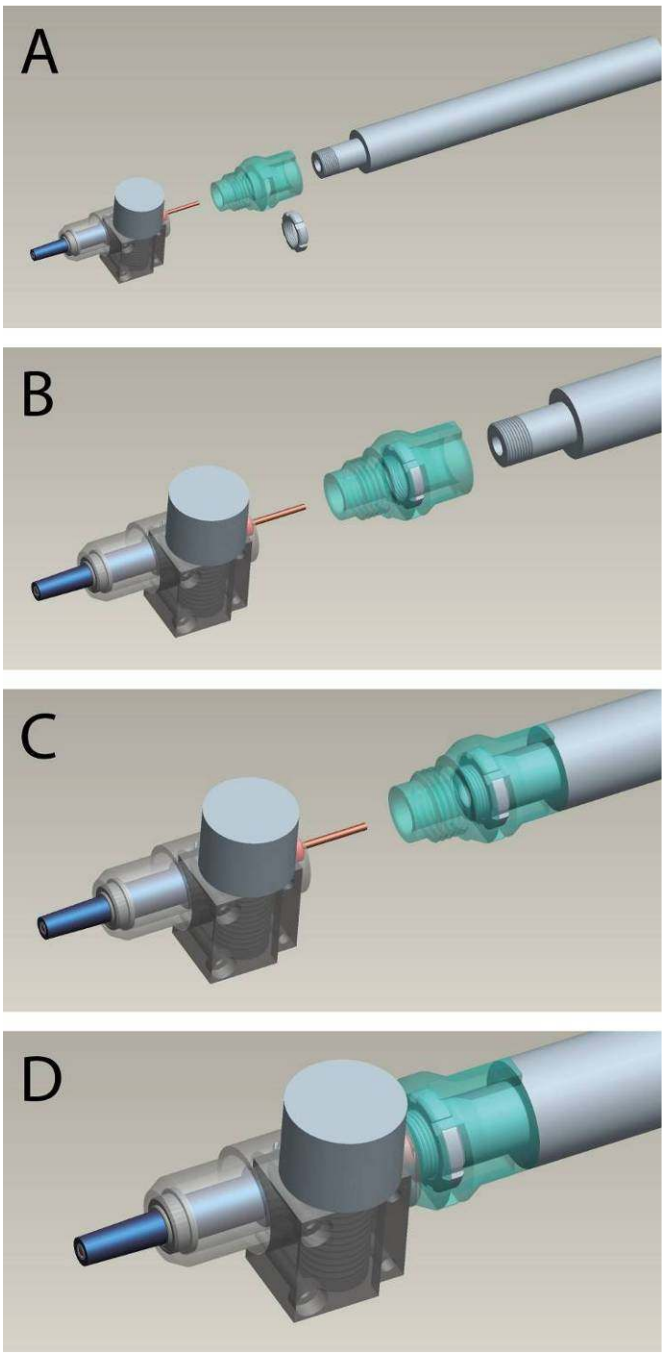


**Figure 3.27**: Schematic of a custom built coupler designed to physically and functionally connect the mechanical controller to the Newport linear actuator. (A, B) The coupler works by sliding over the mounting column of the linear actuator, where a (C) specialized nut is screwed into the threaded section of the mounting column of the linear actuator, and (D) then the coupler is threaded into the rear of the docking station.

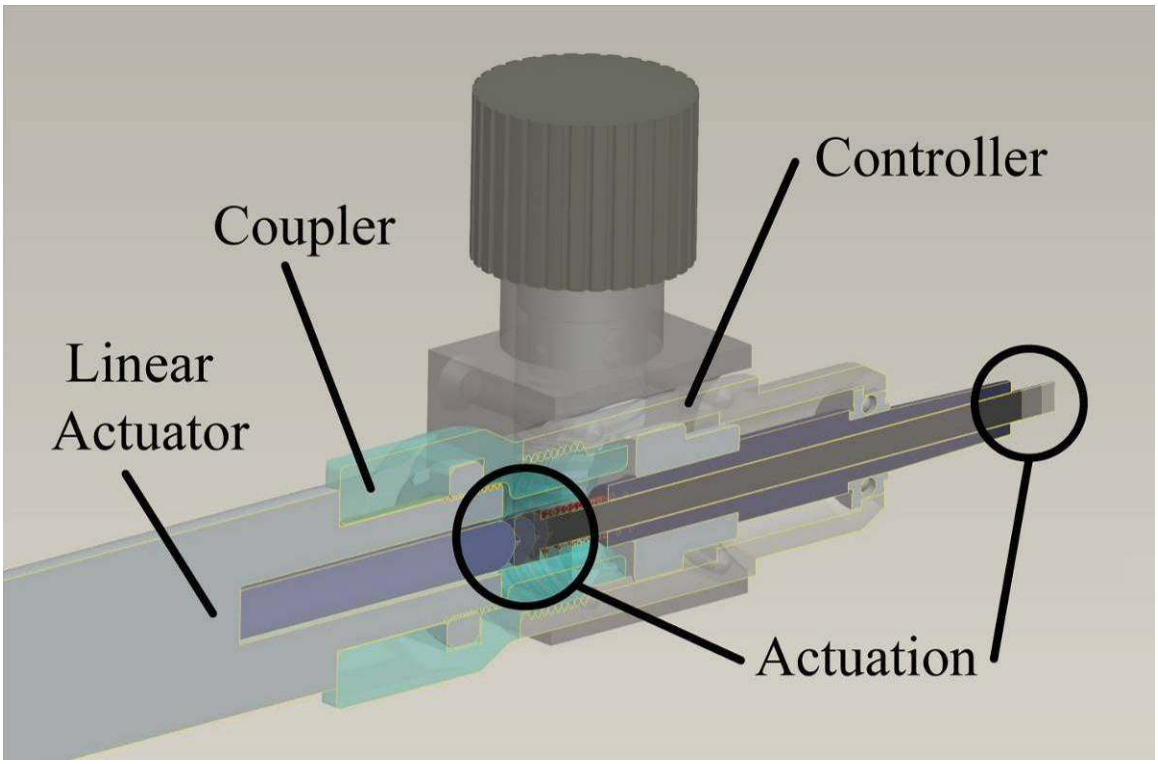


**Figure 3.28**: Schematic of the interface between the linear actuator, coupler, and mechanical controller, and the moving components during actuation. The length of the coupler and controller drive rod need to be tailored to ensure that upon assembly, the actuator was engaging the drive rod, and the drive rod was not engaging the drive cable.

### 3.4.3 - Materials

The materials for the manual linear actuator were selected based on mechanical durability, surface to surface interfacing of moving parts, weight, and ease in machining. For housing and structural components aluminum was selected, and for most parts with direct metal to metal motion contact, brass was used (Figure 3.18, "puck", "cable nut") due to its reduced static coefficient of friction[140]. The luer interfaces and ball bearings were polished stainless steel.

The tether-cable system that connected the manual linear actuator to the controller was composed of a nitinol tube and cable. This material has good mechanical properties to allow both flexibility and tensile strength and good surface properties to reduce friction and stiction during actuation.

The coupler used to connect the automated linear actuator to the mechanical controller was made from the stereolithography polyurethane resin. Threads were incorporated into this design and were strong enough to provide excellent fastener-type connections with both the linear actuator and the controller.

### 3.4.4 - Construction

The extensions of the micrometer head that interfaced with the nitinol cable were assembled first and threaded through the "spring container" housing. Both the "actuator cap," which contained the "cable end sleeve," and the micrometer head were attached to this housing using a collar and set screw connection. For the preliminary manual design, the nitinol pieces were glued, but for the secondary designs, a clamp system was utilized. The automated system assembly simply required the threading of the coupler to the controller housing and to the linear actuator.

### 3.5 - Staging

The stage was a commercially available positioning system that allowed for gross movement of the mechanical controller and attached microtweezer in three-plus dimensions. Because the interchangeable controller mounting brackets were designed with modular fastener surfaces, the controller housing was successfully attached to a variety of micromanipulators and micropositioners. Given that the controller and linear actuator are connected together in the automated solution, custom-designed mounting brackets that attached to the actuator instead of the controller were used as well

#### 3.5.1 - Signatone Micropositioner

The original stage attached to the manual microtweezer system was a Signatone (Lucas Signatone, Gilroy, CA) micromanipulator (SP-170x) (Figure 3.29). The manual linear actuator control knob to direct microtweezer actuation was augmented to the side of the positioner with a custom bracket. The positioner contained a double knuckle feature where the docking station was mounted, allowing two additional degrees of movement freedom for setting the vertical insertion angle of the microtweezer. Additionally, the weight of the stage mitigated mechanical artifact and noise introduced by turning the knobs at its rear.

Use of this stage allowed a variety of manipulation and positioning applications. Coupled with a probing station during testing, the microtweezer system has had the ability to manipulate image markers, crystals, and other small structures, as well as large devices such as MEMS stators and micro-gears (Figure 3.30).

### 3.5.2 - Narishige Micropositioning Stage

A custom designed bracket was built to clamp around the automated linear actuator and attach to the head of a 6-axis manual Narishige (Narishige, Japan) positioning stage (MMN-1, B and C Clamps) (Figure 3.31). This stage was used to precisely direct the microtweezer location within cell culture systems for the preliminary biological studies, and for positioning of the microtweezers next to the load cell during the mechanical characterization (Figure 3.32). For the biological studies, a custom-built stand was design, fabricated, and installed into one of the mounting posts on the microscope imaging station to secure the Narishige stage. This stand provided height adjustment, lateral movement in one direction, and an additional angel of rotational movement (Figure 3.33).

### 3.5.3 - Sutter Micromanipulator

A custom bracket was built to clamp around the automated linear actuator and attach to the mounting block of a Sutter motorized micromanipulator (Sutter Instrument Company, Novato, CA; MP-285). This manipulator was effective at removing mechanical noise that was present when positioning with the manual systems. It also had automated home positions to facilitate experimentation. This manipulator was used to position the microtweezer into the cell culture systems for the majority of biological studies (Figure 3.34).

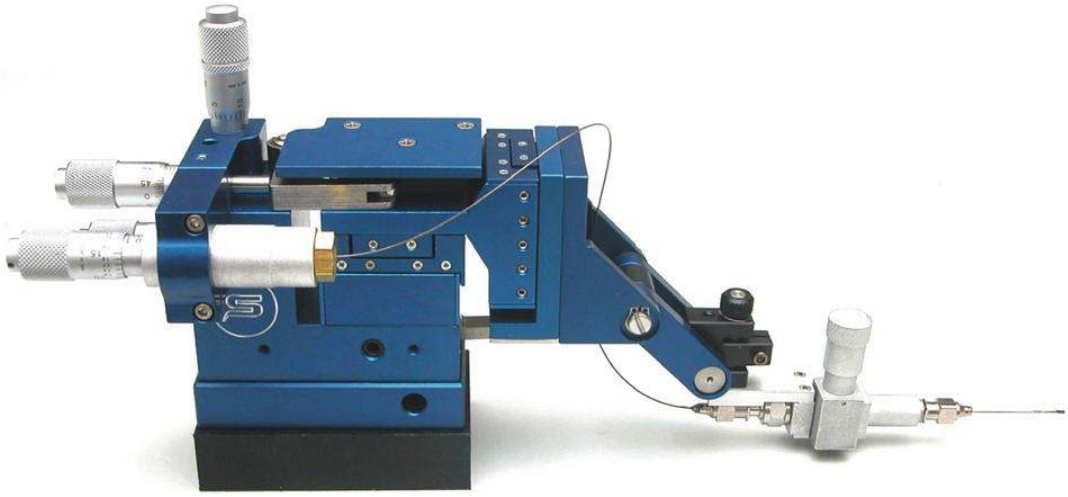

**Figure 3.29**: Photograph of a prototype mechanical controller and manual linear actuator mounted onto a Signatone micropositioner. The nitinol tether-cable system can be seen traveling from the linear actuator to the controller.

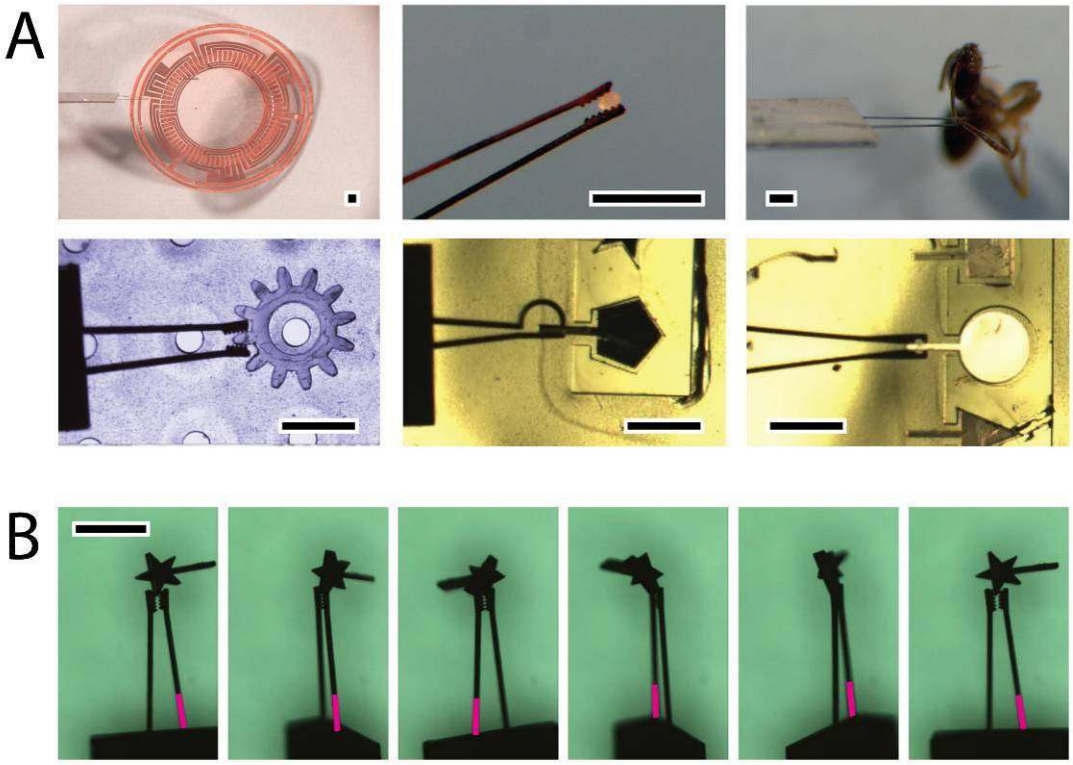


**Figure 3.30**: (A) Stereoscopic and microscopic photographs demonstrating the wide range of applications for microtweezers with varying tip styles. Microtweezers are shown positioning MEMS devices and material samples as well as interfacing with biological samples. (B) The continuous rotational functionality of the microtweezer about its axis is demonstrated in a series of photographs. The same tweezer beam is labeled in pink in each photo to assist in visualizing the rotation. All microtweezers shown here have thickness of 25 µm, and beam widths of 40 µm, and all scale bars are 500 µm.

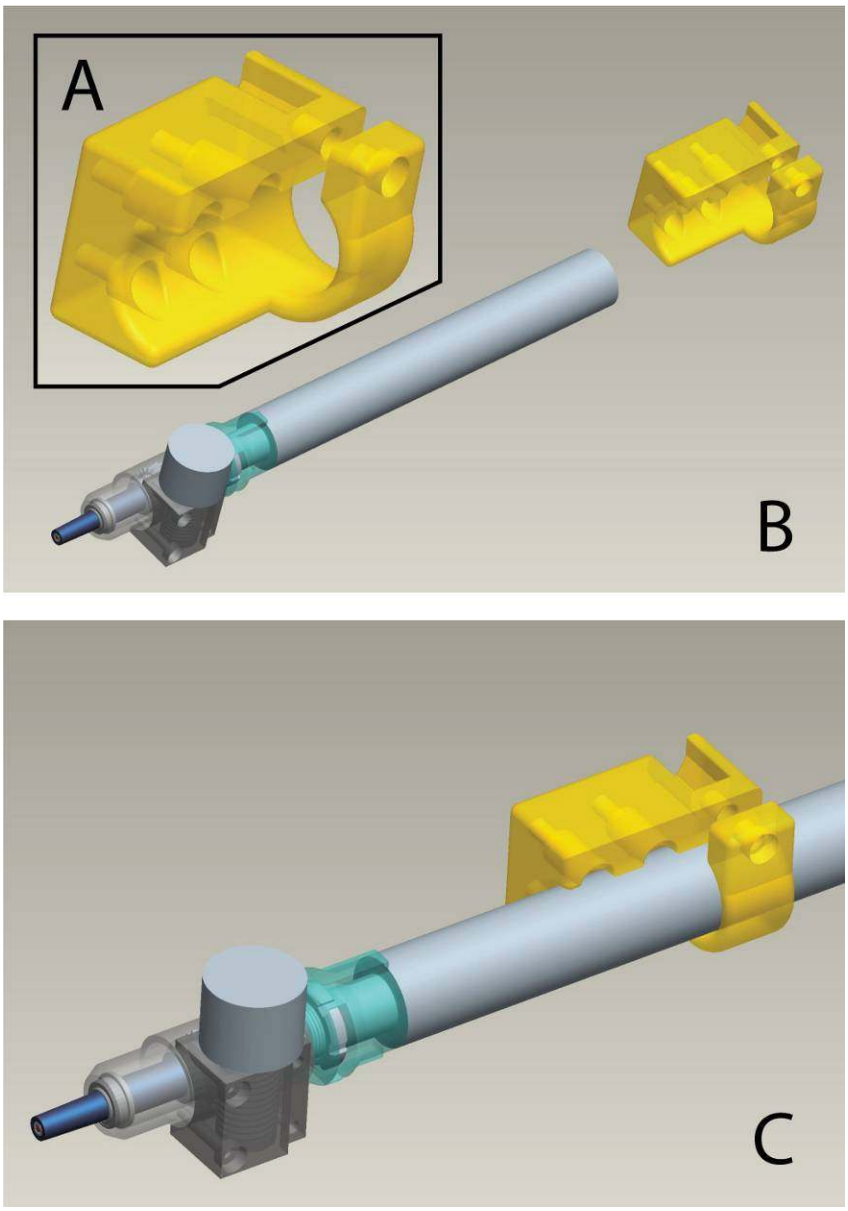


**Figure 3.31**: Schematic of a custom-built mounting bracket to attach the linear actuator to the manual 6-axis positioning stage. (A) This mounting bracket has a bolt-and-nut tightening clamp to secure the linear actuator column, and through-holes where bolts are used to mount the bracket to the chuck of the positioning stage. (B, C) The electrical signal and power cable is inserted through the opening in the clamp, and the bracket is slid over the column of the linear actuator. This bracket allows for coarse forward and backward positioning, and for axial rotation of the linear actuator and controller.

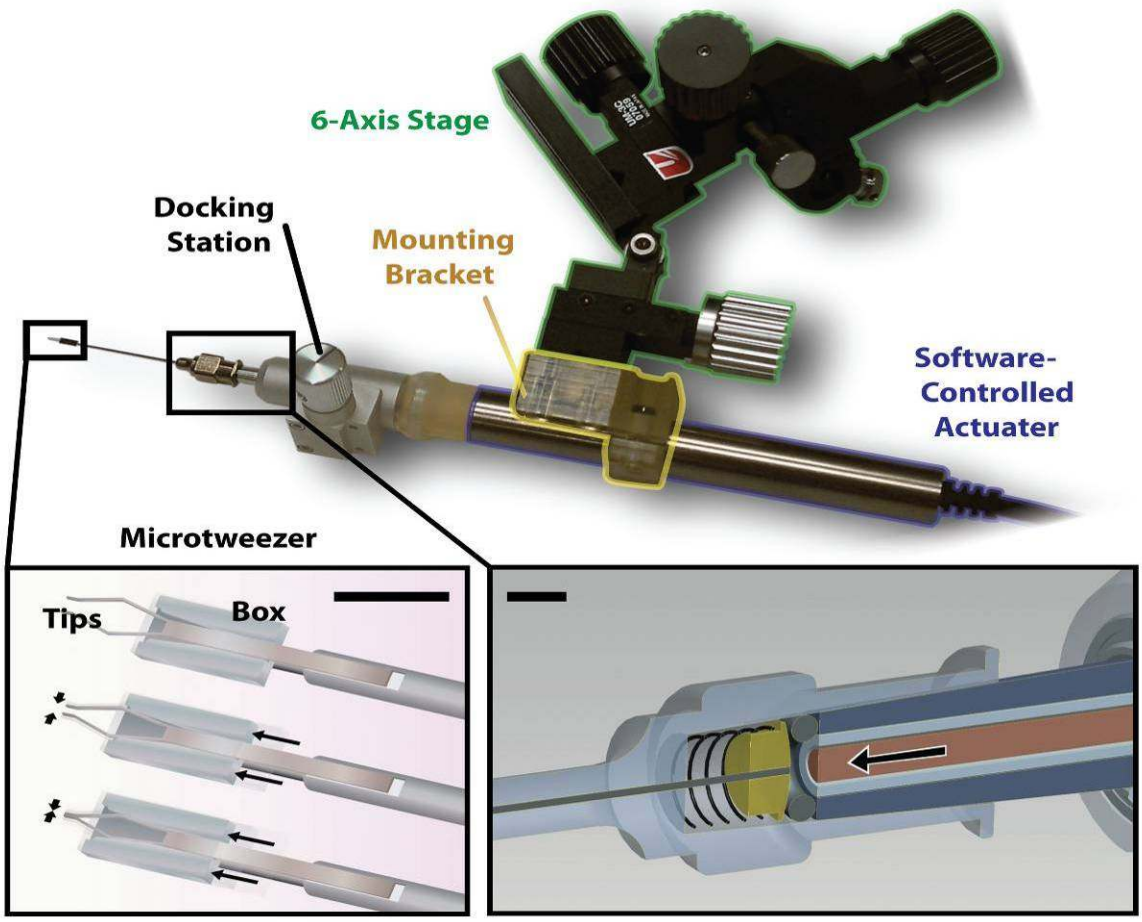


**Figure 3.32**: Photograph of the manual-stage-mounted mechanical controller (labeled docking station here) and linear actuator with affixed packaged microtweezer. The mechanical controller with direct-drive mechanism and rotational functionality are connected to the software-controlled linear actuator with a custom-designed coupler. A custom-designed mounting bracket was used to mount this mechanical controller to a Narishige manual 6-axis stage to provide a large range of positioning motions. The direct drive mechanism and rotational functionality are denoted by arrows.

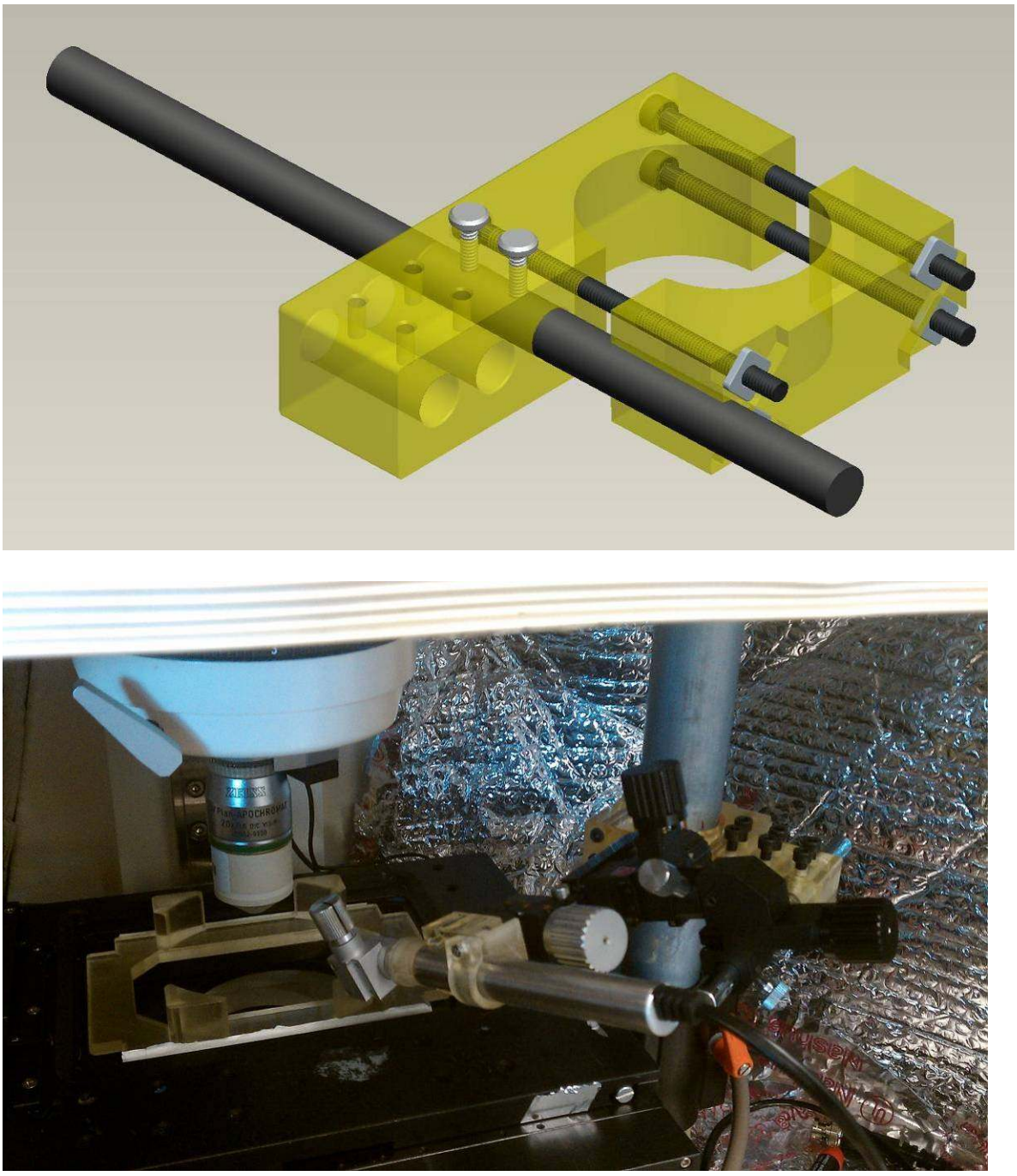

**Figure 3.33**: CAD drawing of the stand to secure the Narishige stage to a 2" OD post (top), and a photograph of the manual-stage-mounted mechanical controller and linear actuator in the neuronal calcium imaging station (bottom). This stand allows for coarse height, lateral, and rotational (around the post) adjustment. In the bottom picture, a custom built chuck for loading the cell culture systems can be seen below the microscope objective.

**Figure 3.34**: Photographs of the microtweezer system attached to a Sutter motorized micromanipulator inside of the neuronal calcium imaging station. The micromanipulator is secured with a rotational stand that is bolted into the air table surface.

# CHAPTER 4

# MECHANICAL MODELING AND CHARACTERIZATION

## 4.1 - Introduction

This chapter presents: (1) the geometric and force models used to aid in the geometric design of the microtweezer beams and the mechanical design of the microtweezer packaging system; (2) the measurement of tip force and comparison to models; (3) endurance testing to evaluate long-term tweezer performance and consistency; and, (4) speed testing and hysteresis examination of tweezer tip closure.

As part of the design process, models can be used to predict the performance of a device prior to construction. Following construction, mechanical characterization determines if the device performs as the model predicted and as designed. Over the iterative design process and prior to construction of the final microtweezer style used in the third aim, various microtweezer-beam and tip designs with different dimensions and geometries were modeled and evaluated. The overall goal of this mechanical characterization was to assess tweezer performance to ensure that it could deliver consistent mechanical input during the injury studies.

## 4.2 - Geometric and Force Modeling

Geometric and force loading models were created to predict the mechanical performance of a variety of tweezer designs. The tweezer designs that were originally examined with models took into account the dimensions of the eventual cell targets for interfacing and the size of the overall device. The model results and the eventual

comparison between these theoretical predictions and the mechanical characterization facilitated substantive design modifications.

### 4.2.1 - Geometric Modeling

The geometric models presented in this section used statics equations to calculate the mechanics of the tweezer beam during closure. They were used to examine: (1) the tweezer tip position during closing; (2) the required box actuation needed to close the tips; (3) the resolution or mechanical advantage of the closing; (4) the linearity of the actuation-to-closure relationship; and, (5) the rate of closure. The calculation of the tweezer tip position and rate of closure was important to understanding the strain and strain rate inputs delivered by the tweezer during the cell injury model. The required box actuation for tip closure, which was constrained by dimensions such as the luer hub length, was important for the design of the microtweezer packaging and docking station. The resolution and linearity of the tip closure was critical to ensuring consistent and precise tweezer tip movements.

In the sections that follow, the tweezer beam and box channel dimensions considered in this model are explained first, followed by the system of equations used to model the tweezer tip closing. A brief description is also given of a custom developed software program used to facilitate the use of these geometric models.

#### 4.2.1.1 - Geometric Modeling System

The microtweezer tips are composed of two beam structures with rectangular cross sections. Because of the micro-scale dimensions of the device, and the same dimensional magnitude for both the width and thickness of the beam, the strength and mechanics of the tip motion can be modeled using beam theory [127, 154-158].

The cross sectional dimensions and predicted contact locations of the box channel wall and tweezer beams were used to calculate the geometries of the tweezer beams and tweezer tips throughout the actuation range of the box. Geometric equations were then solved to create an expected actuation of the tweezer beams based on the beam geometries, the box channel geometries, and the box location relative to the tweezer body and beams (Table 4.1, Figure 4.1, and Table 4.2). Table 4.1 presents the constant and variable dimensions of the tweezer beam and box, and Figure 4.1displays their location. Table 4.2 lists the series of equations used to input the tweezer beam and box geometries to calculate the static position of the tweezer tip. Eulerian solving methods used these static measurements over the actuation range of the box to calculate the tip closing regimen, rate of closure, and total box actuation required for complete closure.

**Table 4.1**: Table depicts the calculated constraints and the dependent and independent values that were used in the various geometric and force models. This table shows the pertinent values in the model, and the equations used to determine the initial conditions and values during both drive and overdrive scenarios for actuation.

| | |
|---|---|
| Constrained Values: | |
| Tweezer Body, Beams, and Tips: | |
| Upper Arm Length: | $C_U$ |
| Forearm Length: | $C_F$ |
| Elbow Angle: | $\Theta_{TOT}$ |
| Beam Thickness: | $T_{TIP}$ |
| Body Thickness: | $T_{BODY}$ |
| Initial Shoulder Angle: | $\Phi o$ |
| Box: | |
| Notch Separation: | N |
| Overdrive Angle: | $\Omega$ |
| Dependents and Calculated Values: | |
| Shoulder Angle: | $\Phi$ |
| Upper Arm Vertical Vector: | $A_U$ |
| Upper Arm Horizontal Vector: | $B_U$ |
| Forearm Vertical Vector: | $A_F$ |
| Forearm Horizontal Vector: | $B_F$ |
| Elbow Angle – Upper Arm Sector: | $\Theta_U$ |
| Elbow Angle – Forearm Sector: | $\Theta_F$ |
| Elbow Separation/Width: | W |
| Moment Vertical Vector: | $A_1$ |
| Moment Length: | $C_1$ |
| Moment Horizontal Vector: | $B_1$ |
| Actuation Distance Transition: (When actuation transitions from drive to overdrive) | $A_{U,Trans}$ |
| Tip Separation: | $T_S$ |
| Input / Independent Variable | |
| Actuation Distance: | Actuation |

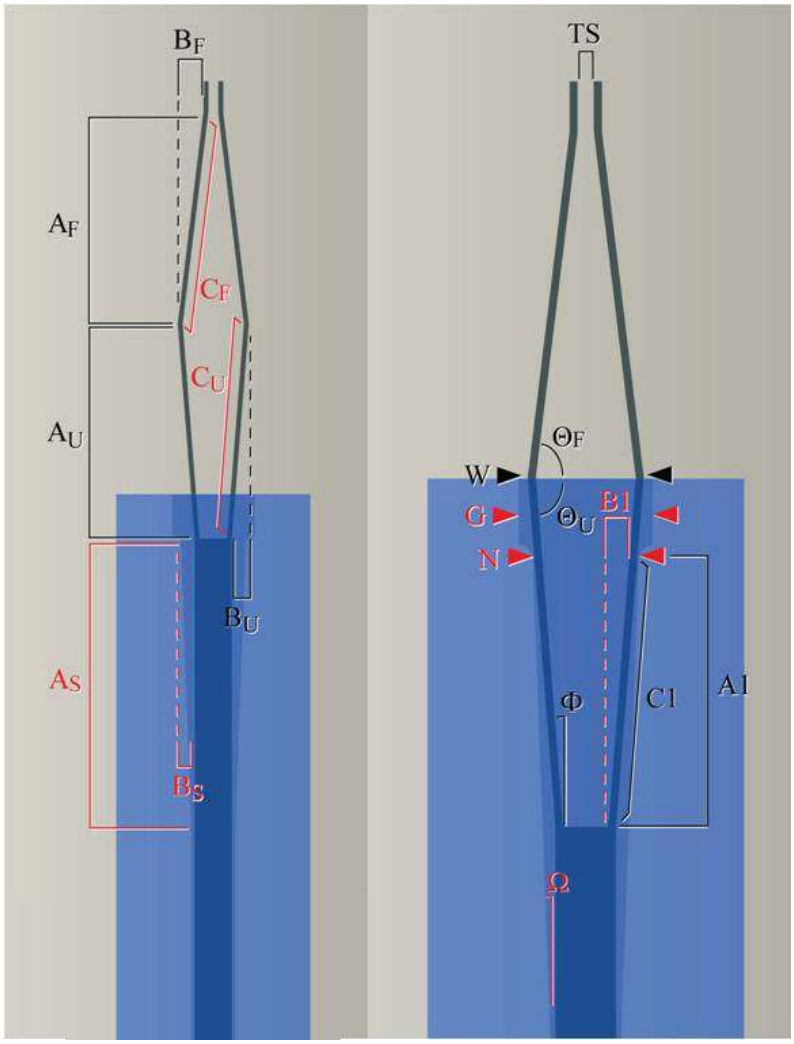


**Figure 4.1**: Schematic of the tweezer body and beams housed within the channel, and the pertinent geometric dimensions that are considered when calculating the predicted actuation behavior. Constant/Static dimensions are highlighted in red, and dependent/dynamic dimensions, which change value over the course of actuation, are in black.

**Table 4.2**: Table depicts the calculated values for the modeling of tweezer beam actuation. This table shows the pertinent values in the model, and the equations used to determine the initial conditions and values during both drive and overdrive scenarios for actuation.

* Assumes tweezer beams and channel notch at initial contact point.

** When action turns from drive to overdrive

| Calculated Values: | | *Initial Value | Actuation Value |
|---|---|---|---|
| Shoulder Angle: | $\Phi$ | $\Phi_o$ | $\Phi = \tan^{-1}(\frac{B_1}{A_1})$ |
| Upper Arm Vert. Vector: | $A_U$ | $A_{Uo} = C_U \cdot \cos(\Phi_o)$ | $A_U = C_U \cdot \cos(\Phi)$ |
| Upper Arm Horz. Vector: | $B_U$ | $B_{Uo} = C_U \cdot \sin(\Phi_o)$ | $B_U = C_U \cdot \sin(\Phi)$ |
| Elbow Angle – Up. Arm: | $\Theta_U$ | $\Theta_{Uo} = 90 - \Phi_o$ | $\Theta_U = 90 - \Phi$ |
| Elbow Angle – Forearm: | $\Theta_F$ | $\Theta_{Fo} = \Theta_{TOT} - \Theta_{Uo}$ | $\Theta_F = \Theta_{TOT} - (90 - \Phi)$ |
| Forearm Vert. Vector: | $A_F$ | $A_{Fo} = C_F \cdot \sin(\Theta_{Fo})$ | |
| Forearm Horz. Vector: | $B_F$ | $B_{Fo} = C_F \cdot \cos(\Theta_{Fo})$ | $B_F = C_F \cdot \cos(\Theta_F)$ |
| Elbow Separation: | W | | $W = (B_U + T_{BODY}) \cdot 2$ |
| Moment Vert. Vector: | $A_1$ | $A_{1o} = \frac{B_{1o}}{\tan(\Phi_o)}$ | $A_1 = A_{1o} - Actuation$ |
| Moment Length: | $C_1$ | $C_{1o} = \frac{B_{1o}}{\sin(\Phi_o)}$ | $C_1 = \frac{B_1}{\sin(\Phi)}$ |
| Moment Horz. Vector: | $B_1$ | $B_{1o} = \frac{N + T_{BODY}}{2}$ | $B_{1,Drive} = \frac{N + T_{BODY}}{2}$<br>$B_{1,Overdrive} = B_{1o} - (A_1 - A_{U,Trans}) \cdot \tan(\Omega)$ |
| **Actuation Transition: | $A_{U,Trans}$ | $A_{U,Trans} = \frac{B_{1o}}{\tan(\sin^{-1}(B_{1o}/C_U))}$ | |
| Tip Separation: | $T_S$ | | $T_S = (B_U - B_F - T_{BEAM}) \cdot 2 + T_{BODY}$ |

4.2.1.2 - Tweezer and Box Designs Examined

For the following mechanical modeling and characterization, two main tweezer beam designs were examined (Figure 4.2). The first design was a "narrow" gap tweezer that had a tip separation of 80 μm, an upper arm length of 1.740 mm, and a lower arm length of 1.718 mm. The second design was a "wide" gap tweezer that had a tip separation of 320 μm, an upper arm length of 1.740 mm, and a lower arm length of 1.713 mm. Testing these two designs would cover the range of tip separations of all the microtweezer designs considered.

For all mechanical modeling and characterization, a single microtweezer box design was used. This design was successful during preliminary performance tests and had a large drive and over-drive range that was capable of closing microtweezer designs with tip separations greater than the wide-style (320 μm) tested. Given the limited range of shoulder and elbow tweezer beam angles explored, it also provided roughly 3:1 mechanical advantage for increased actuation resolution. These successes resulted in the design being used in the single run of the silicon box fabrication, and subsequently, the mechanical characterization tests. In the inner channel of this box design, the separation of the drive-contacts was 0.513 mm, and the angle of the over-drive plane was $2.2^{o}$ inward from the point of the drive contact. This over-drive wall angle was continued until the wall separation of the channel was 330 μm, which provided room for the 300 μm-wide tweezer body to slide during actuation.

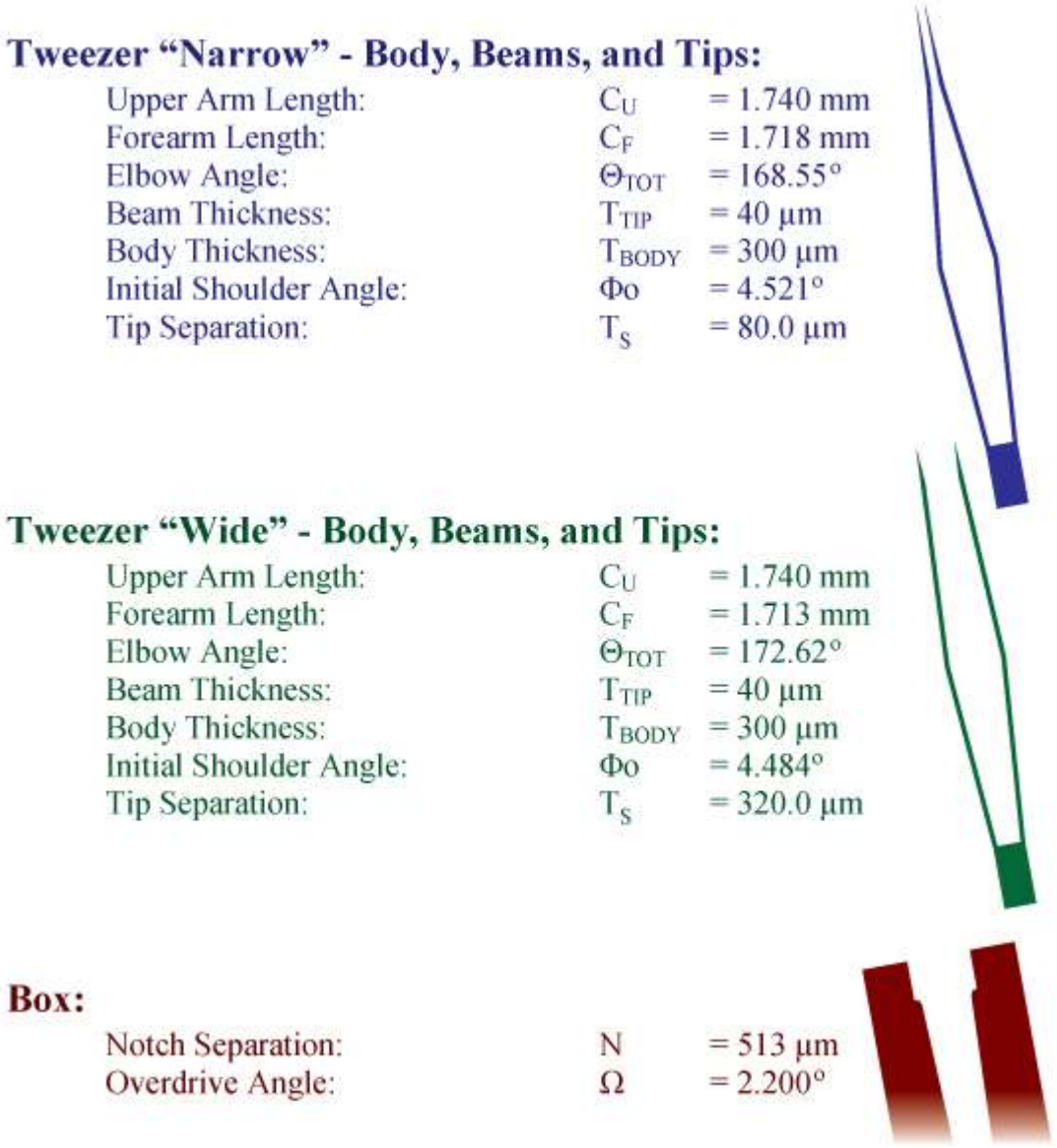


**Figure 4.2**: Schematic of the tweezer body and beams housed within the channel, and the pertinent geometric dimensions that are considered when calculating the predicted actuation behavior. Constant/Static dimensions are highlighted in red, and dependent/dynamic dimensions, which change value over the course of actuation, are in black.

4.2.1.3 - Tip Closure and Closure Rate Modeling

The separation of the tips for two selected tweezer beam geometries ("wide" tips separated by 320 μm, and "narrow" tips separated by 80 μm) are shown based on the actuation distance of the box (Figure 4.3). The narrow tips could close completely with just the drive range of the actuation, where the box channel width is constant as the box advanced forward over the tweezer beams. This length of the drive range depends on the geometries of the upper arm of the tweezer beam and the separation of the drive contacts within the channel of the box. For the tweezers systems modeled here, which both had the same channel and tweezer upper arm geometries, the drive range was 390 μm from the point of contact between the beam and drive contact. The wide tips required a total box actuation of ~1100 μm to close completely, and needed the additional use of the over-drive range of actuation, where the channel width narrows as the box moves forward.

From the tip closure regimen, it appears that as the angle of deflection of the tweezer beam increases, the rate of closure decreases right before the over-drive range is reached. Despite this slight non-linearity, an averaged mechanical advantage can still be calculated for the closure. For a tweezer with a tip separation of 330 μm, a box actuation of 1.09 mm is required to close the tips, providing a mechanical advantage of roughly 1:3. Tailoring this mechanical advantage could be accomplished by altering a number of dimensions, such as the shoulder angle, the tweezer body width, or the drive contact separation in the box channel. The shoulder angle of the tweezer beam could be increased to reduce or even flip the mechanical advantage (tip closes faster than actuation of box), or the shoulder angle could be decreased to close the tweezer tips slower and

improve the advantage. With this model, tweezer and box geometries could be designed to provide a variety of closing regimens through both regular and overdrive box actuation.

For the design of the tweezer used in the single-cell injury studies, a constant tip closure rate was important to ensure consistent strain rate during the cellular injury studies. The expected actuation range of the prescribed cell injury regimen was predicted based on average rat neuron soma size (~10 μm) from cell culture microscopy (Chapter 5, [159]). Based on this cell size, and the strain injury, the closure rate for the entire movement range of the tweezer tips during the mechanical strain deliver was examined for consistency. For a cell injury with a 50% strain, and the rate was shown to only change from 0.306 μm of closure for every 1 μm of box actuation to a rate of 0.300 (Figure 4.4).

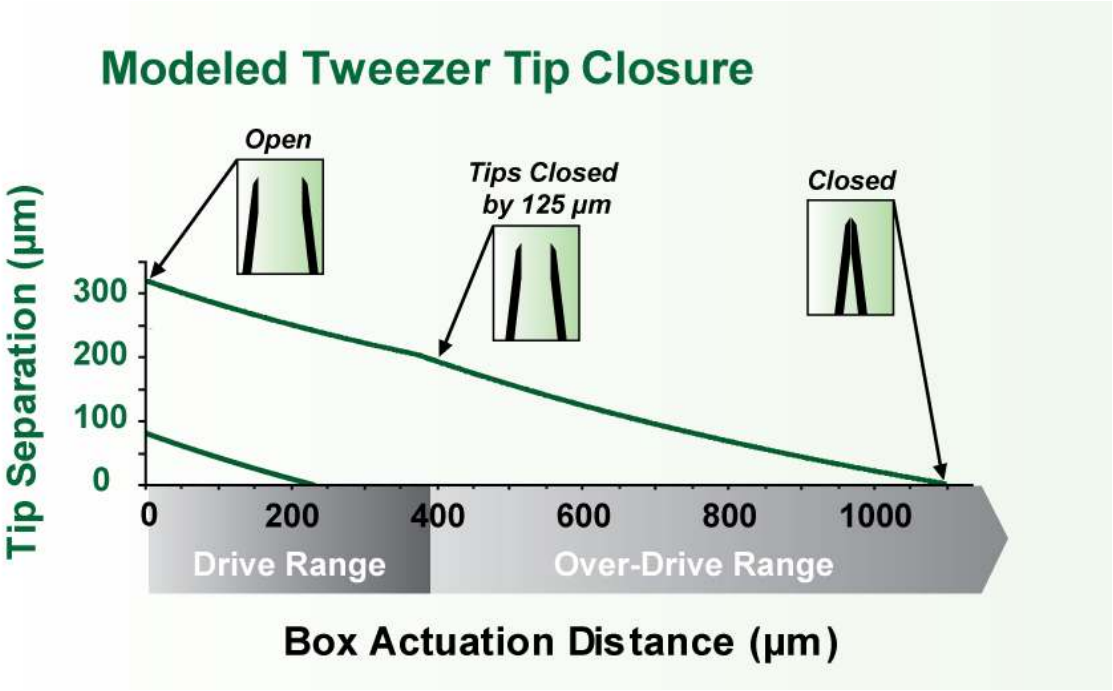


**Figure 4.3**: Modeling data for separation of tips based on actuation distance of box for two tweezer models (320 µm gap, 80 µm gap). The actuation of the box is the distance traveled after contact of channel with tweezer beams.

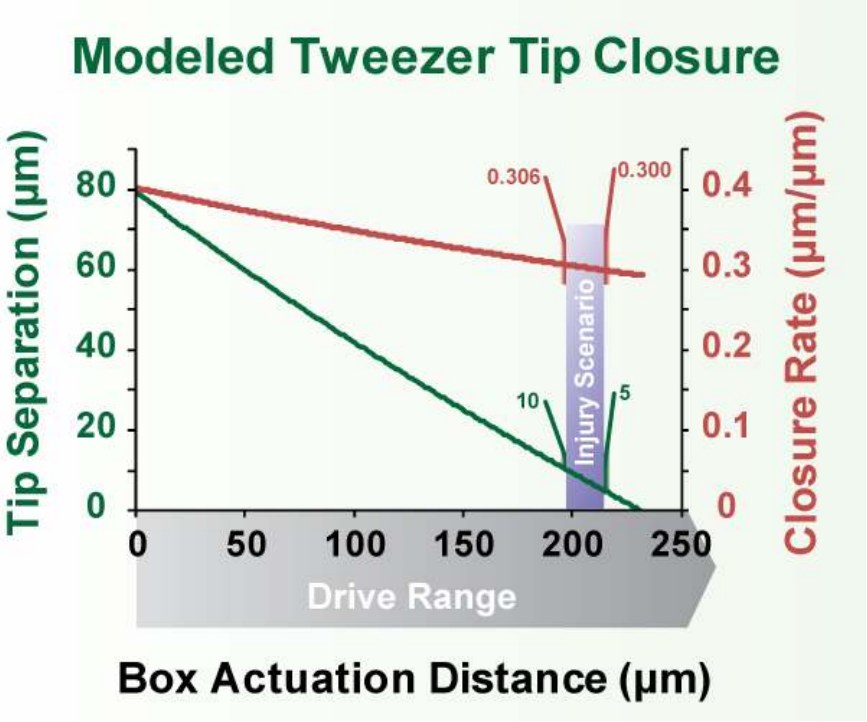


**Figure 4.4**: Modeling data for the narrow tip style (80 µm gap) for separation of tips and rate of closure based on actuation distance of box. The expected range of the prescribed cell injury regimen is displayed with the noted changes in separation and rate of closure. This shows that a consistent rate of closure is expected during the injury studies, which suggests a consistent injury strain rate. The actuation of the box is the distance traveled after contact of channel with tweezer beams.

4.2.1.4 - Geometric Modeling Software

To aid the design of the tweezer geometries, custom developed software programs were coded in Microsoft's Visual Studio (Figure 4.5). These tools provided data for the functional relationship between the box linear actuation and tweezer tip closure. This information assisted in the calculation of the mechanical advantage, or increase in the resolution, provided by each tweezer-beam design. Closure rate and expected forces seen at the tweezer tips were also elucidated to aid overall geometric tailoring of each design. The use of this tool ensured rapid translation from concept to model.

The software program visually and mathematically demonstrated the tweezer positions over the range of actuation and the actuation resolution of the tweezer tips over the actuation range determined by the geometries and driving force. Fundamental geometric equations (displayed previously) defined the software model, and the interface allowed the user to specify the tweezer and box geometries, and the mechanical controller actuation resolution and movement. During the entry of specifications, built in value-checks prevented the evaluation of tweezer tips that would not achieve closure. If this occurred, the program suggested changes in either the box or tweezer geometries. A video of the tip closing was also viewable at different box actuation speeds.

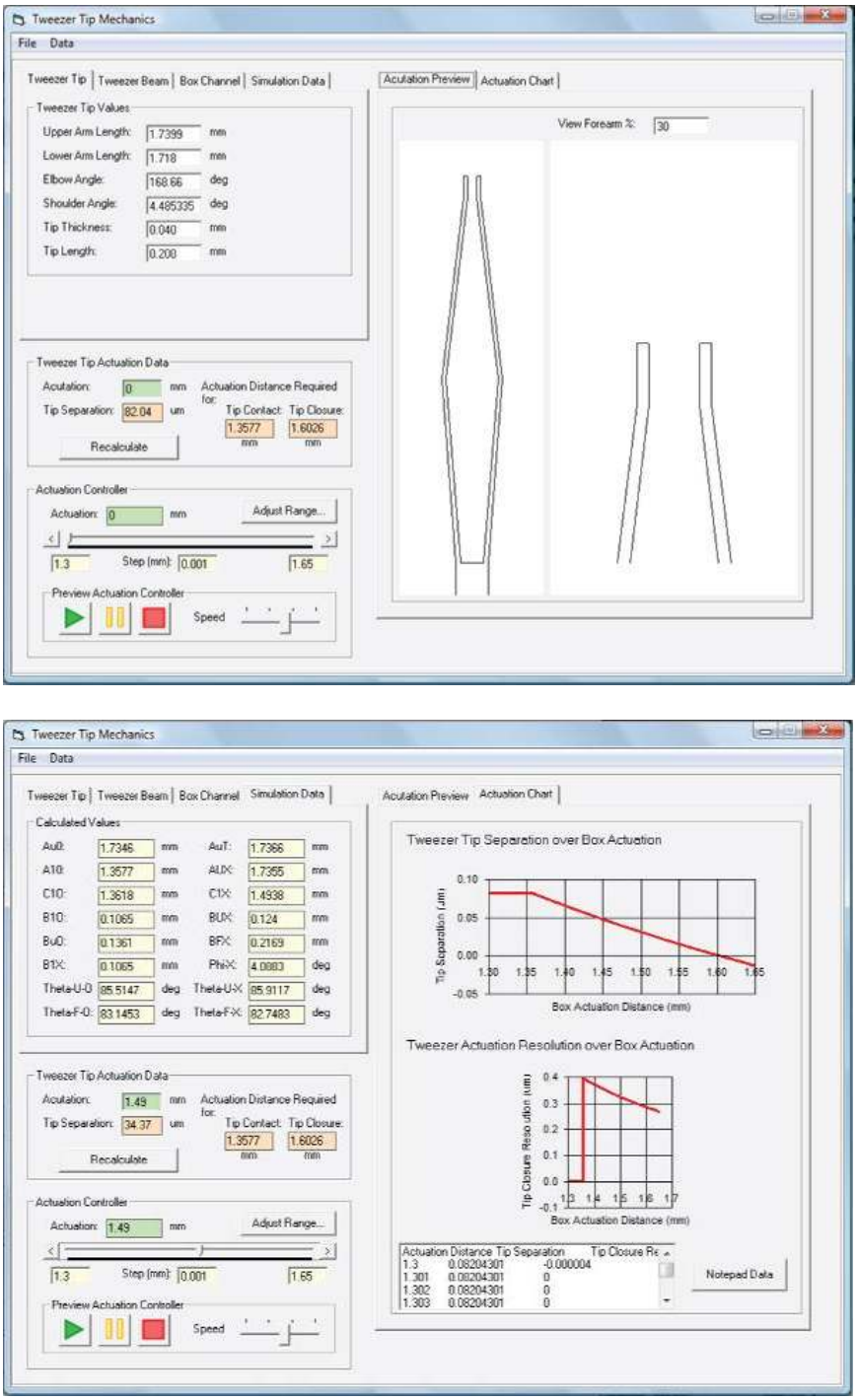


**Figure 4.5**: Screen shots of a custom written tweezer mechanics software program which allows quick parameter adjustment and assessment of tweezer actuation paradigm. With the modeling data stored and processed in this program, additional functionality, such as force modeling, could be subsequently integrated.

### 4.2.2 - Force Modeling

The force models presented in this section used the previously established geometric models along with the tweezer beam elastic moduli (nickel) to calculate the maximal forces seen at the tweezer tips during closure. The geometric models were used to determine the moment-arm of the tweezer beam from the shoulder to the point of contact on the channel wall (drive/over-drive), and also the moment from this point of contact to the tweezer tips. Using this double moment-arm model, the force seen at the inside of the tweezer tip face was predicted, which was then compared to experimentally obtained results. The moment arm was also used to determine the force required by the box to push on the tweezer beam. This aided in the prediction of the spring-loaded button, spring-loaded drive rod, and linear actuator head loading.

In the sections that follow, the beam modeling system and force equation used to calculate the tip loading are explained, and then tweezer tip force modeling data is presented for the previously described tweezer designs. A brief explanation of the loading on the microtweezer box during actuation is also provided.

#### 4.2.2.1 - Double Moment-Arm Model

The bending and deflection forces of the tweezer beams were predicted based on the expected moment-force arm that exists on the shoulder of the tweezer beam. The force required to bend the tweezer beam was dependent on this moment length, the cross-sectional geometry of the beam, and the elastic modulus of the beam material (discussed in Section 4.2.2.2). The force placed on the beam originated from the contact point on the box channel, and was normal to the side of the beam. Constituent horizontal and vertical force vectors were created from this contact force vector to determine the force

required to advance the box and push the tweezer beam (discussed in Section 4.2.2.3). This contact point between the channel wall and tweezer beam formed the origin of the second moment-arm. The second moment, which is the beam deflection from this point to the tip, was used to calculate the forces seen on the inside of the tweezer tip face (Figure 4.6).

The bending location for the first moment was assumed to be the shoulder of the tweezer, as this created the longest moment arm with the smallest bending force. Likewise, the bending location for the second moment was assumed to be the point of contact between the channel wall and tweezer beam (as the angel of the elbow is very shallow – 168.5$^{o}$). During box actuation, which advances the channel forward along the tweezer beam, this point of contact changed on the tweezer beam. During the closing movement, the moment arm increased in length and the angle of the tweezer beam changed. For beam design, this created several considerations: 1) the force normal to the beam required to cause deflection reduced through the closing regimen; 2) the angle of the tweezer beam shoulder decreased, resulting in a change in the normal vector of deflection; 3) the change in this normal vector of deflection changed the relative linear driving force required by the box to push the tweezer; and, 4) the change in the normal vector of the deflection changed the relative force that results in friction between the box and tweezer beam. This complicated the force calculation, as each of the moment arm lengths changed during tweezer tip loading.

Specific geometric features (cross-sectional thickness tailoring) were incorporated into the beam of some tweezer designs to attempt to keep the second bending location, and thus second moment arm length, consistent through the actuation (Figure 4.7). The

first moment, however, still maintained its moving moment length over actuation. Given that this length was variable, stepwise Eulerian solving was used to calculate the force for each step in the actuation.

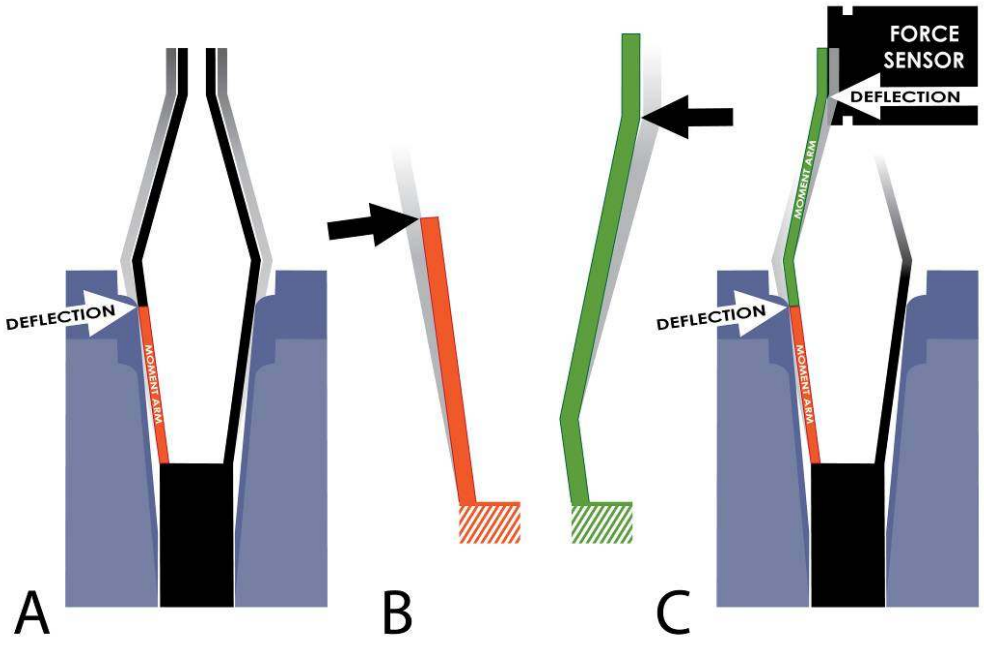


**Figure 4.6**: Cartoon demonstrating the geometric modeling used to predict forces seen at the tip. This tip force calculation, along with calculation of frictional and loading forces seen on the tweezer beams and in the mechanical packaging, aids in the geometric and packaging design process and enhances understanding of performance. (A) Denotes normal tweezer deflection performance, and (B, C) show the double moment arm on the tweezer beam caused by movement isolation from loading on the force sensor.

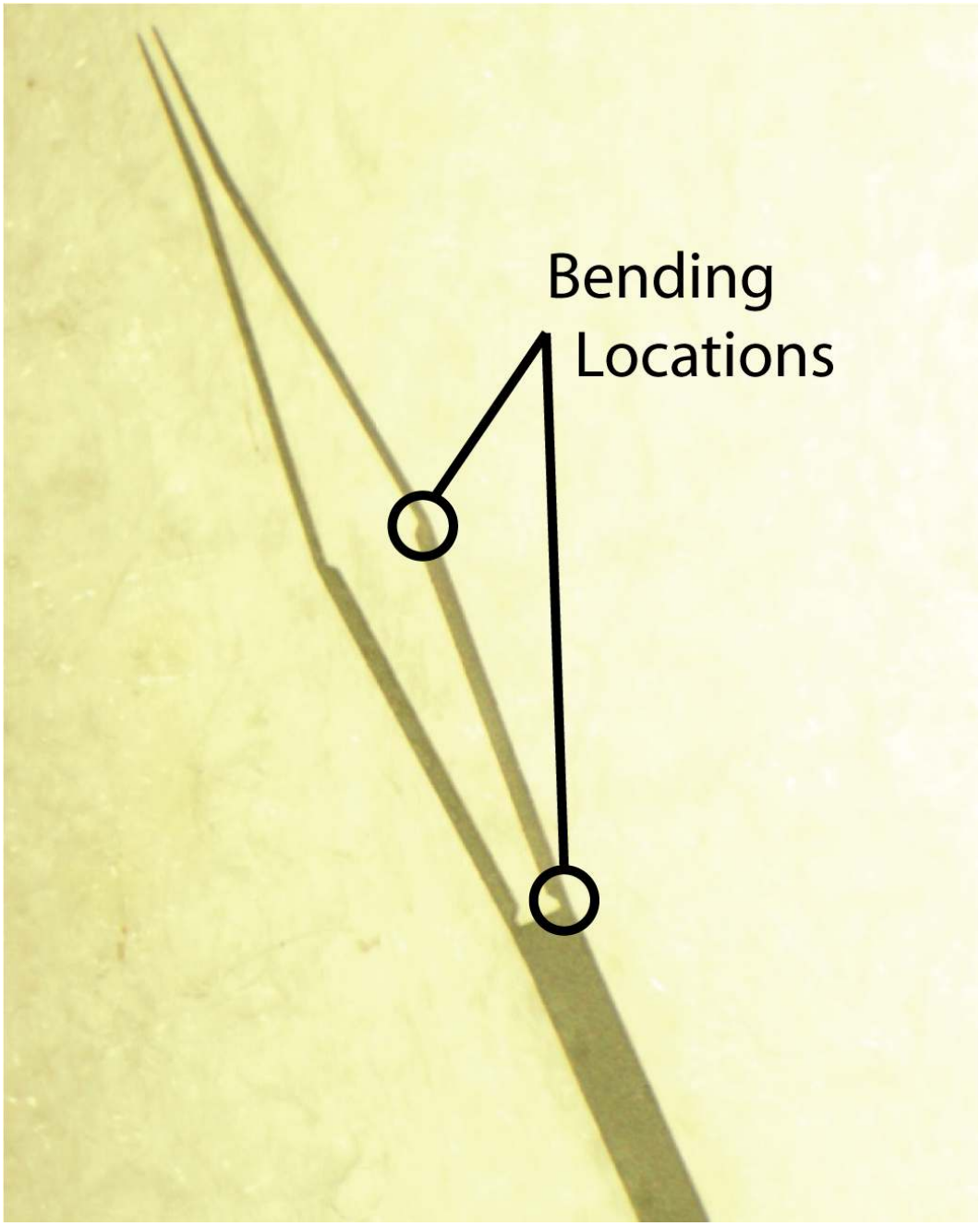


**Figure 4.7**: Bright-field photo of a tweezer beam design with features incorporated to promote beam bending at specific locations (tweezer beam shoulder and elbow).

4.2.2.2 - Microtweezer Tip Force Equations

Because of the predictable bending behavior of the tweezer beam moment arms, Castigliano's second theorem of beam deflection was used to calculate the forces required to cause specified deflections of the tweezer beams [127, 160, 161]. This modeling method considered the cross sectional geometries of the beam, the beam material and modulus, the moment of inertia, and moment arm of force loading. Cantilever deflection models were less relatable as the thickness of the beam on the axis of deflection was neither 'thin' in micro structure considerations, and was not considerably smaller in dimension than the width (or the normal cross sectional dimension). Castigliano's theorem was rearranged (4.1, 4.2) to calculate force (F) as a function of single-axis deflection (δ) and strain energy (U):

$$F_i = \frac{\partial U}{\partial \delta_i} \tag{4.1}$$

$$\delta = \frac{\partial U}{\partial F} \tag{4.2}$$

$$\delta = \frac{\partial}{\partial F}\int_0^L \frac{M^2}{2 \cdot E \cdot I} dl \tag{4.3}$$

$$\delta = \int_0^L \frac{F \cdot l^2}{E \cdot I} dl \tag{4.4}$$

$$\delta = \frac{F \cdot L^3}{3 \cdot E \cdot I} \tag{4.5}$$

$$F = \frac{3 \cdot \delta \cdot E \cdot I}{L^3} \tag{4.6}$$

Strain energy (U) was calculated (4.3) from the known quantities of the point of bend to moment length (l), elastic modulus (E), and Inertia (I). After moving the force

load into the integral (4.4), and integrating with respect to the moment length (4.5), the equation was re-arranged to determine force (4.6).

This model calculated the maximal force that can be delivered by the tweezer tip at each stage of the box actuation for the following condition: (1) the tweezer tip started at its normal location determined by its fabricated geometry; (2) the tweezer tip is immobilized by an equal force being placed on the inner face of the tweezer; (3) the tweezer tip neither closes nor is forced to open past its normal location; (4) the box is actuating; and, (5) the tweezer beam (not the tip) is allowed to deflect. This condition was defined to match the condition that was experienced during force loading caused by box actuation (Section 4.3.1). Maximal forces of roughly 358 μN were calculated to be seen at the inner face of the tweezer tip during a closing regimen of 125 μm (Figure 4.8).

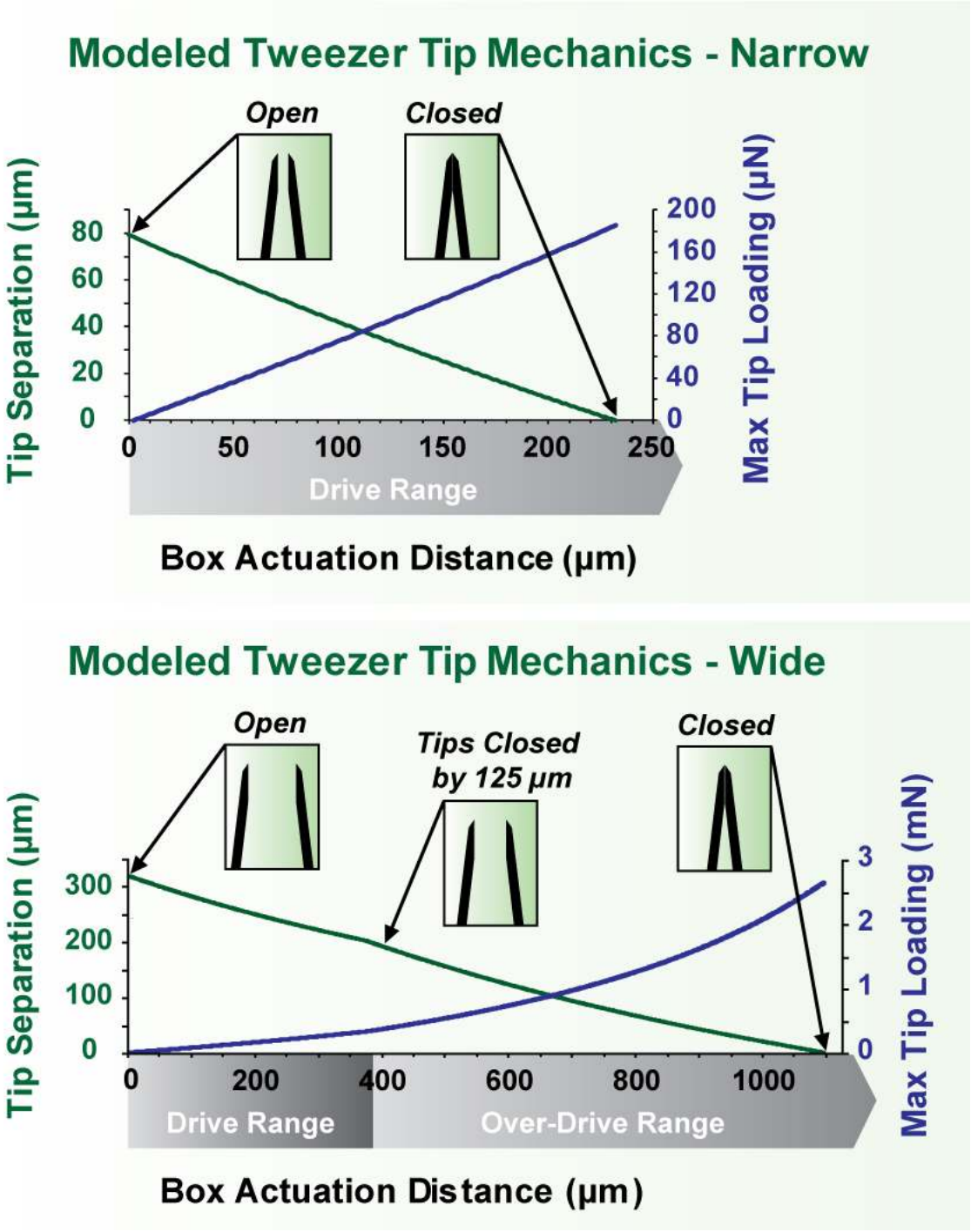


**Figure 4.8**: Modeling data for separation of two tip styles ('narrow tip' with 80 µm gap-top chart; 'wide tip' with 320 µm gap – bottom chart) are based on actuation distance of box, and maximal force loading seen at the inner face of the tweezer for the specified actuation location. For the narrow model, the tip closure and tip loading are near linear for the entire closure.

4.2.2.3 - Microtweezer Box Actuation Force Modeling

Data from both measured tweezer tips forces and mechanical modeling were used to predict static and kinetic frictional loading at the tweezer beam-box channel interface, and the force required by the box to push the tweezer beam. The calculation of these forces would aid in determining the maximal loading required by the controller and linear actuator system.

For this model, single-point contact surfaces were assumed for both the drive contact (rounded drive-contact surface on linear tweezer beam) and over-drive contact (flat over-drive contact surface on pointed tweezer beam elbow) conditions. For a sample calculation, a box actuation of 400 μm resulted in 125 μm of tweezer tip closing. Using the previously defined force equation for the first moment arm, the force loading at the drive contact-tweezer beam interface was calculated to be 341 μN. With a shoulder angle at this actuation point of 3.45$^{o}$, maximal frictional forces of 4.832 mN were expected normal to the tweezer beam deflection angle. Given the shallow angle, almost all of this frictional force contended with the forward actuation of the box. The exact calculated tweezer beam moment and frictional loading for this 400 μm actuation suggested that a minimal forward force of 4.835 mN is required to advance the box at this point. Because the tweezer beam moment arm length changes over the course of actuation, a linear spring constant was difficult to calculate due to the cubic relationship between moment length and force. A semi-linear spring constant region over the 400 μm box actuation suggests a spring constant of 12.09 mN/mm exists on the first moment arm.

For the MEMS luer-needle packaging, these calculated forces were used to determine the minimal spring rate (k) required of the spring-loaded button to overcome

slip-stick across the tweezer beam-box channel interface. A spring, with a constant of 21.0 mN/mm (converted from lb/in), was selected for the luer packaging.

### 4.3 - Force Measurement and Mechanical Characterization

Prior to use in the cellular studies outlined in Aim 3, the microtweezers needed to be mechanically characterized to ensure that they provide established and consistent strain injuries onto the somata of neurons. Following assembly and development of the packaged MEMS devices, mechanical controller, and linear actuator, the forces exerted by the inner faces of the tweezer tips during prescribed actuation regimens were measured. The force data was collected using a load sensor with sub-micronewton resolution (MTS NanoUTM system, Oak Ridge, TN).

Force data was collected from a variety of actuation regimens to: (1) allow for comparison with force data computed by the predictive models; (2) measure the consistency in actuation; (3) determine the durability and cycle lifetime for an assembled microtweezer; and, (4) analyze the effect of actuation and tip closure speed on performance.

In the sections that follow, the preliminary mechanical characterization performed by the manual actuator is presented, followed by the cycle testing and speed analysis performed by the automated actuator. The data from the preliminary testing was used to verify the modeled force data. The cycle testing assessed the longevity and consistency of the microtweezer device. The speed data was examined to determine the qualitative effect of dynamics on the actuation of the tweezer beam, which has a length to width ratio of roughly 40:1.

#### 4.3.1 - Microtweezer Tip Force Measurement

To assess the validity of the force models previously presented (Section 4.2.2), and to ensure that the tweezer was performing as designed, forces during repeating close-open actuations were collected. This section will describe the preparation of the microtweezer sample for force measurement, the actuation regimen used during force testing, and the data collected. A brief discussion of the force loading and subsequent spring constant is included.

4.3.1.1 - Microtweezer Sample Preparation

To prepare for testing, a wide-style MEMS microtweezer with a flat-style inner tip surface (forceps-shape) was assembled and packaged. Following visual inspection under microscope of viable close-open performance, the lower arm (past the elbow) of one of the tweezer beams was cut off. The cut location was important to ensure that the upper arm was still present to contact the inner wall of the box channel during actuation. Removal of any portion below the elbow affected alignment during actuation, which would result in a tweezer performance that deviated from the mechanical model.

The manual mechanical controller was attached to the Signatone stage, and with the tweezer docked, was positioned to align the inner face of the remaining tweezer tip with the surface of the load sensor head. Lateral micropositioning of the controller and microtweezer toward the sensor head was continued until the load sensor system displayed any force input, which indicated contact of the tweezer. Therefore, the tweezer loaded the sensor from the beginning of the close-open cycle.

4.3.1.2 - Force Testing Regimen and Data

During the mechanical testing with the manual actuator, a variety of actuation regimens were used to collect force data. For each test cycle, an actuation regimen of

400 µm close-400 µm open (62.5 µm of expected tip movement each way) was used, which coincided with the actuation distance of the mechanical models. During quickly delivered oscillations, average maximal forces of 367 µN with a standard deviation of 1.1 µN were observed. This force level compared well with the modeled force of the double-moment-arm model from the previous section (~360 µN) (Figure 4.9).

Given the distance of the actuation, the deflection of the tweezer beam, and the force observed at the tweezer tip, these measured forces suggested a tweezer beam spring constant of 2.936 N/m for this actuation regimen. While this small spring constant enables manipulation of delicate microstructures like biological constructs, the tip force is strong enough to overcome the adhesion of cells to substrates [119] and to lift solid structures over 10 mg. Over-actuation of the tweezer beams, which would cause deflection of the beam toward the channel wall and increased inner-tip face forces, allowed far heavier objects to be lifted by the microtweezers.

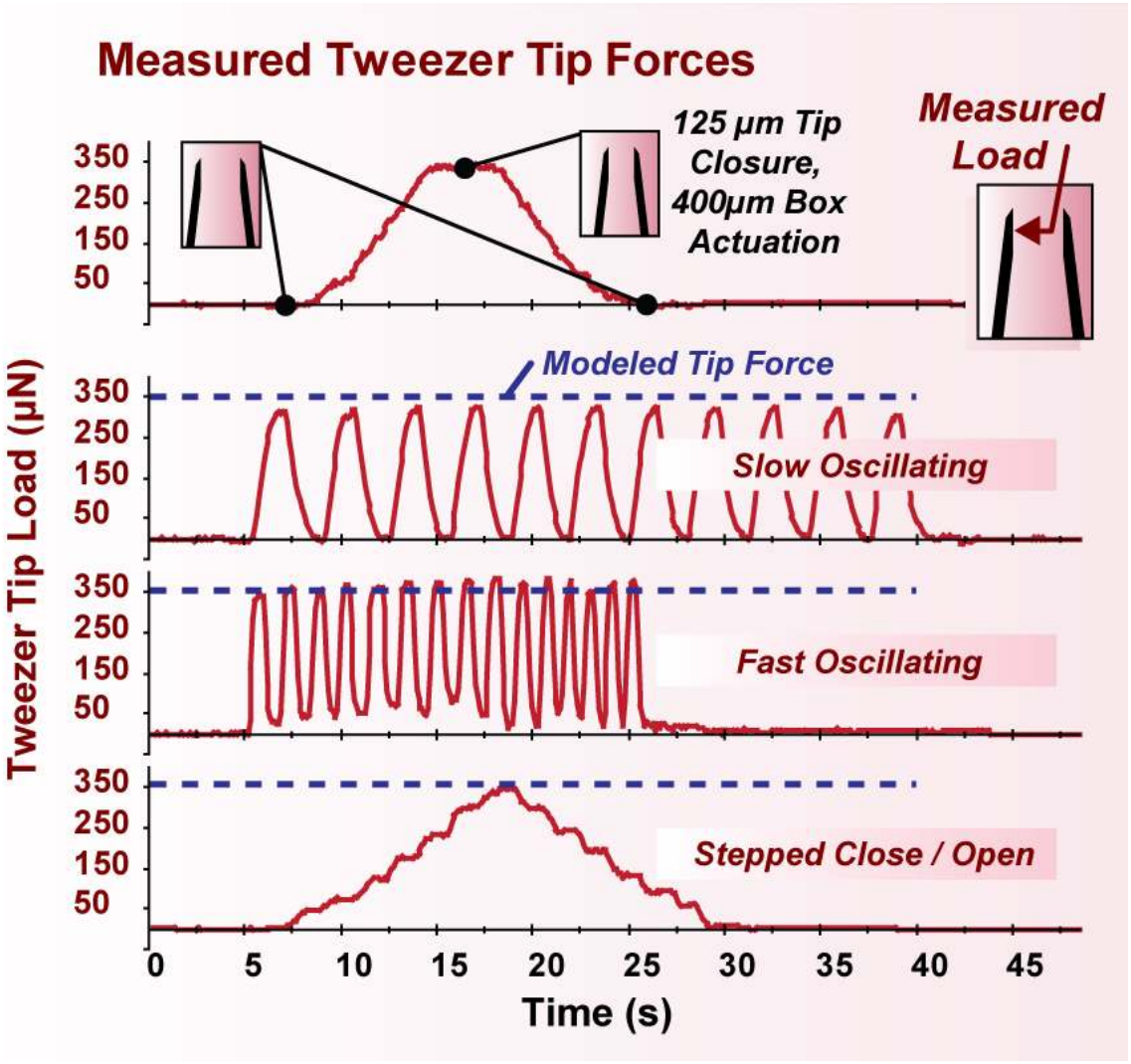


**Figure 4.9**: Measured force on the inner face of closing tweezer tip. Average maximal forces from 125 µm tip deflections were 0.321 mN, 0.367 mN, 0.339 mN, and 0.335 mN for oscillating, fast oscillating, slow close/open, and stepped close/open actuations respectively. The dashed blue line denotes the maximal force calculated for a 125 µm closing.

### 4.3.2 - Microtweezer Cycle and Endurance Testing

To ensure that the microtweezer performance had limited variability and consistent actuation for the biological studies, cycle testing was performed. This section will describe the preparation of the microtweezer sample, collection of mechanical artifact data, the actuation regimen used for the cycle testing, and the data analysis.

#### 4.3.2.1 - Microtweezer Sample Preparation

While the previously collected force data was measured from tweezer tips controlled by the manual controller, the automated controller was required to provide the consistent and highly repeated actuation regimens. The automated mechanical controller and actuator were mounted to the Narishige manual positioner, and like the previous test, the wide-style microtweezer was positioned to the load sensor head.

#### 4.3.2.2 - Mechanical Artifact/Noise Measurement

Prior to testing the actuation of the microtweezer, a mechanical artifact trace was collected to ensure that the linear actuator motor was not introducing noise into the force recordings. This recording also provided a general noise level to allow for a signal to noise ratio to be calculated (if necessary). This force measurement was recorded during a non-actuating (tweezer beam was not contacted by box channel) cycle of the linear actuator motor (Figure 4.10). The mechanical artifact level displayed in this recording suggests a total noise level in the 10s of nN. This recording also verifies the proper mechanical buffering, isolation, and consistency in the force measurement equipment.

#### 4.3.2.3 - Cycle Testing

For the cycle testing, force traces of close-open iterations were collected every 1000 cycles and averaged to determine if the performance of the tweezer was affected following repeated use. The actuation distance of the tweezer box was 0.6 mm forward and 0.6 mm backwards (an arbitrary location in the tweezer actuation cycle was selected), and the actuation speed was 0.4 mm/s. The test was carried out to 5000 cycles (Figure 4.11). Over the course of the endurance test, a decrease in the overall magnitude of force was observed, but the cycle magnitude of force had diminished by less than 10% from baseline.

To determine the change in the force magnitude at the tweezer tips, measurements were taken over fourteen cycles at every 1000 cycles and averaged (Figure 4.12). Based on the trend line of the collected data, this tweezer open-close cycle would have to be repeated 7000 total times to see a change in 10% from the baseline force magnitude at the start of the study.

This change in force could have resulted from either plastic deformation in the tweezer beam arm, such as the opening of the elbow or shoulder angles, or possibly material fatigue in nickel. Because of the consistency of the tweezer performance after thousands of cycles, the source of the change in force, which did not need to be addressed, was not examined here.

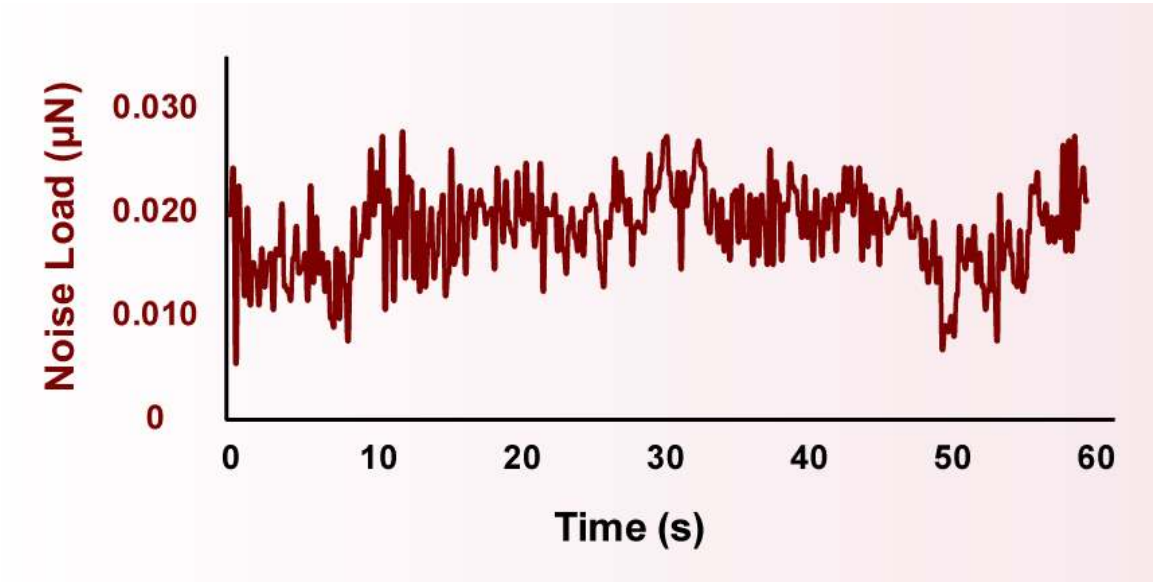


**Figure 4.10**: This graph displays a force measurement of the loaded microtweezer during movement, but not actuation, of the automated linear actuator. The mechanical artifact level displayed in this recording suggests a total noise level in the 10s of nN. This recording also verifies the proper mechanical buffering, isolation, and consistency in the force measurement equipment.

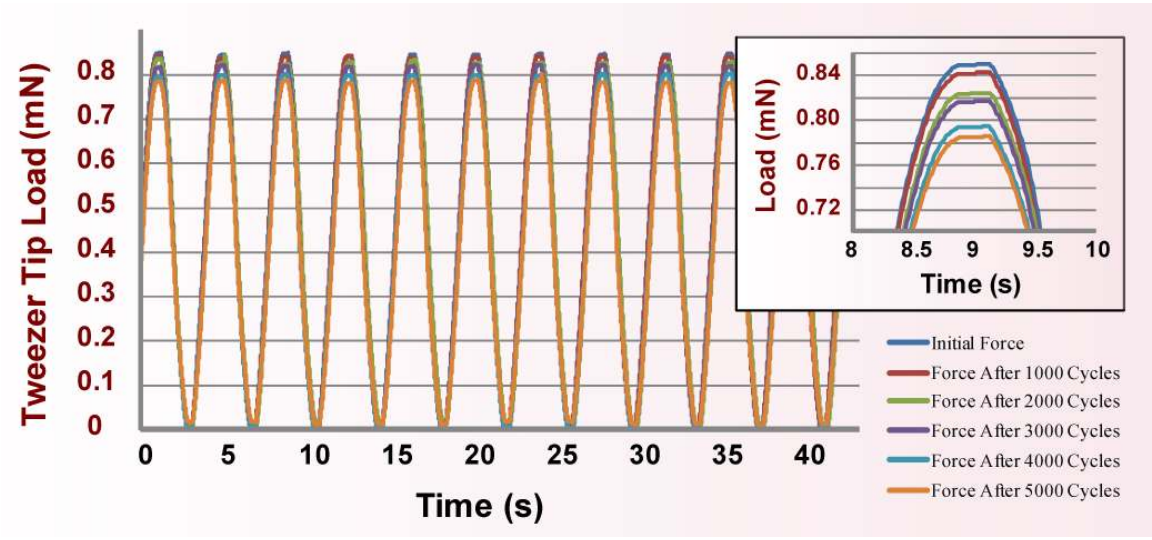


**Figure 4.11**: This graph shows the cycle test data for 0-5000 cycles. Over time, the force exhibited by the tweezer tip onto the force sensor diminishes. This could have resulted from either plastic deformation in the tweezer beam arm, such as the opening of the elbow or shoulder angles, or possibly material fatigue in nickel.

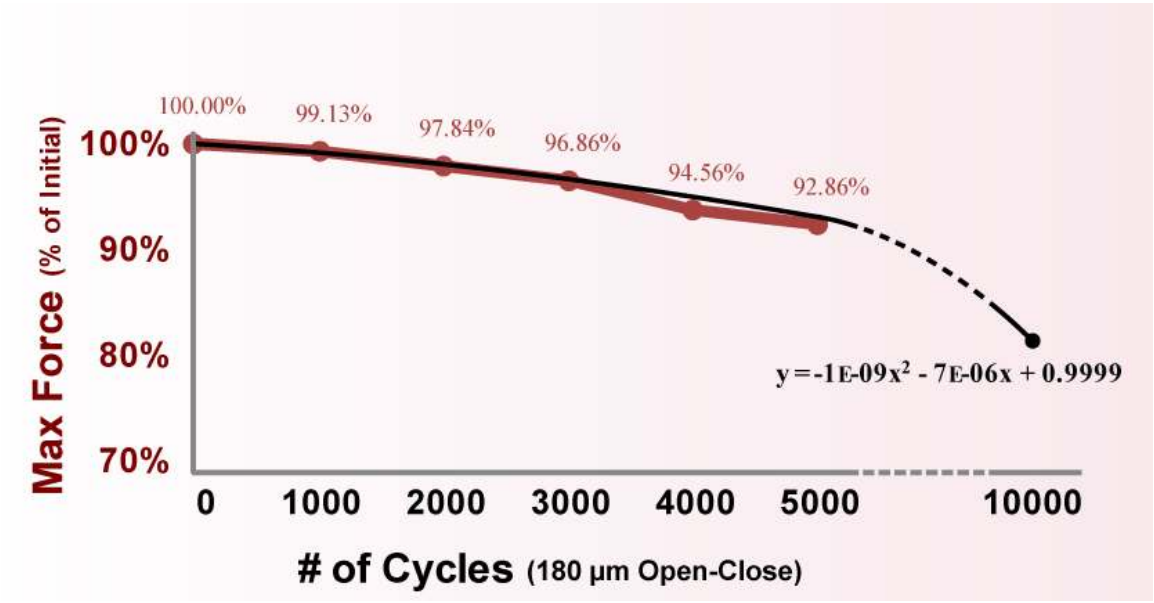


**Figure 4.12**: This graph shows the % change in the maximal force measurement from the same opening and closing tweezer actuation regimen over 5000 cycles. To determine this maximal loading at the tweezer tips, measurements were taken over fourteen cycles at every 1000 cycles and averaged. Over time, the force exhibited by the tweezer tip onto the force sensor diminishes.

### 4.3.3 - Microtweezer Actuation Speed Analysis

Speed tests of the microtweezer actuation were conducted to determine if speed affected the performance, and the input-output relationship of the linear actuator movement and microtweezer tip closure. Given the aspect ratio of the tweezer beam length to width (~40:1), it was possible that quick actuations of the microtweezer box would result in a delay in the complete movement of the tweezer tip compared to the box movement. Any delay in the action of the tweezer beam could potentially impact the strain rate, the strain magnitude, and the overall consistency of the tweezer movement during cell injury. Therefore, the goal of this test was to identify the threshold speed for when the delay emerged. This threshold ideally needed to occur above the speed planned for the injuries in Aim 3 to insure that the speeds used resulted in consistent and un-delayed movement.

For example, one of the single cell injuries delivered in Aim 3 was a 0.5 strain injury, with a 1.0/s strain rate. To deliver a 0.50 strain injury to a cell with a 10 um diameter, the cell needed to compress 50% of its diameter or 5 um. With a strain rate of 1/s, this compression needed to occur in 0.5 seconds. Therefore, the tweezer needed to close 1 um per 0.1 seconds, or 0.01 mm per second. Given the mechanical advantage of the microtweezer box to beam design examined here, a 0.01 mm tweezer closure would require 0.033 mm of box actuation. Therefore, a linear box actuation speed of 0.033 mm/s was used for this particular injury. The actuation at this speed needed to be close to real time to ensure a consistent injury deliver.

This section will describe the preparation of the microtweezer sample, the actuation regimen used for the speed testing, the processing of the speed testing data to allow for analysis, and the data analysis.

4.3.3.1 - Microtweezer Sample Preparation

Similar to the cycle testing, the automated mechanical controller and actuator were mounted to the Narishige manual positioner, and a wide-style microtweezer was positioned to the load sensor head.

4.3.3.2 - Speed Testing

To ensure that the tip closure for a particular box actuation speed was near-real-time with the user input (no delay), force measurements from the inner face of the tweezer were collected over repeated open-close regimens. The automated controller and actuator were mounted to the Narishige stage and a docked microtweezer was positioned to the sensor head as described previously. The box actuation speeds tested were 0.05 mm/s, 0.10 mm/s, 0.15 mm/s, 0.20 mm/s, 0.25 mm/s, 0.30 mm/s, 0.35 mm/s, and 0.40 mm/s. Independent of actuation speed, the same actuation regimen (0.6 mm box actuation forward and backward) and the same start location in the actuation stroke on the same tweezer were used for each test. The force loading magnitude and delay in closure were measured for several cycles for each speed tested. While greater in actuation distance, this close-open cycle was similar to the cycle used to injury the cell (compress and release).

4.3.3.3 - Speed Data Processing and Analysis

To interpret the effects of speed on the input-output relationship of linear actuation and tweezer tip closure, the various force traces for the different actuation speeds were superimposed for comparison. For analysis, the time values for all traces were factored so that they would overlay on the same time scale. To accomplish this, the time-step for each trace was converted to the time-step of the trace with the fastest box actuation (0.4 mm/s). For example, the time values for the trace with the 0.1mm/s actuation speed were multiplied by (0.1mm/s)/(0.4mm/s) , or essentially compressed by a factor of four. This resulted in the force trace from the 0.1 mm/s actuation speed superimposing with the trace of the 0.4 mm/s speed (Figure 4.13).

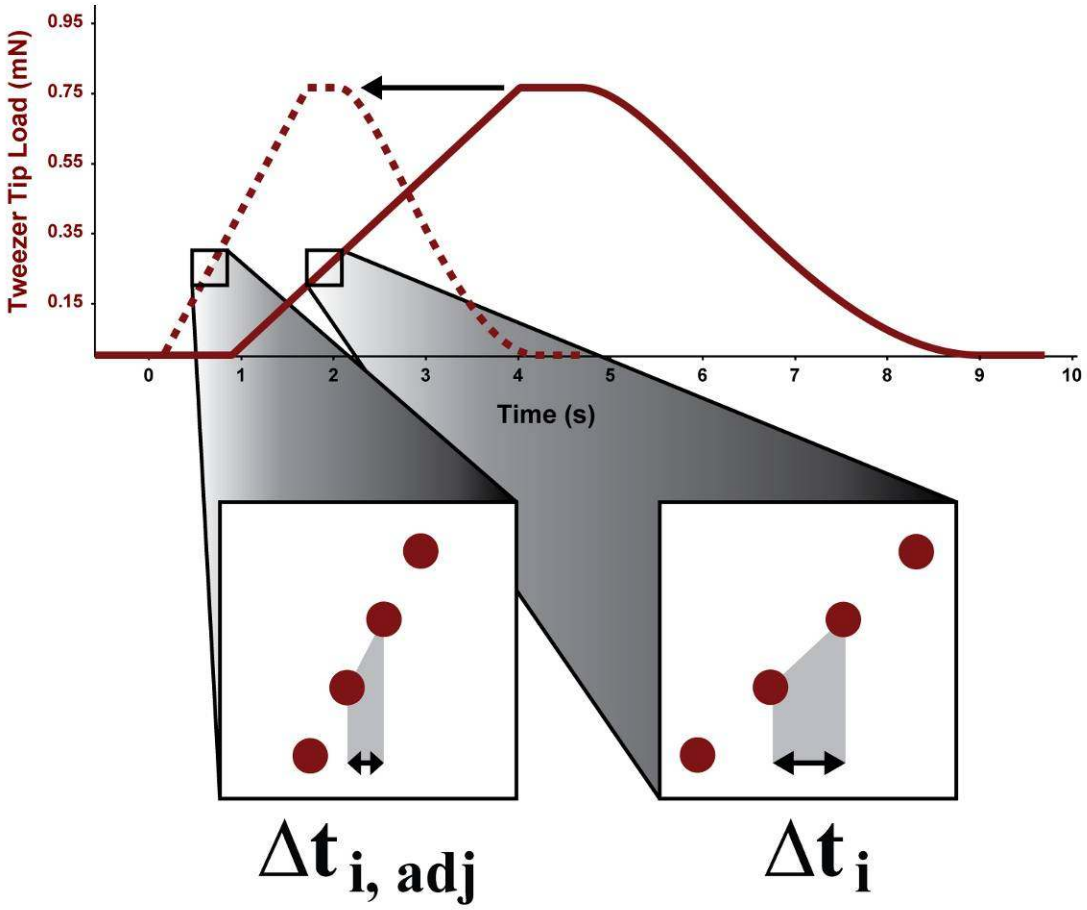


**Figure 4.13**: This cartoon demonstrates the time compression algorithm used in the speed analysis to superimpose the force traces for the tests with different speeds. In this cartoon, the time values between each data point are compressed by a factor to allow superposition of each trace.

Once overlapped, the affects of changing the speed of actuation were observed by the different shapes of the curves. During the tweezer tip opening phase of each cycle, a speed-dependent delay in the completion of the tweezer beam deflection was observed (Figure 4.14). As the speed of the actuation increased, so did the delay in completing the opening movement. A diminishing in the total force magnitude measured during the cycle was also observed at higher speeds. This relationship of speed to delay and force demonstrated a 'low-pass filtering' type phenomena. This could be the result of a delayed settling of the tip at the end of the cycle as a result of the upper-arm beam length to cross-sectional width (aspect) ratio (~40:1). This filtering activity was used to build a chart that displayed the percentage change in the tip closure time, and a Bode plot for the change in force magnitude based on speed.

For data processing, the average times required to open and close the tweezer for varying actuation speeds were determined (4.7-9), and then the previously described time scaling adjustment was made to allow superimposed analysis (4.10, 4.11). A graphical representation of the methodology on how the average tweezer open and close times were obtained from the force traces for the various linear actuator speeds is displayed in Figure 4.15. The original average and converted values can be seen in Table 4.3.

$$i = 0.50\,\frac{mm}{s},\ 1.00\frac{mm}{s},\ \cdots\ 4.00\frac{mm}{s} \tag{4.7}$$

$$\overline{t_{close,i}} = \frac{1}{n}\cdot\sum_{j=1}^{n} t_{close,i,j} \tag{4.8}$$

$$\overline{t_{open,i}} = \frac{1}{n}\cdot\sum_{j=1}^{n} t_{open,i,j} \tag{4.9}$$

$$\overline{t_{close,adj,i}} = t_{close,i}\cdot\frac{v_i}{v_{4\frac{mm}{s}}} \tag{4.10}$$

$$\overline{t_{open,adj,i}} = t_{open,i} \cdot \frac{v_i}{v_{4\frac{mm}{s}}} \tag{4.11}$$

Following the conversion of the time scale for each value, a chart displaying the percent change in the open and close cycle time based on actuation speed was constructed (Figure 4.16). The Bode plot for the magnitude of the force curve was then compiled by similarly averaging the forces for both the "open-to-close" and "close-to-open" phases of each cycle for each actuation speed (4.12).

$$\overline{|Force|}_i = \frac{1}{n} \cdot \sum_{j=1}^{n} Force_{i,j} \tag{4.12}$$

The Bode plot was graphed by converting the force magnitude averages (4.13) and graphing versus actuation speed in logarithmic scale (Figure 4.17).

$$A_{dB} = 20 \cdot \log(\overline{|Force|}_i) \tag{4.13}$$

A suggested trend line that matches the data was included with a decay of -6dB per order of speed magnitude and a cut-off (speed) of 0.07 mm/s (Figure 4.17, black line). For visualization of a potential trend with the data on this charted Bode plot, a line was graphed with a decay of -6 dB per order of magnitude, and a cut-off (box actuation speed) of 0.07 mm/s. The speed of this trend line was higher than the 0.033 mm/s speed used for the example cell injury described above. The -3dB cut-off value for this trend line resided between the actuator speeds of 0.25 mm/s and 0.30 mm/s.

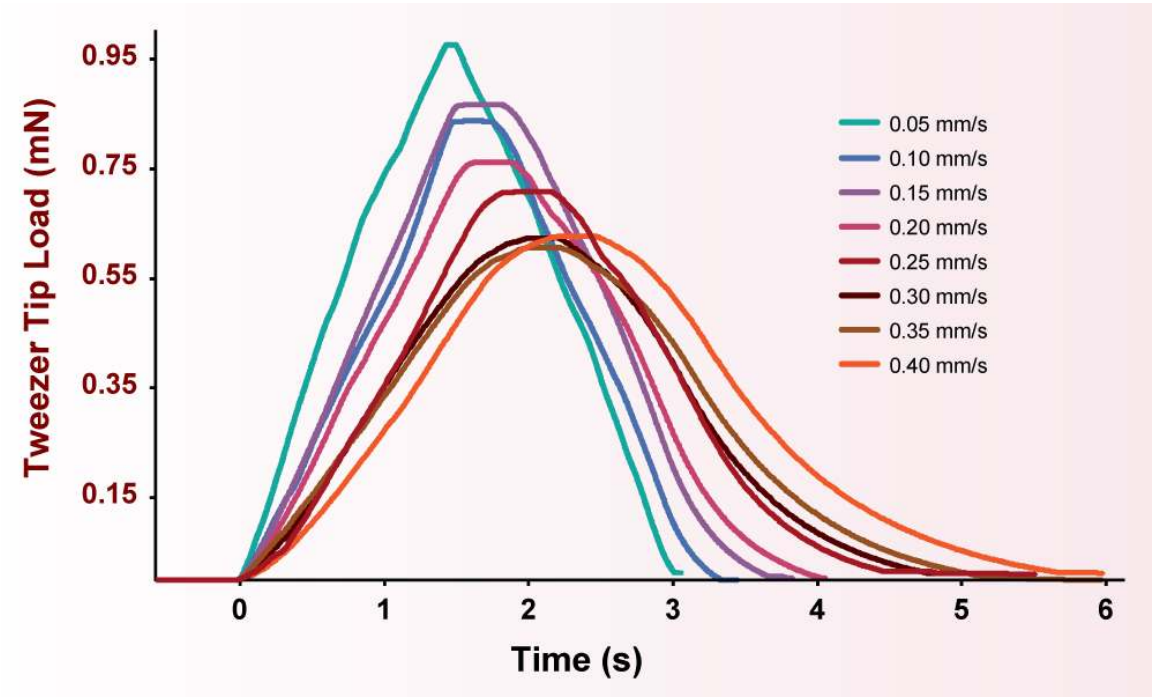


**Figure 4.14**: This graph overlays the tweezer tip forces measured under varying speeds of tweezer actuation. The traces displayed are examples of many traces collected for each speed. The time scale for each trace was converted to the time scale of the fastest trace (0.4 mm/s) so that they could be superimposed. For example, the time scale or $\Delta t$ for the 0.1mm/s actuation speed trace was multiplied by (0.1mm/s)/(0.4mm/s), or 0.25, so that this trace would superimpose with the trace of the 0.4 mm/s speed. Once overlapped, a delay in microtweezer actuation or 'low-pass filtering' was observed, suggesting that at certain speeds, the tweezer tip closing was delayed.

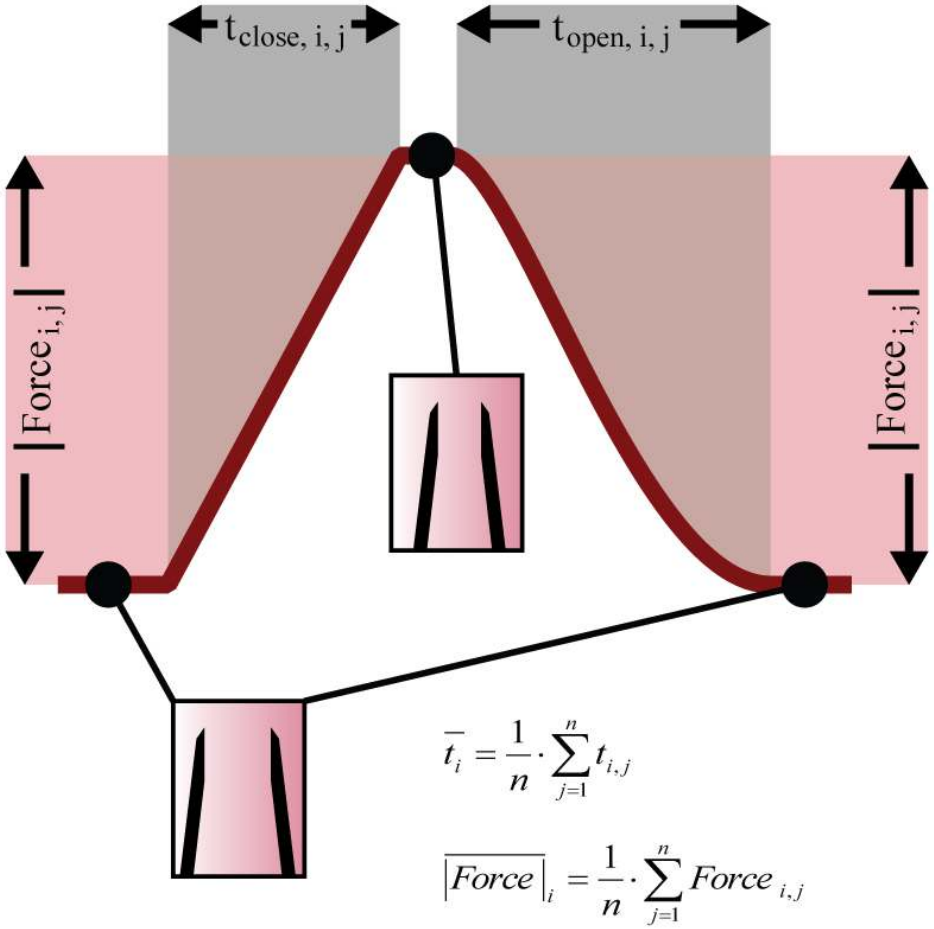


**Figure 4.15**: This cartoon explains the methodology in obtaining the average close and open times, and the average magnitude in force over the open-close regimen. The values are achieved by average over *j* close-open regimens for each *i* speed. These values were collected for a variety of speeds for microtweezer box actuation.

**Table 4.3**: This is a table of the calculated values for the average and adjusted-average tweezer open and close times, and the force magnitude during a close-open cycle. Also, the difference in the tweezer open and close time is displayed.

| | 0.50 $\frac{mm}{s}$ | 1.00 $\frac{mm}{s}$ | 1.50 $\frac{mm}{s}$ | 2.00 $\frac{mm}{s}$ | 2.50 $\frac{mm}{s}$ | 3.00 $\frac{mm}{s}$ | 3.50 $\frac{mm}{s}$ | 4.00 $\frac{mm}{s}$ |
|---|---|---|---|---|---|---|---|---|
| $t_{close}$ | 11.247 | 6.083 | 4.335 | 3.395 | 3.017 | 2.457 | 2.277 | 2.174 |
| $t_{open}$ | 12.060 | 6.293 | 4.810 | 4.265 | 3.770 | 3.348 | 3.241 | 3.218 |
| $t_{close,\ adj}$ | 1.41 | 1.52 | 1.63 | 1.70 | 1.89 | 1.84 | 1.99 | 2.17 |
| $t_{open,\ adj}$ | 1.51 | 1.57 | 1.80 | 2.13 | 2.36 | 2.51 | 2.84 | 3.22 |
| $\Delta t_{adj}$ | 0.10 | 0.05 | 0.18 | 0.44 | 0.47 | 0.67 | 0.84 | 1.04 |
| \|Force\| | 1.029 | 0.828 | 0.844 | 0.792 | 0.647 | 0.640 | 0.607 | 0.621 |

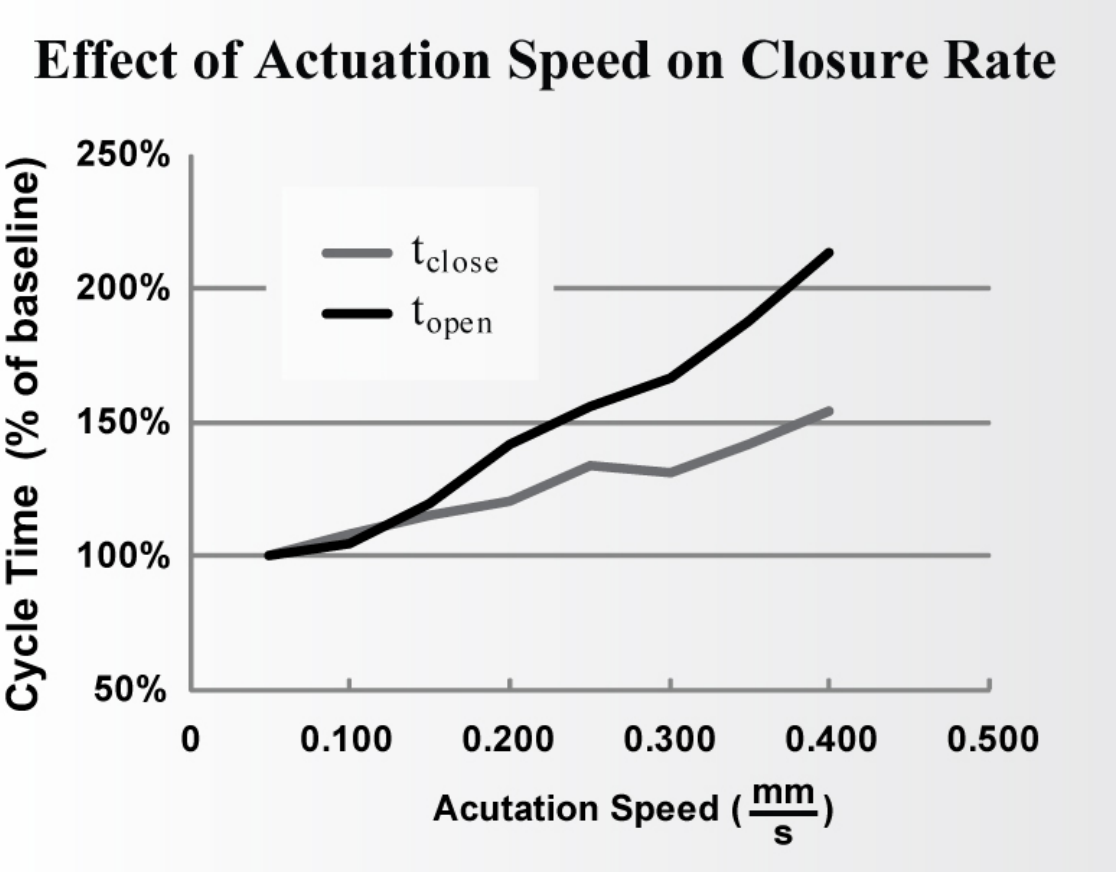


**Figure 4.16**: Graph of the percentage change in total open and close times for the same actuation regimen for different actuation speeds. The faster the actuation speed, the more the comparative delay in the movement of the tweezer beam tip.

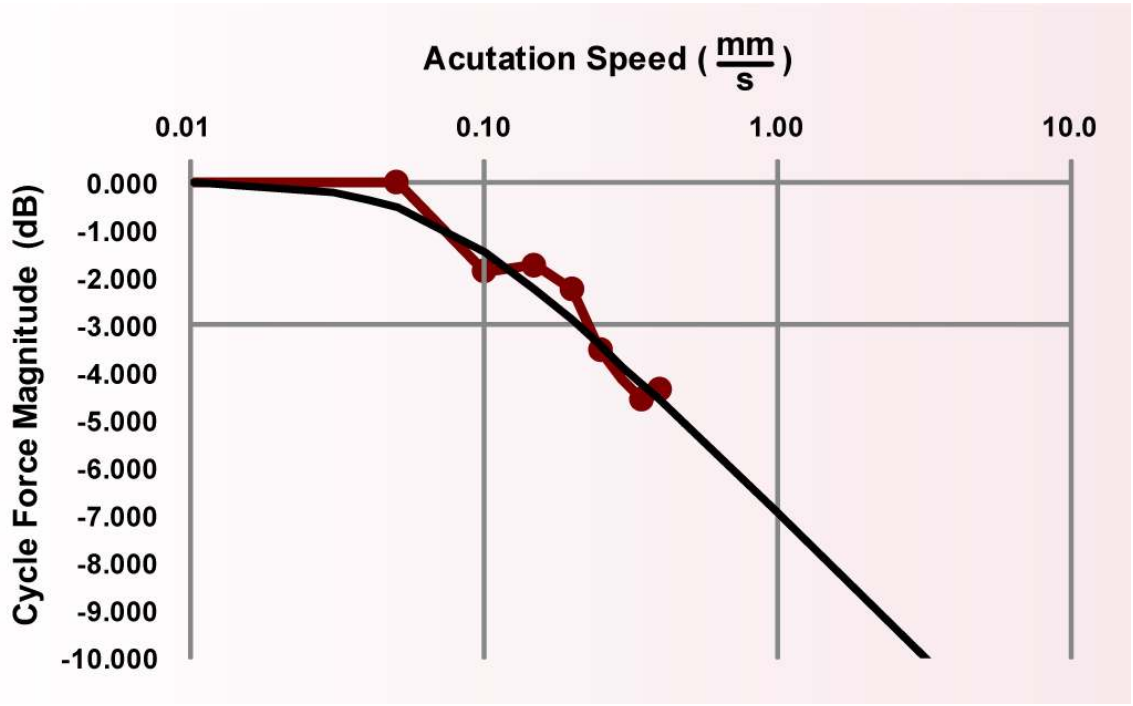


**Figure 4.17**: Bode plot of the magnitude of tweezer tip force during tested open-close cycle over a range of actuation speeds (0.05 mm/s, 0.10 mm/s, 0.15 mm/s, 0.20 mm/s, 0.25 mm/s, 0.30 mm/s, 0.35 mm/s, and 0.40 mm/s). For visualization of a potential trend, a trend line was graphed with a decay of -6 dB per order of magnitude, and a cut-off (box actuation speed) of 0.07 mm/s, which was faster than the 0.033 mm/s speed used for the example cell injury. The -3dB cut-off of this trend line resided between the actuator speeds of 0.25 mm/s and 0.30 mm/s.

### 4.3.4 - Microtweezer Actuation Hysteresis

A hysteresis curve of the forces measured at the tweezer tip during a close-open cycle was constructed for the box actuation speeds observed in the speed testing (Figure 4.18). The force traces collected for the speed testing were used for this analysis as well. This hysteresis curve determined if the loading and unloading of the tweezer tip was symmetrical during the closing and opening phases of the actuation cycle. Ultimately, this test helped to ensure that the loading and unloading action from the microtweezer tip onto cell membranes exhibited consistent strain rate during both the compression and decompression stages of the injury. Similar to a loading and unloading test for determining mechanical properties of a material (i.e. stress/strain curve), this trace displayed the tip force loading based on actuation for a compression/closing motion and a releasing/opening motion.

The force from an opening cycle is displayed from left to right, which continues with the force from a closing cycle displayed from right to left (usually the lower trace). Traces were charted for different speeds of actuation to determine if the dynamics of speed change would affect the symmetry of the loading and unloading.

Extrapolating the traces suggested that the max actuation speed selected for the cell injury (less than 0.05 mm/s) has a force hysteresis curve that was symmetrical. This data helped to ensure a consistent loading and unloading over the mechanical insult cycle for the cell studies.

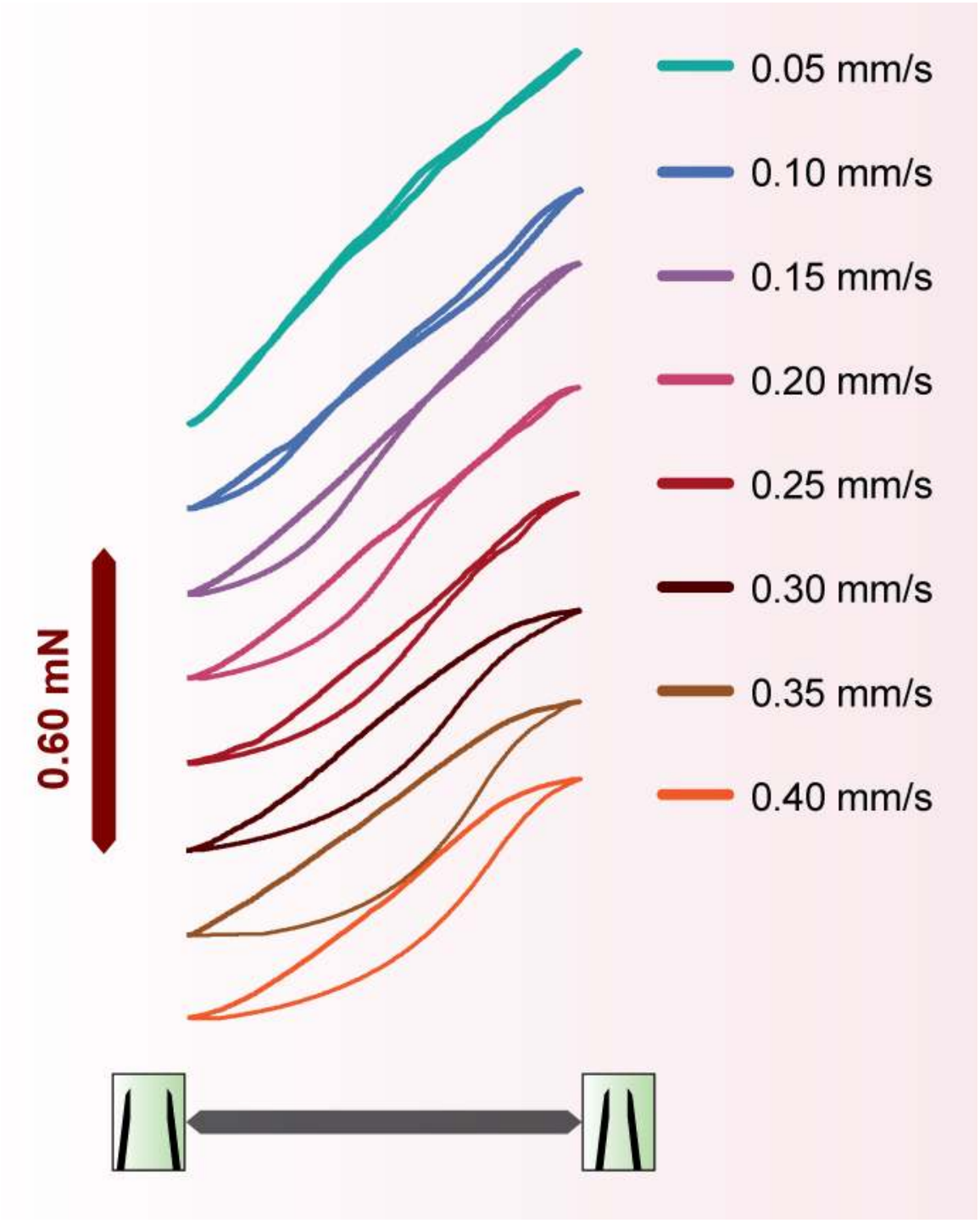


**Figure 4.18**: This graph shows the force-based hysteresis based on the closing and opening force seen at the inside tip of the microtweezer. Hysteresis traces plotted were for the same speeds examined in the speed analysis.

# CHAPTER 5

# SINGLE-CELL MODEL OF TRAUMATIC BRAIN INJURY

## 5.1 - Introduction

This chapter covers the development of the single-cell injury model, which required a specialized testing and imaging system, and a specialized *in vitro* cell system. The cell culturing techniques used to create the biological samples for testing are discussed first, followed by a presentation of a conservative biocompatibility study and the development of the injury testing rig and conducting of the single-cell injury model.

The detailed description of the established and novel cell culture methods covers the cell harvest, plating system, and cell maintenance. The methods and results of the biocompatibility study that uses the cells cultured from the described techniques provide analysis of potential microtweezer toxicity. The injury study methods detail the design of the injury system rig, the use of imaging and staging equipment to conduct the single-cell mechanical insults, and analysis used to evaluate cellular response. Results and discussion of the cell responses recorded from the injury studies is then provided.

## 5.2 - Cell Culture Methods

Both established [86, 162] and novel cell culture methods were utilized to prepare primary cortical neurons for the cell injury studies. Two cell plating systems were used to create samples for the injury studies: (1) a blanket-coverage of cells over a thin glass cover slip; and, (2) a patterned coverage of cells into small islands of cells that are physically separated over a glass disc.

The general cell culture methods that were used to harvest and maintain the cells are described first, and then the techniques used to pattern the plating of the cells into islands is subsequently described.

### 5.2.1 - Neuron Harvest, Plating, and Maintenance

Cortical neurons were harvested from the dissected cortical hemispheres of embryonic day 18 (E18) neonatal rat brains (Charles River, Wilminton, MA). The harvested tissues were then mechanically and chemically dissociated to produce a cell suspension. These cells were then plated onto glass cover slips (VWR Scientific, Media, PA) inside well plates (Corning Inc, Corning, NY). A single cortical hemisphere produced roughly 3-5 million neurons that were ready for plating. Plating with a density of 50,000-100,000 cells/cm$^2$, this tissue provided enough neurons to plate an entire 6-well plate with inserted 25 mm diameter cover slips, or an entire 12-well plate with inserted 18 mm diameter cover slips. A single 25 mm diameter cover slip with a top surface area of 6.25 cm$^2$ from a cell plating of 100,000 cells/cm$^2$ could contain anywhere from 500,000 to 750,000 cells.

Cultures were fed every 2-3 days so that they could mature and grow processes and connections to other cells to produce a culture that is more analogous to an in vivo neural system. Plating on glass cover slips allows the cell culture itself to be removed from the well plate to be placed into a chuck with a low-wall cell medium well (using forceps). This low-wall chuck fits under an upright microscope with an immersion objective lens while permitting the shallow-angle insertion of a microtweezer between the culture and the objective.

The following sections describe in more detail the harvesting of the cortical hemispheres, the dissociation of neurons from this tissue, and the plating of the neurons onto the cover slips.

5.2.1.1 - Tissue Harvest

The timing of the harvest (E18) in the developmental cycle of the embryonic rat, and the locations of the collected tissues, are selected to increase the yield of cortical neurons during the dissociation [163]. Once the rats were removed from the uterine horns and their brains were extracted, a precise series of cuts were made in each brain to isolate the cortical hemispheres and remove the non-cortical portions in that hemisphere (Figure 5.1).

The hemispheres were placed inside of a 15 mL conical tube and stored temporarily on ice for an immediate dissociation. The tissue, however, could be stored in the refrigerator for up to a day following harvest [164]. This required the addition of L-15 (Leibovitz Formula; Invitrogen, Carlsbad, CA) supplemented with B-27 (Invitrogen) to allow for longer-term solution buffering without the presence of carbon dioxide (the conical tube was sealed and stored on its side to increase the surface area to volume ratio).

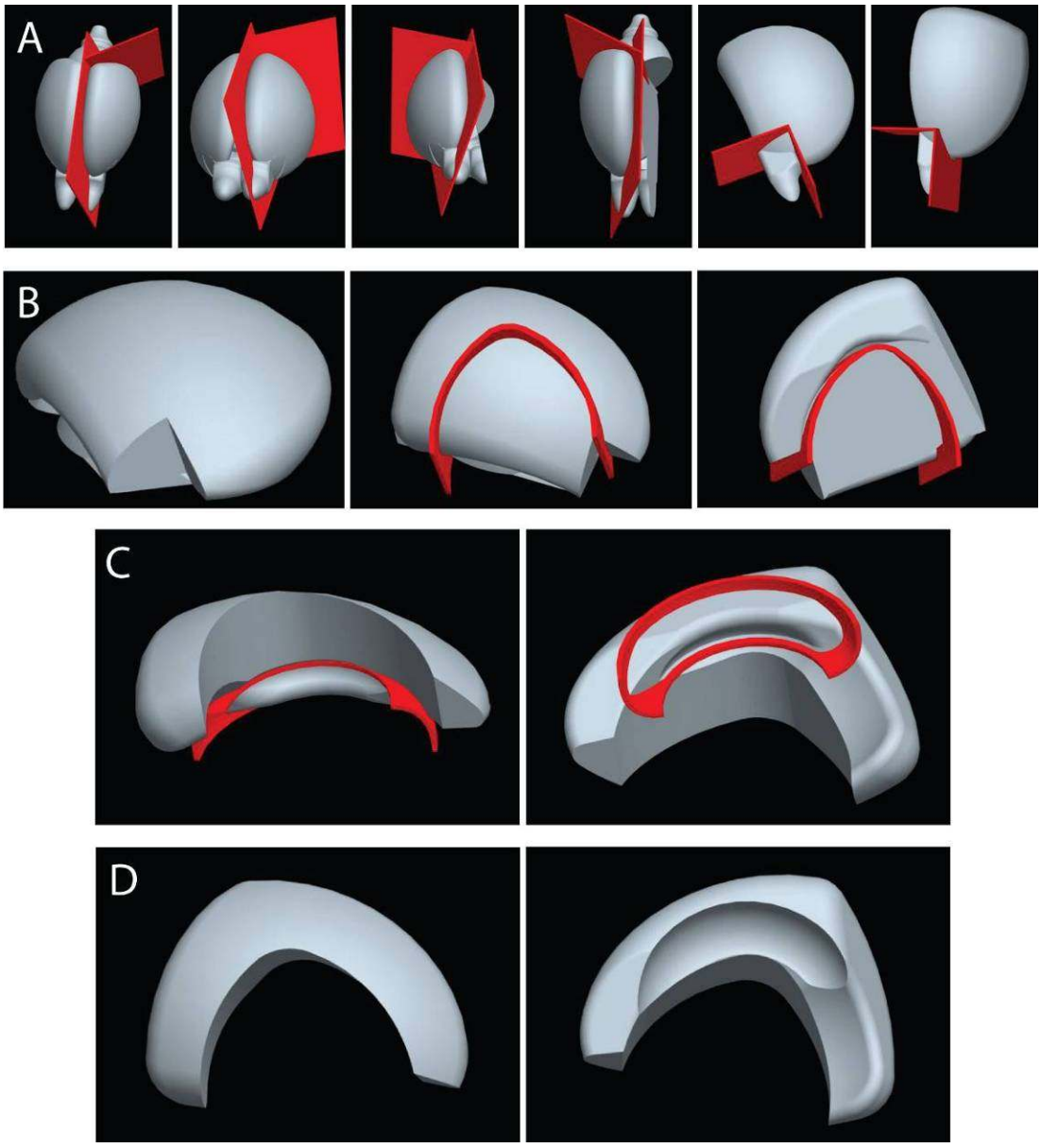


**Figure 5.1**: Gross representation of the dissection cuts made onto the neonatal rat brain to remove non-cortical regions of the brain. (A) The hemispheres were separated from the brain using angled cuts to remove mid brain areas, and the olfactory bulb was removed using a corner cut. (B) From this corner cut, the meninges were peeled back and removed from the hemisphere. The lateral non-cortical regions were removed with a circular cut. (C) The hippocampal portions attached to the medial side of the cortices were then removed. (D) Completed hemicortices, which have a high number of cortical neurons.

5.2.1.2 - Neuronal Dissociation

The harvested hemicortices were first washed 3 times with cold Hank's Buffered Salt Solution without calcium and magnesium (CMF-HBSS; Invitrogen), which is a buffered (7.1-7.3 pH) and biologically isotonic (~280 mmol/kg) solution. The use of cold CMF-HBSS was continued for each subsequent rinsing step. Trypsin (3-5 mL, 0.25% + 1 mM EDTA (Ethylenediaminetetraacetic acid), a divalent metal-ion chelator), which is a digestion enzyme, was added to chemically break down the cortical tissue to promote the dissociation of cells from the extracellular matrix. After a prescribed period of time (10-12 minutes) in a warm water bath (37$^{o}$ C), which allowed sufficient time for breakdown of the tissue, the trypsin was removed with aspiration and with several rinses of cold HBSS to prevent excessive chemical damage to the cells. DNase (0.15-0.3 mg/mL) was then added to break down DNA in solution that may have emerged from damaged or destroyed cells. The cell solution was triturated using mechanical shear by drawing and discharging the solution through pipette tips of decreasing sizes. This process was continued until the cells were dissociated from the tissue. The cell solution was then centrifuged (200 relative centrifugal force, 5 min) so that the DNase and broken cellular material (supernatant) could be removed, leaving the cells to be re-suspended in fresh neuronal medium (Neurobasal Medium, 2% B-27, 0.5 mM GlutaMAX™) for plating.

Neurons were plated at a density of 50,000-100,000 cells/cm$^2$ depending on the culture system, and placed in the incubator (Figure 5.2). The incubator provided an environment with ambient oxygen (air source), injected carbon dioxide (5%), maintained humidity (99%), and heating (37 $^{o}$C) to ensure consistent medium-dissolved gas, pH, and temperature for the mammalian cells.

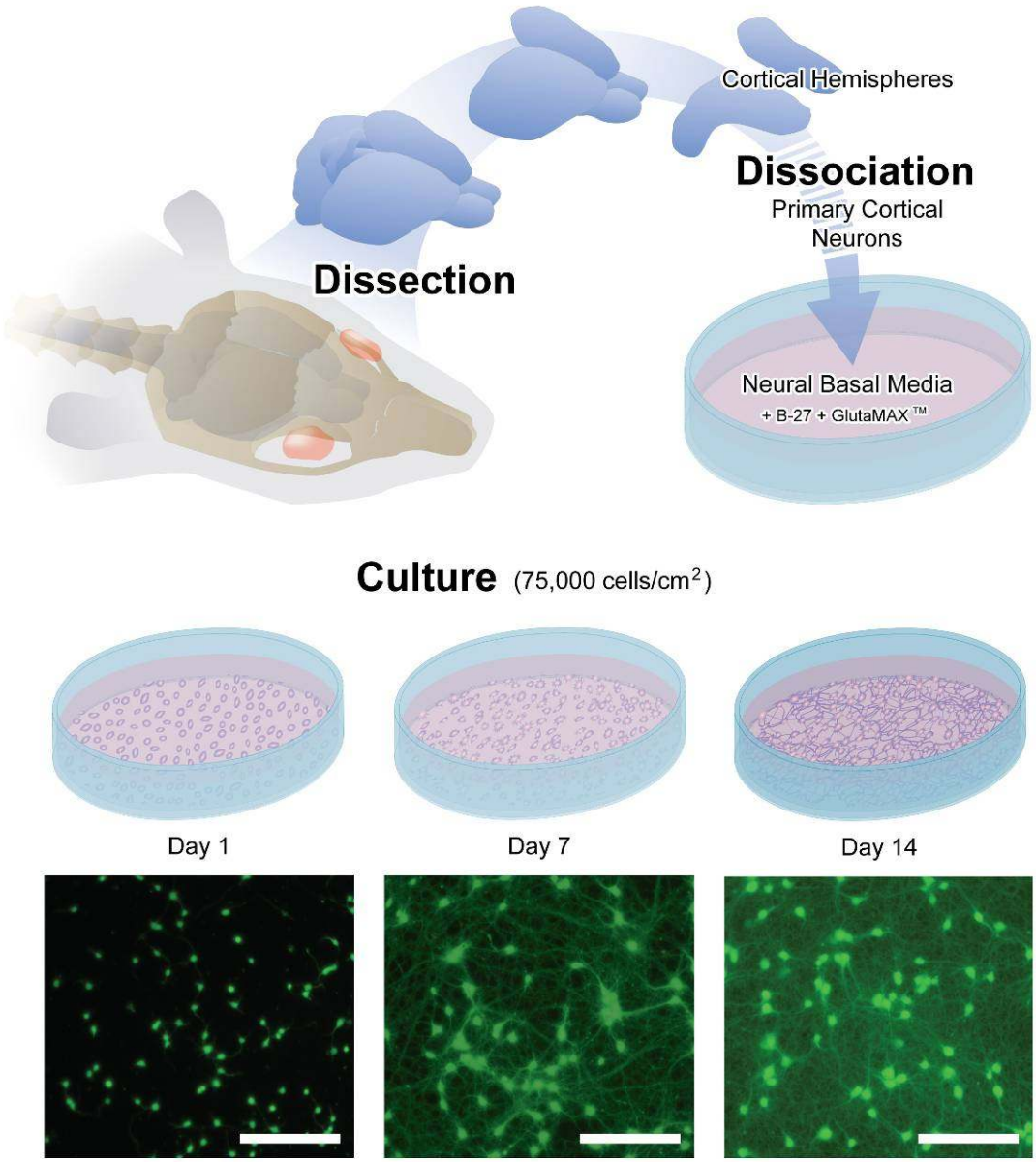


**Figure 5.2**: Cartoon of the neuronal harvest, dissociation, and plating procedures, and fluorescent microscopy photos of neurons at day 1, day 7, and day 14.

5.2.1.3 - Well Plate and Glass Slide Preparation

To promote the adhesion of neurons through integrin binding [165, 166], a layer of charged protein was coated onto the glass surface. Prior to cell plating, a sterile circular 25mm diameter glass slide cover was placed into each well of a 6-well plate and immersed in a 100 µg/mL poly-D-lysine (PDL) solution. For a 12-well plate, 18 mm diameter glass slides were used. Following 1 hour in the cell culture incubator (37$^{o}$ C, 99% Humidity, 5% $CO_2$), sufficient PDL should have adhered to the glass slide and well plate surface to promote adhesion of neurons for plating. After taking the well plate out of the incubator, each well and glass cover slip was then rinsed twice with sterile de-ionized water to remove excessive unbound PDL. This unbound PDL, which cannot be metabolized by neurons, could become cytotoxic if left in the cell medium. The well plate with glass slides was allowed to air-dry completely, after which it was ready for cell plating.

5.2.1.4 - Neuronal Culture Maintenance

Neurons were fed every 2-3 days with fresh Neurobasal/B27 + GlutaMAX medium. During the feeding cycle, half of the old medium (1 mL for a 6-well plate, ½ mL for a 12-well plate) was first removed from each well and then replaced with fresh medium at physiological temperature (37 $^{o}$C). Removing half of the medium reduced waste materials in the well, but did not remove all of the beneficial and physiologic chemical and hormonal factors that the neurons release into their immediate environment. Temporarily removing half of the medium affects the medium surface area-to-volume ratio, which can affect the dissolution and concentration gradient of various gases in the

medium. However, by not removing the entire old medium, exposure of the cells to air is limited which, if prolonged, could affect cell viability

### 5.2.2 - Multi-Island Cell Culture System

A single glass cover slip could contain hundreds of potential experiments, even if only a marginal fraction of neurons were candidates for injury when considering: (1) the orientation of the cell next to the tweezer tips (described in Section 5.4); (2) isolation of target cells from neighboring cells to reduce variability in experimental conditions; (3) the proximal location of previously injured neurons; and, (4) the cells on the periphery (~2-3 mm from edge minimum) of the cover slip cannot be accessed with the microtweezer due to positioning of the microscope objective and the angle of entry of the microtweezer. This makes the lifetime of the fluorescent dye in culture, which can be photo-bleached from excessive exposure to a light source, the limiting factor in the size of data collected from one cover slip.

This system where multiple injury experiments can be conducted on a single culture, however, considers that one injured cell will have minimal affect on a subsequently injured cell (discussed in Section 5.4.1). The mature neurons in culture, which have expansive cellular processes that connect to multiple other neurons (Figure 5.2 – Day 7, 14), can provide electrochemical input to connected cells that alter the electrochemical state [167]. This altered state can include action potential activation and activation of ionic gates and channels. This activity can ultimately affect the intracellular calcium level [168-170], which is what is being examined in the experiments outlined in Section 5.4. The communication between the neurons can be mitigated by adding neurotransmitter blockers to the cell medium (discussed below).

However, this addition of neurotransmitter blockers affects the normal physiology of the neurons. If only membrane permeability is being examined, which, given the time-course of the strain insult is a mostly mechanical response, the communication of neurons will minimally affect the cellular response. Overall, however, this muting of the cells can limit the experimental space of the system, as the electrophysiology and neighboring affects of single cell injury to the surrounding cells (penumbra) cannot be effectively evaluated. Therefore, to ensure the undisturbed examination of multi-cellular or electrical response to single-cell injury, only one cell within an established culture can be injured.

A one-injury-per-culture experimental system would have very low experimental throughput. However, if multiple physically-separated islands of cells are pattern-plated onto the glass surface in one culture, then each island could be an individual experiment. The harvest, maintenance, and preparation (described in Section 5.4.2) of the culture for experimental testing would follow the same protocols established for a blanket-covered glass slide. Only the cell plating step would require changes in the overall sample preparation. Therefore, a multi-island culture plating system was developed to create a culture that consists of multiple isolated islands of cells each with a large cell population (10,000s - 100,000s of cells).

5.2.2.1 - Multi-Island Patterning Strategy

Similar to patterning with photolithography and microfabrication, a mini-colony culture system with small islands of cells could be created using a variety of techniques: 1) control the location of the cells during the plating process; 2) preferentially control the adhesion of cells to specific areas of the well floor; or, 3) preferentially remove cells in

specific regions. Given that the removal of cells is difficult to control, and that the release of intracellular material into the medium can cause pro-apoptotic behavior in neurons [171], the third option was avoided.

As discussed previously (Section 5.1.1.3), following harvest of fetal rat brain tissue and dissociation of the neurons from this tissue, the neurons are plated onto glass cover slips that are coated with poly-D-lysine (PDL), which is a charged polypeptide that facilitates cell adhesion. Cells preferentially adhere to these coated surfaces, as well as to other cells that have already plated onto another surface. If the PDL surface can be patterned, then the adhesion of cells into specific regions on the glass cover slip surface can be controlled to potentially define the islands of cells. Techniques for the use of stamps to contact-transfer a patterned cell-adhesion surface have been previously reported [172], but a PDL immersion method that was more consistent with the current coating protocols was preferred. A physical mask could be attached to the surface of the glass to control and pattern the location and thus adhesion of the PDL. Similarly, a physical mask could also be used to control the location of the cells during plating. Therefore, the same technology and process could be attempted for both techniques.

5.2.2.2 - Physical Mask Development

*5.2.2.2.1 - Dimensions*

The physical mask would be attached to a 25 mm diameter cover slip which could fit into the well of a 6-well plate. The mask would effectively define miniature wells onto the glass surface that would control the patterning of cell adhesion surface and locations of cells. To increase the throughput of this experimental system, the number of wells, and thus, mini-colonies were maximized. The size, orientation, and spacing of the

wells would be distributed by: 1) the opening size of the well to allow insertion and removal of liquid with a pipette tip; 2) the separation of the mini-colonies to minimize connection of cellular processes from one colony to the next; and, 3) the footprint or surface area of the mask-glass interface, which ideally would be maximized to increase attachment force. An initial well-separation of 2 mm was selected to reduce the possibility of cellular process attachment between colonies (limit chemo-attraction and create a distance large enough that 2 weeks of culture life would be insufficient to grow a long enough process). This width of PDMS defining the wells was selected to provide sufficient total surface area for contact between the mask and the glass.

*5.2.2.2.2 - Materials*

Given the dimensions of the glass slide being used (25 mm), the physical mask would have to be constructed using either a mold-casting or machining technique. Machinable materials typically have limited flexibility, which would prevent good conformity to the glass surface for adhesion. Elastic moldable materials would provide conformity, but would need to be susceptible to sterilization techniques and be biocompatible. A commonly used cast-moldable material, poly-dimethyl-siloxane (PDMS), is both chemically inert, allowing it to be cleaned with solvents, and resistant to high heat and pressure, allowing it to be autoclaved [173]. A combination of the two techniques was utilized for sterilization. PDMS is also biologically compatible, eliminating the need for surface treatment or coating to prevent cytotoxicity prior to PDL coating. Lastly, based on preliminary testing, despite low surface energy (~19.6 mN/m) [174] [175], PDMS can also successfully adhere to surfaces with the use of pressure and heat, or by creating surface charging on both the PDMS and the recipient surface.

*5.2.2.2.3 - Construction*

A variety of master molds for the PMDS casting were fabricated. Stereolithography was used to 3D-print molds that were designed in CAD software (Pro-Engineer; PTC, Needham, MA). The resin materials for the master mold needed to be carefully selected, as casted PDMS will not cure properly in the presence of many of the monomer and polymer materials used by these printers (i.e. polyurethane). This precluded the use of the 3D printer utilized in Aim 1, which uses a polyurethane-based resin. Therefore, the mold was formed using a wax stereolithography printer.

Following construction of the mold, the PDMS monomer and cross-linker components were mixed in their recommended ratios (10:1), degassed to remove bubbles, and cast. The casted mold was placed on a level table and allowed to cure for 24 hours. A tab-feature was patterned into the mold to facilitate the demolding of the PDMS (Figure 5.3). This feature would later be removed prior to use in cell culture to allow placement inside of the well of a 6-well plate. An inset-flange was also incorporated into the bottom of the PDMS mask to promote additional conformity to the glass shape. Bright-field photographs of the printed molds and PDMS features are displayed in Figure 5.4.

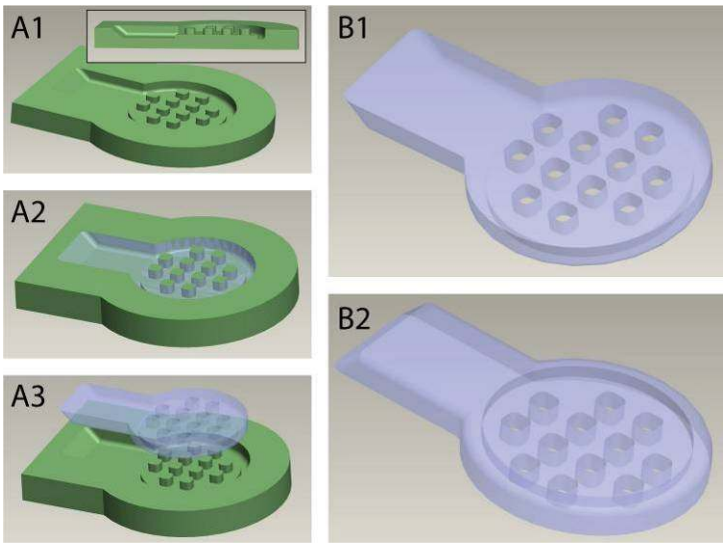


**Figure 5.3**: Schematic of the molding process to create the physical mask for mini-colony cell culture patterning. (A1) Stereolithographical printing of wax mold used to hold the pre-cured PDMS (A2). Following overnight curing, the PDMS is gently removed from the wax mold (A3). Top (B1) and underside of mold (B2), where the inset-flange is visible.

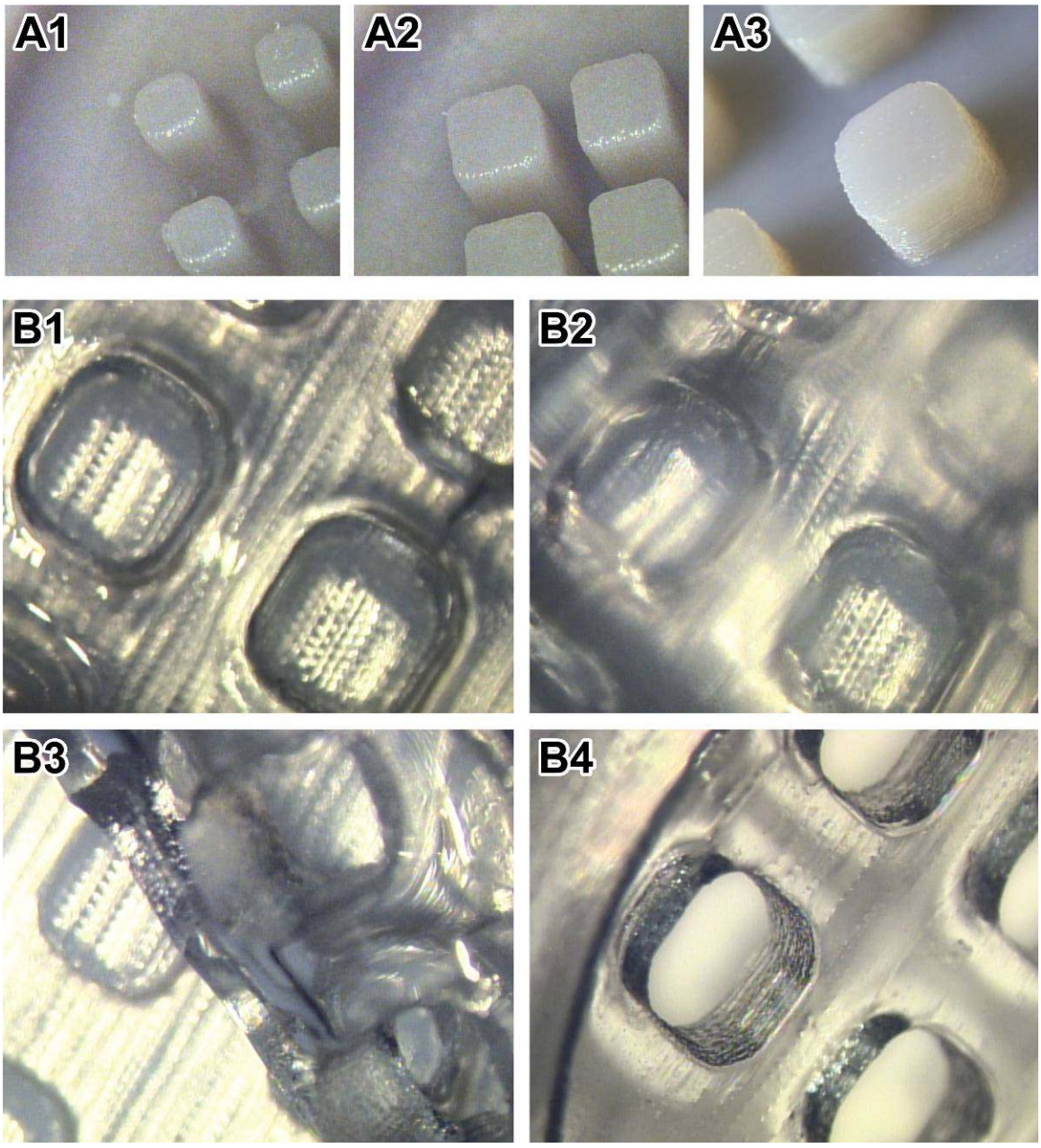


**Figure 5.4**: Bright-field photographs of the stereolithographically printed master molds (A1-3), delamination of the casted PDMS (B1-3), and surface of the final PDMS mask (B4).

*5.2.2.2.4 - Assembly - Mask Adhesion to Glass*

One of the challenges inherent in this system is to prevent unintended delamination of the mask from the glass surface. The PDMS must be bonded sufficiently with the glass to create a liquid-proof seal between each well, but this has to be accomplished without permanent bonding as the mask needs to be delaminated prior to regular cell maintenance (Figure 5.5). While PDMS can readily stretch conform to surfaces, the texture of the molded PDMS surface can prevent this seal from forming if it is too rough. Therefore, the master mold used to cast ideally would have a smooth surface that would be transferred to the PDMS.

Oxygen plasma treatment (Electron Microscopy Sciences, Hatfield, PA; EMS100x Glow Discharge) of the PDMS allows for a strong seal between the glass and PDMS for the majority of the well walls. For plasma treatment, the plasma chamber was evacuated to $10^{-1}$ mbar pressure, an oxygen gas flow then raised the pressure to $2x10^{-1}$ mbar, and 25 mA of relative discharge was created between the gun and target/sample to induce a plasma field. This process was maintained for 30 seconds to ensure complete charge coverage on the PDMS surface. This glass-PDMS seal lasted through the PDL surface coating process, and the cell plating process. However, the delamination of the PDMS and glass failed, resulting in broken cover slips. These 0.27 mm thick cover slips were substituted with 1.52 mm thick glass discs to reduce the likelihood of fracture or breakage. Delamination attempts with the glass discs resulted in tearing of the PDMS and deposited remains of PDMS fragments left on the glass surface. Reductions in the plasma treatment time of the PDMS surface still resulted in incomplete delaminations.

Instead of surface charging with oxygen plasma, the use of pressure and heat to facilitate PDMS attachment to the glass was attempted to create a more temporary seal. The glass disc and PDMS mold were aligned together and placed into an autoclave bag. A 10 lb weight was placed on top of the bag, and a regular dry autoclave cycle was run. Following a dry cycle, a complete seal was present over the surface of the PDMS-glass interface. However, given the durations of the PDL coating (hours) and plating (1 day), this seal failed eventually and permitted the movement of fluid from one mini-well to another from between the PDMS and glass. Following the movement of liquid into the interface between these two components, delamination of this PDMS was readily accomplished.

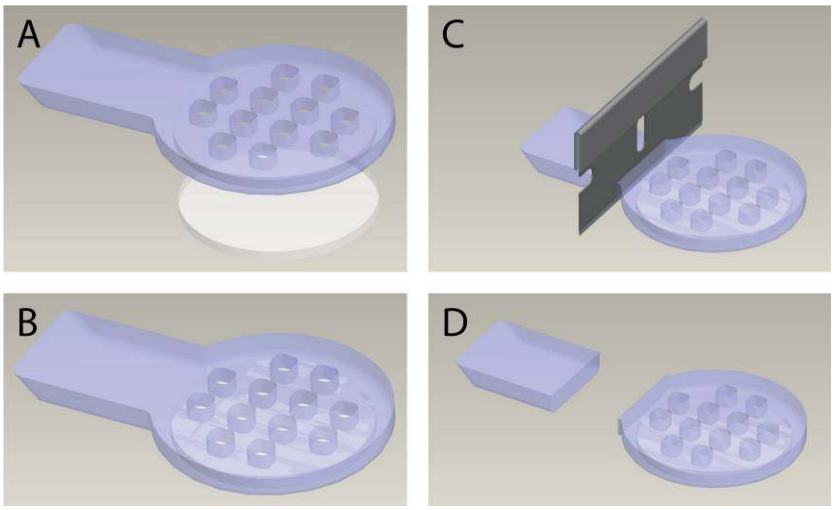


**Figure 5.5**: Schematic of the process used to adhere the molded PDMS mask to the glass slide (or custom cut glass piece). (A) PDMS mask, which is designed to have a snug fit over the glass edge and top surface, is placed over the glass (B). Following placement and application of downward force to ensure a good seal, the PDMS tag, which assisted in the removal of the mask from the wax mold, is removed by cutting with a razor blade (C, D). This sample is then placed inside of an autoclave bag, and into the autoclave chamber. A large metal weight is placed on top to provide additional pressure for adhesion.

5.2.2.3 - Cell Plating and Patterning

*5.2.2.3.1 - PDL Coating Patterning*

The initial strategy to form mini colonies was to use the sterilized physical mask made of molded PDMS that was pressure-heat adhered to the glass surface to control the locations where PDL can surface bind. Similar to the regular glass slide preparation, prior to cell plating, the 100 µg/mL PDL solution was added to each mini-well of the mask, and the well plate was placed in an incubator for 1 hour minimum to allow adsorption. The mask was then removed with forceps, and the glass slide was rinsed twice with de-ionized water and allowed to dry.

While PDL coating was successfully patterned in some of the wells, and neurons were preferentially plated on these surfaces, there were a few neurons that intermittently adhered on the glass surface that was not coated. While these glass-attached neurons were inconsistently spaced, they acted as surfaces where other neurons could bind, and these readily became loci of collected neurons which in many cases formed physical connections via axons and dendrites from one island to another, negating the isolated benefits of the islands.

A major challenge of this strategy was the use of the PDMS physical mask to control PDL exposure. Temporary adhesion of the PDMS to the glass to permit detachment following PDL coating was often incomplete, and leaking under the mask was possible.

*5.2.2.3.2 - Cell Plating Patterning*

The second strategy was to use the physical PDMS mask to control not only the PDL coating pattern, but to also control the location of the cell plating solution so that free floating neurons would be physically constrained to specific areas where plating is preferred (Figure 5.6). The same PDL coating procedures from above were following, but instead of peeling off the mask prior to plating, the plating medium containing the cells was delivered to the mini-wells of the mask. One day after plating, the mask was removed, and the entire glass piece was placed inside of a well of a new 6-well plate, and given 2 mL of fresh medium.

While this method did not ensure patterned coating of the PDL surface, as the PDL solution could freely move between the glass and PDMS, the cells were too large to fit underneath the PDMS, and were thus restricted to the wells. Bright-field microscope images of a patterned week-old mini-colony (4x), and its cells (10x, 40x) are displayed in Figure 5.7.

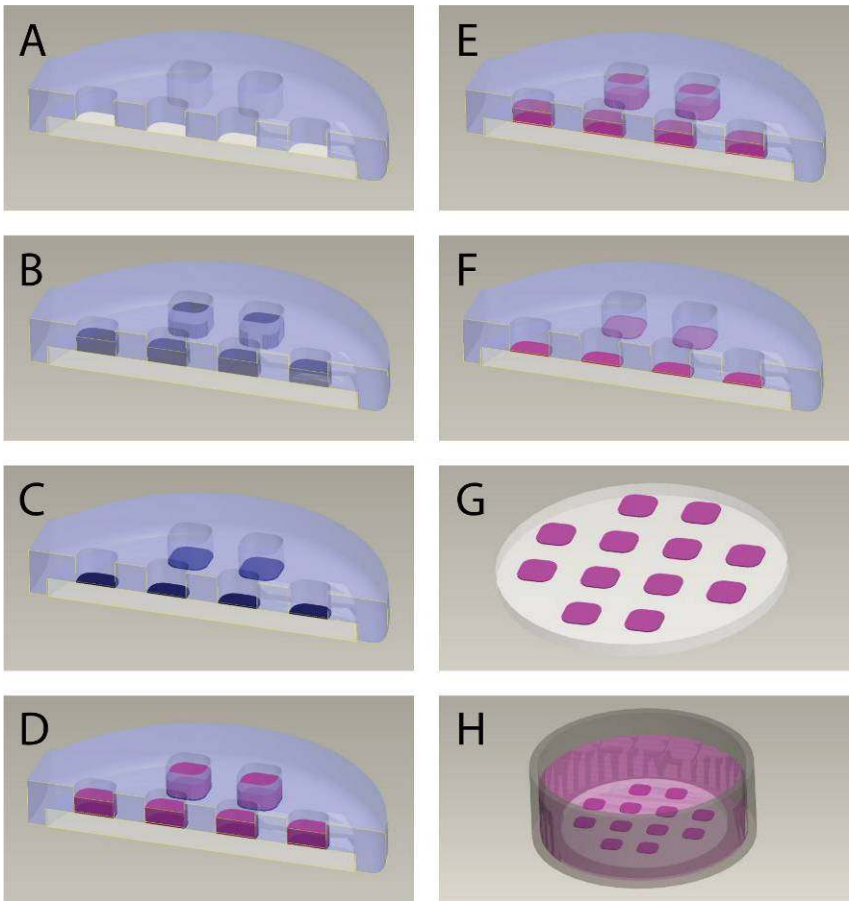


**Figure 5.6**: Schematic of the mini-colony patterning protocol. (A) Following adhesion of the PDMS mask to the glass surface, the 100µg/mL poly-D-lysine solution is placed in each mini-well (B) and allowed to coat (C). Following a rinse step, plating medium with dissociated primary cortical neurons is placed in each well overnight (D, E, F). The PDMS mask is then removed (G) and the glass slide with patterned mini-colonies with plated neurons is placed in a standard multi-plate well (H).

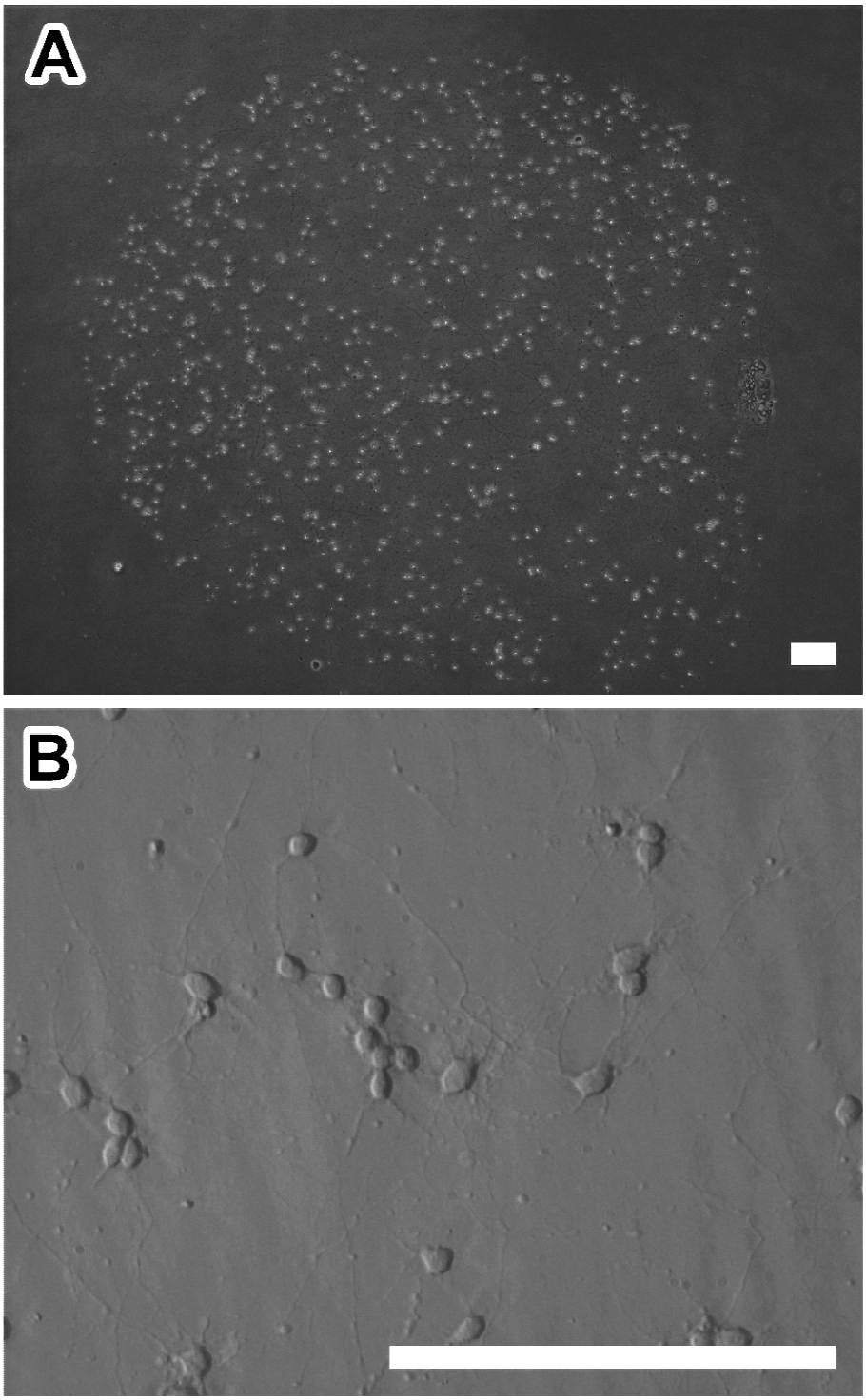


**Figure 5.7**: Bright-field microscope photographs of the 1-week old culture islands (A – 4x magnification), and of the primary cortical neurons (B – 40x magnification). All scale bars are 200 μm.

## 5.3 - Microtweezer Biocompatibility Study

Prior to the use of the microtweezer device to induce mechanical insult onto neurons in culture, potential detrimental effects of the microtweezer's presence in cell medium needed to be identified to determine impact on the outcome of any biological studies. The microtweezer component of the device, which is what physically interfaced with the cell membrane during each study, was composed almost entirely of nickel. As previously mentioned in Section 2.3, both the timeframe of cell exposure to the MEMS device during the injury study and the device's physical dimensions assuage many of the nickel toxicity concerns. However, a conservative biocompatibility study was conducted to verify that the nickel MEMS device itself and timeframe of the studies would minimize any influence of potential cytotoxicity on the cellular outcome.

Given maximum possible medium concentration of nickel calculated in Section 2.3 (~1 μM), the dissociation of nickel is unlikely to affect the medium tonicity, or unbalance the concentration of another extracellular ion. Given nickel's propensity for oxidation, however, it is possible that reactive species or other cytotoxic chemical compounds could be produced or increased from its presence in solution [131].

Therefore, a live-dead viability study was performed to see if the electroplated nickel material in the microtweezer would cause cellular death. A study examining the osmolarity of the cellular medium following this exposure was also conducted.

### 5.3.1 - Methods

#### 5.3.1.1 - Live-Dead Staining

2D primary cortical neurons were cultured as previously described to 1 week in a 12-well plate. Nickel microtweezer bodies (the base of the microtweezer that is attached to the luer needle, the beam portions were removed from these portions of the body) were cut in half, and each piece was placed into the culture well. An equal number of nickel-exposed cultures and negative control cultures were examined, and roughly a thousand cells were counted during quantification for each study. Only a negative control was used in this study, as the maximum calculated nickel concentrations possible from microtweezer exposure were less than those reported for toxicity [130, 135].

Following one day of exposure to the nickel body, a live-dead staining medium using calcein AM (4 mM) to identify live cells, and ethidium homodimer (2 mM, bromide) to identify dead cells, was loaded into the culture for 30 minutes in the incubator [86, 162]. Following three rinses with D-PBS, the cultures were imaged under fluorescent microscopy and entire fields of view under 20x magnification were captured for subsequent quantification of live and dead cells.

5.3.1.2 - Neuronal Cellular Medium Osmolarity

The osmolarity of unused cellular medium, medium with the negative control cells, and the medium with cells and the added nickel component were tested to see if observable changes in medium tonicity occurred from immersion of the nickel component.

**5.3.2 - Results**

5.3.2.1 - Live-Dead Staining

All fluoresced green cells were counted as live cells, and as a conservative measure, all loci of ethidium homodimer fluorescence were counted as dead cells (Figure 5.8). The results of the live-dead staining shows that no significant change in cell viability occurred as a result of exposure to the nickel component for 24 hours. The viabilities reported for the control were 79.9% with a standard deviation of 6.3% (n=6). The viability for the cultures exposed to nickel were 82.0% with a standard deviation of 2.2% (n=6) (Figure 5.9). As a comparison to previous neuronal cultures developed by this laboratory group, this viability is regularly low (viabilities of 85-95% are preferred). However the composition of the cells, growth and connectivity of neuronal processes, and the density of live cells suggest a very healthy culture. The contributing factors to the reduced viability count are: (1) the lack of a DNase digestion step one day following cell plating, which removes all DNA debris from the cell culture that resulted from the dissociation; and, (2) the conservative count of each and every spot of fluoresced ethidium homodimer.

5.3.2.2 - Neuronal Cellular Medium Osmolarity

Osmolarity of the culture medium for unused NBM (220.00 mmol/kg), the negative control cultures (220.55 mmol/kg), and cultures with medium exposed to nickel (220.80 mmol/kg) showed no significant difference. While little observable change in the average tonicity occurred, the variability in osmolarity measurements of medium from cultures did increase. This increase in variability, however, occurred for both the negative control medium and the medium exposed to the nickel.

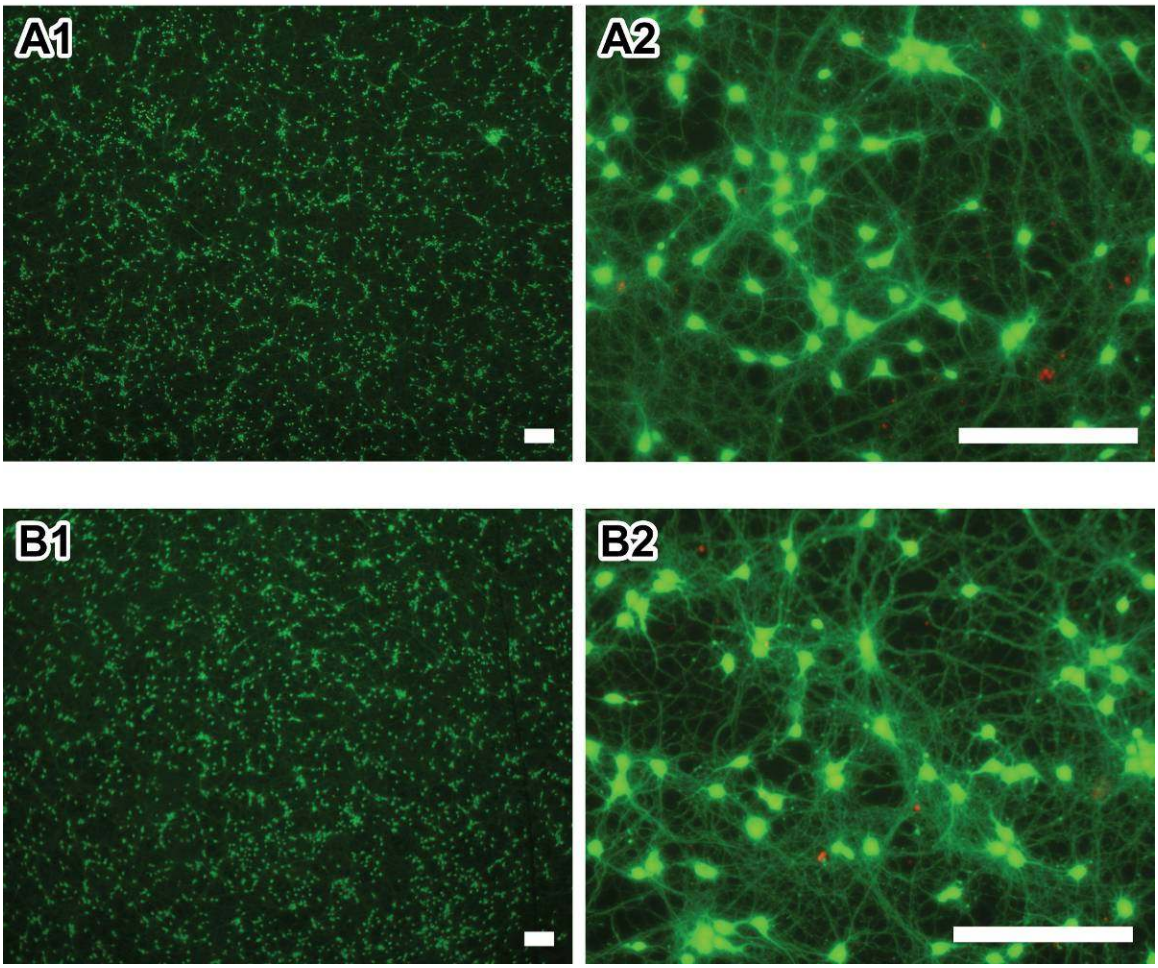


**Figure 5.8**: Fluorescent microscope photos of live-dead staining after 8 days in culture (4 mM Calcein-AM for live cells, and 2 mM Ethidium Homodimer for dead cells): (A1) 4x magnification of regular culture, (A2) 20x magnification of regular culture, (B1) 4x magnification of culture exposed to nickel tweezer component for 24 hours, and (B2) 20x magnification of culture exposed to nickel tweezer component for 24 hours. Distribution and connectivity of cells for each culture is indicative of a healthy culture. All scale bars are 200 μm.

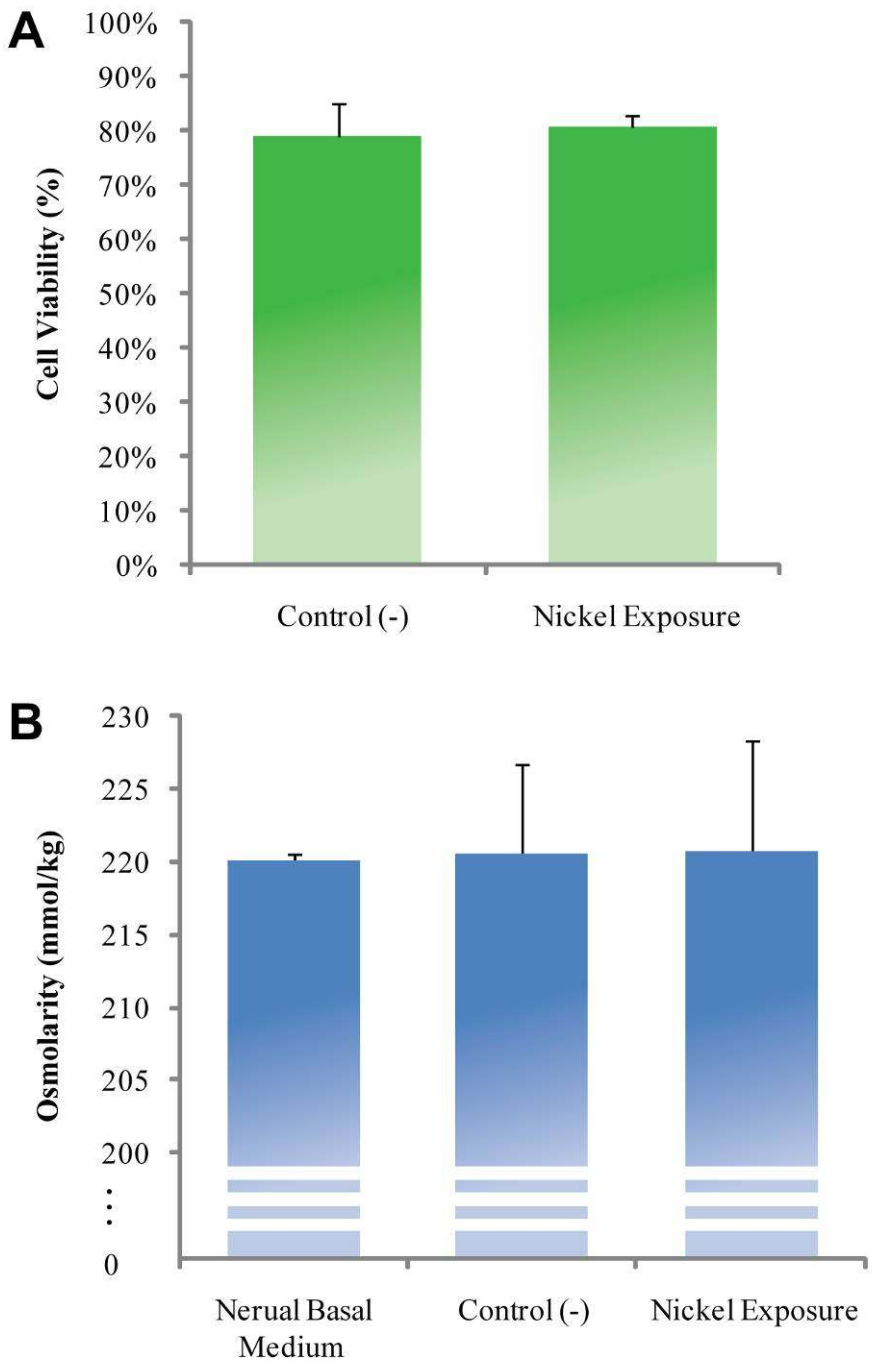


**Figure 5.9**: (A) Live-dead counting results for the negative control neuronal culture (n=6, 78.9%, standard deviation 6.3%) and the culture after being exposed to nickel component for 24 hours (n=6, 80.6%, standard deviation 2.2%). (B) Osmolarity of the culture medium for unused NBM, the negative control, and medium exposed to nickel. No observable change in the average tonicity occurred (but the variability increased)

### 5.3.3 - Discussion

The lack of difference in the cell viabilities measured suggests that short term exposure to the nickel component did not promote additional cell death. Additionally, an insignificant change in the medium osmolarity (difference of 0.8 mmol/kg) and a slight change in the variability of osmolarity measurements were observed. While a limited number of biocompatibility experiments were conducted, the conditions examined were amplified from those used in a normal injury experimental: (1) the nickel component that the cell culture was exposed to was larger than that normally entered into the cellular medium during an experiment; and, (2) a longer time course (almost 25x) of nickel exposure was used. The lack of increased cell death or cell medium tonicity from this conservative study should assuage concerns about nickel toxicity and its introduction of variability into the scientific studies.

## 5.4 - Single Cell Injury Studies

This section will provide background of the injury model definition, the general methods and equipment used to prepare and injure the sample, and the analysis and results of the injury study.

This injury study examines the qualitative change in intracellular calcium concentration indicated by intensity changes in a fluorescent calcium-sensitive dye (Fluo-5F). Because of the real-time visual assessment of each injury, the preliminary testing of the range of strain rates that were assumed based on the literature was rapid. Based on the previous discussion, and the discussion below, the time course of the injury (speed of fluorescence change, delay in resolution of the basal intracellular calcium concentration) can be helpful in elucidating the source of the rise in intracellular calcium.

The change in fluorescence (outcome measure) was used to suggest thresholds of mechanical input required to induce cell membrane permeability and cell death (discussed below).

### 5.4.1 - Background

The background will provide an outline for the determination of the mechanical input used in the model, the behavior of the utilized calcium sensitive dye (Fluo-5F), and the control of the experimental environmental to allow isolation of cellular responses.

#### 5.4.1.1 - Mechanical Input Criteria for Single-Cell Injury

To determine the mechanical input criteria needed for the proposed single-cell injury studies, previously presented *in vivo* and *in vitro* models, their levels and types of mechanical input, and the composition of their tissue/culture samples injured need to be considered. The microtweezer developed in this work will deliver a uniaxial compression injury to the neuron soma; i.e. the two beams of the microtweezer will symmetrically squeeze the neuron cell body in one dimension. Given the novelty of this *in vitro* injury (non-systemic single cell injury, and most *in vitro* models employ tensile and shear mechanisms of insult), an initial extent (strain) and speed (strain rate) of the compression needs to be determined. This characterization of the mechanical input from the injury device will follow the characterization of other *in vitro* injury devices [90, 94, 107].

The criteria for the mechanical loading input for the previously discussed *in vitro* models were determined from extrapolation of mechanical data collected from *in vivo* injury measurements, FEM modeling, and various models [4, 107, 176, 177]. The predicted ranges of strain seen at the tissue level during TBI have varied from 0.10 to

above 0.50, and the maximal strain rates have also varied (10 $s^{-1}$ to 15 $s^{-1}$) [4, 15, 107, 178]. An extrapolation of these TBI mechanical inputs to the inputs used in injury models that induce system-wide injuries have been readily translated; equal strain inputs and strain rate inputs from *in vivo* measurements have been used in both *in vivo* and *in vitro* models.

*5.4.1.1.1 - Mechanical Input Criteria: Strain*

To determine the strain injury used in this model, the mechanical inputs for two established *in vitro* models were preliminarily examined [99, 179]. For a well characterized shear injury of 3D neuronal cultures [99], a mechanical input with a strain of 0.50 (compared to culture height) and a strain rate of 30 $s^{-1}$ was delivered to the top of the culture surface. With a cell culture height of roughly 500 μm, 250 μm of translational movement was used to create 0.50 strain. With a shear angle of 45°, and a consistent gradient of tissue displacement through the depth of the culture, a strain at the cellular level of 0.50 should be seen throughout the culture. This assumption of strain distribution can be extended to equi-biaxial strain models that use stretchable membranes, where the distribution of tensile strain within a certain distance of the center can be close to uniform [90]; a tensile strain of 0.50 across the culture can equate to a tensile strain of 0.50 at the cellular level [107].

The extrapolation of this 0.50 strain injury onto the tissue down to the cellular level has several considerations: (1) consistency in tissue displacement throughout the sample, which as previously discussed, is dependent on the success of the interface between the mechanical input and the tissue/cells; (2) homogeneity of the sample

material and modulus; and (3) the type of mechanical input, which in various models can range from axial and biaxial tension, to shear, to compression.

Large changes in compressibility and elastic modulus across the tissue will result in gradients of strain and shear [180]. It can then be assumed that tissue slices and 3D culture constructs with higher cell density will be more immune to the formation of these gradients and provide for more consistency in translation of mechanical input. Given the morphology of the examined neurons, however, consistent distribution in tissue displacement is more likely to impact the neuronal processes, which, given their cross sectional dimensions, will experience higher rates of strain, strain rate, and shear. This supposition is supported by the idea that diffuse axonal injury (DAI) is a significant contributor to the initiation of the traumatic brain injury following mechanical input [181, 182].

Thus, in general, these critical factors will impact the selection of ranges of mechanical inputs that emulate TBI *in vivo*. Given the difficulty in translating the affects of strain field uniformity across the tissue/cell sample, the variety of mechanical inputs, and the influence of cellular response based on the difference in localized mechanical loading on the neuronal soma and its processes, the selection of an appropriate compressive strain input onto the soma to emulate the cellular conditions seen during in vivo TBI will be benefitted by these preliminary single-cell injury examinations. To start, an assumption of homogeneity for the 3D constructs and tissue slice will be considered, and the strain selected for this single-cell injury study will be 0.50.

*5.4.1.1.2 - Mechanical Input Criteria: Strain Rate*

Determination of the strain rate seen at the cellular level is more difficult considering the previous discussion of neuronal morphology (processes are injured more readily than cell bodies) and the affect of scaling the dimension/size [183]. Some cell mechanics and single-cell neuron injury models studies suggest that the high strain rates that are delivered in bulk-loading models are required to elicit injury response (30 $s^{-1}$) [12], while others show that injury response, including cell permeability, can be observed at substantially lower strain rates (0.5 – 10 $s^{-1}$) [88, 89, 120]. A range of strain rates to be examined can be determined by comparison of the proposed model with these previously reported models.

Quasi-static strain (effective strain rate of 0) induction on giant squid axons of 0.50 caused no change in membrane potential, suggesting limited compromise in the membrane integrity. However, dynamic stretches of the axon resulted in structural failure with strain rates above 10 $s^{-1}$ (strain of 0.25 – 30) [88, 89]. Similar findings were reported in frog sciatic nerves [184]. Other axonal stretching models suggest that the strain rate needed to be elevated (30 $s^{-1}$), but the delivery of mechanical input to the cell in this model was reliant on adhesion of the axon to a deformable substrate [12]. This adhesion is not guaranteed, and following injury, micrographs of the axons show conformational changes and migration in comparison with the deformable membrane, which suggests delamination. In contrast, the physical stretching of the squid and frog axons provided a more confirmable mechanical input. While not completely translatable to traumatic brain injury research, the stretching of vascular smooth muscle cell bodies, which are substantially larger in size and thus have a larger surface area of contact on a

deformable membrane, showed that strain rates of 0.5 $s^{-1}$ were sufficient to produce membrane permeability [120].

Given the range of strain rates reported to induce injury response, strain rates of 1 $s^{-1}$, 2 $s^{-1}$, and 3 $s^{-1}$ were chosen for this injury study. Should cellular response not be elicited at these rates, then the rate will be elevated to determine the threshold.

5.4.1.2 - Intracellular Calcium Concentration and Signaling

During normal physiological firing of the neurons, the intracellular calcium concentration will fluctuate, as membrane depolarization will cause a variety of voltage sensitive calcium channels to open [185, 186]. The opening of these channels causes calcium ions to enter the cell via both electromotive forces from the membrane potential and from the concentration gradient that exists across the cell membrane [167]. At the synapses between neurons, the main site of neuronal communication, the increase in intracellular calcium causes the presynaptic neuron to release neurotransmitters into the synaptic cleft [167]. If bound to neurotransmitter receptors on the postsynaptic cell, these neurotransmitters can cause ion channels to open, allowing ions to enter and depolarize that cell's membrane potential and initiate an action potential.

In addition to neurotransmitter release, calcium presence plays a role in a gene expression, activation of additional ion channels (i.e. calcium-gated $K^+$ channels), membrane polarization, and apoptosis [168-170, 187-190]. To tightly control the signaling that results from localized increases in calcium concentration, the cell uses a variety of mechanisms to buffer, chelate, and remove free calcium from the cellular cytosol [168-170]. These include calcium exchange pumps on the plasma membrane and calcium buffering systems via reticulum and molecules. With these mechanisms, the

intracellular calcium concentration is kept at a very low level (~100 nM) compared to the extracellular concentration (~2 mM) [170]. This creates a steep gradient across the cell plasma membrane (4 orders of magnitude).

5.4.1.3 - Calcium Influx and Spiking

Following localized spikes in intracellular calcium concentration from various mechanisms, the activity of the cellular pump and buffering systems can reinstate the resting calcium concentration gradient. These homeostatic systems, paired with the use of the plasma membrane and intracellular reticulum that are mostly impermeant to calcium influx, reduce the incidence of unintended calcium-initiated signaling. However, any compromise in the integrity, or permeability, of the plasma membrane can quickly disrupt the ability of the cell to maintain this gradient, as calcium from outside the cell can rush down the gradient into the cell. Given the resting membrane potential of neurons (~-70 mV), electromotive forces can also work to bring calcium ions through openings in the membrane into the cell [167]. Disturbance of intracellular calcium sources like the endoplasmic reticulum could potentially also release calcium into the cellular cytosol.

5.4.1.4 - Intracellular Calcium Measurement

These, quick elevations in the intracellular calcium concentration from either neuronal firing or membrane permeability can be examined visually by calcium-sensitive fluorescing dyes like Fluo-5F, that chelate calcium and resultantly change in fluorescent intensity [98, 191]. Isolation of the cause of intracellular calcium increase can be facilitated by the quieting of neuronal firing, which if limited will reduce the changes in membrane potential that initiate calcium channel opening.

5.4.1.5 - Calcium Sensitive Dye - Fluo-5F

Fluo-5F is a high affinity calcium imaging dye that exhibits unchelated intracellular calcium presence [192]. While substantially lower in affinity compared to Fluo-4 dye ($K_D$ = 345 nM), the $K_D$ value of Fluo-5F for $Ca^{2+}$ binding is 2.3 μM. Because the intracellular calcium concentration ($[Ca^{2+}]_i$) is 100 nM, which is much closer to the binding constant of Fluo-4, the use of Fluo-5F will comparatively allow for identification of a higher range of calcium influx (Figure 5.10). Given that the half-binding concentration (KD) for Fluo-5F is 2.3 μM, not even half of the available fluorescent dye will be chelated and activated at physiological intracellular concentrations of calcium (100 nM) [192]. Visual evidence of baseline measurements showed that at the normal intracellular concentration, the Fluo-5F molecules do fluoresce. Therefore, the available concentration spectrum in which available Fluo-5F can continue to bind and increase fluorescence intensity extends several orders of magnitude above the physiological concentration (from to 100 nM to 2.3 μM and higher).

The Fluo-5F molecule is originally bound with an acetoxymethyl ester (AM) group, which due to hydrophobic properties of the chemical structure, allows movement of the complete molecule across a cellular plasma membrane. Once a complete molecule moves into a cell, this AM group is cleaved by intracellular enzymes (specifically esterases), which causes the Fluo-5F molecule to remain inside the cell as subsequent plasma membrane transport is prevented. If Fluo-5F AM molecules are added to culture medium, a portion of the Fluo-5F molecules are eventually internalized into the cells via this one-way mechanism.

An intracellular Fluo-5F molecule will chelate with free calcium ions and, if excited in this state with energy in the proper wavelength, will emit fluorescence. The fluorescence intensity emitted from Fluo-5F is dependent on the localized concentration of free calcium; the higher the calcium concentration, the more the occurrence of calcium chelation, and the more fluorescence emission.

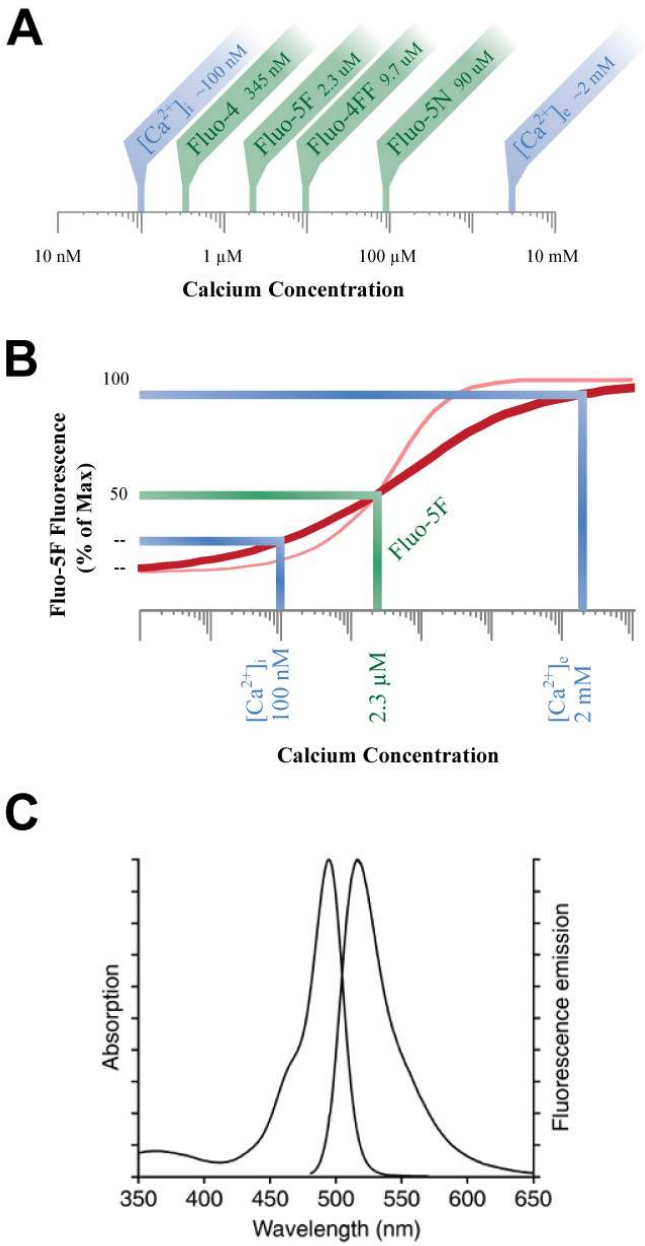


**Figure 5.10**: (A) Chart showing intracellular and extracellular calcium concentrations, and variety of calcium sensitive dyes and the concentrations of their 50% fluorescence intensity. (B) Qualitative curve (red) of the fluorescence intensity of Fluo-5F over a range of calcium concentrations (curve slope not determined, so alternative pink curve shown as another example with smaller range of fluorescence resolution). The fluorescence at the intracellular concentration ($[Ca^{++}]_i$ should be consistent from cell to cell), will provide the baseline and all other measurements compare to this. Fluorescence baseline will vary from cell to cell based on loading and photo-bleaching. (C) Spectrum of absorption/emission wavelengths for Fluo-4 (comparable to Fluo-5F). All information and spectrum chart (C) provided by Invitrogen (www.invitrogen.com).

5.4.1.6 - Neurotransmitter Blocking - Neuronal Fast-Receptor Agonists

Without disrupting the normal physiology of the neurons, the quieting of electrical activity of cells can be accomplished by limiting the neurotransmitter-based chemical communication between neurons. Neurotransmitter blockers, or neurotransmitter receptor antagonists, preferentially bind with the neurotransmitter receptors and prevent their activation. Given the number and types of neurotransmitters used by primary cortical neurons, a variety of neurotransmitter blockers can be required to successfully reduce inter-neuronal communication [193, 194].

Based on work by Bakkum, a combination of Bicuculline (BMI), 2-amino-5-phosphonova-leric acid (APV), and 6-cyano-7-nitroquinoxaline-2,3-dione (CNQX), can be added to the cell medium to disrupt both the inhibitory and excitatory neuron communication [194]. BMI binds with the γ-aminobutric acid or GABA receptor, limited inhibitory input to neurons [195]. Bicuculline also inhibits or blocks some calcium activate potassium channels [195]. The APV receptor antagonist binds with the N-methyl d-aspartate or NMDA receptor. NMDA is a fast-acting receptor that is a coincidence detector, as it is gated by both glycine and glutamate, and forms a calcium channel when activated. APV, which prevents the binding of glutamate that activates NMDA, can prevent the formation of the calcium channel [28]. The CNQX receptor antagonist binds with the α-amino-3-hydroxy-5-methyl-4-isoxazolepropionic acid receptor AMPA receptor, also preventing the binding of glutamate that causes AMPA to form into a channel that allows influx of sodium, potassium, and calcium [196].

**5.4.2 - General Injury Methods**

The following methods define the microtweezer injury system, and outline the preparation of the microtweezer prior to use, and the preparation of the cell culture sample prior to imaging and injury, and the analysis methods uses to process the injury response data from the experiments.

5.4.2.1 - Microtweezer Injury System

The injury system consisted of: (1) the microscope and imaging equipment used to visualize the cell culture; (2) the light source and camera used to activate and capture the activity of the Fluo-5F molecule; (3) the microscope stage with a chuck that holds the cell culture sample; and, (4) microtweezer device that is used to induce the mechanical insult onto the neurons and the micromanipulator stage that positions it.

*5.4.2.1.1 - Calcium Imaging System*

The calcium imaging system, which consisted of a microscope, isolation table, camera, filter cube, and light source, was used to capture the Fluo-5F fluorescence activity of the examined neurons. This fluorescence was activated when the Fluo-5F molecule was exposed to a light with a wavelength of ~494 nm. A light with this wavelength was produced using a specific light-emitting-diode (LED) source (TLCC-01-Triple LED; Prizmatix, Modiin Ilite, Israel). This emitted light was channeled through a fluorescein isothiocyanate or FITC filter cube and then an immersion microscope objective into the cell culture being imaged (Zeiss Axioscop2, 20x). Following exposure to this light, the Fluo-5F molecule emits fluorescence with a spectral peak in the 516-518 nm wavelength range. This fluorescence emission passed back through the microscope objective and FITC filter cube and was captured using a CCD camera (QuantEM 512S;

Photometrics, Tucson, AZ). The captured image was recorded using a software imaging program (Slidebook; Intelligent Imaging Innovations, Denver, CO).

*5.4.2.1.2 - Microtweezer Device Staging*

The assembled and characterized microtweezer and controller were augmented to a positioning stage that was secured to the calcium imaging system isolation table. For the preliminary work, the Narishige stage was used to position the microtweezer into the neuronal culture. As described in Section 3.5.2, the Narishige stage was attached to bracket that clamped to a 2" diameter post that was screwed into the isolation table. This stage provided over 6 degrees of movement freedom.

Following microtweezer characterization and finalization, a Sutter micromanipulator stage was used for the injury experiments. As described in Section 3.5.3, the Sutter stage was mounted to a rotating swivel stand. This stage provided 4 degrees of freedom movement, but it was controllable using a joystick, which prevented the introduction of mechanical noise from user input. This controller had a pre-programmed home position, and allowed the use of an inclined entry angle, which if set, could be used to easily enter and remove the microtweezer from the culture.

*5.4.2.1.3 - Microscope Stage and Injury Chuck (for holding cover slip sample)*

To facilitate the insertion of the microtweezer into the cell culture, a specialized chuck was machined out of polycarbonate to hold the glass cover slip sample. Similar to a culture well, the chuck contained a recessed cavity that would allow the insertion of a cover slip with neurons. However, this cavity was much more shallow than a normal well-plate well (0.08" compared to ~0.75"), which allowed the tweezer to be inserted at a more shallow angle ($14^{o}$). This shallow angle of insertion ensured a more flat tweezer tip

surface relative to the culture system bottom, which facilitated interfacing with low-profile neurons. The cavity of the chuck was designed to fit the cover slip tightly so that minimal shifting would occur during microscope stage movement. A lateral tab, which was deeper than the well cavity floor was machined into the edge of this cavity to facilitate the removal of the cover slip after experiments. This tab also provided a location to deliver medium to the culture without directing fluid flow directly at the cells.

To secure the injury chuck to the motorized microscope stage, a custom injury chuck holder was designed in CAD and fabricated using the stereolithography printer (Figure 5.11). The holder had two components: (1) a base to fit snugly into the slot of the microscope stage; and, (2) a post with a nest where the chuck could be seated using a friction lock. Posts with a variety of heights and bases with a variety of sizes could be fabricated to allow attachment of the injury chuck to any microscope stage.

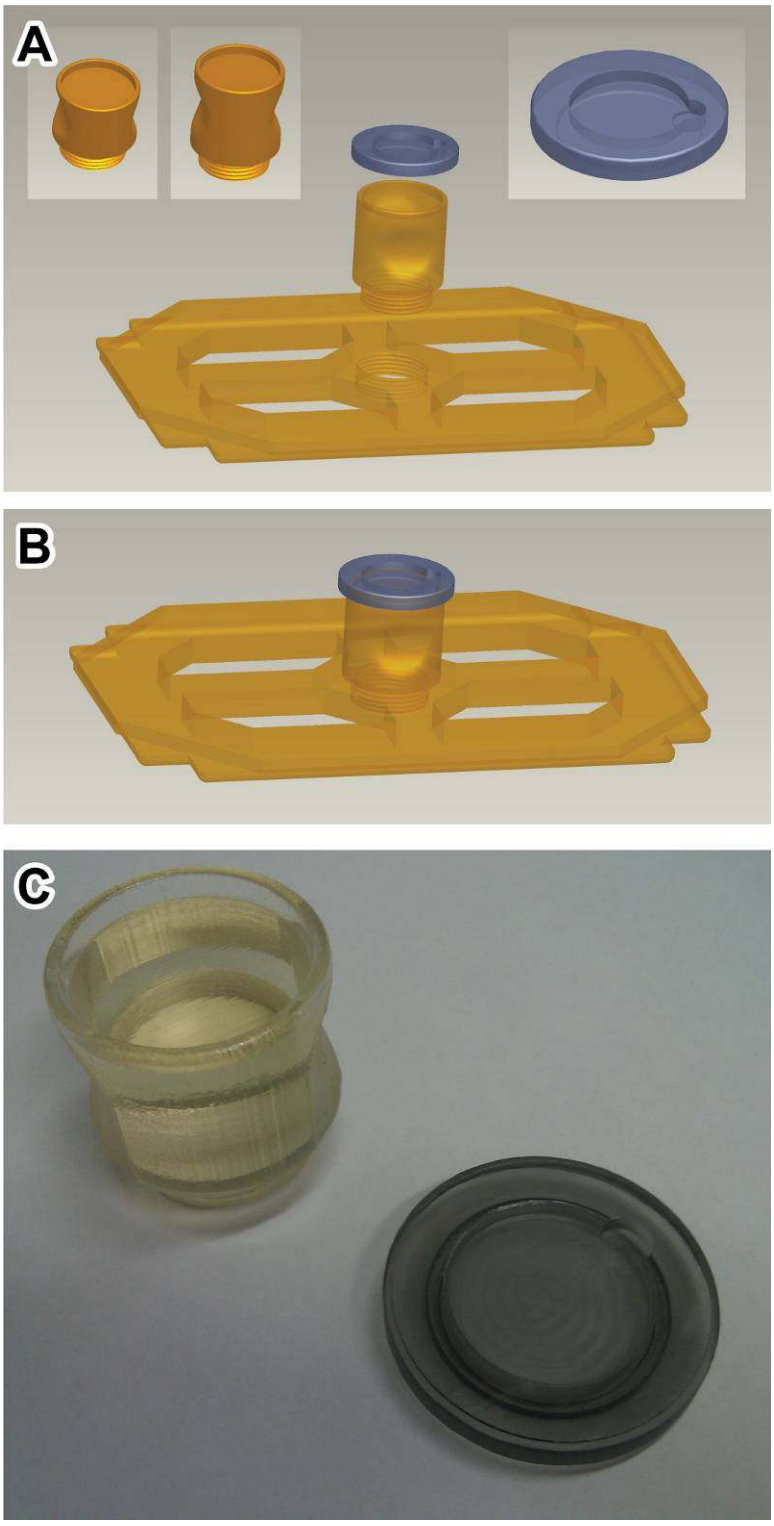


**Figure 5.11**: (A, B) CAD drawings of the unassembled and assembled injury chuck holder (orange pieces), and the injury chuck (blue piece). Bright-field photo of the injury chuck holder post (upper left) and the injury chuck (bottom right).

*5.4.2.1.4 - Microtweezer Positioning into Culture, Programming, and Injury Induction*

The microtweezer itself was controlled using the automated controller and software described in Section 3.4.2.3. Pre-programmed actions, including a prescribed closing and then subsequent opening of the microtweezer could be executed with a single mouse click. Once positioned into the culture under the microscope objective, the microscope focus was adjusted to see the microtweezer tips. Care needed to be taken to ensure that the microtweezer tips were not pushed into either the microscope objective lens (difficult given the angle of entry ~14$^{o}$) or the cell culture surface.

To program the movement of the box to produce the injury conditions, the microtweezers were first actuated using software commands until they closed completely. This state and box location was recorded. Using this state, and considering the tweezer tip style, tweezer tip separations could be calculated and determined based on relative box actuations. This information was used to preprogram the injury regimens into the software. The software provided the ability to deliver specific box actuation locations, or relative actuations to the microtweezer device.

When ready, the opened microtweezer was lowered over a target neuron. The focal plane of the imaging field was used to determine the relative z-plane of both the microtweezer and the culture surface and neurons. Care was taken not to disturb the axonal and dendritic processes of the neuron. This could be accomplished by adjusting the x- and y-location of the microtweezer prior to lowering over the neuron. The recording software was started to get a baseline fluorescence image, and then the injury was initiated. Video recording of the injury before, during, and after was captured.

*5.4.2.1.5 - Microtweezer Tip Coating*

Following preliminary injury studies, it was noticed that microtweezer tips would occasionally get covered in cellular or extracellular material after multiple injuries. This was potentially caused by the surface topography of the nickel microtweezer, or the surface binding by integrins and other proteins from the cell surface onto the nickel. To reduce the surface energy of the nickel microtweezer tips, a protein-coating protocol was developed.

Bovine Serum Albumin (BSA) is a protein that binds well to surfaces, but once bound, can inhibit the adhesion of cellular proteins to the bound surface [197]. A 1% (g / 100 mL) solution of BSA (Bovine Serum Albumin - Fraction V; Thermo Fischer Scientific, Waltham, MA) was prepared. Using the Signatone micropositioner, the tips of the microtweezer were lowered into a shallow tray containing the BSA solution, and allowed to coat for 20 minutes. This coating provided a sufficient reduction in the adhesion of cellular material for at least one hour-long experiment (subsequent experiments showed reduced adhesion as well).

5.4.2.2 - Cell Culture Sample Preparation and Loading

For the injury assessment of single-cells, either the simple culture system with just glass slides, or the multi-cell-island culture system can be used. Cell culture preparation and maintenance was as previously described (Section 5.2.1). Because multi-cellular responses for this study were not examined, multiple cells were injured per culture per experiment, and cell to cell communication was muted with neurotransmitter blockers. Following the loading of the Fluo-5F fluorescent dye into the neurons, and several rinsing steps, a buffered solution containing the neurotransmitter blockers was used as the cellular medium during the injury experiments.

The sections that follow describe the preparation of the culture sample from the culture well-plate, to loading of the Fluo-5F dye and neurotransmitter blockers, to insertion into the injury system chuck.

*5.4.2.2.1 - Fluo-5F Cellular Loading*

The culture well containing the cover slip sample was used to load the Fluo-5F dye. All neural medium was removed from the well, and the medium with the Fluo-5F was added. For a 6-well-plate, the well got 1 mL of the Fluo-5F medium, and for a 12-well-plate, the well got 0.5 mL of Fluo-5F medium. The well-plate was then placed into the incubator for 35 minutes. Following this time, the Fluo-5F medium was removed from the well, and rinsed 3-5 times with artificial cerebral spinal fluid (ACSF), which is an isotonic solution that contains the cationic, anionic, osmotic, pH, and pH buffer conditions that exist in the central nervous system. A detailed protocol for mixing and delivering this solution is included in Appendix D.1.

*5.4.2.2.2 - Neurotransmitter Blocking - Neuronal Fast-Receptor Agonists*

Following loading of the Fluo-5F dye and rinsing, the cover slip sample was removed from the well-plate and placed into the dry injury chuck. A dry chuck allowed the glass surface of the cover slip to sit flush with the bottom of the chuck. This ensured flatness of the glass cover slip when viewing under the microscope objective. 0.5 mL of medium containing ACSF and the neurotransmitter blockers was quickly added to the injury chuck at the lateral tab on the side. Adding the medium to this location prevented a direct spray of fluid at the cell culture, which could cause delamination of the cell layer.

The blocker medium containing the fast synaptic receptor antagonists was composed of Bicuculline methiodide (BMI, 50 μM), 2-amino-5-phosphonova-leric acid

(APV, 100 μM), and 6-cyano-7-nitroquinoxaline-2,3-dione (CNQX, 10 μM) [194]. A detailed protocol for mixing and delivering this solution is included in Appendix D.2.

*5.4.2.2.4 - Sample Loading and Microtweezer Insertion*

Following the insertion of the injury chuck into the holder, the microscope stage was used to position the chuck below the immersion microscope objective. The objective is lowered to the fluid level and focused onto the cells, which can be visualized using the LED to excite the intracellular Fluo-5F. The microtweezer was then inserted and positioned into the culture under the objective by directing the positioning stage. Using a moving focal plane of the objective, the microtweezer was lowered to just above the culture floor. From this location, the microtweezer could be micropositioned onto a selected neuron within the culture for injury.

5.4.2.3 - Microtweezer Mechanical Input

As previously described, following baseline measurements of fluorescence intensity, the microtweezer was then actuated to induce mechanical strain insult on a single-cell basis (Figure 1.5). The strain injury for each neuron was held constant at 0.50 (the cell diameter was compressed by a factor of 50%), and the strain rate was varied (1 $s^{-1}$, 2 $s^{-1}$, 3 $s^{-1}$). The change in strain rate was accomplished by changing the motor speed of the linear actuator, and thus, the actuation speed of the microtweezer box. Each injury had two phases: (1) a compression phase where the tweezer tips are closing onto the neuron, compressing the soma; and, (2) a release phase where the tweezers are opened, allowing the cell to decompress. The strain rate for both phases of the injury was exact.

Experimental trials of n=25+ were performed for each strain scenario. Maximal fluorescence intensities for all trails were averaged over the group, and groups were compared.

5.4.2.4 - Cellular Response Assessment

*5.4.2.4.1 - Intracellular Calcium Concentration*

Real-time cellular response in this injury model was indicated by the cellular uptake of calcium, which was comparatively measured by changes in intensity of measured Fluo-5F fluorescence. Following baseline measurements of fluorescence intensity, fluorescence intensity immediately following injury was video captured. These video files were converted into layer TIFF files, which each layer being a frame in the video. These layered TIFF files were then loaded into MATLAB® (MathWorks, Natick, MA) and analyzed using custom developed signal processing scripts. All fluorescence levels for each video frame were normalized to the background of the current frame. The fluorescence level of the injured cell (pixel of highest intensity) was compared to baseline (exact same pixel). Given the resolution of the high speed calcium camera, a cell could be composed of a pixel array of roughly 5x5. This normalized change in intensity from baseline was used to assess the qualitative activity or injury level for each injury scenario.

The motivation for using a normalized percentage comparison to baseline as the change in the fluorescence, instead of the before and after hard fluorescence intensity values, resulted from: (1) the variation in fluorescence from injury to injury due to potential photo-bleaching during positioning of the tweezer and searching through the culture for injury candidates; (2) the intracellular concentration of free calcium, which should be fairly consistent from one neuron to the next (~100 nM), so even if baseline

fluorescence intensity varies from trial to trial, the baseline calcium concentration should not; (3) the variation in fluorescence from one loading of the dyes to the next and from one cell to the next, even with strict adherence to the loading protocol; and, (4) the relative fluorescence intensity, which is functionally related to the number of Fluo-5F molecules loaded into the cell and can be compared across experimental groups.

The video capture of the entire injury regimen was also used to ensure consistent strain induction. Data was disregarded from failed mechanical insults. The occurrence of cell death following a mechanical insult was also recorded.

### 5.4.3 - Results

The following sections provide the calcium imaging fluorescent study results, and overall cell death results over the three varieties of mechanical insult examined here. As a comparison with final calcium imaging data, the data for the preliminary studies is provided to show the enhancement in injury precision over the iterations of the microtweezer fabrication, microtweezer controlling, and the stage positioning.

#### 5.4.3.1 - Intracellular Calcium Concentration

##### *5.4.3.1.1 - Preliminary Studies*

Figure 5.12 shows the Fluo-5F fluorescence of day 14 2D cortical neurons before and after injury using a base microtweezer tip. The microtweezer was positioned using the Narishige manual stage. Images were acquired at a sampling rate of 15 Hz, down-sampled and averaged to reduce noise, and plotted on a normalized color scale. Receptor antagonists present in media limited fluorescence change from sporadic and network activity. This control allowed fluorescence change to be more attributed to injury-induced cellular uptake of $Ca^{2+}$. Fluorescence is shown acutely following injury. Based on movement of tweezer in this preliminary study, the fluorescence appeared directly following mechanical insult, and cells were strained between 50-100% (some cells were sheared), and the strain rate was roughly 2 $s^{-1}$. During mechanical injury, multiple cells demonstrated increased fluorescence due to physical contact of relatively non-sharp precursor microtweezer with somata and processes (dendrites, axons). Duration of enhanced Fluo-5F fluorescence following strain was minutes, compared to seconds for an action potential [98, 198]. Raw baseline subtractive change in fluorescent intensity before and following injury suggest that changes ($\Delta F/F$) of up to 87% were observed.

This change is significantly higher than normally observed fluorescence change due to electrophysiological bursting or sporadic firing in same experimental apparatus.

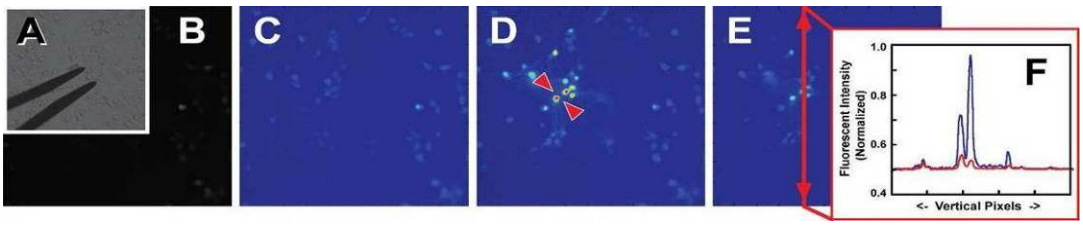


**Figure 5.12**: Bright-field photo of tweezer in culture(A), raw fluorescence image of Fluo-5F dye fluorescence (B), normalized baseline fluorescence for intracellular calcium (C) and fluorescence after injury (D), baseline subtractive change in fluorescence (E), and normalized quantitative histogram of pre and post injury fluorescence along one vertical line of image (F).

*5.4.3.1.2 - Intracellular Calcium Examination During Mechanical Insult*

Figure 5.13 and Figure 5.14 each show a sample single-cell injury using a strain of 0.50 and a strain rate of 1 $s^{-1}$. The microtweezer was positioned using the Sutter motorized staging. Images were captured with an exposure of 50 ms, sampling rate of (~20 Hz), and were averaged over 3 frames, to make an effective frame rate of 6.49 frames/sec, or 150 ms per frame. Receptor antagonists present in media limited fluorescence change from sporadic and network activity. An increase in fluorescence in the injured cell is shown immediately during and following mechanical insult and the elevated fluorescence intensity is maintained for minutes (Figure 5.15). This duration in elevated intracellular calcium is non-physiologic. To verify, Fluo-5F calcium imaging on the same rig with primary cortical neurons shows that neuronal firing, which also causes spikes in intracellular calcium, causes a brief elevation and then fall of the Fluo-5F fluorescence intensity. The average time required for the Fluo-5F to return to baseline intensity is 1.416 sec with a standard deviation of 0.6260 (n=8, collected by Ms. Michelle Kuykendal and Mr. Gareth Guvanasen). The microtweezer tip shape, positioning, and actuation were refined sufficiently to adequately prevent the disturbance of neighboring neurons during injury.

When examining the fluorescence response to the various mechanical injury severities, we see some relationship, but additional trails are required to reduce the variance (Figure 5.16). Also, during a scenario where the fluorescence drops quickly after injury (death), the fluorescence may never have reached the maximal potential intensity. This may alter the lack of increase in the trend from 1 $s^{-1}$ injuries, which saw very limited death, to the injuries with 3 $s^{-1}$ (discussed later).

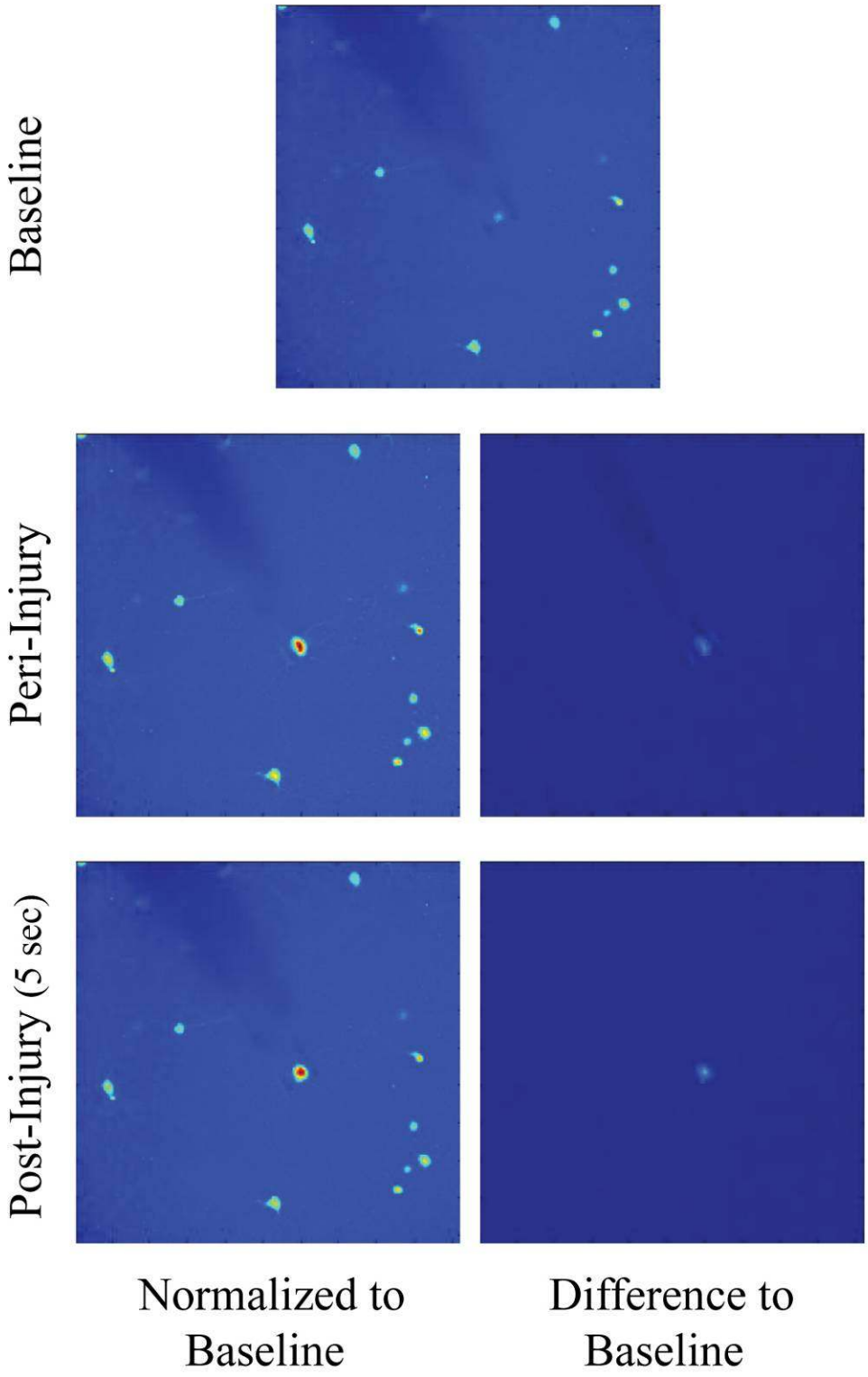


**Figure 5.13**: Normalized Fluo-5F fluorescent intensity jet-images for the baseline, peri-injury, and post-injury video frames.

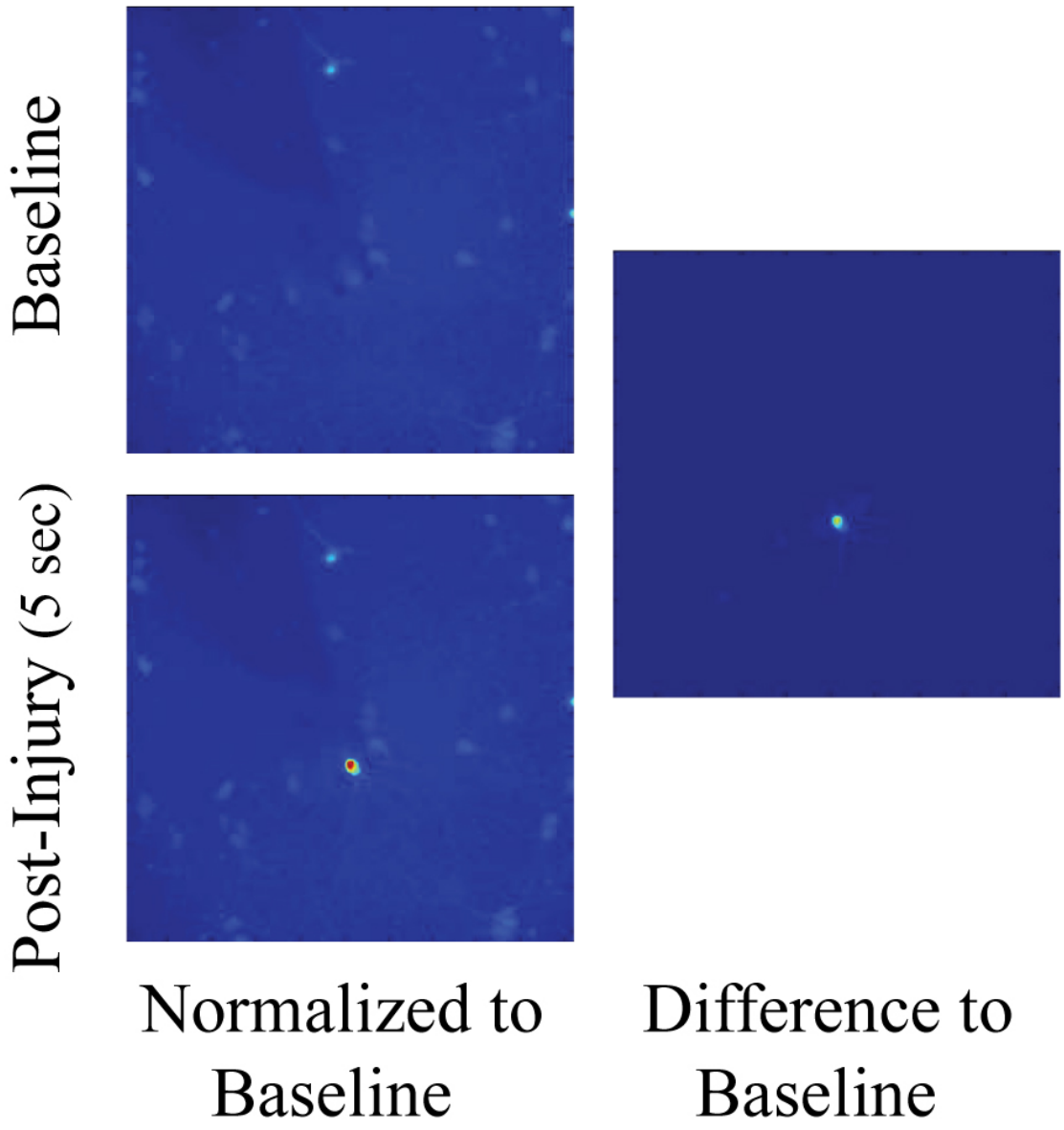


**Figure 5.14**: Normalized Fluo-5F fluorescent intensity jet-images for the baseline, peri-injury, and post-injury video frames.

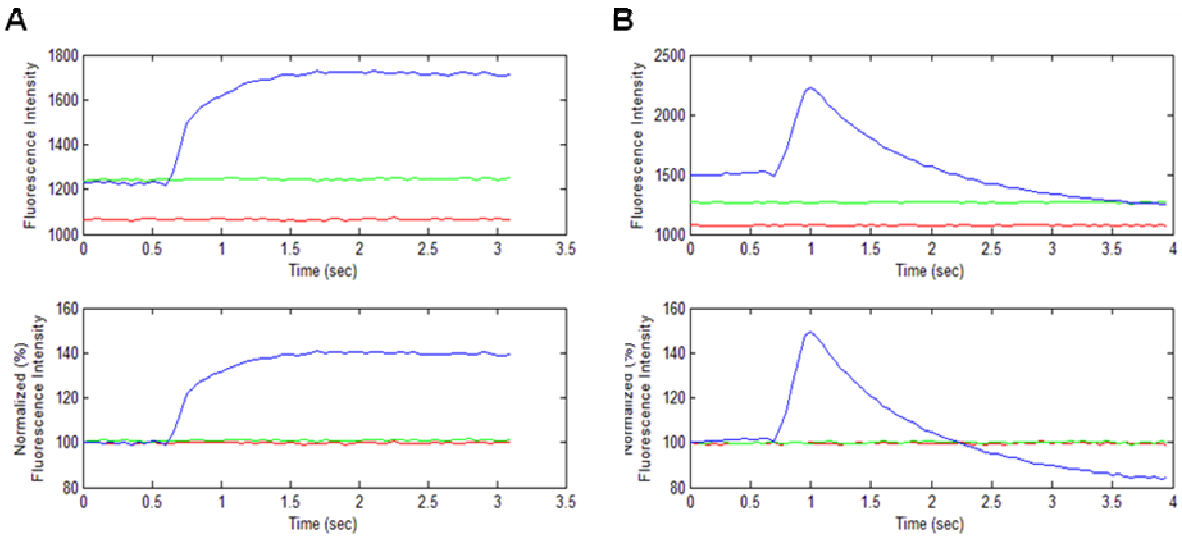


**Figure 5.15**: Traces of the raw (bottom) and normalized (top) fluorescence intensity over the time course of injury of the background (red), another non-injured cell (green), and the injured cell (blue). In the scenario from (A), the fluorescence remains high after injury, and in scenario (B) the fluorescence drops quickly following injury to a value below the baseline, indicating sustained cell permeability.

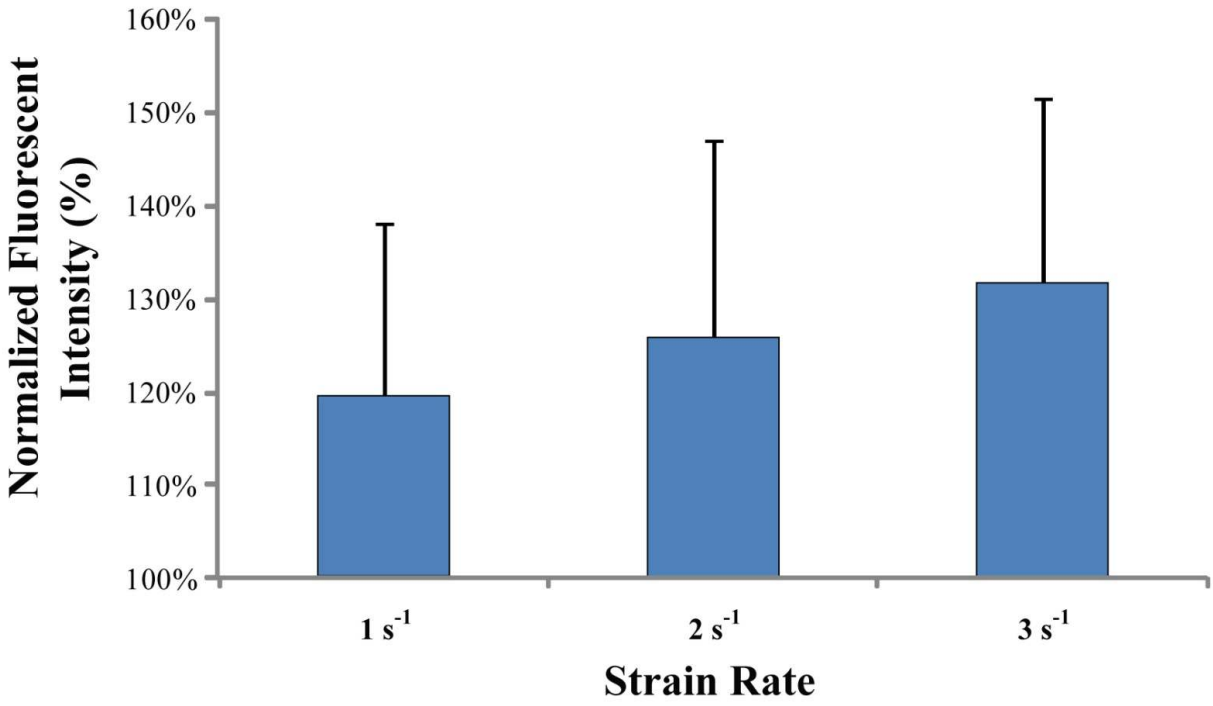


**Figure 5.16**: Normalized Fluo-5F fluorescent intensity changes following varieties of mechanical input (all with a strain of 0.50).

5.4.3.2 - Cell Death

Despite the consistency in the tweezer tip actuation, there was variability in the cellular injury response. This could have resulted from the variability in the orientation and positioning of the neuronal processes for each injury. The chance of the microtweezer hitting a process during mechanical strain induction was high. For a number of the injuries, acute cell death occurred. In some scenarios, the cell died immediately (the compression of the soma punched a hole in the soma, forcing out the cytosolic fluid and any intracellular Fluo-5F dye) (Figure 5.17-A). Cell death also occurred more gradually, and in one case was observed roughly 5 minutes following injury (Figure 5.17-B). For each scenario, the fluo-5 intensity of the cell diminishes considerably, while the change in intensity of the neighboring cells is negligible.

The occurrence of this immediate cell death was related to the injury severity. The percentage of cases in which death occurred was 3.3% for a 1 $s^{-1}$ strain rate injury, 16.7% for a 2 $s^{-1}$ strain rate injury, and a 52.3% for a 3 $s^{-1}$ strain rate injury (Figure 5.18).

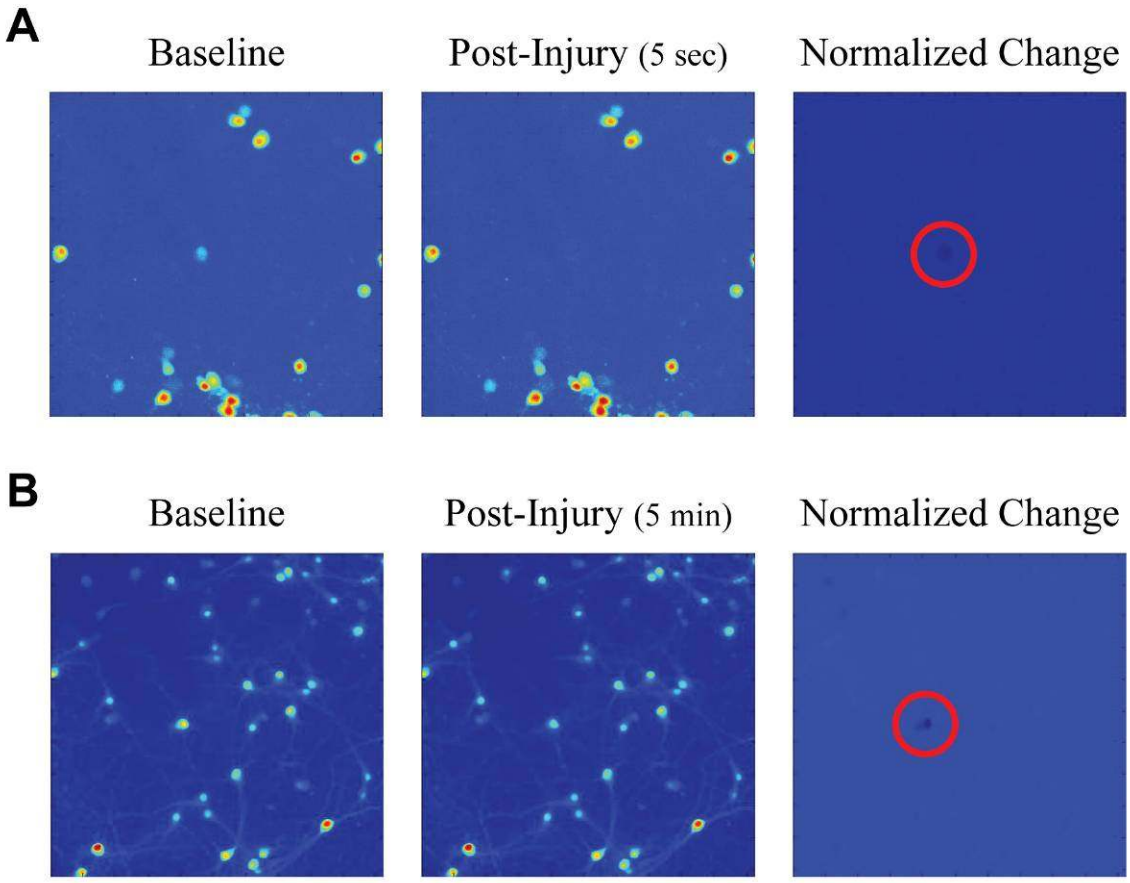


**Figure 5.17**: Video frames of a injury scenarios where: (A) the cell died immediately from mechanical insult, as the cytosol was visibly pushed out from the cell through a hole in the top of the neuron during the compression phase of the injury, and all fluorescence faded in 5 seconds (1 $s^{-1}$ strain rate); and, (B) a slow-dying cell, as the fluorescence in the cell continued to fade for 5 min (2 $s^{-1}$ strain rate). As can be seen the deaths occurred at all strain rates, and the variance in injury from strain rate to strain rate was high.

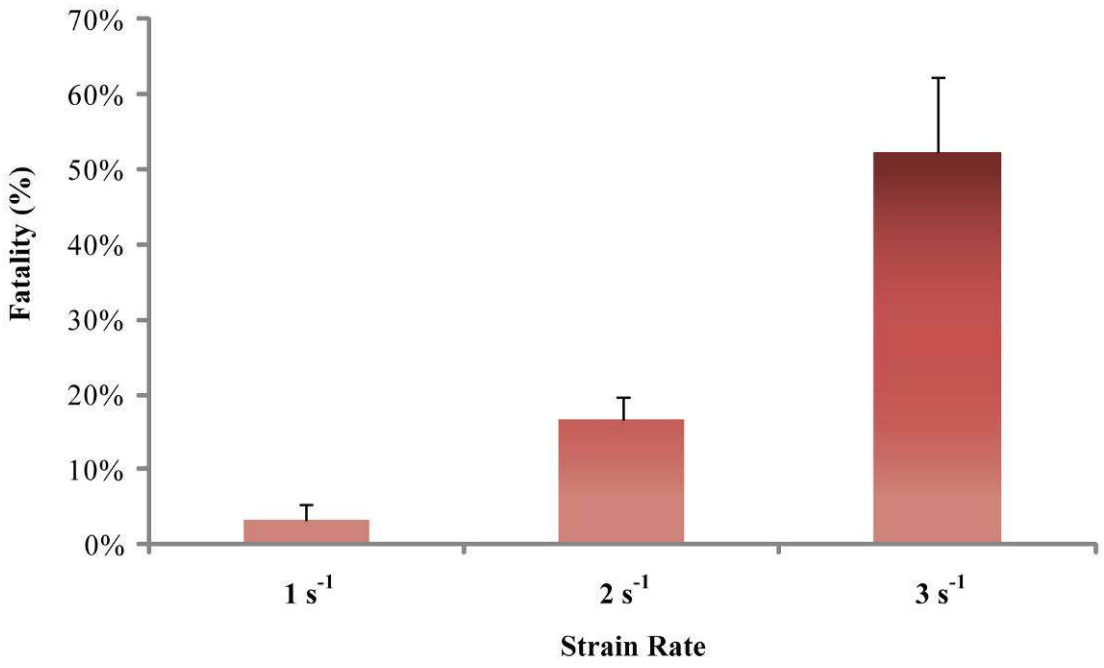


**Figure 5.18**: Chart showing the percentages of cells that died (according to assumptions above) following specific mechanical input by the tweezer (over 112 single-cell injuries).

### 5.4.4 - Discussion

5.4.4.1 - Intracellular Calcium Concentration

In choosing the experimental variable, varying the strain rate instead of the strain allowed a wider variety of injury severities to be tested more quickly. As injuries were taking place, it was clear that small deviations in the strain from injury to injury were present (a best estimate of the cell body size was made during the experiment, which dictated the displacement of the tweezer).

Other inconsistencies could have existed in the delivery of the mechanical insult. However, using visual inspection, any poorly conducted injuries could be removed from inclusion in the calculated results. This is one of the most important benefits of this particular model. In addition to real-time assessment, an evaluation of the mechanical insult delivery itself can be assessed. Obvious 'game-over' cues existed, such as the striking of an axon during either tweezer positioning or injury delivery that would lead to the spiking in fluorescence of the struck neuron (Figure 5.19). The compression of the neuron could be examined as well to ensure that a proper bi-axial strain loading had taken place during the insult.

While there was some correlation between the mechanical input, and normalized percentage change in fluorescence intensity, the variance was high. The variance in data could be reduced by collecting additional data. However, several enhancements to the imaging and tweezer stating systems would not only increase precision of tweezer placement, and thus, injury delivery, but it would reduce the time between injuries. A single 20x immersion objective was augmented to this upright-microscope calcium imaging station. The alternative use of an inverted microscope would not only provide

clearance above the culture for inserting and positioning the tweezer, but it would permit the changing of objectives to increase the positioning and imaging resolution.

5.4.4.2 - Cell Death

For the cell death scenarios described previously, the Fluo-5F intensity of the cell diminishes considerably, while the changes in intensity of the neighboring cells are negligible. The diminishing in the intensity of the neuron following injury could have resulted from the following: (1) the displacement of Fluo-5F molecules from the cytosol from membrane permeability or from the tweezer mechanical insult forcing out portions of cytosol; (2) the drastic reduction in the intracellular calcium concentration (which is unlikely given a basal concentration of 100 nM and the baseline fluorescence intensity at this concentration); and, (3) the complete loss in integrity of the plasma membrane, allowing fluid flow into and out of the cell. The fluorescent intensity drop suggests that scenarios either (1) and (3) are possible given the time course.

Depending on degrees of cellular response to these injuries, some adjustment in the strain and strain rates might be required to cover an appropriate range of injury and to more closely identify injury thresholds: no response, minimal response, severe injury, and death (fluorescence fades to below baseline measurement).

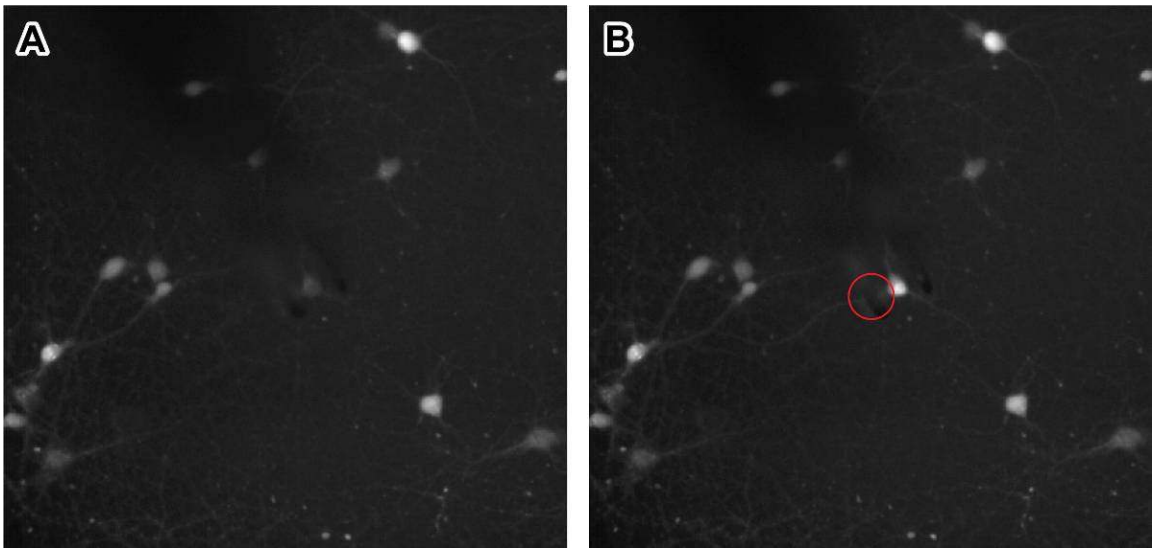


**Figure 5.19**: The positioning of the tweezer both laterally and vertically was critical to ensuring a successful mechanical insult. Vertical positioning was most difficult given that only the focal plane could be used as a reference. In this scenario, as the tweezer is being positioned around a target neuron, it was accidentally lowered too far, causing it to strike a neuronal process of the very cell to be injured. This failure to position correctly resulted in a pass of the trial, and no collection of data, as the cell is no longer in an undisturbed state prior to induction of the prescribed mechanical insult.

# CHAPTER 6
# CONCLUSIONS AND FUTURE DIRECTIONS

## 6.1 - Conclusions

The development of novel models to elucidate the cellular and biomechanical events occurring during traumatic brain injury (TBI) is critical to the identification of reliable targets for therapy. These models provide the means to more quickly test a wider range of inputs, perturbations, and potential therapies in a physiological or pathophysiological system. Although we are focusing on using this microtweezer system, and future system iterations, to examine acute changes after TBI, the technology and techniques developed here may also be useful for examining injuries to different types of structures, such as neuronal processes. We expect that the results of this work will enable a range of cellular interfacing, cellular injury experiments, and bio-mechanical analysis previously not possible.

While the selection of the mechanical actuation mechanism limited the complexity in modeling, fabrication, and integration into biological environments, the increased design time on the packaging implementation and the mitigation of stiction during actuation presented multifaceted challenges. Ultimately, due to this mechanical actuation, and the resolution of the microtweezer tip closure is reliant on increasingly smoother surface interfaces between components sliding across one another. However, the final microfabrication processes developed for the microtweezer and box components of the MEMS microtweezer were repeatable, high-yield, and provided high-resolution features with aspect ratios of nearly 20:1. Additionally, the mechanical performance was

consistent, and repeatable, and permitted the induction of high resolution strain injuries onto neuron cell bodies.

### 6.1.1 - Fabrication

Based on the directed application, the established fabrication protocols can be easily repeated to make tweezers with new planar geometries or tip shapes, or even modified to accommodate non-planar geometric changes and use of alternative materials.

Given the complexity in constructing, assembling, and interfacing the microscale MEMS components with a functional interface, the incorporation of modularity in the system was paramount for both process refinement and packaging. Even though the microfabrication process refinement was iterative, the separation of the microtweezer body/beam/tips and box was critical to increasing the speed of process refinement and eventually, the development of a viable prototype that could be mechanically characterized. Despite the accessory technologies and resources required for post-fabrication MEMS assembly, and the need to iteratively refine a second process, the additional benefits of increase in yield, simplification in fabrication (e.g. reduced alignment steps), and flexibility in geometries and materials provided ample justification.

Prior to the use of the multi-layer microtweezer fabrication process, the increase in the aspect ratio for the photoresist mold to accommodate the higher silicon box channel forced a reduction in the feature resolution of the tweezer tips. For the fabrication of future microtweezer tips, a scheme that employed the multi-layer strategy would be effective in tightly controlling the tip geometries.

### 6.1.2 - Packaging and Controller

Based on the inherent modularity in the interfaces between the packaging, controller, and actuator components, any refinement or alterations in the actuation mechanism or control (e.g. a higher resolution, faster actuation speed) should require minimal developmental time. There are few constrained dimensions to the system, but if necessary, an additional coupling component can be inserted that can confer dimensional shift, mechanical advantage, or rotational or translational isolation and buffering.

The internalization and compartmentalization of moving components lowered the tool's susceptibility to damage and unintended external input.

### 6.1.3 - Tweezer Tip Modeling, Mechanics, and Characterization

The linearity of the relationship between box actuation and tip closure (closing rate consistency) was important to ensuring consistent strain rate during injury. Based on the geometric modeling data for the two main tweezer types examined in Chapter 4, it appears that the tip closing during the regular drive range was more linear than the closure that took place during the over drive range.

The need to use the over-drive range to completely close the tips was necessary for many of the microtweezer designs with wider tip separations. The tweezer beam and/or box channel design could, however, be compensated to preclude the need for over-drive actuation. This would require an increase in the length of the tweezer beams or a narrowing of the drive contacts in the box channel. Excessive increase in the tweezer beams length could lead to vertical deflection or sag caused by gravitational forces. Speed-dependent hysteresis in the tweezer tip location over a close-open cycle, which was observed in the mechanical characterization, could also be amplified by increased tweezer beam length. Alternatively, narrowing the width of the drive contacts in the

channel would affect the closing rate of the tweezer tips, which could reduce the overall actuation resolution of the system.

In subsequent designs, the over-drive section of the box channel and/or the tweezer beam could be patterned with a curved geometry. This curve could compensate for any non-linearity expected in the relationship between the box actuation and the tip closure, but ultimately allows for specific control of the speed and overall regimen of the closing. Both the beam and channel geometries could also be tailored to each other to linearize the actuation-tip closure relationship and ensure constant closing rate.

The cycle testing showed that while performance was consistent and repeatable, there was a slight degradation in the maximal force output over time. We can speculate that this reduction in the magnitude of force over cycling can result from: (1) plastic deformation of the nickel tweezer beam from its originally defined geometries; (2) material fatigue or wearing of the nickel beam at the beam-channel interface; and/or, (3) material fatigue or wearing of the silicon at the face of the box channel. Overall, a metal-ceramic mechanical interface for translational and rotational sliding parts has been used in MEMS mechanical devices due to tribological benefits [199, 200], and can be more attractive than purely ceramic-ceramic interfaces, which have limited flaw-tolerance, causing cracking, wear-based debris, and structural failure [201-205]. This Ni-Si interface, which couples a relatively pliable, compliant material with a mechanically rigid surface, can potentially provide longevity and fidelity in mechanical performance [199, 206]. However, the coefficient of static friction at this interface can actually reduce over progressive wear from polishing effects [199], and this polishing can potentially affect the geometries and translation of position/deflection at the microtweezer tips. This

material wear, combined with even just slight plastic deformations of the tweezer beam, which only rotates 2.65$^{o}$ at the shoulder over a tip closure of 320 μm, can be responsible for the change in force seen at the tips.

While the actuation characterization suggested that the motor had a speed limit after which real-time performance delayed, the speeds selected for this particular biological study were shown to be repeatable with a consistent acceleration, velocity, and force loading for both opening and closing. For other applications, and for faster speeds, however, the delay in tweezer movement responding to box actuation might limit the experimental study. Geometric changes could be incorporated into the tweezer to allow for faster response times, ultimately increasing the application space of the tweezer.

### 6.1.4 - Single-Cell Injury

The selection of the mechanical input criteria (e.g. strain, strain rate) for testing was critical to the refinement and subsequent use of the single-cell injury model. Based on the previously reported characterization papers for other novel neural injury devices [90, 99, 107], the need for this refinement was consistent with the development of other models.

To demonstrate success as a model, the literature suggests that in vitro models of TBI require consistency of tissue displacement across the sample, and from sample to sample. While the mechanical characterization of the device is necessary to demonstrate the capability to deliver the prescribed mechanical input, it does not prove that this mechanical input will be successfully translated to the tissue being examined. A variety of factors, such as adhesion (or lack of adhesion) between the device and the tissue, and the alignment between the direction of mechanical input and the boundary of the tissue,

are critical to ensuring fidelity of the model, and subsequently, the data provided by that model. Feedback helps to validate the functioning of the model. In this particular model, visual feedback is used. However, in the future, sensors that provide tactile/force feedback could be integrated into the tweezer to further ensure the performance.

## 6.2 - Future Directions

In the sections that follow, future directions for the fabrication of the microtweezer, mechanical characterization, and biological studies are outlined.

### 6.2.1 - Future Fabrication Directions

Future efforts may focus on the optimization of the performance of the MEMS component, the integration of sensors onto the tweezer substrate, the expansion of available tweezer materials or tweezer fabrication processes, or the scaling of the microtweezer geometries to allow positioning in different environments.

The tweezer-box interface could be geometrically or materially altered to reduce friction and improve the fluidity of the actuation. This may also increase the lifetime and consistency of each microtool. This could be accomplished with a variety of additional microfabrication processes, post fabrication treatments, or material coatings.

Sensor integration, including microelectrodes and strain gauges, could greatly enhance the functionality of the tweezer, and allow additional experimental protocols. Microelectrodes have already been patterned onto the tweezer tips, but a viable electrical packaging scheme would need to be determined (Figure 6.1-6.3).

The current microtweezer fabrication process is established for created metal-based microtweezers. To fabricate ceramic-based tweezers, alternative fabrication processes would have to be developed (Figure 6.4).

Alternative fabrication methods could be employed to reduce manufacturing time by using a molding process that would reduce the number of photoresist patterning steps (Figure 6.5).

The scaling down of the tweezer tips to a micron or smaller in size would allow the manipulation of sub-micron sized structures, and could facilitate an injury model that damages neuronal processes. To decrease the dimension of the tweezer tips, a wet etching protocol could be utilized to sharpen the tips so that they can be used to manipulate and interface with smaller structures, such as cellular processes like axons and dendrites (Figure 6.6). The tweezers could also be inserted inside SEM and AFM environments where characterization and manipulation of sub-micron sized objects could be performed (Figure 6.7).

6.2.1.1 - Microtweezer Surface Treatments

More extensive mechanical testing data might demonstrate a need for future changes in the surface material or texture of the microtweezer. Depending on the application and the type of sample being interfaced, the microtweezer surfaces might require post fabrication treatment to mitigate frictional forces, wear, stiction and other surface effects that arise at the micro-scale. Wet etch polishing, nanodot array patterning, and atomic layer deposition (ALD) coating could reduce surface energies and tailor surface roughness in the physical interfaces between the actuation surfaces (tool body and box). Such surface treatments can be incorporated into the box channel wall in order to

increase surface hydrophobicity and reduce adhesion and friction **[207]**. The channel wall will be treated to reduce ICP etching artifacts and irregularities. This can be accomplished utilizing process modifications such as etching of a thermally grown oxide **[208]**, wet chemical etching using KOH and IPA **[209]** or usage of plasma treatments **[210]**. Alternatively, a nickel nanodot array patterning can be utilized as a post-fabrication technique to achieve improved surface properties and reduce friction **[207, 211, 212]**. Stiction can be also overcome with atomic layer deposition (ALD) of stiction-release low surface energy reagents like diphenyl siloxane **[213]**, alkyl trichloro silane **[214]**, other self-assembled-monolayer (SAM) layers **[215]**, or process modifications like change in surface roughness of the device material **[216]**. Manufacturers like Cambridge Nanotech have commercially available ALD tools that can deposit various materials like insulating metal-nitrides and SAMs with high conformity and improved step coverage in high aspect ratio structures **[217, 218]** to suit a variety of applications. It is however estimated that these coatings will support the microtool/box assembly use for a limited number of experimental iterations, at which point replacement of the assembly becomes necessary.

6.2.1.2 - Microtweezers with Embedded Microelectrodes

A preliminary microtweezer microelectrode was fabricated with a single electrode in each tip (Figure 6.1). The augmentation of additional electrodes onto the tweezer tip might require the creation of a thicker tweezer beam. In the sections that follow, a fabrication scheme for this microtweezer with embedded microelectrodes is provided, along with a potential electrical packaging strategy.

*6.2.1.2.1 - Microtweezer Microelectrode Microfabrication*

The microtweezer microelectrode is fabricated by first depositing a thick electroplating seed layer made of Ti/Al (Figure 6.2-A). A thick negative PR layer is spun and patterned using UV exposure and development to create an electroplating mold (Figure 6.2-A). Nickel is electroplated to the top of the mold to form the tweezer platform (Figure 6.2-B). To pattern the microelectrodes, SU-8 2000 series is spun onto the wafer to form a thin film layer and then patterned using UV exposure and development to completely cover the top layer of the tweezer body and tips (Figure 6.2-C). A blanket layer of gold is evaporated, and a thin protective layer of positive PR is patterned to outline the conduction lines and contact sites onto the tweezers (Figure 6.2-D, E). The exposed gold is wet etched, and all exposed PR surfaces are stripped with a quick acetone bath (protective PR layer, electroplating mold) (Figure 6.2-F). A final layer of SU-8 is spun and patterned to insulate the conduction lines (Figure 6.2-G). The final tweezer bodies with embedded microelectrodes are lifted off from the wafer with an oxide etch, which removes the electroplating seed layer (Figure 6.2-H). One or more microelectrodes could be patterned on to each tweezer tip, allowing for bimodal electrode recording and microenvironment impedance measurements. Additional patterning of microelectrodes in the formation of an array could allow spatial resolution in electrical recording.

Because of the potentially uneven topography of the tweezer and mold surface following both electroplating and gold conduction line patterning, spinning and patterning of SU-8 could be non-uniform across the wafer. The adhesion of SU-8 layers to the nickel during excessive tool use could also be compromised which could result in delamination. Additionally, for longer term experiments with biological samples, an

alternative more biocompatible material such as parylene is preferred. A contingency approach to patterning the microelectrodes onto the nickel surface is to substitute the spinning, baking, exposure, and development processing of SU-8 to the uniform vapor-deposition and patterned-etching of parylene.

*6.2.1.2.2 - Microtweezer Microelectrode Packaging*

The current internal mechanical packaging scheme inside the luer needle can be continued for the microelectrode packaging. The electrical packaging, which would conduct signals from the microelectrode contact pads to a DIP socket, can be augmented on the outside of the luer needle and housing. The universal DIP socket allows for easy wire connection to filters, amplifiers and recording devices. The electrical package could consist of thin-film-polyimide-encased wires that conduct signals from the contact pads to a dual-inline-pin (DIP) socket attached to outside of the luer hub. The wires can be affixed with epoxy to the luer needle section that is posterior to the microtweezer body attachment, and exposed ends of the wires can adhere to the microelectrode contact pads with conductive epoxy. The other end of the wires could be soldered to the backside connections of the DIP socket (Figure 6.3).

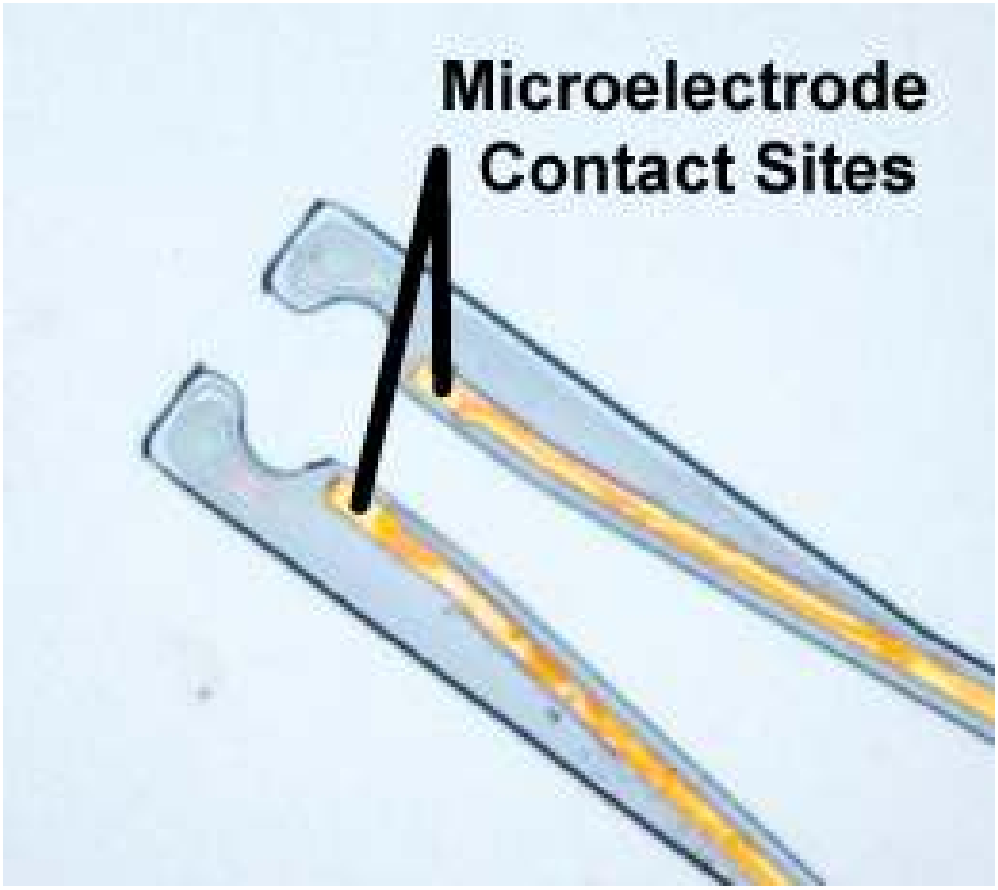


**Figure 6.1**: Bright-field image of microelectrodes embedded onto the tweezer substrate. Electrodes are electrically isolated by SU-8, and are composed of thin-film gold that was evaporated and patterned.

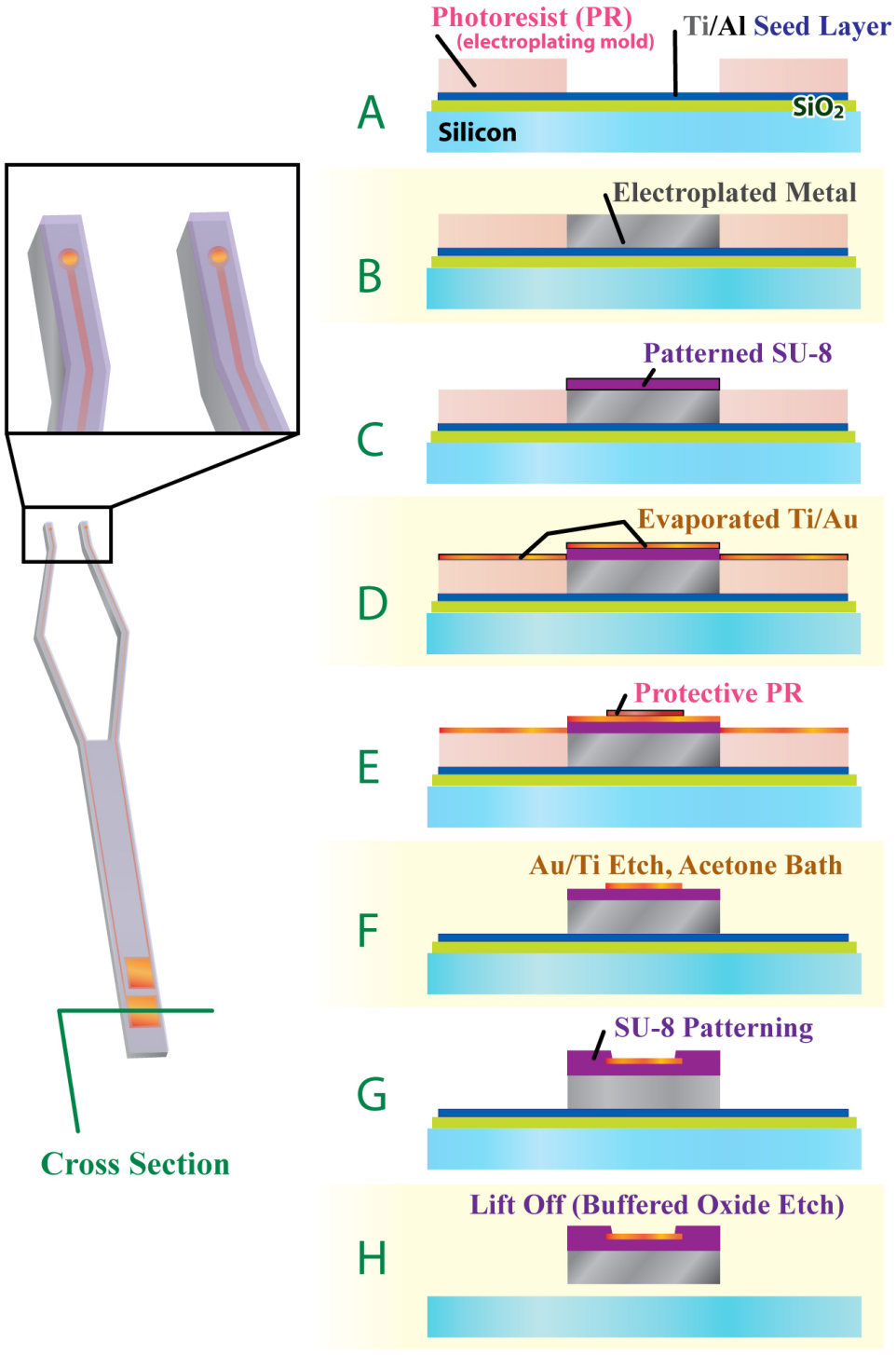


**Figure 6.2**: Fabrication processes for construction of a microtweezer with embedded electrodes.

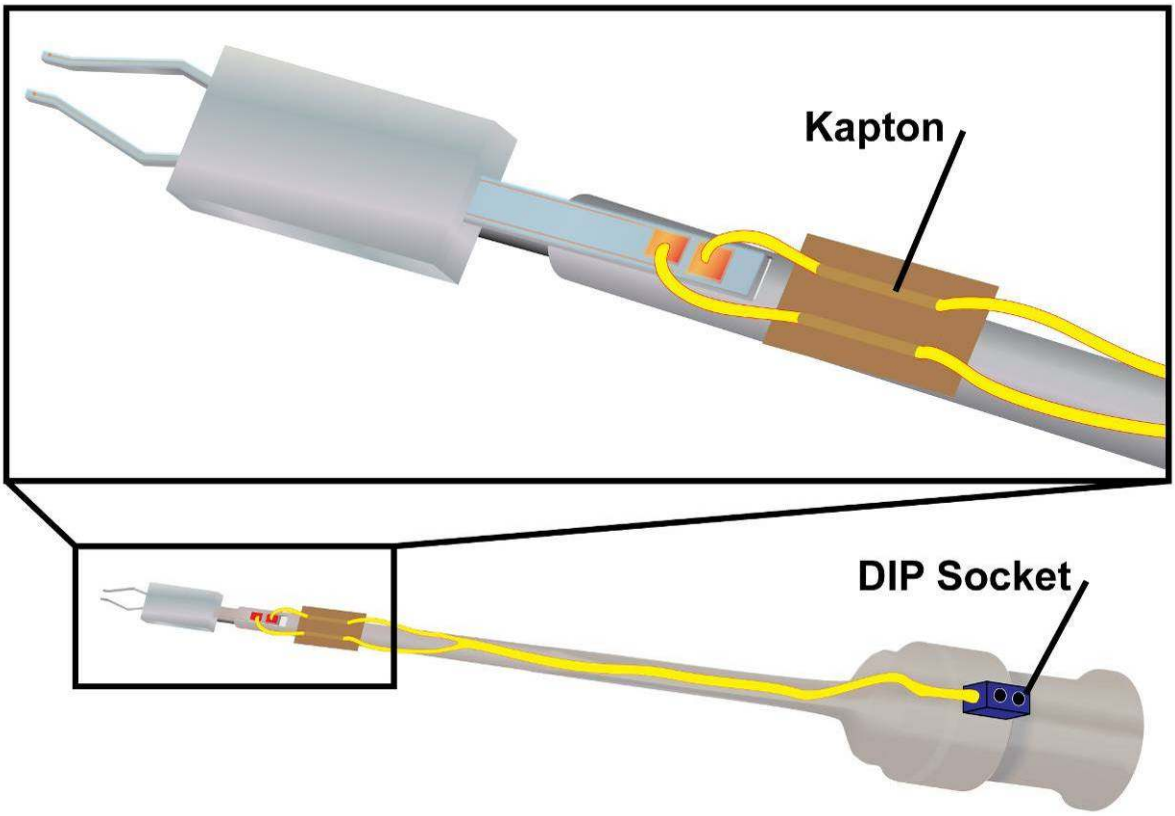


**Figure 6.3**: Proposed packaging scheme for microtweezers with embedded microelectrodes. This scheme would translate to packaging for alternative sensors.

6.2.1.3 - Ceramic-Based Microtweezers

Depending on the range of deflection required for the specific application, ceramic materials could be used as the substrate for the microtweezer. For construction, a Silicon-on-Insulator (SOI) process is envisioned, where the top layer of silicon will be patterned into the tweezer. An SOI wafer with specified top silicon and silicon dioxide layer thicknesses, handle layer, and buried oxide thicknesses can be purchased off the shelf. The tweezer beam and body could be etched using a multi-step ICP process on the top layer silicon of the SOI wafer (Figure 6.4-A-D). A layer of plasma enhanced chemical vapor deposition (PECVD) silicon dioxide can then be deposited (Figure 6.4-E), patterned, and etched (Figure 6.4-F-H) to expose the crystalline silicon at the tweezer tips. The geometry and crystalline planes of this volume of silicon could be carefully designed in order to achieve nanoscale sharpness in the subsequent etch process. Further, this could be accomplished in a batch fabrication approach utilizing an anisotropic etch step with potassium hydroxide (KOH). Atomic scale sharpness is achieved due to the fact that during the etching, the process comes to a complete halt when the (111) plane is exposed due to substantially lower etch rate of this plane compared to fast etching planes around it (Figure 6.4-I) [65]. The tweezers are released in the final step from the SOI wafer using a wet etch of silicon dioxide (Figure 6.4-J).

For future applications and large scale production, it is of interest to expand the scope of materials beyond silicon, particularly for specific applications where silicon may not be the material of choice [219]. This could be application driven (e.g. biomedical applications) or mechanical strength driven (silicon's Young's modulus 125 GPa, [220]).

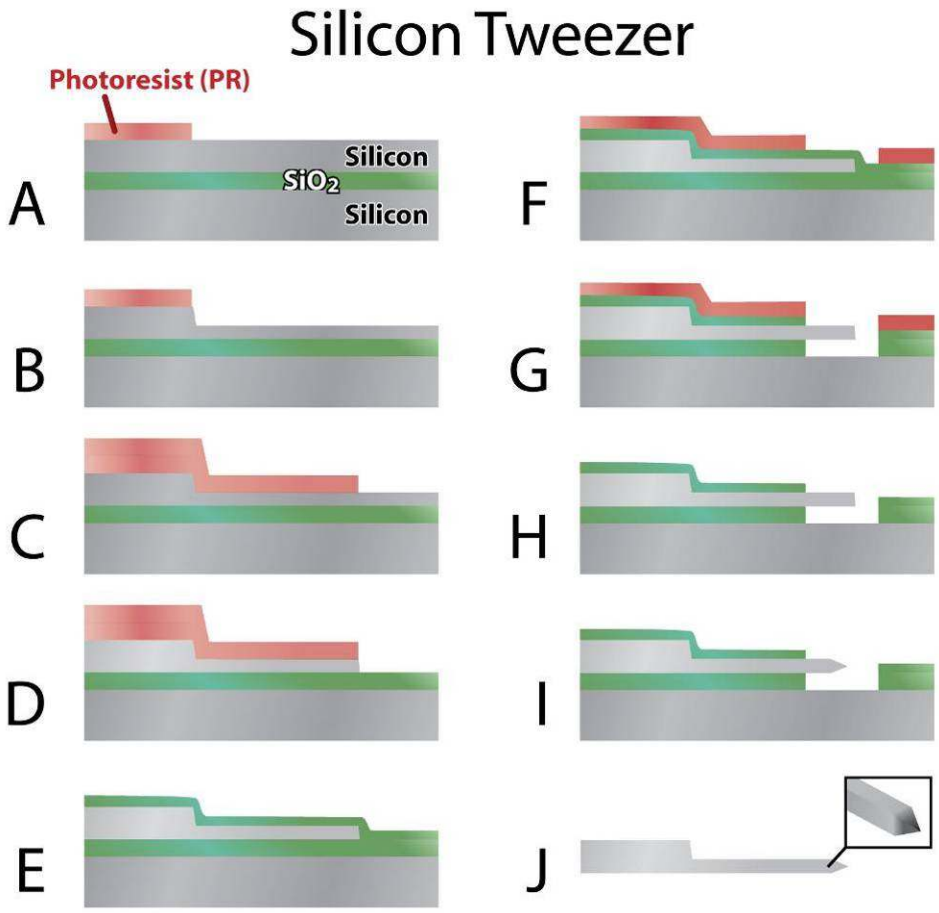


**Figure 6.4**: Proposed fabrication scheme for silicon based microtweezers. This process flow would require a silicon-on-insulator (SOI) wafer substrate and ICP and wet etching.

6.2.1.4 - Nanotweezer Fabrication using Nano-Imprinting

Nanoimprint lithography is a low cost, high throughput, non-conventional lithographic technique that enables creation of sub 100 nm structures in a large area batch fabrication compatible format [221]. This technique is promising for overcoming resolution issues of repeated photolithography beyond a certain size. The process involves two basic steps – creation of a nanomaster stamp (which resembles the final device) that is pressed on an imprint-compatible resist to create the opposite structure on the mold. A variety of processes can follow this step (example electrodeposition of metal) to create the final structure. The fabrication of nanotweezers using this technique is briefly described below (Figure 6.5).

The silicon tweezers that described previously have a dual application – they not only can be used as tweezers themselves but they can also be used as master stamp structures in nanoimprint lithography [222]. The tweezers master stamp is imprinted on a silicon wafer that is processed along current microtool fabrication technologies [136, 139] in combination with preparation for nanoimprinting. Additionally, a reverse master of the silicon nanotweezers could be used to pattern a nanoimprint mold (Figure 6.5). The advantages of this technique include: (1) integration of a variety of materials (for instance Rhodium tips for RF probing) in nanotweezer fabrication; and, (2) low cost batch fabrication of non-silicon material set. Electroplating metals with nano-scale features in electroplating molds can be challenging due to grain size of the electroplated structure, but this can be overcome with a selective etch strategy that also serves as a technique to sharpen current nickel-based microtweezer tips [136, 139]. A mechanical controller (similar to the one described in Chapter 3) can be developed for z-scale

movement of a wafer containing nanotweezers. This is controlled to be lowered into a wet etch solution that can isotropically etch a certain volume of metal for sharpening. This will polish the edge of the nanotweezer and, with optimization of the process, would produce sharper tips than what can be achieved utilizing electroplating. The technique used in this process is simpler version of the established process of electropolishing of microneedle tip geometries to achieve sharper tips for insertion into the skin [223].

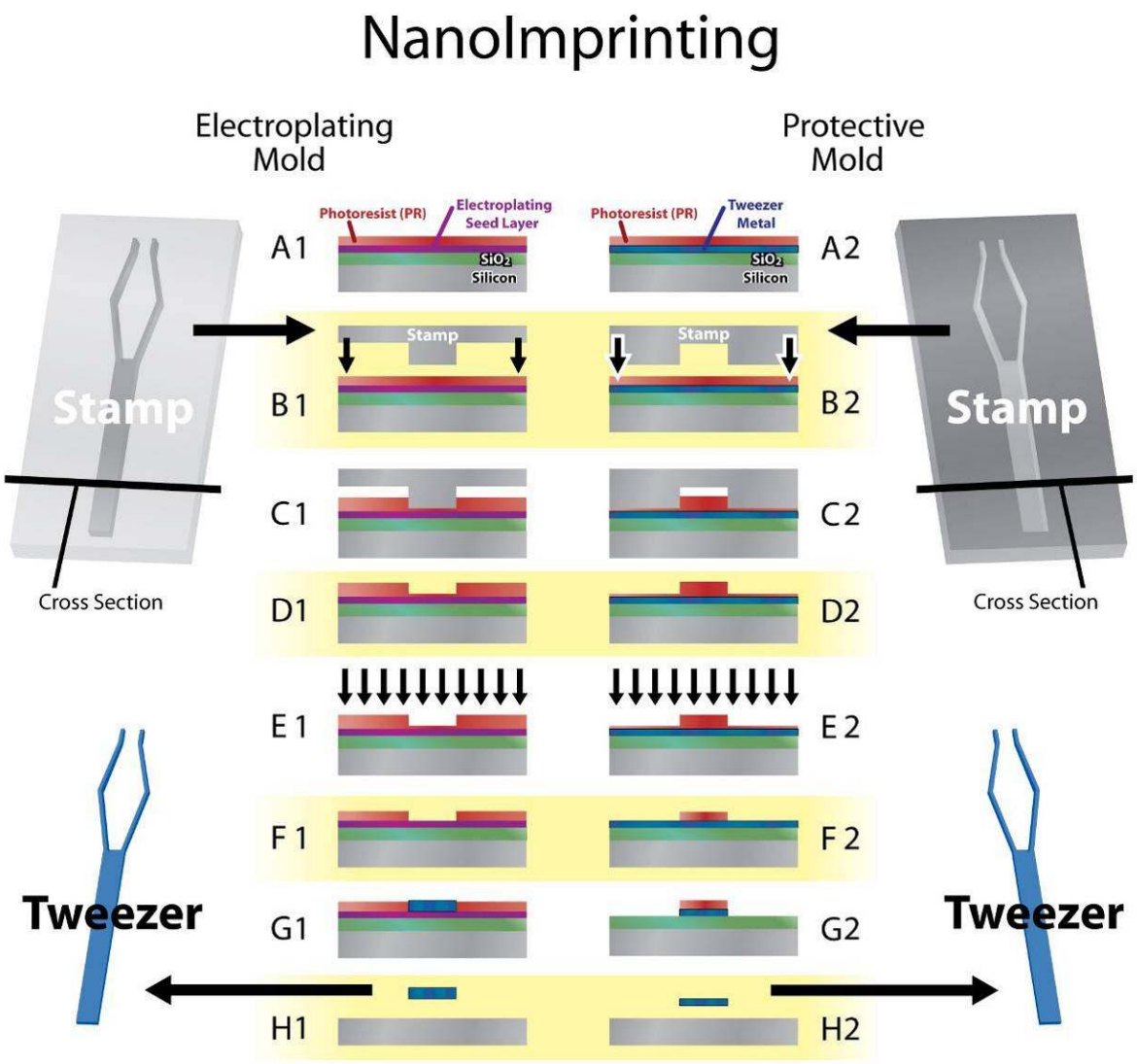


**Figure 6.5**: Proposed fabrication scheme for using nanoimprinting methods to mass-fabricate tweezers. Two methods are proposed, one that creates an electroplating mold which can be used to create metal tweezers, and one that creates a patterned protective layer for wet etching that can be used to make tweezers out of a variety of materials.

6.2.1.5 - Microtweezer Scaling (NanoTweezer) and Integration into SEM

*6.2.1.5.1 - Microtweezer Scaling*

To scale the tweezer to the sub-micron size, the device surfaces will require post fabrication treatment to mitigate frictional forces, wear, stiction and other surface effects that arise at the nano-scale. Wet etch polishing (Figure 6.6), nanodot array patterning, and atomic layer deposition (ALD) coating could reduce surface energies and tailor surface roughness not only in the physical interfaces between the actuation surfaces, but the tool tips as well where stiction release becomes increasingly challenging [217]. Such surface treatments are required for both the box channel and the tool tip in order to increase surface hydrophobicity and reduce adhesion and friction [207].

*6.2.1.5.2 - Integration into SEM*

Integration of the developed mechanical controller into a SEM mounting stage could provide a additional metrology functionality for the MEMS and microfabrication industry. To accomplish this, an experimental mounting stage adapter could be constructed utilizing a single linear actuator similar the automated control system. This could provide the ability to advance the tweezer to the SEM sample floor for interfacing with a micron and sub-micron scale objects (Figure 6.7). Such integration with high resolution SEMs has been previously performed by Kleindiek Nanotechnik and Klocke Nanotechnik. Integration into the staging setups of the SEM will entail modification of the standard stage design to accommodate for the imaging tool in question. This process of integration would likely involve a collaborative effort between the developer and the commercial vendors of these tools, such as Zeiss, Veeco Instruments, or Agilent.

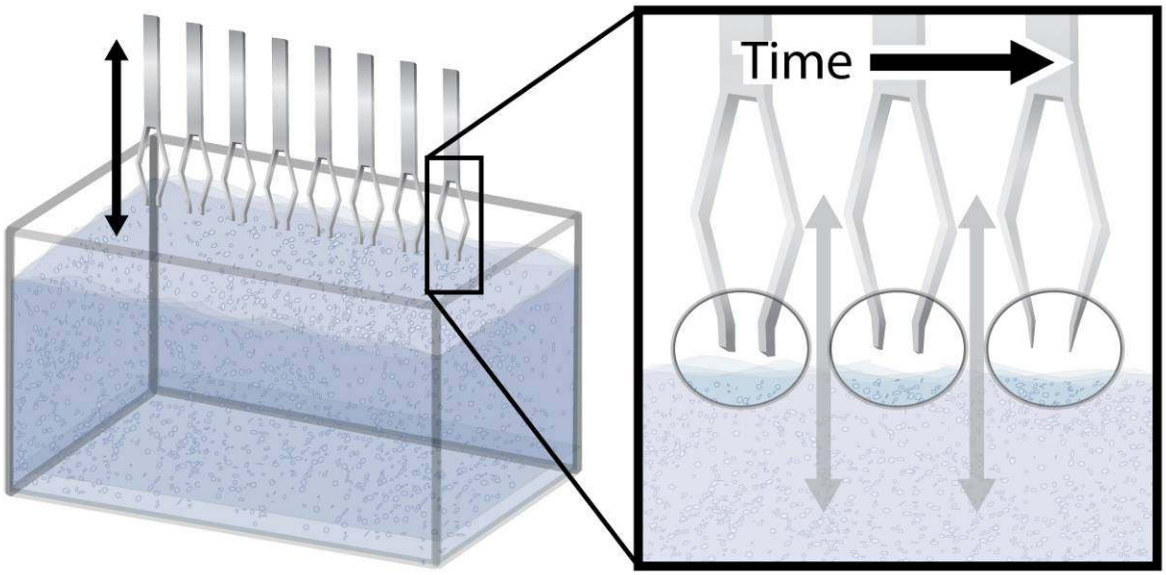


**Figure 6.6**: Wet etching procedure to sharpen the tweezer tips to allow for manipulation of smaller objects.

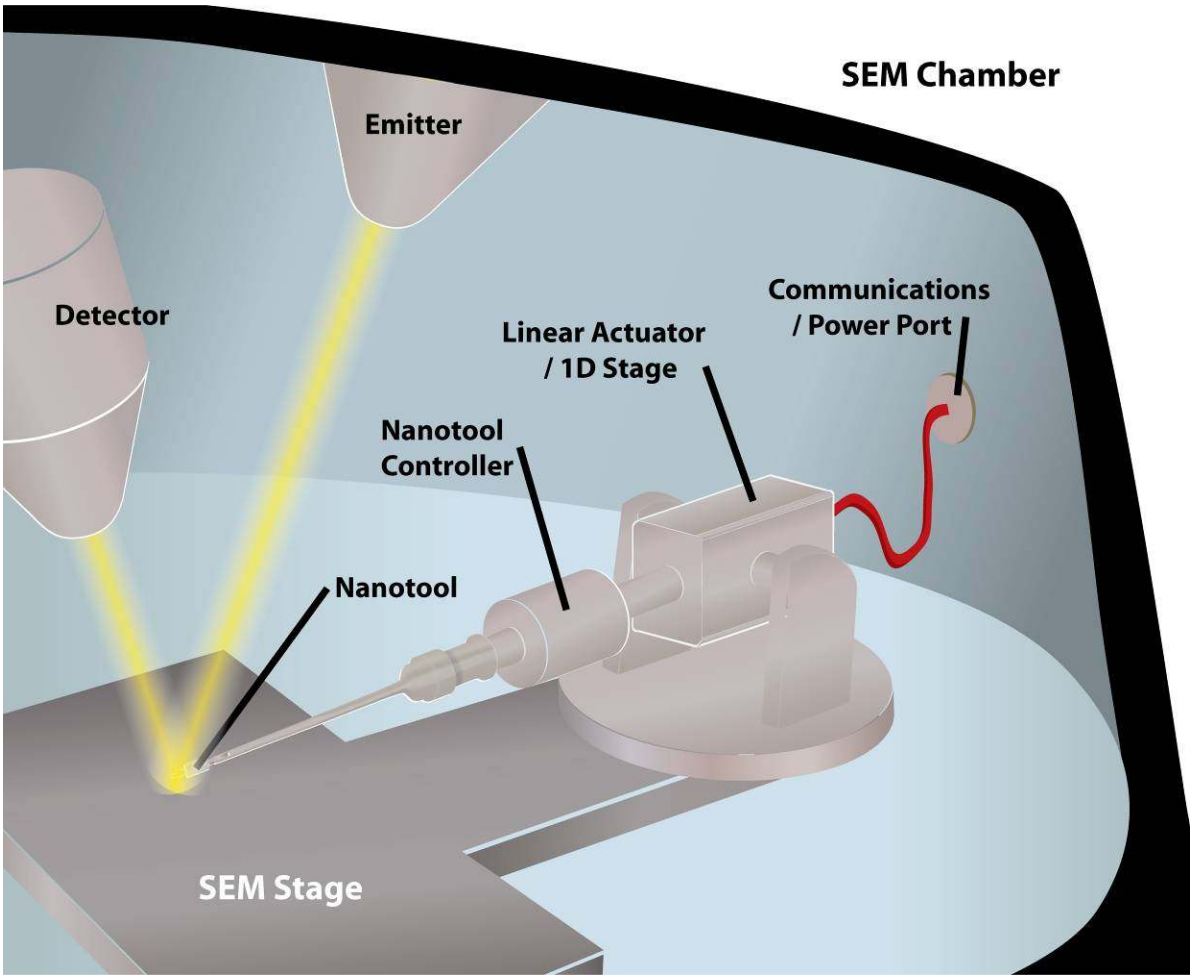


**Figure 6.7**: Integration of the microtweezer into a SEM chamber.

### 6.2.2 - Future Mechanical Analysis Directions

#### 6.2.2.1 - Geometric and Force Modeling

##### *6.2.2.1.1 - Geometric Modeling Software*

While the current modeling software program can take in a series of geometric parameters and predict the actuation paradigm and closing speed, it could also be used to predict tweezer tip geometric and elastic behavior, frictional forces, and tolerance analysis over the desired actuation ranges. Currently, these models are implemented manually using Eulerian solving methods, and incorporation into the code of the modeling software would be trivia.

##### *6.2.2.1.2 - Modeling Using Dynamics*

Based on the force measurements taken during the speed analysis, it is clear that at faster closure rates, the tweezer movement can no longer be modeled using semi-static geometric equations. Calculations that take into account the dynamic affects of closure could be used to create new tweezer designs that can perform more consistently at higher speeds. Additionally, these dynamics could be incorporated into the modeling software.

#### 6.2.2.2 - Mechanical Characterization

While a variety of force testing regimens (endurance cycle testing, speed analysis, etc.) were employed to test the performance of the microtweezer, additional cycle testing that collects longer-term data (10,000 cycles), and recording of force deflections for additional speeds around the speed used for injury would be useful.

The source of the reduction in the maximal tip loading force from cycling could also be examined to provide a target for improved tool longevity. A variety of metrology techniques (microscopy, SEM, AFM, etc.) could be employed to look for wearing of the materials at the box channel – tweezer beam interface. Any change in the geometry of the tweezer beam could be examined as well to determine if plastic deformation is playing a role in the reduction in tip loading.

Material property measurement of the microtweezer under different electroplating protocols might be useful in optimization of the microtweezer construction process.

6.2.2.3 - Real-time Force Measurement and Feedback

The incorporation of microelectrodes into the tips of the microtweezers demonstrates the fidelity in incorporating other kinds of sensors, such as strain gauges and force transducers. These elements could be introduced into specific regions of the beam to provided real-time feedback data that could allow for position assessment and force measurement during microtweezer use.

Each of these sensors could be calibrated using either visual assessment or from actual force measurement at the tip. Visual assessment is possible due to the development and verification of the double-moment arm model used to predict the forces seen at the inner tweezer tip. Visually measured deflections could be correlated to these real-time measurements to provide a discrete or function-based relationship reference. Force measurements of the tips caused by deflection during actuation could then be used to validate these relationships.

The electrical packaging of these calibrated force and strain sensors could be inputted to a computer through a serial connection, and the measured real-time data could

be inputted into the software that was used to control the tweezer. Such a setup could provide for an actuation system with closed-loop control, allowing the delivery of prescribed forces in addition to strains.

### 6.2.3 - Future Cell Culture and Injury Directions

#### 6.2.3.1 - Intracellular Calcium Identification

##### *6.2.3.1.1 - Calcium Source Identification*

The source of intracellular calcium rise during injury was not identified with this single-cell injury study. These sources include the extracellular space and the various buffered intracellular sources like the mitochondria. To indentify the impact of the various available calcium sources on the role of intracellular calcium rise, these sources could be controlled during injury.

Calcium chelators, which bind to the available calcium, could be added to the cellular medium to limit the ability of free calcium to bind to and activate Fluo-5F. Various calcium chelators such as EDTA (ethylenediaminetetraacetic acid) and EGTA (ethylene glycol tetraacetic acid) could be added in various concentrations to affect this extracellular source.

##### *6.2.3.1.2 - Calcium Channel Activation*

The method by which extracellular calcium enters the cell was not examined in this study. The timeline and level of gradient change would suggest that mechanoporation of the plasma membrane from injury provided entry points for calcium to pass into the cytoplasm. However, physiologic entry methods, such as calcium channels and pumps were not deactivated prior to injury, and the method of entry cannot

be completely attributed to holes being punched into the cell. A subsequent study where calcium channel blockers are added to suppress the channel activity could be used to ensure that the majority of calcium influx is from membrane permeability.

6.2.3.2 - Gene Expression Following Injury

*6.2.3.2.1 - Gene Expression Imaging Using Quantum Dots*

While the intracellular concentration of one particular ion was examined following mechanical insult, which is in the very acute period of neuronal injury, changes in the cellular behavior could be identified as well; some of which could be used as metrics to indentify levels of injury of even preludes to cell death. Quantum dots attached to genes associated with specific behaviors could be loaded into the culture to identify if gene expression is taking place. The quantum dot activation could be compared to various injury inputs to quantify thresholds.

*6.2.3.2.2 - Protein Expression Analysis Using Single-Cell PCR*

This injury model could be expanded to examine changes in protein expression following injury. An additional micromanipulator can be used to insert a patch clamp electrode into the culture medium to extract the intracellular material of the cell following injury. Multiple cells could be harvested to increase the source DNA prior to amplification. This output metric could be easily correlated with other *in vitro* and *in vivo* injury assessments of change in protein expression.

6.2.3.3 - Morphological Changes Following Injury

In addition to chemical and genetic changes in cellular activity, morphological changes in the cell structure can be identified by freeze-fracturing the cell culture. SEM

micrographs could then be collected of the plasma membrane and underlying structures of control and injured cells to identify specific structural and morphological changes.

6.2.3.4 - Injury of Neuronal Processes

With the proper geometric modifications to tweezer design, micropositioner and microscope staging, and actuation resolution, this system has the potential to induce prescribed mechanical loading on a variety of neuronal targets, including processes.

6.2.3.5 - Rotating Injury Chuck Stage

To increase the number of experiments per culture, and to improve the orientation and alignment of the microtweezer with each neuron, a rotational functionally incorporated into the injury chuck stage would be very beneficial. This could be motorized and controlled remotely so that mechanical artifact input by the user is minimized. An automated controller will also increase the rotational resolution.

# SUPPLEMENTAL CHAPTER 1

# FLEXIBLE ELECTRODE WORK

## S1.1 - Introduction

While electrical activity is the ultimate attribute of neuronal tissue, recording that activity has remained one of the key technical challenges in neuroscience. One aspect of this challenge is the mechanical mismatch between rigid electrodes and compliant brain tissue. Inflammation, tissue reactivity, and scar formation can occur around implanted electrodes from even normal physiologic micromotion of brain tissue, such as that resulting from breathing. In addition to the difficulty in sustaining stable chronic recordings in long term studies, rigid electrodes also cause additional accessory mechanical damage when used in the study of traumatic brain injury (TBI). Prior to this study, no recordings at the cellular level have been made during cortical impact and in the initial post-trauma period. Such information is important to understanding the secondary injury cascades that initiate during this period.

This analysis and correlation with tissue damage is central to this research. To this end, the initial goal of this research is to develop a recording system that can viably record before, during, and immediately following the large tissue deformations experienced during cortical impact. This recording system uses custom-developed, insertable flexible electrodes that are mechanically compatible with nervous tissue. The individual elements of this system follow iterative cycles of development and testing in an in vivo test bed for TBI. Following the refinement of electrode design, as well as the

electrode insertion and mounting methods used to mitigate mechanical artifacts, electrical activity in regions of the cortex will be examined during and following mechanical insult.

### S1.2 - Research Plan

The objective of this research was to develop a system that can electrically record in cortical and sub cortical structures before, during, and immediately following mechanical insult to determine if resulting changes in electrical activity are direct correlates to tissue damage. A prototypic electrode design was fabricated that can be stably inserted and incorporated into brain tissue, and used to successfully record electrophysiological function before, during, and immediately after a mechanical insult.

The overall approach had multiple iterative steps. The first iterative approach was to optimize electrode mechanical and electrical characteristics over several design and fabrication cycles. Following the selection of viable electrodes, insertion and recording performance was evaluated using a well-defined in vivo paradigm of injury with whisker stimulation/barrel cortex activity. Then, recordings were collected during injury.

### S1.3 - Background and Significance

Traumatic brain injury (TBI) affects 1.4 million people a year in the United States and despite the fact that 96% of people survive a TBI, the health and socioeconomic consequences can be grave, partially due to the fact that very few clinical treatments are available to reduce the damage and subsequent dysfunction following TBI [1]. Identification of critical events that occur in neuronal tissue during and acutely following a traumatic insult, as well as their relationship to cellular outcome, may lead to the development of improved protective systems and effective clinical therapies. However, direct electrical recordings of neuronal tissue at the cellular level in subcortical regions

during the impact and in the critical initial post-trauma period remain elusive due to limitations in recording technology. One important aspect of this technical challenge in is the mechanical mismatch between rigid insertable electrodes and compliant brain tissue [224, 225]. Alternative non-inserting electrode recordings, such as those by non-invasive electroencephalogram (EEG) offer some promise to elucidate large-scale neuronal activity. However, EEGs of mild and moderate post-TBI clinical subjects have not been found to provide useful diagnostic measures [226], possibly due to the lack of resolution and specificity. Although the technique has been used to monitor cortical network activity [227], embedded microelectrodes can provide superior spatial resolution and enable recording at deeper brain structures, such as the hippocampus, which is one region severely compromised by TBI [34, 42]. Initial changes in ion homeostasis and mass depolarization, which could be recorded with an in-dwelling electrode, may lead to altered cellular signaling and gene expression that result in deafferentation and delayed cell death [73, 77].

While some studies have evaluated important aspects of electrophysiological changes following mild and moderate in vitro TBI [24, 48], fewer have investigated this phenomenon in the in vivo environment [40]. Gross measures of electrophysiology post-injury with EEGs in animals have reported a depression of activity during the immediate time period after TBI, which often returns to normal after a few minutes [226]. Cortical network activity has also been monitored using similar techniques [227]. However, while some changes in neural activity following TBI are pervasive enough to be recorded by EEG, they may also be localized. Only by inserting an electrode that can ride-out the injury itself and record during the acute stages following TBI, can this activity be mapped

and correlated with ultimate outcome measures. However, TBI studies using a mechanical insult could displace brain tissue sufficiently to prevent the use of in-dwelling rigid electrodes. The mechanical mismatch between brain tissue and rigid electrodes, which is seven orders of magnitude difference in elastic modulus, is a pervasive concern with in vivo neural recording, as even normal movements and autonomic functions such as breathing and vascular pulsatility can cause micromotion at the interface of the brain tissue and electrode [228, 229]. The ensuing micromotion can initiate or exacerbate inflammation and scar formation, ultimately limiting electrode function [230]. In addition to the accessory damage caused to tissue surrounding the rigid electrode, the TBI would likely lead to substantial recording site migration and could even induce irrecoverable mechanical damage on the conduction lines of rigid electrodes, which would reduce recording efficacy. In-dwelling flexible electrodes offer a high degree of spatio-temporal resolution that can be used to track activity at multiple regions in the brain during injury. Flexible electrodes also overcome the mechanical limitations of rigid electrodes, as well as the spatial limitations of EEG without compromising the temporal dimension. Finite element analysis (FEA) has shown a significant reduction in the strain induced on tissue at the electrode tip in flexible versus rigid electrodes, as well as a reduction in mechanical failure from compression and deflection tests with surrogate tissue [229]. The results demonstrate a mechanical discrepancy with the silicon-based electrode, which is seven orders of magnitude stiffer than brain tissue (Young's modulus comparison [229]). Tissue strains in response to a 1 μN longitudinal force, estimated to be in the range of 0.01 to 0.10, were highest at the electrode tip [229]. In a separate finite element analysis, materials with a lower modulus (e.g., polyimide) caused less strain at

the tip, as expected [231]. Flexible structures have been shown to greatly reduce mechanical failure in compression and deflection tests with surrogate tissue (gelatin) as compared to rigid electrode designs [232]. These findings support the hypothesis that "softer" materials are advantageous for reducing strain induced on surrounding tissue.

### S1.3.1 - Development of Flexible Electrodes

As a result of the previously mentioned benefits, and technological advancements, there has been a recent surge in development of flexible electrodes for a variety of neural recording applications. Since their inception, flexible electrodes have been primarily composed of a single biocompatible polymer, such as polydimethylsiloxane (PDMS), polyimide, or parylene. Several groups have proposed various materials for flexible electrodes (e.g., [232-234]). Polyimide has been presented as a candidate material [232, 233], due to its compatibility with both microfabrication processing and with biological tissue. Parylene C has a comparable elastic modulus to polyimide and, moreover, it has superior flexibility and resistance to moisture absorption. While the elastic moduli of both materials are 2-3 orders of magnitude lower than that of metal and silicon electrodes, parylene has recently been favored for its ease of fabrication, superior resistance to moisture absorption, and reduced tensile strength. Given the relatively soft mechanical properties of parylene and other flexible polymers, previous designs of flexible electrodes have required the development of an assistive insertion method to introduce the electrode into brain tissue. A variety of technologies, including accessory and detachable rigid devices, polymeric coatings, and microfluidic channels have been employed to reduce the likelihood of insertion failure due to buckling [232, 234, 235]. Other methods use polymers as either an external coating or a microfluidic channel

filling. These assistive methods all require additional fabrication processes and surgical steps, which complicate their development and use.

However, predictive mathematical models can be used with high confidence to determine minimum electrode dimensions required to prevent the possibility of electrode buckling during insertion into brain tissue [233]. The forces required to buckle a column, which is highly dependent on the size of the smallest cross sectional dimension of the column, can be determined for a range of electrode designs. Maximal forces experienced during the insertion of rigid probes into rat brain tissue following removal of the dura mater have been determined for a variety of electrode shapes, point types, and cross sectional dimensions [236]. Forces of roughly 500-1000 μN are exerted onto pointed rigid electrodes upon insertion in rat brain. Considering these experimentally determined insertion forces, mathematically determined buckling forces of some proposed electrode designs predict that insertion into the brain tissue would require only fixation of the electrode shank column at certain lengths.

The microfabrication techniques used to create flexible electrodes permit the manipulation of application-based size and shape in order to achieve desirable mechanical characteristics, i.e., those which cause minimal damage both during insertion and mechanical insult in a clinically relevant rat model of traumatic brain injury. Electrical characteristics of flexible electrodes are also ideal to monitor electrophysiological activity continuously during injury studies. This provides a pre-injury baseline and a record of the electrophysiological response during the insult and the post-injury period.

The development of flexible electrodes to circumvent the challenges inherent in current electrical recording capabilities has important implications to the fields of neurotrauma and neurobiology. Although the focus of these electrodes is to examine acute changes after TBI, the techniques developed here may also be useful for long-term recording applications due to the reduction of chronic electrode-induced mechanical tissue damage.

**S1.3.2 - Traumatic Brain Injury**

The mechanical impact of TBI has been correlated to disruption of intra- and extracellular ionic homeostasis, neurotransmitter release, and concomitant massive depolarization [226]. Excitotoxic damage is initiated by the gross release of excitatory amino acids [23, 27]. Glucose levels and oxidative metabolism are depressed from ionic balance reestablishment and ischemia [16, 237]. These and other events contribute to the fragile post-trauma state. The initial recovery from mechanical insult creates a highly vulnerable cell population, leading to persistent biochemical and molecular effects that may cause cell death and sustained dysfunction [43, 238, 239]. These events will likely impact the electrophysiological function [11].

The electrophysiology of the hippocampus has particular clinical relevance because it is a region that suffers a disproportionate loss function after TBI (as early as 10 minutes following fluid percussion injury [76, 78]). In the hilar region of the hippocampal formation, induction of immediate early genes such as c-fos, c-jun, and junB have been reported within 5 minutes after fluid percussion injury. A transient loss of the microtubule-associated protein 2 (MAP-2) has been reported 5 minutes following a moderate cortical contusion injury in mice [26]. The trigger mechanisms that initiate

these early cellular responses in neurons have remained largely unexplored. In addition to acute phenomena, hippocampal damage has long-term implications, evidenced though problems with memory and learning [17, 240]. Studies using microelectrodes in anesthetized animals or slices have demonstrated impairment in long-term potentiation (LTP) during the hours to months following TBI [38, 241]. This is significant because the occurrence of LTP is associated with learning and memory formation [242]. Additionally, the hippocampus is also susceptible to seizures after TBI, although the mechanism is poorly understood [243]. The characteristic electrophysiology and regional response to injury has been shown to vary from the dorsal to ventral areas [47] as well as among the hippocampal subregions (CA1, CA3 and dentate gyrus [45, 243]. The cell-level electrophysiology in the immediate time period after TBI has not been investigated, but the literature does present information on the ionic and excitatory amino acid flux in the hippocampus in the seconds to minutes after TBI [23, 27]. The disruption in the homeostatic balance is expected to cause dramatic and immediate changes in the electrophysiology [11, 27]. Additionally, electrophysiological data might provide insight into the documented inhibition of LTP by monitoring changes in characteristic hippocampal signature waves [244]. Specifically sharp rhythmic waves [245], which may have an antagonistic relationship with LTP [242], and the signal propagation from the ventral to dorsal region [246] were noted.

### S1.4 - Methods

Mask designs and fabrication processes were developed for flexible electrode manufacturing. Several batches of electrodes were constructed varying the electrode

width and thickness, conduction line width and thickness, as well as parameters for fabrication processes which affected electrical and mechanical viability (Figure S1.1).

The fabricated flexible electrodes were then electrically tested by measuring the impedance over a physiological range of frequencies prior to, and following severe mechanical deformation. This mechanical and electrical assessment of the various electrode designs was used to make intelligent alterations in a subsequent design and fabrication iterations.

Following mechanical and electrical validation, a successful design was implanted into rat brain tissue and used to record somatosensory responses. Electrical data was then recorded prior to, during, and following injury to assess electrode performance and to ensure minimal electrode migration and/or electrode damage.

### S1.4.1 - Flexible Electrode Iterations

#### S1.4.1.1 - Prototype Flexible Electrode

The prototype, or 1st generation electrodes were designed and electrically validated both prior to and following mechanical deflections of the electrode shank. They have been successfully used to collect barrel cortex activity during and immediately following mechanical insult.

#### S1.4.1.2 - 2nd Generation Flexible Electrode

A 2nd generation recording system was designed and development of the electrode was initiated. These designs are displayed, although only preliminary mechanical testing was accomplished.

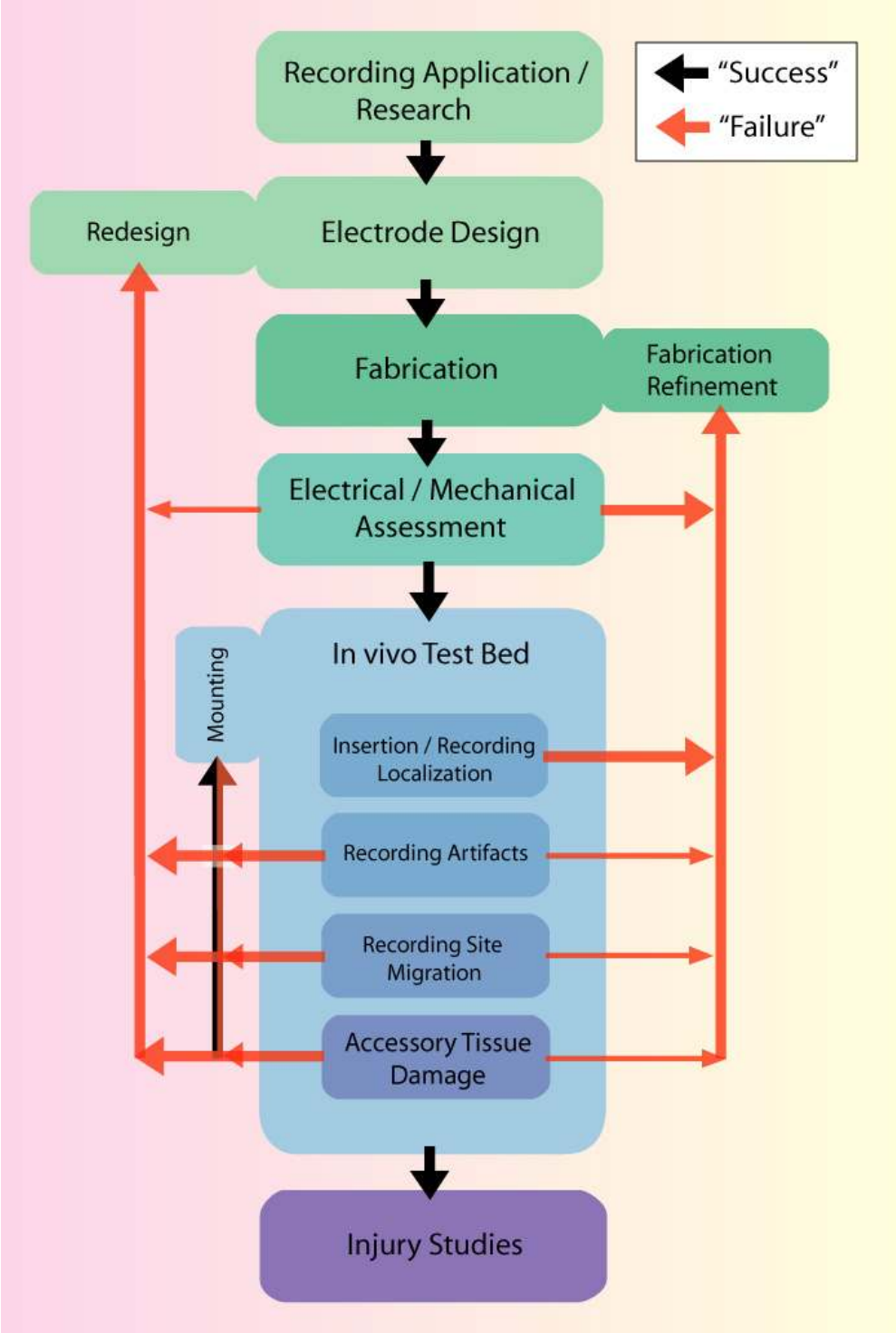


**Figure S1.1**: Flow chart explaining the iterative design cycle for the flexible electrode. Design is followed by characterization, and then either redesign or *in vivo* testing, after which substantive design changes are made.

### S1.4.2 - Flexible Electrode Design

Electrode dimensions are determined based on specific recording application. For recording in layer IV of the cortex an electrode shank minimum length of 700 μm and a contact site diameter of roughly 30-40 μm to record field potentials is required. Mathematically determined buckling forces provide minimal electrode thicknesses of 18-20 μm, and minimum electrode widths of 100 μm are dictated by the size, number, and orientation of the contact sites.

#### S1.4.2.1 - Prototype Flexible Electrode

The prototype flexible electrode shank containing a single 30μm or 40μm contact site was designed and fabricated (Figure S1.2). Although multiple shank arrays provide enhanced recording coverage, non-independently fixed multi-shank electrode arrays could potentially cause increased mechanical damage due to non-uniform tissue deformation during cortical injury across the length of the array, which limits the mechanical compliance of each shank with the tissue. The fabrication approach provides a platform that permits the addition of multiple contact sites, and ultimately allows for enhanced recording capabilities such as spike sorting. In addition, these techniques allow custom-based mechanical features (e.g., size and shape). The bead and barb features on the electrode act as a physical insertion depth control, and allow additional mechanical adherence to the dura mater to prevent electrode relocation during mechanical disturbances. Following insertion, a long portion of the flexible parylene shank extends beyond the dura, providing strain relief between the tissue and electrode packaging. Recording targets in the rat brain (e.g., cortex, 0-2 mm deep) determined the designed length of the embedded section of the electrode shank (Figure S1.2b-c).

Stereotactic attachment to the electrode bead during surgical insertion decreases the electrode column length, allowing the electrode to be introduced into the tissue by effectively increasing the buckling force threshold. Cross sectional electrode geometry was selected to provide sufficient tensile strength to achieve insertion, to minimize the tissue footprint, and to maximize mechanical compliance between the electrode and tissue [236]. The width (b) of the electrode shank, set to 100 μm, was dictated both by contact site diameter and minimum photolithography feature size. A conservative single fixed-point, single pinned-point column bucking equation model (S1.1, S1.2), which assumes perfect column conditions such as no initial curvature, was used to calculate the minimal cross sectional thickness (h) to prevent shank buckling during insertion into tissue.

$$P_{cr} = \frac{K \cdot \pi^2 \cdot E \cdot I}{L^2} \tag{S1.1}$$

$$I = \frac{1}{12} \cdot b \cdot h^3 \tag{S1.2}$$

where,

Pcr = buckling force threshold = 1000 μN

K = column effective length factor (one pinned end, one fixed end) = 2.045

E = elastic modulus = 3.778 GPa

I = area moment of inertia

L = unsupported column length

b = column width = 100 μm

h = column thickness (smallest cross sectional dimension)

Calculations using column lengths (bead to electrode tip) of 1 mm and 2.5 mm determined that insertion could be accomplished with minimum electrode thicknesses of

12 μm and 22 μm, respectively. A conservative thickness of 25 μm was selected for the prototype electrode. Because planar photolithography was selected as the fabrication method, electrode thicknesses can be easily adjusted without redesign of the electrode shape.

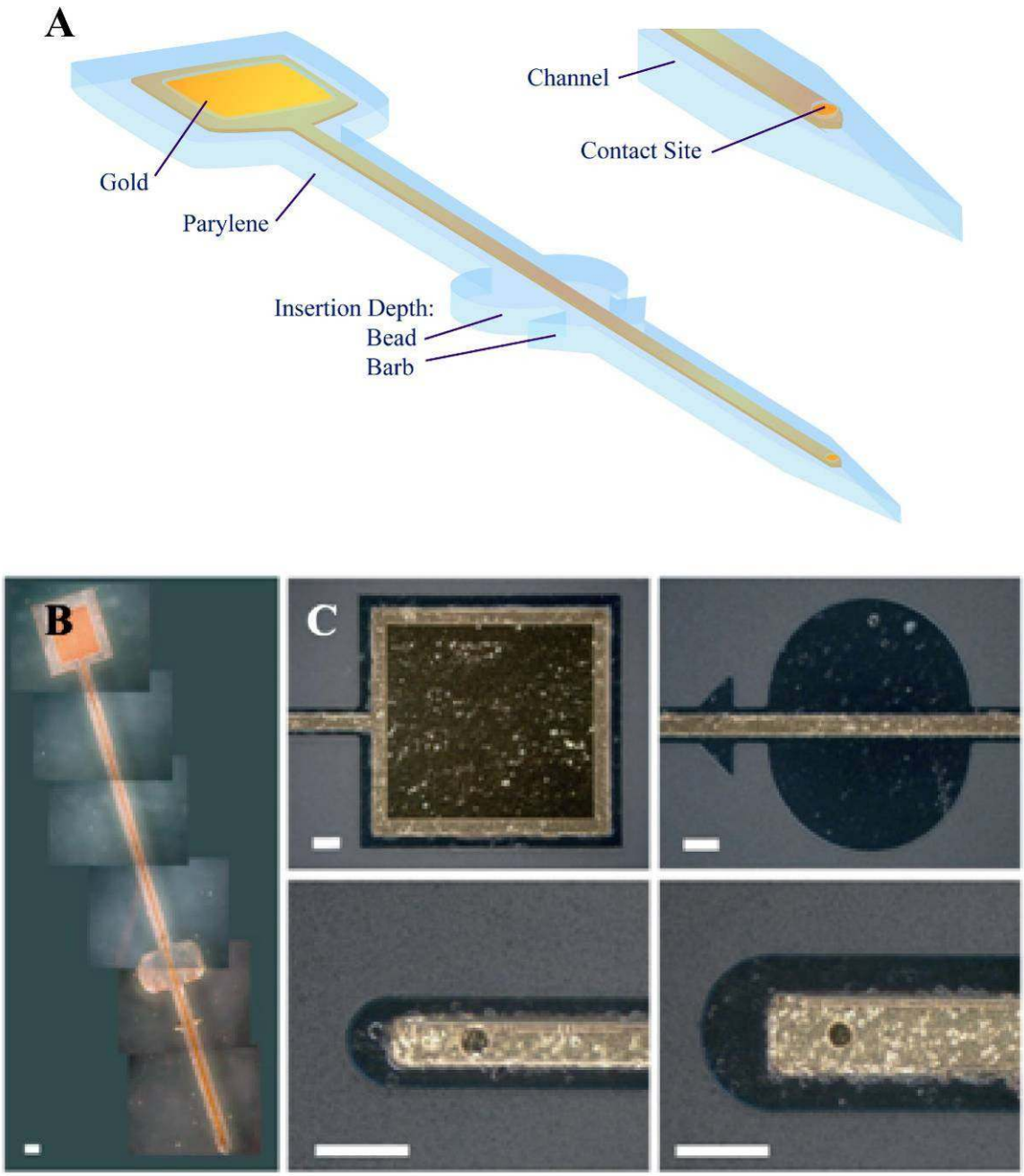


**Figure S1.2**: (A) Schematic of the flexible electrode prototype design showing the orientation of the gold leads (not-to-scale). Insertion depth control is accomplished using the fabricated bead and barb. (B) Montage of photomicrographs of a prototype flexible electrode with an insertion section of 0.5 cm past barb. (C) Dark-field images of various features of finalized flexible electrode, including exposed 1 mm x 1 mm Au contact pad for pin attachment, bead and barb structural features for controlled insertion depth, and Exposed Au contact sites for 100 μm and 200 μm wide electrodes. Contact sites are 40 μm in diameter, and all scale bars are 100 μm.

S1.4.2.2 - 2nd Generation Flexible Electrode

While the prototype, or 1st generation electrode design, could effectively record following a mechanical insult, there were some complications with the insertion of the electrode to a specified depth. The packaging system was mechanically restrictive, and the extraneous length of shank of the electrode between the barb and bead and the contact pad, where the DIP pin was adhered, is unnecessary to the electrode function. The electrode was stereotactically fixed, but the 1.5 cm long shank of the electrode made buckling of the electrode during insertion inevitable unless a secondary fixed end was induced on the shank closer to the insertion using teflon coated forceps. To alleviate this issue in the next generation of electrode design, the unidirectional shank from the barb and bead to the contact pad, or packaging, was removed entirely, and replaced with a coiled, floating parylene wire. This wire was then led to a floating contact pad where mechanically isolated packaging was installed. Insertion complications also resulted in lowered insertion depth control, which was a significant problem when locating recording targets at specified depths. To increase the fidelity in finding recording targets, three additional recording sites were added lengthwise along the shank, spaced 100 μm apart. This new design allows more possibilities for electrode insertion with micro-forceps or micro-tweezers (Figure S1.3, S1.15).

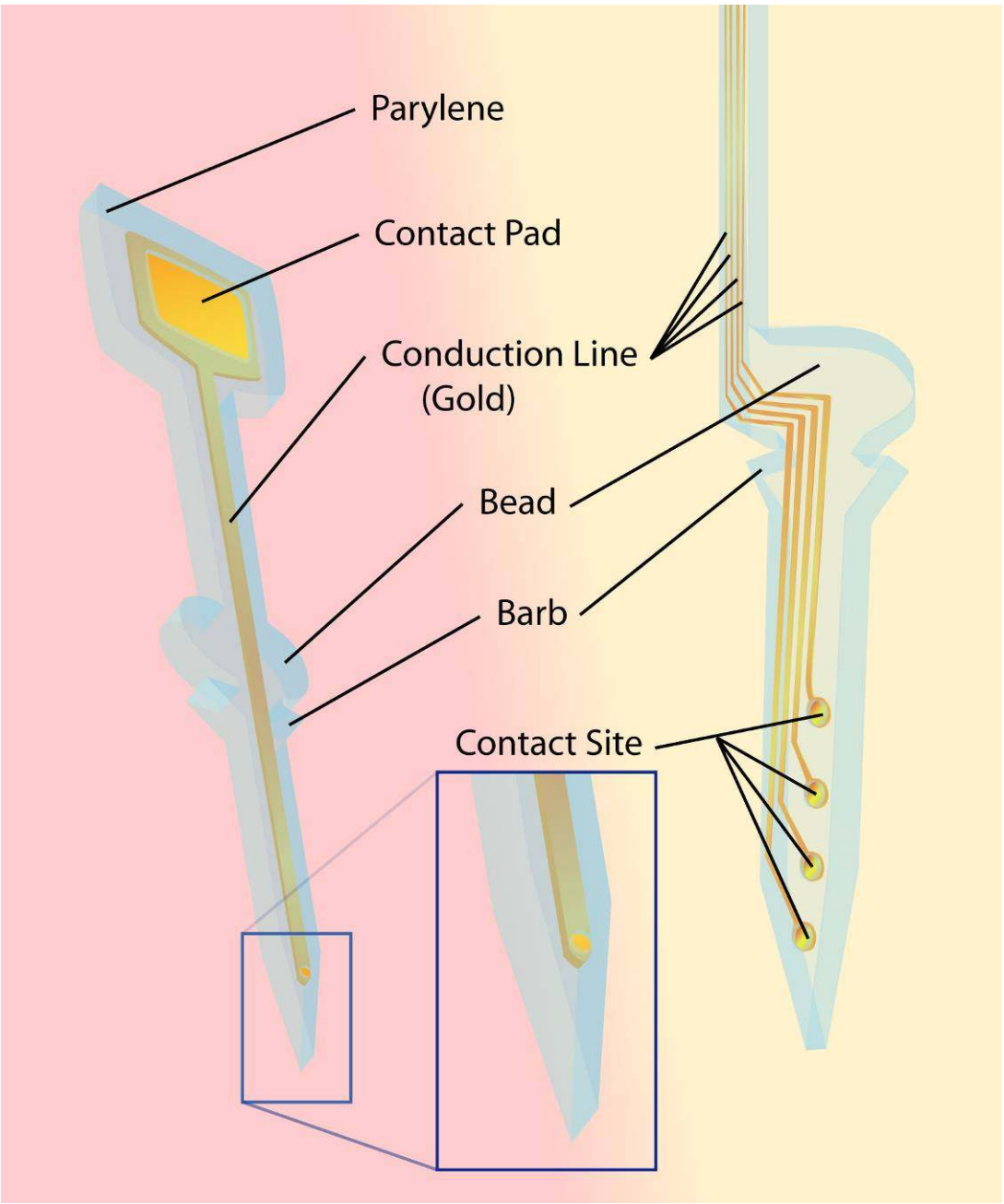


**Figure S1.3**: Flexible electrode schematic of 2nd generation flexible electrode design compared to prototype flexible electrode (not to scale). This shows the orientation of the four contact sites and gold leads. Insertion depth control is accomplished using the fabricated bead and barb. Stereotactically attached micro-tweezers and micro-forceps can be used to accurately insert the electrode.

Despite these significant changes in electrode shape, electrical capability, and mechanical isolation, photolithography for the 2nd generation electrodes was identical in processing steps, but refinement of photoresist exposure, pre- and post-baking, and development was necessary to define the smaller features. Gold patterning of the 10 µm-thick conduction lines was accomplished using the same processing. These conduction lines resided both within the electrode, as well as within the wire connecting the electrode to the contact pad and packaging (Figure S1.4).

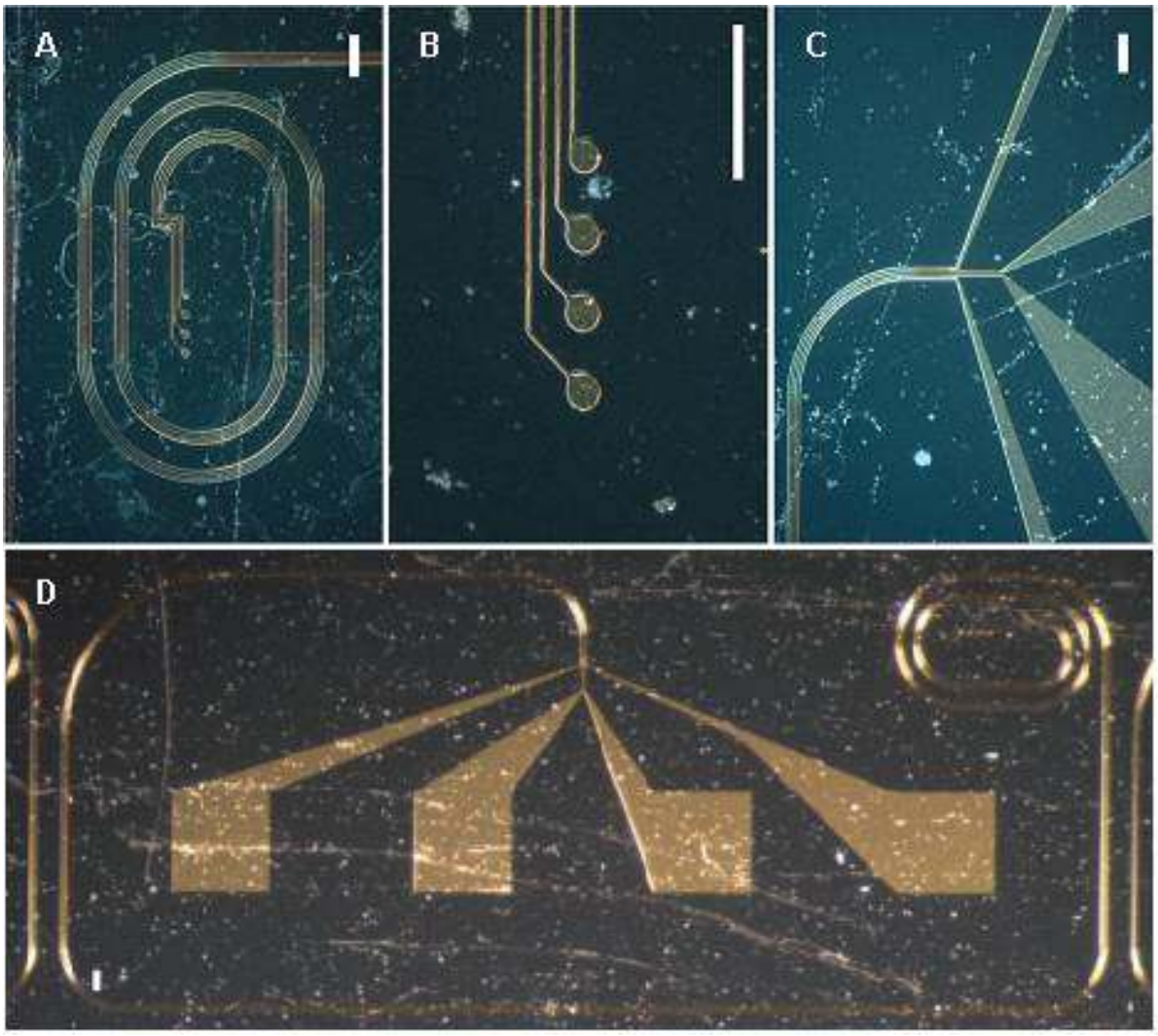


**Figure S1.4**: (A,B,C,D) Dark-field images of 2nd generation flexible electrode Au conduction lines. Gold contact sites are 40 μm in diameter and conduction lines are <10 μm in width. Coiling of conduction line wire begins directly above non-inserted region of electrode shank. All scale bars are 100 μm.

### S1.4.3 - Flexible Electrode Construction

S1.4.3.1 - Microfabrication

Photolithographic processing was used to outline and deposit the conduction leads and physical features of the electrode (Figure S1.5). A base layer of parylene was deposited onto polished soda ash glass using the Specialty Coating Systems Parylene Labcoater (Indianapolis, Indiana). A deposition of NR5-8000 photoresist was then patterned for the electrode conduction lines, and 0.5 μm of gold was deposited using the CVC E-Beam Evaporator (SC 5000; Fontana, California). An acetone wash for 3 hours resulted in lift-off processing of the NR5-8000 photoresist and definition of the conduction lines. Following a second deposition of parylene encasing the conduction lines, lift-off processing using NR9-8000 photoresist was used to pattern a protective layer of aluminum to outline the contact sites, pads, and exterior electrode shape. $O_2$ plasma processing with a Plasma Therm Reactive Ion Etcher (790 Series; Prosper, Texas) was used to remove unprotected parylene down to the substrate. The protective aluminum layer was removed with a wet etch and physical detachment of the electrode from the glass substrate was accomplished with Teflon forceps.

Each 4”x4” chrome mask contains patterns for 100+ electrodes. This allows several designs to be fabricated in one batch with a large number of copies, if needed. Due to the high level of successful fabrication with preliminary runs, sufficient numbers of electrodes will be available for all mechanical and electrical testing.

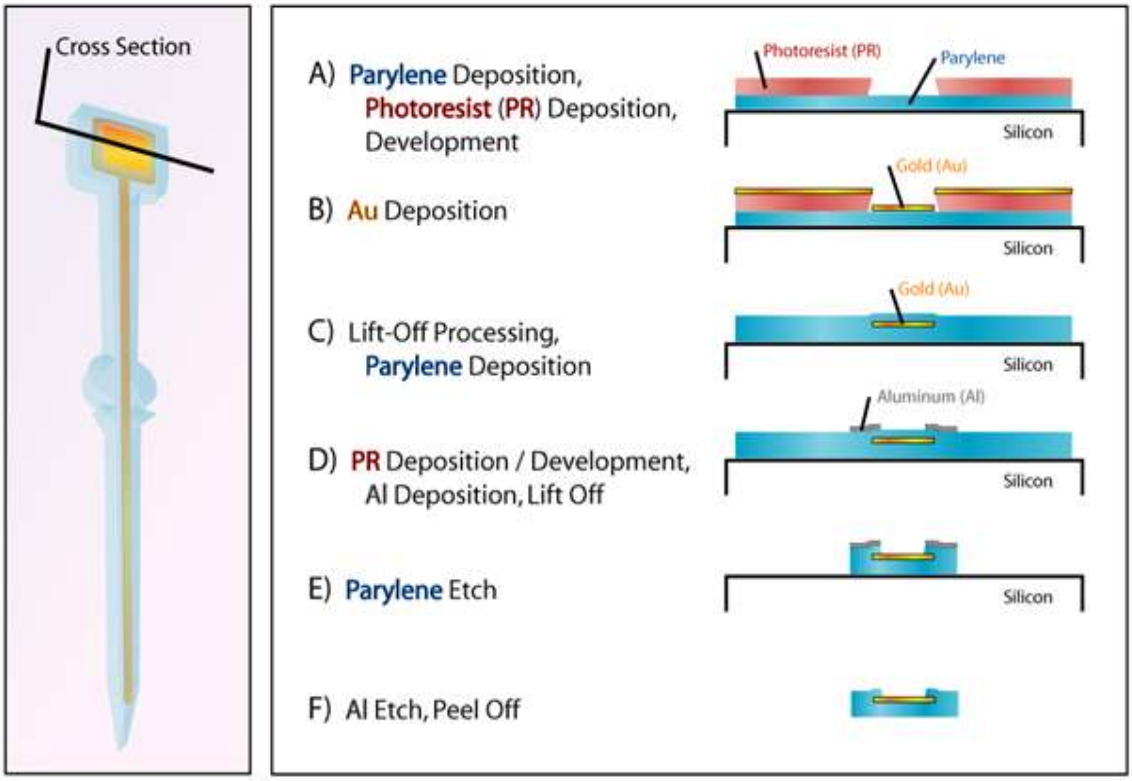


**Figure S1.5**: (A) Fabrication processes: 15 μm parylene deposited on glass substrate. AZ 4620 Positive photoresist is patterned for electrode lines. (B) Gold is vertically deposited using the CVC E-Beam Evaporator. (C) Acetone wash is used for lift-off processing to remove photoresist from the electrode surface. A top layer of parylene is deposited, embedding the gold lines. (D) Photoresist is patterned, and a protective aluminum layer is deposited. Lift-off processing with an acetone wash defines the electrode contact sites and electrode shape. (E) Unprotected parylene is etched with $O_2$ plasma using the Plasma Therm Reactive Ion Etcher. (F) Protective aluminum layer is wet etched, and mechanical separation releases the electrode from the substrate.

S1.4.3.2 - Electrode Packaging

Packaging of the electrode to allow connection to a Michigan Probe headstage (ADP/16o50-MICH; Ann Arbor, Michigan) was accomplished by attaching a dual inline package (DIP) pin to the electrode contact pad with silver conductive epoxy (Insulating Materials Inc.; New Haven, CT). Dow Corning Sylgard® was used to cover and electrically isolate the connection between the electrode and DIP pin. This packaging apparatus is adequate for the terminal acute recording studies of pre- and post-electrophysiology in the rat cortex because the rat is anesthetized and immobilized during the entire experiment.

**S1.4.4 - Mechanical Characterization**

Given the expected mechanical deformations of the brain tissue during a traumatic insult [247], mechanical integrity of any implanted probe is crucial. Mechanical properties of 25μm thick flexible prototype electrodes were assessed prior to electrical and in vivo evaluation.

S1.4.4.1 - Material Properties

Nano-indentation tests on 16 prototype electrodes were conducted with a MTS Nano-Indenter (XP; Oak Ridge, Tennessee) to determine the elastic modulus and tensile strength of each. These tests provided mechanical property data, and, when taken to failure, provided yield stress data. While electrode flexibility is essential for recording during and immediately following injury, the flexibility makes it inherently difficult to introduce the electrode into brain tissue.

S1.4.4.2 - Bucking Force

Mathematical modeling for the minimal electrode cross-sectional dimensions was therefore performed to ensure that the buckling force threshold exceeds the experimentally measured maximal force of 1000 μN placed on the electrode tip during insertion. Buckling force tests were then performed on five prototype electrodes fixed 2.5 mm from the tip of the electrode. Force loads on electrode tips were measured using the MTS NanoUTM (Oak Ridge, Tennessee) until both visual inspection and measured data confirmed electrode shank buckling.

### S1.4.5 - Electrical Characterization

Even though the flexible electrode is designed to be compliant, large displacements may result in deflection of the electrode, possibly separating the sequentially deposited electrically-insulating parylene layers. In addition, it is possible that the gold conduction lines will fracture, reducing or eliminating the electrical viability of the electrode. Electrical evaluation of polyimide electrodes following repeated mechanical deflections, as well as electrodes with an induced permanent $90^{o}$ bend, have been shown to result in minimal changes in electrical impedance material [233].

#### S1.4.5.1 - Impedance Testing

A $90^{o}$ bend test was performed (Figure S1.6), comparing the electrode impedance prior to and following the bend to demonstrate the mechanical reliability of the insulating parylene layers and structural integrity of the conduction lines. Measurements of the electrical impedance for the flexible electrodes (100 μm wide, 25 μm thick, n=7) over a frequency range of 100 Hz to 100 kHz were made using a Stanford Research SR785® two-channel dynamic signal analyzer. This was augmented by a custom-built, controlled switching board with known resistance that allowed for rapid, automated measurements

of the magnitude and phase of electrode impedances across a large range of frequencies. Impedance measurements were performed between the electrodes and ground using Hank's Balanced Salt Solution (HBSS) as the conducting medium.

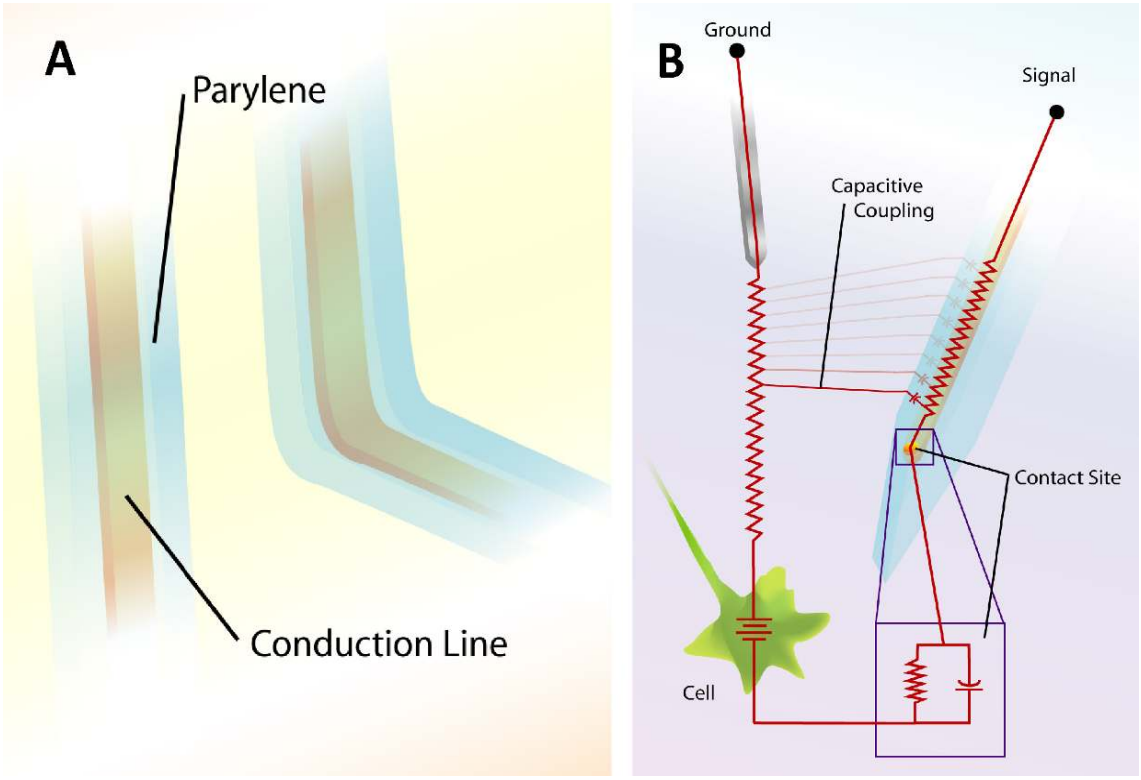


**Figure S1.6**: Schematics demonstrating the induction of a permanent bend in the electrode (A), as well as a simplification of the electrical circuit from the electrode to a ground wire (B).

**S1.4.6 - Surgical Methods**

As mentioned, this system would be developed using the iterative processes of electrode design and fabrication, followed by testing in an in vivo platform (rat). Following optimization using the in vivo test bed, the changes in electrical activity of cortical regions resulting from mechanical insult would be recorded and analyzed. This optimized recording system incorporated a custom-built flexible electrode and a specific insertion and mounting scheme, and could mitigate mechanical artifacts in recording as well as accessory mechanical damage to brain tissue.

System testing and recording viability assessment was performed using the whisker deflection paradigm prior to and following mechanical insult. In vivo optimization within the well-defined barrel cortex preparation permits rapid, consistent evaluation of electrode performance and required redesign. For example, accessory tissue damage may necessitate a change in electrode geometry to increase flexibility. Overall, the key interrelated issues that need to be overcome for success are: (1) development of stable insertion and mounting methods that minimize damage; and, (2) mechanical/electrical properties that ensure stable recordings.

An important problem with making electrodes flexible is that they may not insert into the desired region of the brain by simply pushing them into tissue. It was determined that the prototype electrode does insert into the brain when microsurgical forceps are used after a small slit is made in the dura mater. As design iterations to the electrode continue in order to reduce tissue damage and increase flexibility, accurate insertion of the flexible electrodes into desired cell fields (barrel cortex and potentially various hippocampal subregions) remains a necessary constraint. In addition, the need for stable

mounting to the skull or stereotactical frame while allowing the electrode to move with the tissue is imperative for reliable recording during the large deformations that occur during TBI and long-term studies. Complete optimization of the recording system would require in vivo testing of multiple designs of flexible electrodes and currently available alternative electrodes, as well as testing of multiple insertion and mounting schemes.

The in vivo testing platform of the recording system took place in the somatosensory barrel cortex of a rat prior to, during, and following mechanical insult. In vivo optimization within the well-defined barrel cortex preparation permits rapid, consistent evaluation of electrode performance (Figure S1.7). All procedures involving animals conformed to guidelines set forth in the Guide for the Care and Use of Laboratory Animals (U.S. Department of Health and Human Services, Pub no. 85-23, 1985) in accordance with the Georgia Tech Institutional Animal Care and Use Committee.

S1.4.6.1 - Surgical Preparation

Anesthetized adult male rats (Sprague Dawley, 300-350 g, n=159 in total) were mounted in a stereotactic frame and prepared for controlled cortical impact (CCI) or sham conditions. Animals were maintained narcotized with a rat cocktail (ketamine - 50 mg/kg / xylazine - 10 mg/kg / acepromazine - 1.67 mg/kg). An alternative anesthesia could be a combination of isoflurane and fentanyl (5-10 μg/kg) (induction at 3% isoflurane). Rats were immobilized with pancuronium bromide (1.6 mg/kg) and artificially respired using a positive pressure respirator. Vital signs were monitored throughout the procedure and experiment was terminated by pentobarbital overdose if normal physiological ranges were not maintained. After exposing the skull, a

craniectomy (diameter 6 mm) was performed over the left fronto-parietal cortex with the center 3.0 mm posterior to bregma and 3.0 mm lateral to the midline. A second smaller (1-2 mm) hole was drilled to allow for stereotactic placement of the electrode (the location varied based on destination and orientation required to reach placement location). Electrode holes were made as far away from the cortical impact craniectomy as possible. A small slit into the dura mater was introduced with surgical microscissors and electrodes were stereotactically inserted with the assistance of forceps to a depth of up to 700 μm to locate a layer IV pyramidal neuron field (Figure S1.8).

S1.4.6.2 - Electrode Insertion

Electrodes were stereotactically implanted in cortical layer IV in the barrel region of the somatosensory cortex in the brain prior to controlled cortical impact (CCI) or sham surgery using a 3-axis micropositioning stage. Exact placement depth of electrodes were stereotactically determined according to coordinates for a single field within the barrel cortex (-2mm/+5mm/-3 mm A-P, L-M, D-V from Bregma). Intended placement could have been confirmed with actual placement by verification with histological analysis, which was not performed.

S1.4.6.3 - Barrel Cortex Stimulation and Recording

As the electrode was inserted and localized to the recording region, whiskers on the contralateral mystacial pad were stimulated manually to determine when the electrode had entered the area of whisker representation. The principal whisker corresponding to the electrode placement was determined as the whisker that elicits the strongest response by manual deflection. The principal whisker was deflected at a 45º angle using an electrically isolated rod. Baseline layer IV barrel cortex signals following mechanical

whisker stimulation were recorded using a Plexon in vivo system with a headstage gain of 10, and an amplifier gain of 1000. Stimulus-response data was accumulated into peristimulus time histograms and compared over the sampled populations. Electrical activity was recorded during and for 1hr following the injury. Cortical impact recordings were also collected from the barrel cortex at 10, 11, and 12 min following brain death from separate animals. These were used to determine the extent and duration of mechanically induced recording artifacts which originated both from the CCI and micromotion of the electrode from resulting tissue deformation.

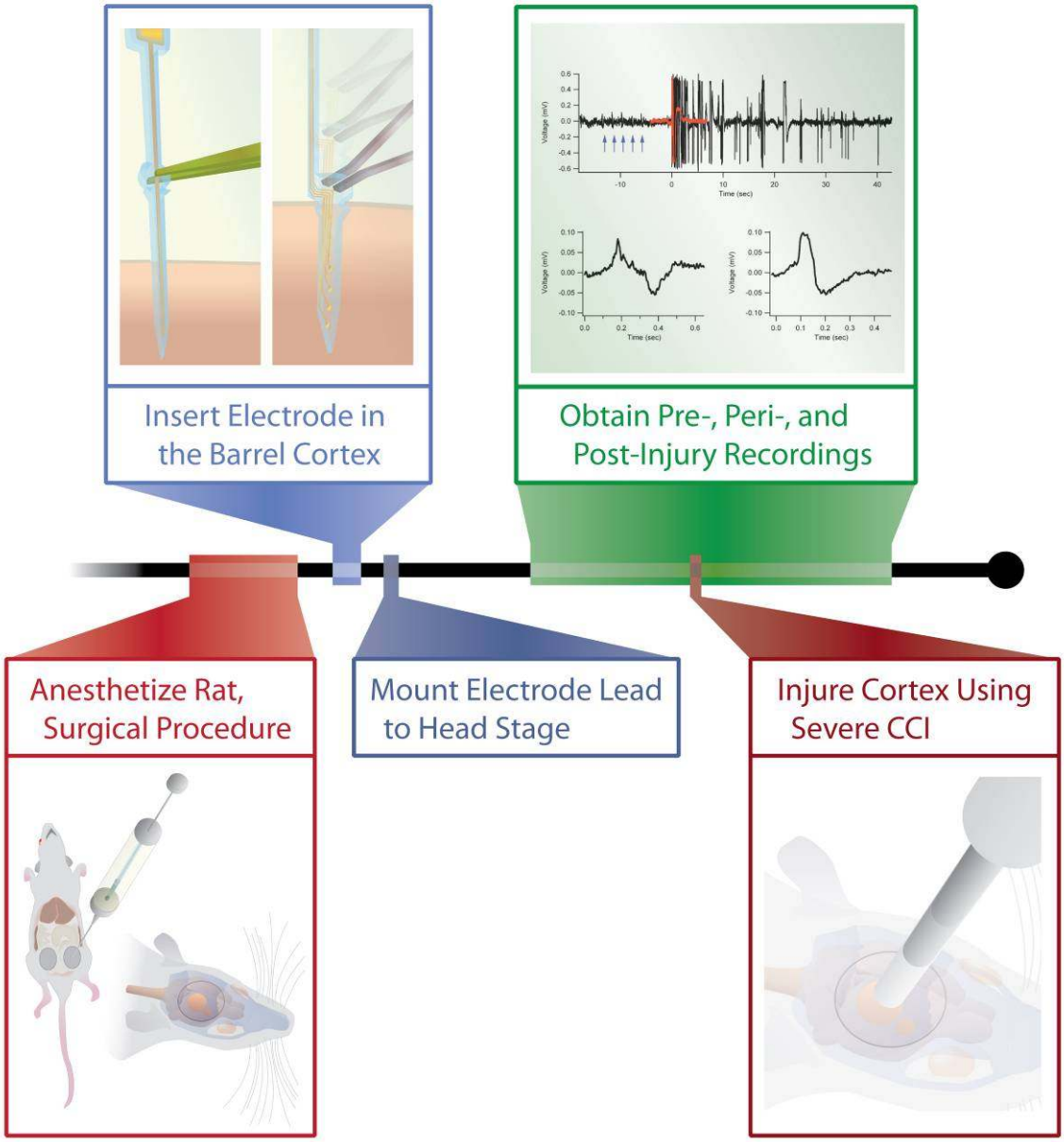


**Figure S1.7**: Timeline of the surgical and injury protocol. Following the intraperitoneal injection of anesthesia and double craniectomy surgical procedure, the electrode is inserted to the recording target, and mounted. Recordings are collected prior to, during, and following controlled cortical impact.

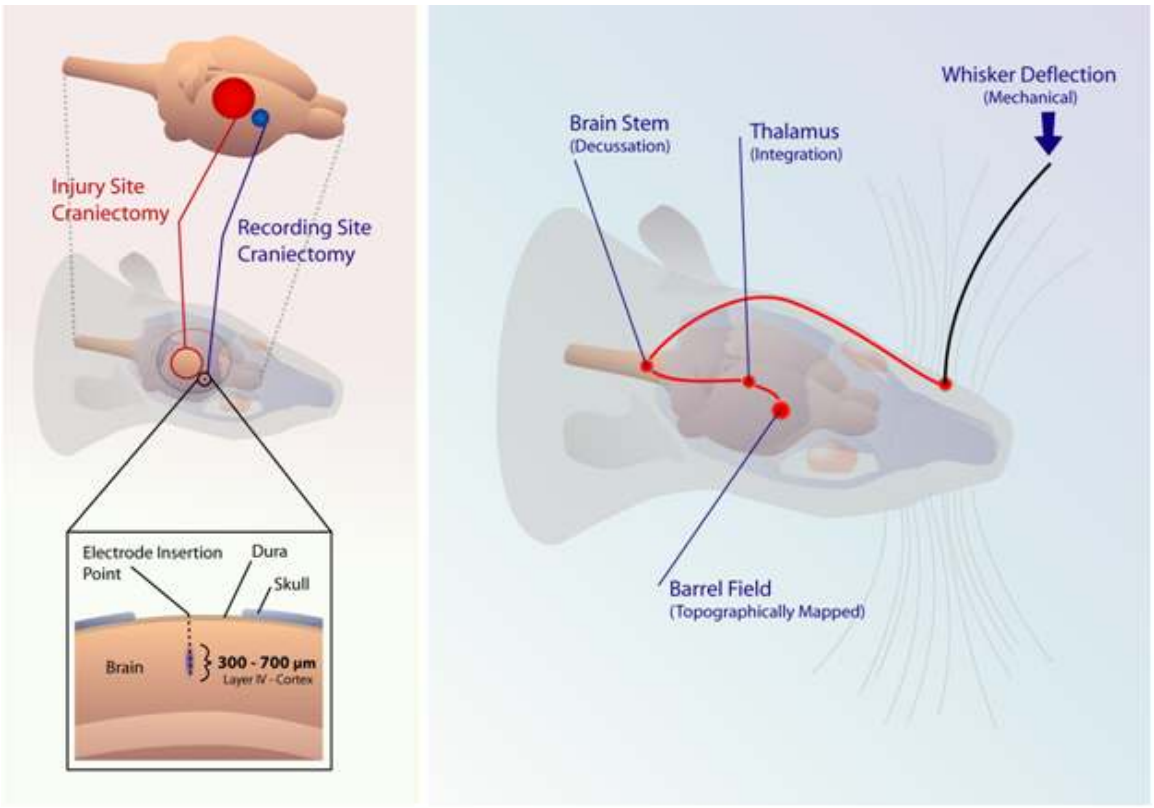


**Figure S1.8**: Schematic outlining the whisker-barrel cortex recording protocol. Whiskers were manually stimulated, which elicited a consistent, repeatable neuronal response from the layer IV of the barrel field cortex.

S1.4.6.4 - Controlled Cortical Impact

Unilateral contusions of the lateral fronto-parietal cortex were delivered using the Pittsburg Precision Instruments (PPI) pneumatic impactor device. To produce the CCI injury, a 5-mm pneumatically-operated metal impactor from PPI was contacted with the brain at 2.85 m/s and 2 mm of depth below surface. The impactor rod was angled so that it is perpendicular to the tangential plane of the brain curvature at the impact surface (15° to the vertical). The impactor travel distance was 5 cm, the impact contact hold time was 250 ms and the total duration of the impactor travel was 285 ms. A linear variable differential transformer (LVDT) connected to the impactor recorded velocity and duration to verify the consistency of the injuries. After the CCI injury, bleeding was stopped, the incision was left open and the animals were kept on warm pads during post-insult recording. All animals were sacrificed at most 2 hours post-insult recording. Sham animals received the same surgical preparations but did not undergo cortical impact.

## S1.5 - Results

### S1.5.1 - Mechanical Characterization

S1.5.1.1 - Material Properties

Mechanical property tests of vapor deposited parylene yielded an average elastic modulus of 3.778 GPa (vs. 140 GPa for silicon) and hardness of 0.183 GPa (vs. 8.5 GPa for silicon) (Figure S1.9).

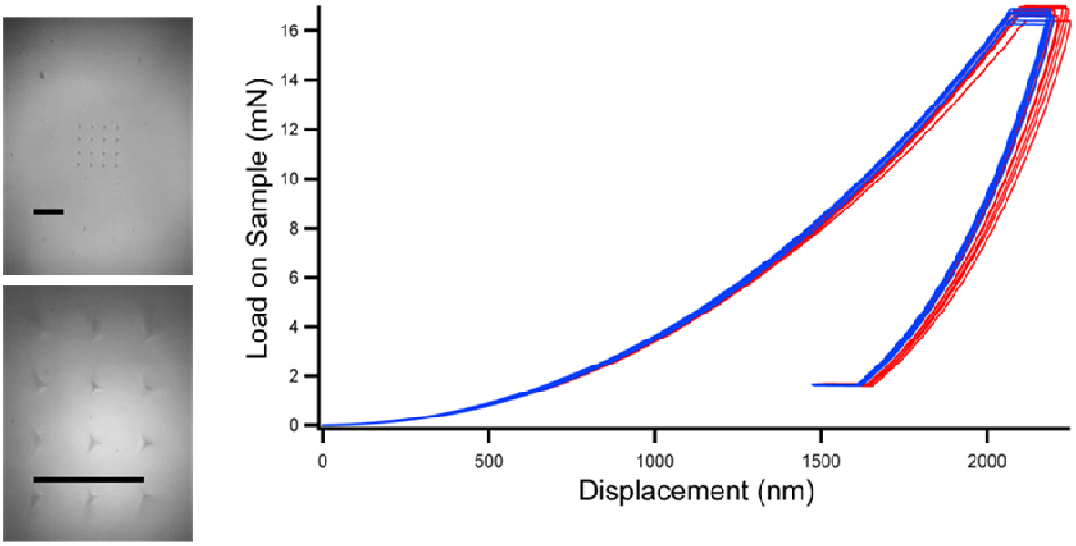


**Figure S1.9**: Nano-Indentation of flexible electrode (indents in photos on left) demonstrating required loads to induce displacement. This test yielded average elastic moduli (3.778 GPa) and hardness (0.183 GPa). For comparison, Si mechanical properties (Load on sample of 500 mN at 1600 nm displacement, Modulus~=140 GPa, Hardness~=8.5 GPa). Scale bars are 40 nm. Red traces are from the prototype electrode design, and the blue traces are from the 2$^{nd}$ generation electrode design.

S1.5.1.2 - Bucking Force

Due to the inherent flexibility of the electrode substrate (Figure S1.10), the prototype flexible electrode geometries were designed based on experimental and theoretical insertion force predictions that required fixation of the electrode column at specified lengths. Buckling force threshold tests on five prototype electrodes fixed 2.5 mm from the tip of the electrode verified these predictive models (Figure S1.11). Mean buckling force thresholds of 1970 μN for the 25μm thick electrodes with a column length of 2.5 mm exceed the model values of 1586 μN. These data show that this mathematical approach can predict the minimum electrode dimensions to prevent buckling during insertion.

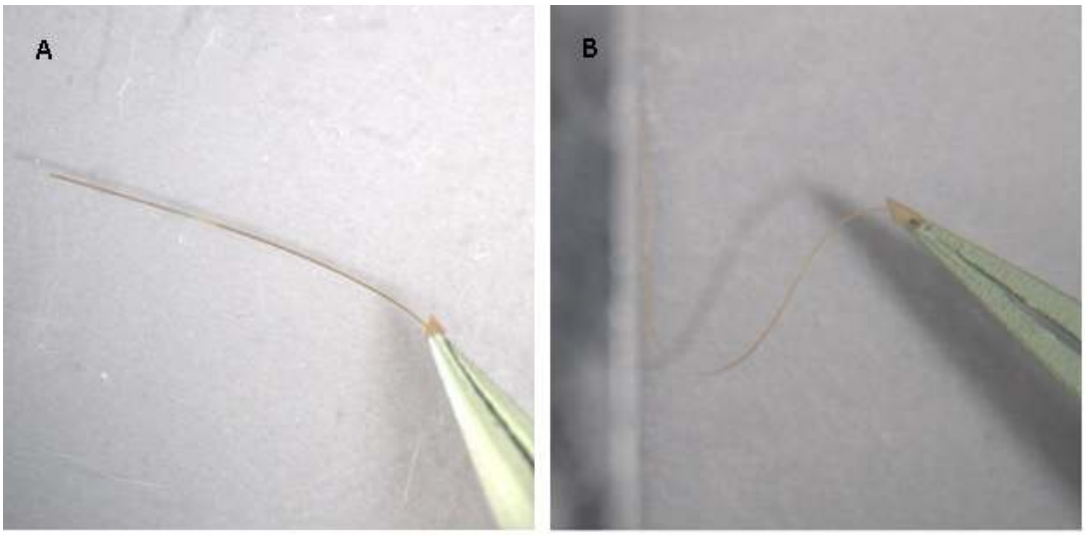


**Figure S1.10**: (A) Bright field photograph of the physical detachment of the electrode from the substrate with Teflon coated forceps. Following RIE etching of parylene and wet etching of aluminum protective layer, flexible electrodes partially detach from substrate, easing lift off. (B) Demonstration of the flexibility of the electrode by introducing two simultaneous bends in the shank. Featured electrode is 100 µm wide at the shank with a 50 µm wide gold conduction line, and 1mm wide at the contact pad, where coarse manipulation of the electrode can occur with forceps.

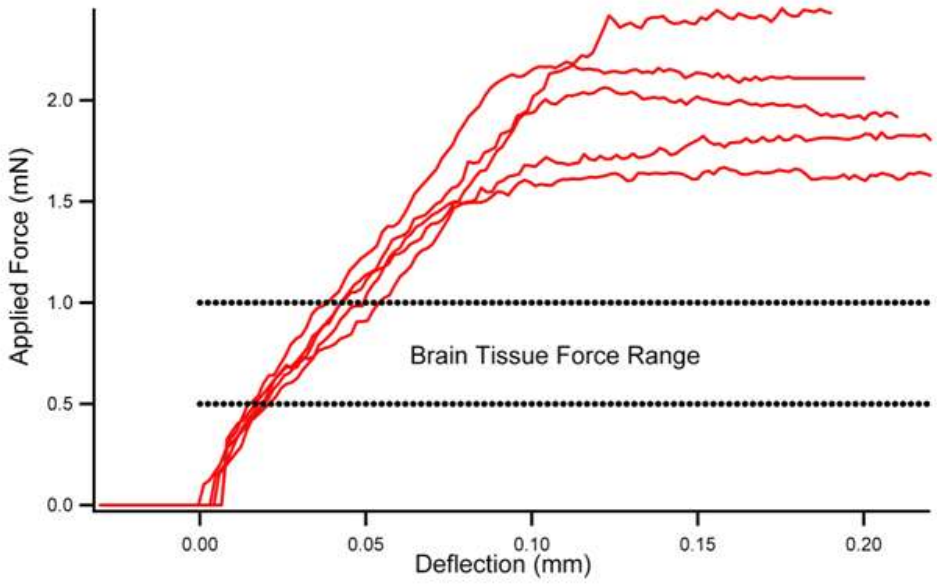


**Figure S1.11**: Buckling force tests were performed on five prototype electrodes fixed 2.5 mm from the tip of the electrode. Force loads on electrode tips were measured using an MTS NanoUTM until both visual inspection and measured data confirmed electrode shank buckling. Mean buckling force thresholds of 1970 μN for the 25μm thick electrodes with a column length of 2.5 mm were measured.

### S1.5.2 - Electrical Characterization

Flexible electrode impedances for the 30 and 40 micron diameter contact sites were recorded over a frequency range from 100 Hz to 100 kHz (Figure S1.12). The 40 μm contact sites had a lower impedance range, and were selected for the final prototype design, and were shown to have a minimum of 44 kΩ and maximum of 81 kΩ at a frequency of 1 kHz. Following a permanently induced 90$^{o}$ bend in these electrodes, this range of impedances increased to 86-126 kΩ (Figure S1.13). Examination of electrical impedance following wear suggests that the 0.5 μm gold conduction layer of intact electrodes may contain partial fractures due to the increased series resistance component of the impedance, but also confirms that the integrity of the insulation layer is maintained.

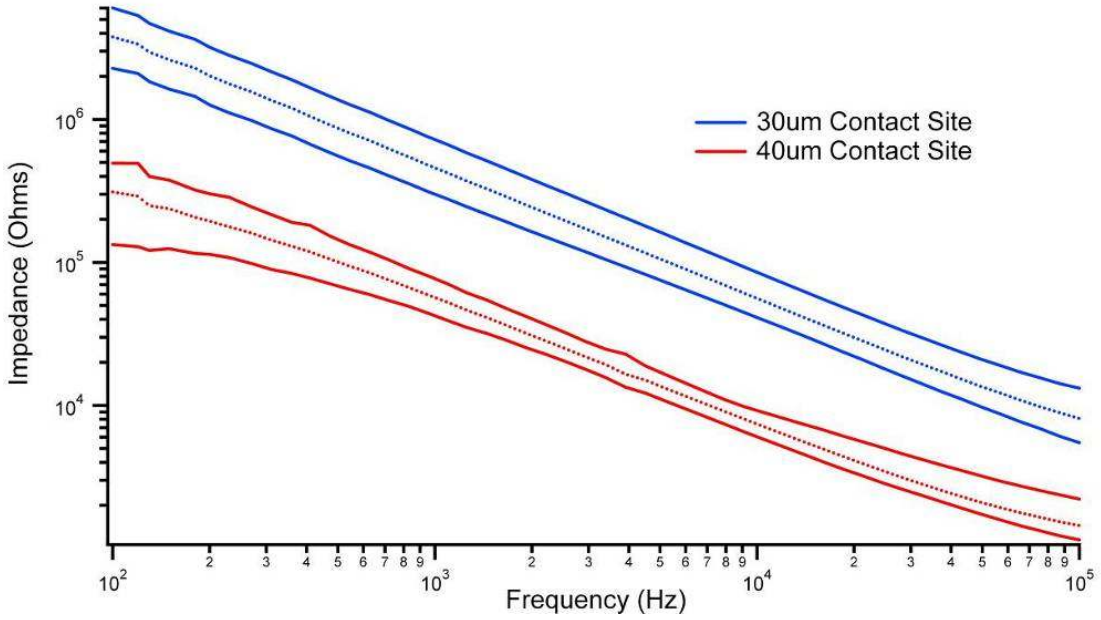


**Figure S1.12**: Magnitude of the max, min, and mean electrode impedances as a function of frequency. Measurements are taken for eight prototype Au electrodes (blue traces, contact site 40 μm diameter), and six second generation electrodes (red traces, contact site 30 μm diameter). The electrical impedance of the flexible electrodes was measured using a Stanford Research SR785 two-channel dynamic signal analyzer augmented by a custom-built, controlled switching board that allows for rapid, automated measurements of the magnitude and phase of electrode impedances across a large range of frequencies (100 Hz to 100 kHz).

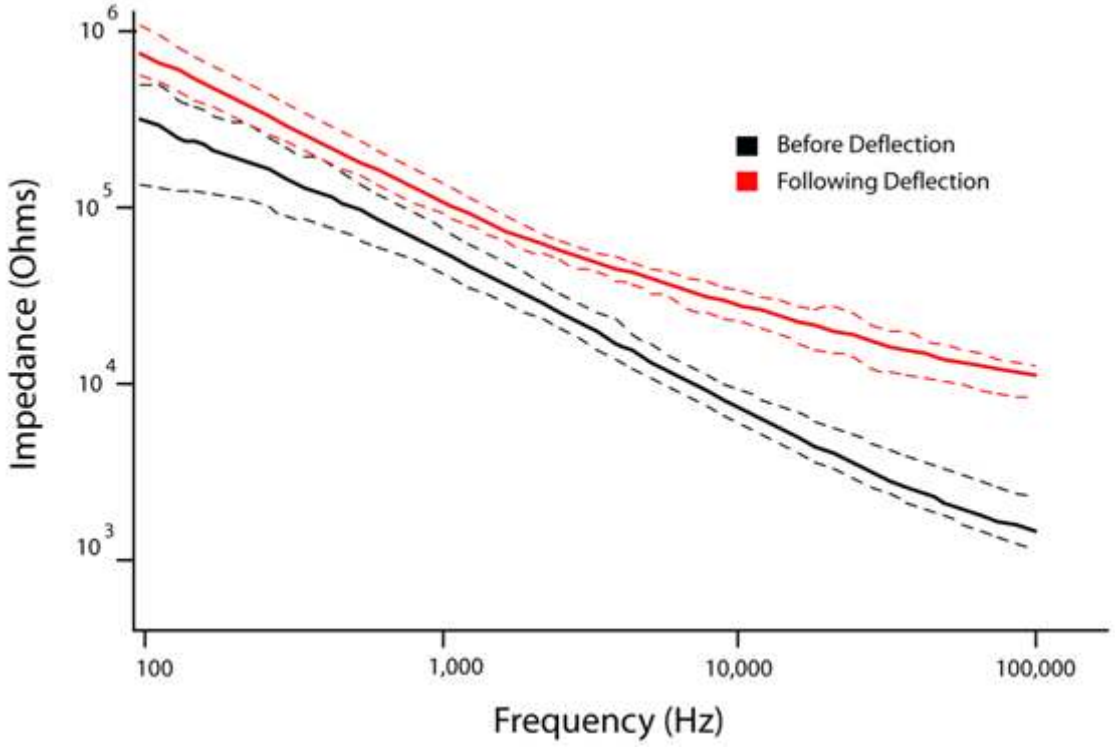


**Figure S1.13**: Average, Min, and Max magnitude of the electrode impedance as a function of frequency prior to, and then following induced bend (n=7). Featured electrodes are 100 μm wide at the shank with a 40 μm diameter contact site. Mechanical deflection is induced on the electrode shank by an Instron Tensile Testor, and consists of a permanent 90$^{o}$ bend 5 mm from the tip of the shank across the smallest cross sectional dimension. Prior to the bend, the magnitude of impedance at 1 kHz ranges from 44 kΩ to 81 kΩ, with an average of 59 kΩ. After the bend, the magnitude of impedance at 1 kHz ranges from 86 kΩ to 126 kΩ, with an average of 101 kΩ.

### S1.5.3 - *In Vivo* Testing

Electrical recording of whisker stimulation responses, and of activity during and following cortical impact demonstrate the successful use of the flexible electrode design. Following the large tissue displacements inherent in a controlled cortical impact (n=4), the electrode recording ability was not compromised (see representative recordings in Figure S1.14).

#### S1.5.3.1 - Recording, Mechanical Artifact and Electrode Migration

Recordings of the barrel cortex in a dead animal during cortical injury (n=2) determined the extent and duration of mechanically induced recording artifacts which originate both from the controlled cortical impact (CCI) and micromotion of the electrode from resulting tissue deformation. This recording from dead brain tissue can be used to determine the presence of mechanical artifacts, and indicate the initiation of viable recordings following injury. These recordings, which max out our rail to rail voltage recording range, indicate that following cortical impact, viable recordings can be collected successfully after less than 5 seconds. Even subsequent injuries and recordings on the same brain tissue resulted in similar mechanical artifacts, which range in duration from 1.059 to 2.473 seconds, and average 1.512 seconds. Because the duration of the cortical impactor movement is roughly 585 ms, these results suggest minimal migration of the electrode during tissue displacement.

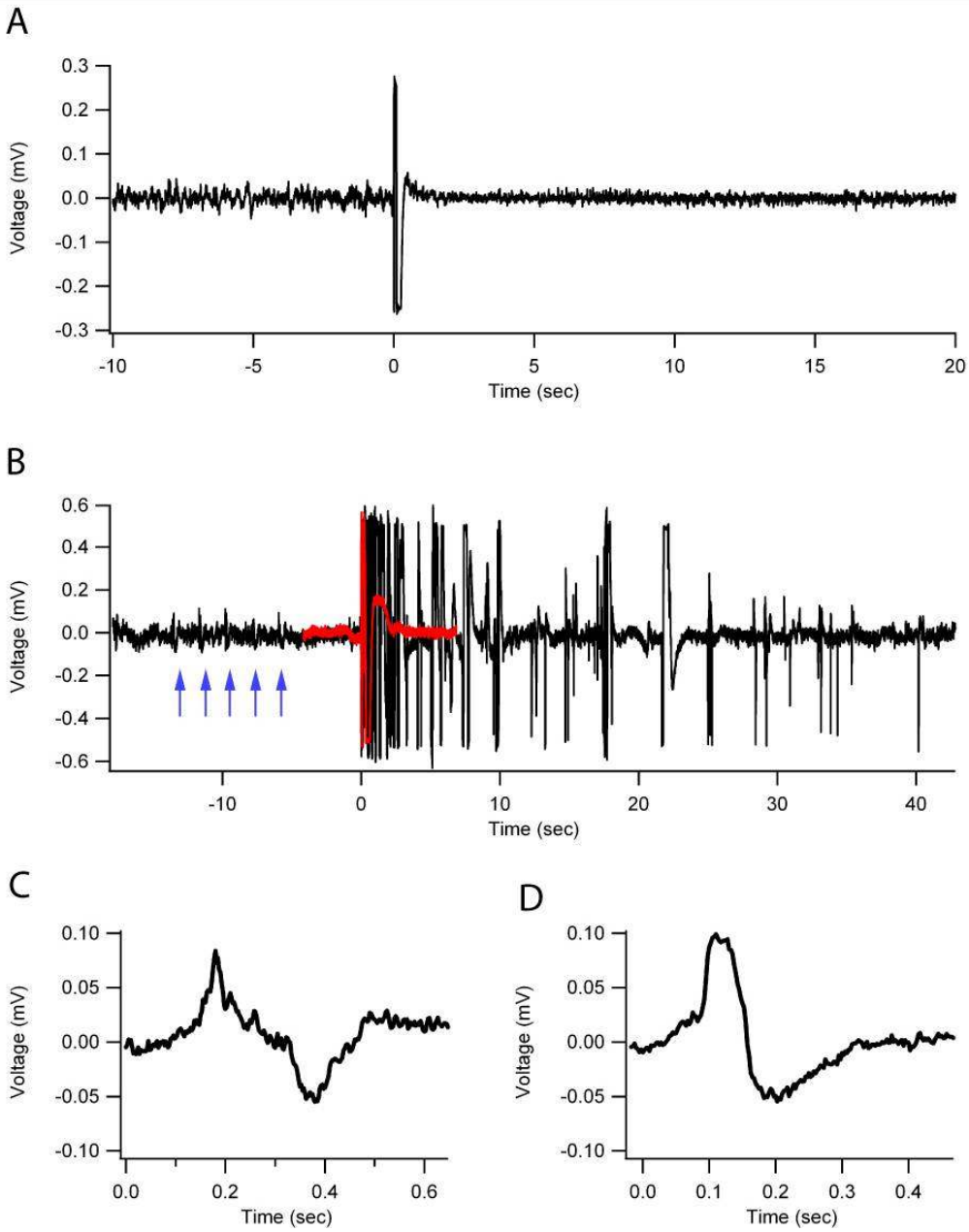


**Figure S1.14**: Electroencephalogram recording (A) on the skull and flexible electrode recording (B) from layer IV pyramidal cells prior to, during, and following cortical impact in a representative animal. Injury occurs when time = 0 seconds. Whisker stimulations prior to injury are denoted in blue. Red mechanical artifact trace obtained from recording in the barrel cortex in a dead animal. Typical whisker responses are also shown before (C), and following cortical impact (D). Gains for all recordings shown are the same. Signals were filtered with a 4$^{th}$ degree notch filter at 60 Hz.

S1.5.3.2 - Electrical Recording Analysis

Central to this research is the hypothesis that neural activity may contribute to secondary injury following TBI. Neuronal injury can readily lead to wide spread depolarizing events due to compromised membranes and ionic channels, and alterations in extracellular ionic concentrations. These depolarization events can then result in substantial increases in neuronal discharge, which, if generally excitatory, can result in further depolarizing pressures. Thus, under this scenario, neuronal activity could greatly exacerbate and even propagate an excitotoxic wave across affected regions. Recordings in the somatosensory cortex following mechanical insult present preliminary evidence of this effect (Figure S1.14). Upon insult, a massive barrage of electrical activity ensues for many seconds and ultimately subsides to a sustained elevated level of activity. This recording was taken in the barrel cortex where stereotyped responses to whisker stimulation can be quantified. Post-injury whisker stimulation responses at post-injury 1 hour are exaggerated. This indicates that the circuitry itself is still functionally intact and that the circuitry is in an excited state. While some of this activity is likely pervasive enough to be recorded by EEG, it may also be localized. Only by placing a flexible electrode, which can withstand the injury itself within specific brain regions, can this activity be mapped and correlated with outcome measures.

Previous studies of electrical recordings of field potentials in layer IV of the barrel cortex before, and at time points 1 and 2 hours after injury, suggest that injury results in an increase in initial post-stimulus excitation and prolongation of post-excitatory inhibition [21, 248]. Pre-injury baseline recordings from layer IV pyramidal cells following whisker response yield responses with an average initial excitation of

~380 μV and a post-excitatory inhibition of ~190 ms. Post-injury recordings (1 hr) from layer IV pyramidal cells following whisker response yield responses with an increased average initial excitation of ~540 μV and a prolonged post-excitatory inhibition of ~400 ms. Comparison of electrical recordings of layer IV of the barrel cortex at equivalent time points with these previous TBI studies validate the electrical recording fidelity of the electrode following mechanical insult, as well as minimal migration of the contact site.

### S1.6 - Conclusions and Future Directions

The work presented here shows for the first time ipsilateral electrophysiological recordings from the same cellular field obtained before, during, and immediately following traumatic brain injury. While we were unable to correlate electrical activity to acute damage in the brain, this was a first demonstration of flexible electrode recording during a traumatic (i.e. large deformation) insult, and subsequent tests could allow examination of this important hypothesis.

#### S1.6.1 - Electrical Recording and Analysis

The metric of electrical activity examined here may not provide sufficient fidelity to differentiate between conditions, but more sophisticated recording techniques and alternate metrics can be examined to evaluate changes in electrical activity. EEG recordings could also be employed as a reference for the barrel cortex response, or for any electrical activity during recording with an embedded electrode. While this is an excellent control for surface and rodent cortex recording, it may not provide the cellular resolution that will allow for histological correlation, nor will EEG be useful as recordings move to deeper structures like the hippocampus. A variety of analytical approaches can be used on subsequently collected electrical data. Signal rectification,

and squaring the rectified signal, which emphasizes peaks more than the base method, are simple methods to identify overall increases in electrical activity. Should injury induce periodic or patterned electrical activity, changes in periodicity, duration, and amplitude could be good metrics for identifying direct relationships between mechanical insult severity and changes in electrical activity.

Relative measures of staining contrast or cell number may also be employed to compare tissue and cellular damage across injury groups. Following electrophysiological recordings, animals could be sacrificed and perfused, and electrodes could be removed and the brains removed for post-fix and sectioning. Cellular and tissue damage could be assessed using multiple methods, including: (1) Lucifer yellow (an aldehyde fixable, cell impermeant dye) uptake in surrounding tissue; and, (2) loss of Nissl stain / electrode track volume. We have found that Lucifer yellow is a stable, fluorescent marker of cell permeability alterations that is indicative of acute cell damage induced by a traumatic event. Histological damage may also be targeted at later time points and/or by measuring more specific markers for reactive astrocytes (GFAP immunostaining) or infiltrated inflammatory cells (isolectin 4). Alternative chemical agents could prove more effective at sufficiently controlling the electrical environment of these brain regions, and there are numerous levels of control that can be considered.

**S1.6.2 - Mechanical Properties, Insertion, and Tissue Damage**

Given the flexible mechanical properties of these designed electrodes, overall non-uniformity of brain tissue, and depth of insertion, mechanical and material properties are a major concern. Because the goal of this research is the overall viability of the electrode for these injury studies, a variety of mechanical property constraints exist: (1)

structural rigidity is required for insertion; (2) elasticity is required to prevent tissue damage during injury; and, (3) elasticity and anchoring into the dura mater is important to prevent electrode movement and ensure recording site accuracy during injury. These factors and the reduction of mechanical recording artifacts are interrelated. To maintain electrode flexibility, difficulty with electrode insertion into tissue could be alleviated with two potential modifications to the design: (1) incorporating an internal channel to inject temperature or pH-sensitive polymers such as reverse transition hydrogels [249, 250] to provide controllable but temporary stiffening structures [234]; and, (2) increasing the cross sectional geometry but incorporate physical features in the electrode substrate to increase overall flexibility. The latter option has several possibilities, including segmenting the backbone of the electrode to result in a reduction in width at evenly spaced locations along the shank, or creating pockets inside the electrode structure to reduce overall density and increase flexibility (Figure S1.15). By manipulating the geometry (and hence the moment of inertia), the flexibility is increased. A reduction in width could not exceed 1/3 of the original shank width, and would need to sufficiently insulate the narrowed conduction lines. Fabrication of the segmented shank would require an additional mask for the electrode shape and conduction leads. During fabrication, the absence of sonication during acetone wash and a more delicate lift-off process for the gold and photoresist would also be necessary to reduce the chance of introducing damage to the thinner locations of gold along the conduction leads. A considerably longer acetone wash would be required as well for lift-off processing and removal of any photoresist layers. Fabricating truly hollow closed pockets is technically challenging as lithography requires laying material down on a solid substrate.

Fabrication of the perforations, or encapsulated air into the parylene layers would require an additional mask for patterning and an additional parylene etching process prior to the final deposition of parylene. A protective layer of silver could be used to outline any portions of parylene to be etched from the electrode, and etching rates of 0.3 μm/min would prevent etching the entire depth of any deposited parylene to ensure complete encapsulation of air. However, ablating or etching very small diameter holes into and evenly through the electrode is possible, and subsequent coating (with parylene C) could close these holes without filling them. Thus, pin-hole ablations of a percentage of the total mass could reduce the overall density of the electrode to that approaching brain tissue.

The mechanical and electrical characterizations of the flexible electrode did verify that the expected mechanical deformations experienced during cortical impact do not compromise the integrity of the parylene insulator or gold conduction lines. The electrical impedance averages of roughly 100 kΩ at 1 kHz for this electrode size compares well to commercially available neural probes of similar size, and impedance changes were minimal following a permanently induced bend in the electrode substrate. In addition, the forces required for insertion with our flexible electrodes were estimated and compared to measured forces for rigid electrodes and predicted to be in a non-buckling range. Mechanical testing and successful surgical insertion validated these predictions. Following insertion, barrel cortex response recordings were successfully acquired prior to, during, and immediately following injury, and the resulting changes in electrical activity compare well with the results of previous studies.

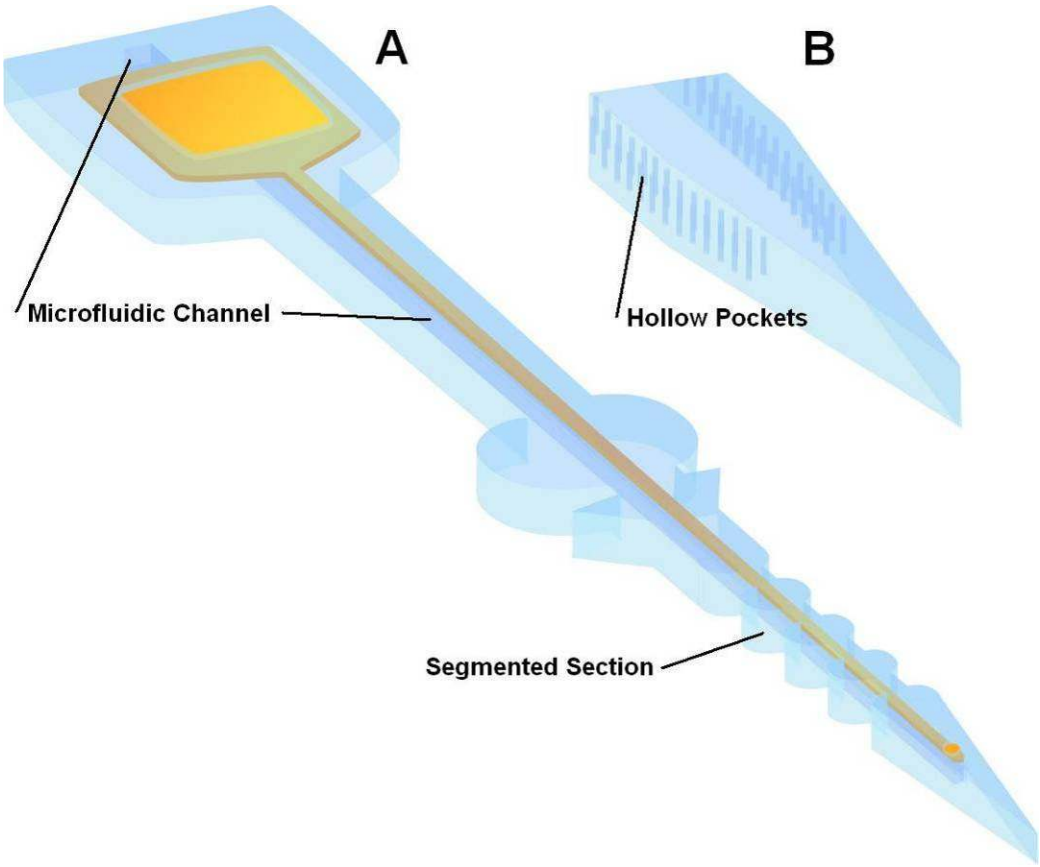


**Figure S1.15**: Alternative design incorporations for the flexible electrode to enhance material and mechanical properties. (A) Microfluidic channel that can contain stiffening agents that can be removed following insertion, and a segmented region that can increase compliance of the electrode to reduce movement within the brain. (B) Inclusion of hollow pockets to decrease substrate density.

### S1.6.3 - Alternative Surgical Methods - Electrode Insertion

Stereotactic insertion could be accomplished with custom-fabricated microtweezers and a 3-axis micromanipulator (Figure S1.16). Custom built microtweezers are an already completed design [139].

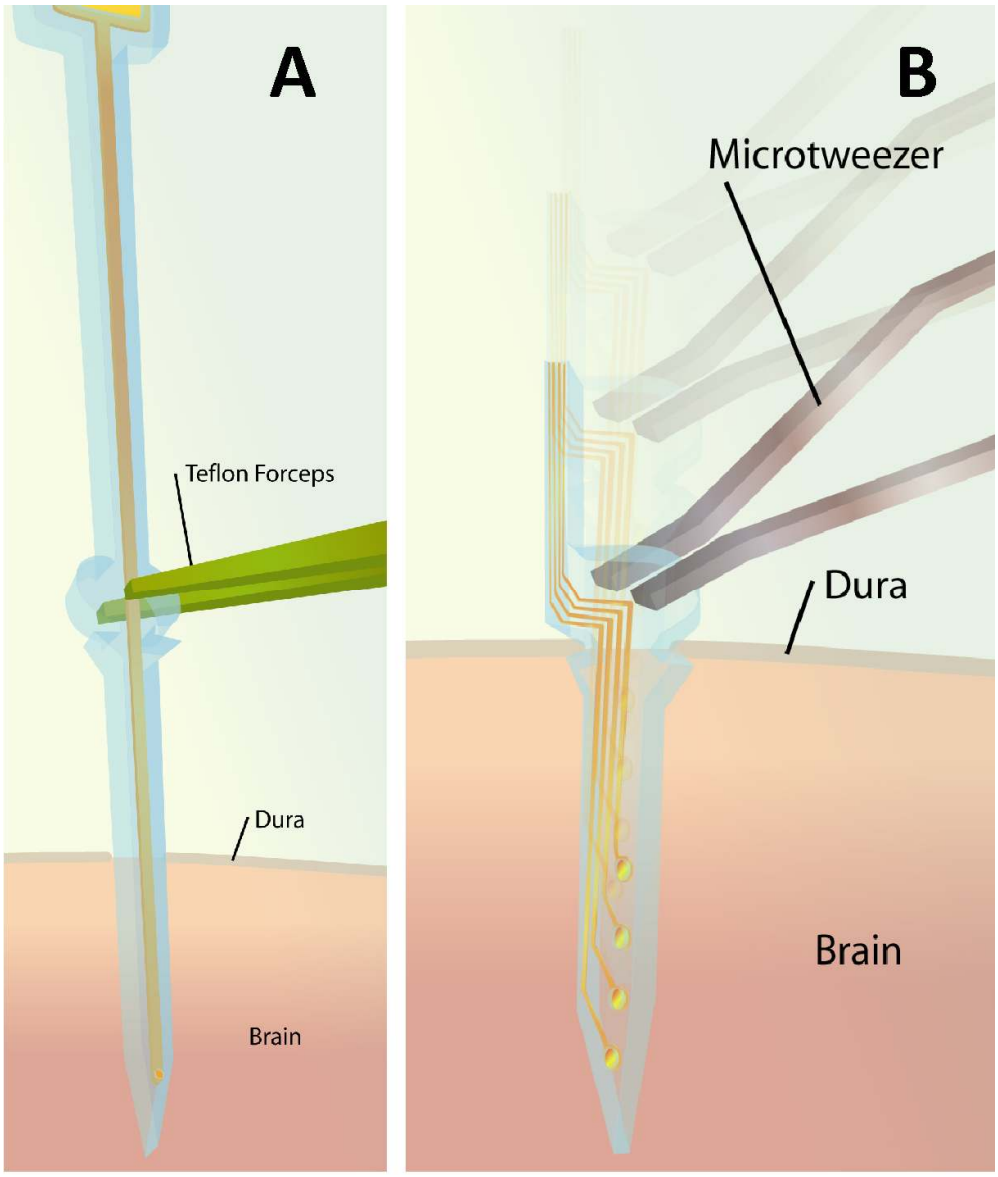


**Figure S1. 16**: Schematic demonstrating the method of reducing buckling column length by assisting insertion with Teflon forceps for the primary electrode design (A), and the microtweezers for the second electrode design (B).

### S1.6.4 - Alternative Surgical Methods - Electrode Mounting

Electrode flexibility includes not only the ability of the electrode to bend as the brain tissue deforms, but also the ability to tolerate gross brain movement relative to the electrode mount. One of the main goals of this project was to assure that the flexible electrodes move with the brain tissue as much as possible to both reduce electrode-induced tissue damage and record from the same position within the cellular field before and after impact. The electrode designs presented include a thin section of fabricated wiring that acts as a tether, the end of which could be mounted to the skull with dental acrylic or another adhesive away from the electrode brain surface. This tether would have slack between the brain surface and the adhesion point that would act as strain relief for any movement between the brain and the adhesion point. The anchor of the electrode tether would be a rigid adhesion to a brace, such that force directed onto the electrode from the external environment will be taken up by the stiff adhesion arm between the anchor point and the skull (Figure S1.17).

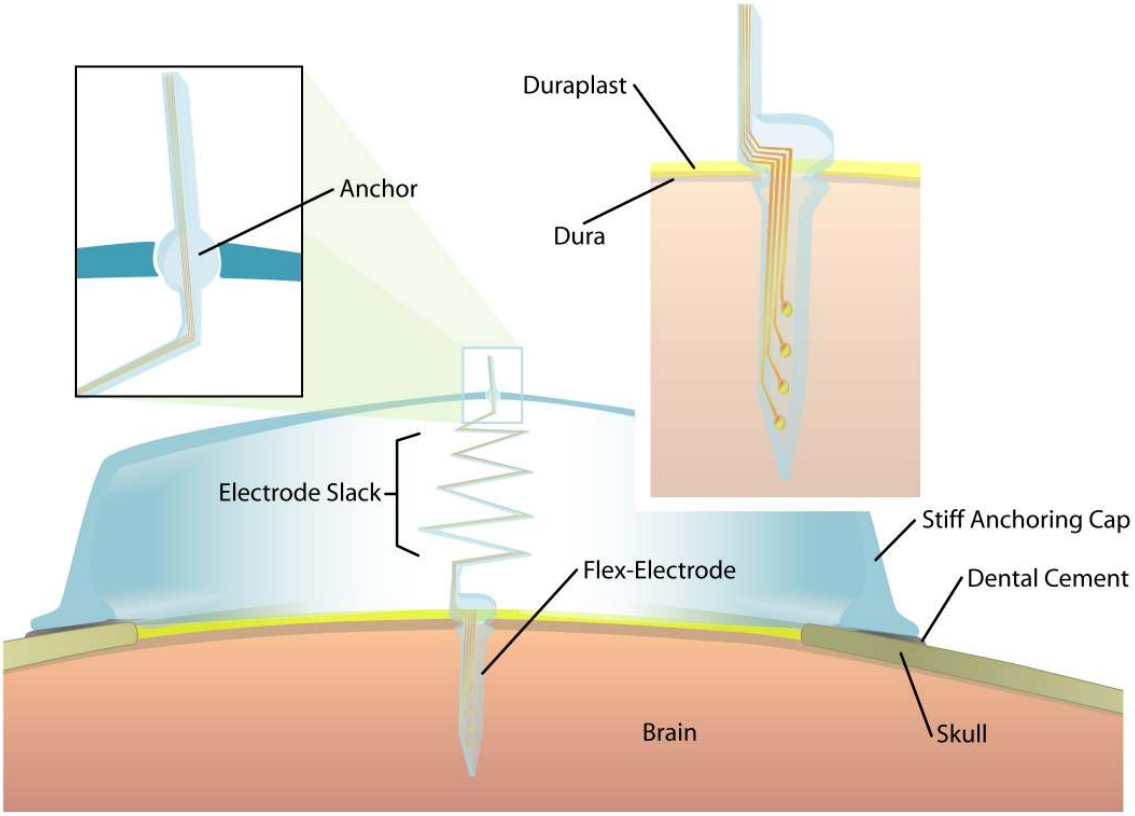


**Figure S1.17**: Schematic of the Flex-electrode (top right) with the mounting scheme to affix the electrode to the skull while allowing the electrode shank to move with the brain during deformation.

### S1.6.5 - Alternative Surgical Methods - Whisker Stimulation

The data currently collected was from electrical recordings from the cortical barrel field following manual whisker deflections. A more prescribed, repeatable deflection could be accomplished using a modified two-axis piezoelectric whisker stimulator [251]. The stimulus protocol could include ramp-and-hold stimuli (for example) or could include cyclic mechanical inputs (repeated 10 or more times) with an interstimulus interval of 2-3 seconds at standard deflection parameters [252, 253]. Velocity and amplitude of deflections could be held more constant throughout the experiment to remove variability from response in the cortex.

### S1.6.6 - Future Electrode Designs and Tests

The fabrication techniques utilized within this project have an enormous potential to incorporate several features that vastly increase the potential for flexible electrodes developed here to be used for diagnostic and therapeutic research in the laboratory setting. Alternative design features can be easily augmented to the current design and can be used to increase flexibility, length, and incorporate more recording sites, as well as combine material coatings to reduce inflammation, deliver diffusible molecules in a time-release fashion, and provide biocompatible integration with surrounding tissue. For example, the addition of an internal channel to the electrode probes may be suitable for microfluidic delivery of agents (e.g., Tetrodotoxin) to manipulate cell function, reduce excitability locally and trace the outcome of cells, and look for windows of opportunity for pharmaceutical therapies (e.g., targeted membrane sealants and channel blockers). These techniques could be combined with extracellular matrix (e.g., laminin) coatings on

the electrode to improve adhesion (and thus limit strain) and/or addition of anti-inflammatory factors.

Recording site localization, recording artifacts, accessory tissue damage from the electrode itself, and the strength, if present, of any correlations between electrophysiology and tissue damage could contribute to redesign of future flexible electrodes, and selection of the most successful designs. The most important diagnostic, however, is the strength of correlations discovered between electrophysiology and tissue damage from each tested system. As refinement of the system progresses, it is expected that these correlations, if present, will become less ambiguous. Following an iterative design cycle with development and construction, and then in vivo testing, it is expected that variations in measured correlations from in vivo data compared to injury severity from one design to the next would diminish.

Flexible electrode designs, as well as alternative electrode types such as rigid electrodes, and EEG could be tested using the whisker deflection paradigm over a variety of mounting and insertion schemes to determine the most effective setup. Activity recorded from cortical regions before, during, and following mechanical insult could also be used to refine system design. This overall comparison between flexible and rigid electrodes, using both electrical performance and tissue damage assessment as metrics, is an important area of need in the field of electrophysiology.

**S1.6.7 - Final Thoughts**

Flexible polymeric electrodes were developed that can be inserted into the brain and can withstand the large deformations associated with TBI. The flexible electrodes were characterized to ensure durability and recording fidelity during in vivo conditions.

The mechanical and electrical characterization verifies that mechanical deformations experienced during cortical impact do not compromise the integrity of the parylene insulation or gold conduction lines. Based on planned electrode geometries and features, the forces required for insertion were predicted and verified to be in a non-buckling range, precluding the need for assistive delivery vehicles, mechanisms and procedures [232, 234, 235]. In addition, due to a simplified manufacturing process, application based customization of electrode geometries is easily accomplished. Through the in vivo validation studies, the flexible electrode design presented here was functional for intracerebral insertion. The electrodes demonstrated electrical viability before and following a traumatic mechanical insult. These electrodes have electrical impedances (averages of 59 kΩ at 1 kHz) at or lower than those of other electrodes with similar geometries and tissue footprints [229]. With the integration of additional electrode contact sites, impedances are also expected to compare well to commercially available neural probes of similar size.

Both clinical data and in vivo TBI models have revealed that selective regions in the brain are more vulnerable to mechanical insult than others, suggesting that monitoring of regional and subregional network activity may yield important information about acute function. The technology and methodology developed here could be used to further investigate TBI-induced changes in electrophysiological activity in various brain regions, comparing and contrasting heavily damaged areas with those that are not as damaged by the impact. In addition, analogous studies in a traumatic spinal cord injury (SCI) model would be an improvement over currently available technology. The established methods in both TBI and SCI and will combine the electrophysiology techniques developed here

with ongoing studies investigating membrane permeability changes and the relationship with electrophysiological disturbances.

The in vivo applications focus on the examination of acute changes after TBI, and the techniques developed here can be applied to a variety of recording applications and situations [136, 254-256]. The development of flexible electrodes to circumvent the challenges inherent in current electrode capabilities has important implications in many neurophysiological applications [255]. We expect that this prototype electrode and future multielectrode versions will enable a range of electrophysiological experiments not previously possible in a variety of CNS recording systems where movement has been an issue, including TBI. It is expected that damage over a larger time course and across several other brain regions could be subsequently examined. A scientific study examining electrical activity before, during, and after TBI could be performed in the hippocampus, which is a region that is known to be vulnerable to traumatic cortical insults. Recorded data could be partitioned into "immediate," "early," and "late" time periods (<60 seconds, 1 – 60 minutes, and 60-120 minutes) and then quantified as to the degree of activity.

### S1.7 - Project Related Acknowledgements

This work was supported by the NSF (DGE-0333411) and the NIH (NINDS/NIMH/NIBIB NS046851 and NIBIB EB000786). Thank you to: (1) Dr. Yoonsu Choi for his guidance with fabrication processing; (2) Dr. Scott Kasprzak and Dr. Ken Gall for support with mechanical testing; (3) Dr. George McConnell for surgical training; (4) Dr. Jim Ross for help with impedance testing; and, (5) Mr. Ashish Patil for assistance with mechanical and electrical evaluation.

# APPENDIX A

# FABRICATION PROTOCOLS

## A.1 - Fabrication Materials

| Materials | | | Process Notes, Parameters | Notes |
|---|---|---|---|---|
| **Wafer, Wafer Accessories** | | | | |
| Si Wafer, 4" | | | | 4 inch diameter<br>500um thickness<br>1-100 ohm-cm<br>Single Side Polish<br>P-type (100)<br>"Mechanical Grade" |
| Wafer Boxes | 1 | per wafer | | 4"x4"x3/4" plastic box |
| Tex Wipes | 1 | per wafer | | Used as cushion for wafer in box |
| **Cleanroom** | | | | |
| NR-7-1500 Negative PR | | | | |
| NR-9-8000 Negative PR | | | | |
| SU-8 2000 Series Negative PR | | | | |
| TetrachloroEthylene | | | | |
| Acetone | | | | |
| Isopropanal | | | | |
| DI Water | | | | |
| N2 Gun System | | | | |
| Tex Wipes | | | | |
| Droppers | | | Used for application of PR to wafer prior to spinning | |
| Wafer Tweezers | 2 | per user | | |
| **Electroplating** | | | | |
| Current Power Supply | 1 | per station | | |
| Plating Bath Tub | 1 | per station | | |
| Banana Cables | 2 | per station | | |
| Alligator Clips | 2 | per station | | |
| Nickel Sulfamate Plating Solution | varies | | | |
| Nickel Sulfamate Brightener Solution | varies | | | |
| Buffer Oxide Etchant | varies | | | |
| Polyethelene Container for BOE | 1 | per station | | |
| Container for DI Rinsing | 1 | per station | | |
| Backside Tape | 1 | per wafer | | Blue backside tape sheets are 6x6 inches |
| Wafer tweezer | 1 | per station | | |
| **Tweezer-Box Assembly** | | | | |
| Magnetic Forceps | 2 | per station | Used to manipulate micro structures | |
| Non-Magnetic Forceps | 2 | per station | Used to manipulate micro structures | |
| Gel Super Glue | 1 | per station | Epoxy for adherance of Cable to Box, and Body to Needle | |
| Table Clamp | 1 | per station | To secure Needle/Docking Code structure for assembly | |
| Stereoscope | 1 | per station | Visual aid for use during assembly | |
| Stainless Steel Needle | | | | Assembled Needle and Cone |
| Cable Spring | | | | |
| Spring Stopper | | | | |
| Rubber O-ring | | | | |
| Fabricated Tweezer | | | | |
| Fabricated Box | | | | |
| Snips | | | Use to cut cable to length | |

# A.2 - Fabrication Process Details

| Process | Materials | Material Amount | Material Unit | Time (hours) | Time Note | Process Notes, Parameters | | | Notes |
|---|---|---|---|---|---|---|---|---|---|
| **Wafer Preperation** | | | | | | | | | |
| Cleaning - Pre Backside Prep | | | | 0.2 | per wafer | Clean with each chemical in order: TCE, Acetone, IPA, DI H20. Requires 2 iterations | | | Removal of Debris to ensure good processing |
| | TetraChloroEthelene | 30 | ml | | | Use Spray bottle to thoroughly rinse wafer, both sides | | | Detergent, removes oils and debris |
| | Acetone | 30 | ml | | | Use Spray bottle to thoroughly rinse wafer, both sides | | | Solvent, removes oils, and TCE, 98-99% solvent grade |
| | Isopropanol | 30 | ml | | | Use Spray bottle to thoroughly rinse wafer, both sides | | | Solvent, removes Acetone, 98-99% solvent grade |
| | DI Water | | | | | Use Spray bottle to thoroughly rinse wafer, both sides | | | Wash, removes IPA |
| | N2 Spray Gun | | | | | Use N2 Gun to remove all traces of DI Water | | | |
| | Tex Wipes | 2 | units | | | | | | Used to assist in drying wafer following rinse |
| Wafer Backside Passivation | | | | 1 | per batch (4) | | | | Reducing or Eliminating the conductivity of the backside surface to prevent plating of metal material during the electroplating stages of fabrication |
| PECVD | | | | | 4 max | PECVD Deposition of SiN, Standard Nitride Recipe, 1 hr | | | |
| Cleaning - Post Backside Prep | | | | 0.2 | per wafer | Clean with each chemical in order: TCE, Acetone, IPA, DI H20. Requires 2 iterations | | | Removal of Debris to ensure good processing |
| | TetraChloroEthelene | 30 | ml | | | Use Spray bottle to thoroughly rinse wafer, both sides | | | Detergent, removes oils and debris |
| | Acetone | 30 | ml | | | Use Spray bottle to thoroughly rinse wafer, both sides | | | Solvent, removes oils, and TCE, 98-99% solvent grade |
| | Isopropanol | 30 | ml | | | Use Spray bottle to thoroughly rinse wafer, both sides | | | Solvent, removes Acetone, 98-99% solvent grade |
| | DI Water | | | | | Use Spray bottle to thoroughly rinse wafer, both sides | | | Wash, removes IPA |
| | N2 Spray Gun | | | | | Use N2 Gun to remove all traces of DI Water | | | |
| | Tex Wipes | 2 | units | | | | | | Used to assist in drying wafer following rinse |
| **Sacrificial Release Layer** | | | | 1 | per wafer * | | | | Non Conductive, uniform thickness, washable (with Acetone) material deposited to allow easy, cheap, and gentle removal of electroplated units from each wafer. Given the volatility of the electroplating bath, and potential for the PR to be corroded, hard baking, and use of a negative photoresist is recommended. |
| Sacrifical Oxide Layer | | | | 1 | per batch (4-15) | | | | |
| PECVD | | | | | 4 max | PECVD Deposition of SiO2, Standard Oxide Recipe, 1 hr | | | |
| **or** | | | | | | | | | |
| Lindberg Furnace | | | | | 15+ max | Baking wafers in environment with Oxygen to promote growth of SiO2 | | | Backside oxide growth difficult to predict on nitride surface |
| Sacrificial Photoresist Layer | | | | | | | | | Deposits photoresist evenly over entire surface of circular wafer |
| Spin Photoresist | | | | | | Top Speed: | 3000 | rev/min | |
| | | | | | | Ramp Speed: | 1000 | rev/min | |
| | | | | | | Spin Duration: | 30 | sec | |
| | NR-7-1500 Negative PR | 5 | ml | | | | | | GT Cleanroom Provides for Free |
| | Dropper | 1 | unit | | | Used to apply PR to wafer | | | |
| | Tex Wipes | 6 | units | | | | | | Used to protect and clean spinning system |
| Soft Bake | | | | | | Bake wafer with spun photoresist in oven | 15 min | 80 C | |
| Expose | | | | | | Expose photoresist without patterning (no mask). | 340nm | 1000mJ | |
| Post-Exposure Bake | | | | | | Bake wafer with spun photoresist in oven | 10 min | 80 C | |
| **Electroplating Seed-Layer Deposition** | | | | 2 | per batch (1-6) | PVD Deposition of Cr/Cu OR DC Sputterer Deposition of Ti/Cu/Ti OR Unifilm Sputterer Deposition of Cr/Cu | | | Deposition of uniform layer of conductive material (copper) to seed electroplating for exposed areas of seed metal. Requires thin adhesion layer (Ti, Cr) of 'sticky' metal, and potentially, a thin protective layer of non-corroding metal (Ti). |
| DC Sputterer | | | | | 6 max | Titanium - 3" Gun | 500 sec | 7% power | Adhesion Layer |
| | | | | | | Aluminum - 6" Gun | 3000 sec | power | Seed layer for electroplating |
| **or** | | | | | | | | | |
| DC Sputterer | | | | | 6 max | Titanium - 6" Gun | 100 sec | power | Adhesion Layer |
| | | | | | | Copper - 6" Gun | 3000 sec | power | Seed layer for electroplating |
| **or** | | | | | | | | | |
| Unifilm Sputterer | | | | | 6 max | Chrome | 200 | A/min | Adhesion Layer |
| | | | | | | Gold | 300 | A/min | Seed layer for electroplating |
| **Electroplating Mold Patterning** | | | | 2 | per wafer * | | | | Depositing Photoresisit layer, and developing to pattern the features that will be electroplated. This mold will have a selectively deposited or spun thickness, which will correspond with, and serve as a guide to specify and validate electroplating thickness. Given the volatility of the electroplating bath, and potential for the PR to be corroded, hard baking, and use of a negative photoresist is recommended. |
| Photoresist Mold - NR-9-8000 | | | | | | | | | |
| Spin Photoresist ~30 um | | | | | | Top Speed: | 800 | rev/min | Deposits photoresist evenly over entire surface of circular wafer. |
| | | | | | | Ramp Speed: | 300 | rev/min | This Top Speed, Ramp Speed, and Duration will lead to a thickness of: |
| | | | | | | Spin Duration: | 30 | sec | 20-22um |
| | NR-9-8000 Negative PR | 15 | ml | | | | | | |
| | Dropper | 1 | unit | | | Used to apply PR to wafer | | | |
| | Tex Wipes | 6 | unit | | | | | | Used to protext and clean spinning system |
| Soft Bake | | | | | | Bake wafer with spun photoresist in oven | 15 min | 80 C | |
| Expose | | | | | | Expose photoresist without patterning (no mask). Use near-340nm wavelength source | 340nm | 1200mJ | |
| Post-Exposure Bake | | | | | | Bake wafer with spun photoresist in oven | 10 min | 80 C | |
| Develop | | | | | | Use RD6 Developer with no dilution, rinse with DI water | 2.5 min | No Dilution | |
| | RD6 Developer | 100 | ml | | | | | | GT Cleanroom Provides for Free |
| | DI Water | | | | | Thoroughly rinse wafer following development, both sides | | | Rinse, removes traces of developer from all features |
| | N2 Spray Gun | | | | | Use N2 Gun to remove all traces of DI Water | | | |
| | Tex Wipes | 2 | unit | | | | | | Used to assist in drying wafer following rinse |
| Profile Mold | | | | | | Set profile height range sensing for 10-100um wall | | | Use Profilometer to determine the height or thickness of PR mold |
| **or** | | | | | | | | | |
| Photoresist Mold - NR-21-20000 | | | | | | | | | |
| Spin Photoresist ~30 um | | | | | | Top Speed: | 3000 | rev/min | Deposits photoresist evenly over entire surface of circular wafer. |
| | | | | | | Ramp Speed: | 1000 | rev/min | This Top Speed, Ramp Speed, and Duration will lead to a thickness of: |
| | | | | | | Spin Duration: | 30 | sec | 20-22um |
| | NR-21-20000 Negative PI | 15 | ml | | | | | | |
| | Dropper | 1 | unit | | | Used to apply PR to wafer | | | |
| | Tex Wipes | 6 | unit | | | | | | Used to protext and clean spinning system |
| Soft Bake | | | | | | Bake wafer with spun photoresist on hotplate | 1 min | 150 C | |
| | | | | | | Bake wafer with spun photoresist on hotplate | 3 min | 90 C | |
| Expose | | | | | | Expose photoresist without patterning (no mask). Use near-340nm wavelength source | 340nm | 1200mJ | |
| Post-Exposure Bake | | | | | | Bake wafer with spun photoresist in oven | 3 min | 80 C | |
| Develop | | | | | | Use RD6 Developer with no dilution, rinse with DI water | 2.5 min | No Dilution | |
| | RD6 Developer | 100 | ml | | | | | | GT Cleanroom Provides for Free |
| | DI Water | | | | | Thoroughly rinse wafer following development, both sides | | | Rinse, removes traces of developer from all features |
| | N2 Spray Gun | | | | | Use N2 Gun to remove all traces of DI Water | | | |
| | Tex Wipes | 2 | unit | | | | | | Used to assist in drying wafer following rinse |
| Profile Mold | | | | | | Set profile height range sensing for 10-100um wall | | | Use Profilometer to determine the height or thickness of PR mold |

| Process | Materials | Material Amount | Material Unit | Time (hours) | Time Note | Process Notes, Parameters | Notes |
|---|---|---|---|---|---|---|---|
| **Lift Off** | | | | 0.5-2 | per wafer * | | This final processing step will remove the desired units from the wafer. Due to pre-processing and electroplating seed layer thickness and material selection, this will only require sonication in an acetone bath. |
| Oxide Layer | | | | | | | |
| Placement of Units in Quiescent Acetone Bath, Rinse | | | | | | Immersion in acetone bath for 30 min - 2 hours, depending on feature dimensions. Rinsing of acetone from box is accomplished by placement of units into IPA bath, and then DI Water bath. | Structural PR layers will be removed |
| | Acetone | 100 | ml | | | | 98-99% solvent grade acetone |
| | Isopropanol | 100 | ml | | | | 98-99% solvent grade IPA |
| | DI Water | 200 | ml | | | | |
| Removal of Oxidation Layer | | | | | | Immerse into BOE or dilute HF Bath for until units begin to delaminate | |
| | DI Water | 500 | ml | | | | |
| | BOE | 200 | ml | | | | |
| | DI Water | 200 | ml | | | Rinse following exposure to HF | |
| Drying | | | | | | Units are removed from DI Water bath and placed on a Tex Wipe until dry. | |
| | Tex Wipes | 1 | unit | | | | Used to assist in drying |
| **or** | | | | | | | |
| Sacrificial Photoresist Layer | | | | | | | |
| Place into Sonicating Acetone Bath | | | | | | 98-99% solvent grade acetone is placed in container large enough to fit wafer, but small enough to fit sonication bath. The container is placed into a sonication bath, and as units lift from the wafer, they should be removed individually and placed into a quiescent acetone bath so that removal of all debris from the surface and channel of box can be completed. | Structural PR layers will be removed, and thin electroplating seed layers will break up |
| | Acetone | 500 | ml | | | | 98-99% solvent grade acetone |
| Placement of Units in Quiescent Acetone Bath, Rinse | | | | | | Following removal from sonication bath, individual units will be placed into acetone bath for 30 min - 2 hours, depending on Box channel cross sectional dimensions. Rinsing of acetone from box is accomplished by placement of units into IPA bath, and then DI Water bath. | |
| | Acetone | 100 | ml | | | | 98-99% solvent grade acetone |
| | Isopropanol | 100 | ml | | | | 98-99% solvent grade IPA |
| | DI Water | 200 | ml | | | | |
| Drying | | | | | | Units are removed from DI Water bath and placed on a Tex Wipe until dry. | |
| | Tex Wipes | 1 | unit | | | | Used to assist in drying |
| **then** | | | | | | | |
| Visual Examination | | | | | | Visual Examination can be used to determine if units are viable (clean, structurally sound, channel present without debris or malformation of channel hole). | |

Key Words:

| | |
|---|---|
| Photoresist | PR |
| TetraChloroEthylene | TCE |
| Buffered Oxide Etch | BOE |

* Wafers processing times can be reduced with parallel processing, due to fixed times of baking, metalization, etc.

** A maximumm of one wafer can be plated per power supply, and as set up (but could be changed) plating bath. Time is dependent on current applied, surface area, and plating solution used

# A.3 - MEMS Device Assembly

| Process | Time (min) | Time Note | Process Notes, Parameters |
|---|---|---|---|
| **Tweezer-Box Assembly** | 10 | per unit | |
| Visual Examination | | | are viable (clean, structurally sound, without debris or malformation). |
| Position Box | | | Place flat surfaced object (block) with tacky/sticky surface (can be accomplished with double sided tape, or rolled tape) into clamp. Using forceps, place Nickel/Silicon Box unit onto tacky surface, with wider channel opening placed upwards, clearing top of tacky area. Check channel opening positioning with assistance of stereoscope. |
| Slide Tweezer Beam into Box Channel | | | Using forceps, slide the beam of the tweezer unit into the opening of the secured box. Feed the beam until it comes out of the smaller channel opening on the opposite side of the box. |
| Removal of Assembled Unit, Visual Examination | | | Gently remove tweezer-box assembly from tacky surface and using two forceps, examine the motion of tweezer and box relative to one another. Should check for clear, fluid motion (clean channel/beam), and also tweezer tip actuation. |
| **Needle/Docking Cone Assembly** | 10 | per unit | Prior to assembly of the tweezer and box, the Needle or Docking Cone structure must be assembled. This structure will house the tether-cable structures allowing independent motion of the tether and cable, and thus, tweezer and box. This Docking Cone Assembly consists of the Stainless Steel Needle (tether), Cable (cable), Spring, Stopper, O-ring, and some epoxy. |
| Visual Examination | | | are viable (clean, structurally sound, without debris or malformation). |
| Cut Length of Cable | | | Measure and cut length of cable, dependent on length of stainless steel needle, always allowing some excess to protrude from the tip of the needle, so that it can be attached to the tweezer box. |
| Attach Cable to Stopper | | | The stopper, which is larger in diameter than the inner diameter of the O-ring, prevents substantial backwards movement of the cable-stopper-box. Attach stopper to cable using pressure to force cable into small stopper hole (center of cylinder), and secure with glue. |
| Stopper | | | This small cylindrical plastic stopper can be manufactured using a variety of processes, including rapid 3D prototyping |
| Position Spring over cable | | | Spring, with radial diameter smaller than outer diameter of stopper, is placed around cable (non stopper-ed end) and slid to other end of cable, against stopper |
| Slide Cable Assembly through Needle Tract | | | Slide the cable (non stopper-ed/spring end) through needle tract from inside the docking cone housing to the tip of needle so that stopper and spring are inside housing. |
| Secure O-Ring inside Docking Cone Housing | | | Drop O-Ring into Docking Cone Housing, and press against stopper position, until snug. This can be accomplished by pushing the Needle/Docking Cone onto Syringe (no needle attached). |
| **Final Assembly** | 20 | per unit | |
| Visual Examination | | | are viable (clean, structurally sound, without debris or malformation). |
| Position Needle/Docking Assembly | | | Using the Docking Cone as a structurally sound base, clamp the Docking Cone Assembly to the table, with minimal angle from table of needle trajectory (so that focal plane of needle tip is close to same over length of needle tip). Orient/rotate needle so that tweezer beam track is facing top. |
| Cut Cable to Length | | | Using a tweezer-box assembly as a guide, determine length of exposed cable (from needle tract) required for 75-100% of box to overlap with exposed cable. Given final space between box and needle tip, this should provide a final overlap of roughly 50-75% of box and cable, allowing for secure adherance with epoxy. Cut cable with snips one length is determined. |
| Position Tweezer Beam over Needle | | | Using forceps, position tweezer beam of tweezer from assembled tweezer-box (beam is exposed out the smaller channel opening of box) over the slot in top of Needle. Before securing tweezer beam to Needle, ensure that facing surface of Box contains the slot for the cable. Secure with epoxy. |
| Position Box over Cable | | | Using forceps, position box (slides along tweezer beam) over exposed length of cable (coming out of needle tract). Positioning will need consideration of tweezer tip actuation threshold position, exposed length of cable. Secure with epoxy. |
| Visual Examination | | | Examine under stereoscope the motion of tweezer tip actuation. Make adjustments in tweezer/box positioning relative to Needle/Cable prior to curing of epoxy so that motion is fluid, and has minimal angle of slide (so that tips close concurrently). |

# APPENDIX B

# MECHANICAL CONTROLLER AND LINEAR ACTUATOR COMPONENTS

## B.1 - Luer-Based Mechanical Packaging

| | Part Description | | | | |
|---|---|---|---|---|---|
| Part Name | Picture | Description | Key Dimensions (Critical) | Key Dim. Value (Inch is default) | Material |
| Needle | 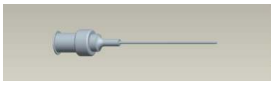 | Main Housing for actuation mechanisms for tweezer box. Houses o-ring, cable and cable butt. | | | Stainless Steel |
| Needle_Cable |  | Will translate actuation from docking head to tweezer box. | Outer Diameter<br>Length | 0.01000<br>2.25000 | Stainless Steel |
| Cable_Butt | 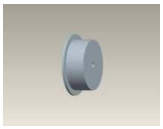 | Use to hold spring in place, and to provide target for actuation rod from docking head. Will interface with o-ring | Outer Diameter<br>Hub Diameter<br>Shaft Diameter<br>Hub Length<br>Total Length | 0.14500<br>0.12000<br>0.01200<br>0.04500<br>0.31500 | SLA Plastic |
| O_Ring | 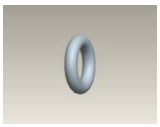 | Used as a stopper to hold cable butt in place. | Outer Diameter<br>Inner Diameter<br>Thickness | 0.16200<br>0.09800<br>0.03200 | |

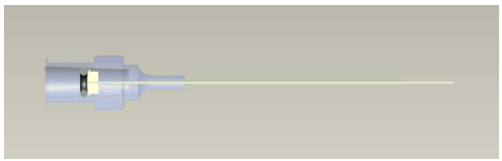

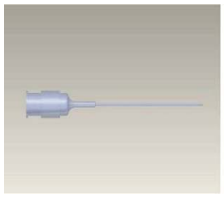

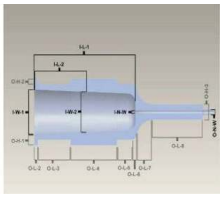

# B.2 - Mechanical Controller

## B.2.1 - Lower Housing

| Part Name | Part Description: Picture | Description | Key Dimensions (Critical) | Key Dim. Value (Inch is default) | Material |
|---|---|---|---|---|---|
| Luer_Bushing | 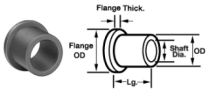 | Bushing for lower housing end fitting/luershaft. Flanged Sleeve Bearing. | Shaft Diameter - 3/16<br>Outside Diameter - 1/4<br>Flange Outside Diameter - 3/8<br>Flange Thickness - 1/32<br>Length - 1/2 | 0.18750<br>0.25000<br>0.37500<br>0.03125<br>0.50000 | Plastic, Peek |
| Luer_Bearing | 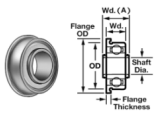 | Bearing for lower housing luershaft. Flanged Double Sheilded with Extended Inner Ring. General Purpose. | Shaft Diameter - 3/16<br>Outside Diameter - 5/16<br>Flange Outside Diameter - 0.359<br>Flange Thickness - 0.036<br>Width - 1/8<br>Width (A) - 5/32 | 0.18750<br>0.31250<br>0.35900<br>0.03600<br>0.12500<br>0.15625 | Stainless Steel |
| Worm_Gear |  | Worm gear for rotational functionality of luershaft | Shaft Diameter (B) - 0.187<br>Hub Diameter (C) - 11/32<br>Gear Diameter<br>Hub Projection (D) - 3/16<br>Gear Face Width (F) - 3/16<br>Length (E) - 3/8<br>Pitch - 48<br>Number of Teeth - 20<br>Pressure Angle (P.A.) - 20<br>Gear Ratio - 10<br>Lead Angle - 7.12 | 0.18700<br>0.34375<br>0.45000<br>0.18750<br>0.18750<br>0.37500<br>48.00000<br>20.00000<br>20.00000<br>10.00000<br>7.12000 | Acetyl |
| Luershaft | 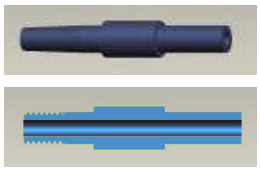 | Luershaft allows docking of needle assembly, and rotation of needle assembly via worm/worm wheel actuation. | Shaft Diameter - was 0.0937<br>Outer Diameter<br>Flange Diameter<br>Flange Length<br>Hub Length<br>Length<br>Luer Angle | 0.09500<br>0.18750<br>0.25000<br>0.42000<br>0.50000<br>1.55000<br>7.00000 | Stainless Steel |
| Lower_Housing | 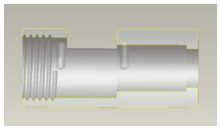 | Houses the rotational elements, and screws onto the end fitting, which houses the actuation elements. | Shaft Diameter (bearing flange)<br>Bearing Diameter (bearing)<br>Inner Diameter - was 0.45<br>Outer Diameter<br>Thread Pitch<br>Thread Angle<br>Thread Length<br>Thread Height<br>Thread Diameter<br>Bearing Length<br>Length | 0.36000<br>0.31250<br>0.48500<br>0.60000<br>0.05000<br>60.00000<br>0.03750<br>0.0271<br>0.5000<br>0.0890<br>1.3950 | Aluminum |
| Inner_Tubing |  | Inserts into luershaft. Outer diameter conforms to luershaft and end fitting shaft diameters, and inner diameter sets the size of the push rod. Use of this piece allows for modularity. | Shaft Diameter<br>Outer Diameter - 3/32<br>Length | 0.05380<br>0.09370<br>1.50000 | Stainless Steel<br>304 |
| Inner_Tubing_Short |  | Inserts into end fitting. Outer diameter conforms to luershaft and end fitting shaft diameters, and inner diameter sets the size of the push rod. Use of this piece allows for modularity. | Shaft Diameter<br>Outer Diameter - 3/32<br>Length | 0.05380<br>0.09370<br>0.53000 | Stainless Steel<br>304 |

Images from www.mcmaster.com included.

| | Part Description | | | | |
|---|---|---|---|---|---|
| **Part Name** | **Picture** | **Description** | **Key Dimensions (Critical)** | **Key Dim. Value (Inch is default)** | **Material** |
| **Drive_Rod** |  | Inserts into the inner tubing, allows for actuation of tweezer/needle housing button. | Outer Diameter<br>Length | 0.04900<br>2.44000 | Steel, Brass |
| **Rod_Collar** |  | Provides physical stopper for actuation, setting the limits for the actuation range. Is glued to push rod, and rests against inside shaft of end fitting from spring tension on second, bored out disk (slides). | Shaft Diameter<br>Outer Diameter<br>Thickness<br>Flange Diameter<br>Flange Thickness<br>Set Screw Size | 0.05000<br>0.18000<br>0.22500<br>0.15000<br>0.12500<br>'0', 1/16" length | SLA Plastic |
| **Rod_Bushing** | 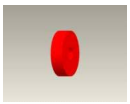 | Provides physical stopper for actuation, setting the limits for the actuation range. Is glued to push rod, and rests against inside shaft of end fitting from spring tension on second, bored out disk (slides). | Shaft Diameter<br>Outer Diameter<br>Thickness | 0.07500<br>0.18650<br>0.05000 | Plastic:<br>Nylon<br>Acetyl<br>Teflon |
| **Rod_Spring** | 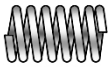 | Provides resistance and allows for home location for actuation assembly (rod and disk). | Outer Diameter<br>Thickness<br>Compressed Length<br>Length<br><br>Inner Diameter | 0.18750<br>0.01200<br>0.24000<br>0.93750<br><br>0.16350 | Steel |
| **End_Fitting** | 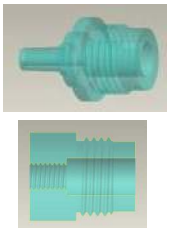 | Screws into lower housing, contains the entire range of push rod/disk actuation (exists inside bushing). A luer fitting on the end is where the actuator cable inserts. | Shaft Diameter - was 0.0937<br>Inner Diameter<br>Outer Diameter<br>Thread Pitch<br>Thread Angle<br>Thread Length<br>Thread Height<br>Thread Diameter<br>Hub Diameter<br>Inner Length - was 0.25, 0.4688<br>Length<br>Luer Angle | 0.09500<br>0.25000<br>0.60000<br>0.05000<br>60.00000<br>0.03750<br>0.02706<br>0.50000<br>0.44600<br>0.48000<br>0.98000<br>7.00000 | Steel |
| **Luer_Front_Fitting** | 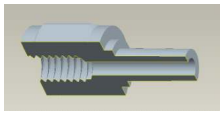 | | Body OD (housing)<br>Body ID (shaft)<br>Term 1 Thread **(female)**<br>Term 2 OD (luer male fitting) | 0.37500<br>0.09300<br>10-32<br>0.25000 | Stainless Steel |
| **Luer_Back_Fitting** | 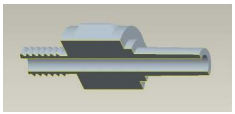 | | Body OD (housing)<br>Body ID (shaft)<br>Term 1 Thread **(male)**<br>Term 2 OD (luer male fitting) | 0.37500<br>0.09300<br>10-32<br>0.25000 | Stainless Steel |

Images from www.mcmaster.com included.

## B.2.2 - Upper Housing

| Part Description | | | | | |
|---|---|---|---|---|---|
| Part Name | Picture | Description | Key Dimensions (Critical) | Key Dim. Value (Inch is default) | Material |
| Worm_Bearing | 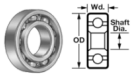 | Bearing for upper housing worm wheel assembly. Open Bearing Style. General Purpose. | Shaft Diameter - 1/8<br>Outside Diameter - 3/8<br>Width - 0.1094 | 0.12500<br>0.37500<br>0.10940 | Stainless Steel |
| Worm_Bushing | 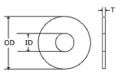 | Bushing for upper housing worm wheel assembly. Thrust Sleeve Bearing. | Shaft Diameter - 1/8<br>Outside Diameter - 3/8<br>Thickness - 0.040 | 0.12500<br>0.37500<br>0.04000 | Teflon |
| Worm |  | Worm wheel in upper housing for rotation functionality of lower housing luershaft. Double Teeth | Shaft Diameter (B) - 0.1248<br>Pitch Diameter (P.D.) - 0.333<br>Set Screw Size - #2-56<br>Lead Angle - 7'7'<br>Lead - 0.0654<br>Face Width - 9/16<br>Length - 3/4<br>Outside Diameter - 3/8<br>Hub Diameter - 0.312<br>Pressure Angle - 20 | 0.12480<br>0.33300<br>#2-56<br>7-7'<br>0.06540<br>0.56250<br>0.75000<br>0.37500<br>0.31200<br>20.00000 | Stainless Steel |
| Worm_Shaft |  | This shaft will connect the worm wheel, worm bearing, and worm bushing inside the upper housing. | Outer Diameter<br>Length | 0.12480<br>1.00000 | Steel, Stainless<br>Steel |
| Upper_Housing |  | This will house the upper assembly, the worm wheel, bearing, bushing, and then allow for attachment to lower housing and assembly. | Shaft Diameter<br>Outer Length<br>Outer Width<br>Outer Depth<br>Screw Hole Size | 0.38000<br>0.98000<br>0.75000<br>0.55750<br>0.08750 | Stainless Steel |
| Knob |  | Knob will allow user to rotate worm wheel and rotate luershaft and tool tip. | Shaft Dimension<br>Diameter<br>Shaft Length<br>Total Length<br>Set Screw Type | 0.37500<br>0.50000<br>0.52<br>0.63000<br>#6-32 | Aluminum |
| Mounting_Bracket_Signatone | 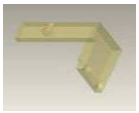 | Used to mount the integration device to the Signatone Micropositioner | Top Thickness<br>Side Thickness<br>Screw Hole Size<br>Mounting Screw Hole Size | 0.18750<br>0.18750<br>0.08750<br>0.18750 | Stainless Steel |
| Mounting_Bracket_Narishige | 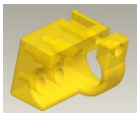 | Used to mount the integration device to the Narishige Micropositioner stage | Top Thickness<br>Side Thickness<br>Screw Hole Size<br>Mounting Ring Size | 0.18750<br>0.18750<br>0.08750<br>0.18750 | Stainless Steel |
| Mounting_Bracket_Sutter | 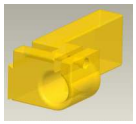 | Used to mount the integration device to the Sutter Micromanipulator | Top Thickness<br>Side Thickness<br>Screw Hole Size<br>Mounting Ring Size | 0.18750<br>0.18750<br>0.08750<br>0.18750 | Stainless Steel |

Images from www.mcmaster.com and www.sdp-si.com included.

# B.3 - Manual Linear Actuator

| | Part Description | | | | |
|---|---|---|---|---|---|
| Part Name | Picture | Description | Key Dimensions (Critical) | Key Dim. Value (Inch is default) | Material |
| Actuator_Cap | 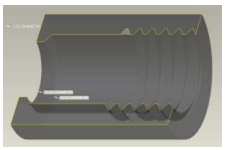 | Bearing for upper housing worm wheel assembly. Open Bearing Style. General Purpose. | Outer Diameter<br>Shaft Diameter<br>Shaft Thread Diameter<br>Lip Diameter<br>Lip Length<br>Shaft Length<br>Total Length<br>Thread Pitch<br>Thread Angle<br>Thread Length<br>Thread Height<br>Thread Diameter | 0.50000<br>0.30000<br>0.37500<br>0.25000<br>0.03125<br>0.55000<br>0.60000<br>0.05000<br>60.00000<br>0.30000<br>0.02706<br>0.37500 | Aluminum |
| Cable_Sleeve_End |  | Bushing for upper housing worm wheel assembly. Thrust Sleeve | Outer Diameter<br>Hub Diameter<br>Cable Hole Diameter<br>Shaft Diameter<br>Hub Length<br>Cable Hole Length<br>Shaft Length<br>Total Length | 0.30000<br>0.25000<br>0.22000<br>0.25000<br>0.05000<br>0.10000<br>0.25000<br>0.35000 | Aluminum |
| Cable_Nut |  | Worm wheel in upper housing for rotation functionality of lower housing luershaft. Double Teeth | Outer Diameter<br>Shaft Diameter<br>Shaft Thread Diameter<br>Cable Hole Diameter<br>Shaft Length<br>Cable Hole Length<br>Total Length | 0.17050<br>0.10000<br>0.10250<br>0.01000<br>0.31500<br>0.03000<br>0.20000 | Aluminum |
| Ball_Bearing |  | This shaft will connect the worm wheel, worm bearing, and worm bushing inside the upper housing. | Outer Diameter | 0.12500 | Steel, Stainless Steel |
| Actuator_Spring | 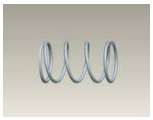 | | Outer Diameter<br>Inner Diameter<br>Wire Thickness<br>Length | 0.31250<br>0.25000<br>0.02200<br>1.00000 | Stainless Steel |

| | Part Description | | | | |
|---|---|---|---|---|---|
| Part Name | Picture | Description | Key Dimensions (Critical) | Key Dim. Value (Inch is default) | Material |
| Actuator_Puck |  | Knob will allow user to rotate worm wheel and rotate luershaft and tool tip. | Outer Diameter<br>Hub Diameter<br>Hub Thread Diameter<br>Sleeve Diameter<br>Shaft Diameter<br>Hub Length<br>Sleeve Length<br>Shaft Length<br>Total Length | 0.25000<br>0.10000<br>0.14000<br>0.31000<br>0.20000<br>0.15000<br>0.15000<br>0.40000<br>0.95800 | Brass |
| Actuator_Housing | 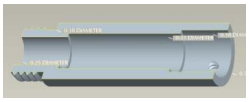 | Houses the actuator puck and micrometer, providing location for internal actuation. | Outer Diameter<br>Shaft Diameter<br>Inner Diameter<br>Hub Internal Diameter<br>Hub Outer Diameter<br>Hub Length<br>Hub Internal Length<br>Shaft Length<br>Total Length | 0.50000<br>0.37500<br>0.31250<br>0.25000<br>0.37500<br>0.25000<br>0.35000<br>1.20000<br>1.55350 | Aluminum |
| Nitinol Cable |  | Driving cable that is actuated by micrometer, and that sends actuation from actuator to the docking head. | Outer Diameter<br>Length | 0.01050<br>12.00000<br>.0085?? | |
| Nitinol Sleeve |  | Sleeve that nitinol cable runs throught, provides tether-cable system, allowing actuation to translate from remote actuator to docking head. | Outer Diameter<br>Inner Diameter<br>Length | 0.02150<br>>0.0105<br>12.00000 | Nitinol |
| Needle Housing | 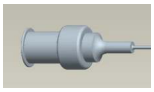 | Houses the actual projecting nitinol cable from the sleeve, directing this actuating element to the drive components of docking head and providing protection. With needle shaft, can help house nitinol tubing. | Gauge | 20.00000 | |

Images from www.memry.com included.

# APPENDIX C

# SOFTWARE CODING SAMPLES

## C.1 - Geometric Modeling Software Program - Graphical User Interface

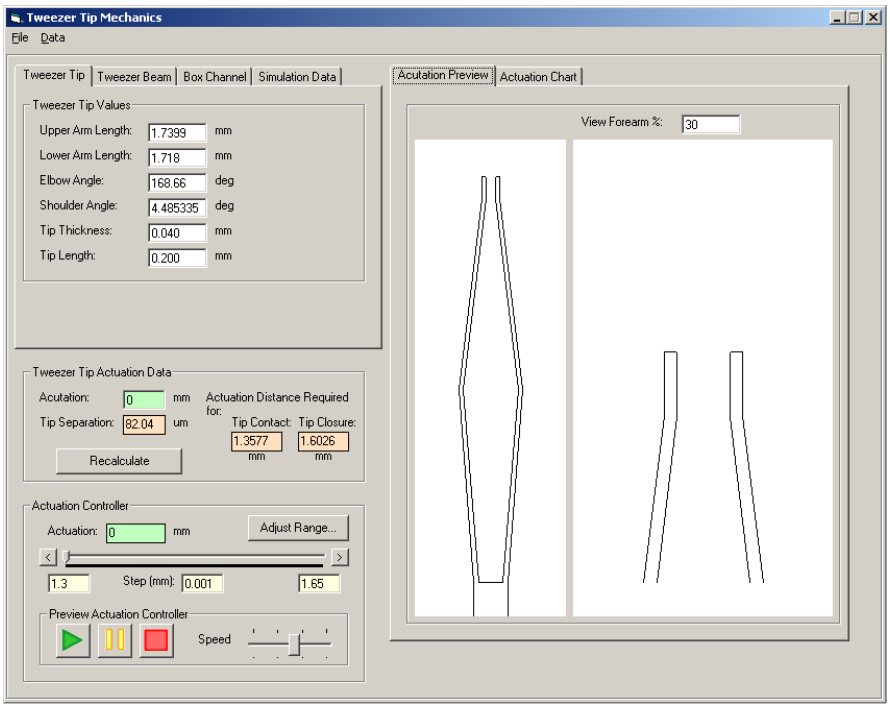


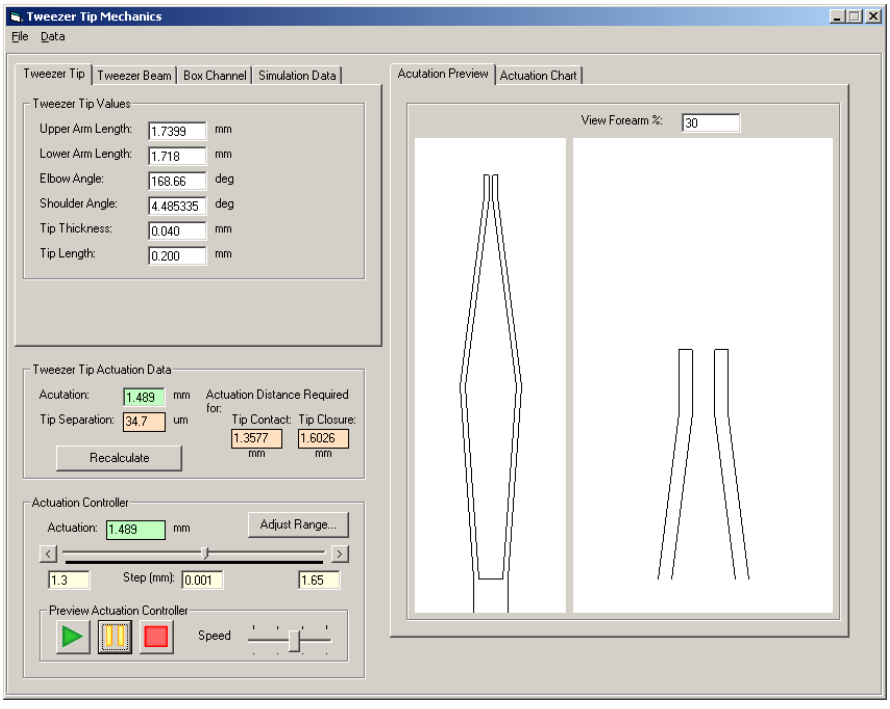

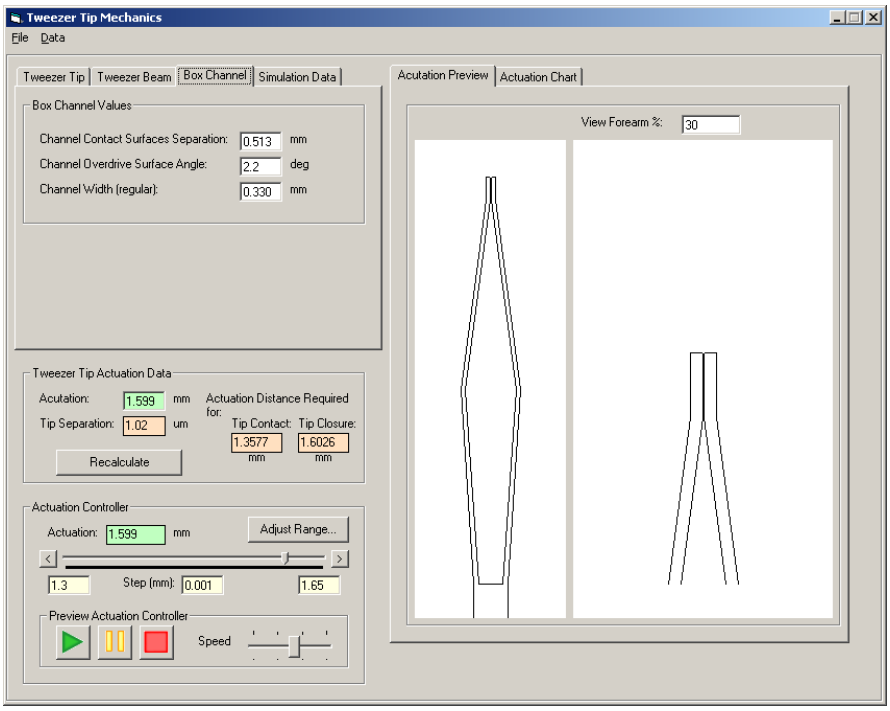


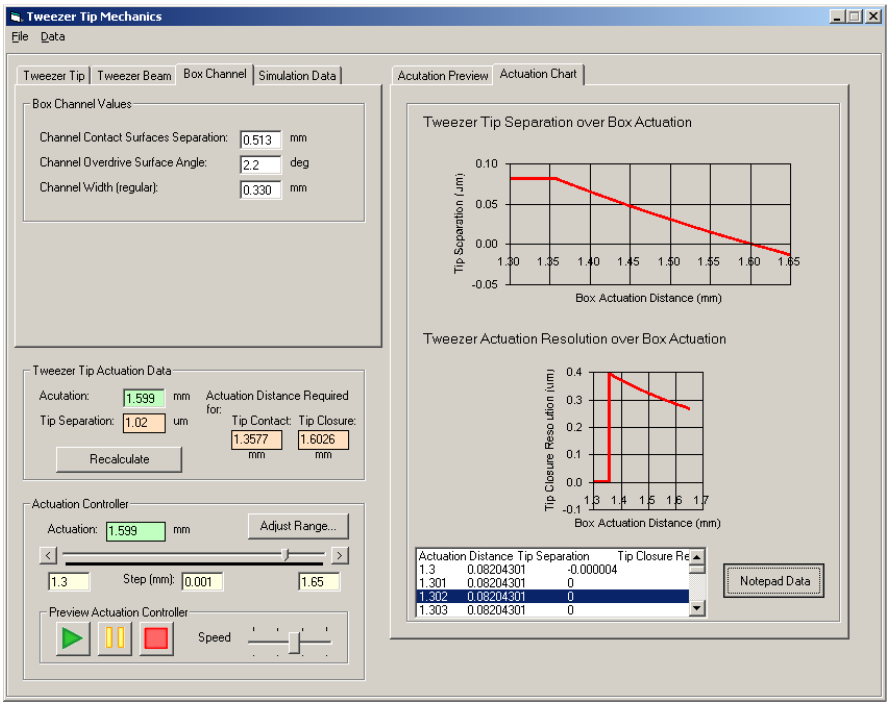

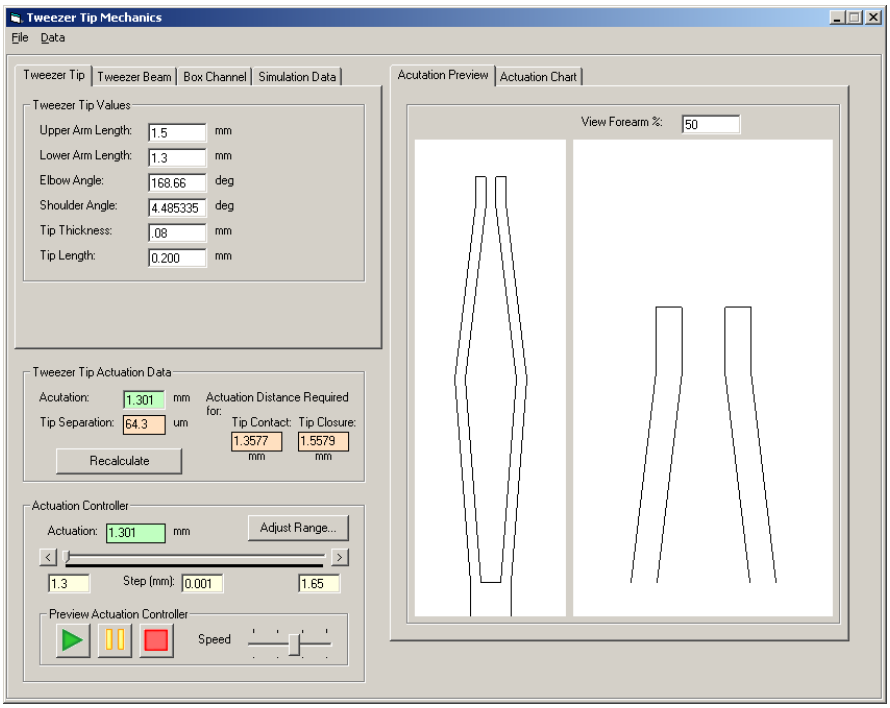


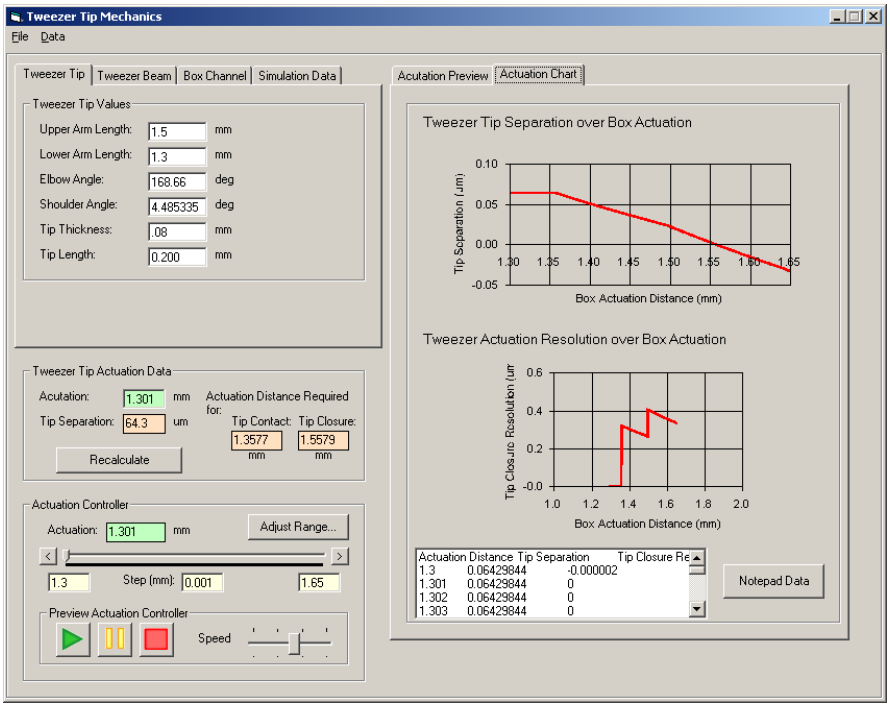

## C.2 - Geometric Modeling Software Program - Code

```
'CALCULATE PARAMETERS
    Public Sub CalculateParameters()
        'This function will calculate the non-static parameters for tweezer tips
        Dim dMMVertMax1, dMMHorzMax1, dMMVertMax2, dMMHorzMax2 As Double
        Dim iTemp As Integer

        On Error GoTo ErrorProcess
            'Non-Variable Dependent
            dBUO = Sin(dPhiO * PI / 180) * dCU
            dAUO = Cos(dPhiO * PI / 180) * dCU
            dB1O = (dN / 2) - dBeam
            dA1O = dB1O / (Tan(dPhiO * PI / 180))
            dC1O = dB1O / Sin(dPhiO * PI / 180)
            dAUT = Sqr(dCU ^ 2 - dB1O ^ 2)
            dThetaUO = 90 - dPhiO
            dThetaFO = dThetaTotal - dThetaUO
            dAFO = dCF * Sin(dThetaFO * PI / 180)
            dBFO = dCF * Cos(dThetaFO * PI / 180)

            dTSO = (dBUO - dBFO - dTipThickness + dBeam) * 2


        'PICTURE SCALING DETERMINATION
          iDrawSpace = 500
          'TOTAL TWEEZER PICTURE
            'VERTICAL MAX - determine vertical limit of tweezer in millimeters (arbitrary value here)
            dMMVertMax1 = (dCU + dCF + dTipLength) * DRAWING_MAX_DIMENSION_MULTIPLIER
            dMMHorzMax1 = (dBUO + dBFO) * 2 * DRAWING_MAX_DIMENSION_MULTIPLIER

            'SCALE FACTOR FOR PICTURE BOX (number of pixels per millimeter)
            iTemp = (ActuationPreviewPictureBox.Height - iDrawSpace * 2) / dMMVertMax1
            iDrawScaleFactor1 = (ActuationPreviewPictureBox.Width - iDrawSpace * 2) / dMMHorzMax1

            'Determine is more scaling is needed in horzontal direction or vertical,
            '  set all scaling to lower scaling value
            If (iDrawScaleFactor1 > iTemp) Then
                iDrawScaleFactor1 = iTemp
            End If ' test for lower scaling factor (so scaled image doesnt exceed dimensions of picture box



            'Variable Dependent
            'CalculateVariables
            UpdateTextBoxes (UPDATE_TEXT_BOX_PARAMETERS)

        Exit Sub

ErrorProcess:

        MsgBox "Inputted parameter values are invalid"

    End Sub 'CalculateParameters
```

```
'CALCULATE VARIABLES
    Public Sub CalculateVariables()
        'This function will calculate the non-static parameters for tweezer tips
        'For clarity:
        '  A1X - is the actuation distance (input variable)
        '  A1O - minimum actuation distance required for contact
        '  B1O - horizontal/lateral distance from shoulder to contact surface
        '  PhiX - angle of shoulder
        '  AUX - current vertical length of upper arm

            'Variable Dependent

        'DRIVE / OVERDRIVE ACTUATION RANGE determination
            'If the tweezer elbow is past the box contact points,
            '  then the 'overdrive' angled inner contact point (B1) shrinks
            If (dA1X > dAUT) Then
                dB1X = dB1O - ((dA1X - dAUT) * (Tan(dOmega * PI / 180)))
            Else
                dB1X = dB1O
            End If 'test to see if elbow is past contact points

        'UPPER ARM GEOMETRY calculations
            'If the tweezer tips have made contact with the box contact points
            If (dA1X >= dA1O) Then
                'CONTACT
                  'Shoulder angle
                    dPhiX = Atn(dB1X / dA1X) * 180 / PI
                  'Upper(U) arm - Current vertical length of upper (U) arm
                    dAUX = dCU * Cos(dPhiX * PI / 180)
                  'Upper(U) arm - Current horizontal length of upper (U) arm
                    dBUX = dCU * Sin(dPhiX * PI / 180)

            Else
                'NO CONTACT made yet (not actuated enough...)
                dPhiX = dPhiO
                dAUX = dAUO
                dBUX = dBUO

            End If 'test to see if tips in contact with box

        'ELBOW, FOREARM GEOMETRY calculations
            'Calculate values based on set values above
              'Hypothetudinal length from shoulder to contact point
                dC1X = dB1X / Sin(dPhiX * PI / 180)
              'Overall Horz width from elbow to elbow - includes Horz length and beam thickness
                'dW = (dBUX + dBeam) * 2
              'Elbow angle of upper arm
                dThetaUX = 90 - dPhiX
              'Elbow angle of forearm
                dThetaFX = dThetaTotal - dThetaUX
              'Horz length of forearm (helps determine tip separation)
                dBFX = dCF * Cos(dThetaFX * PI / 180)
                dAFX = dCF * Sin(dThetaFX * PI / 180)

                dTSX = (dBUX - dBFX - dTipThickness + dBeam) * 2

    End Sub 'CalculateVariables
```

```
    Public Sub CalculateTipClosure()
        'This function will calculate the actuation distance required to close tips

        Dim Const1 As Double
        Dim Const2 As Double
        Dim Const3 As Double
        Dim dTAR As Double

        'TIP SEPARATION '
              'Tip Separation '
                Const1 = -dCF * Sin(dThetaTotal * PI / 180)
                Const2 = (dCU - dCF * Cos(dThetaTotal * PI / 180))
                Const3 = (dTipThickness - dBeam) ^ 2

                'dTSX = (dCU * Sin(Atn(dB1X / dA1X)) - dCF * Cos((dThetaTotal - 90 + Atn(dB1X / dA1X) * 180 / P
                'dTSX = ((((-1) * dCF * Sin(dThetaTotal * PI / 180)) + (dCU + (-1) * dCF * Cos(dThetaTotal * PI
                'dTSX = ((Const1 + Const2 * (dB1X / dA1X)) / (1 + (dB1X / dA1X) ^ 2) ^ 0.5 - dTipThickness + dB

                dTAR = (-(2 * Const1 * Const2) - ((2 * Const1 * Const2) ^ 2 - 4 * (Const2 ^ 2 - Const3) * (Cons

                dATipClosure = dB1O / dTAR
                'Test if Drive/Overdrive required for tip closure - more calculations needed for overdrive
                If (dATipClosure > dAUT) Then

                    dATipClosure = (dB1O / dTAR + (dAUT * Tan(dOmega * PI / 180) / dTAR)) * (1 / (1 + Tan(dOmeg

                End If ' test to see if overdrive needed to get to tip closure

    End Sub 'CalculateTipClosure
```

```
'UPDATE TEXT BOXES
    Public Sub UpdateTextBoxes(Optional UpdateWhichBoxes As Integer = 0)
        'This will update the parameter text boxes with the current
        '  values, and will only updated visible text boxes to save
        '  processor time

            'PARAMETERS ONLY
            If (UpdateWhichBoxes = UPDATE_TEXT_BOX_PARAMETERS) Then

                ThetaUOText.Text = Round(dThetaUO, OUTPUT_VARIABLE_RESOLUTION)
                ThetaFOText.Text = Round(dThetaFO, OUTPUT_VARIABLE_RESOLUTION)
                AUOText.Text = Round(dAUO, OUTPUT_VARIABLE_RESOLUTION)
                BUOText.Text = Round(dBUO, OUTPUT_VARIABLE_RESOLUTION)
                AUTText.Text = Round(dAUT, OUTPUT_VARIABLE_RESOLUTION)
                A1OText.Text = Round(dA1O, OUTPUT_VARIABLE_RESOLUTION)
                B1OText.Text = Round(dB1X, OUTPUT_VARIABLE_RESOLUTION)
                C1OText.Text = Round(dC1O, OUTPUT_VARIABLE_RESOLUTION)

            'VARIABLES ONLY
            ElseIf (UpdateWhichBoxes = UPDATE_TEXT_BOX_VARIABLES) Then

                AUXText.Text = Round(dAUX, OUTPUT_VARIABLE_RESOLUTION)
                B1XText.Text = Round(dB1X, OUTPUT_VARIABLE_RESOLUTION)
                BFXText.Text = Round(dBFX, OUTPUT_VARIABLE_RESOLUTION)
                BUXText.Text = Round(dBUX, OUTPUT_VARIABLE_RESOLUTION)
```

```
Sub ValidateModelValues()
    'This function will run simple checks on tweezer tip values given to
    '  make sure they are within tolerances
    Dim dVertLengthOverdriveSurface As Double

    'CHECK TO MAKE SURE TWEEZER WILL ACTUALLY CLOSE

    'TWEEZER TIP
        'CHECK ELBOW ANGLE
        'If ((180 - 2 * dPhiO) <= dThetaTotal) Then
        If (180 <= dThetaTotal) Then
             MsgBox "The Elbow Angle is too wide, tweezer tips will not close"

        End If


    'BOX
        'CHECK ACTUATION RANGE
            'OVERDRIVE RANGE
              'Calculate the vertical length of overdrive surface
                dVertLengthOverdriveSurface = (dN - dChannelWidth) / (2 * Atn(dOmega * PI / 180))
              'Calculate the total actuation range considering entire vertical length of overdrive surface
                dMaxActuationRangePastOverdrive = dVertLengthOverdriveSurface + dAUT
                If (dATipClosure > dMaxActuationRangePastOverdrive) Then
                    MsgBox "There is not sufficient actuation range to close a tweezer with these geometrie
                End If 'test actuation max range

            'BOX COVERING THE TIPS FROM ACTUATION
              'Calculate the distance from actuation start to overdrive begin, then add vertical length of
                dMaxActuationRangeCovered = (dAUT + (dCF * Sin(dThetaFO * PI / 180)))
                If (dATipClosure > dMaxActuationRangeCovered) Then
                    MsgBox "There is not sufficient actuation range to close a tweezer without tips being w
                End If 'test actuation max range


    'VIEW PERCENTAGE OF FOREARM for tip picture
    If (Trim(ViewForearmText.Text) = "") Then ViewForearmText.Text = 0
    If (CInt(ViewForearmText.Text) <= 100) Then

        If (CInt(ViewForearmText.Text) >= 0) Then

        Else
            MsgBox "The Forearm View Percentage value must be between 0 and 100"
            ViewForearmText.Text = 50
        End If

    Else
        MsgBox "The Forearm View Percentage value must be between 0 and 100"
        ViewForearmText.Text = 50

    End If 'Test view Forearm Percentage


End Sub 'ValidateModelValues
```

```
'CHART SETUP
    'This will set the chart axis, labels, grids, and general design
    Public Sub SetUpCharts(Optional whichChart As Integer = 1)

      'TIME TO NUCLEUS CHART
        'Type
        'TimeToNucleusMSChart(whichChart).chartType = VtChChartType2dCombination

        'Specifying types of charts for frequency and distribution graphs
        'ActuationChart.Plot.SeriesCollection(1).SeriesType = VtChSeriesType2dXY
        'TimeToNucleusMSChart(whichChart).Plot.SeriesCollection(CHART_TIME_TO_NUCLEUS_DISTRIBUTION).SeriesType

        'Y/X Axis Label, Ticks
        ActuationChart.Plot.Axis(VtChAxisIdY).AxisTitle = "Tip Separation (um)"
        ActuationChart.Plot.Axis(VtChAxisIdX).AxisTitle = "Box Actuation Distance (mm)"
        ActuationResolutionChart.Plot.Axis(VtChAxisIdY).AxisTitle = "Tip Closure Resolution (um)"
        ActuationResolutionChart.Plot.Axis(VtChAxisIdX).AxisTitle = "Box Actuation Distance (mm)"
        'MSChart.Plot.Axis(VtChAxisIdY).AxisTitle = "Tip Separation (mm)"
        'MSChart.Plot.Axis(VtChAxisIdX).AxisTitle = "Box Actuation Distance (mm)"
```

-

-

-

```
    'Normal Distribution
    'Poisson Distribution
    Public Sub SimTipClosureGraph(Optional whichChart As Integer = 1)

        Dim counter, counter2, numMotorsAtNucleus, iLoopCount As Integer
        Dim dA1Xtemp, dB1Xtemp, dPhiXtemp, dBUXtemp, dBFXtemp As Double
        Dim tempChart() As Variant

        iLoopCount = ((dActuationControlMax - dActuationControlMin) / dActuationControlStep)
        ActuationDataList.Clear
        ActuationDataList.AddItem ("Actuation Distance" & vbTab & "Tip Separation" & vbTab & "Tip Closure Resol

        'Set Chart data to size for simulation
        'ReDim chartData(1 To 2, iLoopCount - 1)
        ReDim chartData(iLoopCount, 1)
        ReDim chartDataResolution(iLoopCount, 1)

        chartData(0, CHART_POS_ACTUATION_POS) = "Box Actuation Distance (mm)"
        chartData(0, CHART_POS_TIP_CLOSURE) = "Tip Closure (um)"
        chartDataResolution(0, CHART_POS_ACTUATION_POS) = "Box Actuation Distance (mm)"
        chartDataResolution(0, CHART_POS_TIP_CLOSURE) = "Tip Closure Resolution (um)"

        chartData(1, CHART_POS_ACTUATION_POS) = dActuationControlMin
        chartData(1, CHART_POS_TIP_CLOSURE) = dTSO

        'Initializing arrays
        For counter = 2 To iLoopCount

            dA1Xtemp = dActuationControlMin + ((counter - 2) * dActuationControlStep)

            'DRIVE / OVERDRIVE ACTUATION RANGE determination
                'If the tweezer elbow is past the box contact points,
                '  then the 'overdrive' angled inner contact point (B1) shrinks
```

-

-

-

```
'TWEEZER DRAWING
    'Will draw next motor positions on Simulation Replay Picture Box
    Public Sub DrawTweezerPosition()

        'TEMP VARIABLES
        Dim counter, counter2, numMotorsToDisplay As Integer
        Dim iCircleRadiusBig As Integer
        Dim dMMVertMax1, dMMHorzMax1, dMMVertMax2, dMMHorzMax2 As Double
        Dim iTemp As Integer
        Dim iHorzCenter, iVertCenter As Integer
        Dim sX1, sY1, sX2, sY2, sXTemp, sYTemp As Single
        Dim iDrawBeamThickness As Integer

        ActuationPreviewPictureBox.Cls
        ActuationPreviewTipsPictureBox.Cls

    'TWEEZER: PICTURE POSITIONING
        'Determine where to start drawing the tweezer beam
        iHorzCenter = ActuationPreviewPictureBox.Width / 2
        iVertCenter = ActuationPreviewPictureBox.Height / 2
        iDrawBeamThickness = dTipThickness * iDrawScaleFactor1

    'DRAW TWEEZER
        ActuationPreviewPictureBox.AutoRedraw = True
        ActuationPreviewPictureBox.DrawWidth = 1
        'iDrawSpace = 500
```

-

-

-

# APPENDIX D

# BIOLOGICAL PROTOCOLS

## D.1 - Fluo-5F Fluorescence Imaging

### D.1.1 - Background (derived from www.invitrogen.com documentation)

Fluo-5F is a high affinity calcium imaging dye that exhibits unchelated intracellular calcium presence. While substantially lower in affinity compared to Fluo-4 dye (Kd = 345 nM), the Kd value of Fluo-5F for Ca2+ binding is 2.3 μM. This will allow identification of events where calcium influx are more intense, as regular intracellular calcium concentration ($[Ca^{2+}]_i$) is 100 nM which is much closer to the binding constant of Fluo-4. When the calcium concentration reaches The Fluo-5F molecule is originally bound with an acetoxymethyl ester (AM) group, which due to hydrophobic properties allows movement of the complete molecule across a cellular plasma membrane. Once a complete molecule moves into a cell, this AM group is cleaved by intracellular enzymes, which causes the Fluo-5F molecule to remain inside the cell as subsequent plasma membrane movement is prevented. If Fluo-5F AM molecules are added to culture media, a substantial portion of the Fluo-5F molecules are eventually internalized into the cells via this one-way mechanism. Because intracellular calcium concentration is substantially lower than the extracellular concentration, the extracellular Fluo-5F molecules will fluoresce more readily than those inside the cell. Given the ubiquity of the culture media, cellular contrast can only be resolved if the extracellular Fluo-5F molecules are removed, which requires the replacement of the culture media with fresh media.

When exposed to a FITC light (or more specifically, an energy source with a wavelength of 494 nm), the spectral emission of the Fluo-5F molecule is at 516-518 nm. Fluorescent images can be captured using a CCD camera (ex: Photometrics QuantEM 512SC) that can capture this wavelength. The Fluo-5F dye can be excited using a LED

source with the proper wavelength (ex: Prizmatix TLCC-01-Triple LED). Following baseline measurements of fluorescent intensity, fluorescence level (intensity, duration or rate of change) can be collected for either electrical activity or mechanical insult/injury (membrane permeability resulting in increased intracellular calcium). This level can be compared to baseline, and used to assess activity or injury level for one or more neurons in an established neuronal network.

For injury studies, fast-receptor neurotransmitter antagonists (Section D.2) present in culture media during imaging can limit fluorescence changes due to sporadic and network electrical activity. This measure of control allows fluorescence change to be more attributed to injury-induced cellular uptake of $Ca^{2+}$.

### D.1.2 - Calcium Affinity

| | **Kd Value ($Ca^{2+}$)** |
|---|---|
| Fluo-4 | 345 nM |
| Fluo-5F | 2.3 uM |
| Fluo-4FF | 9.7 uM |
| Fluo-5N | 90 uM |
| Mag-Fluo-4 | 22 uM (also selective for Mg2+) |

$[Ca^{2+}]_i$: ~100 nM; $[Ca^{2+}]_e$: 1.8 mM -> ($10^4$ membrane gradient)

### D.1.3 - Absorption / Emission Spectrum

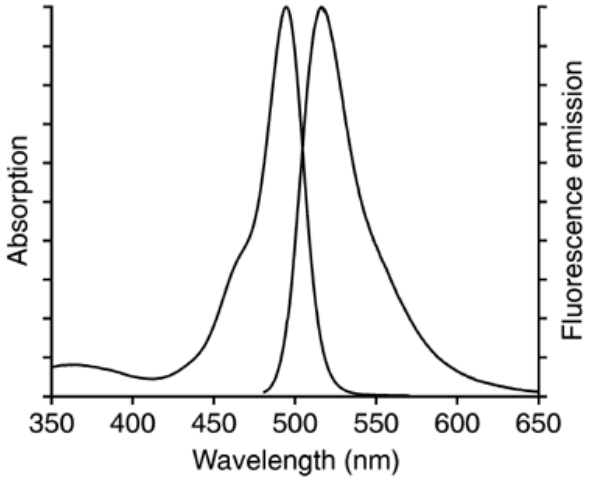


**Figure D.1**: Absorption and Emission Spectrum for Fluo-4, which is comparable to other dyes in the Fluo family. This chart is from the Invitrogen website (www.invitrogen.com).

### D.1.4 - Preparation of Fluo-5F Aliquots

D.1.4.1 - Solution Components (from www.invitrogen.com and www.sigmaaldrich.com)

*Fluo-5F*

MW: 1100.92 g/mol

$C_{50}H_{47}F_3N_2O_{23}$

Ordering: Fluo-5F, AM *cell permeant* - Invitrogen (F-14222)

Store: Solid at -20°C, Aliquot at -20°C

*Dimethylsulfoxide (DMSO)*

MW: 78.13 g/mol

$C_2H_6OS$

Ordering: Dimethyl sulfoxide anhydrous, ≥99.9% - Sigma Aldrich (276855)

Store: Room Temperature

*Pluronic F-127 (purchased in DMSO solution)*

MW: ~12500 g/mol

$C_{50}H_{47}F_3N_2O_{23}$

Ordering: Pluronic® F-127 *20% solution in DMSO* - Invitrogen (P-3000MP)

Store: Liquid at -4°C, Aliquot at -20°C

D.1.4.2 - Solution Preparation (Fluo-5F+DMSO+pluronic f-127 ) - 1 mL of solution

When preparing the dye, care should be taken to minimize light exposure (e.g. wrap foil around the 15 ml centrifuge tube used for preparing the mixture). This recipe is primarily derived from Ikegaya [191], and adapted by Dr. Steve Potter's research group and Dr. Jim Ross.

1. Begin with one 50 µg vial of Fluo-5F powder (Invitrogen)
2. Add 45 µL of anhydrous DMSO into the Fluo-5F vial

   Note: Mix gently but thoroughly with the micro-pipetter to dissolve powder
3. Add the DMSO-Dye solution to 1 ml of artificial cerebral spinal fluid (ACSF) (use the foil-wrapped 15 mL centrifuge tube)
4. Add 1 µl of pluronic F-127 and vortex the whole solution
5. Partition into 10 aliquots of 100 µl units. Store in -80 ºF freezer

**D.1.5 - Loading of Fluo-5F into Neuronal Cultures**

When loading the dye, care should be taken to minimize light exposure (e.g. wrap foil around the top and bottom (independently) of a petri-dish and use to transport vials

and dishes). This protocol is primarily derived from Ikegaya [191], and adapted by Dr. Steve Potter's research group and Dr. Jim Ross.

1. Remove all of the media from the culture dish
2. Add back in 400 µl of ACSF to the culture dish
3. Add 100 µl of aliquoted Fluo-5F dye to the center of the dish
4. Store dish in 34 ºF incubator for 35 minutes
5. Remove dye-rich media from culture dish and apply 1 ml of preferred media

## D.2 - Neurotransmitter Blockers (fast-receptor antagonist)

### D.2.1 - Background

Neurons can release neurotransmitters from the cell membrane into neuronal synapses during changes in plasma membrane potential and other external stimuli. These released neurotransmitters can bind to receptors on the post-synaptic plasma membrane of a neighboring neuron, which can then affect a variety of cellular properties and mechanisms, including membrane potential (via combination with ion channels), gene expression, and/or subsequent uptake of additional neurotransmitter. This mechanism of neurotransmitter release by the effector neuron and response by neighboring neurons is considered neuronal communication. Chemical agents in the synapse, including neurotransmitters, compete with each to bind with the various receptors on the surface of the post-synaptic neuron. Receptor antagonists are physiological or non-physiological molecules that closely mimic a specific neurotransmitter, but that do not, upon binding with a receptor, affect the cellular properties or mechanisms of the post-synaptic neuron. Thus, with the systemic presence of receptor antagonists in the culture media (and

subsequently, the synapse), the communication ability from one neuron to the next is severely reduced.

The fast synaptic receptor antagonist media that inhibits network activity and spontaneous firing is composed of Bicuculline methiodide (BMI, 50 μM), 2-amino-5-phosphonova-leric acid (APV, 100 μM), and 6-cyano-7-nitroquinoxaline-2,3-dione (CNQX, 10 μM) [194]. BMI is a receptor antagonist of the γ-aminobutric acid (GABA) receptor, which is a major inhibitory neurotransmitter use in the brain. BMI also inhibits or blocks some calcium activated potassium channels [195]. APV is a receptor antagonist of the N-methyl d-aspartate (NMDA) receptor, which is a fast receptor that is a coincidence detector, as it is gated by both glycine and glutamate, and that forms a calcium channel when activated. APV inhibits the glutamate binding site of the NMDA receptor [28]. CNQX is a receptor antagonist for the α-amino-3-hydroxy-5-methyl-4-isoxazolepropionic acid receptor (AMPA), which is a receptor activated by glutamate binding that forms a channel that is permeable to sodium, potassium, and calcium [196].

### D.2.2 - Preparation of Fast-Receptor Antagonist Aliquots

D.2.2.1 - Solution Components (from www.sigmaaldrich.com)

*Bicuculline methiodide (BMI)*

MW: 509.29 g/mol

$C_{21}H_{20}INO_6$

Ordering: 1(S),9(R)-(−)-Bicuculline methiodide - Sigma Aldrich (14343)

Store: Solid at -20°C, Aliquot at -20°C

*2-amino-5-phosphonova-leric acid (APV)*

MW: 197.13 g/mol (anhydrous base)

$C_9H_2N_4Na_2O_4 \times H_2O$

Ordering: DL-2-amino-5-phosphonopentoic-acid - Sigma Aldrich (A5282)

Store: Solid at -20°C, Aliquot at -20°C

*6-cyano-7-nitroquinoxaline-2,3-dione (CNQX)*

MW: 276.12 g/mol (anhydrous base)

$C_9H_2N_4Na_2O_4 \times H_2O$

Ordering: CNQX disodium salt hydrate - Sigma Aldrich (C239)

Store: Solid at -20°C, Aliquot at -20°C

*Artificial Cerebral Spinal Fluid (ACSF)*

Combine into DI $H_2O$ (start with 700 mL, add chemicals, fill to 1 L)

| | Concentration (mM) | Grams (1 L) | Grams (2 L) |
|---|---|---|---|
| NaCl | 126 | 7.335 | 14.61 |
| KCl | 2.5 | 0.186 | 0.373 |
| $MgCl_2 \times 6H_2O$ | 1 | 0.204 | 0.407 |
| $CaCl_2 \times 2H_2O$ | 2 | 0.290 | 0.588 |
| $NaH_2PO_4 \times H_2O$ | 1.25 | 0.173 | 0.345 |
| $NaHCO_3$ | 26 | 2.18 | 4.36 |
| Glucose | 25 | 4.51 | 9.01 |
| Phenol Red (optional) | 0.5% | 5mg | 10mg |

*Always check pH and adjust to 7.4 (+/-) 0.1 and osmolarity to 300 (+/-) 20*

D.2.2.2 - Final Solution Concentrations (in ACSF) - (developed by Dr. Douglas Bakkum):

100 µM - (APV)

50 µM - (BMI)

10 µM - (CNQX)

Osmolality: 285

**D.2.3 - Using the Fast-Receptor Antagonists**

The concentration of blockers sufficient to block virtually all spontaneous activity was derived by Dr. Douglas Bakkum, and this protocol was developed by Dr. Steve Potter's research group and Dr. Jim Ross.

1. Following 35 minutes of bulk load of Fluo-5F dye, mix up 50 µM BMI, 100 µM APV, and 10 µM CNQX) in1 ml of ACSF in a 15 ml centrifuge tube
2. Vortex the ACSF and synaptic blockers
3. Withdraw all of the dye-rich media from the culture dish
4. Add in the ACSF with synaptic blockers.
5. After concluding experiments performed with loaded dyes and added blockers, sequentially rinse the dish 3 times with 1 ml of ASCF.
6. Finally, add back in 1 ml of your preferred culturing media.

# REFERENCES


[1] CDC, "Key Resources on Traumatic Brain Injury (TBI)," *http://www.cdc.gov/ncipc/,* 2004.

[2] M. C. LaPlaca, C. M. Simon, G. R. Prado, and D. K. Cullen, "Neurotrauma: New Insights into Pathology and Treatment," *Progress in Brain Research,* pp. 13-26, 2007.

[3] R. S. Cargill and L. E. Thibault, "Acute alterations in [Ca2+]i in NG108-15 cells subjected to high strain rate deformation and chemical hypoxia: An in vitro model for neural trauma," *Journal of Neurotrauma,* vol. 13, pp. 395-407, Jul 1996.

[4] M. C. LaPlaca, V. M. Y. Lee, and L. E. Thibault, "An in vitro model of traumatic neuronal injury: Loading rate-dependent changes in acute cytosolic calcium and lactate dehydrogenase release," *Journal of Neurotrauma,* vol. 14, pp. 355-368, Jun 1997.

[5] M. C. LaPlaca and L. E. Thibault, "An in vitro traumatic injury model to examine the response of neurons to a hydrodynamically-induced deformation," *Annals of Biomedical Engineering,* vol. 25, pp. 665-677, Jul-Aug 1997.

[6] P. L. McNeil and R. A. Steinhardt, "Loss, restoration, and maintenance of plasma membrane integrity," *Journal of Cell Biology,* vol. 137, pp. 1-4, Apr 7 1997.

[7] E. H. Pettus, C. W. Christman, M. L. Giebel, and J. T. Povlishock, "Traumatically Induced Altered Membrane-Permeability - Its Relationship to Traumatically Induced Reactive Axonal Change," *Journal of Neurotrauma,* vol. 11, pp. 507-522, Oct 1994.

[8] E. H. Pettus and J. T. Povlishock, "Characterization of a distinct set of intra-axonal ultrastructural changes associated with traumatically induced alteration in axolemmal permeability," *Brain Research,* vol. 722, pp. 1-11, May 25 1996.

[9] G. R. Prado, Ross, J.D. DeWeerth, S.P., LaPlaca, M.C. , "Traumatic loading to cultured neurons induces transient membrane permeability increases that

modulate electrophysiological activity," in *Society for Neuroscience Annual Meeting*, 2003.

[10] G. R. Prado, C. L. Caltagirone, and M. C. LaPlaca, "Neuronal plasma membrane disruption in the traumatically injured brain," *Journal of Neurotrauma,* vol. 21, pp. 1331-1331, Sep 2004.

[11] G. R. Prado, J. D. Ross, S. P. DeWeerth, and M. C. LaPlaca, "Mechanical trauma induces immediate changes in neuronal network activity," *J Neural Eng,* vol. 2, pp. 148-58, Dec 2005.

[12] D. H. Smith, J. A. Wolf, T. A. Lusardi, V. M. Y. Lee, and D. F. Meaney, "High tolerance and delayed elastic response of cultured axons to dynamic stretch injury," *Journal of Neuroscience,* vol. 19, pp. 4263-4269, Jun 1 1999.

[13] M. Ankarcrona, J. M. Dypbukt, E. Bonfoco, B. Zhivotovsky, S. Orrenius, S. A. Lipton, and P. Nicotera, "Glutamate-Induced Neuronal Death - a Succession of Necrosis or Apoptosis Depending on Mitochondrial-Function," *Neuron,* vol. 15, pp. 961-973, Oct 1995.

[14] D. Arciniegas, L. Adler, J. Topkoff, E. Cawthra, C. M. Filley, and M. Reite, "Attention and memory dysfunction after traumatic brain injury: cholinergic mechanisms, sensory gating, and a hypothesis for further investigation," *Brain Inj,* vol. 13, pp. 1-13, Jan 1999.

[15] A. C. Bain, R. Raghupathi, and D. F. Meaney, "Dynamic stretch correlates to both morphological abnormalities and electrophysiological impairment in a model of traumatic axonal injury," *J Neurotrauma,* vol. 18, pp. 499-511, May 2001.

[16] F. Barone, E. Ohlstein, A. Hunter, C. Campbell, S. Hadingham, A. Parsons, Y. Yang, and E. Shohami, "Selective antagonism of endothelin-A-receptors improves outcome in both head trauma and focal stroke in rat," *Journal of Cardiovascular Pharmacology,* vol. 36, pp. S357-S361, 2000.

[17] T. L. Butler, C. A. Kassed, P. R. Sanberg, A. E. Willing, and K. R. Pennypacker, "Neurodegeneration in the rat hippocampus and striatum after middle cerebral artery occlusion," *Brain Res,* vol. 929, pp. 252-60, Mar 8 2002.

[18] D. W. Choi, "Ionic Dependence of Glutamate Neurotoxicity," *Journal of Neuroscience,* vol. 7, pp. 369-379, Feb 1987.

[19] D. W. Choi, "Glutamate Receptors and the Induction of Excitotoxic Neuronal Death," *Neuroscience: From the Molecular to the Cognitive,* vol. 100, pp. 47-51, 1994.

[20] W. D. Dietrich, Z. C. Feng, H. Leistra, B. D. Watson, and M. Rosenthal, "Photothrombotic Infarction Triggers Multiple Episodes of Cortical Spreading Depression in Distant Brain-Regions," *Journal of Cerebral Blood Flow and Metabolism,* vol. 14, pp. 20-28, Jan 1994.

[21] M. Ding, E. Tejima, E. H. Lo, and G. B. Stanley, "Electrophysiology of the rat barrel cortex following traumatic brain injury," in *Society for Neuroscience*, 2005.

[22] M. Fabricius, S. Fuhr, R. Bhatia, M. Boutelle, P. Hashemi, A. J. Strong, and M. Lauritzen, "Cortical spreading depression and peri-infarct depolarization in acutely injured human cerebral cortex," *Brain,* vol. 129, pp. 778-90, Mar 2006.

[23] A. I. Faden, P. Demediuk, S. S. Panter, and R. Vink, "The role of excitatory amino acids and NMDA receptors in traumatic brain injury," *Science,* vol. 244, pp. 798-800, May 19 1989.

[24] P. B. Goforth, E. F. Ellis, and L. S. Satin, "Enhancement of AMPA-mediated current after traumatic injury in cortical neurons," *J Neurosci,* vol. 19, pp. 7367-74, Sep 1 1999.

[25] H. Hansen, B. Moesgaard, H. Hansen, and G. Petersen, "N-acylethanolamines and precursor phospholipids - relation to cell injury," *Chemistry and Physics of Lipids,* vol. 108, pp. 135-150, Nov 2000 2000.

[26] J. W. Huh, R. Raghupathi, H. L. Laurer, M. A. Helfaer, and K. E. Saatman, "Transient loss of microtubule-associated protein 2 immunoreactivity after moderate brain injury in mice," *J Neurotrauma,* vol. 20, pp. 975-84, Oct 2003.

[27] Y. Katayama, D. P. Becker, T. Tamura, and D. A. Hovda, "Massive increases in extracellular potassium and the indiscriminate release of glutamate following concussive brain injury," *J Neurosurg,* vol. 73, pp. 889-900, Dec 1990.

[28] R. G. M. Morris, "Synaptic Plasticity and Learning - Selective Impairment of Learning in Rats and Blockade of Long-Term Potentiation Invivo by the N-Methyl-D-Aspartate Receptor Antagonist Ap5," *Journal of Neuroscience,* vol. 9, pp. 3040-3057, Sep 1989.

[29] H. Ozawa, S. Shioda, K. Dohi, H. Matsumoto, H. Mizushima, C. J. Zhou, H. Funahashi, Y. Nakai, S. Nakajo, and K. Matsumoto, "Delayed neuronal cell death in the rat hippocampus is mediated by the mitogen-activated protein kinase signal transduction pathway," *Neuroscience Letters,* vol. 262, pp. 57-60, Feb 26 1999.

[30] M. J. Passineau, W. Zhao, R. Busto, W. D. Dietrich, O. Alonso, J. Y. Loor, H. M. Bramlett, and M. D. Ginsberg, "Chronic metabolic sequelae of traumatic brain injury: prolonged suppression of somatosensory activation," *Am J Physiol Heart Circ Physiol,* vol. 279, pp. H924-31, Sep 2000.

[31] K. R. Pennypacker, S. Eidizadeh, C. A. Kassed, J. P. O'Callaghan, P. R. Sanberg, and A. E. Willing, "Expression of fos-related antigen-2 in rat hippocampus after middle cerebral arterial occlusion," *Neurosci Lett,* vol. 289, pp. 1-4, Jul 28 2000.

[32] K. R. Pennypacker, C. A. Kassed, S. Eidizadeh, and J. P. O'Callaghan, "Brain injury: prolonged induction of transcription factors," *Acta Neurobiol Exp (Wars),* vol. 60, pp. 515-30, 2000.

[33] K. R. Pennypacker, C. A. Kassed, S. Eidizadeh, S. Saporta, P. R. Sanberg, and A. E. Willing, "NF-kappaB p50 is increased in neurons surviving hippocampal injury," *Exp Neurol,* vol. 172, pp. 307-19, Dec 2001.

[34] L. L. Phillips and T. M. Reeves, "Interactive pathology following traumatic brain injury modifies hippocampal plasticity," *Restor Neurol Neurosci,* vol. 19, pp. 213-35, 2001.

[35] R. Raghupathi, D. I. Graham, and T. K. McIntosh, "Apoptosis after traumatic brain injury," *Journal of Neurotrauma,* vol. 17, pp. 927-938, Oct 2000.

[36] R. Raghupathi, "Cell death mechanisms following traumatic brain injury," *Brain Pathol,* vol. 14, pp. 215-22, Apr 2004.

[37] K. E. Saatman, B. Abai, T. Grosvenor, C. K. Vorwerk, D. H. Smith, and D. F. Meaney, "Traumatic axonal injury results in biphasic calpain activation and retrograde transport impairment in mice," *Journal of Cerebral Blood Flow and Metabolism,* vol. 23, pp. 34-42, Jan 2003.

[38] M. J. Sanders, T. J. Sick, M. A. Perez-Pinzon, W. D. Dietrich, and E. J. Green, "Chronic failure in the maintenance of long-term potentiation following fluid percussion injury in the rat," *Brain Res,* vol. 861, pp. 69-76, Apr 7 2000.

[39] G. Serbest, J. Horwitz, and K. Barbee, "Involvement of MAPKs and cell death after mechanical injury," *Journal of Neurotrauma,* vol. 21, pp. 1335-1335, Sep 2004.

[40] N. A. Shaw, "The neurophysiology of concussion," *Prog Neurobiol,* vol. 67, pp. 281-344, Jul 2002.

[41] R. Shi and J. D. Pryor, "Pathological changes of isolated spinal cord axons in response to mechanical stretch," *Neuroscience,* vol. 110, pp. 765-777, 2002.

[42] M. Shimamura, J. M. Garcia, D. S. Prough, D. S. Dewitt, T. Uchida, S. A. Shah, M. A. Avila, and H. L. Hellmich, "Analysis of long-term gene expression in neurons of the hippocampal subfields following traumatic brain injury in rats," *Neuroscience,* vol. 131, pp. 87-97, 2005.

[43] S. J. Tavalin, E. F. Ellis, and L. S. Satin, "Mechanical perturbation of cultured cortical neurons reveals a stretch-induced delayed depolarization," *Journal of Neurophysiology,* vol. 74, pp. 2767-73, 1995.

[44] P. M. Vespa, W. J. Boscardin, D. A. Hovda, D. L. McArthur, M. R. Nuwer, N. A. Martin, V. Nenov, T. C. Glenn, M. Bergsneider, D. F. Kelly, and D. P. Becker, "Early and persistent impaired percent alpha variability on continuous electroencephalography monitoring as predictive of poor outcome after traumatic brain injury," *J Neurosurg,* vol. 97, pp. 84-92, Jul 2002.

[45] B. M. Witgen, J. Lifshitz, M. L. Smith, E. Schwarzbach, S. L. Liang, M. S. Grady, and A. S. Cohen, "Regional hippocampal alteration associated with cognitive deficit following experimental brain injury: a systems, network and cellular evaluation," *Neuroscience,* vol. 133, pp. 1-15, 2005.

[46] J. A. Wolf, P. K. Stys, T. Lusardi, D. Meaney, and D. H. Smith, "Traumatic axonal injury induces calcium influx modulated by tetrodotoxin-sensitive sodium channels," *Journal of Neuroscience,* vol. 21, pp. 1923-1930, Mar 15 2001.

[47] C. P. Wu, G. Cheung, N. Rakhshani, S. Parvardeh, M. N. Asl, H. L. Huang, and L. Zhang, "Ca3 neuronal activities of dorsal and ventral hippocampus are differentially altered in rats after prolonged post-ischemic survival," *Neuroscience,* vol. 130, pp. 527-39, 2005.

[48] L. Zhang, B. A. Rzigalinski, E. F. Ellis, and L. S. Satin, "Reduction of voltage-dependent $Mg^{2+}$ blockade of NMDA current in mechanically injured neurons," *Science,* vol. 274, pp. 1921-1923, 1996.

[49] B. A. Wester, R. H. Lee, and M. C. LaPlaca, "Development and characterization of in vivo flexible electrodes compatible with large tissue displacements," *Journal of Neural Engineering,* p. 024002, 2009.

[50] A. Manz, N. Graber, and H. M. Widmer, "Miniaturized Total Chemical-Analysis Systems - a Novel Concept for Chemical Sensing," *Sensors and Actuators B-Chemical,* vol. 1, pp. 244-248, Jan 1990.

[51] A. Stett, U. Egert, E. Guenther, F. Hofmann, T. Meyer, W. Nisch, and H. Haemmerle, "Biological application of microelectrode arrays in drug discovery and basic research," *Analytical and Bioanalytical Chemistry,* vol. 377, pp. 486-495, Oct 2003.

[52] K. D. Wise, "Silicon microsystems for neuroscience and neural prostheses," *Ieee Engineering in Medicine and Biology Magazine,* vol. 24, pp. 22-29, Sep-Oct 2005.

[53] C. G. Keller, R. T. Howe, and Ieee, "Hexsil tweezers for teleoperated micro-assembly," in *IEEE 10th Annual International Workshop on Micro Electro Mechanical Systems*, Nagoya, Japan, 1997, pp. 72-77.

[54] M. Goldfarb and N. Celanovic, "A flexure-based gripper for small-scale manipulation," *Robotica,* vol. 17, pp. 181-187, Mar-Apr 1999.

[55] F. Beyeler, A. Neild, S. Oberti, D. J. Bell, Y. Sun, J. Dual, and B. J. Nelson, "Monolithically fabricated microgripper with integrated force sensor for manipulating microobjects and biological cells aligned in an ultrasonic field," *Journal of Microelectromechanical Systems,* vol. 16, pp. 7-15, Feb 2007.

[56] A. Celedon, I. M. Nodelman, B. Wildt, R. Dewan, P. Searson, D. Wirtz, G. D. Bowman, and S. X. Sun, "Magnetic Tweezers Measurement of Single Molecule Torque," *Nano Letters,* vol. 9, pp. 1720-1725, Apr 2009.

[57] N. Chronis and L. P. Lee, "Electrothermally activated SU-8 microgripper for single cell manipulation in solution," *Journal of Microelectromechanical Systems,* vol. 14, pp. 857-863, Aug 2005.

[58] M. B. Cohn, K. F. Bohringer, J. M. Noworolski, A. Singh, C. G. Keller, K. Y. Goldberg, and R. T. Howe, "Microassembly technologies for MEMS," in *Materials and Device Characterization in Micromachining*, Santa Clara, CA, 1998, pp. 2-16.

[59] N. Dechev, W. L. Cleghorn, and J. K. Mills, "Microassembly of 3-D microstructures using a compliant, passive microgripper," *Journal of Microelectromechanical Systems,* vol. 13, pp. 176-189, Apr 2004.

[60] C. Haber and D. Wirtz, "Magnetic tweezers for DNA micromanipulation," *Review of Scientific Instruments,* vol. 71, pp. 4561-4570, Dec 2000.

[61] S. K. Jericho, M. H. Jericho, T. Hubbard, and M. Kujath, "Micro-electro-mechanical systems microtweezers for the manipulation of bacteria and small particles," *Review of Scientific Instruments,* vol. 75, pp. 1280-1282, May 2004.

[62] W. Nogimori, K. Irisa, M. Ando, Y. Naruse, and Ieee, "A laser-powered micro-gripper," in *IEEE 10th Annual International Workshop on Micro Electro Mechanical Systems*, Nagoya, Japan, 1997, pp. 267-271.

[63] R. Tharmann, M. Keller, J. Uhde, and A. Bausch, "Active networks studied by magnetic tweezers microrheometry and torsional macrorheometry," *Biophysical Journal,* vol. 84, pp. 247a-247a, Feb 2003.

[64] R. Tharmann, J. Zhang, M. Barmann, and A. Bausch, "Active networks studied by magnetic tweezers microrheometry and torsional macrorheometry," 2004, pp. 53A-54A.

[65] G. T. A. Kovacs, *Micromachined Transducers: Sourcebook*: McGraw Hill, 1998.

[66] C. E. Dixon, M. F. Kraus, A. E. Kline, X. C. Ma, H. Q. Yan, R. G. Griffith, B. M. Wolfson, and D. W. Marion, "Amantadine improves water maze performance without affecting motor behavior following traumatic brain injury in rats," *Restorative Neurology and Neuroscience,* vol. 14, pp. 285-294, 1999.

[67] P. D. Adelson, C. E. Dixon, and P. M. Kochanek, "Long-term dysfunction following diffuse traumatic brain injury in the immature rat," *Journal of Neurotrauma,* vol. 17, pp. 273-282, Apr 2000.

[68] S. T. Fujimoto, L. Longhi, K. E. Saatman, and T. K. McIntosh, "Motor and cognitive function evaluation following experimental traumatic brain injury," *Neuroscience and Biobehavioral Reviews,* vol. 28, pp. 365-378, Jul 2004.

[69] J. T. Povlishock and D. I. Katz, "Update of neuropathology and neurological recovery after traumatic brain injury," *Journal of Head Trauma Rehabilitation,* vol. 20, pp. 76-94, Jan-Feb 2005.

[70] T. A. Gennarelli, K. S. Waxman, and F. D. Lewis, "Serious traumatic brain injury: An evaluation of functional outcomes - Discussion," *Journal of Trauma-Injury Infection and Critical Care,* vol. 41, pp. 263-264, Aug 1996.

[71] J. Olesen and M. Leonardi, "The burden of brain diseases in Europe," *European Journal of Neurology,* vol. 10, pp. 471-477, Sep 2003.

[72] T. K. McIntosh, "Neurochemical sequelae of traumatic brain injury: therapeutic implications," *Cerebrovascular & Brain Metabolism Reviews,* vol. 6, pp. 109-62, 1994.

[73] T. K. McIntosh, K. E. Saatman, R. Raghupathi, D. I. Graham, D. H. Smith, V. M. Lee, and J. Q. Trojanowski, "The Dorothy Russell Memorial Lecture. The molecular and cellular sequelae of experimental traumatic brain injury: pathogenetic mechanisms," *Neuropathol Appl Neurobiol,* vol. 24, pp. 251-67, 1998.

[74] D. H. Smith, X. H. Chen, J. E. S. Pierce, J. A. Wolf, J. Q. Trojanowski, D. I. Graham, and T. K. McIntosh, "Progressive atrophy and neuron death for one year following brain trauma in the rat," *Journal of Neurotrauma,* vol. 14, pp. 715-727, Oct 1997.

[75] B. Brett, G. Krishnan, and D. S. Barth, "The effects of subcortical lesions on evoked potentials and spontaneous high frequency (gamma-band) oscillating potentials in rat auditory cortex," *Brain Research,* vol. 721, pp. 155-166, May 20 1996.

[76] W. S. Carbonell and M. S. Grady, "Regional and temporal characterization of neuronal, glial, and axonal response after traumatic brain injury in the mouse," *Acta Neuropathol (Berl),* vol. 98, pp. 396-406, Oct 1999.

[77] H. L. Hellmich, J. M. Garcia, M. Shimamura, S. A. Shah, M. A. Avila, T. Uchida, M. A. Parsley, B. A. Capra, K. A. Eidson, D. R. Kennedy, J. H. Winston, D. S. DeWitt, and D. S. Prough, "Traumatic brain injury and hemorrhagic hypotension suppress neuroprotective gene expression in injured hippocampal neurons," *Anesthesiology,* vol. 102, pp. 806-14, Apr 2005.

[78] R. R. Hicks, H. D. Soares, D. H. Smith, and T. K. McIntosh, "Temporal and spatial characterization of neuronal injury following lateral fluid-percussion brain injury in the rat," *Acta Neuropathol,* vol. 91, pp. 236-246, 1996.

[79] M. R. Nuwer, D. A. Hovda, L. M. Schrader, and P. M. Vespa, "Routine and quantitative EEG in mild traumatic brain injury," *Clinical Neurophysiology,* vol. 116, pp. 2001-2025, Sep 2005.

[80] A. Yoshino, D. A. Hovda, Y. Katayama, T. Kawamata, and D. P. Becker, "Hippocampal Ca3 Lesion Prevents Postconcussive Metabolic Dysfunction in Ca1," *Journal of Cerebral Blood Flow and Metabolism,* vol. 12, pp. 996-1006, Nov 1992.

[81] A. C. Conti, R. Raghupathi, J. Q. Trojanowski, and T. K. McIntosh, "Experimental brain injury induces regionally distinct apoptosis during the acute and delayed post-traumatic period," *Journal of Neuroscience,* vol. 18, pp. 5663-5672, Aug 1 1998.

[82] H. M. Bramlett and W. D. Dietrich, "Quantitative structural changes in white and gray matter 1 year following traumatic brain injury in rats," *Acta Neuropathologica,* vol. 103, pp. 607-614, Jun 2002.

[83] P. M. Kochanek, K. S. Hendrich, C. E. Dixon, J. K. Schiding, D. S. Williams, and C. Ho, "Cerebral blood flow at one year after controlled cortical impact in rats: Assessment by magnetic resonance imaging," *Journal of Neurotrauma,* vol. 19, pp. 1029-1037, Sep 2002.

[84] T. K. McIntosh, D. H. Smith, D. F. Meaney, M. J. Kotapka, T. A. Gennarelli, and D. I. Graham, "Neuropathological sequelae of traumatic brain injury: Relationship to neurochemical and biomechanical mechanisms," *Laboratory Investigation,* vol. 74, pp. 315-342, Feb 1996.

[85] B. R. Blackman, K. A. Barbee, and L. E. Thibault, "In vitro cell shearing device to investigate the dynamic response of cells in a controlled hydrodynamic environment," *Annals of Biomedical Engineering,* vol. 28, pp. 363-372, Apr 2000.

[86] D. K. Cullen and M. C. LaPlaca, "Neuronal response to high rate shear deformation depends on heterogeneity of the local strain field," *Journal of Neurotrauma,* vol. 23, pp. 1304-1319, Sep 2006.

[87] E. F. Ellis, J. S. Mckinney, K. A. Willoughby, S. Liang, and J. T. Povlishock, "A New Model for Rapid Stretch-Induced Injury of Cells in Culture - Characterization of the Model Using Astrocytes," *Journal of Neurotrauma,* vol. 12, pp. 325-339, Jun 1995.

[88] J. Galbraith and L. E. Thibault, "Mechanically induced depolarizations in the squid giant axon," *Journal of Biomechanical Engineering,* vol. 115, pp. 13-22, 1993.

[89] J. A. Galbraith, L. E. Thibault, and D. R. Matteson, "Mechanical and electrical responses of the squid giant-axon to simple elongation," *Journal of Biomechanical Engineering-Transactions of the Asme,* vol. 115, pp. 13-22, Feb 1993.

[90] D. M. Geddes and R. S. Cargill, "An in vitro model of neural trauma: Devise characterization and calcium response to mechanical stretch," *Journal of Biomechanical Engineering-Transactions of the Asme,* vol. 123, pp. 247-255, Jun 2001.

[91] D. M. Geddes, R. S. Cargill, and M. C. LaPlaca, "Mechanical stretch to neurons results in a strain rate and magnitude-dependent increase in plasma membrane permeability," *Journal of Neurotrauma,* vol. 20, pp. 1039-1049, Oct 2003.

[92] J. A. Gilbert, P. S. Weinhold, A. J. Banes, G. W. Link, and G. L. Jones, "Strain profiles for circular cell-culture plates containing flexible surfaces employed to mechanically deform cells in-vitro," *Journal of Biomechanics,* vol. 27, pp. 1169-1177, Sep 1994.

[93] D. M. Hallow, R. A. Seeger, P. P. Kamaev, G. R. Prado, M. C. LaPlaca, and M. R. Prausnitz, "Shear-induced intracellular loading of cells with molecules by controlled microfluidics," *Biotechnology and Bioengineering,* vol. 99, pp. 846-854, Mar 1 2008.

[94] M. C. LaPlaca, D. K. Cullen, J. J. McLoughlin, and R. S. Cargill, "High rate shear strain of three-dimensional neural cell cultures: a new in vitro traumatic brain injury model," *Journal of Biomechanics,* vol. 38, pp. 1093-1105, May 2005.

[95] J. L. Schaffer, M. Rizen, G. J. Litalien, A. Benbrahim, J. Megerman, L. C. Gerstenfeld, and M. L. Gray, "Device for the Application of a Dynamic Biaxially Uniform and Isotropic Strain to a Flexible Cell-Culture Membrane," *Journal of Orthopaedic Research,* vol. 12, pp. 709-719, Sep 1994.

[96] K. Okiyama, D. H. Smith, T. A. Gennarelli, R. P. Simon, M. Leach, and T. K. Mcintosh, "The Sodium-Channel Blocker and Glutamate Release Inhibitor Bw1003c87 and Magnesium Attenuate Regional Cerebral Edema Following Experimental Brain Injury in the Rat," *Journal of Neurochemistry,* vol. 64, pp. 802-809, Feb 1995.

[97] R. Ichord, M. Naim, A. Pollock, M. Nance, C. Christian, and S. Margulies, "Hypoxic ischemic injury complicates traumatic brain injury in young children: The role of diffusion weighted magnetic resonance (DWI) imaging," *Journal of Neurotrauma,* vol. 23, pp. 1001-1001, Jun 2006.

[98] B. A. Wester, J. D. Ross, S. Rajaraman, M. Kuykendal, G. Guvanasen, M. G. Allen, and M. C. LaPlaca, "A single-unit neural injury model using mechanically actuated microtweezers," in *Society for Neuroscience*, 2009.

[99] D. K. Cullen, Vukasinovic, J., Glezer, A. and LaPlaca, M.C., "High cell density three-dimensional neural co-cultures require continuous medium perfusion for survival," in *Proceedings of the 28th Annual International Conference IEEE Engineering in Medicine and Biology Society (EMBS)*, 2006.

[100] C. E. Dixon, G. L. Clifton, J. W. Lighthall, A. A. Yaghmai, and R. L. Hayes, "A controlled cortical impact model of traumatic brain injury in the rat," *J Neurosci Methods,* vol. 39, pp. 253-62, 1991.

[101] D. M. Geddes-Klein, K. B. Schiffman, and D. F. Meaney, "Mechanisms and consequences of neuronal stretch injury in vitro differ with the model of trauma," *Journal of Neurotrauma,* vol. 23, pp. 193-204, Feb 2006.

[102] H. R. Irons, D. K. Cullen, N. P. Shapiro, N. A. Lambert, R. H. Lee, and M. C. LaPlaca, "Three-dimensional neural constructs: a novel platform for neurophysiological investigation," *Journal of Neural Engineering,* vol. 5, pp. 333-341, Sep 2008.

[103] M. LaPlaca, G. Prado, L. Y. Zhang, and K. Yang, "Correlation of traumatic brain injury-induced strain with cell damage," *Journal of Head Trauma Rehabilitation,* vol. 21, pp. 414-414, Sep-Oct 2006.

[104] T. K. McIntosh, R. Vink, L. Noble, I. Yamakami, S. Fernyak, H. Soares, and A. L. Faden, "Traumatic brain injury in the rat: Characterization of a lateral fluid percussion model," *Neuroscience,* vol. 28, pp. 233-44, 1989.

[105] S. I. Svetlov, S. F. Larner, D. R. Kirk, J. Atkinson, R. L. Hayes, and K. K. W. Wang, "Biomarkers of Blast-Induced Neurotrauma: Profiling Molecular and Cellular Mechanisms of Blast Brain Injury," *Journal of Neurotrauma,* vol. 26, pp. 913-921, Jun 2009.

[106] J. M. Cheng, J. W. Gu, Y. A. Ma, T. Yang, Y. Q. Kuang, B. C. Li, and J. Y. Kang, "Development of a rat model for studying blast-induced traumatic brain injury," *Journal of the Neurological Sciences,* vol. 294, pp. 23-28, Jul 15 2010.

[107] B. Morrison, D. F. Meaney, and T. K. McIntosh, "Mechanical characterization of an in vitro device designed to quantitatively injure living brain tissue," *Annals of Biomedical Engineering,* vol. 26, pp. 381-390, May-Jun 1998.

[108] B. Morrison, D. F. Meaney, S. S. Margulies, and T. K. McIntosh, "Dynamic mechanical stretch of organotypic brain slice cultures induces differential genomic expression: Relationship to mechanical parameters," *Journal of Biomechanical Engineering-Transactions of the Asme,* vol. 122, pp. 224-230, Jun 2000.

[109] B. J. Pfister, T. P. Weihs, M. Betenbaugh, and G. Bao, "An in vitro uniaxial stretch model for axonal injury," *Annals of Biomedical Engineering,* vol. 31, pp. 589-598, May 2003.

[110] T. A. Lusardi, J. Rangan, D. Sun, D. H. Smith, and D. E. Meaney, "A device to study the initiation and propagation of calcium transients in cultured neurons after mechanical stretch," *Annals of Biomedical Engineering,* vol. 32, pp. 1546-1558, Nov 2004.

[111] M. J. Sanderson and E. R. Dirksen, "Mechanosensitivity of Cultured Ciliated Cells from the Mammalian Respiratory-Tract - Implications for the Regulation of Mucociliary Transport," *Proceedings of the National Academy of Sciences of the United States of America,* vol. 83, pp. 7302-7306, Oct 1986.

[112] A. C. Charles, J. E. Merrill, E. R. Dirksen, and M. J. Sanderson, "Intercellular Signaling in Glial-Cells - Calcium Waves and Oscillations in Response to Mechanical Stimulation and Glutamate," *Neuron,* vol. 6, pp. 983-992, Jun 1991.

[113] M. J. Sanderson, A. C. Charles, and E. R. Dirksen, "Mechanical Stimulation and Intercellular Communication Increases Intracellular Ca-2+ in Epithelial-Cells," *Cell Regulation,* vol. 1, pp. 585-596, Jul 1990.

[114] K. Paemeleire and L. Leybaert, "Ionic changes accompanying astrocytic intercellular calcium waves triggered by mechanical cell damaging stimulation," *Brain Research,* vol. 857, pp. 235-245, Feb 28 2000.

[115] G. W. Gross, J. H. Lucas, and M. L. Higgins, "Laser Microbeam Surgery - Ultrastructural-Changes Associated with Neurite Transection in Culture," *Journal of Neuroscience,* vol. 3, pp. 1979-1993, 1983.

[116] J. B. Kirkpatrick, M. L. Higgins, J. H. Lucas, and G. W. Gross, "Invitro Simulation of Neural Trauma by Laser," *Journal of Neuropathology and Experimental Neurology,* vol. 44, pp. 268-284, 1985.

[117] D. G. Emery, J. H. Lucas, and G. W. Gross, "The Sequence of Ultrastructural-Changes in Cultured Neurons after Dendrite Transection," *Experimental Brain Research,* vol. 67, pp. 41-51, 1987.

[118] C. E. Hampton, H. C. Gabler, and B. Rzigalinski, "Numerical simulation of a cellular-level experiment to induce traumatic injury to neurons," *Biomedical Sciences Instrumentation,* vol. 42, pp. 205-2010, 2006.

[119] P. H. Tsang, G. L. Li, Y. V. Brun, L. Ben Freund, and J. X. Tang, "Adhesion of single bacterial cells in the micronewton range," *Proceedings of the National Academy of Sciences of the United States of America,* vol. 103, pp. 5764-5768, Apr 11 2006.

[120] K. A. Barbee, "Mechanical cell injury," *Cell Injury: Mechanisms, Responses, and Repair,* vol. 1066, pp. 67-84, 2005.

[121] D. R. Berlowitz and D. M. Brienza, "Are all pressure ulcers the result of deep tissue injury? A review of the literature," *Ostomy Wound Management,* vol. 53, pp. 34-38, Oct 2007.

[122] R. G. M. Breuls, C. V. C. Bouten, C. W. J. Oomens, D. L. Bader, and F. P. T. Baaijens, "Compression induced cell damage in engineered muscle tissue: An in vitro model to study pressure ulcer aetiology," *Annals of Biomedical Engineering,* vol. 31, pp. 1357-1364, Dec 2003.

[123] A. Gefen, B. van Nierop, D. L. Bader, and C. W. Oomens, "Strain-time cell-death threshold for skeletal muscle in a tissue-engineered model system for deep tissue injury," *Journal of Biomechanics,* vol. 41, pp. 2003-2012, 2008.

[124] M. I. Almeida-Silveira, D. Lambertz, C. Perot, and F. Goubel, "Changes in stiffness induced by hindlimb suspension in rat Achilles tendon," *European Journal of Applied Physiology,* vol. 81, pp. 252-257, Feb 2000.

[125] R. J. Minns and D. S. Muckle, "Mechanical-Properties of Traumatized Rat Tendo-Achilles and the Effect of an Anti-Inflammatory Drug on the Repair Properties," *Journal of Biomechanics,* vol. 15, pp. 783-&, 1982.

[126] H. Lorenz, M. Despont, N. Fahrni, N. LaBianca, P. Renaud, and P. Vettiger, "SU-8: a low-cost negative resist for MEMS," *Journal of Micromechanics and Microengineering,* vol. 7, pp. 121-124, Sep 1997.

[127] J. M. Gere, *Mechanics of materials* vol. 5: Brooks-Cole, 2000.

[128] D. Schneider and M. D. Tucker, "Non-destructive characterization and evaluation of thin films by laser-induced ultrasonic surface waves," *Thin Solid Films,* vol. 291, pp. 305-311, Dec 15 1996.

[129] J. D. Heck and M. Costa, "Extracellular Requirements for the Endocytosis of Carcinogenic Crystalline Nickel Sulfide Particles by Facultative Phagocytes," *Toxicology Letters,* vol. 12, pp. 243-250, 1982.

[130] G. Repetto, A. del Peso, P. Sanz, and M. Repetto, "In vitro effects of lithium and nickel at different levels on Neuro-2a mouse Neuroblastoma cells," *Toxicology in Vitro,* vol. 15, pp. 363-368, Aug-Oct 2001.

[131] K. S. Kasprzak, B. A. Diwan, N. Konishi, M. Misra, and J. M. Rice, "Initiation by Nickel Acetate and Promotion by Sodium Barbital of Renal Cortical Epithelial Tumors in Male F344 Rats," *Carcinogenesis,* vol. 11, pp. 647-652, Apr 1990.

[132] M. Misra, R. E. Rodriguez, and K. S. Kasprzak, "Nickel Induced Lipid-Peroxidation in the Rat - Correlation with Nickel Effect on Antioxidant Defense Systems," *Toxicology,* vol. 64, pp. 1-17, Oct 1990.

[133] R. E. Rodriguez, M. Misra, and K. S. Kasprzak, "Effects of Nickel on Catalase Activity Invitro and Invivo," *Toxicology,* vol. 63, pp. 45-52, Jul 1990.

[134] S. C. Xu, M. D. He, M. Zhong, Y. W. Zhang, Y. A. Wang, L. Yang, J. Yang, Z. P. Yu, and Z. Zhou, "Melatonin protects against Nickel-induced neurotoxicity in vitro by reducing oxidative stress and maintaining mitochondrial function," *Journal of Pineal Research,* vol. 49, pp. 86-94, Aug 2010.

[135] M. Luebbert, D. Radtke, R. Wodarski, N. Damann, H. Hatt, and C. H. Wetzel, "Direct activation of transient receptor potential V1 by nickel ions," *Pflugers Archiv-European Journal of Physiology,* vol. 459, pp. 737-750, Apr 2010.

[136] Y. Choi, J. Ross, B. Wester, and M. G. Allen, "Mechanically driven microtweezers with integrated microelectrodes," *Journal of Micromechanics and Microengineering,* vol. 18, pp. -, Jun 2008.

[137] V. Nazmov, E. Reznikova, A. Snigirev, I. Snigireva, M. DiMichiel, M. Grigoriev, J. Mohr, B. Matthis, and V. Saile, "LIGA fabrication of X-ray nickel lenses," *Microsystem Technologies-Micro-and Nanosystems-Information Storage and Processing Systems,* vol. 11, pp. 292-297, Apr 2005.

[138] P. E. Bakeman, H. K. Lee, and S. E. Luce, "Protection of aluminum metallization against chemical attack during photoresist development." vol. 5480748 USA, 1996.

[139] B. A. Wester, J. D. Ross, S. Rajaraman, and M. G. Allen, "Packaging and Characterization of Mechanically Actuated Microtweezers for Biomedical Applications," in *IEEE EMBC* Minneapolis, MN, 2009.

[140] K. Gieck and R. Gieck, *Engineering Formulas*, 7 ed.: McGraw-Hill, 1997.

[141] D. Kopeliovich, "Substances and Technologies, www.substech.com," 2010.

[142] T. Velten, H. H. Ruf, D. Barrow, N. Aspragathos, P. Lazarou, E. Jung, C. K. Malek, M. Richter, and J. Kruckow, "Packaging of bio-MEMS: Strategies, technologies, and applications," *Ieee Transactions on Advanced Packaging,* vol. 28, pp. 533-546, Nov 2005.

[143] R. R. Tummala, *Fundamentals of Microsystems Packaging*: McGraw-Hill, 2001.

[144] B. A. Wester, S. Rajaraman, J. D. Ross, M. C. LaPlaca, and M. G. Allen, "Development and Characterization of a Packaged Mechanically Actuated Microtweezer System," *Sensors and Actuators,* p. (In Review), 2010.

[145] A. Wick, O. Vohringer, and A. R. Pelton, "The bending behavior of NiTi," *Journal De Physique Iv,* vol. 5, pp. 789-794, Dec 1995.

[146] A. R. Pelton, J. DiCello, and S. Miyazaki, "Optimisation of processing and properties of medical grade Nitinol wire," *Minimally Invasive Therapy & Allied Technologies,* vol. 9, pp. 107-118, Mar 2000.

[147] T. W. Duerig, A. R. Pelton, and D. Stockel, "The utility of superelasticity in medicine," *Bio-Medical Materials and Engineering,* vol. 6, pp. 255-266, 1996.

[148] S. A. Shabalovskaya, "On the nature of the biocompatibility and on medical applications of NiTi shape memory and superelastic alloys," *Bio-Medical Materials and Engineering,* vol. 6, pp. 267-289, 1996.

[149] C. M. Putman, J. C. Chaloupka, P. Kailasnath, and J. Alderman, "Technical feasibility and performance studies of a 0.009-inch nitinol microguidewire for potential neuroendovascular applications," *Investigative Radiology,* vol. 32, pp. 241-247, Apr 1997.

[150] J. Ryhanen, E. Niemi, W. Serlo, E. Niemela, P. Sandvik, H. Pernu, and T. Salo, "Biocompatibility of nickel-titanium shape memory metal and its corrosion behavior in human cell cultures," *Journal of Biomedical Materials Research,* vol. 35, pp. 451-457, Jun 15 1997.

[151] A. R. Pelton, S. M. Russell, and J. DiCello, "The physical metallurgy of Nitinol for medical applications," *Jom-Journal of the Minerals Metals & Materials Society,* vol. 55, pp. 33-37, May 2003.

[152] X. J. Wen, N. Zhang, X. H. Li, and Z. W. Cao, "Electrochemical and histomorphometric evaluation of the TiNiCu shape memory alloy," *Bio-Medical Materials and Engineering,* vol. 7, pp. 1-11, 1997.

[153] G. Tepe, T. Zeller, S. Heller, J. Wiskirchen, A. Fischmann, S. Coerper, B. Balletshofer, S. Beckert, and C. D. Claussen, "Self-expanding nitinol stents for treatment of infragenicular arteries following unsuccessful balloon angioplasty," *European Radiology,* vol. 17, pp. 2088-2095, Aug 2007.

[154] M. Dafflon, B. Lorent, R. Clavel, F. Beyeler, and B. J. Nelson, "Characterization of Micro Manipulation Tasks Oriented with Various Controlled Conditions by MicroTweezers," in *International Workshop on MIcroFactories*, 2006.

[155] J. Fraser, T. Hubbard, and M. Kujath, "Theoretical and experimental analysis of an off-chip microgripper," *Canadian Journal of Electrical and Computer Engineering-Revue Canadienne De Genie Electrique Et Informatique,* vol. 31, pp. 77-84, Spr 2006.

[156] I. P. F. Harouche, C. Shafai, and R. G. Gordon, "Design and simulation of microtweezers using a controlled displacement comb drive," in *Canadian Conference on Electrical and Computer Engineering*, 2006, pp. 341-3.

[157] D. H. Kim, M. G. Lee, B. Kim, and Y. Sun, "A superelastic alloy microgripper with embedded electromagnetic actuators and piezoelectric force sensors: a numerical and experimental study," *Smart Materials & Structures,* vol. 14, pp. 1265-1272, Dec 2005.

[158] K. P. Larsen, A. A. Rasmussen, J. T. Ravnkilde, M. Ginnerup, and O. Hansen, "MEMS device for bending test: measurements of fatigue and creep of electroplated nickel," in *Micro Electro Mechanical Systems, 2002. MEMS '02, Proceedings, IEEE., Fifteenth Annual International Workshop on*
Las Vegas, Nevada, 2002, pp. 156-164.

[159] R. L. Mcbride, E. R. Feringa, M. K. Garver, and J. K. Williams, "Prelabeled Red Nucleus and Sensorimotor Cortex Neurons of the Rat Survive 10 and 20 Weeks after Spinal-Cord Transection," *Journal of Neuropathology and Experimental Neurology,* vol. 48, pp. 568-576, Sep 1989.

[160] L. S. Li, X. D. Meng, and L. H.X., "Analysis and Stress Optimization Design of an S-shaped Micro Spring," *Manufacturing Science and Engineering,* pp. 2500-2504, 2009.

[161] Y. B. Wu, G. F. Ding, C. C. Zhang, J. A. Wang, S. P. Mao, and H. Wang, "Design and implementation of a bistable microcantilever actuator for magnetostatic latching relay," *Microelectronics Journal,* vol. 41, pp. 325-330, Jun 2010.

[162] V. N. Vernekar, D. K. Cullen, N. Fogleman, Y. Choi, A. J. Garcia, M. G. Allen, G. J. Brewer, and M. C. LaPlaca, "SU-8 2000 rendered cytocompatible for neuronal bioMEMS applications," *Journal of Biomedical Materials Research Part A,* vol. 89A, pp. 138-151, Apr 2009.

[163] B. Clancy, R. B. Darlington, and B. L. Finlay, "Translating developmental time across mammalian species," *Neuroscience,* vol. 105, pp. 7-17, 2001.

[164] G. J. Brewer and P. J. Price, "Viable cultured neurons in ambient carbon dioxide and hibernation storage for a month," *Neuroreport,* vol. 7, pp. 1509-1512, Jun 17 1996.

[165] J. H. McCarty, "Cell adhesion and signaling networks in brain neurovascular units," *Current Opinion in Hematology,* vol. 16, pp. 209-214, May 2009.

[166] Y. J. Ren, H. Zhang, H. Huang, X. M. Wang, Z. Y. Zhou, F. Z. Cui, and Y. H. An, "In vitro behavior of neural stem cells in response to different chemical functional groups," *Biomaterials,* vol. 30, pp. 1036-1044, Feb 2009.

[167] R. R. Llinas, "Calcium in Synaptic Transmission," *Scientific American,* vol. 247, pp. 56-&, 1982.

[168] D. E. Clapham, "Calcium Signaling," *Cell,* vol. 80, pp. 259-268, Jan 27 1995.

[169] D. E. Clapham, "Calcium signaling," *Cell,* vol. 131, pp. 1047-1058, Dec 14 2007.

[170] H. P. Cheng and W. J. Lederer, "Calcium sparks," *Physiological Reviews,* vol. 88, pp. 1491-1545, Oct 2008.

[171] G. Haase, B. Pettmann, C. Raoul, and C. E. Henderson, "Signaling by death receptors in the nervous system," *Current Opinion in Neurobiology,* vol. 18, pp. 284-291, Jun 2008.

[172] P. LeDuc, E. Ostuni, G. Whitesides, and D. Ingber, *Methods in Cell Biology-Matrix Adhesion* vol. 69: Academic Press Inc., 2002.

[173] A. Mata, A. J. Fleischman, and S. Roy, "Characterization of polydimethylsiloxane (PDMS) properties for biomedical micro/nanosystems," *Biomedical Microdevices,* vol. 7, pp. 281-293, Dec 2005.

[174] H. W. Fox, P. W. Taylor, and W. A. Zisman, "Industrial and Engineering Chemistry," p. 1401, 1947.

[175] DataPhysics-Instruments, "Solid Surface Energy Data (SFE) for Common Polymers," 2007.

[176] S. S. Margulies and L. E. Thibault, "A Proposed Tolerance Criterion for Diffuse Axonal Injury in Man," *Journal of Biomechanics,* vol. 25, pp. 917-923, Aug 1992.

[177] C. J. Zhou, T. B. Khalil, and A. I. King, "A new model comparing impact responses of the homogeneous and inhomogeneous human brain," *Stapp Car Crash Journal,* pp. 121-137, 1995.

[178] D. I. Shreiber, A. C. Bain, and D. F. Meaney, "In vivo thresholds for mechanical injury to the blood-brain barrier," in *Stapp Car Crash Conference*, 1997, pp. 277-291.

[179] B. Morrison, H. L. Cater, C. D. Benham, and L. E. Sundstrom, "An in vitro model of traumatic brain injury utilising two-dimensional stretch of organotypic hippocampal slice cultures," *Journal of Neuroscience Methods,* vol. 150, pp. 192-201, Jan 30 2006.

[180] R. J. H. Cloots, H. M. T. Gervaise, J. A. W. van Dommelen, and M. G. D. Geers, "Biomechanics of traumatic brain injury: Influences of the morphologic heterogeneities of the cerebral cortex," *Annals of Biomedical Engineering,* vol. 36, pp. 1203-1215, Jul 2008.

[181] D. T. Boss, D. F. Meaney, M. K. Sabol, D. H. Smith, and T. A. Gennarelli, "Distribution of Forebrain Diffuse Axonal Injury Following Inertial Closed-Head Injury in Miniature Swine," *Experimental Neurology,* vol. 126, pp. 291-299, Apr 1994.

[182] T. A. Gennarelli, L. E. Thibault, and D. I. Graham, "Diffuse axonal injury: An important form of traumatic brain damage," *Neuroscientist,* vol. 4, pp. 202-215, May 1998.

[183] S. Kleiven and H. von Holst, "Consequences of head size following trauma to the human head," *Journal of Biomechanics,* vol. 35, pp. 153-160, Feb 2002.

[184] J. A. B. Gray and J. M. Ritchie, "Effects of Stretch on Single Myelinated Nerve Fibres," *Journal of Physiology-London,* vol. 124, pp. 84-99, 1954.

[185] P. F. Baker, A. L. Hodgkin, and E. B. Ridgway, "Depolarization and Calcium Entry in Squid Giant Axons," *Journal of Physiology-London,* vol. 218, pp. 709-&, 1971.

[186] S. W. Jones, "Overview of voltage-dependent calcium channels," *Journal of Bioenergetics and Biomembranes,* vol. 30, pp. 299-312, Aug 1998.

[187] R. Kretz, E. Shapiro, and E. R. Kandel, "Post-Tetanic Potentiation at an Identified Synapse in Aplysia Is Correlated with a Ca-2+-Activated K+ Current in the Pre-Synaptic Neuron - Evidence for Ca-2+ Accumulation," *Proceedings of the National Academy of Sciences of the United States of America-Biological Sciences,* vol. 79, pp. 5430-5434, 1982.

[188] M. J. Berridge, M. D. Bootman, and H. L. Roderick, "Calcium signalling: Dynamics, homeostasis and remodelling," *Nature Reviews Molecular Cell Biology,* vol. 4, pp. 517-529, Jul 2003.

[189] M. J. Berridge, "Calcium microdomains: Organization and function," *Cell Calcium,* vol. 40, pp. 405-412, Nov-Dec 2006.

[190] R. Rizzuto and T. Pozzan, "Microdomains of intracellular Ca2+: Molecular determinants and functional consequences," *Physiological Reviews,* vol. 86, pp. 369-408, Jan 2006.

[191] Y. Ikegaya, M. Le Bon-Jego, and R. Yuste, "Large-scale imaging of cortical network activity with calcium indicators," *Neuroscience Research,* vol. 52, pp. 132-138, Jun 2005.

[192] Invitrogen, "Invitrogen - Fluo-5F, AM *cell permeant*," Invitrogen Corporation, 2010.

[193] E. R. Kandel, J. H. Schwartz, and T. M. Jessell, *Principles of Neural Science*, 4th ed.: McGraw-Hill, 2000.

[194] D. J. Bakkum, Z. C. Chao, and S. M. Potter, "Long-Term Activity-Dependent Plasticity of Action Potential Propagation Delay and Amplitude in Cortical Networks," *Plos One,* vol. 3, pp. -, May 7 2008.

[195] R. Khawaled, A. Bruening-Wright, J. P. Adelman, and J. Maylie, "Bicuculline block of small-conductance calcium-activated potassium channels," *Pflugers Archiv-European Journal of Physiology,* vol. 438, pp. 314-321, Aug 1999.

[196] N. Imamachi, Y. Saito, K. Hara, S. Sakura, and Y. Kosaka, "The non-NMDA glutamate receptor antagonist CNQX augments lidocaine antinociception through a spinal action in rats," *Anesthesia and Analgesia,* vol. 89, pp. 416-421, Aug 1999.

[197] R. Ardehali, L. Shi, J. Janatova, S. F. Mohammad, and G. L. Burns, "The inhibitory activity of serum to prevent bacterial adhesion is mainly due to apo-transferrin," *Journal of Biomedical Materials Research Part A,* vol. 66A, pp. 21-28, Jul 1 2003.

[198] J. D. Ross, N. E. Reddy, D. J. Bakkum, S. M. Potter, and S. P. DeWeerth, "Experimental Platform for the study of region specific excitation and inhibition of neural tissue," in *IEEE EMBC*, 2007.

[199] D. Mathieson, U. Beerschwinger, S. J. Yang, R. L. Reuben, M. Taghizadeh, S. Eckert, and U. Wallrabe, "Effect of progressive wear on the friction characteristics of nickel LIGA processed rotors," *Wear,* vol. 192, pp. 199-207, Mar 1996.

[200] E. Rabinowicz, "Tribology of magnetic recording systems - an overview," in *ASME/ASLE Tribology Conference*. vol. 3, 1986, pp. 1-7.

[201] M. Mehregany, S. D. Senturia, and J. H. Lang, "Measurement of Wear in Polysilicon Micromotors," *Ieee Transactions on Electron Devices,* vol. 39, pp. 1136-1143, May 1992.

[202] N. G. Milne, U. Beerschwinger, S. J. Yang, R. L. Reuben, D. Mathieson, H. Ziad, and S. Spirkovitch, "Finite-Element Analysis of Rotor Stability in an Axial-Drive Micromotor," *Journal of Micromechanics and Microengineering,* vol. 4, pp. 74-83, Jun 1994.

[203] U. Beerschwinger, T. Albrecht, D. Mathieson, R. L. Reuben, S. J. Yang, and M. Taghizadeh, "Wear at Microscopic Scales and Light Loads for Mems Applications," *Wear,* vol. 181, pp. 426-435, Feb 1995.

[204] W. Y. Yan, E. P. Busso, and N. P. O'Dowd, "A micromechanics investigation of sliding wear in coated components," *Proceedings of the Royal Society of London Series a-Mathematical Physical and Engineering Sciences,* vol. 456, pp. 2387-2407, Oct 8 2000.

[205] W. M. Zhang and G. A. Meng, "Friction and wear study of the hemispherical rotor bushing in a variable capacitance micromotor," *Microsystem Technologies-Micro-and Nanosystems-Information Storage and Processing Systems,* vol. 12, pp. 283-292, Mar 2006.

[206] D. Kim, D. Cao, M. D. Bryant, W. J. Meng, and F. F. Ling, "Tribological study of microbearings for MEMS applications," *Journal of Tribology-Transactions of the Asme,* vol. 127, pp. 537-547, Jul 2005.

[207] M. Zou, L. Cai, and H. Wang, "Adhesion and friction studies of a nano-textured surface produced by spin coating of colloidal silica nanoparticle solution," *Tribology Letters,* vol. 21, pp. 25-30, Jan 2006.

[208] A. A. Ayon, R. L. Bayt, and K. S. Breuer, "Deep reactive ion etching: a promising technology for micro- and nanosatellites," *Smart Materials & Structures,* vol. 10, pp. 1135-1144, Dec 2001.

[209] D. Nilsson, S. Jensen, and A. Menon, "Fabrication of silicon molds for polymer optics," *Journal of Micromechanics and Microengineering,* vol. 13, pp. S57-S61, Jul 2003.

[210] H. T. Pham, S. F. Yoon, K. H. Tan, and D. Boning, "Effects of nitrogen incorporation in InSb1-xNx grown using radio frequency plasma-assisted molecular beam epitaxy," *Applied Physics Letters,* vol. 90, pp. -, Feb 26 2007.

[211] Z. Burton and B. Bhushan, "Hydrophobicity, adhesion, and friction properties of nanopatterned polymers and scale dependence for micro- and nanoelectromechanical systems," *Nano Letters,* vol. 5, pp. 1607-1613, Aug 2005.

[212] B. Bhushan and Z. Burton, "Adhesion and friction properties of polymers in microfluidic devices," *Nanotechnology,* vol. 16, pp. 467-478, Apr 2005.

[213] E. J. Thoreson, J. Martin, and N. A. Burnham, "Recommendations for the use of an atomic force microscope as an in-fab stiction monitor," *Journal of Microelectromechanical Systems,* vol. 16, pp. 694-699, Jun 2007.

[214] U. Srinivasan, M. R. Houston, R. T. Howe, and R. Maboudian, "Alkyltrichlorosilane-based self-assembled monolayer films for stiction reduction in silicon micromachines," *Journal of Microelectromechanical Systems,* vol. 7, pp. 252-260, Jun 1998.

[215] R. L. Alley, G. J. Cuan, R. T. Howe, and K. Komvopoulos, "The effect of release-etch processing on surface microstructure stiction," in *IEEE Solid-State Sensor and Actuator Workshop*, 1992, pp. 202-207.

[216] C. C. Lee and W. Hsu, "Method on surface roughness modification to alleviate stiction of microstructures," *Journal of Vacuum Science & Technology B,* vol. 21, pp. 1505-1510, Jul-Aug 2003.

[217] A. Rugge, J. S. Becker, R. G. Gordon, and S. H. Tolbert, "Tungsten nitride inverse opals by atomic layer deposition," *Nano Letters,* vol. 3, pp. 1293-1297, Sep 2003.

[218] J. S. Becker, E. Kim, and R. G. Gordon, "Atomic layer deposition of insulating hafnium and zirconium nitrides," *Chemistry of Materials,* vol. 16, pp. 3497-3501, Sep 7 2004.

[219] J. Y. Chang, B. K. Min, J. Kim, S. J. Lee, and L. W. Lin, "Electrostatically actuated carbon nanowire nanotweezers," *Smart Materials & Structures,* vol. 18, pp. -, Jun 2009.

[220] B. Bhushan and X. D. Li, "Micromechanical and tribological characterization of doped single-crystal silicon and polysilicon films for microelectromechanical systems devices," *Journal of Materials Research,* vol. 12, pp. 54-63, Jan 1997.

[221] P. R. Krauss and S. Y. Chou, "Fabrication of planar quantum magnetic disk structure using electron beam lithography, reactive ion etching, and chemical mechanical polishing," *Journal of Vacuum Science & Technology B,* vol. 13, pp. 2850-2852, Nov-Dec 1995.

[222] L. J. Guo, P. R. Krauss, and S. Y. Chou, "Nanoscale silicon field effect transistors fabricated using imprint lithography," *Applied Physics Letters,* vol. 71, pp. 1881-1883, Sep 29 1997.

[223] H. S. Gill and M. R. Prausnitz, "Coated microneedles for transdermal delivery," *Journal of Controlled Release,* vol. 117, pp. 227-237, Feb 12 2007.

[224] D. H. Szarowski, M. D. Andersen, S. Retterer, A. J. Spence, M. Isaacson, H. G. Craighead, J. N. Turner, and W. Shain, "Brain responses to micro-machined silicon devices," *Brain Res,* vol. 983, pp. 23-35, Sep 5 2003.

[225] J. N. Turner, W. Shain, D. H. Szarowski, M. Andersen, S. Martins, M. Isaacson, and H. Craighead, "Cerebral astrocyte response to micromachined silicon implants," *Exp Neurol,* vol. 156, pp. 33-49, Mar 1999.

[226] M. R. Nuwer, D. A. Hovda, L. M. Schrader, and P. M. Vespa, "Routine and quantitative EEG in mild traumatic brain injury," *Clin Neurophysiol,* vol. 116, pp. 2001-25, Sep 2005.

[227] B. Brett, G. Krishnan, and D. S. Barth, "The effects of subcortical lesions on evoked potentials and spontaneous high frequency (gamma-band) oscillating potentials in rat auditory cortex," *Brain Res,* vol. 721, pp. 155-66, May 20 1996.

[228] M. S. Fee, "Active stabilization of electrodes for intracellular recording in awake behaving animals," *Neuron,* vol. 27, pp. 461-8, Sep 2000.

[229] H. Lee, R. V. Bellamkonda, W. Sun, and M. E. Levenston, "Biomechanical analysis of silicon microelectrode-induced strain in the brain," *J Neural Eng,* vol. 2, pp. 81-9, Dec 2005.

[230] A. C. Hoogerwerf and K. D. Wise, "A three-dimensional microelectrode array for chronic neural recording," *IEEE Trans Biomed Eng,* vol. 41, pp. 1136-46, Dec 1994.

[231] J. Subbaroyan, D. C. Martin, and D. R. Kipke, "A finite-element model of the mechanical effects of implantable microelectrodes in the cerebral cortex," *J Neural Eng,* vol. 2, pp. 103-13, Dec 2005.

[232] D. P. O'Brien, T. R. Nichols, and M. G. Allen, "Flexible microelectrode arrays with integrated insertion devices," in *Proceedings of the 14th IEEE International Conference on Micro Electro Mechanical Systems*, 2001, pp. 216-219.

[233] P. Rousche, D. Pellinen, D. J. Pivin, J. Williams, R. Vetter, and D. Kipke, "Flexible polyimide-based intracortical electrode arrays with bioactive capability," *IEEE Trans Biomed Eng,* vol. 48, pp. 361-71, 2001

[234] S. Takeuchi, D. Ziegler, Y. Yoshida, K. Mabuchi, and T. Suzuki, "Parylene flexible neural probes integrated with microfluidic channels," *Lab Chip,* vol. 5, pp. 519-23, May 2005.

[235] T. Suzuki, K. Mabuchi, and S. Takeuchi, "A 3D flexible parylene probe array for multichannel neural recording," in *Proceedings of the 1st International IEEE EMBS*, Capri Island, Italy, 2003, pp. 154-156.

[236] A. Ortega, K. Gall, D. Restrepo, and A. Sharp, "Mechanics of neuronal probe insertion at micrometer scales," in *Coleman Institute Conference*, 2006.

[237] A. Yoshino, D. A. Hovda, Y. Katayama, T. Kawamata, and D. P. Becker, "Hippocampal CA3 lesion prevents postconcussive metabolic dysfunction in CA1," *J Cereb Blood Flow Metab,* vol. 12, pp. 996-1006, Nov 1992.

[238] D. M. Geddes and R. S. Cargill, 2nd, "An in vitro model of neural trauma: device characterization and calcium response to mechanical stretch," *J Biomech Eng,* vol. 123, pp. 247-55., 2001.

[239] M. C. LaPlaca, V. M. Lee, and L. E. Thibault, "An in vitro model of traumatic neuronal injury: loading rate-dependent changes in acute cytosolic calcium and lactate dehydrogenase release," *J Neurotrauma,* vol. 14, pp. 355-68, 1997.

[240] H. S. Levin, "Head trauma," *Curr Opin Neurol,* vol. 6, pp. 841-6, Dec 1993.

[241] S. Miyazaki, Y. Katayama, B. G. Lyeth, L. W. Jenkins, D. S. DeWitt, S. J. Goldberg, P. G. Newlon, and R. L. Hayes, "Enduring suppression of hippocampal long-term potentiation following traumatic brain injury in rat," *Brain Res,* vol. 585, pp. 335-9, Jul 10 1992.

[242] L. L. Colgin, D. Kubota, Y. Jia, C. S. Rex, and G. Lynch, "Long-term potentiation is impaired in rat hippocampal slices that produce spontaneous sharp waves," *J Physiol,* vol. 558, pp. 953-61, Aug 1 2004.

[243] G. Golarai, A. C. Greenwood, D. M. Feeney, and J. A. Connor, "Physiological and structural evidence for hippocampal involvement in persistent seizure susceptibility after traumatic brain injury," *J Neurosci,* vol. 21, pp. 8523-37, Nov 1 2001.

[244] B. Kocsis, A. Bragin, and G. Buzsaki, "Interdependence of multiple theta generators in the hippocampus: a partial coherence analysis," *J Neurosci,* vol. 19, pp. 6200-12, Jul 15 1999.

[245] C. Wu, H. Shen, W. P. Luk, and L. Zhang, "A fundamental oscillatory state of isolated rodent hippocampus," *J Physiol,* vol. 540, pp. 509-27, Apr 15 2002.

[246] C. Wu, W. P. Luk, J. Gillis, F. Skinner, and L. Zhang, "Size does matter: generation of intrinsic network rhythms in thick mouse hippocampal slices," *J Neurophysiol,* vol. 93, pp. 2302-17, Apr 2005.

[247] H. Mao, L. Zhang, K. H. Yang, and A. I. King, "Application of a finite element model of the brain to study traumatic brain injury mechanisms in the rat," *Stapp Car Crash J,* vol. 50, pp. 583-600, Nov 2006.

[248] W. D. Dietrich, O. Alonso, R. Busto, and M. D. Ginsberg, "Widespread metabolic depression and reduced somatosensory circuit activation following traumatic brain injury in rats," *J Neurotrauma,* vol. 11, pp. 629-40, Dec 1994.

[249] M. C. Tate, D. A. Shear, S. W. Hoffman, D. G. Stein, and M. C. LaPlaca, "Biocompatibility of methylcellulose-based constructs designed for intracerebral gelation following experimental traumatic brain injury," *Biomaterials,* vol. 22, pp. 1113-1123, 2001.

[250] S. E. Stabenfeldt, A. J. Garcia, and M. C. LaPlaca, "Thermoreversible laminin-functionalized hydrogel for neural tissue engineering," *J Biomed Mater Res A,* vol. 77, pp. 718-25, Jun 15 2006.

[251] D. J. Simons, "Multi-whisker stimulation and its effects on vibrissa units in rat SmI barrel cortex," *Brain Res,* vol. 276, pp. 178-82, Oct 3 1983.

[252] D. J. Simons and G. E. Carvell, "Thalamocortical response transformation in the rat vibrissa/barrel system," *J Neurophysiol,* vol. 61, pp. 311-30, Feb 1989.

[253] J. Chmielowska, G. E. Carvell, and D. J. Simons, "Spatial organization of thalamocortical and corticothalamic projection systems in the rat SmI barrel cortex," *J Comp Neurol,* vol. 285, pp. 325-38, Jul 15 1989.

[254] K. Fujimoto, J. H. Kim, and S. Shiratori, "Characterization of Self-Assembled Flexible Multilayer Electrode Film by Roll-to-Roll Process," *Japanese Journal of Applied Physics,* vol. 47, pp. 8644-8647, Nov 2008.

[255] S. Myllymaa, K. Myllymaa, H. Korhonen, K. Djupsund, H. Tanila, and R. Lappalainen, "Fabricating and testing of flexible microelectrode arrays for neural recordings," *Tissue Engineering Part A,* vol. 14, pp. 735-736, May 2008.

[256] H. Y. Yu, L. S. Ai, M. Rouhanizadeh, D. Patel, E. S. Kim, and T. K. Hsiai, "Flexible Polymer Sensors for In Vivo Intravascular Shear Stress Analysis," *Journal of Microelectromechanical Systems,* vol. 17, pp. 1178-1186, Oct 2008.

# VITA

## BROCK A. WESTER

Brock A. Wester (M'02) was born in Okinawa, Japan, in 1981. He attended public schools in McLean, Virginia, received a B.S. degree with highest honors in computer engineering, a minor in Biomedical Engineering, and a Pre-Med from the Georgia Institute of Technology, Atlanta, Georgia, in 2004 before pursuing a doctorate in Biomedical Engineering from Georgia Institute of Technology and Emory University, Atlanta, GA.

During his graduate studies, Brock Wester was awarded and supported with the National Science Foundation (NSF) Integrative Graduate Education and Research Traineeship (IGERT) Fellowship, the NSF Student Teaching Enhancement Program (STEP) Fellowship, and the Gandy-Diaz Teaching Fellowship. For work in student government as president of the graduate students, senator, and coordinating officer, as well as leadership and mentorship roles in several on-campus organizations, Brock received the Georgia Tech Impact Scholarship in 2009.

Brock joined Matsushita Mobile Communications Division in 2000 as a computer engineering cooperative student employee. In 2007, he co-founded Teneo MicroInstruments, LLC. and held the position of Vice President of Research and Development. In 2010, he co-founded NanoGrip Technologies, Inc. from Teneo MicroInstruments and held the position of Chief Technology Officer and Board Member. Upon Completion of his doctorate degree, he will work as an engineer for John Hopkin's Applied Physics Lab in Columbia, MD.

His research interest areas include microfabrication, MEMS, packaging, prototyping, machining, software engineering, and biomedical engineering. While not in work, Brock enjoys large-scale home improvement projects, playing guitar, and traveling.

Mr. Wester is a member of the Institute of Electrical and Electronics Engineers, the Society for Neuroscience and the National Neurotrauma Society.